

Lecture Notes in Civil Engineering

Amit Prashant
Ajanta Sachan
Chandrakant S. Desai *Editors*

Advances in Computer Methods and Geomechanics

IACMAG Symposium 2019 Volume 2

 Springer

Lecture Notes in Civil Engineering

Volume 56

Series Editors

Marco di Prisco, Politecnico di Milano, Milano, Italy

Sheng-Hong Chen, School of Water Resources and Hydropower Engineering,
Wuhan University, Wuhan, China

Ioannis Vayas, Institute of Steel Structures, National Technical University of
Athens, Athens, Greece

Sanjay Kumar Shukla, School of Engineering, Edith Cowan University, Joondalup,
WA, Australia

Anuj Sharma, Iowa State University, Ames, IA, USA

Nagesh Kumar, Department of Civil Engineering, Indian Institute of Science
Bangalore, Bangalore, Karnataka, India

Chien Ming Wang, School of Civil Engineering, The University of Queensland,
Brisbane, QLD, Australia

Lecture Notes in Civil Engineering (LNCE) publishes the latest developments in Civil Engineering - quickly, informally and in top quality. Though original research reported in proceedings and post-proceedings represents the core of LNCE, edited volumes of exceptionally high quality and interest may also be considered for publication. Volumes published in LNCE embrace all aspects and subfields of, as well as new challenges in, Civil Engineering. Topics in the series include:

- Construction and Structural Mechanics
- Building Materials
- Concrete, Steel and Timber Structures
- Geotechnical Engineering
- Earthquake Engineering
- Coastal Engineering
- Ocean and Offshore Engineering; Ships and Floating Structures
- Hydraulics, Hydrology and Water Resources Engineering
- Environmental Engineering and Sustainability
- Structural Health and Monitoring
- Surveying and Geographical Information Systems
- Indoor Environments
- Transportation and Traffic
- Risk Analysis
- Safety and Security

To submit a proposal or request further information, please contact the appropriate Springer Editor:

- Mr. Pierpaolo Riva at pierpaolo.riva@springer.com (Europe and Americas);
- Ms. Swati Meherishi at swati.meherishi@springer.com (Asia - except China - and Australia/NZ);
- Ms. Li Shen at li.shen@springer.com (China).

Indexed by Scopus

More information about this series at <http://www.springer.com/series/15087>

Amit Prashant · Ajanta Sachan ·
Chandrakant S. Desai
Editors

Advances in Computer Methods and Geomechanics

IACMAG Symposium 2019 Volume 2

 Springer

Editors

Amit Prashant
Indian Institute of Technology Gandhinagar
Gandhinagar, Gujarat, India

Ajanta Sachan
Indian Institute of Technology Gandhinagar
Gandhinagar, Gujarat, India

Chandrakant S. Desai
University of Arizona
Tucson, AZ, USA

ISSN 2366-2557 ISSN 2366-2565 (electronic)
Lecture Notes in Civil Engineering
ISBN 978-981-15-0889-9 ISBN 978-981-15-0890-5 (eBook)
<https://doi.org/10.1007/978-981-15-0890-5>

© Springer Nature Singapore Pte Ltd. 2020

This work is subject to copyright. All rights are reserved by the Publisher, whether the whole or part of the material is concerned, specifically the rights of translation, reprinting, reuse of illustrations, recitation, broadcasting, reproduction on microfilms or in any other physical way, and transmission or information storage and retrieval, electronic adaptation, computer software, or by similar or dissimilar methodology now known or hereafter developed.

The use of general descriptive names, registered names, trademarks, service marks, etc. in this publication does not imply, even in the absence of a specific statement, that such names are exempt from the relevant protective laws and regulations and therefore free for general use.

The publisher, the authors and the editors are safe to assume that the advice and information in this book are believed to be true and accurate at the date of publication. Neither the publisher nor the authors or the editors give a warranty, expressed or implied, with respect to the material contained herein or for any errors or omissions that may have been made. The publisher remains neutral with regard to jurisdictional claims in published maps and institutional affiliations.

This Springer imprint is published by the registered company Springer Nature Singapore Pte Ltd. The registered company address is: 152 Beach Road, #21-01/04 Gateway East, Singapore 189721, Singapore

Preface

The Symposium of the International Association for Computer Methods and Advances in Geomechanics (IACMAG) was held at the Indian Institute of Technology Gandhinagar, Gujarat, India, during the period 5–7 March 2019. Computer applications of geomechanics have been gaining much popularity from the early days of the International Conference on Numerical Methods in Geomechanics at Vicksburg, in 1972, Blacksburg, in 1976, and Innsbruck, Austria, in 1988. It was in that very context the IACMAG was established and it has been growing ever since with various stakeholders contributing significantly from different nations across the world. IACMAG aims at fostering multidisciplinary research and ideas pertaining to geomechanics with particular emphasis on integrating both the practical and the fundamental aspects. The field of geomechanics has evolved with time, and in this regard, IACMAG takes into account the need for judicious simplification of fundamental aspects of geomechanics with proper amalgamation of theory and experimentation in order that they find their use in practical problems and challenges faced in the industry today.

IACMAG has grown steadfastly in its scope and size encompassing various aspects of constitutive modelling of geomaterials, computational methods and emerging fields of bio-cementation as well as treatment of geomaterials. The Symposium at IIT Gandhinagar aimed at providing a platform for exchanging ideas and recent developments as well as for discussing future visions related to the field of geomechanics and geotechnical engineering. A pre-symposium workshop on “Behaviour of Civil Engineering Materials” was also held in this regard on 4 March 2019 with its focus on the material models commonly used in analysis and design of structures. It also included a hands-on session for implementing simple computer applications of geotechnical engineering for industry and the academia. The IACMAG Symposium 2019 included 11 keynote/invited speakers of repute from different backgrounds of the geotechnical engineering community. It involved four parallel sessions with main themes of the symposium being primarily focussed on (i) geomaterial behaviour and material modelling, including multi-scale modelling, micro-structural instabilities, liquefaction, chemical and bio-effects in geomaterials, field/laboratory testing; (ii) earthquake engineering, including dynamics

of geomaterials, earth embankments, and dams; (iii) geosynthetics and ground improvement with thrust areas on bio-treatment, soft and expansive clays; and (iv) analysis and design of structures, including bridges and foundations as well as soil–structure interaction problems.

We thank all the authors for their contribution to the IACMAG Symposium 2019 that has resulted in the proceedings which is being published in two volumes. IACMAG follows its long-standing tradition in selecting and reviewing these papers with great rigour, and we hope that the proceedings will provide a glimpse of the state-of-the-art practices followed in different fields related to geomechanics and its allied branches. We would also like to express our sincerest of appreciation to the reviewers of the papers and to various technical and financial sponsors for making this event a grand success.

Gandhinagar, India
Gandhinagar, India
Tuscon, AZ, USA

Amit Prashant
Ajanta Sachan
Chandrakant S. Desai

Contents

Exfoliation and Extraction of Nanoclay from Montmorillonite Mineral Rich Bentonite Soil	1
Naman Kantesaria and Sudhanshu Sharma	
Uncertainties in Water Retention Curve of Bentonite	13
A. Prakash, B. Hazra and S. Sreedeeep	
Comparative Study of Backfill Retaining Systems for Onshore RCC Pile Berth Under Different Site Conditions	25
Soumyakanti Dhavala, Dhara Shah and Sanjeev Kapasi	
The Effect of Saline Fluid on Hydraulic Properties of Clays	41
Koteswaraarao Jadda and Ramakrishna Bag	
Influence of Shape of Cross Section on the Load–Settlement Behaviour of Strip Footings	55
J. Jayamohan, P. Sajith, Shilpa Vijayan, Anusha Nair, S. Chandni and Akhila Vijayan	
Effect of Biopolymers on Soil Strengthening	65
Lekshmi P. Nair and K. Kannan	
Examination of Present Subsurface Investigation Data for Valuation of Liquefaction Potential for Ahmadabad City by Means of SPT-N Value	73
Manali S. Patel and Tejas P. Thaker	
Improving “Shrinkage-Swelling” Response of Expansive Soil Using Bio-calcite and Exopolysaccharide Produced by Bacillus sp.	83
V. Guru Krishna Kumar, Kaling Taki, Sharad Gupta and Ajanta Sachan	
Mitigation of Soil Liquefaction Under Strip Footing by Densification: A Numerical Investigation	99
N. Dinesh, Subhadeep Banerjee and K. Rajagopal	

Effect of Strain Rate on Strength Behaviour of Cohesionless Soil	109
Amit Singh and Manash Chakraborty	
Compaction and Strength Characteristics of Bentonite Rock-Quarry Dust Mixtures	121
Hemanga Das, Tinku Kalita and Malaya Chetia	
Synthesis of Bentonite Clay-Based Geopolymer and Its Application in the Treatment of Expansive Soil	133
Kaling Taki and Sudhanshu Sharma	
A Micromechanical Study on the Effect of Initial Static Shear Stress on Cyclic Shearing Response	145
R. Kolapalli, M. M. Rahman, M. R. Karim and H. B. K. Nguyen	
Study on the Behaviour of NATM Tunnel Face During Seismic Activities	157
R. B. Jishnu, Ramanathan Ayothiraman and Raghvendra Sahu	
A PSO-Based Estimation of Dynamic Earth Pressure Coefficients of a Rigid Retaining Wall	169
Swarnima Subhadarsini, Sushree Paritweshha Pradhan, Jayanti Munda and Pradip Kumar Pradhan	
Analytical Study on the Influence of Rigidity of Foundation and Modulus of Subgrade Reaction on Behaviour of Raft Foundation	181
Sujay Teli, Palak Kundhani, Virag Choksi, Pritam Sinha and Kannan K. R. Iyer	
Numerical Study on the Undrained Response of Silty Sands Under Static Triaxial Loading	195
M. Akhila, K. Rangaswamy and N. Sankar	
Seismic Hazard Estimation for Southwest India	207
C. Shreyasvi and Katta Venkataramana	
Assessment of Bond Strength on Geosynthetic Interlayered Asphalt Overlays Using FEM	221
S. Shiyamalaa and K. Rajagopal	
Influence of Variabilities of Input Parameters on Seismic Site Response Analysis	233
C. Shreyasvi, N. Badira Rahmath and Katta Venkataramana	
3D-Continuum Numerical Analysis of Offshore Driven Pipe Pile Using Finite Difference Method	245
D. S. Murthy, Ramesh Gedela, Rajagopal Karpurapu and R. G. Robinson	

A Study on the Seismic Behaviour of Embankments with Pile Supports and Basal Geogrid	257
Radhika M. Patel, B. R. Jayalekshmi and R. Shivashankar	
Parametric Investigation of Bridge Piers Reinforced with Shape-Memory Alloys in Plastic Hinge Regions	269
Kanan Thakkar and Anant Parghi	
Response of Single Pile to Lateral Load with Constant Uplift	283
Poulami Ghosh, Sibapriya Mukherjee, Narayan Roy and Subhadeep Banerjee	
Correlation Between Shear Strength of Soils and Water Content Ratio as a Substitute for Liquidity Index	299
Harshdeep Singh and Ashok Kumar Gupta	
Numerical Study of Embankments Supported by Ordinary and Encased Granular Columns in Peat	307
J. Jayapal and K. Rajagopal	
Experimental Investigation for Damage Evaluation of Bridges Using Piezo-Transducers	319
Umesh T. Jagadale, Rutuja D. Kharade, Chittaranjan B. Nayak and Wasudeo D. Deulkar	
Effect of Magnesium Incorporation in Enzyme-Induced Carbonate Precipitation (EICP) to Improve Shear Strength of Soil	333
Alok Chandra and K. Ravi	
Performance of Structural Concrete Using Recycled Plastics as Coarse Aggregate	347
P. R. Admille and P. D. Nemade	
Effect of Ground Water Level and Seismic Intensity on Failure of a Slope	361
Sreyashi Dutta, R. K. Dubey, Sibapriya Mukherjee and Narayan Roy	
Stability of Two-Layered Earth Slope Under Varying Rainfall Intensity	373
Dooradarshi Chatterjee and A. Murali Krishna	
Studies on Embankment Foundations with Soft Soil Reinforced with Prestressed Geosynthetic Encapsulated in Thin Layer of Granular Soil	385
R. Anciya Fazal, J. Jayamohan and S. R. Soorya	
Influence of Reinforcement Pattern on the Performance of Geotextile-Reinforced Slopes	397
Veerabhadra M. Rotte and Hardik V. Gajjar	

Use of Polypropylene Fibres for Cohesive Soil Stabilization	409
Trudeep N. Dave, Dhavalkumar Patel, Gafur Saiyad and Nirmal Patolia	
Analytical Investigation on High and Low Seismic Response of Zero Liquid Discharge Steel Structure	419
B. Nambiyanna, Mohammed Younus Salman and R. Prabhakara	
Chemical Compatibility of Fly Ash–Bentonite Based Hydraulic Barrier	429
G. Suneel Kumar, Kami Venkata Balaiah and Rabi Narayan Behera	
Retrofitting of Beam–Column Joint Under Seismic Excitation	441
Marimuthu Sumathi and Sivasankarapillai Greeshma	
Study on Effect of Particle Shape on Interlocking	455
Ashwani Kumar Bindal, Arghya Das and Animesh Das	
Correlation of Shear Wave Velocity with Standard Penetration Resistance Value for Allahabad City	467
Manjari Singh, S. K. Duggal, Kumar Pallav and Keshav Kr. Sharma	
Experimental Studies on Controlled Low Strength Materials Using Black Cotton Soils and Comparison of Results with Taguchi Model	483
B. N. Skanda Kumar, M. P. Naveena, Anil Kumar, A. Shashishankar and S. K. Darshan	
Strength Improvement of Locally Available Sand Using Enzymatically-Induced Calcite Precipitation	495
P. B. Kulkarni and P. D. Nemade	
Bio-treatment of Fly Ash	505
Archika Yadav, K. Vineeth Reddy, Md. Muzzaffar Khan, G. Kalyan Kumar and Amitava Bandhu	
A Review of Expansive Soil—Effects and Mitigation Techniques	519
Trudeep N. Dave and Arshad K. Siddiqui	
Vibration Control of Flexible Retention Systems	529
Nisha Kumari and Ashutosh Trivedi	
Sequential Drawdown and Rainwater Infiltration Based Stability Assessment of Earthen Dams	541
Priyanka Talukdar and Arindam Dey	
Water-Soluble Super Absorbent Polymer as Self-curing Agents in High-Strength Cement Concrete Mixes	553
N. T. Suryawanshi and S. B. Thakare	

Pounding Probability of Three-Span Simply Supported Bridge Subjected to Near-Field and Far-Field Ground Motions 565
 Lopamudra Mohanty, Rahul Das and Goutam Mondal

Review of Seismic Performances of Partial Infill RC Frames..... 577
 Narayan Muduli, Suresh R. Dash and Goutam Mondal

An Artificial Intelligence Approach for Modeling Shear Modulus and Damping Ratio of Tire Derived Geomaterials 591
 Siavash Manafi Khajeh Pasha, Hemanta Hazarika and Norimasa Yoshimoto

Rutting Performance of PPA-Modified Binders Using Multiple Stress Creep and Recovery (MSCR) Test..... 607
 Shivani Rani, Rouzbeh Ghabchi, Musharraf Zaman and Syed Ashik Ali

2D Coupled Poro-Elastic Analysis for Dynamic Behaviour of CPRF 617
 Patchamatla J. RamaRaju, Pavan K. Emani and Shashank Kothari

Performance-Based Evaluation of Building With and Without Soil Flexibility 625
 S. Deepa, I. R. Mithanthaya and S. V. Venkatesh

Application of TS Method in Dynamic UH Model 637
 Zheng Wan, Chenchen Song and Wensheng Gao

Effect of Lime and Cement on Strength and Volume Change Behavior of Black Cotton Soil 651
 Majid Hussain

Strength and Deformation Characteristics of Jointed Block Rock Matrix Using Triaxial System 665
 Manish Shah and Arpit Patel

Fundamental Time Period of Vibration in Seismic Analysis..... 679
 Prabhat K. Soni, Prakash Sangamnerkar and S. K. Dubey

Case Studies on Ground Improvement for Heavy Infrastructure on Soft Soil Using Basal Reinforcement 691
 Vikalp Kamal, Minimol Korulla and P. S. Meenu

Effect of Fascia Gravity on the Design of Reinforced Soil Walls 709
 Homit Singh Pal and Mohan Krishna Kolli

Geotechnical and Electrical Resistivity Properties of Gypsum Rich Sands 717
 Raghava A. Bhamidipati and Michael E. Kalinski

About the Editors

Amit Prashant is a Professor in Indian Institute of Technology Gandhinagar, India. After his PhD and post-doctoral work in the University of Tennessee at Knoxville (USA), he went on to work as an Assistant Professor in IIT Kanpur from 2005 to 2010, before joining IIT Gandhinagar in 2010. His research interests include constitutive modeling for granular materials, numerical modeling of geotechnical structures, and earthquake geotechnical engineering. In 2005, he received the Young Researcher Fellowship Award from Massachusetts Institute of Technology, Cambridge (USA) during the 3rd M.I.T. Conference on Computational Fluid and Solid Mechanics. He has also been awarded the Excellence Award in Institution Building and Outreach in 2013 and 2015 respectively. Prof Prashant has published more than 60 research articles in reputed journals and conferences, and organizes activities to encourage student initiatives and increase industry-academia interaction.

Ajanta Sachan is an Associate Professor in Indian Institute of Technology Gandhinagar, India. After her B.E in Civil Engineering, she worked in WAPCOS Limited and IIT Kanpur, India before pursuing her PhD in University of Tennessee at Knoxville, USA. Her research interests include material characterization, studying shear strength and compressibility behavior in soils, etc. Dr Sachan serves as a reviewer in 7 journals and is a member of American Society of Civil Engineers (ASCE), USA, Earthquake Engineering Research Institute (EERI), USA and the National Information Centre for Earthquake Engineering (NICEE), India. She has published more than 50 research papers, and has served in various administrative capacities.

Chandrakant S. Desai is a Regents' Professor (Emeritus) in the Department of Civil and Architectural Engineering and Mechanics at the University of Arizona, Tucson, USA. After completing his MS and PhD from Rice University Houston and University of Texas, Austin in 1966 and 1968 respectively, he joined the U.S. Army Corps of Engineers' Waterways Experiment Station, where he worked till 1974. Subsequently, he joined The University of Arizona, where he has served on various capacities. Prof Desai has authored or edited 23 books and over 345

research papers over the course of his career, which has involved the development and application of constitutive laws with design and fabrication of new and innovative test devices, and of computer methods for solution of a wide range of problems in civil, mechanical and electronics engineering. He has been the founding president of the IACMAG and founding Editor-in-Chief for two international journals in Geomechanics. He has received many awards and distinctions, and is a member of a number of technical societies including an elected Distinguished Member of the American Society of Civil Engineers, USA.

Exfoliation and Extraction of Nanoclay from Montmorillonite Mineral Rich Bentonite Soil



Naman Kantesaria and Sudhanshu Sharma

Abstract Nanoclay is a fine-grained crystalline material, which contains a mineral of alumina and silica with high aspect ratio and at least one dimension of a particle in the nanometer ($1 \text{ nm} = 10^{-9} \text{ m}$) range. Nanoclays have various applications in many fields, including problematic soil treatment, pharmacy, medicine, catalysis, cosmetics, food packaging, and textile industry. The raw cost of Nanoclay is high due to its costly manufacturing process that involves heavy chemicals and machinery. Therefore, the aim of the current research is to extract Nanoclay from the montmorillonite-rich commercially available Bentonite soil using a cost-effective method. The process involves the exfoliation of the nanosized lamina from the stacked 2:1 tetrahedral–octahedral laminae of montmorillonite minerals with the help of surfactant. Three different types of surfactants (cationic, nonionic, and anionic) were chosen in the current study to evaluate their effect on the exfoliation process of highly expansive Bentonite soil. A series of chemical processes including solution preparation, sonication, centrifugation, and drying were performed using selected proportion of surfactant and Bentonite soil mixture. Physical and chemical properties of the end product were investigated by performing X-ray diffraction (XRD) technique and scanning electron microscope (SEM) image analysis. Nanoclay of the particle size range of 10–15 nm is successfully exfoliated from montmorillonite sheet structure by the chemical interaction between cationic surfactant and Bentonite soil. Nonionic surfactant was observed to be just intercalated between the sheets of montmorillonite mineral with additional growth of small needle-like structures. Anionic surfactant has no prominent effect on Bentonite soil.

Keywords Nanoclay · Exfoliation · Montmorillonite · Bentonite soil · Surfactant · SEM · XRD

N. Kantesaria (✉)

Civil Engineering, Indian Institute of Technology Gandhinagar, Gandhinagar, India

e-mail: naman.kantesaria@iitgn.ac.in

S. Sharma

Chemistry Department, Indian Institute of Technology Gandhinagar, Gandhinagar, India

e-mail: ssharma@iitgn.ac.in

© Springer Nature Singapore Pte Ltd. 2020

A. Prashant et al. (eds.), *Advances in Computer Methods and Geomechanics*, Lecture Notes in Civil Engineering 56, https://doi.org/10.1007/978-981-15-0890-5_1

1 Introduction

Bentonite soil is a high plasticity clayey soil made from the very high amount of montmorillonite $((\text{Na}, \text{Ca})_{0.33}(\text{Al}, \text{Mg})_2(\text{Si}_4\text{O}_{10})(\text{OH})_2 \cdot n\text{H}_2\text{O})$ minerals. Due to the presence of these minerals, the expansiveness of this soil is very high. Montmorillonite minerals are alumino silicates generated from the combination of sheet-like structures attached together by weak Van der Waals forces. Each sheet of this structure is a 2:1 structure in which, two tetrahedral silica $(\text{SiO}_4)^{4-}$ are connected to one octahedral alumina $[\text{AlO}_3(\text{OH})_3]_6$ sheet. The thickness of this single sheet can be 1 nm. When these single sheets are combined together by Van der Waals forces, their thickness increases to a few hundreds of nanometers. In nature, montmorillonite mineral is present in the stacked form only. Hence, the aim of the current research is to break this stacked structure and separate the individual 2:1 sheet of montmorillonite mineral termed as Nanoclay.

Nanoclays are fine-grained crystalline materials where at least one dimension is in nanoscale [6]. They are synthesized from artificial or natural bulk clay fraction by various procedures such as centrifugation, ultracentrifugation, and freezing–drying [1, 5, 6, 8]. All these processes required high-end equipment and costly raw products. Nanoclays have various applications in many fields, including problematic soil treatment, pharmacy, medicine, catalysis, cosmetics, food packaging, and textile industry [2, 5, 7, 8]. Usefulness of Nanoclays in various fields is attributed to the amenability of Nanoclays for modification, and the dispersion characteristics of clay layers into individual lamellae [7]. Amenability of Nanoclays for modification is due to the interchangeability of the desired cations or other molecules on their negatively charged surface [1, 5, 7, 8]. Simple procedures are required to interchange the desired ions and modify the surface chemistry of Nanoclays. The biggest advantage of Nanoclays are the high specific surface area (SSA) and that increases scope for altering the properties of clays like their polarity, zeta potential, acidity, cation exchange capacity (CEC), pore size, and many others that govern their performances in various applications [1, 5, 6, 8].

The current study presents a brief insight of economical extraction procedure of Nanoclay from commercially available Bentonite soil. Effect of different types of surfactant on the chemical and physical properties of Bentonite soil is determined. An attempt was made to give chemical hypothesis regarding surfactant and Bentonite reaction in the extraction procedure of Nanoclay. X-ray diffraction technique (XRD) and scanning electron microscopy (SEM) were used to determine chemical and physical properties of various reaction products.

2 Experimental Program

2.1 Material Properties

2.1.1 Bentonite Soil

The soil used for the current study was the commercially available Bentonite soil supplied by local suppliers. Bentonite soil was chosen because of the presence of high amount of montmorillonite mineral in it. The soil is classified as clay of high plasticity (CH) type of soil according to Indian Standard Soil Classification. Differential free swell index (DFSI) value of Bentonite soil is 662%, which indicates the soil is highly expansive in nature (IS: 2911 Part III-1980). Basic geotechnical properties of Bentonite soil including liquid limit, plastic limit, shrinkage limit, and specific gravity are mentioned in Table 1.

2.1.2 Surfactant

Surfactants are defined as the compounds which reduced the surface tension between liquid and solid, between two liquids or between liquid and gas. Surfactants may act as wetting agents, detergents, emulsifiers, dispersants, and foaming agents. In the present study, surfactants are chosen to perform the function of dispersing agents. They consist of mainly two part structures: a hydrophilic head and a hydrophobic tail. Surfactants are classified into four main groups based on the ions present into their hydrophilic tail as described in Fig. 1. In the current study, the surfactants chosen were Cetrimonium Bromide (CTAB), Polyethylene glycol (PEG), and Trisodium citrate as the cationic, nonionic, and anionic surfactants, respectively. The chemical formulas of these surfactants are shown in Table 2.

2.2 Testing Procedure

The exfoliation and extraction procedure of Bentonite soil was done by performing a series of chemical procedures. The total testing procedure is divided into four major portions and they are explained as follows.

Table 1 Geotechnical properties of Bentonite soil

Specific gravity G_s	Liquid limit, w_L (%)	Plastic limit, w_P (%)	Shrinkage limit, w_S (%)	Plasticity index, I_p (%)	DFSI (%)
2.8	609	51	6	558	662

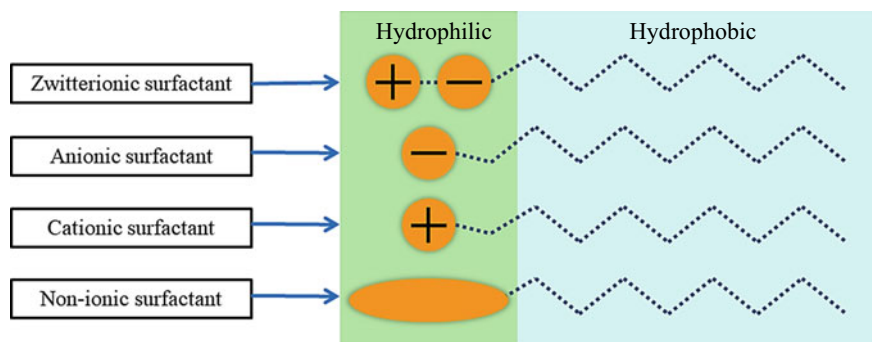


Fig. 1 Types of surfactants

Table 2 Types of surfactant used and sample prepared

Sample number	Surfactant used	Type of surfactant group	Chemical composition
S-0	Sonication of pure Bentonite (without the addition of any surfactant)		
S-1	Cetrimonium bromide (CTAB)	Cationic	$C_{19}H_{42}BrN$
S-2	Polyethylene glycol (PEG)	Nonionic	$C_{2n}H_{4n+2}O_{n+1}$
S-3	Trisodium citrate	Anionic	$Na_3C_6H_5O_7$

2.2.1 Solution Preparation

The molar solution of the chosen surfactant is prepared in 100 ml of distilled water. To dissolve it properly into the water, the sonication was done for 10 min. Five gram of 75-micron sieve passed Bentonite soil is then mixed with a prepared solution and stirred well for proper mixing. This procedure is shown in Fig. 2. Four different samples were prepared and details of these samples with the chosen surfactant are provided in Table 2. For S-0 sample, pure Bentonite soil is sonicated for 90 min without any addition of surfactant.

2.2.2 Sonication

The prepared mixture was sonicated for 90 min to break down the structure of the soil and mixed uniformly with the surfactant. In this procedure, ultrasonic waves were applied to the mixture through the sonicator. This will impart extra energy to break the structure.

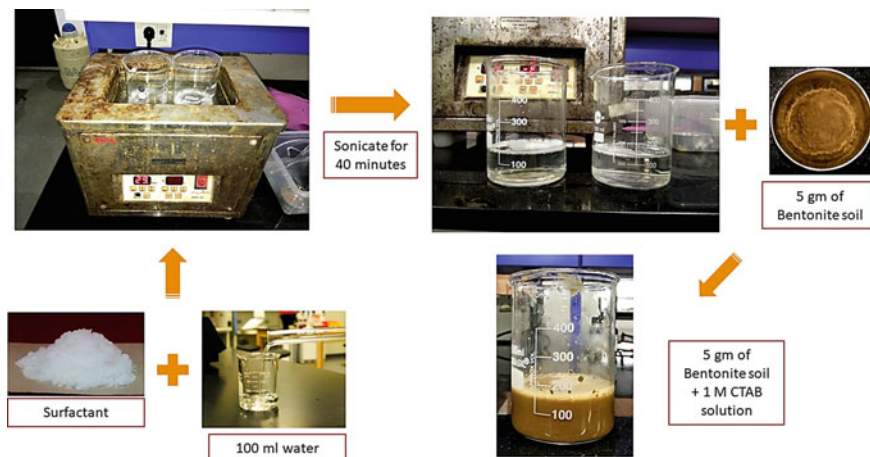


Fig. 2 Solution preparation stage

2.2.3 Washing

To remove the surfactant from the mixture, washing was done with the help of centrifuge. Initially, the mixture was centrifuged at 8000 RPM for 20 min. Settled parts in the tube were extracted and again mixed with water. This mixture was again centrifuged at the same RPM and for the same time duration. This procedure was repeated twice to remove most part of the surfactant from the mixture.

2.2.4 Drying

The settled samples were collected in the container and put inside the oven for drying at 105 °C for at least 24 h. After drying, it was crushed into fine powder for further analysis. The detailed procedure of stage 2–4 is shown in Fig. 3.

3 Results

X-ray diffraction (XRD) analysis and scanning electron microscope (SEM) analysis were performed to evaluate the results of the chemical process. Both the analysis was performed on pure Bentonite soil and processed soil. To characterize the modification of the lattice structure quantitatively, the XRD analysis was performed. SEM analyses were performed to identify the changes visually by seeing the modified clay structure through a microscope with high zoom-in capacity.

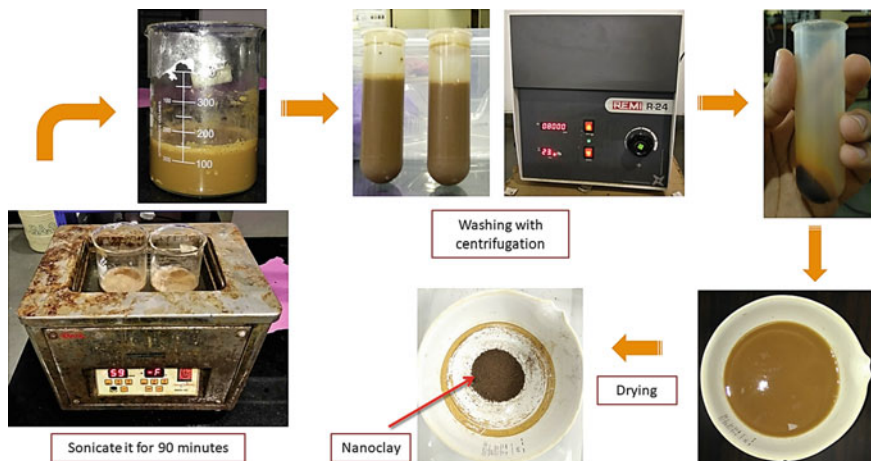


Fig. 3 Sonication, washing, and drying stage

3.1 X-Ray Diffraction (XRD) Analysis

Pure Bentonite soil and S-0–S-3 samples were analyzed in the powder form on Bruker AXS D8 Discover XRD equipment. The plot of the intensity versus 2θ (angle) were plotted for both the samples. It is shown in Fig. 4. The intensity is plotted in terms of arbitrary units (a.u.) to compare the results of different samples on a single curve. In Fig. 4, the values of the intensity have no significance, hence these values were removed. The 2θ values were limited to 25° as the montmorillonite mineral presence is majorly indicated until this value only. As seen from the curve, there was no change observed for the XRD patterns of pure Bentonite soil and samples S-0, S-2, and S-3. This indicates no change in the crystal lattice structure by interaction with anionic and nonionic surfactant. Widening of the montmorillonite mineral peak (0 0 1) is observed for S-1 sample when pure Bentonite soil was processed with Cationic surfactant (CTAB). This is the indication of a particular mineral's particle size reduction. The reduction in the particle size can be quantitatively determined by Scherrer's equation. Scherrer's equation can give lower bound of reduced particle size. It is expressed as follows:

$$d_c = \frac{k * \lambda}{\beta * \cos \theta}$$

where d_c is the averaged dimension of crystallites; K is the Scherrer constant, a somewhat arbitrary value that falls in the range 0.87–1.0 (it is usually assumed to be 1); λ is the wavelength of the X-ray; and β is the integral breadth of a reflection (in radians 2θ) located at 2θ . For S-1 sample's XRD data, lower bound of particle size determined is $d_c = 3.84$ nm. It is the indication of particle size reduction from pure Bentonite soil.

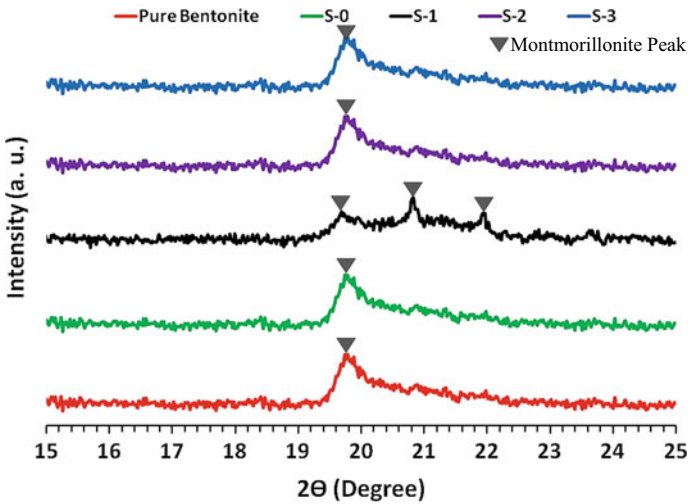


Fig. 4 XRD result: intensity versus 2θ curve for all the samples

3.2 Scanning Electron Microscope (SEM) Analysis

SEM image analysis was done on the powder specimens of pure Bentonite soil and S-0–S-3 specimens. This analysis was done to characterize and identify the changes in the sheet-like structure of montmorillonite mineral with the addition of different surfactants. SEM images of 1 μm –100 nm scale are presented for different samples as follows:

- (a) Pure Bentonite: Sheet-like densely packed structure is observed in the SEM images of pure Bentonite soil. It is the original stacked form of montmorillonite mineral as shown in Fig. 5a.
- (b) S-0 Sample: Due to sonication, very small amount of exfoliation is achieved. But, the effect of sonication alone is not sufficient to exfoliate Bentonite to nanoscale. The observed small fragments in the images were generated due to the breakage of mineral structure from sonication. It is shown in Fig. 5b.
- (c) S-1 Sample: Successfully exfoliated structure of montmorillonite mineral is observed in the SEM images of CTAB surfactant processed Bentonite. Individual sheets of montmorillonite mineral in the scale of nanometer were observed to be separated from the stacked structure. One dimension of Nanoclay is observed in the order of 10–15 nm as shown in Fig. 5c.
- (d) S-2 Sample: Some extent of exfoliation is observed with the intrusion of PEG into the Bentonite soil. But it is not prominently in the nanometre size range. PEG penetrates within the soil mass as observed in the SEM images. The square-shaped particles observed inside the clay sheets were particles of PEG. Small, unidentifiable needle-type structures were observed to grow within the grooves of the particles. It is shown in Fig. 5d.

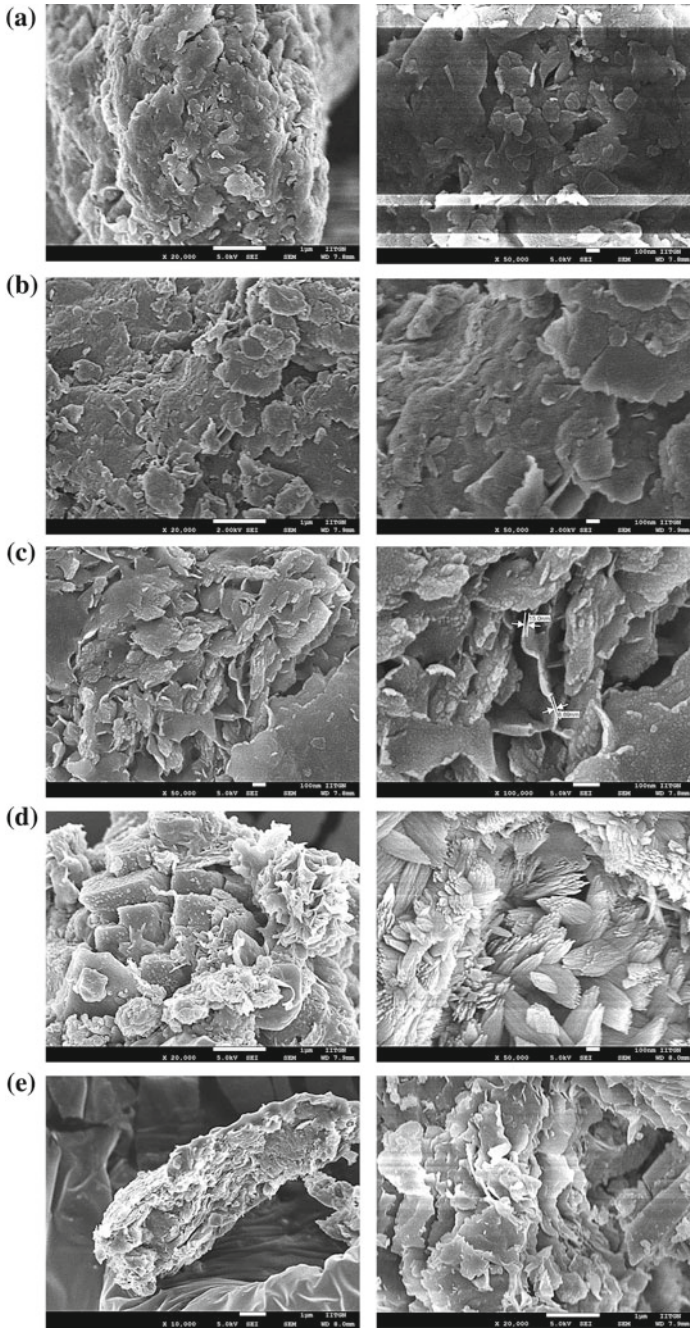


Fig. 5 SEM images of a pure Bentonite, b S-0, c S-1, d S-2, e S-3 samples

- (e) S-3 Sample: No effect of Trisodium Citrate on the layers of Bentonite was observed. All the layers were in the same stacked position as shown in Fig. 5e. The side view of a staked particle is shown in Fig. 5e, whereas the top view of the staked particles were presented for pure Bentonite and S-0 samples. They resembled the same original microstructure of the montmorillonite mineral with different orientations of the particle.

4 Theory

The montmorillonite clay minerals are negatively charged particles that create high affinity of these minerals toward cations and bipolar water molecules. The aim of the current study is to exfoliate these sheets-like structures, and water molecules alone cannot exfoliate the complete structure. Hence, the additional ions are required to assist the process of exfoliation. Due to the negative charges on the clay surface, the best-suited surfactants are considered as cationic surfactants. Though, the other types of surfactants may have some different effects on the montmorillonite mineral and to study that, three different types of surfactants were chosen. The modification of the structure due to the chemical process is explained as follows.

4.1 Effect of Cationic Surfactant

Due to isomorphous substitution within the silica tetrahedral and alumina octahedral sheets of the montmorillonite mineral, the net negative charge is generated on the surface of the clay particles. Hence, when a cationic surfactant is added to the solution, the cations in the hydrophilic head are attached with the negatively charged clay surface [4–6, 8]. Due to this process, all the hydrophilic tails come closer to each other. These tails repeal each other and the distance between the two montmorillonite mineral units increases. This process is still not sufficient to break the structure completely. Hence, sonication is performed and the ultrasound waves during sonication impart additional energy to break down the structure. To remove the attached cationic surfactant from the surface of the clay particles, washing process is done. Nanoclay is determined after drying and crushing of this final product. As there were no distinct peaks observed for the CTAB surfactant in the XRD analysis, it was confirmed that almost all the hydrophilic heads were removed through the process of washing. Apart from that, no foreign material traces were observed in the SEM images. The schematic representation of this process is shown in Fig. 6.

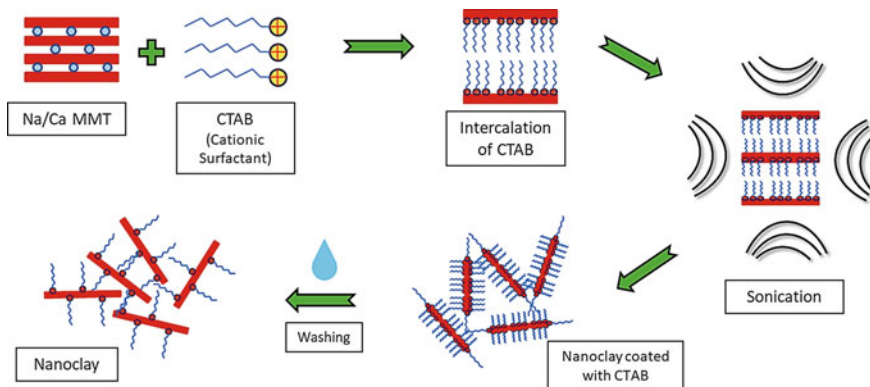


Fig. 6 Effect of cationic surfactant

4.2 Effect of Nonionic Surfactant

When nonionic surfactant is added to the solution, the oxygen in the nonionic surfactant may build the covalent bond with the negatively charged clay particles [2, 3, 9]. Their reaction with the mineral can be either in the form of microcomposite, intercalation, or exfoliation. In the present study, intercalation of PEG into the clay layers is observed from the SEM images of S-2. The possible other modes of interaction of nonionic surfactants are presented in Fig. 7. There was no remarkable effect of the anionic surfactant that was observed in the current study which further supports the given hypothesis. The reaction of the anionic surfactant with the montmorillonite mineral could have been same as the “Microcomposite” structure shown in Fig. 7.

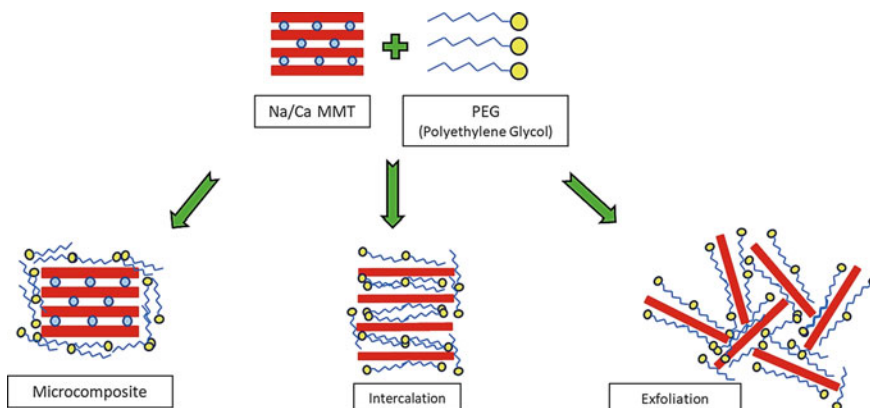


Fig. 7 Effect of nonionic surfactant

5 Conclusions

The current study examined the effect of various surfactants on the exfoliation and extraction procedure of Nanoclay from commercially available Bentonite soil. The experiments were conducted on the raw and processed Bentonite and results were analyzed in terms of X-ray diffraction (XRD) and scanning electron microscope (SEM) responses. Key observations are summarized as follows:

- With the use of cationic surfactant (CTAB), Nanoclay of the particle size range of 10–15 nm is extracted from the commercially available Bentonite soil. Successful intercalation of this surfactant and exfoliation of montmorillonite mineral was observed from both the XRD and SEM analyses.
- Effect of nonionic surfactant (PEG) on the Bentonite soil is not clearly visible in the SEM images and XRD pattern. Intercalation of PEG due to the covalent bond of oxygen with clay particles was observed with the growth of additional unidentified needle-like structures.
- No prominent exfoliations of sheets were observed in pure sonicated Bentonite and treated soil with the anionic surfactant (Trisodium Citrate).
- Less-expensive laboratory method of Nanoclay extraction from easily available Bentonite soil is successfully developed.

Acknowledgements Financial support from IIT Gandhinagar is gratefully acknowledged. The authors are indebted to Mr. Kaling Taki for providing the Bentonite soil basic property data. Any opinions, findings, and conclusions or recommendations expressed in this material are those of authors and do not necessarily reflect the views of IIT Gandhinagar.

References

1. Baki MH, Shemirani F, Khani R, Bayat M (2014) Applicability of diclofenac–montmorillonite as a selective sorbent for adsorption of palladium (II); kinetic and thermodynamic studies. *Anal Methods* 6(6):1875–1883
2. Bensadoun F, Kchit N, Billotte C, Trochu F, Ruiz E (2011) A comparative study of dispersion techniques for nanocomposite made with nanoclays and an unsaturated polyester resin. *Nanomater* 2011:6
3. Carretero-González J, Valentín JL, Arroyo M, Saalwächter K, Lopez-Manchado MA (2008) Natural rubber/clay nanocomposites: influence of poly (ethylene glycol) on the silicate dispersion and local chain order of rubber network. *Eur Polymer J* 44(11):3493–3500
4. Fontana JP, Camilo FF, Bizeto MA, Faez R (2013) Evaluation of the role of an ionic liquid as organophilization agent into montmorillonite for NBR rubber nanocomposite production. *Appl Clay Sci* 83:203–209
5. Laske S (ed) (2015) *Polymer nanoclay composites*. William Andrew
6. Mintova S, Jaber M, Valtchev V (2015) Nanosized microporous crystals: emerging applications. *Chem Soc Rev* 44(20):7207–7233

7. Nazir MS, Kassim MHM, Mohapatra L, Gilani MA, Raza MR, Majeed K (2016) Characteristic properties of nanoclays and characterization of nanoparticulates and nanocomposites. In: Nanoclay reinforced polymer composites. Springer, Singapore, pp 35–55
8. Saba N, Jawaid M, Asim M (2016) Recent advances in nanoclay/natural fibers hybrid composites. In: Nanoclay reinforced polymer composites. Springer, Singapore, pp 1–28
9. Zhu S, Peng H, Chen J, Li H, Cao Y, Yang Y, Feng Z (2013) Intercalation behavior of poly (ethylene glycol) in organically modified montmorillonite. *Appl Surf Sci* 276:502–511

Uncertainties in Water Retention Curve of Bentonite



A. Prakash, B. Hazra and S. Sreedeep

Abstract Bentonites are increasingly used for various geoenvironmental applications (e.g. hydraulic barriers and waste containment) owing to its low hydraulic conductivity and high water retention capacity. Investigating the aforementioned problems necessitates the knowledge of the water retention curve (WRC) of bentonite, which maps the variation of the degree of saturation (S) with suction (ψ). It is now well established that there are various uncertainties associated with WRC. In this study, a database exclusively for the WRC of bentonite is presented. The uncertainties in the WRC parameters of the database are quantified using the copula approach and thereafter confidence intervals are created. Finally, as an application example, the confidence intervals are used to calculate uncertainty bounds in an unsaturated transient seepage problem.

Keywords Bentonite · Water retention · Uncertainty · Copula

1 Introduction

Bentonite finds its use in various geotechnical and geoenvironmental applications such as underground disposal of nuclear waste [32, 36] and waste containment [10, 14]. The reason for preferring bentonite over other materials in these projects is due to its high water retention capacity and extremely low hydraulic conductivity. Modelling the hydraulic response in the aforementioned projects essentially require the water retention curve of bentonite. Water retention curve (WRC), also known as

A. Prakash (✉) · B. Hazra · S. Sreedeep
Department of Civil Engineering, Indian Institute of Technology Guwahati, Guwahati
781039, Assam, India
e-mail: atma.prakash@iitg.ac.in

B. Hazra
e-mail: budhaditya.hazra@iitg.ac.in

S. Sreedeep
e-mail: srees@iitg.ac.in

soil water characteristic curve (SWCC) is one of the most important constitutive equations which maps two key hydraulic state variables: water content and suction ψ .

However, the measurement of WRC for bentonites is not a straightforward but a time-consuming, expensive and cumbersome task. For example, obtaining a single data point (water content and suction) in the WRC of bentonites in some cases may take up to 50 days [9]. Also, given the fact that volumetric measurements are also required in the case of bentonites, the process becomes even more tedious. Even after being measured, the obtained WRC is not sufficient as there are various sources which contribute to non-uniqueness of WRC. Some of them are choice of suction measuring instruments [1, 16–23], initial state of the material [19, 38], hysteresis [8, 37], etc. Though the WRC or SWCC is supposed to be a ‘characteristic’ or is unique for a material, the aforementioned and many other sources of uncertainty essentially imply that measurement of a single WRC is not sufficient. But as already mentioned, the measurement of even a single WRC is difficult for bentonites; obtaining multiple WRCs is not practically feasible.

In such cases, statistical estimate from soils of similar class or texture is extremely useful and has been successfully employed in the past for various other classes of soils. Carsel and Parrish [4] was perhaps the first one to demonstrate the usefulness of probability theory to quantify the uncertainties in various WRC parameters using the UNSODA database. A preliminary statistical analysis was conducted by Sillers and Fredlund [28] over 230 WRCs and the first and second moment was thereafter reported for various WRC parameters. Phoon et al. [20] proposed a first-order estimate from the statistical generalizations of WRCs belonging to similar class of soils. A joint lognormal model for vG WRC parameters was thereafter proposed. Chiu et al. [6] used Bayesian approach to obtain the updated PDF of uncertain parameters associated with WRC and created confidence interval for various classes of soil. Prakash et al. [21, 22] used the copula theory to construct the joint PDF of vG parameters accounting for instrumental and material uncertainty in fly ash.

It should be noted that performing a statistical analysis requires a database, with preferably at least 30 soils in the same class. While there are databases (e.g. UNSODA) for sandy or silty soils, the same is missing for highly expansive clays like bentonite. Therefore, a database for WRC of bentonite is presented. Using the vG (1980) model, the scatter in the compiled database is reduced to a set of curve fitting parameters. Thereafter, the joint distribution of the same is evolved using Gaussian copula and thereafter the confidence intervals are created. Finally, as an application example, the confidence intervals are used to calculate uncertainty bounds in an unsaturated transient seepage problem.

2 Database

This study presents a large database for WRC of bentonites compiled from the literature in Prakash et al. [24]. For a deformable material like bentonite, S versus ψ is widely accepted as the most informative form of representation for bentonite WRC [17] since the key parameters such as air entry value (AEV) and residual degree of saturation are better identified on S versus ψ curve rather than on the θ_w versus ψ or w versus ψ curves. Hence only the sources where WRCs are reported in the form of S versus ψ were collected. The total number of WRCs compiled from the literature is 60 which corresponds to a total of 565 data points with an average of 9.4 data points per WRC. The WRCs in the database correspond to different bentonites, various initial densities, temperature, and are also subjected to different paths such as wetting or drying. As already discussed, all of these factors contribute to the non-uniqueness of WRC. An ideal case would have been to further quantify the uncertainties based on the above factors but unfortunately the number of WRCs available on further breakdown will be too less for satisfactory statistical estimation and inference. Details of the compiled database with its sources are summarized in Table 1.

Table 1 Details of the compiled database for bentonite WRC

S.I. No.	References	Bentonite	No. of WRCs
1	Zhu et al. [39]	GMZ	4
2	Chen et al. [5]	GMZ	1
3	Lloret et al. [15]	FEBEX	9
4	Villar [34]	FEBEX	2
5	Villar [36]	FEBEX	3
6	Alonso et al. [2]	FEBEX	3
7	Dai et al. [7]	FEBEX	1
8	Villar and Loret [35]	FEBEX	3
9	Tripathy et al. [31]	MX-80	1
10	Tripathy et al. [32]	MX-80	5
11	Seiphoori et al. [27]	MX-80	3
12	Hökmark et al. [13]	MX-80	1
13	Rizzi et al. [26]	MX-80	1
14	Villar [36]	MX-80	12
15	Ravi and Rao [25]	BARMER	10
16	Baille et al. [3]	German	1
		Total	60

Note GMZ = Gaomiaozi (China), FEBEX = Full-scale Engineered Barriers Experiment (Spain), MX-80 = Wyoming (USA), BARMER (India)

3 Copula Approach

This section presents a brief overview of the copula theory with respect to bivariate distribution functions. A comprehensive and more general overview of copulas can be found in Nelsen [18]. For usage of the copula theory specific to WRCs, one can refer to the literature (e.g. [16–23]). Sklar [30] theorem forms the foundation of the copula theory. According to it, every multivariate cumulative distribution function of a random vector can be expressed in terms of a copula and its marginals. When applied to bivariate case, it means that

$$H(x_1, x_2) = C(F(x_1), F(x_2); \theta) = C(u_1, u_2; \theta) \quad (1)$$

where $H(x_1, x_2)$ is the bivariate joint cumulative distribution function and $u_1 = F(x_1)$ and $u_2 = F(x_2)$ are the marginal cumulative distribution functions (CDFs), respectively, and C is the copula with parameter θ . It also states that for a bivariate distribution $H(x_1, x_2)$, the copula is unique on the Cartesian product of the range of marginal CDFs $RanF(x_1) \times RanF(x_2)$. This provides uniqueness of the copula when the marginals are continuous.

A two-dimensional copula is a function C of two variables that provides a link between its one dimensional marginal and joint distribution function. It is defined over a unit square $[0, 1]^2$ with uniform marginals. Even when strictly increasing, the transformations are applied to associated random variables, copula remain invariant. This is an advantage since the copula can exactly capture the joint distribution properties even under strictly increasing transformation. The bivariate probability density function (PDF) can be obtained by taking the derivative of the joint CDF given by Eq. (1) as follows:

$$f(x_1, x_2) = f_1(x_1)f_2(x_2)D(u_1, u_2; \theta) \quad (2)$$

where $D(u_1, u_2; \theta) = \partial^2 C(u_1, u_2; \theta) / \partial u_1 \partial u_2$ is the copula density function and $C(u_1, u_2; \theta)$ is the copula function with parameter θ . For the estimation of copula parameter θ , Kendall's τ was used. Kendall's τ can be expressed in terms of copula and its parameter θ as [26]:

$$\tau = 4 \int_0^1 \int_0^1 C(u_1, u_2; \theta) dC(u_1, u_2; \theta) - 1 \quad (3)$$

Solving the above integral equation for different copulas yields a unique relationship between Kendall's τ and copula parameter θ for each copula. For evaluation of the goodness of fit among the copulas, Cramer–von Mises statistic [11] is used here. The CM statistic (S_n) represents the distance between the true and

observed copula and is based on the comparison of empirical copula with derived copula under null hypothesis. The same is given by

$$S_n = \int_{[0,1]^p} C_n^2(u) dC_n(u) = \sum_{i=1}^n (C_n(U_i) - C_{\theta_n}(U_i))^2 \quad (4)$$

where $C_n(u) = \sqrt{n}\{C_n(u) - C_{\theta_n}(u)\}$ is the empirical copula and C_{θ_n} is the copula under hypothesis and θ_n is the estimator of θ , computed using the ranked pseudo-observations. Large value of S_n indicate rejection of the null hypothesis H_0 . Approximate p value for the test statistic S_n can be computed using parametric bootstrap simulation approach [12]. p value represents the degree by which the null hypothesis is not rejected, hence large value of p results in a better fit.

4 Results and Discussions

4.1 Construction of Multivariate Probabilistic Model for WRC

Figure 1a presents the compiled database of the degree of saturation (S) versus suction (ψ). The WRCs were fitted using the van Genuchten [33] equation with constraints $S_r = 0$ and $m = 1 - 1/n$. The vG (1980) model has been used successfully to model the S, ψ variation for bentonites (e.g. [3, 32]). It can be noted that the scatter in the figure is very high as the apparent air entry value can be observed to vary from 0.1 to 100 MPa. This is mainly due to the cumulative effect of multiple sources of uncertainty such as grades of bentonites, initial state, hysteresis, and temperature. The vG parameters α and n for the database are presented in Fig. 1b. It

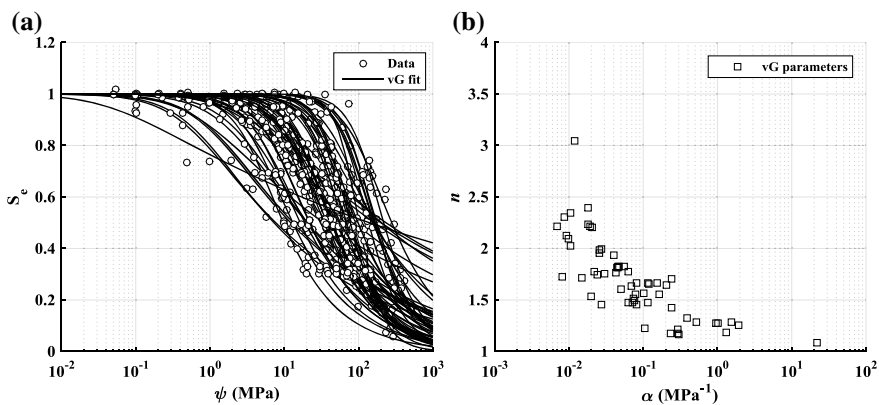


Fig. 1 Database of WRC of bentonite, **a** fitted to van Genuchten [33] equation, **b** vG parameters

Table 2 van Genuchten [33] parameter statistics for the database

Parameter	Statistics	Value
α^a	Mean	0.5549
	Median	0.0631
	SD	2.7836
	Range	0.0070–21.56
n	Mean	1.6924
	Median	1.6606
	SD	0.3796
	Range	1.09–3.05
(α, n)	τ	-0.64

Note SD refers to standard deviation, τ refers to Kendall's τ

^aThe unit for α parameter is MPa^{-1}

should be noted that the scale for α is presented in logarithmic axis as the variation in α parameter (Ref. Table 2) is too high to be legible on a normal scale. Upon observing the scatter, it can be noted that an increase in α value is associated with a decrease in n value. This suggests a negative correlation between the two variables. The same can be confirmed with the statistics provided in Table 2 wherein the rank correlation coefficient Kendall's τ for (α, n) is -0.64 . This is in agreement with the negative correlation observed elsewhere for various other classes of soils. (e.g. [20]). This negative correlation implies that the vG parameters form a joint distribution and the same will be modelled using Gaussian copula in this study. Figure 2a presents the rank transformed value for α, n on a unit square space.

This is useful not only in calculating the rank correlation coefficient but also in visually comparing the copula random numbers with the measured data since a bivariate copula is defined over a unit square. The simulated copula random numbers using Gaussian copula along with the measured data are depicted in

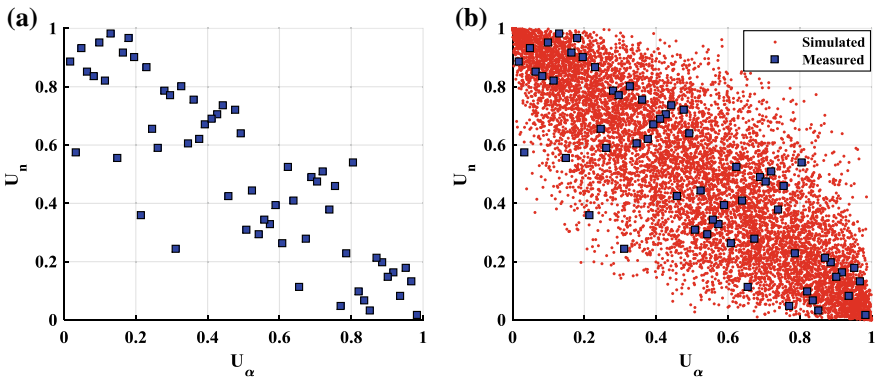


Fig. 2 a Measured and b simulated vG parameters using Gaussian copula on unit square space

Fig. 2b. For checking the appropriateness of Gaussian copula for the current dependence structure, S_n statistics was calculated using Eq. (4) and found to be 0.023. The p value for the S_n statistics was calculated using the bootstrap simulation approach and found to be 0.56. It can be noted that the S_n statistics for Gaussian copula is very low and the p value is high. This means that the null hypothesis for Gaussian copula has a very low evidence against rejection and therefore, Gaussian copula can be considered an appropriate candidate to model the asymmetric dependence structure among vG parameters. Given that the vG parameters are strictly defined for positive values only, the lognormal distribution is selected as the potential candidate for modelling the univariate distribution of vG parameters. The lognormal marginals are also compared against the empirical PDF (histogram) and empirical CDF as presented in Fig. 3 and it can be observed that the empirical and calculated CDF compares well at least visually. For a statistical confirmation, K-S (Kolmogorov–Smirnov) test [16] was performed. The test quantifies the distance between empirical and observed CDF under the null hypothesis. p value for the K-S test is also presented in Fig. 3. High values of $p (> 0.05)$ observed, in this case, suggest that there is no evidence to reject the lognormal distribution. Lognormal marginals were used for α and n parameters by Phoon et al. [20]. Prakash et al. [21, 22] found lognormal distribution to be successful for modelling the vG parameters

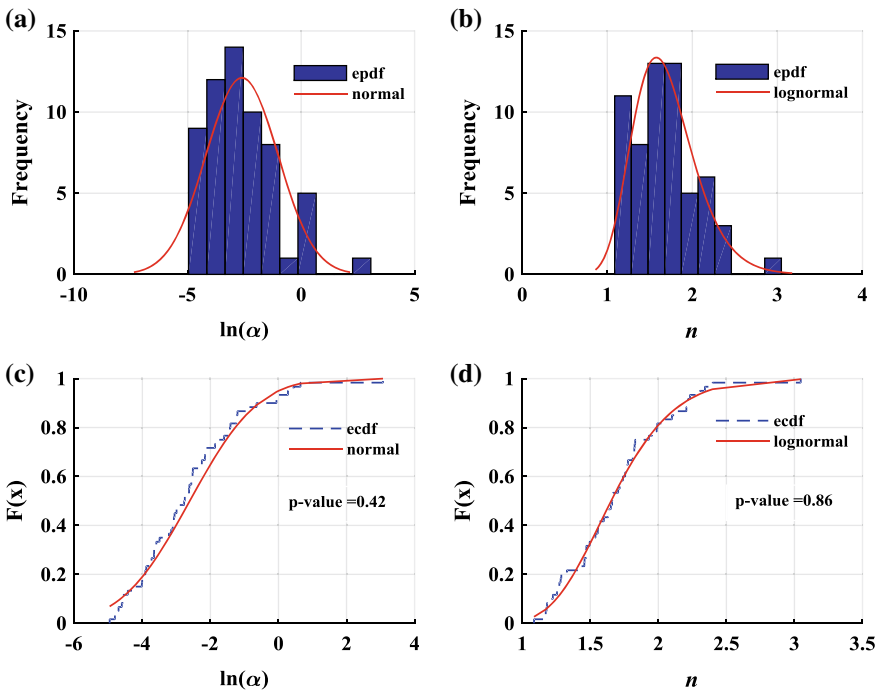


Fig. 3 Empirical and calculated probability density function along with cumulative density function for vG parameters α and n

Table 3 Lognormal parameters for a and n

Curve parameter	Lower bound	Parameters	
		λ	ζ
a	0	-2.61	1.59
n^a	1	-0.50	0.51

λ and ζ are parameters of lognormal distribution

^aparameters of n are of lognormal distribution truncated from below at 1

α, n of fly ash. Given the consistent and successful application of lognormal distribution in the literature for various soil classes along with the one for bentonite observed in this study, it can be stated that vG parameters can be satisfactorily modelled using lognormal distribution.

The distribution parameters were obtained using the maximum likelihood approach and the ones corresponding to the lognormal distribution for the α, n are provided in Table 3. It should be noted that the distribution parameters for n are corresponding to the lognormal distribution truncated from below at 1. The same is also called the three-parameter or translational lognormal distribution. For more details with respect to modelling parameter n with truncated lognormal distribution, one can refer to [20] and Prakash et al. [21, 22]. Given the identified marginals and parameters of the desired copula, the next step is to simulate the original data and check if the dependence structure is modelled correctly. Measured and simulated parameters using the lognormal marginals along with Gaussian copula are shown in Fig. 4a. It can be observed that the prescribed copula along with lognormal marginals can adequately model the shape associated with the measured vG parameters. However, it is difficult to judge the adequacy of fit visually. The measured ρ and τ for the current dataset were -0.27 and -0.65 , respectively. The simulated one using Gaussian copula is calculated to be -0.17 and -0.64 , respectively. It can be seen that the simulated rank correlation coefficient is in close agreement with the

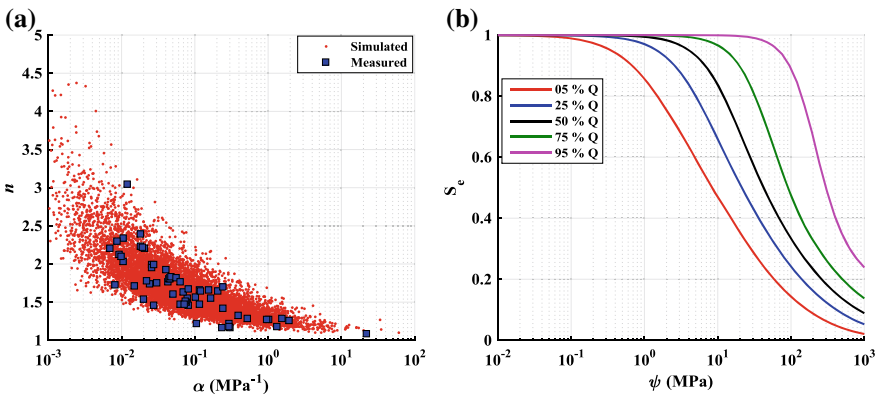


Fig. 4 **a** Measured and simulated vG parameters in the original scale, **b** various quantiles of WRC created using simulated vG parameters

measured one. This confirms the S_n statistics mentioned previously which showed that Gaussian copula is an appropriate choice for the current dataset.

4.2 Application

4.2.1 Confidence Intervals for WRC of Bentonite

In this section, confidence intervals for bentonite WRCs are created using the bivariate distribution evolved in this study. However, it should be noted that the outcome of the copula approach is not limited to just confidence intervals, instead, the WRC is described completely by their joint distribution. 10,000 samples of correlated α, n and m are simulated using the prescribed marginals and copula. Finally, WRC corresponding to a particular quantile is created as an envelope of S_e . Figure 4b shows the various confidence intervals created for bentonite WRC simulated using Gaussian and t-copula.

5 and 95% quantile refer to the lower and upper limit respectively for the 90% confidence interval. Similarly, 25 and 75% quantile refer to the lower and upper limit of the 50% confidence interval respectively and 50% quantile refers to the median curve. It can be easily observed that there is a significant wide dispersion in the confidence interval. This wide degree of dispersion essentially implies that the degree of uncertainty associated with bentonite WRCs is very high. The aforementioned confidence intervals are valuable for assessment of uncertainty bounds related to flow and seepage modelling in the geoenvironmental problems where bentonites are used. The vG parameters for the confidence intervals are summarized in Table 4.

4.2.2 Unsaturated Transient Seepage Analysis

In this section, a simple one-dimensional vertical transient seepage analysis is conducted using Hydrus-1D code [29]. Depth of the soil profile is assumed to be 100 cm. Saturated hydraulic conductivity (k_{sat}) is taken as 10^{-12} m/s. Residual and

Table 4 van Genuchten [33] parameters for the confidence intervals created using Gaussian copula

Quantile (%)	α	n	Remark
05	0.594	1.45	Lower limit of 90% CI
25	0.184	1.49	Lower limit of 50% CI
50	0.077	1.54	Median
75	0.028	1.63	Upper limit of 50% CI
95	0.006	1.93	Upper limit of 90% CI

Note CI denotes confidence interval

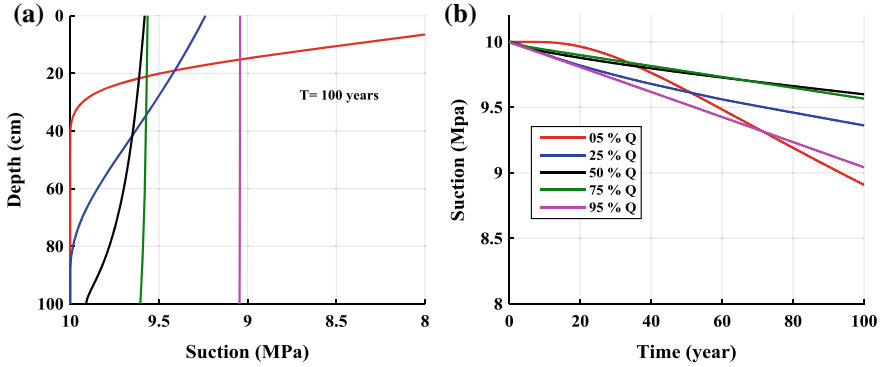


Fig. 5 a Suction profile with depth and b suction variation with time, corresponding to various quantiles of WRC

saturated water content are taken as zero and 0.45, respectively. A constant flux boundary condition equal to k_{sat} is applied at the upper end. This was done purposely to avoid ponding of water at the top surface. At the lower end, free drainage boundary condition is assumed. A uniform initial suction head of 10 MPa was assumed throughout the column. The simulations are conducted for 100 years. The confidence intervals formulated in the previous section are utilized to obtain the uncertainty bounds for suction variation with time and depth. Figure 5a demonstrates the variation of profile of suction with depth across time. Figure 5b presents the variation of suction with time for a soil element at the depth of 15 cm. The variation in the profile and time variation across various quantiles of WRC can be noted. Although the boundary conditions applied are not very realistic, these examples demonstrates the usefulness of the confidence intervals presented in this study towards establishing uncertainty bounds related to applications requiring WRC as an input.

5 Conclusions

This study presented a database of water retention curve (WRC) exclusively for bentonite. The scatter in the database was reduced to a set of van Genuchten [33] curve fitting parameters, α and n . To quantify the uncertainty in WRC of the database, the joint distribution of vG parameters was established using the copula approach. Gaussian copula and lognormal marginals were found to be adequate to represent the dependence structure and the randomness associated with the vG parameters. Finally, for practical application purposes, confidence intervals were created for the WRC of bentonite. The confidence intervals were thereafter utilized to demonstrate the evaluation of uncertainty bounds in a simple unsaturated transient seepage problem.

References

1. Abhijit D, Sreedeeep S (2014) Evaluation of measurement methodologies used for establishing water retention characteristic curve of fly ash. *J Test Eval* 43(5):1066–1077
2. Alonso EE, Romero E, Hoffmann C (2011) Hydromechanical behaviour of compacted granular expansive mixtures: experimental and constitutive study. *Géotechnique* 61(4):329–344
3. Baille W, Tripathy S, Schanz T (2014) Effective stress in clays of various mineralogy. *Vadose Zone J* 13(5)
4. Carsel RF, Parrish RS (1988) Developing joint probability distributions of soil water retention characteristics. *Water Resour Res* 24(5):755–769
5. Chen B, Qian L, Ye W, Cui Y, Wang J (2006) Soil-water characteristic curves of Gaomiaozi bentonite. *Yanshilixue Yu Gongcheng Xuebao/Chin J Rock Mech Eng* 25(4):788–793
6. Chiu CF, Yan WM, Yuen KV (2012) Reliability analysis of soil–water characteristics curve and its application to slope stability analysis. *Eng Geol* 135:83–91
7. Dai Z, Samper J, Wolfsberg A, Levitt D (2008) Identification of relative conductivity models for water flow and solute transport in unsaturated bentonite. *Phys Chem Earth Parts A/B/C33: S177–S185*
8. Gallipoli D (2012) A hysteretic soil-water retention model accounting for cyclic variations of suction and void ratio. *Geotechnique* 62(7):605
9. Gatabin C, Talandier J, Collin F, Charlier R, Dieudonné AC (2016) Competing effects of volume change and water uptake on the water retention behaviour of a compacted MX-80 bentonite/sand mixture. *Appl Clay Sci* 121:57–62
10. Gates WP, Bouazza A, Churchman GJ (2009) Bentonite clay keeps pollutants at bay. *Elem* 5 (2):105–110
11. Genest C, Rémillard B, Beaudoin D (2009) Goodness-of-fit tests for copulas: a review and a power study. *Insurance: Math Econ* 44(2):199–213
12. Genest C, Favre AC, Béliveau J, Jacques C (2007) Metaelliptical copulas and their use in frequency analysis of multivariate hydrological data. *Water Resour Res* 43(9)
13. Hökmark H (2004) Hydration of the bentonite buffer in a KBS-3 repository. *Appl Clay Sci* 26 (1–4):219–233
14. Kumar S, Yong WL (2002) Effect of bentonite on compacted clay landfill barriers. *Soil Sediment Contam* 11(1):71–89
15. Lloret A, Romero E, Villar MV (2004) FEBEX II Project Final report on thermo-hydro-mechanical laboratory tests (No. ENRESA–10/04). CENTRO DE INVESTIGACIONES ENERGETICAS
16. Massey FJ Jr (1951) The Kolmogorov-Smirnov test for goodness of fit. *J Am Stat Assoc* 46 (253):68–78
17. Mbonimpa M, Aubertin M, Maqsood A, Bussièrre B (2006) Predictive model for the water retention curve of deformable clayey soils. *J Geotech Geoenviron Eng* 132(9):1121–1132
18. Nelsen RB (2006) An introduction to copulas. Springer Science and Business Media
19. Nuth M, Laloui L (2008) Advances in modelling hysteretic water retention curve in deformable soils. *Comput Geotech* 35(6):835–844
20. Phoon KK, Santoso A, Quek ST (2010) Probabilistic analysis of soil-water characteristic curves. *J Geotech Geoenviron Eng* 136(3):445–455
21. Prakash A, Hazra B, Sreedeeep S (2018) Uncertainty quantification in water retention characteristic curve of fly ash using copulas. *J Test Eval* 47(4)
22. Prakash A, Hazra B, Sreedeeep S (2018) Probabilistic analysis of unsaturated fly ash slope. *J Hazard Toxic Radioact Waste* 23(1):06018002
23. Prakash A, Hazra B, Deka A, Sreedeeep S (2017) Probabilistic analysis of water retention characteristic curve of fly ash. *Int J Geomech* 17(12):04017111
24. Prakash A, Hazra B, Sreedeeep S (Accepted) Probabilistic analysis of soil water characteristic curve of bentonite: a multivariate copula approach. *Int J Geomech*

25. Ravi K, Rao SM (2013) Influence of infiltration of sodium chloride solutions on WRC of compacted bentonite–sand specimens. *Geotech Geol Eng* 31(4):1291–1303
26. Rizzi M, Seiphoori A, Ferrari A, Ceresetti D, Laloui L (2011) Analysis of the behaviour of the granular MX-80 bentonite in THM-processes. *Lausanne Swiss Fed Inst Technol Orders* 7:928
27. Seiphoori A, Ferrari A, Laloui L (2014) Water retention behaviour and microstructural evolution of MX-80 bentonite during wetting and drying cycles. *Géotechnique* 64(9):721–734
28. Sillers WS, Fredlund DG (2001) Statistical assessment of soil-water characteristic curve models for geotechnical engineering. *Can Geotech J* 38(6):1297–1313
29. Simunek J, Van Genuchten MT, Sejna M (2005) The HYDRUS-1D software package for simulating the one-dimensional movement of water, heat, and multiple solutes in variably-saturated media. *Univ Calif-Riverside Res Rep* 3:1–240
30. Sklar M (1959) Fonctions de repartition an dimensions et leurs marges. *Publ Inst Stat Univ Paris* 8:229–231
31. Tripathy S, Tazda MYM, Thomas HR (2014) Soil-water characteristic curves of clays. *Can Geotech J* 51(8):869–883
32. Tripathy S, Thomas HR, Bag R (2015) Geoenvironmental application of bentonites in underground disposal of nuclear waste: characterization and laboratory tests. *J Hazard Toxic Radioact Waste* 21(1):D4015002
33. Van Genuchten MT (1980) A closed-form equation for predicting the hydraulic conductivity of unsaturated soils 1. *Soil Sci Soc Am J* 44(5):892–898
34. Villar Galicia MV (2002) Thermo-hydro-mechanical characterisation of a bentonite from Cabo de Gata. A study applied to the use of bentonite as sealing material in high level radioactive waste repositories. *Publicación técnica (Empresa Nacional de Residuos Radiactivos)* 4:15–258
35. Villar MV, Lloret A (2004) Influence of temperature on the hydro-mechanical behaviour of a compacted bentonite. *Appl Clay Sci* 26(1–4):337–350
36. Villar MV (2005). MX-80 bentonite. Thermo-hydro-mechanical characterisation performed at CIEMAT in the context of the Prototype Project. *Informes Técnicos CIEMAT* 1053:39
37. Wheeler SJ, Sharma RS, Buisson MSR (2003) Coupling of hydraulic hysteresis and stress–strain behaviour in unsaturated soils. *Géotechnique* 53(1):41–54
38. Zhou AN, Sheng D, Carter JP (2012) Modelling the effect of initial density on soil-water characteristic curves. *Géotech* 62(8):669
39. Zhu Z, Sun DA, Zhou A, Qiu Z (2016) Calibration of two filter papers at different temperatures and its application to GMZ bentonite. *Environ Earth Sci* 75(6):509

Comparative Study of Backfill Retaining Systems for Onshore RCC Pile Berth Under Different Site Conditions



Soumyakanti Dhavala, Dhara Shah and Sanjeev Kapasi

Abstract The study is focused on analyzing and designing backfill retaining systems for a berth with respect to permissible deflection and overall consumption of concrete and steel. It includes analyzing and designing of RCC piled jetty with three types of earth retaining systems, namely slope fill (Type 1), diaphragm wall separate from the jetty (Type 2), cantilever wall attached to the jetty (Type 3), and with two different vessels of 5000 DWT (V_1) and 3000 DWT (V_2) under different site conditions. The different conditions consist of different water depth, different soil conditions (loose, medium, and hard), different seismic zone (II, III, IV, and V), and earth pressure for different backfill soil parameters and slope fill. The Axial force, Moments (M_y and M_z), and Concrete and Steel consumption are compared with respect to different water depths for all the zones and type of soils. The three systems are then compared against one another to find the most economical section. Also, the material consumption factor is found. It was observed that the slope fill (Type 1) and 9 m system are most suitable in terms of economy as a backfill retaining system for onshore RCC pile berth. With the change in soil from hard to loose, the pile diameter increases. Also as the width of jetty increases, in case of Type 1 system, the structure becomes less economical due to increased forces.

Keywords Retaining wall · Diaphragm wall · RCC Pile · Berthing structure · Backfill retaining system

S. Dhavala (✉)

M.Tech Structural Engineering Design, CEPT University, Ahmedabad, Gujarat, India
e-mail: dhavala.soumyakanti@gmail.com

D. Shah

Faculty of Technology, CEPT University, Ahmedabad, Gujarat, India

S. Kapasi

Grid Consultant, Ahmedabad, Gujarat, India

© Springer Nature Singapore Pte Ltd. 2020

A. Prashant et al. (eds.), *Advances in Computer Methods and Geomechanics*, Lecture Notes in Civil Engineering 56,
https://doi.org/10.1007/978-981-15-0890-5_3

1 Introduction

More onshore berthing structures need to be constructed because of the increased focus on waterway transportation systems. It is a contributing mode to the Indian economy. For bulk transportation of materials and passengers, waterway proves to be the cheapest mode of transportation. This study is focused on analyzing and designing of backfill retaining systems for onshore RCC pile berth with respect to permissible deflection and overall consumption of concrete and steel. It includes analyzing and designing of RCC piled jetties with three types of earth retaining systems—slope fill, cantilever wall attached to the jetty, and a diaphragm wall separate from the jetty—subjected to different site conditions. The different conditions consist of different water depth, different soil conditions (loose, medium, and hard), and different seismic zones (II, III, IV, and V).

Soil, which is soft marine clay or loose sand in most of the coastal regions, is usually under consolidated with low shear strength values. Most of the coastlines have surfaces which are sloping toward the waterfront. Slope instability, a common problem, is due to the low shear strength of the soil. The instability of seabed slope is due to creep deformation of clayey soil, self-weight, surcharge load, earthquake, wave force, etc. This instability results from the failure due to large displacements of the pile head, causing additional forces on the piles which are constructed on these slopes. Hence, it is very important from a practical viewpoint to understand the forces acting on the piles, the behavior of such structures under these forces, design of the structure to withstand these forces, and comparing the different earth retaining systems to find out the most feasible system to counter the abovementioned forces.

2 Problem Formulation

Forces like Berthing force, Mooring force, Current Force, and Wave Force have been computed as per IS 4651 (Part 3)—1974. Wave force has been confirmed as per Shore Protection Manual Volume II, 1984. The Hydrodynamic and Seismic Forces are computed as per IS 1893 (Part 1)—1984 and 1893 (Part 1)—2002, respectively. The Wind Forces have been calculated as per the clauses mentioned in IS 875 (Part 3): 2015. IS 1893 (Part 1): 2002 has been referred to determine the seismic forces. The load combinations have been taken from IS 4651 (Part 4)—2014.

To carry out a comparative study of the backfill retaining system for onshore RCC pile berth with respect to the following various site conditions.

- Different water depth (6, 8 m),
- Different spacing of piles (6.43, 7.5, 9 m),
- Different seismic zone (II, III, IV and V),
- Different soil condition (Soft—L, Medium—M, Hard—H),

- Different structural systems (Type 1, Type 2, Type 3), and
- Earth pressure for different backfill soil parameters and soil profile.

The following methodology has been adopted.

1. Data collection,
2. Preparing general arrangement layout of RCC pile berth along with different earth retaining systems,
3. Preparing models in STAAD Pro and analyzing it for all load cases and load combinations as per Indian Standard Code of Practice,
4. Designing of piles and beams for critical load combinations considering the strength and serviceability criteria,
5. Calculation of safe pile diameter,
6. Calculation of concrete and reinforcement quantity of structural members, and
7. Comparative study to be done based on obtained results.

3 Structural Layout

See Figs. 1, 2 and 3.

4 Loads and Load Combinations

Dead load, live load, berthing force, mooring force, current force, wave force, hydrodynamic force, wind force, and seismic force have been considered.

IS 4651 (Part IV)—2014 has been referred for load combinations.

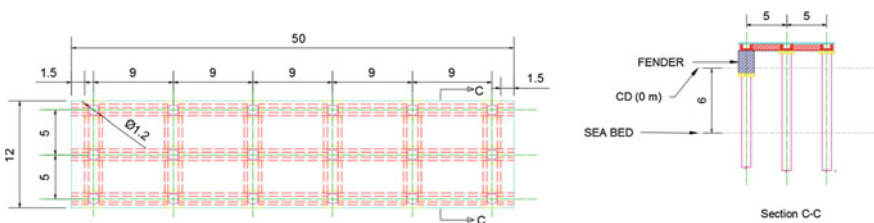


Fig. 1 Plan and elevation of Type 1 structure (slope fill system) (all dimensions in “m”)

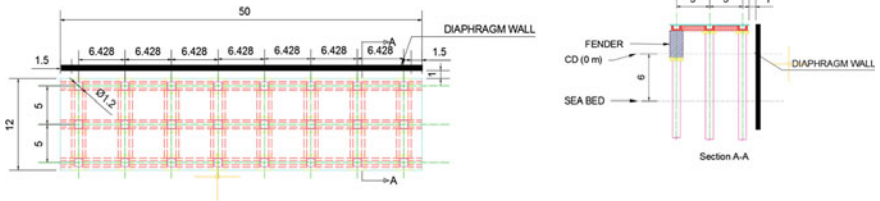


Fig. 2 Plan and elevation of Type 2 structure (diaphragm wall separate from the jetty structure) (all dimensions in “m”)

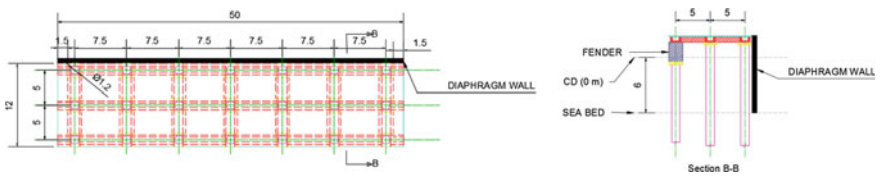


Fig. 3 Plan and elevation of Type 3 structure (cantilever wall attached to the jetty) (all dimensions in “m”)

5 Observation and Conclusions

5.1 Observations

See Charts 1, 2, 3, 4, 5, 6, 7, 8, 9, 10, 11, 12, 13, 14, 15, 16, 17, 18, 19, 20, 21, 22, 23, 24 and 25.

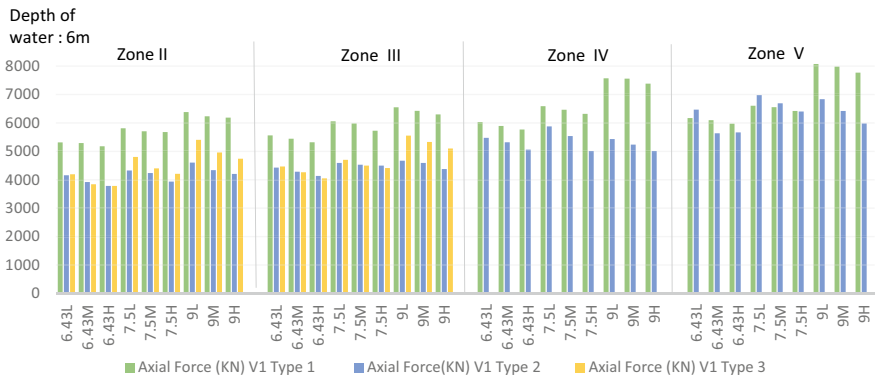


Chart 1 Comparison of axial force w.r.t seismic zone, pile spacing and soil type for Type 1, Type 2 and Type 3 structure and 6 m depth of water

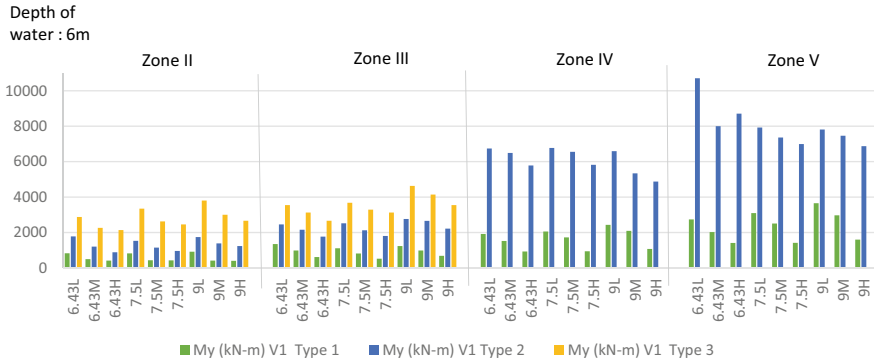


Chart 2 Comparison of M_y (kNm) w.r.t seismic zone, pile spacing, soil type and depth of water for Type 1, Type 2 and Type 3 structures

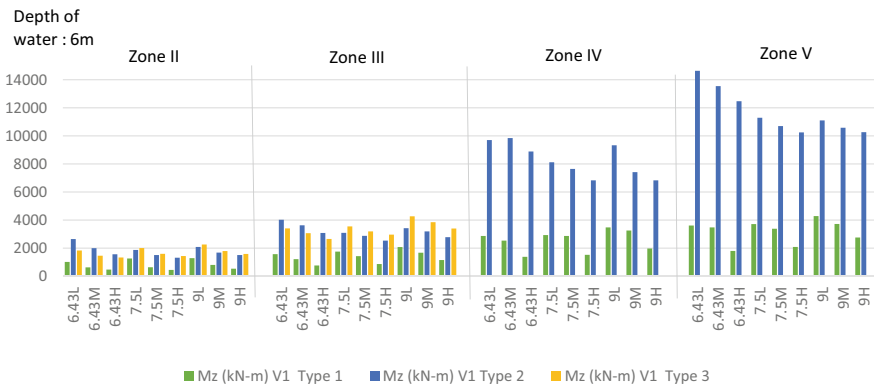


Chart 3 Comparison of M_z (kNm) w.r.t seismic zone, pile spacing and soil type for Type 1, Type 2 and Type 3 structure and 6 m depth of water

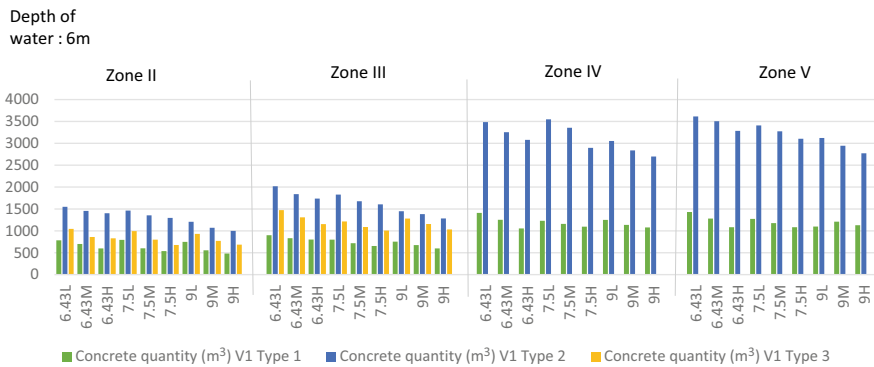


Chart 4 Comparison of concrete quantity (m^3) w.r.t seismic zone, pile spacing and soil type for Type 1, Type 2 and Type 3 structure and 6 m depth of water

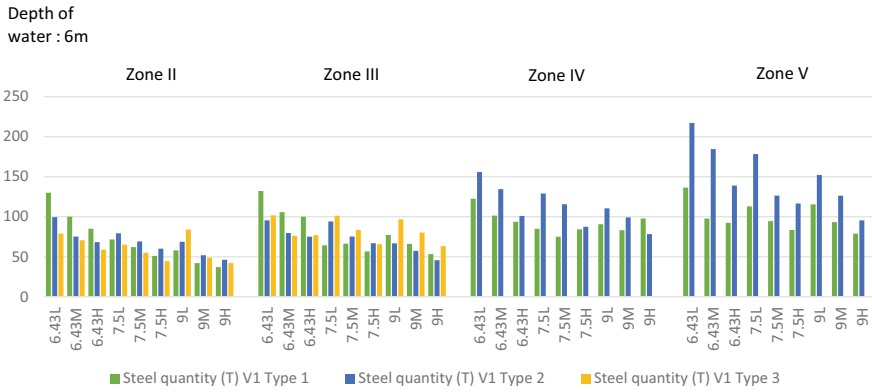


Chart 5 Comparison of steel quantity (MT) w.r.t seismic zone, pile spacing and soil type for Type 1, Type 2 and Type 3 structure and 6 m depth of water

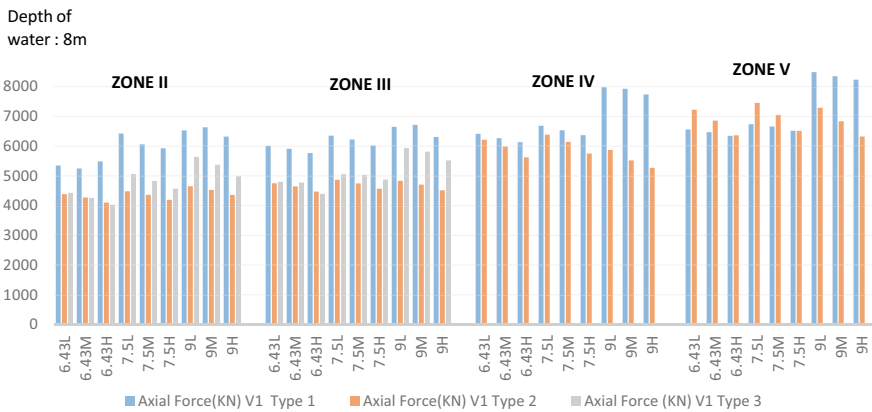


Chart 6 Comparison of axial force w.r.t seismic zone, pile spacing and soil type for Type 1, Type 2 and Type 3 structure and 8 m depth of water

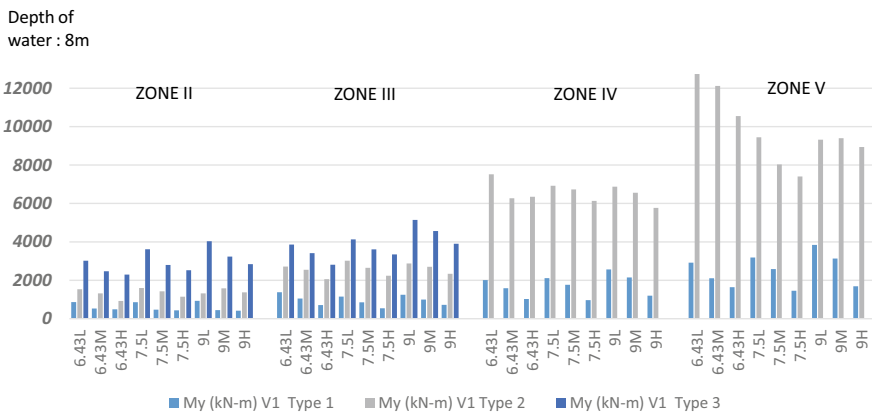


Chart 7 Comparison of M_y (kNm) w.r.t seismic zone, pile spacing and soil type for Type 1, Type 2 and Type 3 structure and 8 m depth of water

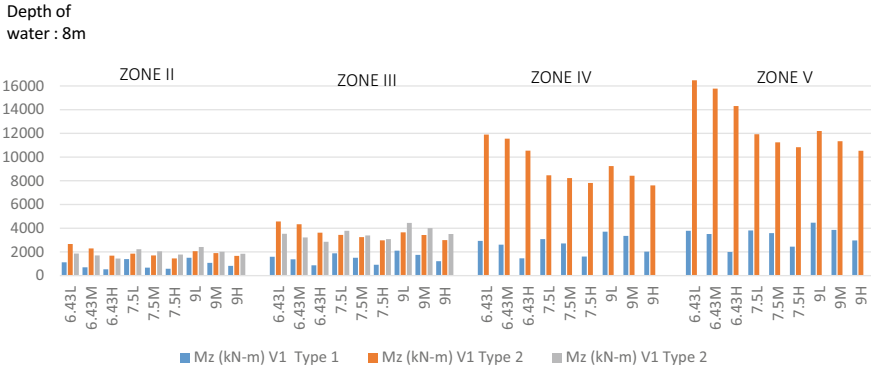


Chart 8 Comparison of M_z (kNm) w.r.t seismic zone, pile spacing and soil type for Type 1, Type 2 and Type 3 structure and 8 m depth of water

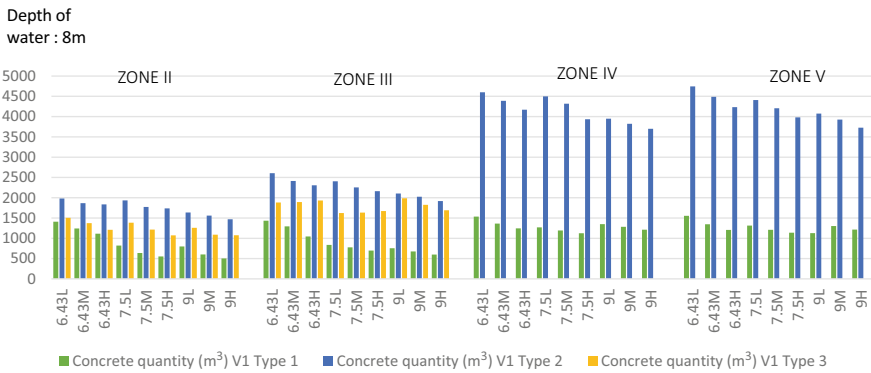


Chart 9 Comparison of concrete quantity (m^3) w.r.t seismic zone, pile spacing and soil type for Type 1, Type 2 and Type 3 structure and 8 m depth of water

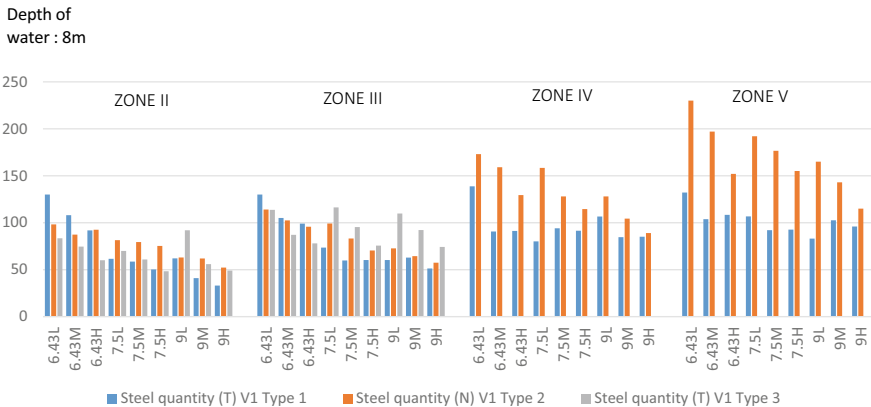


Chart 10 Comparison of steel quantity (MT) w.r.t seismic zone, pile spacing and soil type for Type 1, Type 2 and Type 3 structure and 8 m depth of water

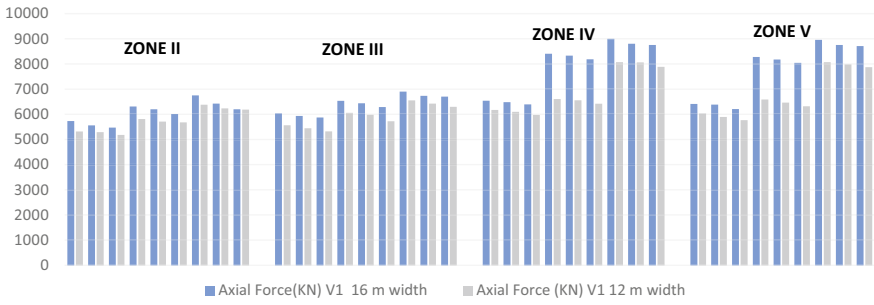


Chart 11 Comparison of axial force w.r.t seismic zone, pile spacing and soil type for two different widths of Jetty in Type 1 structure

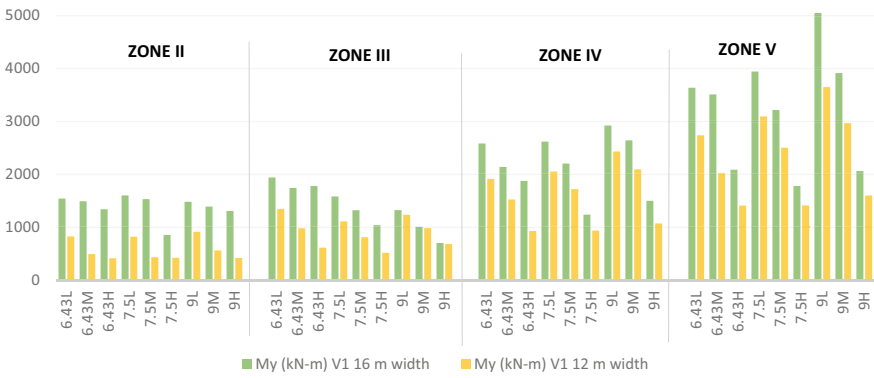


Chart 12 Comparison of M_y (kNm) w.r.t seismic zone, pile spacing and soil type for two different widths of Jetty in Type 1 structure

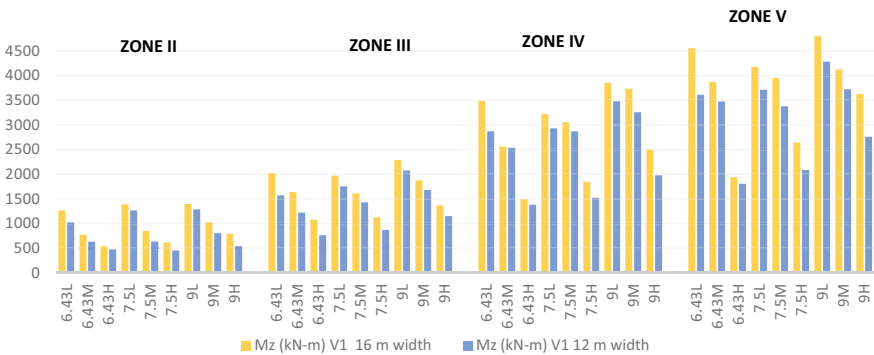


Chart 13 Comparison of M_z (kNm) w.r.t seismic zone, pile spacing and soil type for two different widths of Jetty in Type 1 structure

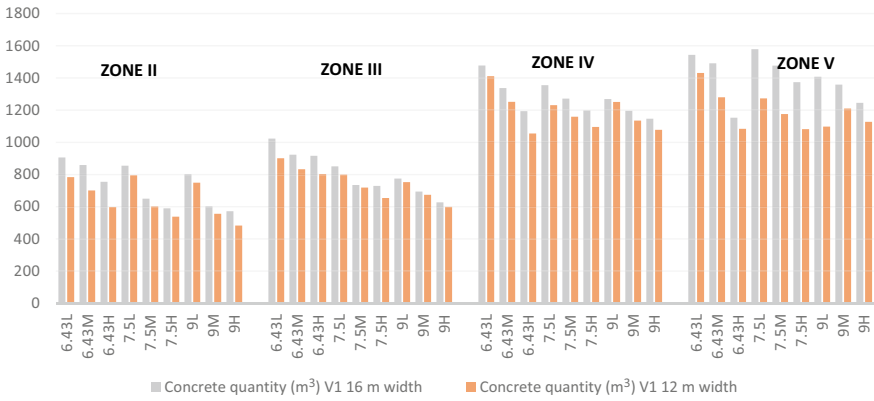


Chart 14 Comparison of concrete quantity (m³) w.r.t seismic zone, pile spacing and soil for two different widths of Jetty in Type 1 structure

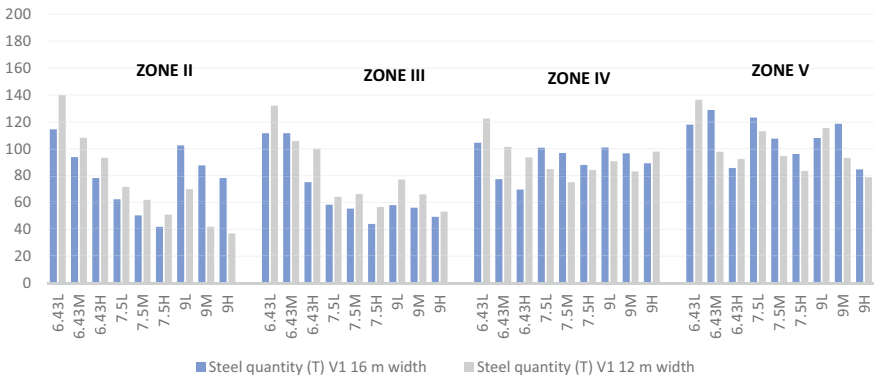


Chart 15 Comparison of steel quantity (MT) w.r.t seismic zone, pile spacing and soil for different widths of Jetty in Type 1 structure

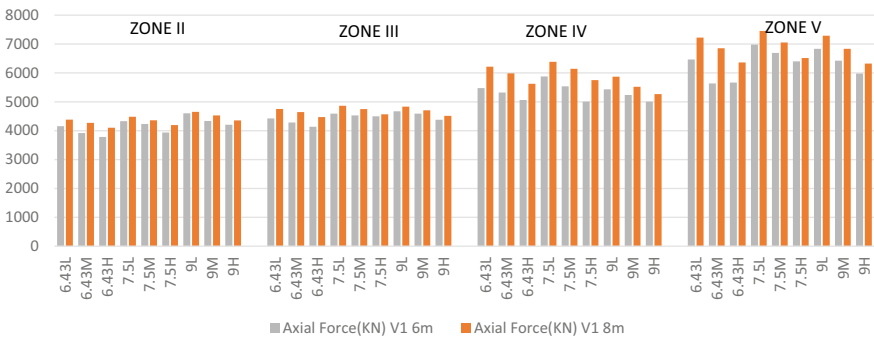


Chart 16 Comparison of axial force w.r.t seismic zone, pile spacing, soil type and depth of water for Type 2 structure

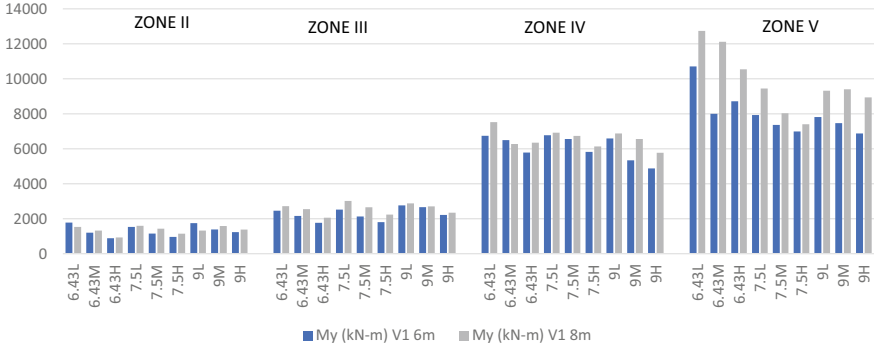


Chart 17 Comparison of M_y (kNm) w.r.t seismic zone, pile spacing, soil type and depth of water for Type 2 structure

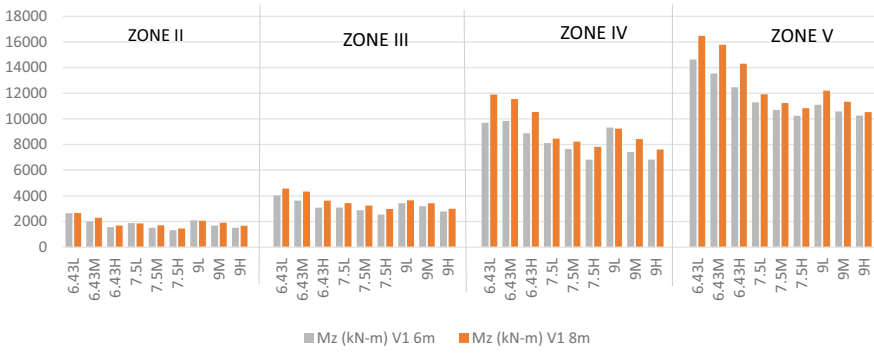


Chart 18 Comparison of M_z (kNm) w.r.t seismic zone, pile spacing, soil type and depth of water for Type 2 structure

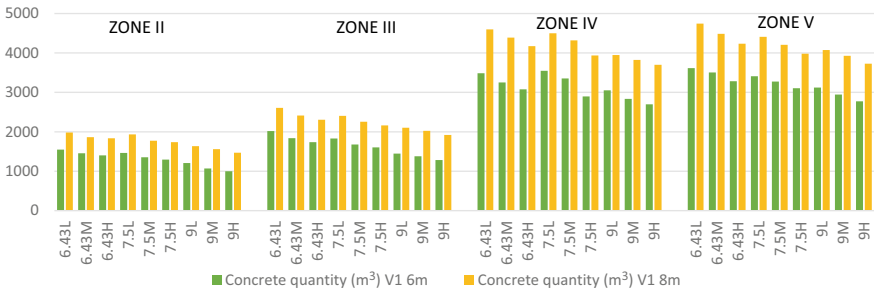


Chart 19 Comparison of concrete quantity (m^3) w.r.t seismic zone, pile spacing, soil type and depth of water for Type 2 structure

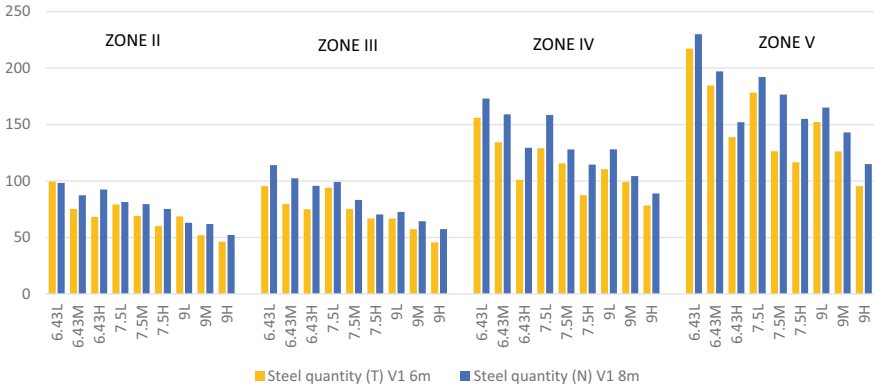


Chart 20 Comparison of steel quantity (MT) w.r.t seismic zone, pile spacing, soil type and depth of water for Type 2 structure

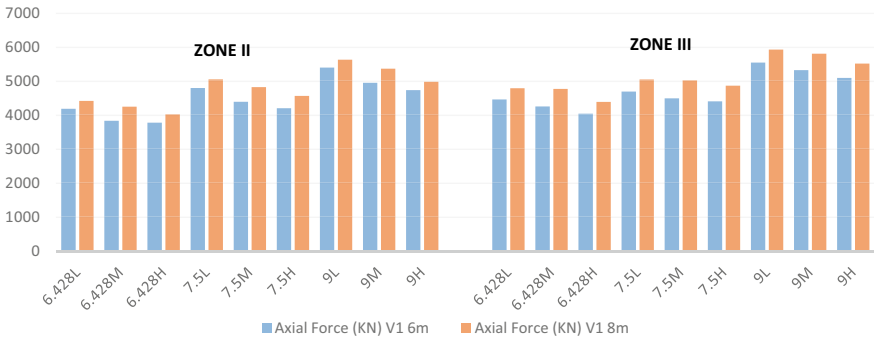


Chart 21 Comparison of axial force w.r.t seismic zone, pile spacing, soil type and depth of water for Type 3 structure

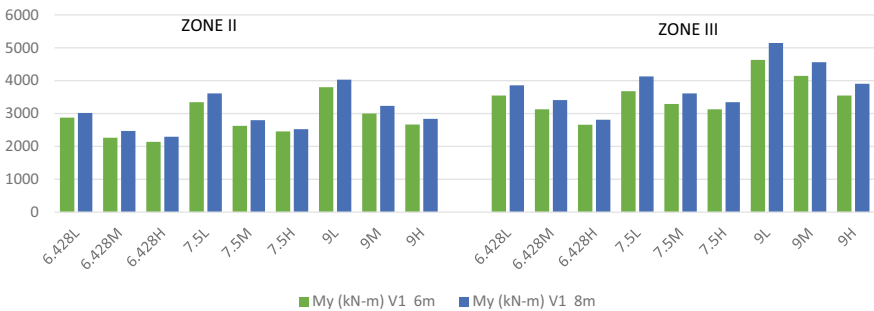


Chart 22 Comparison of M_y (kNm) w.r.t seismic zone, pile spacing, soil type and depth of water for Type 3 structure

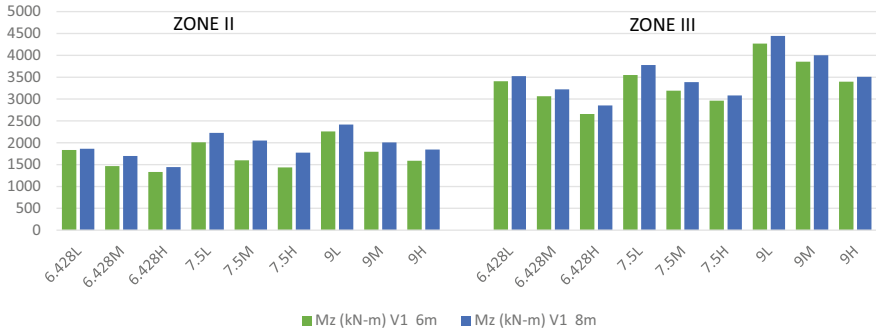


Chart 23 Comparison of M_z (kNm) w.r.t seismic zone, pile spacing, soil type and depth of water for Type 3 structure

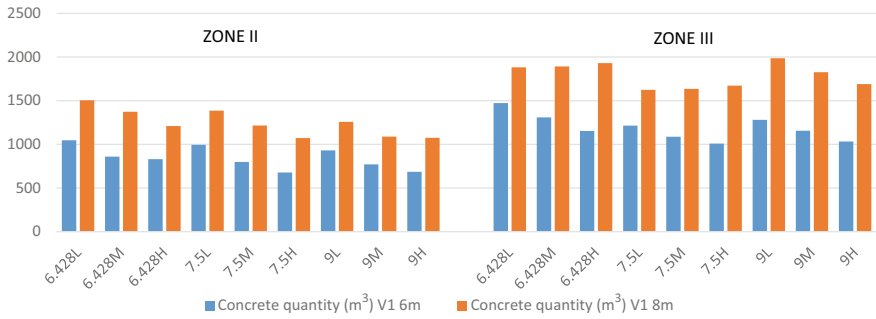


Chart 24 Comparison of concrete quantity (m^3) w.r.t seismic zone, pile spacing, soil type and depth of water for Type 3 structure

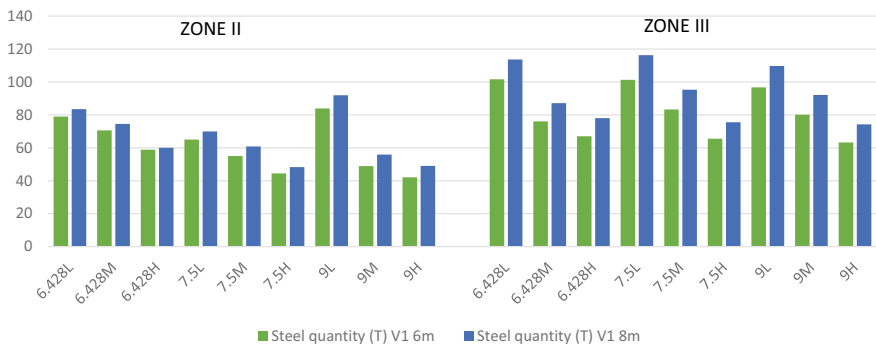


Chart 25 Comparison of steel quantity (MT) w.r.t seismic zone, pile spacing, soil type and depth of water for Type 3 structure

Table 1 Material consumption factor

Zone	Water depth	Soil type	Pile spacing	Concrete consumption factor			Steel consumption factor		
				Type 1	Type 2	Type 3	Type 1	Type 2	Type 3
II	6	L	6.43	1.05	2.07	1.40	1.61	1.78	1.46
II	6	L	7.5	1.06	1.96	1.33	1.39	1.55	1.24
II	6	L	9	1.00	1.61	1.24	1.15	1.35	1.00
II	6	M	6.43	1.26	2.62	1.55	2.19	1.67	1.34
II	6	M	7.5	1.08	2.44	1.44	1.70	1.28	1.20
II	6	M	9	1.00	1.93	1.38	1.44	1.16	1.00
II	6	H	6.43	1.24	2.91	1.72	1.57	1.86	2.27
II	6	H	7.5	1.11	2.68	1.40	1.14	1.40	1.32
II	6	H	9	1.00	2.07	1.42	1.00	1.25	1.14
II	8	L	6.43	1.76	2.48	1.88	1.23	1.62	1.39
II	8	L	7.5	1.03	2.42	1.73	1.17	1.58	1.21
II	8	L	9	1.00	2.05	1.57	1.00	1.50	1.04
II	8	M	6.43	2.07	3.10	2.29	2.17	1.65	1.39
II	8	M	7.5	1.06	2.95	2.02	1.80	1.45	1.24
II	8	M	9	1.00	2.60	1.81	1.53	1.54	1.00
II	8	H	6.43	2.21	3.64	2.39	1.88	1.91	2.78
II	8	H	7.5	1.10	3.44	2.12	1.24	1.87	1.69
II	8	H	9	1.00	2.91	2.13	1.00	1.58	1.49
III	6	L	6.43	1.22	2.80	1.86	1.13	1.66	1.79
III	6	L	7.5	1.10	2.56	1.66	1.17	1.33	1.47
III	6	L	9	1.00	2.46	1.54	1.00	1.18	1.16
III	6	M	6.43	1.12	2.52	1.84	1.73	1.27	1.36
III	6	M	7.5	1.04	2.29	1.63	1.41	1.06	1.01
III	6	M	9	1.00	2.16	1.44	1.33	1.00	1.03
III	6	H	6.43	1.26	2.42	2.14	1.69	1.46	2.12
III	6	H	7.5	1.13	2.31	1.93	1.44	1.26	1.75
III	6	H	9	1.00	2.14	1.72	1.17	1.00	1.38
III	8	L	6.43	1.20	3.45	2.33	1.23	1.66	1.84
III	8	L	7.5	1.11	3.23	2.34	1.00	1.39	1.59
III	8	L	9	1.00	3.10	2.40	1.01	1.18	1.26
III	8	M	6.43	1.37	2.49	1.80	1.69	1.46	1.46
III	8	M	7.5	1.24	2.31	1.81	1.35	1.31	1.12
III	8	M	9	1.00	2.21	1.85	1.27	1.23	1.00
III	8	H	6.43	1.26	3.51	3.32	1.18	1.42	2.26
III	8	H	7.5	1.13	3.38	3.05	1.23	1.25	1.80
III	8	H	9	1.00	3.20	2.82	1.00	1.12	1.45
IV	6	L	6.43	1.12	3.24		1.13	1.72	

(continued)

Table 1 (continued)

Zone	Water depth	Soil type	Pile spacing	Concrete consumption factor			Steel consumption factor		
				Type 1	Type 2	Type 3	Type 1	Type 2	Type 3
IV	6	L	7.5	1.06	3.06		1.00	1.54	
IV	6	L	9	1.00	2.64		1.12	1.16	
IV	6	M	6.43	1.34	3.30		1.31	1.67	
IV	6	M	7.5	1.19	3.08		1.08	1.44	
IV	6	M	9	1.00	2.92		1.00	1.08	
IV	6	H	6.43	1.16	2.83		1.16	1.41	
IV	6	H	7.5	1.05	2.63		1.06	1.27	
IV	6	H	9	1.00	2.50		1.25	1.00	
IV	8	L	6.43	1.13	4.00		1.00	1.98	
IV	8	L	7.5	1.06	3.84		1.17	1.60	
IV	8	L	9	1.00	3.50		1.14	1.43	
IV	8	M	6.43	1.23	3.69		1.46	1.91	
IV	8	M	7.5	1.09	3.52		1.00	1.76	
IV	8	M	9	1.00	3.35		1.01	1.43	
IV	8	H	6.43	1.11	3.25		1.26	1.51	
IV	8	H	7.5	1.06	3.15		1.00	1.23	
IV	8	H	9	1.00	3.05		1.01	1.05	
V	6	L	6.43	1.18	3.15		1.35	2.14	
V	6	L	7.5	1.09	3.03		1.13	1.52	
V	6	L	9	1.00	2.87		1.00	1.40	
V	6	M	6.43	1.32	3.33		1.48	2.35	
V	6	M	7.5	1.18	3.23		1.06	2.00	
V	6	M	9	1.00	3.03		1.00	1.50	
V	6	H	6.43	1.03	2.84		1.46	1.93	
V	6	H	7.5	1.10	2.68		1.18	1.60	
V	6	H	9	1.00	2.53		1.00	1.21	
V	8	L	6.43	1.16	3.88		1.16	2.09	
V	8	L	7.5	1.06	3.70		1.01	1.92	
V	8	L	9	1.00	3.50		1.00	1.68	
V	8	M	6.43	1.29	3.93		1.34	2.21	
V	8	M	7.5	1.12	3.71		1.04	1.89	
V	8	M	9	1.00	3.51		1.00	1.46	
V	8	H	6.43	1.08	3.61		1.17	2.01	
V	8	H	7.5	1.15	3.48		1.25	1.74	
V	8	H	9	1.00	3.30		1.00	1.40	

5.2 Conclusions

1. From the observations, slope fill earth retaining system is most suitable in terms of economy as a backfill retaining system for onshore RCC pile berth. The concrete and steel consumption for slope fill earth retaining system (Type 1) is less as compared to jetty with attached diaphragm wall (Type 2) and jetty with separate diaphragm wall (Type 3).
2. With the change in soil from hard to medium to loose, the pile diameter increases.
3. From the observations, 9 m is the most economical pile spacing for all the conditions studied for the thesis.
4. There is a negligible difference between the forces and moments of 3000 DWT and 5000 DWT vessel.
5. In case of the slope fill earth retaining system, there are two systems, one of 12 m width and the other of 16 m width. As the width of the jetty increases, the structure becomes less economical due to increased forces.

For a particular zone and soil type, the case which shows the least material consumed under different types of structures and different spacing is given a factor of 1. With respect to this, the factors are derived for other cases.

Table 1 shows the material consumption factors for both, concrete and steel, in beams and piles in Type 1, Type 2, and Type 3 system zone-wise. The factor for the system with the lowest material consumption has been highlighted.

For a particular zone and soil type, the case which shows the least material consumed under different types of structures and different spacing is given a factor of 1. With respect to this the factors are derived for other cases.

References

1. IS 4651: 1974—Code of practice for planning and design of ports and harbours, Part 1: Site Investigation, Part 3: Loading
2. IS 4651 (Part 4): 2014—Code of practice for planning and design of ports and harbours—General design considerations (for load combinations)
3. IS 4651 (Part 5): 1980—Code of practice for planning and design of ports and harbours—Layout and functional requirements
4. IS 456: 2000—Plain and reinforced concrete code of practice
5. IS 875 (Part 3): 2015—Code of practice for wind loads on buildings and structures
6. IS 1893 (Part 1): 1984 & 2016—Criteria for earthquake resistant design of structures—General provision and buildings
7. IS 2911 (Part 1): 2010—Code of practice for design and construction of pile foundations (Concrete piles)
8. Shore Protection Manual by U.S. Army Coastal Engineering Research Centre

The Effect of Saline Fluid on Hydraulic Properties of Clays



Koteswaraarao Jadda and Ramakrishna Bag

Abstract The effect of pore fluid concentration on the hydraulic conductivity of barrier material is one of the key factors which are considered in the long-term performance of a geological repository. The current study presents the effect of various NaCl concentrations on Atterberg limits and hydraulic properties of two bentonites and one kaolin clay. The results indicated that the liquid limit, shrinkage limit, and consolidation characteristics of bentonites such as compression index (C_c) and the time required for 90% of consolidation (t_{90}) were decreased significantly with an increase in salt concentrations. Similarly, the hydraulic conductivity and coefficient of consolidation (C_v) increased drastically with increase in salt concentrations; however, the significant impact was found for the high smectite bentonite. The experimental results showed that the hydraulic conductivity of the clays mainly depends on the particle arrangement rather than percentage of clay fraction and consolidation stress. For kaolin soil, both the liquid limit and shrinkage limit were found to be slightly increased up to 0.5 M NaCl, however, the effect was found to be decreased at further increase in concentrations, whereas hydraulic conductivity was found to be increased with increase in NaCl concentration. Further, the effect of molding water content on the consolidation characteristics of the clays was also investigated. The parameter compression ratio was used to evaluate the impact of initial moisture content on the compression index of the soil specimens. The hydraulic conductivity of the clays was noted to be increased at higher pore fluid concentration, due to the diminishing of the diffused double-layer thickness of clay minerals.

Keywords Bentonite · Kaolin · Compression index · Hydraulic conductivity · Saline fluid

K. Jadda (✉) · R. Bag
Indian Institute of Technology Patna, Patna, India
e-mail: Jadda.pce17@iitp.ac.in

© Springer Nature Singapore Pte Ltd. 2020
A. Prashant et al. (eds.), *Advances in Computer Methods and Geomechanics*, Lecture Notes in Civil Engineering 56,
https://doi.org/10.1007/978-981-15-0890-5_4

1 Introduction

Compacted clays have been used as potential buffer/backfill materials in most of the toxic waste disposal repositories due to their inherent properties of low permeability, high swelling potential, self-healing capacity, and good durability under disposal environments. During the long-term operation of a deep geological repository, the contaminants present in the buffer materials or infiltrated pore fluids from the surrounding geological strata may influence the hydromechanical properties of the compacted clays resulting in decreasing the efficiency of the buffer materials. Among all the hydromechanical properties of buffer materials, the hydraulic conductivity is the most important parameter involved in the assessment of contaminant migration in the subsurface and the design of barriers for hazardous waste control. For effective insulation, the barrier material should fulfill some desired specifications such as saturated hydraulic conductivity which should be in the range of 10^{-8} – 10^{-10} m/s and the swelling pressure should be more than 1 MPa [15, 16].

The effect of various salt concentrations on the liquid limit and hydraulic conductivity of different soil–bentonite mixtures was studied by Mishra et al. [9]. The hydraulic conductivity of GMZ bentonites by using different electrolyte concentrations of NaCl and CaCl_2 was studied by Zhu et al. [23]. Similarly, Singh and Prasad [14] reported the effect of ferric chloride and humic acid on the various engineering properties of barrier materials such as differential free swell index, swelling pressure, and hydraulic conductivity of the clays. Ismeik et al. [6] investigated the effect of seawater concentration on the various geotechnical properties of fine-grained soils. Dutta and Mishra [4] reported the effect of heavy metals concentration on the consolidation characteristic of compacted bentonites. The study suggested that C_C , m_v , and t_{90} of bentonites decreased with increases in salt concentration. Tiwari and Ajmera [21] evaluated the effect of saline fluid on compressibility characteristic of various clay minerals. The study suggested that the effect of NaCl solution was significant in montmorillonite clays as compared to illite and kaolinite clays. Sridharan et al. [19] reported that the increases in the pore fluid concentration cause a decrease in free swell index capacity for the smectite-type clay whereas it was found to be increased for kaolinite-type clays. The temperature effect on the swelling pressure and consolidation characteristics of the soils were studied by Bag and Rabbani [1]. Ören and Akar [11] investigated the effect of landfill leachates on the swelling and hydraulic conductivity of bentonites. The study reported a decrease in the free swell capacity of bentonites with increasing leachates concentration whereas the hydraulic conductivities of bentonites was not affected by the leachates concentration. Thyagaraj and Rao [20] and Chen et al. [3] examined the effect of salinization and desalinization cycles on the osmotic swelling and consolidation characteristic of compacted clays. Siddiqua et al. [13] investigated the effect of pore fluid chemistry on the various geotechnical properties of the barrier materials such as hydraulic conductivity and swelling pressure and stiffness. The study found that hydraulic conductivity increases with

electrolyte concentration whereas it decreased with effective montmorillonite dry density. Fan et al. [5] investigated the consolidation characteristics of the sand/clay–bentonite used as backfill materials. The study presented that the effect of sand grain size does not show any significant effect on the compression index and hydraulic conductivity. Komine [8] proposed theoretical equations to evaluate the hydraulic conductivities of buffer and backfilling materials.

Several studies focused on the effect of pore water chemistry on the stiffness and hydraulic conductivity of the clays, however, the impact on the various clay minerals is not very clear. In the current study, the effect of saline fluid concentration on the hydraulic properties of three clays, having different mineralogical characteristics such as Na–bentonite (high smectite content), Ca–bentonite (medium smectite content), and kaolin clay were investigated.

2 Materials and Methodology

2.1 Materials

Commercially available two types of bentonites and one kaolin clay were used in the present study. All the soils were procured from Rajasthan, India. For further discussion, these two bentonites are referred to as bentonite-A and bentonite-B. The basic engineering properties of the clays such as specific gravity, Atterberg limits, and particle size distribution were determined by following Indian Standard (IS) Soil Classification System IS 2720 (Part 3, 1980), IS 2720 (Part 4, 1985), and IS 2720 (Part 5, 1985), respectively. For all the soils used for this study, the percentage of clay fraction was determined from hydrometer analysis. The grain size distribution of the soils is presented in Fig. 1. Here, bentonite-A, bentonite-B, and kaolin have 76%, 82%, and 33% of clay fractions, respectively.

The total specific surface area (SSA) of the soil was determined by using the EGME method [2]. The total cation exchange capacity of the bentonites was determined by using the ammonium acetate method [12]. Cation exchange results suggested that bentonite-A was dominated by sodium cations whereas bentonite-B contains more divalent cations. Therefore, bentonite-A is referred to as Na-type bentonite whereas bentonite-B is classified as Ca-bentonite. The smectite content of the clay was determined as per ASTM C837-09 (2009). The physical properties of the materials used in the current study are listed in Table 1.

In order to find out the specific volume of the clays, the self-compacting dry density of specimens was determined by using the Archimedes principle. After completion of the shrinkage limit test, the dry soil pads were used to determine the dry density of the specimen. The dry density (ρ_d) of the specimen was calculated using Eq. 1.

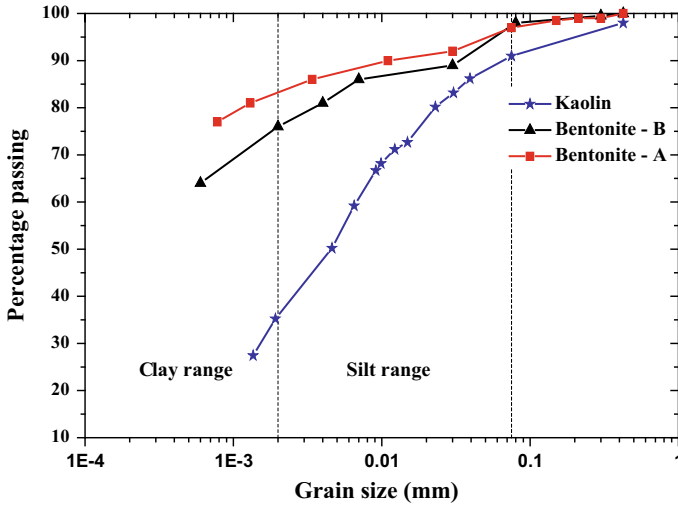


Fig. 1 The grain size distribution of the clays used in the current study

Table 1 Physicochemical properties of the clays used in the current study

Property	Bentonite-A	Bentonite-B	Kaolin
Specific gravity	2.76	2.64	2.62
Liquid limit (%)	220	172	44
Plastic limit (%)	43	52	23
Shrinkage limit (%)	12	26	19
Clay fraction (%)	76	82	33
Cation exchange capacity (meq/100)	65	48	9
Smectite content (%)	76	42	–
Specific surface area (m ² /g)	386	520	58
Soil classification	CH	CH	CI

$$\rho_d = \frac{m_a}{m_a - m_f} \times \rho_f \tag{1}$$

where ρ_f is the density of the immersion liquid (mercury); m_a is the mass of soil specimen in the air; m_f is the mass of soil specimen in mercury (nonpolar liquid).

The measured dry densities of the clays were 1.92, 1.41, and 1.71 Mg/m³ for bentonite-A, bentonite-B, and kaolin, respectively. Due to the higher specific gravity self-compacting capacity of bentonite-A was found to be higher. Similarly, due to the high specific surface area bentonite-B possesses higher specific volume and less self-compaction density.

2.2 Methodology

Free swell void ratio (FSVR) of the clays is defined as the ratio of the swell volume of the void space that is occupied by the expansive clays under no-load condition to the volume of dry clay solids [7]. The free swell void ratio of the clays depend on the type of exchangeable cations, mineralogical compositions, and the type of pore fluid used. In order to measure the free swell voids ratio of clays, about 2 gm of the soil was taken in a graduated 100 ml glass jar and approximately 80 ml of DI water to the soil. Soil particles stuck to the walls of the cylinder were washed with salt solutions and filled up to 100 ml mark. After 24 h of duration, the free swelling volume was noted as V_f . To evaluate the effect of salt concentration on the free swell void ratio, the similar tests were repeated with (0.1, 0.5 and 1 M) concentrations of the NaCl.

The free swell void ratio (e_f) of the bentonites was calculated from Eq. 2.

$$e_f = \left[\frac{\gamma_w G_c V_f - W_c}{W_c} \right] \quad (2)$$

where W_c is the weight of clay, G_c is the specific gravity of clay, and γ_w is the specific gravity of water.

In order to conduct liquid limit tests for fine-grained soils such as clay soils, the dry soil samples were mixed with different moisture contents of water or electrolyte fluids. The clay–water mixtures were placed in airtight plastic bags and these bags were kept in a desiccator to control the moisture exchange from the external environment. After equilibration of 7 days, the soil specimens were taken out from the desiccator and used for performing liquid limit tests. The liquid limit of the clays was determined by using cone penetration method. For shrinkage limit tests, the bulk volume of the soils was measured using a standard mercury displacement method (IS: 2720 Part 6, 1972). To find the significance of NaCl concentration on the liquid limit and shrinkage limit, similar tests were repeated with various pore fluid concentrations such as 0.1, 0.25, 0.5, and 1 M of NaCl.

The effect of saline solution concentration on the stiffness and hydraulic conductivity of the clays were evaluated by using oedometer tests. The oedometer tests were carried out at different concentrations such as 0.1, 0.5 and 1 M of NaCl. The oedometer tests were performed according to the Indian Standard Code IS 2720-15 (1965). After performing the liquid limit tests, the same soil paste was used for oedometer soil specimen preparation, by maintaining the targeted water content of 1.1 time's liquid limit (LL). The required quantity of the clay paste was carefully transferred to oedometer rings. In order to remove air bubbles in the soil paste, the oedometer ring along with soil samples was pressed and tamped. The soil specimen size of 60 mm diameter and 20 mm height was compacted in the oedometer ring. In order to provide double drainage condition, two porous stones along with filter papers were placed on both sides of the soil specimen. The vertical

consolidation stress starts with initial stress of 5 kPa and applied up to 800 kPa with increment ratio of 1.

The change in the void ratio due to overburden pressure was calculated from Eq. 3:

$$\Delta e = \frac{\Delta H}{H}(1 + e_0) \quad (3)$$

where Δe and ΔH are the change in void ratio and change in height of the specimen to each of the corresponding load increments; H and e_0 are the initial height and initial void ratio of the soil specimens.

The coefficient of volume compressibility, the coefficient of consolidation, and saturated hydraulic conductivity (k) of the soils were calculated from Eqs. 4, 5, and 6, respectively,

$$m_v = \frac{a_v}{1 + e_0} \quad (4)$$

$$c_v = \frac{T_v H^2}{t_{90}} \quad (5)$$

$$k = c_v m_v \gamma_w \quad (6)$$

where a_v is the coefficient of compressibility, C_v is the coefficient of consolidation, and γ_w is the unit weight of pore water pressure. The settlement of the soil samples corresponding to various time intervals is recorded by using LVDT. The change in displacement of the samples was measured with a precision of 0.001 mm. The coefficient of consolidation (C_v) was evaluated by using Taylor's square root time (\sqrt{T}) method.

3 Results and Discussions

The effect of NaCl concentrations on the free swell void ratio and liquid limit of the clays were presented in Fig. 2a. The effect of salt concentration on the shrinkage limit of the clays was presented in Fig. 2b. The free swell void ratio of bentonite-A, bentonite-B, and kaolin was found to be 27, 14, and 7.7, respectively. The results showed that the impact of the saline fluid was significant in case of the bentonite having high smectite content; for bentonite-A, both the liquid limit and free swell void ratio were drastically decreased with increase in salt concentration. For both the bentonite-B and kaolin, irrespective of the salt concentration free-swell void ratio was found to be constant. Whereas for the bentonite-B, the liquid limit was decreased linearly with increase in salt concentration, in case of kaolin liquid limit was slightly increased up to 0.5 M of NaCl concentration, subsequently, for higher

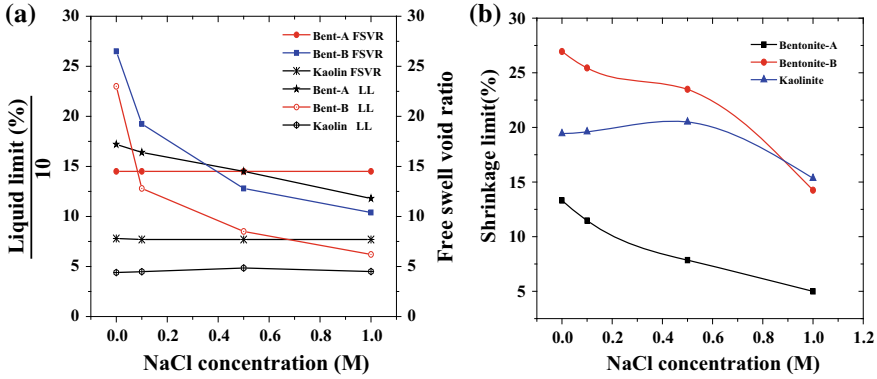


Fig. 2 a The effect of salt concentration on the free swell void ratio and liquid limit of clays; b the effect of salt concentration on the shrinkage limit of the clays

concentrations, the value was found to be decreased. Therefore, the self-healing capacity of the barrier materials decreased when exposed to higher salt concentration.

According to Gouy–Chapman theory, the diffuse double layer repulsion is inversely proportional to the square root of the electrolyte concentration [18].

$$\theta = \sqrt{\frac{\epsilon_0 k R T}{2 F^2 C v^2}} \quad \theta \propto \frac{1}{\sqrt{C}} \quad (7)$$

where θ is the Debye length (m), C is the pore fluid concentration, T is the absolute temperature, k is the relative permittivity of the pore fluid, R is the universal gas constant (8.134 J/mol.K), and F is Faraday’s constant. Equation 7 suggested that Debye length is inversely proportional to the square root of the pore fluid concentration and valency of exchangeable cations present in the clays. In the current study, bentonite-A contained sodium as a predominant cation; thus it possesses higher free swell capacity. The free swell void ratio of bentonite-A was significantly decreased with increase in NaCl concentration whereas for bentonite-B and kaolin, it was found to be constant irrespective of the salt concentration. Therefore, it is difficult to quantify the impact of the pore fluid concentration on the diffused double layer thickness of the clays. The increase in electrolyte concentration causes more flocculation occurred in the crystal lattice of high smectite clays leading to decrease in the total surface area and the absorbed water resulting in decrease in the swell void capacity and the liquid limit.

The shrinkage properties of the clays play a significant role in the performance of the buffer materials. The clays with low shrinkage limit are considered as a good barrier material. Basically, the soil having the higher plasticity index possesses low shrinkage limit. In the current study, both the plasticity index as well as the shrinkage limit of bentonite-B were found to be much higher as compared to kaolin.

It indicates that the shrinkage limit of the soils does not depend upon the plasticity characteristics, and that it primarily depends on the relative grain size distribution of the soil; similar observations made by Sridharan and Prakash [17]. Bentonite-B has a more specific surface area which leads to high micro/mesoporous voids; hence, it possesses the highest shrinkage limit compared to other soils. For all the soils, the shrinkage limit was decreased with increased NaCl concentration, this phenomenon is due to the addition of salt solutions to the clays attributed to bringing the soil particles closer and obtaining a flocculating structure which led to denser clay matrices.

The time versus settlement curves for the various clay soils is presented in Fig. 3. The results showed that both the bentonite-B and kaolin clays possess rapid initial settlement and reach 90% of consolidation (t_{90}) rapidly. For bentonite-A, progressive settlement occurred and the t_{90} values were measured to be much higher than that of the other clay soils. The time required for 90% of consolidation of the clay soils is subjected to effective stress from 10 to 800 kPa which are listed in Table 2. The results showed that irrespective of the consolidation stress, bentonite-A possesses higher t_{90} values. Although bentonite-B contains higher clay fraction, it possesses higher repulsive pressure to any corresponding dry density (observed from e - $\log(p)$ curve); the t_{90} values were found to be much lower as compared to bentonite-A. It can be said that the t_{90} values depend on the particle arrangement and pore size distribution of the clays. The bentonite-A has a higher amount of smectite subjected to a high thickness of the diffused double layer. Although bentonite-B has more specific surface area associated large amount of micro-voids, contains less amount of smectite mineral thus the thickness of the double layer is lower. When the external stress is applied to bentonite-B, the large

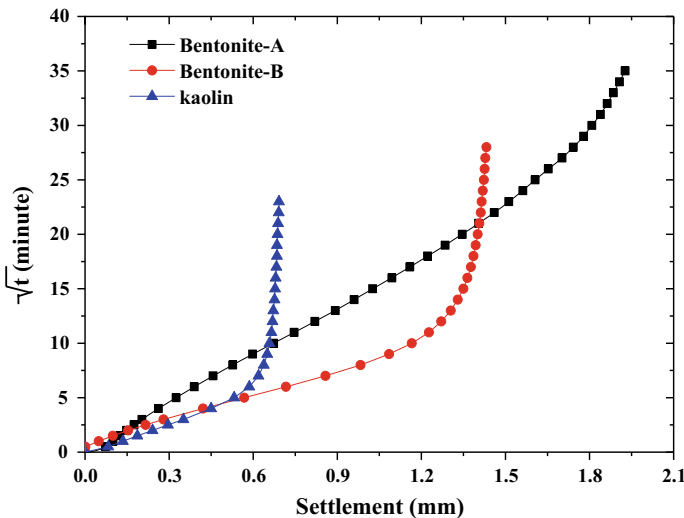


Fig. 3 Typical time settlement curves for different clays for 10 kPa stress by using DI water

Table 2 The time required for 90% of consolidation of the clay soils subjected to effective stress from 10 to 800 kPa

Type of soil	Bentonite-A	Bentonite-B	Kaolin
Consolidation stress (kPa)	Time required for 90% consolidation (min.)		
10	2485	384	58
20	2389	247	29
50	2285	156	19
100	1989	95	12
200	1486	75	9
400	1211	54	8
800	986	45	7

amount of the micro-porous is subjected to rapid settlement subjected to lower t_{90} values. In all the cases, the volume compressibility (m_v) was found to be increased at the initial phase of the loading and decreased to the subsequent loads. As the salt concentration increased, the time required for 90% of consolidation (t_{90}) was decreased whereas the coefficient of consolidation (C_v) significantly increased.

The initial water content plays a significant role in the compression index of the soils. In order to eliminate the effect of initial water content on the compression index, the parameter compression ratio (CR) was used. The compression ratio is the ratio of compression index and initial specific volume [10]. The current experimental results suggested that both the compression index and compression ratio values were slightly decreased with an increase in the pore fluid concentration due to an increase in the NaCl concentration from zero to 1 M; CR values were noticed to decrease from 0.29 to 0.23 for bentonite-A whereas for bentonite-B, it was found to decrease from 0.24 to 0.22. For kaolin, the CR value was noticed to decrease from 0.16 to 0.13. Nagaraj et al. [10] reported that for highly compressible clays, the compression ratio would be relatively close to constant.

The magnitude of the decrease in the void ratio due to the consolidation stress was found to be higher for bentonite-A than that of bentonite-B and kaolin. In the presence of DI water, the compression index values for bentonite-A, bentonite-B, and kaolin were noted as 1.49, 1.14, and 0.26, respectively. The effect of salt concentrations on the consolidation characteristics of the clays was presented in Fig. 4a. The compression index for bentonite-A decreased from 1.49 to 0.62 to the corresponding salt concentration from zero (DI water) to 1 M of NaCl. Similarly, for bentonite-B and kaolin, the compression index values varied from 1.14 to 0.83 and 0.35 to 0.28, respectively. The results indicated that the percentage of decrease in the compression index was maximum for bentonite-A which is about 57%, followed by bentonite-B and kaolin about 27% and 20%, respectively. The effect of salt concentrations on the hydraulic conductivity of the clays was presented in Fig. 5. The saturated hydraulic conductivity of the soils is a monotonic function of its dry density; in a semilogarithmic plane, the hydraulic conductivity of the soils varies linearly with the dry density. The results suggested that for a given dry

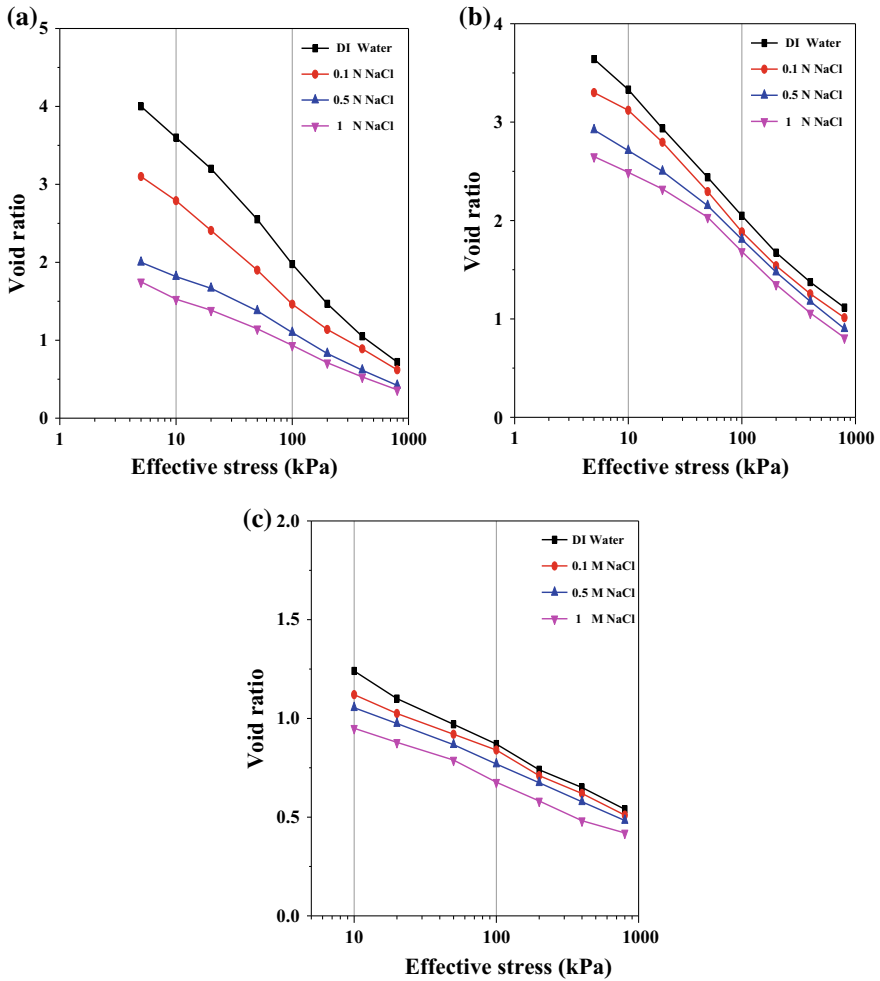


Fig. 4 The e - $\log(p)$ plots for the clay soils **a** bentonite-A; **b** bentonite-B; **c** kaolin

density, the hydraulic conductivity of bentonite-A was found to be minimum in the range of 5.5×10^{-9} – 3×10^{-11} with the corresponding dry density between 0.7 and 1.5 Mg/m^3 . Similarly, the kaolin clay possesses higher hydraulic conductivity of about 1×10^{-8} to the corresponding dry density of 1.76 Mg/m^3 .

The DI water as a pore fluid and for the total consolidation stress of 1.6 MPa the dry density attained by bentonite-A, bentonite-B and kaolin were measured to be 1.6, 1.45 and 1.78 Mg/m^3 , respectively. The results suggested that for obtaining the same dry density, bentonite-B required more consolidation stress. The contrasting results were found in the study for a given dry density where bentonite-B possesses more swelling pressure as well as higher hydraulic conductivity as compared to

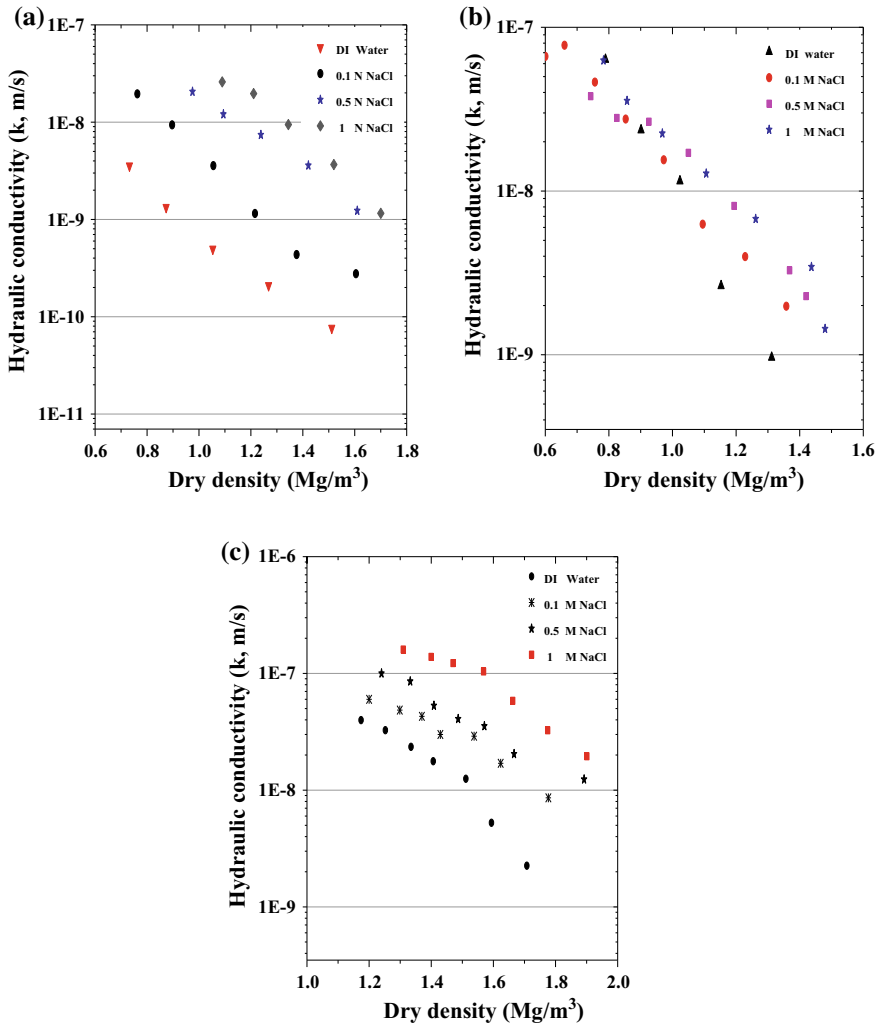


Fig. 5 The hydraulic conductivity versus dry density plots for the clay soils **a** bentonite-A; **b** bentonite-B; **c** kaolin

bentonite-A. Therefore, it can be concluded that the soil structure plays more important role in the hydraulic conductivity of the soils. In order to study the microstructure of clays, scanning electron microscope study was conducted for both the bentonite samples after performing the oedometer tests for DI water conditions; the results are presented in Fig. 7. The microstructure of bentonite-A showed a flocculated structure with equidimensional flakes that have a film-like appearance, whereas, bentonite-B indicates dispersive structure with needle-like poorly distinct, broken structure. Therefore, bentonite-A possesses lower hydraulic conductivity.

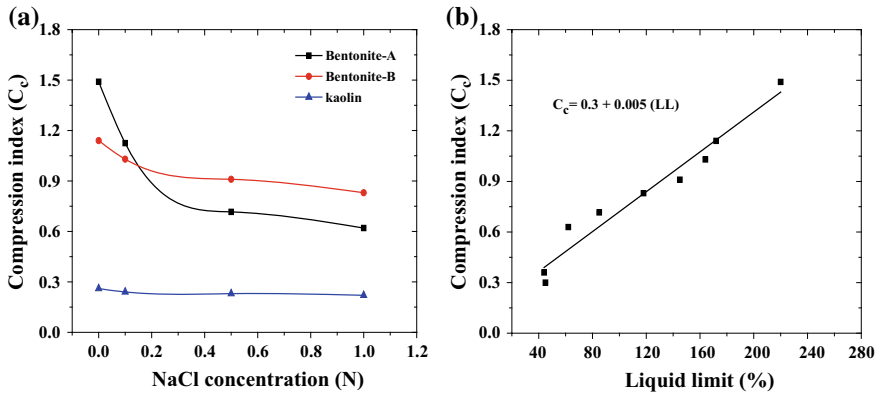


Fig. 6 a The C_c versus NaCl salt concentration plots for clays; b the liquid limit versus compression index of clays

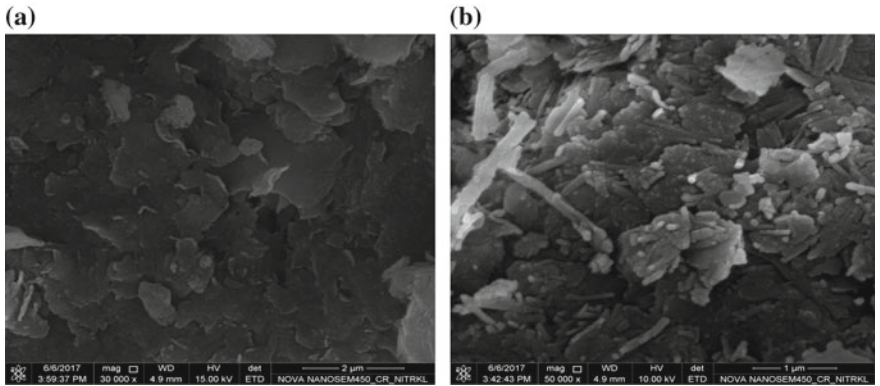


Fig. 7 The FESEM images of the bentonites a bentonite-A; b bentonite-B

The effect of the salt concentration on the hydraulic conductivity was found to be maximum for bentonite-A, whereas, for bentonite-B and kaolin, the effect was found to be marginal. The hydraulic conductivity of the clays was increased with the pore fluid concentration due to the diminishing of the diffused double-layer thickness of the clay minerals [22]. For a given dry density as the salt concentration increased from zero (DI) to 1 molarity, the k value was found to decrease about 100 times for bentonite-A. Whereas for bentonite-B and kaolinite, the hydraulic conductivity values were marginally decreased. The effect of salt concentration was marginal for kaolinite type of clays due to their small diffused double-layer thickness and the presence of stronger hydrogen bond in the crystal lattice. The results indicate that both Ca–bentonite and kaolin have the maximum endurance against the salt concentration. Based on the test results, the relationship between

compression index and liquid limit of the clays is shown in Fig. 6b. The results indicate that both the liquid limit and compression index of the clays are linearly correlated.

SKB report (2004) suggested that the basic criteria for buffer materials are that they should possess swelling pressure of more than 1 MPa and the hydraulic conductivity should be less than 10^{-9} m/s. From the current experimental study, it was observed that both the bentonites meet the basic standards for engineered barriers in terms of hydraulic conductivity. However, in the presence of the salt concentration, the hydraulic conductivity of bentonite-A was drastically increased; hence for the barrier material to be used in the coastal region, a higher density of bentonites is recommended. Although bentonite-B had higher endurance capacity against the salt concentration and also possessed higher k values, for higher dry densities, both the bentonites are recommended as a good barrier material.

4 Conclusions

The current study evaluated the effect of NaCl concentration on the Atterberg limits, free swell capacity, and hydraulic conductivity of two Indian bentonites and kaolin clay. The results suggest that the shrinkage limit of the clays does not depend on the plasticity characteristics; it primarily depends on the pore size distribution of the clays. Due to increase in salt concentration, both the liquid limit and shrinkage limit of the bentonites were found to be decreased whereas for kaolin, it was found to be slightly increased up to 0.5 M NaCl upon that decreases at higher salt concentrations. The experimental results revealed that the salt concentration has a significant effect on the hydraulic conductivity of Na-bentonite containing high smectite content whereas for bentonite with low smectite and kaolin, it does not show any significant effect. For the same consolidation stress, bentonite-A attained higher dry density and possesses low permeability values whereas for bentonite-B, it was found to be the opposite. According to the DDL theories, the thickness of the DDL decreases as the saline concentration increases resulting in increases in the effective pores' size. Therefore, the hydraulic conductivity increases with increase in the pore fluid concentration. The study found a good correlation between the compression index and the liquid limit of the clays.

References

1. Bag R, Rabbani A (2017) Effect of temperature on swelling pressure and compressibility characteristics of soil. *Appl Clay Sci* 136:1–7
2. Cerato AB, Lutenegeger AJ (2002) Determination of surface area of fine-grained soils by the ethylene glycol monoethyl ether (EGME) method. *Geotech Test J* 25(3):315–321

3. Chen YG, Zhu CM, Ye WM, Cui YJ, Wang Q (2015) Swelling pressure and hydraulic conductivity of compacted GMZ01 bentonite under salinization-desalinization cycle conditions. *Appl Clay Sci* 114:454–460
4. Dutta J, Mishra AK (2017) Consolidation behavior of compacted bentonites in the presence of heavy metals. *J Hazard Toxic Radioact Waste* 21(04017003):1–8
5. Fan RD, Du YJ, Liu SY, Chen ZB (2014) Compressibility and hydraulic conductivity of sand/clay–bentonite backfills. In: Reddy KR, Shen SJ (eds) *Geo-Shanghai*
6. Ismeik M, Ashteyat AM, Ramadan KZ (2013) Stabilisation of fine-grained soils with saline water. *Eur J Environ Civ Eng* 17:32–45
7. Kenney TC, Van Veen WA, Swallow MA, Sungaila MA (1992) Hydraulic conductivity of compacted bentonite–sand mixtures. *Can Geotech J* 29(3):364–374
8. Komine H (2008) Theoretical equations on hydraulic conductivities of bentonite-based buffer and backfill for underground disposal of radioactive wastes. *J Geotech Geoenviron Eng* 134:497–508
9. Mishra AK, Ohtsubo M, Li LY, Higashi T, Park J (2009) Effect of salt of various concentrations on liquid limit, and hydraulic conductivity of different soil-bentonite mixtures. *Environ Geol* 57:1145–1153
10. Nagaraj TS, Joshi RC, Srinivasa Murthy BR (1988) Generalized equation for compression Ratio. *J Test Eval* 16(1):86–89
11. Ören AH, Akar RÇ (2017) Swelling and hydraulic conductivity of bentonites permeated with landfill leachates. *Appl Clay Sci* 142:81–89
12. Rao SM, Ravi K (2013) Hydro-mechanical characterization of Barmer 1 bentonite from Rajasthan, India. *Nucl Eng Des* 265:330–340
13. Siddiqua S, Blatz J, Siemens G (2011) Evaluation of the impact of pore fluid chemistry on the hydromechanical behaviour of clay-based sealing materials. *Can Geotechn* 48:199–213 (NRC Research Press)
14. Singh S, Prasad A (2017) Influence of ferric chloride and humic acid on bentonite as clay liner. *Int J Geotech Eng* 4(1):45–53
15. SKB (2004) Interim main report of the safety assessment SR-Can. SKB technical report TR-04-11, Swedish nuclear fuel Management Company limited, Stockholm, Sweden
16. Souli H, Fleureau JM, Trabelsi Ayadi M, Besnard M (2008) Physicochemical analysis of permeability changes in the presence of zinc. *Geoderma* 145:1–7
17. Sridaran A, Prakash K (2000) Shrinkage limit of soil mixtures. *Geotechn Test J* 23(1):3–8 (ASTM)
18. Sridharan A, Jayadeva MS (1982) Double layer theory and compressibility of clays. *Géotechnique* 32(2):133–144
19. Sridharan A, Rao SM, Joshi S (1990) Classification of expansive soils by sediment volume method. *Geotech Test J* 13:375–380
20. Thyagaraj T, Rao SM (2013) Osmotic Swelling and osmotic consolidation behaviour of compacted expansive clay. *Geotech Geol Eng* 31:435–445
21. Tiwari B, Ajmera B (2014) Effects of saline fluid on compressibility of clay minerals. *Environ Geotechn* 1:108–120
22. Tripathy S, Bag R, Thomas HR (2014) Effects of post-compaction residual lateral stress and electrolyte concentration on swelling pressures of a compacted bentonite. *Geotech Geol Eng* 32:749–763
23. Zhu CM, Ye WM, Chen YG, Chen B, Cui YJ (2013) Influence of salt solutions on the swelling pressure and hydraulic conductivity of compacted GMZ01 bentonite. *Eng Geol* 166:74–80

Influence of Shape of Cross Section on the Load–Settlement Behaviour of Strip Footings



J. Jayamohan, P. Sajith, Shilpa Vijayan, Anusha Nair, S. Chandni and Akhila Vijayan

Abstract The bearing capacity of footings has been extensively studied, both theoretically and experimentally over the past decades. In all the type of footings except shell foundations, the shape of the cross section adopted is rectangular and the base has been considered as a plane surface. The pattern of soil movement beneath the footing during loading is a significant factor contributing to the load–settlement behaviour. By altering the shape of the cross section of the footing, it would be possible to provide better confinement of underlying soil thereby improving the load–settlement behaviour. This paper investigates the influence of the shape of the cross section of the footing on its behaviour. The different shapes of the cross section of footing adopted for the study are sloped cross section, curved cross section and rectangular cross section with vertical flanges. A series of non-linear finite element analyses are carried out with the FE software PLAXIS 2D and the results are validated by carrying out laboratory scale load tests and comparing the results. It is observed from the results that the load–settlement behaviour of the footings can be significantly improved by altering the shape of the cross section. The improvement is significant when the shape of the cross section is Curved or Rectangular with flanges. The optimum length of flanges is observed to be 20% of the width of the footing.

Keywords Shape of cross section · Footing · Load–settlement behaviour · Finite element analyses

J. Jayamohan (✉) · P. Sajith · S. Vijayan · A. Nair · S. Chandni · A. Vijayan
LBS Institute of Technology for Women, Thiruvananthapuram, India
e-mail: jayamohan7@gmail.com

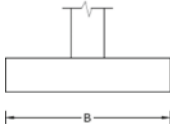
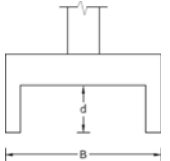
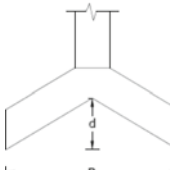
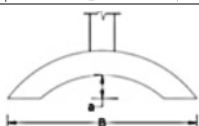
© Springer Nature Singapore Pte Ltd. 2020
A. Prashant et al. (eds.), *Advances in Computer Methods and Geomechanics*, Lecture Notes in Civil Engineering 56,
https://doi.org/10.1007/978-981-15-0890-5_5

1 Introduction

The foundation transmits the load of the structure safely to the ground, without undergoing any shear failure or excessive settlement. Extensive analytical and experimental investigations have been carried out by researchers in the past decades. Prandtl [11] and Reissner [12] initiated the analytical approach and Terzaghi [16] developed the bearing capacity theory considering the engineering parameters of soil. Later, many researchers [2, 3, 7, 9, 10, 13, 15] focused on a more realistic derivation of bearing capacity and various correction factors.

The load bearing capacity of a shallow footing is a classical soil engineering problem. The mechanism of soil failure is general shear failure for a surface footing [1]. It is reported that localized failure occurs for a buried footing [4–6, 17–19]. The ultimate bearing capacity of a deeply buried foundation is considerably larger than that of a shallow foundation [8, 18]. Ming and Radoslaw [20] proposed new shape factors for square and rectangular footings based on the elasto-plastic model of the soil and finite element analyses. Singh and Monika [14] carried out studies on Shell foundations of various shapes of the cross section. In all the types of footings; except shell foundations, the shape of the cross section is rectangular and the base has been considered as a plane surface. The pattern of soil movement beneath the footing during loading is a significant factor contributing to load–settlement

Table 1 Cross-sectional shapes of strip footings

Shape of footing		d/B
	Footing with rectangular cross section	–
	Rectangular cross section with flanges	0.2, 0.4, 0.6, 0.8
	Sloped cross section	0.2, 0.4, 0.6, 0.8
	Curved cross section	0.1, 0.2, 0.3, 0.4, 0.5

behaviour. By altering the shape of the cross section of the footing, it would be possible to provide better confinement of underlying soil thus improving the bearing capacity.

This paper presents the results of numerical and experimental studies carried out to investigate the influence of the shape of the cross section on the load–settlement behaviour of strip footing. A series of non-linear finite element analyses are carried out with the FE software PLAXIS 2D. The results of finite element analyses are validated by carrying out laboratory scale load tests and comparing the results. The different shapes of the cross section of the footing, shown in Table 1, are considered for the analyses.

2 Finite Element Analyses

A series of finite element analyses are carried out using the FE software *PLAXIS* 2D. The behaviour of soil can be modelled by the various constitutive models available in the software. In this study, the soil behaviour is modelled with the Mohr–Coulomb model. This non-linear model mainly uses the basic soil parameters like angle of shearing resistance and cohesion intercept. Plane strain model is adopted in the analyses since strip footing is studied.

The footing is taken as rigid in the analyses. Since the footing is rigid, its settlement is simulated using the prescribed displacement model in the software. At the bottom boundary, both vertical and horizontal displacements are restricted. At the vertical boundaries, the horizontal movement alone is restricted. 15-node triangular elements are used to model the soil. In all the simulations, medium mesh size is used. The width of the model strip footing (*B*) is taken as 100 mm and the dimensions of soil mass are taken as 10*B* in all analyses. The footing and the confining walls are modelled using plate elements. To simulate the interaction between the footing and underlying soil, an interface element is provided at the bottom surface of the footing. The geometric model and pattern of soil movement after loading is shown in Fig. 1. The soil is modelled using 15-node triangular elements. Properties of locally available sand and clay are adopted in the analyses.

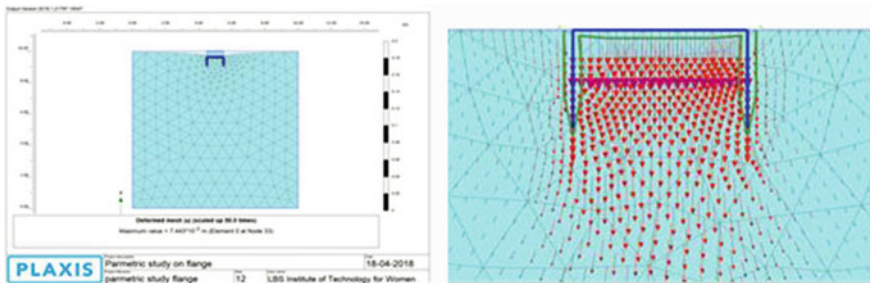


Fig. 1 Geometric model for finite element analyses and pattern of soil movement after loading

3 Laboratory Scale Load Tests

Laboratory scale load tests are carried out on model strip footings of various shapes of cross section, fabricated with mild steel. The width of the model strip footings for all cases is 100 mm. Model strip footings with a flat base and various cross sections are shown in Fig. 2.

The load tests are conducted in a combined test bed and loading frame assembly. The test beds are prepared in a tank which is designed keeping in mind the size of the model footing to be tested and the zone of influence. The dimensions of the test tank are 1000 mm length \times 750 mm width \times 750 mm depth. The width of the model strip footings is taken as 100 mm. The loading tests are carried out in a loading frame fabricated with ISMB 300. The load is applied using a hand-operated mechanical jack of capacity 50 kN. The applied load is measured using a proving ring of capacity 10 kN. The settlement of the model strip footing is measured using two dial gauges kept diametrically opposite each other. The model strip footing is placed exactly beneath the centre of the loading jack to avoid eccentric loading.

In all the tests, the base at the middle of the model strip footing is kept at the soil surface. The soil surface is prepared and compacted according to the shape of the cross section and then the model footings are placed. In the case of model footings with flanges, the sand surface is prepared flat and the footing is driven down with a hammer. The details of the test setup and a photograph are shown in Fig. 3. The soil used in laboratory model tests is locally available sand. Its properties are given in Table 2.

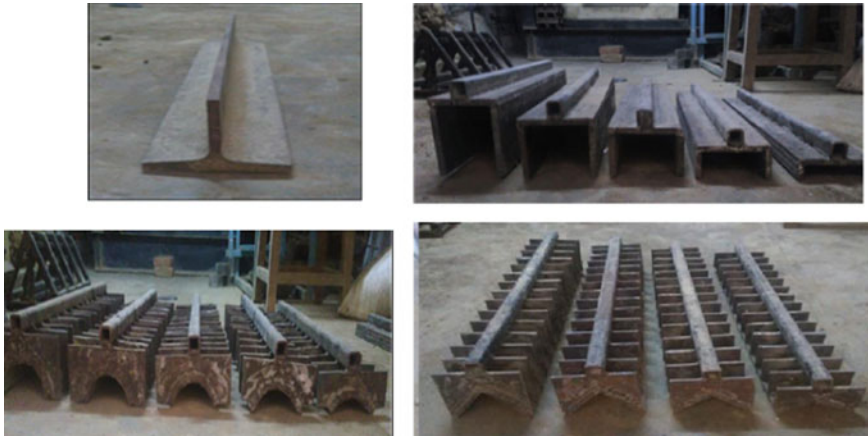


Fig. 2 Model strip footings with flat base, with flanges, curved cross section and sloping cross section with various (d/B)

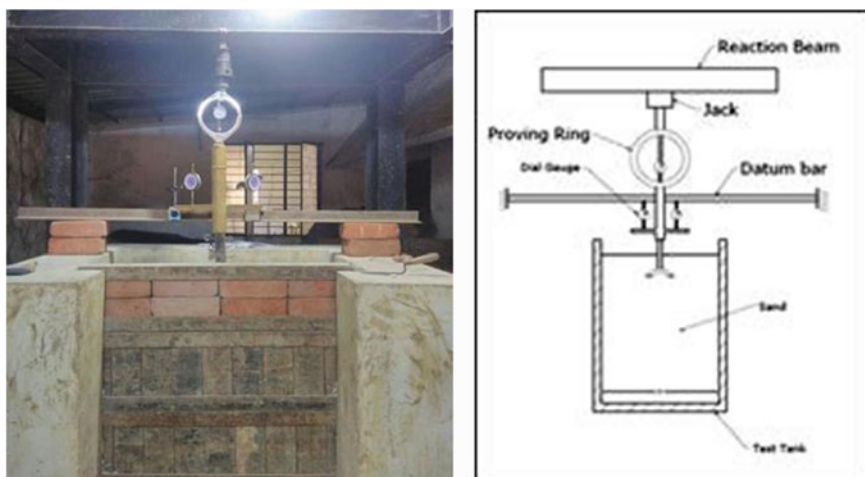


Fig. 3 Details of the test setup

Table 2 Properties of sand

Properties	Sand
Specific gravity	2.65
Friction angle (ϕ°)	31.2
Cohesion (kPa)	0
Dry unit weight (kN/m^3)	16
Effective grain size D10 (mm)	0.15
D60 (mm)	0.60
D30 (mm)	0.30
Coefficient of uniformity C_u	4.00
Coefficient of curvature C_c	1.00
Permeability (m/s)	1.07×10^{-4}
IS classification	SP

4 Results and Discussions

The results obtained from finite element analyses and laboratory scale load tests are presented below.

4.1 Influence of Shape of Cross Section

Figure 4 presents the load–settlement behaviour of model footings of various cross sections when $(d/B) = 0.2$ and 0.4 , obtained from laboratory scale load tests. It is

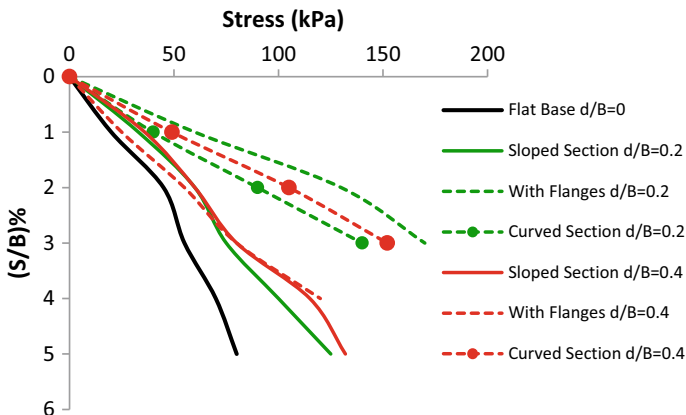


Fig. 4 Load–settlement behaviour of various shapes of cross section at $(d/B) = 0.2$ and 0.4 from laboratory model tests

observed that the load–settlement behaviour can be considerably improved by altering the shape of the cross section. At $(d/B) = 0.2$, footing with flanges shows the best load–settlement behaviour. However at $(d/B) = 0.4$, footings with curved cross section showed the best load–settlement behaviour.

4.2 Influence of Depth of Flange

Figure 5 presents the load–settlement behaviour of model strip footings with sloped cross section with various slopes, obtained from laboratory scale load tests and finite element analyses. It is observed that up to a settlement of 2%, model footing with $(d/B) = 0.4$ is showing better improvement. However at higher settlements, $(d/B) = 0.8$ is showing better results. The results of finite element analyses and laboratory model studies are in a reasonably good agreement up to a settlement of about 1.5%. For higher values of settlement, it underestimates the stress.

From Fig. 6, which presents the results of laboratory scale load tests and numerical analyses on model strip footings with flanges, it is observed that the improvement is maximum when the (d/B) ratio is 0.2. With the further increase in (d/B) ratio, the improvement comes down drastically and reaches a minimum when $(d/B) = 0.4$. With a further increase in (d/B) , there is an improvement in load–settlement behaviour.

The results obtained from laboratory scale load tests on model strip footings with a curved cross section with various curvatures are presented in Fig. 7. Finite element analyses could not be carried out for footings with curved cross section since

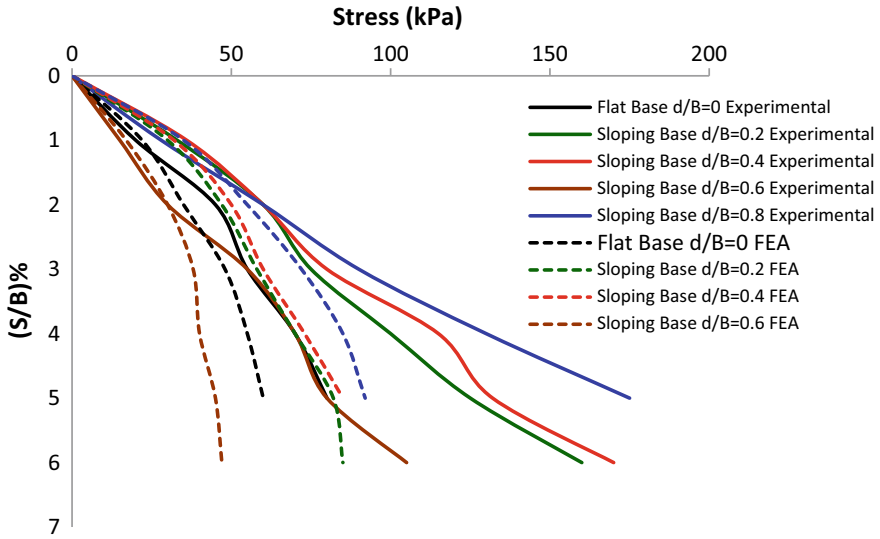


Fig. 5 Load–settlement behaviour of model strip footings with sloped cross section with various (d/B) ratios from laboratory scale load tests and FEA

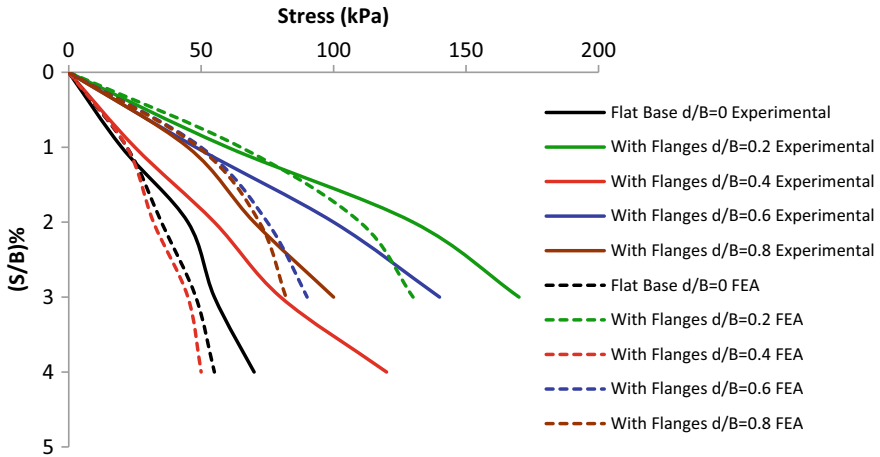


Fig. 6 Load–settlement behaviour of model strip footings with flanges with various (d/B) ratios from laboratory scale load tests and FEA

it is not possible to generate plates with curved cross section in PLAXIS 2D software. It is observed from the results of laboratory scale load tests that maximum improvement is attained when (d/B) is 0.3.

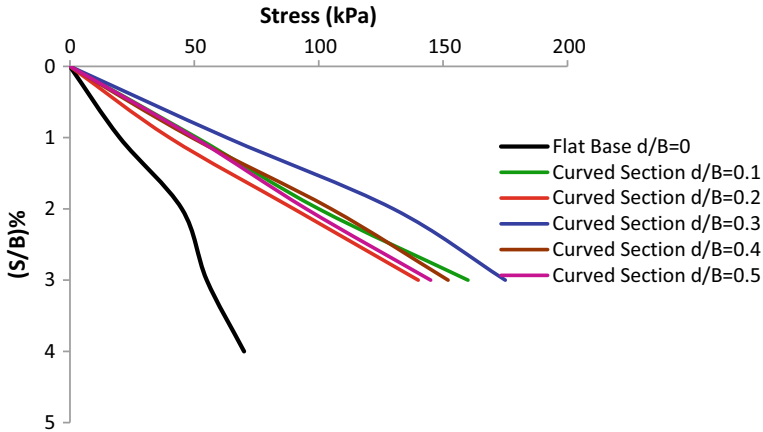


Fig. 7 Load–settlement behaviour of model strip footings with sloped cross section with various (d/B) ratios from laboratory scale load tests

4.3 Bearing Capacity Ratio

To quantify the influence of the shape of the cross section and (d/B) on load–settlement behaviour, the Bearing Capacity Ratio (BCR) at 3% settlement is presented in Fig. 8. Bearing Capacity Ratio is the ratio of Vertical Stress at 3% settlement of model footings with an altered cross section to the stress at the same settlement of model strip footing with a flat base.

It is seen from Fig. 8 that in all the shapes of the cross section of footings, there is an initial increase in BCR, followed by a decrease and a subsequent increase. It is inferred that as the slope/curvature/depth of flange of the cross section is increased, there occurs a change in the pattern of soil movement due to the applied loads and causes the change in BCR.

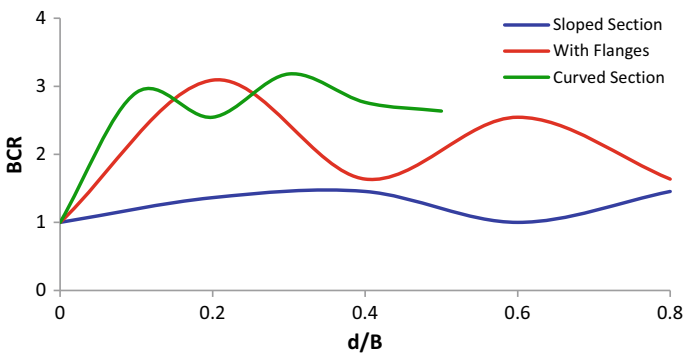


Fig. 8 Bearing capacity ratio of model footings of various cross sections, obtained from laboratory scale load tests

5 Conclusions

From the results of Finite element analyses, and laboratory scale load tests, the following conclusions are drawn.

- The load–settlement behaviour can be improved by altering the shape of the cross section of footings.
- The improvement in load–settlement behaviour depends on the geometrical parameters of the cross section.

References

1. Craig RF (2004) *Craig's soil mechanics*. Taylor & Francis, New York
2. Ericson HL, Drescher A (2002) Bearing capacity of circular footings. *J Geotech Geoenviron Eng ASCE* 128(1):38–43
3. Griffiths DV, Fenton Gordon A, Manoharan N (2002) Bearing capacity of rough rigid strip footing on cohesive soil: probabilistic study. *J Geotech Geoenviron Eng ASCE* 128(9):743–750
4. Hossain MS, Randolph MF (2009) New mechanism-based design approach for spudcan foundations on single layer clay. *J Geotech Geoenviron Eng* 1264–1274. [https://doi.org/10.1061/\(asce\)gt.1943-5606.0000054](https://doi.org/10.1061/(asce)gt.1943-5606.0000054)
5. Hossain MS, Randolph MF (2010) Deep-penetrating spudcan foundations on layered clays: centrifuge tests. *Géotechnique* 60(3):157–170
6. Hu Y, Randolph MF, Watson PG (1999) Bearing response of skirted foundation on non-homogeneous soil. *J Geotech Geoenviron Eng* 125(11):924–935. [https://doi.org/10.1061/\(asce\)1090-0241](https://doi.org/10.1061/(asce)1090-0241)
7. Lee J, Salgado R (2005) Estimation of bearing capacity of circular footing on sands based on CPT. *J Geotech and Geoenviron Eng ASCE* 131(4):442–452
8. Merifield RS, Sloan SW, Yu HS (2001) Stability of plate anchors in undrained clay. *Géotechnique* 51(2):141–153
9. Meyerhof G (1965) Shallow foundations. *J Soil Mech Found Div ASCE* 91(SM2):21–31
10. Michalowski Radoslaw L, Dawson ME (2002) Three-dimensional analysis of limit loads on Mohr-Coulomb soil. *Found Civil Environ Eng* 1(1):137–147
11. Prandtl L (1921) Über die Eindringungsfestigkeit (Härte) plastischer Baustoffe und die Festigkeit von Schneiden. *Zeit Angew Math Mech* 1:15–20
12. Reissner H (1924) Zum Erddruckproblem. In: *Proceedings of first international congress of applied mechanics*. Delft, pp 295–311
13. Salgado R, Lyamin AV, Sloan SW, Yu HS (2004) Two- and three-dimensional bearing capacity of foundation in clay. *Geotechnique* 54(5):297–306
14. Singh SK, Monika K (2016) Load carrying capacity of shell foundations on treated and untreated soils. In: *Indian geotechnical conference 2016, IIT Madras*
15. Taiebat HA, Carter JP (2000) Numerical studies of the bearing capacity of shallow foundation. *Geotechnique* 50(4):409–418
16. Terzaghi K (1943) *Theoretical soil mechanics*. Wiley, New York
17. Wang CX, Carter JP (2002) Deep penetration of strip and circular footings into layered clays. *Int J Geomech* 2(2):205–232. [https://doi.org/10.1061/\(asce\)1532-641](https://doi.org/10.1061/(asce)1532-641)

18. Zhang Y, Bienen B, Cassidy MJ, Gourvenec S (2012) Undrained bearing capacity of deeply buried flat circular footings under general loading. *J Geotech Geoenviron Eng* 385–397 [https://doi.org/10.1061/\(asce\)gt.1943-5606.0000606](https://doi.org/10.1061/(asce)gt.1943-5606.0000606)
19. Zhang Y, Wang D, Cassidy MJ, Bienen B (2014) Effect of installation on the bearing capacity of a spudcan under combined loading in soft clay. *J Geotech Geoenviron Eng* 04014029. [https://doi.org/10.1061/\(asce\)gt.1943-5606.0001126](https://doi.org/10.1061/(asce)gt.1943-5606.0001126)
20. Zhu M, Michalowski RL (2005) Shape factors for limit loads on square and rectangular footings. *J Geotech Geoenviron Eng ASCE* 131(2):223–231

Effect of Biopolymers on Soil Strengthening



Lekshmi P. Nair and K. Kannan

Abstract Kuttanad region is the largest agricultural area in the state of Kerala. Kuttanad clay is an important soil group, well-known for its low shear strength and high compressibility. The typical Kuttanad soil consists primarily of silt and clay fractions. The natural water content of the soil here is very high and close to the liquid limit. Since Kuttanad is the rice bowl of Kerala, any technique adopted in this region should be eco-friendly and should never cause any harm to the soil and water. This paper discusses the stabilization of Kuttanad clay using biopolymers. Two types of biopolymers were (Xanthan gum and Guar gum) used in this study due to their availability with reasonable prices and their stable behavior. A laboratory study was conducted on Kuttanad clay treated with Xanthan gum and Guar gum, and variation in soil properties was analyzed. The biopolymer was added in different concentrations so as to identify an optimum dosage. From various tests, it was observed that with the addition of Xanthan gum the optimum moisture content has decreased by about 7.4% and the Unconfined Compressive Strength has increased by 51.5% and with the addition of Guar gum, the optimum moisture content has decreased by 17.6% and the Unconfined Compressive Strength has increased by 59.5%.

Keywords Kuttanad clay · Xanthan gum · Guar gum · Compressive strength

1 Introduction

The treatment and usage of soil in construction is a long-standing technical field, dating to the beginning of human civilization. Soil is one of the most important materials used in a variety of construction projects including earth canals and earth dams.

L. P. Nair (✉) · K. Kannan

Department of Civil Engineering, Marian Engineering College, Thiruvananthapuram, India
e-mail: lekshmi.rpnair@gmail.com

K. Kannan

e-mail: kk260493@gmail.com

© Springer Nature Singapore Pte Ltd. 2020

A. Prashant et al. (eds.), *Advances in Computer Methods and Geomechanics*, Lecture Notes in Civil Engineering 56,
https://doi.org/10.1007/978-981-15-0890-5_6

Soil stabilization means the improvement of stability and bearing power of the soil by the use of controlled compaction, proportioning and/or the addition of suitable admixtures or stabilizers. The two primary methods that are conventionally applied to produce engineered soil are mechanical improvement and chemical treatment. Mechanical improvement involves physical processes to improve soil properties. This includes compaction, drainage, consolidation, and by other means. Chemical treatments use chemicals and emulsions as compaction aids, water repellents, and binders which initiate chemical reactions such as pozzolanic reactions or hydration inside the soil to create artificial binding.

As an alternative to such traditional soil treatment and improvement techniques, biological approaches are now being actively investigated in the field of geotechnical engineering, including microbe injection and by-product precipitation. Microbial induced polymers have been introduced as a new type of construction binder, especially for soil treatment and improvement [4]. This paper attempts to understand and evaluate the effect of the behaviors of two biopolymers, namely Xanthan gum and Guar gum in terms of engineering properties to Kuttanad clay. Different concentrations of both the biopolymers were used in this study and five effects on compaction characteristics and compressive strength were evaluated.

2 Materials and Experiments

2.1 Soil Properties

Kuttanad denotes the low lying land, comprising the Vembanad lake and its surrounding marshy land.

The typical soil of the Kuttanad region is soft black or gray marine clay. The natural water contents are very high and even close to the liquid limit. The soil is well-known for its high compressibility and low shear strength.

In this study, Kuttanad clay collected from Pallippad region, Alappuzha district was used. Samples were collected from a depth of about 2 m below the surface. The properties of the soil were determined as per IS 2720. The properties of Kuttanad clay are given in Table 1 and the grain size distribution curve is presented in Fig. 1.

2.2 Biopolymers

The biopolymers used in this study were chosen because of their availability at their reasonable prices compared to other biopolymers. Xanthan gum was procured from Kachabo Gums Pvt. Ltd, Maharashtra and Guar gum was procured from Swastik Gum Industries, Ahmedabad.

Table 1 Properties of Kuttanad soil

Property	Value
Specific gravity	2.06
Particle size range	
Clay (%)	46
Silt (%)	46.8
Sand (%)	7.2
Atterberg’s limits	
Liquid Limit, wL	67
Plastic limit, wp	54.7
Shrinkage limit, ws	24
Plasticity index, IP	12.3
Soil classification	MH
Unconfined compressive strength (kN/m ²)	59.6
Standard proctor compaction test	
Maximum dry density (g/cc)	1.2
Optimum moisture content (%)	32

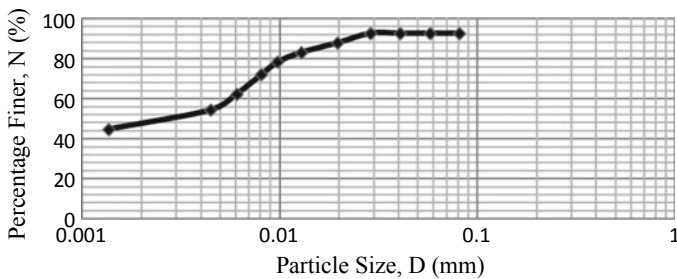


Fig. 1 Particle size distribution of Kuttanad soil

Xanthan gum is a polysaccharide that is made by the *Xanthomonas campestris* bacterium and is generally used as a viscosity thickener due to its hydrocolloid rheology. Xanthan gum has been introduced to geotechnical engineering to reduce the hydraulic conductivity of silty sand via pore filling as well as to increase the undrained shear strength of soil by increasing the liquid limit. Another recent study has reported possibilities for using Xanthan gum as soil strengtheners [1].

Guar gum is also a polysaccharide consisting of the galactose of sugars and mannose. The backbone in Guar gum is a linear chain of β 1, 4—linked mannose remains to which galactose residues are 1, 6—linked at every second mannose, creating short side branches. Guar gum is more solvable than many other biopolymers and is a better stabilizer [1].

2.3 Specimen Preparation

The soil was oven dried for 24 h. The biopolymers used in this study were processed as powders and mixed with water to produce gels which can act as stabilizers and binders. The powder was gently added to water to avoid clumping and then mixed until a homogenous solution was obtained. Biopolymer concentrations of 0.5, 1, 1.5, and 2% by weight were used in this study. The soil was mixed with the solution and tested for variation in properties.

2.4 Test Procedure

A modified Proctor Compaction test as per IS 2720 Part 7 was performed for determining the maximum dry density and its corresponding optimum moisture content. Unconfined compressive strength tests as per IS 2720 Part 10 were performed on soil–biopolymer specimens. The specimen for the test had a diameter about 3.9 cm and length of 7.5 cm. As per the mentioned standard, the loading speed should be about 0.5–2% axial strain/min.

3 Results and Discussion

3.1 Effect of Biopolymers on Compaction Characteristics

Figure 2 shows the variation of dry density for different concentrations of biopolymer contents. In general, both gums show an increase in compaction characteristics. With increasing gum concentrations, the maximum dry density was observed first to increase and then decrease with the biopolymers. For Xanthan gum, the optimum concentration was found as 2% with maximum dry density 1.33/cc and its corresponding optimum moisture content as 29.8%. Similarly, the optimum moisture content was observed first to decrease with increasing gum concentrations and then increases with the biopolymers. For Guar gum, the optimum concentration was found as 1.5% with maximum dry density 1.36 g/cc and its corresponding optimum moisture content as 27.2%. The increasing density up to optimum concentration can be explained based on the nature of the gum which reduces the friction between the particles. Beyond the optimal dosage, the biopolymer content increases the spaces between the clay particles and thereby increases the global volume of void spaces causing a reduction in dry density. Also, the high viscous nature of biopolymers disturbs the compaction mechanism, which causes the particles to shift away from each other, reducing the dry density. Therefore, higher concentrations of biopolymers produce lower densities. The variation of moisture content with optimum dosages of biopolymer concentrations is shown in Fig. 3.

Fig. 2 Variation of dry density for different concentrations of biopolymers

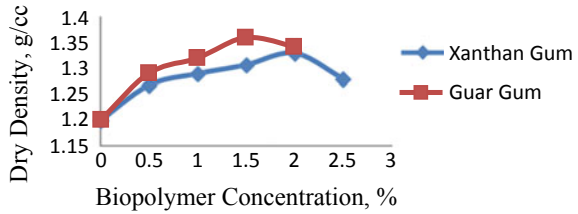


Fig. 3 Variation of compaction curves for different biopolymers

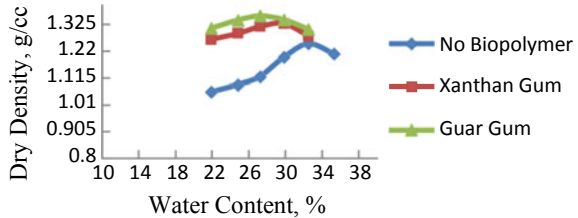
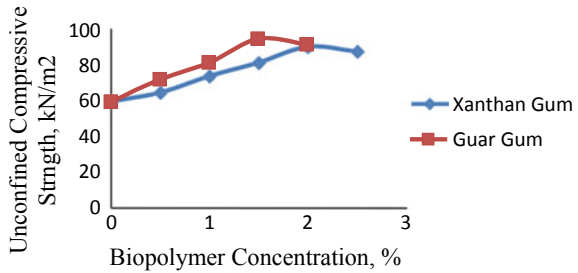


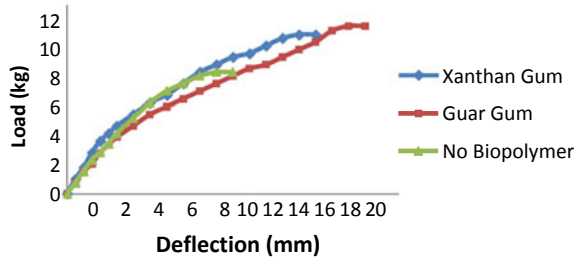
Fig. 4 Variation of compressive strength for different concentrations of biopolymers



3.2 Effect of Biopolymers on Compressive Strength

Figure 4 shows the variation of compressive strength for different concentrations of biopolymer contents. The UCS value increases with an increase in gum concentrations up to optimal content for both the biopolymers. This is because the biopolymers can be directly bonded to clay particles via cation bridging and hydrogen bonding between the electrically charged fine particles which lead to higher mechanical enhancement. Beyond the optimal dosage, the UCS value decreases due to the higher viscosity, which results in lack of bonding between clay–gum–water mixtures. The maximum compressive strength for Xanthan gum was found as 90.3 kN/m² and for Guar gum as 95.1 kN/m². The percentage increment in compressive strength for Xanthan gum and Guar gum was found as 51.2% and 59.6%, respectively. The unconfined compressive strengths for optimal dosages of biopolymers are shown in Fig. 5.

Fig. 5 Variation of compressive strengths for different biopolymers



4 Conclusions

This study investigates the effect of two biopolymers, namely Xanthan gum and Guar gum on Kuttanad soil with different concentrations. Using experimental investigations, the following conclusions can be drawn.

1. Biopolymers are environmentally friendly alternatives to conventional soil stabilizing agents like cement and lime.
2. The dry unit weight increases with increasing concentrations for both Xanthan gum and Guar gum from 1.2 g/cc to about 1.36 g/cc while the optimum water content reduces from 32 to 27%, approximately.
3. Mixing the soil with 2% of Xanthan gum and 1.5% of Guar gum leads to an increase in the compressive strength as much as 60%.
4. Guar gum is more promising than Xanthan gum for increasing the dry density and compressive strength. However, higher viscosity of biopolymers can reduce the soil density, thereby, the strength also.

References

1. Ayseldeen MK, Negm AM, Sawwaf ME (2016) Evaluating the physical characteristics of biopolymer/soil mixtures. *Arab J Geosci* 9(5):371
2. Ayseldeen M, Negm A, Sawwaf ME, Kitazume M (2017) Enhancing mechanical behaviors of collapsible soil using two biopolymers. *J Rock Mech Geotech Eng* 9:329–339
3. Biju MS, Arnepalli DN (2016) Biopolymer modified soil: prospects of a promising green technology. In: *Proceedings of Indian geotechnical conference, Chennai, India*
4. Chang I, Im J, Cho GC (2016) An environmentally-friendly geotechnical approach for soil erosion reduction using microbial biopolymers. In: *Proceedings of geo—Chicago, Chicago*
5. Chang I, Im J, Lee SW, Cho GC (2017) Strength durability of Gellan gum biopolymer treated korean sand with cyclic wetting and drying. *Constr Build Mater* 143:210–221
6. Chang I, Im J, Prasadhi AK, Cho GC (2015) Effects of Xanthan gum biopolymer on soil strengthening. *Constr Build Mater* 74:65–72

7. Hataf N, Ghadir P, Ranjbar N (2018) Investigation of soil stabilization using chitosan biopolymer. *J Clean Prod* 170:1493–1500
8. IS 2720 (Part 10) Determination of unconfined compressive strength. Bureau of Indian Standards
9. IS 2720 (Part 7) Determination of water content—dry density relation using light compaction. Bureau of Indian Standards

Examination of Present Subsurface Investigation Data for Valuation of Liquefaction Potential for Ahmadabad City by Means of SPT-N Value



Manali S. Patel and Tejas P. Thaker

Abstract In the area of geotechnical earthquake engineering, liquefaction is most imperative, difficult, and notorious matter. It is a major contributor to urban risk. Liquefaction is the process whereby soil loses its strength and stiffness under the application of stress, where stresses get developed due to ground vibrations during earthquakes. The subsoil strata of Ahmedabad region consist of silty sand, which is one of the responsible factors for the liquefaction susceptibility. In the present study, Idriss and Boulanger [1] method is used which is based on SPT-N value. Before attempting the rigorous investigation of the liquefaction potential for Ahmedabad region, first qualitative assessment of liquefiable soils was carried out based on the geotechnical characteristics such as SPT-N value, depth of water table, grain size analysis, liquid limit, plasticity index, etc. The qualitative assessment of liquefaction potential was done by SPT method using subsurface data and PGA values were generated. The different hazard maps were generated using SPT values of different depths for the quantitative assessment of liquefaction potential. Analysis reveals that Madhupura, Shyamal, and Vatva area are likely to be liquefied. If groundwater table is assumed to be at ground level in Ahmedabad region, the results show that the severity of liquefaction would be moderate to high due to the thick shallow liquefied deposits.

Keywords Soil liquefaction · Liquefaction potential · Peak ground acceleration · Ground water table

M. S. Patel (✉)

Sardar Vallabhbhai National Institute of Technology, Surat, India
e-mail: davemanali99@gmail.com

T. P. Thaker

Pandit Deendayal Petroleum University, Gandhinagar, India

© Springer Nature Singapore Pte Ltd. 2020

A. Prashant et al. (eds.), *Advances in Computer Methods and Geomechanics*, Lecture Notes in Civil Engineering 56, https://doi.org/10.1007/978-981-15-0890-5_7

1 Introduction

Earthquakes like the Good Friday ($M_w = 9.2$) of Alaska and Niigata ($M_w = 7.5$) of Japan occurred during three months' era in 1964 took the consideration of geotechnical engineers due to its shocking effects. Liquefaction was defined in the simplified method to be a phenomenon in which a cohesionless soil loses strength during an earthquake and acquires a degree of mobility sufficient to permit movements ranging from several feet to several thousand feet [7]. The Sabarmati river of Ahmedabad city was a non-perennial river. Owing to infrastructure development on this riverfront, now it exhibits a continuous flow of water throughout the year through the transported flow of Narmada river. It has increased the chances of rise in ground water table. Moreover, the city consists of silty sand and falls under seismic zone III which is the moderate zone of earthquake. Due to historic seismicity, there is a great need of liquefaction potential assessment in this region and hence certain a prime objective in present study. Furthermore, the severity of liquefaction is plotted for Ahmedabad city.

2 Theoretical Background

The first simplified procedure for liquefaction potential analysis was established by Seed and Idriss in [7]. Later on, many researchers [5, 6, 8–10] have tried to revise and simplify this procedure in their studies. The procedure was updated and augmented lastly, in National Center for Earthquake Engineering Research (NCEER [10] and 1998). Then based on more extensive databases and past experiences Standard Penetration Test (SPT) procedure is generally preferred among different types of in situ tests. In the SPT Based Liquefaction Triggering Procedures by Idriss and Boulanger, it is concluded that NCEER and Idriss-Boulanger [1–3] liquefaction triggering procedures are reasonable for depths covered by the case history database and that the Idriss-Boulanger procedures are better-supported by existing field and laboratory data for extrapolations to greater depth.

3 Methodology

Using SPT based empirical formulas, the quantitative assessment of liquefaction potential for Ahmedabad region [1] has been carried out. From IS 1893 [4], earthquake magnitude and the site-specific surface peak ground acceleration values are taken. The adopted methodology is illustrated in Fig. 1.

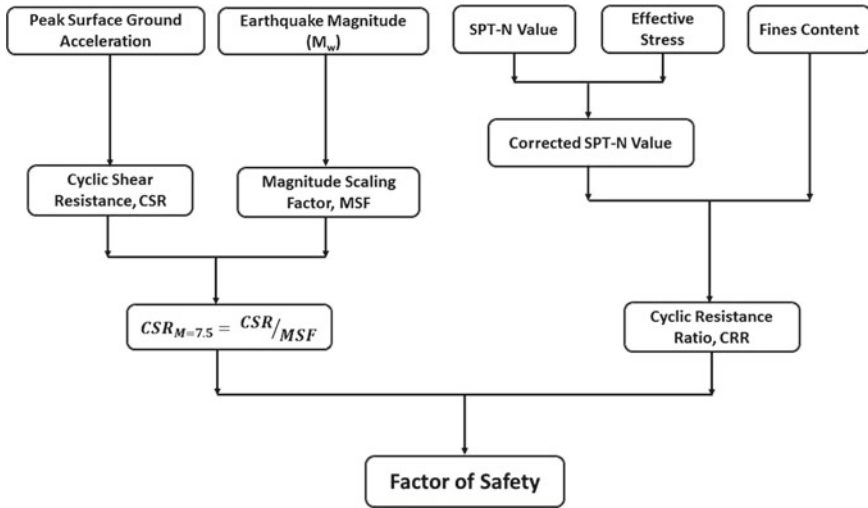


Fig. 1 Flow chart for the liquefaction analysis using simplified method

From the obtained borehole data, the various corrections such as overburden, borehole diameter, rod length, sampling method, and fines content are made to the SPT-N values. Factor of Safety (FS) is defined as the ability of a soil element to resist liquefaction. The soils are classified based on the following conditions, FS less than or equal to 1 and FS greater than 1 indicates that the soil layers are likely and not likely to liquefy, respectively.

4 Results and Discussion

The seismic moment magnitude scale (M_w) and peak ground surface acceleration (PGA) value are the essential seismic input parameter in the liquefaction hazard analysis. In the state of Gujarat, highest magnitude of earthquake ($7.5 M_w$) was recorded at Bhuj in the year 2001. With reference to that the value of M_w was adopted as 7.5 in the present study. For Ahmedabad region, the value of peak ground acceleration is 0.16 g as it falls in seismic zone III [4]. From the collected bore log data, the water table is observed very high (<4 m from ground surface) in nearby areas of Sabarmati river (Fig. 2). In such situations it becomes essential to identify the liquefiable soil layers within upper 10 m strata, especially with loose soil pockets which can be susceptible to liquefy in future. Typical calculations for selected liquefied location is presented in Tables 1 and 2.

Detailed site investigation is essential for the assessment of liquefaction hazard. To determine the liquefaction potential of the soil in Ahmedabad region, the preliminary evaluation is performed to identify the liquefiable soil layers and then the

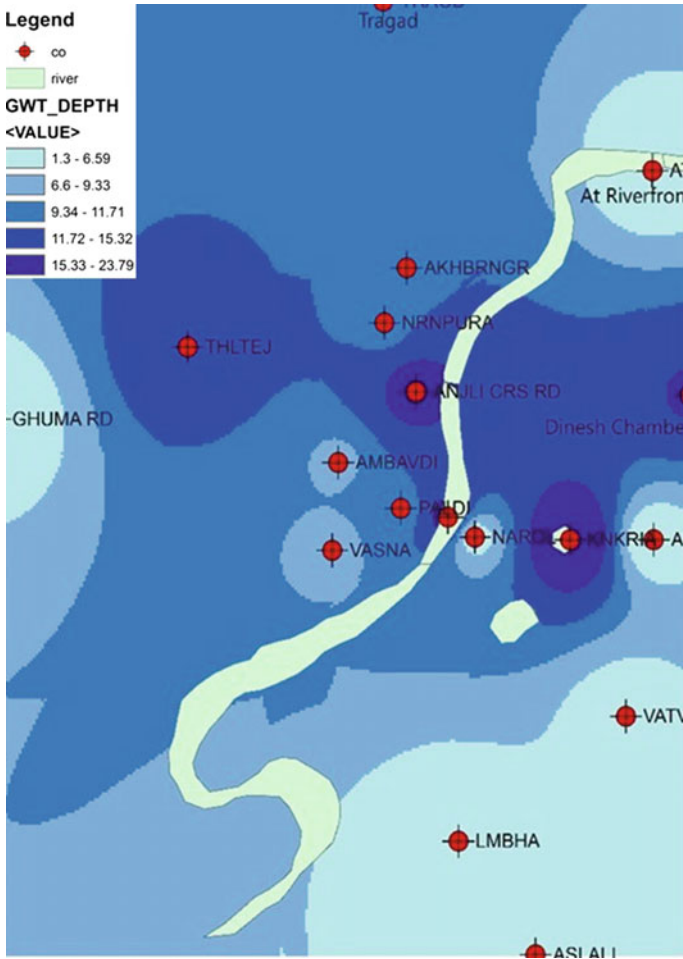


Fig. 2 Present groundwater table scenario of Ahmedabad Region

Table 1 Corrected SPT-N values using Idriss and Boulanger [1]

Depth (m)		Density (Y)	Soil type	Fine content	Liquid limit	Field SPT-N value	SPT-N corrected for field procedure and overburden	Corrected SPT-N
From	To	(kN/m ³)		(F.C.) %	W _L	N _R		
0.00	1.50	FILL	20	3	16.19	22.00	0.00	1.50
1.50	4.50	SM	24	11	16.48	24.00	1.50	4.50
4.50	6.00	SM	25	6	16.68	24.00	4.50	6.00

Table 2 Assessment of liquefaction potential using Idriss and Boulanger approach [1]

Total pressure	Effective pressure	Stress reduction factor	$(CSR)_{M=7.5, \sigma=1}$	Idriss and Boulanger [1]		Liquefaction
σ_v (kN/m ²)	σ'_v (kN/m ²)	r_d		CRR	F.S.	Y/N
24.28	24.28	1.00	0.104	0.10	1.0	N
73.72	73.72	0.97	0.101	0.15	1.5	N
98.74	98.74	0.95	0.099	0.12	1.2	N

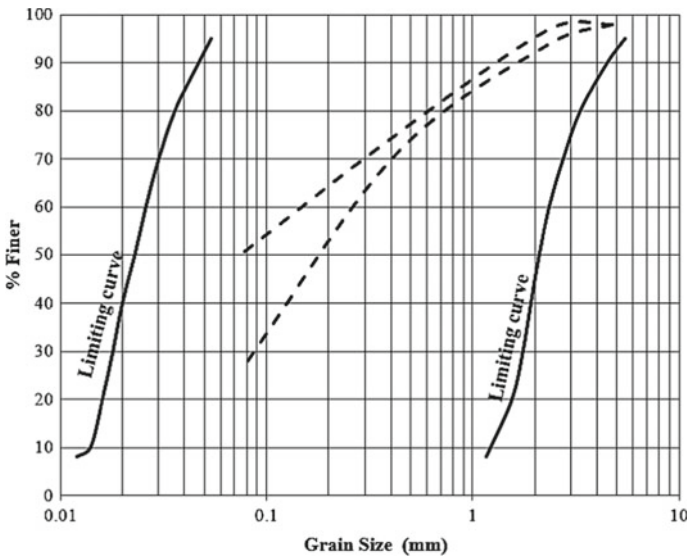


Fig. 3 Grain size distribution curves for Vatva in Ahmedabad region

detailed analysis is performed. For the preliminary assessment of liquefaction potential, the grain size distribution curves of Vatva area are drawn in Ahmedabad region. Figure 3 shows the grain size distribution (GSD) curves of Vatva area which is prone to liquefaction along with the limiting curves given by Tsuchida in 1987.

Factor of safety distribution maps for different depths like 0.0–3.0, 3.0–6.0, and 6.0–10.0 m were drawn along with the liquefaction hazard maps for Ahmedabad region (Figs. 4, 5 and 6).

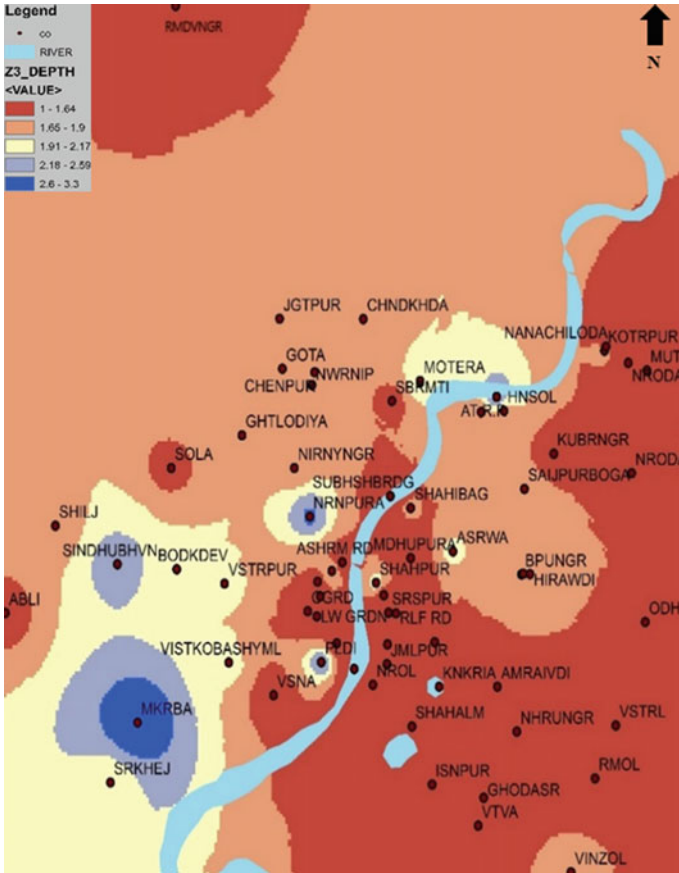


Fig. 4 Factor of safety distribution adopting Idriss and Boulanger [1] method for 0.0–3.0 m depths

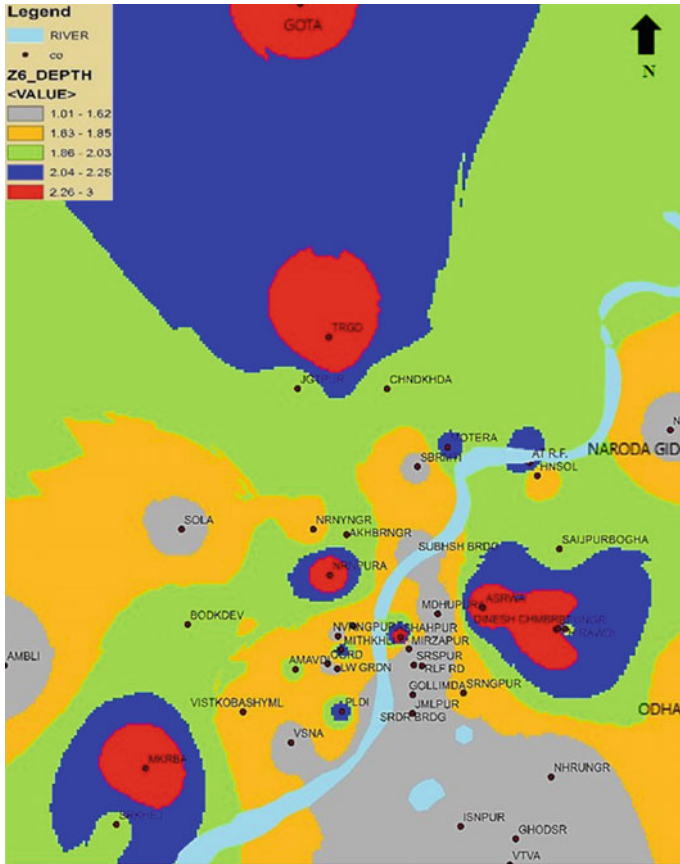


Fig. 5 Factor of safety distribution adopting Idriss and Boulanger [1] method for 3.0–6.0 m depths

5 Summary and Conclusions

Analysis of liquefaction is attempted using SPT based method Idriss and Boulanger [1]. Liquefaction hazard map at various depth intervals has been prepared which show the maximum depth of liquefaction is around 10 m. It is observed that the locations such as Sardar Bridge, Law garden, Saraspur, Vasna, Paldi, etc., near the Sabarmati river, has a great chance of being liquefied. Looking to the scenario of soil profile of the city, the city is having loose silty sand deposits at shallow depths and which are more susceptible to liquefaction. Mostly, the central part of the region is vulnerable to liquefaction.

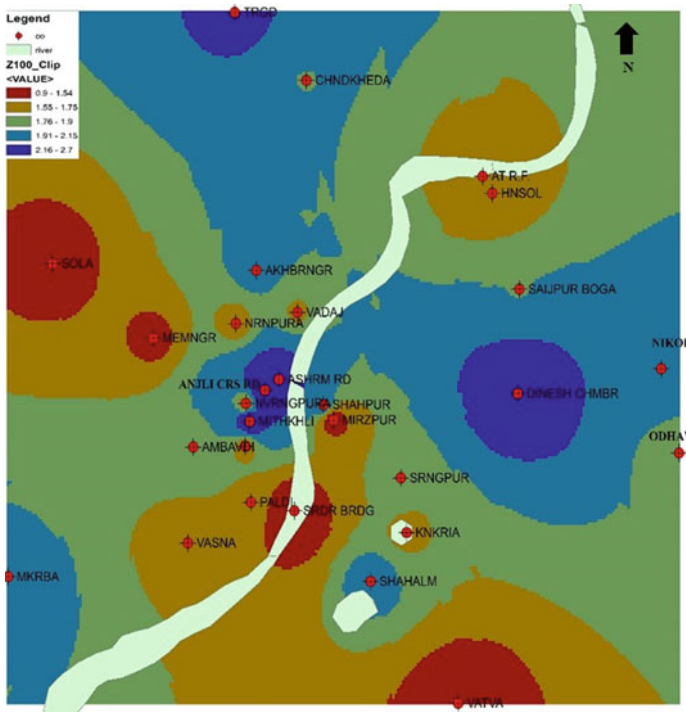


Fig. 6 Factor of safety distribution adopting Idriss and Boulanger [1] method for 6.0–10.0 m depths

References

1. Idriss IM, Boulanger RW (2010) SPT-based liquefaction triggering procedures
2. Idriss IM, Boulanger RW (2004) Semi-empirical procedures for evaluating liquefaction potential during earthquakes. In: Proceedings of 11th international conference on soil dynamics and earthquake engineering and 3rd international conference of earthquake geotechnical engineering, vol 1, pp 32–56
3. Idriss IM, Boulanger RW (2006) Semi-empirical procedures for evaluating liquefaction potential during earthquakes. *Soil Dyn Earthq Eng* 26:115–130
4. IS 1893 (2002) Indian standard criteria for earthquake resistant design of structures. Part-1-General Provisions for Buildings, Bureau of Indian Standards, New Delhi
5. Seed HB, Idriss IM, Arango I (1983) Evaluation of liquefaction potential using field performance data. *J Geotech Eng ASCE* 109(3):458–482
6. Seed HB (1979) Soil liquefaction and cyclic mobility evaluation for level ground during earthquakes. *J Geotech Eng ASCE* 105:201–221
7. Seed HB, Idriss IM (1971) Simplified procedure for evaluating soil liquefaction potential. *J Soil Mech Found ASCE* 97(SM9):1249–1273
8. Seed HB, Idriss IM (1982) Ground motions and soil liquefaction during earthquakes. In: *Earthquake engineering institute monograph*, p 134

9. Seed HB, Tokimatsu K, Harder LF, Chung RM (1985) Influence of SPT procedures in soil liquefaction resistance evaluations. *J Geotech Eng Div ASCE* 111(12):1425–1445
10. Youd TL, Noble SK (1997) Liquefaction criteria based on statistical and probabilistic analyses. In: *Proceedings of NCEER workshop on evaluation of liquefaction resistance of soils*. Technical report NCEER-97-2002. Multidisciplinary Center for Earthquake Engineering Research, Buffalo, New York, pp 201–215

Improving “Shrinkage-Swelling” Response of Expansive Soil Using Bio-calcite and Exopolysaccharide Produced by *Bacillus* sp.



V. Guru Krishna Kumar, Kaling Taki, Sharad Gupta
and Ajanta Sachan

Abstract Biological phenomena stand out as a key towards green method for improving the properties of engineering construction material. The present study investigates the effect of Microbial Induced Calcite Precipitation (MICP) and Extracellular Polymeric Substance (EPS) produced by *Bacillus cereus* (*B. cereus*) SG4 on “shrinkage-swelling” behavior of expansive soil. The soil used for the study was commercially available Bentonite cohesive soil. The critical soil parameters such as Liquid Limit (LL), Plastic Limit (PL), and Differential Free Swell Index (DFSI) were found to be very high (LL = 608%, PL = 50%, and DFSI = 661%) due to the presence of Montmorillonite mineral. The results showed that treatment of Bentonite expansive soil with bio-calcite and EPS containing *B. cereus* SG4 culture media worked effectively. Bentonite soil was treated with bacteria along with culture medium for 5 and 10 days. It was observed that there was no significant reduction in geotechnical properties after 10th day of treatment. Maximum effect was observed at the end of 5th day exhibiting the efficiency and strong capability of proposed soil treatment method. After 5th day, LL, PL, and DFSI values were observed to be decreased; 177%, 39%, and 371% for EPS, respectively. The similar response was observed for Bio-calcite technique, which exhibited a significant reduction in LL, PL, and DFSI values (158%, 39%, and 271%), respectively. Both the treatment techniques worked successfully in improving the shrinkage-swelling response of Bentonite soil, but bio-calcite treatment was observed to be more effective than EPS treatment to control the shrinkage-swelling response.

V. G. Krishna Kumar · S. Gupta
Biological Engineering, Indian Institute of Technology Gandhinagar, Gandhinagar, India
e-mail: guru_krishnakumar@iitgn.ac.in

S. Gupta
e-mail: sharad@iitgn.ac.in

K. Taki (✉) · A. Sachan
Civil Engineering, Indian Institute of Technology Gandhinagar, Gandhinagar, India
e-mail: kaling.taki@iitgn.ac.in

A. Sachan
e-mail: ajanta@iitgn.ac.in

Keywords *Bacillus cereus* SG4 • Bio-calcite • EPS • Expansive soil • Montmorillonite

1 Introduction

Last decade has seen the emergence of Construction Biotechnology as a new area of Science and Engineering and a significant contribution has come from the development of microbial products or processes for the enhancement of the properties of construction materials [12, 19, 29]. A wide variety of microorganisms in the environment exhibit the phenomenon of mineralization of diverse nature and chemical composition, including carbonates, silicates, and iron and manganese oxides. Metabolites from microbes using specific substrates often contribute to products such as insoluble organic compounds and salts which have cementation and clogging properties [17, 35]. Biocalcification also known as Microbial Induced Calcite Precipitation (MICP) is dependent upon the ability of a microorganism to secrete the urease enzyme leading to the production of insoluble calcium carbonate [4]. Certain microorganisms occur in the form of microbial aggregates made of structural elements called Extracellular Polysaccharides (EPS) [14, 34]. The EPS, secreted by microorganisms into the surrounding for their survival are widely used as emulsifiers, gelling agents, binders, coagulants, and thickening agents [24]. Studies on the application of biocalcification produced by several microorganisms have been extensively carried out in concretes, bricks, cement mortar, and sand [1, 11, 16, 25, 28, 33]. Furthermore, there are reports of augmentation of functional properties and geotechnical aspects of soil by treatment with EPS biofilms produced by bacteria [5, 9].

Bentonite clay used in the current study has very high shrinkage and swelling response owing to the presence of large amounts of montmorillonite mineral [8]. Expansive soil such as black cotton soil (Gujarat, India) has nearly 30–60% of montmorillonite mineral which swells on the absorption of water and shrinks when dried out. Cycles of swelling-shrinkage place repetitive stress on structures resulting in a huge commercial loss. The present research focuses on two aspects (i) isolation and characterization of a unique *Bacillus cereus* strain which could produce bio-calcite and EPS (ii) a soil treatment technique which could significantly lower swelling-shrinkage response of expansive soil. In this study, Bentonite cohesive soil has been treated using bio-calcite and EPS produced from the same microbe *Bacillus cereus* SG4 to control the said response. The proposed method has excellent potential for effective treatment of expansive soil.

2 Experimental Program

2.1 Material Properties

For the study Bentonite soil was taken the soil is classified as clay with high compressibility (CH) type. The properties of Bentonite soils have been given in Table 1.

2.2 Soil Collection for Bacterial Isolation

Soil samples were collected from twelve different locations in Gujarat (India) where the nature of the soil was cohesive with significant variations in clay content. The soil was sampled into a clean plastic box and stored in 4 °C before use.

2.3 Bacterial Isolation

Bacterial isolation was carried out by first mixing 1 g of soil sample into 10 mL ddH₂O and the supernatant was further diluted 10-fold, 100-fold, and 1000-fold. A 100 µL aliquot from each dilution was spread onto nutrient agar plates and incubated at 37 °C for 24 h. All grown colonies were screened for urease and EPS production by using selective media such as Ammonium-Yeast extract agar plates for urease and nutrient broth (NB) supplemented with glucose media for EPS production. Microorganisms which yielded both urease and EPS were further characterized.

Table 1 Basic properties of Bentonite soil

Particulars	Specifications
Material used	Bentonite (Brown color)
Liquid limit (%)	608
Plastic limit (%)	50
Plasticity index (%)	558
Soil classified	Highly compressible
Differential free swell index (DFSI) (%)	661

2.4 Microbial Characterization

Gram staining was performed using Grams Stain-Kit (HiMedia). Biochemical tests such as Malonate, Citrate, Arginine, Sucrose, Mannitol, Glucose, Arabinose, Trehalose, Vogue's Proskauer, Catalase, Nitrate reduction and ONPG were performed by using HiBacillus identification kit (HiMedia). The changes in the color of API strips were used to characterize the strains based upon their response towards different tests. HiChrome bacillus agar (HiMedia) was used for species identification based on colony color.

2.5 Testing Procedure

2.5.1 Procedure for MICP and EPS Production

NB supplemented with 2% urea and 0.3% CaCl₂ was used as growth media to produce MICP. In brief, the strain was inoculated in sterile media and incubated at 37 °C and 250 rpm for one week. Baffled Erlenmeyer flasks were used to provide extra aeration and agitation to the bacterial culture. A switch in media to NB supplemented with 5% glucose was used for EPS production under similar growth conditions for three days.

2.5.2 EPS Extraction and Quantification

Extraction of EPS was done by using cold ethanol method [3]. In brief, three days old culture media was centrifuged at 7,000 g for 15 min at 4 °C to pelletize the bacterial cells. The supernatant was mixed with four volumes of ice cold ethanol and the suspension was stored at -20 °C overnight. Precipitated EPS was separated by centrifugation at 12,000 g for 30 min at 4 °C and lyophilized. Carbohydrates were quantified by the phenol-sulfuric acid method as reported by Dubios et al. [13]. Protein content was estimated by Bradford's method using BSA as standard.

2.5.3 Scanning Electron Microscopy

Precipitated calcite crystals were collected on Whatman No. 1 filter by filtration, washed with sterile distilled water, and air-dried at 37 °C for 48 h. Dried crystals were sputter coated with platinum and FE-SEM analysis was carried out using JEOL JSM-7600F at accelerating voltage of 35 kV and working distance of 9 mm. Energy Dispersive Spectroscopy (EDS) was performed to identify the composition of elements and their relative proportions in the precipitated bio-calcite.

2.5.4 Genomic and In Silico Analysis

Genomic DNA extraction was performed using DNeasy Blood & Tissue Kit (Qiagen). The amplification of 16S gene was carried out using the universal primers 27f and 1492r [15]. The reaction was performed in 50 μ L reaction volume and the PCR conditions were as follows: primary denaturation at 94 °C for 5 min, followed by 30 cycles of 94 °C for 1 min, 55 °C for 1 min, 72 °C for 1.2 min, and final extension at 72 °C for 5 min. The PCR amplicons were analyzed on a 1% agarose gel along with a DNA molecular weight marker. Sequencing of 16S rDNA gene was performed on an ABI PRISM 377 genetic analyzer (Applied Biosystems, USA) by Eurofins Scientific, Bangalore India. NCBI’s BLAST program (www.blast.ncbi.nlm.nih.gov/Blast.cgi) was used to identify the sequences that are homologous to extracted 16S rDNA sequence. Multiple sequence alignment was performed using the CLUSTALW program [20]. Phylogenetic analyses were carried out in MEGA v6.0 using the neighbor joining algorithm with 1000 bootstrap replicates [30]. Sequence information was submitted to NCBI GenBank (Accession number: KX817272).

2.5.5 Urease and Protease Activity

Urease activity was determined for the bacterial isolate in nutrient broth (NB) containing 2% urea and 0.3% CaCl_2 by measuring the amount of ammonia released on hydrolysis of urea using phenol-hypochlorite method [23]. One unit of urease activity is defined as the amount of enzyme hydrolyzing one μ mole of urea per minute. Protease activity was determined according to the method of Tsuru et al. [31] using casein as a substrate and L-tyrosine (1.1 mM) as the standard [31]. One unit of protease activity is defined as tyrosine equivalents in μ moles released from casein per minute.

2.5.6 Geotechnical Test on Bacteria Treated Bentonite Soil

The following geotechnical tests were carried out on treated and untreated Bentonite clay.

- (a) *Liquid Limit (LL) test*: [IS: 2720 (Part 5)—1985 (Reaffirmed 2006)].
- (b) *Plastic limit (PL) test*: [IS: 2720 (Part 5)—1985 (Reaffirmed 2006)].
- (c) *Differential free swell index (DFSI) test*: [IS: 2720 (Part XL)—1977 (Reaffirmed 2002)].

3 Results and Discussion

3.1 Screening of Bacterial Strains and Strain Identification

Soil samples were collected from twelve parts of Gujarat, India to isolate EPS and urease producing microorganism. Soil samples were serially diluted in ddH₂O and the extract was spread on NB agar containing glucose and isolated 33 different strains based on the colony morphology (Fig. 1 and Table 2).

Bacteria which produced mucoid secretion were identified and further tested for urease production by their ability to grow in Ammonium-Yeast extract media. Four strains namely Strain 1, Strain 2, Strain 3, and Strain 4 were screened for urease production form which strain 4 had maximum urease activity, which corresponds to 829.6 U/min (Fig. 2). Comparison of strain 4 with previously reported urease positive strain *B. megaterium* CT-5 was also performed and the urease activity was found to be qualitatively similar (Fig. 3).

Gram staining was performed to differentiate bacteria based on their cell wall constituent (Fig. 4). Isolated Strain 4 (hereafter referred to as SG4) which gave the highest urease activity was found to be Gram positive and rod-shaped bacteria. To identify whether the screened strains 1–4 were of *Bacillus* sp they were grown in HiCrome *Bacillus* agar. SG4 showed a luxuriant growth in this media exhibiting large colonies with blue centered morphology, which was a characteristic response for *Bacillus cereus*. HiBacillus identification kit was used to further characterize the bacteria based on its biochemical properties (Table 3). Positive test results suggested that the isolate SG4 can potentially be *Bacillus cereus*. To study the phylogeny and taxonomy of SG4 at genome level, 16s rRNA sequencing was performed. In silico sequence analysis of the 16S rDNA gene revealed that there was a significant level of similarity (>99%) between the sequence obtained in this



Fig. 1 Isolated strains from 12 different soil samples were tested on NB-Glucose agar for EPS production * (Note * Images have been taken by the authors during the experiment at Biological Engineering Lab IITGN)

Table 2 Bacteria screened on NB-glucose agar plates based on the colony morphology

Strain No.	Morphology	Obtained from Soil
1	With dot	S-III
2	With yellow sheen	S-VII
3	Light spread	S-VII
4	Full spread	S-XI
5	Dark	S-VIII
6	With flagella	S-IX
7	Radiating	S-VIII
8	Thick dot	S-VII
9	Crystal	S-XII
10	Round	S-XI
11	Zone from side	S-V
12	Light yellow	S-II
13	Dark yellow	S-II
14	Red	S-II
15	Spread yellow sheen	S-VII
16	Flat spread	S-II
17	Star	S-5
18	Small	S-II
19	Big	S-II
20	With sheen	S-VII
21	Like film from center	S-I
22	Double layer	S-VI
23	Yellow	S-XI
24	Outgrowth	S-II
25	Shine	S-II
26	Criss cross spread	S-X
27	Like film from side	S-I
28	Zone from center	S-V
29	Crystal center	S-VI
30	Crystal side	S-VI
31	White small dot	S-XII
32	Bluish yellow	S-III
33	Middle dark with translucent edge	S-III

study with the sequences reported earlier from *Bacillus cereus*. The phylogenetic tree analysis further divulged the closeness of the bacterial isolate SG4 with *Bacillus cereus* strains (Fig. 5). The tree also indicated that *Bacillus anthracis* and *Bacillus thuringiensis* formed a separate clade altogether. These results further affirmed that the bacterial isolate SG4 belonged to genus: *Bacillus* and species: *cereus*.

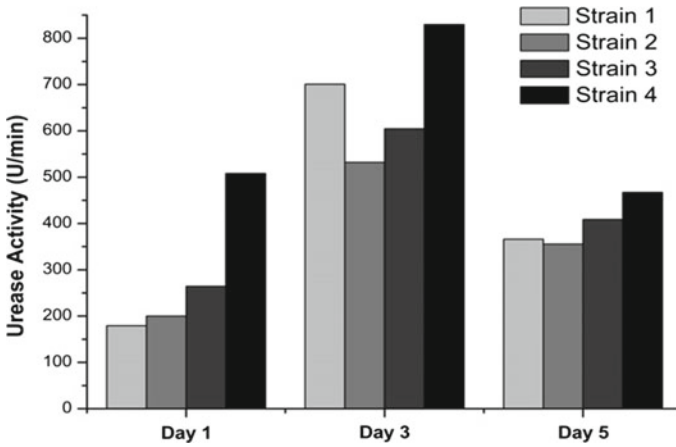


Fig. 2 Isolated bacterial strains tested for urease production in NB-Urea-CaCl₂ media

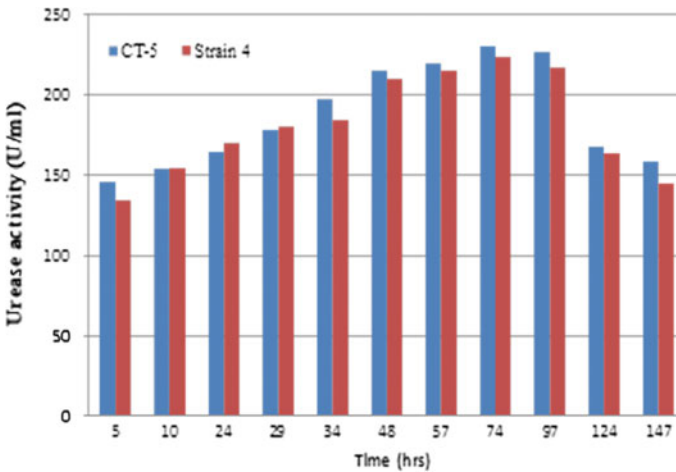


Fig. 3 Comparison of urease activity from *B. megaterium* CT-5 and Strain 4

3.2 Urease/Protease Activity and EPS Production

Bacillus cereus SG4 showed maximum urease productivity corresponding to 206 U/mL on the third day, in nutrient broth containing Urea-CaCl₂. Protease activity increased with time and showed maximum productivity on the fifth day corresponding to 1.4 U/ml (Fig. 6). It was also noted that the urease production gradually reduced after the third day, which is in agreement with increased protease concentration leading to the degradation of urease in culture media. *B. cereus* SG4 yielded a total of 1.8 g/L of dried calcium carbonate in NB-urea-CaCl₂ media and

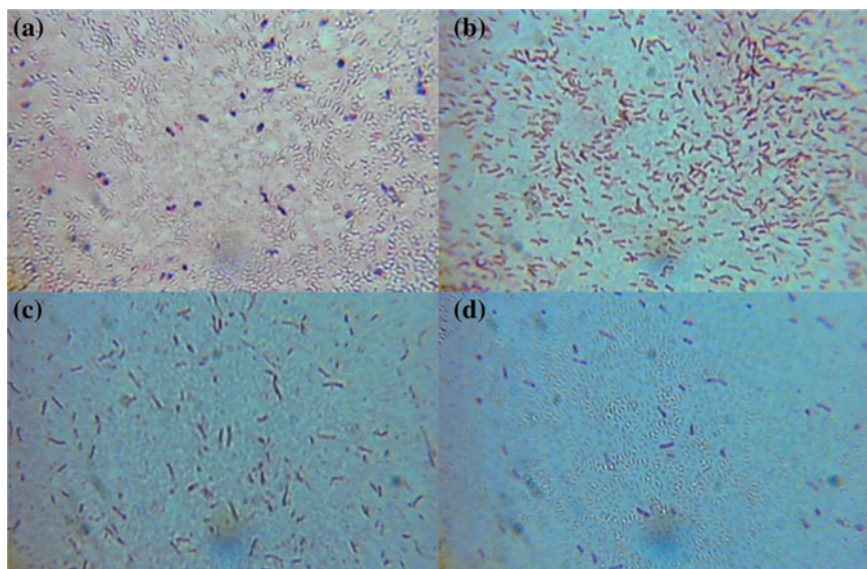


Fig. 4 Gram staining performed to differentiate bacteria based on their cell wall constituent, **a** Strain 1, **b** Strain 2, **c** Strain 3, and **d** Strain 4

Table 3 Comparison of distinctive biochemical characteristics of bacterial strains which tested positive for urease and EPS production

Characteristics	Strain 1	Strain 2	Strain 3	Strain 4
Malonate	–	+	–	–
VP	–	–	+	+
Citrate	–	+	+	–
ONPG	–	+	+	–
Nitrate reduction	+	–	–	+
Catalase	+	+	+	+
Arginine	–	+	–	
Sucrose	+	–	+	+
Mannitol	–	–	+	–
Glucose	+	–	+	+
Arabinose	–	–	–	–
Trihalose	+	+	+	+

300 mg/L of dried EPS in NB-glucose media. Crude EPS consisted of 85% carbohydrates and 6% proteins Fig. 7. Bio-calcite was visualized by SEM as shown in Fig. 8. The size of calcite crystals formed by *B. cereus* SG4 was about 10–50 μm in diameter. The composition of thus examined crystals was determined with EDS which verified the presence of calcium carbonate based on weight %.

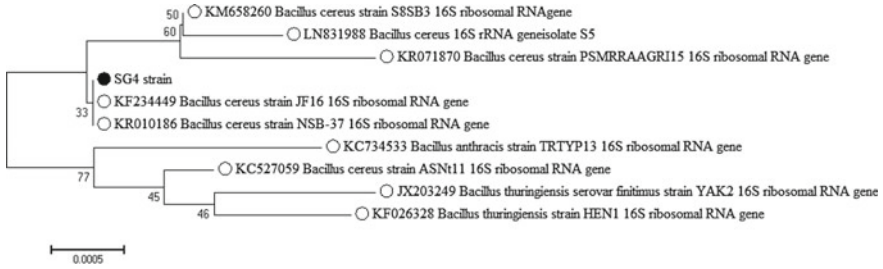


Fig. 5 Phylogenetic tree based on 16S rDNA sequence using neighbor joining algorithm with 1000 bootstrap replicates for *Bacillus cereus* SG4 strain. Branch distances represent nucleotide substitution rate and the scale bar represents the number of changes per nucleotide position

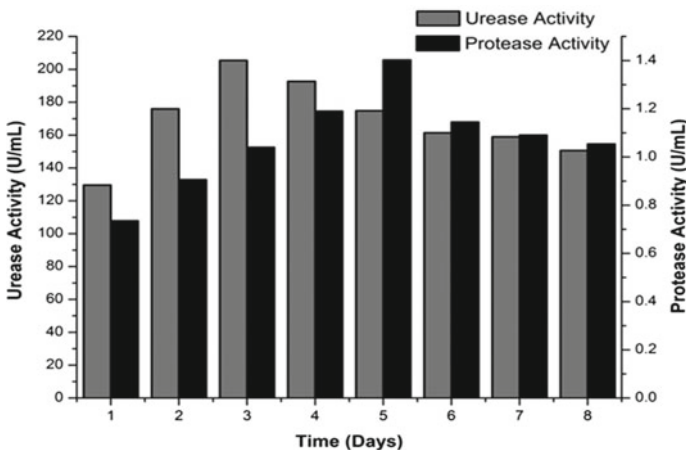


Fig. 6 Urease and Protease production by *Bacillus cereus* SG4

3.3 Improvement in the Geotechnical Properties of Bentonite Soil

Geotechnical properties of soil can be enhanced by the treatment with microbial-mediated processes or microbial products, e.g., microbial induced calcite precipitation and extracellular polysaccharides. The process of calcification involves decomposition of urea into ammonia and CO₂ by extracellular urease enzyme produced by bacteria [22]. Earlier studies state that bacteria can hydrolyze urea and utilize resulting ammonia as the nitrogen source for its metabolism [18]. Presence of ammonia raises the pH of media, thus increasing the concentration of CO₃²⁻ which reacts with supplemented Ca²⁺ ions to form insoluble calcium carbonate precipitate (Fig. 9). To achieve a higher yield of bio-calcite an organism exhibiting enhanced urease activity is required. EPS is an extracellular polymeric metabolite produced by bacteria utilizing sugars present in the culture media [7].

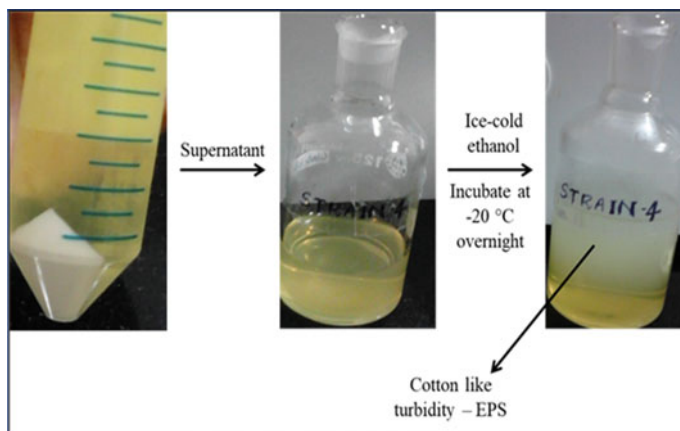


Fig. 7 Extraction of Extracellular Polysaccharide by cold ethanol method* (Note * Images have been taken by the authors during the experiment at Biological Engineering Lab IITGN)

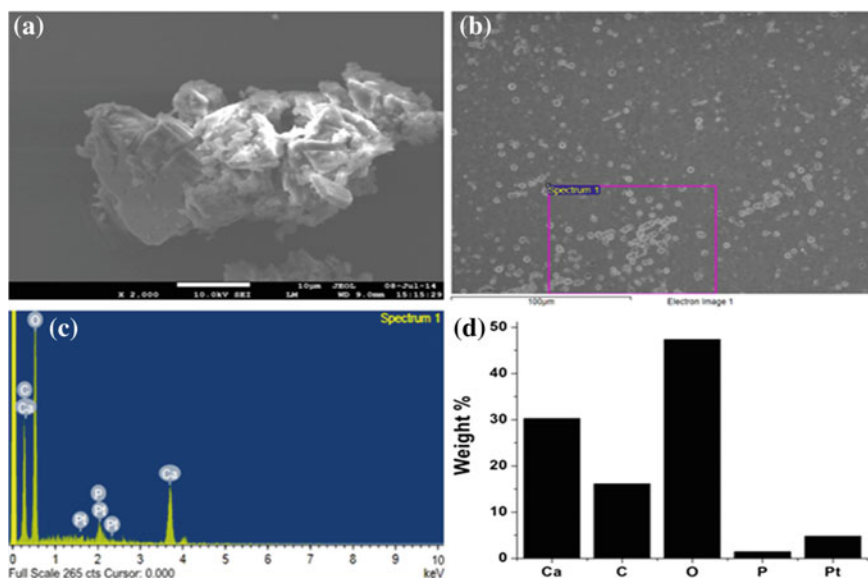


Fig. 8 Analysis of precipitated Bio-calcite using electron microscopy, **a** SEM of Bio-calcite precipitated by *Bacillus cereus* SG4 in NB-Urea-CaCl₂ media, **b** selection area for EDS analysis, **c** elemental analysis plot by EDS, **d** prevalence of calcium, carbon, and oxygen in weight%

Microbial polysaccharides have found wide applications as admixture for concrete and grout but have not been used for soil properties enhancement. Thus, we set out to extract urease or EPS producing bacteria which could potentially be used for soil treatment. We screened 33 bacteria isolated from 11 soil samples across Gujarat,

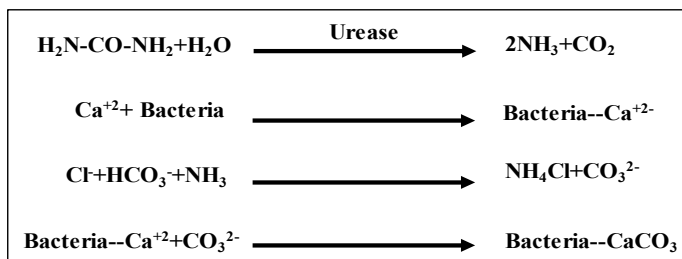


Fig. 9 Mechanism of calcite precipitation by bacteria [27]

India, and successfully identified as bacterial strain *Bacillus cereus* SG4 which not only exhibited significantly higher urease activity than previously isolated bio-calcite producing bacteria but also produced EPS when a suitable culture media with glucose as substrate was used.

Lian and co-workers have shown that the bacterial cell surface induces mineral deposition by providing nucleation sites [21]. Calcium carbonate crystal formation by ureolytic bacteria involved the nucleation of calcite on the microbial cell wall. Bacterial metabolic processes do not utilize Ca^{2+} ions, and thus they start accumulating outside the cell. Meanwhile, enzymatic reversible hydration of CO_2 leads to the formation of HCO_3^- or the dissolved CO_2 transformation to CO_2^{3-} commences the growth of CaCO_3 around the cell [2]. A similar mechanism can also be predicted for bio-calcite from *Bacillus cereus* SG4 where the analysis of a precipitated crystal by SEM and EDS confirmed the composition to be CaCO_3 . EPS forms a surface film which reduces the absorption properties of soil resulting in bioclogging of soil. As *Bacillus cereus* SG4 could produce substantial quantities of EPS using glucose as a substrate. It was hypothesized that this property could be utilized to enhance the soil properties. After characterizing the extracellular metabolites, viz., bio-calcite and EPS, culture media containing bacteria was tested on expansive bentonite clay which has drastic shrinkage and swelling properties rendering it highly unusable for civil constructions.

Geotechnical properties of soil can be enhanced by the treatment with microbial-mediated processes or microbial products, e.g., microbial induced calcite precipitation and extracellular polysaccharides. When media containing bio-calcite was added to Bentonite the soil exhibited a large decrease in LL, PL, and DFSI. The calcium ion from calcite is released into the pores of soil and as a result divalent Ca^{2+} ions replace the monovalent Na^+ ions present in Bentonite clay. This replacement of ions causes an increase in electrolytic concentration, which may reduce the thickness of “diffuse double layer” (an ionic layer found around the clay particle). Reduction in thickness will lessen water absorption, retention, and swelling properties of soil leading to decrease in LL, PL, and DFSI [10]. In addition, CaCO_3 forms an aggregated structure (0.02–0.05 mm in diameter) which is larger than the size of clay particle (0.002 mm in diameter). These particles behave as silt sealing the pores and further enhance the clay properties [6, 32].

Treatment of Bentonite clay with culture media containing EPS also leads to a significant reduction in LL, PL, and DFSI. EPS was found to decrease the pore size of soil thus hampering the permeability of water [9]. When the culture containing EPS was added to Bentonite, it gave rise to tiny clumps of $\sim 3\text{--}5$ mm diameter after five days of curing as shown in Fig. 10. This is owing to the binding and encapsulating nature of EPS which holds the soil particles together. EPS coating to soil might stop the inflow of water thereby reducing the swelling property of Bentonite. Moreover, it is reported that biofilm formed by EPS has water retaining capacity [26]. When water was added to soil, EPS retained water and only a small portion may get exposed to soil particles. Thus, a low permeability nature of biofilm acts as a barrier for water molecules to interact with the soil which results in the minimal swelling index.

The results showed that treatment of expansive soil with bio-calcite and EPS containing *B. cereus* SG4 culture media worked effectively. As shown in Tables 4 and 5, these treatment strategies have considerably reduced LL, PL, and DFSI values of Bentonite clay. It was interesting to note that there was no significant reduction in geotechnical values after the tenth day of treatment showing the quickness and efficiency of proposed method. Both treatment strategies worked successfully in improving shrinkage-swelling response of Bentonite clay; with bio-calcite treatment proving more beneficial than EPS treatment.

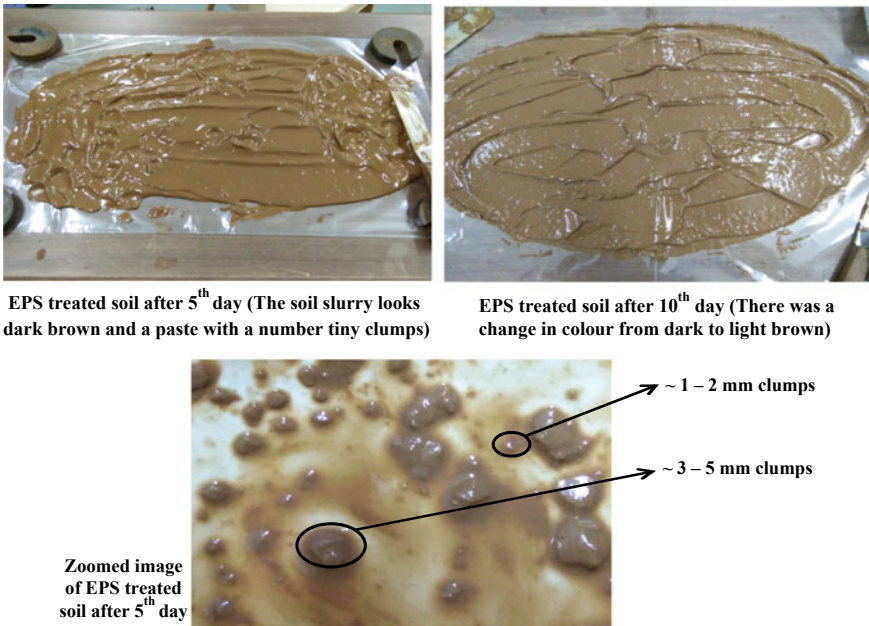


Fig. 10 EPS treatment on Bentonite cohesive soil* (Note * Images have been taken by the authors during the experiment at Geotechnical Engineering Lab IITGN)

Table 4 Bentonite clay treated with EPS produced by *B. cereus* SG4

S. No.	Properties	Control (%)	5 days		10 days	
			Treatment (%)	Percentage reduction (%)	Treatment (%)	Percentage reduction (%)
1	LL	608	177	70	171	72
2	DFSI	661	371	43	357	46
3	PL	50	39	22	37	27

Table 5 Bentonite clay treated with Bio-Calcite produced by *B. cereus* SG4

S. No.	Properties	Control	5 days		10 days	
			Treatment (%)	Percentage reduction (%)	Treatment (%)	Percentage reduction (%)
1	LL	608	158	73	150	75
2	DFSI	661	271	58	243	63
3	PL	50	39	22	36	29

4 Conclusions

In summary, *Bacillus cereus* SG4 was isolated and characterized for urease and EPS production. *B. cereus* SG4 effectively produced bio-calcite and EPS in Urea-CaCl₂ and glucose substituted nutrient broth, respectively. Culture media containing bio-calcite and EPS was used to treat expansive Bentonite clay, which had a severe shrinkage-swelling problem. The results showed that both bio-calcite and EPS treatments have capabilities to effectively reduce the geotechnical properties such as LL, PL, and DFSI. The most interesting aspect of the identified bacteria is that it can switch the metabolic pathway as per the availability of the medium and produce bio-calcite as well as EPS and both strategies can be applied to expansive soil to effectively control its shrinkage-swelling response.

Acknowledgements Authors thank Indian Institute of Technology Gandhinagar for providing financial support for this work. Authors also thank Ms. Gundeep Kaur Sudan, Ms. S. Smita for their assistance in bacterial screening and Mr. R. Vijayaraghavan (NIOT, Chennai) for his help with genomic characterization and analysis. Authors are very grateful to Dr. Abhijit Mukherjee for valuable discussions and Dr. V. Veeraraghavan for proofreading the manuscript.

References

1. Achal V, Mukherjee A, Reddy MS (2011) Effect of calcifying bacteria on permeation properties of concrete structures. *J Ind Microbiol Biotechnol* 38:1229–1234
2. Anbu P, Kang C-H, Shin Y-J, So J-S (2016) Formations of calcium carbonate minerals by bacteria and its multiple applications. *Springerplus* 5:250

3. Antón J, Meseguer I, Rodríguez-Valera F (1988) Production of an extracellular polysaccharide by *Haloferax mediterranei*. *Appl Environ Microbiol* 54:2381–2386
4. Bachmeier KL, Williams AE, Warmington JR, Bang SS (2002) Urease activity in microbiologically-induced calcite precipitation. *J Biotechnol* 93:171–181
5. Banagan BL, Wertheim BM, Roth MJS, Caslake LF (2010) Microbial strengthening of loose sand. *Lett Appl Microbiol* 51:138–142
6. Bell FG (1996) Lime stabilization of clay minerals and soils. *Eng Geol* 42:223–237
7. Ceyhan N, Ozdemir G (2008) Extracellular polysaccharides produced by cooling water tower biofilm bacteria and their possible degradation. *Biofouling* 24:129–135
8. Cui Y-J, Tang A-M, Qian L-X et al (2011) Thermal-mechanical behavior of compacted GMZ bentonite. *Soils Found* 51:1065–1074
9. Daniels J, Cherukuri R (2005) Influence of biofilm on barrier material performance. *Pract Period Hazard Toxic Radioact Waste Manag* 9:245–252
10. Dash S, Hussain M (2011) Lime stabilization of soils: reappraisal. *J Mater Civ Eng* 24:707–714
11. De Muynck W, Debrouwer D, De Belie N, Verstraete W (2008) Bacterial carbonate precipitation improves the durability of cementitious materials. *Cem Concr Res* 38:1005–1014
12. DeJong JT, Mortensen BM, Martinez BC, Nelson DC (2010) Bio-mediated soil improvement. *Ecol Eng* 36:197–210
13. DuBois M, Gilles KA, Hamilton JK et al (1956) Colorimetric method for determination of sugars and related substances. *Anal Chem* 28:350–356
14. Flemming H-C, Wingender J (2010) The biofilm matrix. *Nat Rev Micro* 8:623–633
15. Frank JA, Reich CI, Sharma S et al (2008) Critical evaluation of two primers commonly used for amplification of bacterial 16S rRNA. *Genes. Appl Environ Microbiol* 74:2461–2470
16. Ghosh S, Biswas M, Chattopadhyay BD, Mandal S (2009) Microbial activity on the microstructure of bacteria modified mortar. *Cem Concr Compos* 31:93–98
17. Ivanov V, Chu J (2008) Applications of microorganisms to geotechnical engineering for bioclogging and biocementation of soil in situ. *Rev Environ Sci Bio/Technol* 7:139–153
18. Jahns T, Zobel A, Kleiner D, Kaltwasser H (1988) Evidence for carrier-mediated, energy-dependent uptake of urea in some bacteria. *Arch Microbiol* 149:377–383
19. Krishnapriya S, Venkatesh Babu DL, Pa G (2015) Isolation and identification of bacteria to improve the strength of concrete. *Microbiol Res* 174:48–55
20. Larkin MA, Blackshields G, Brown NP et al (2007) Clustal W and Clustal X version 2.0. *Bioinformatics* 23:2947–2948
21. Lian B, Hu Q, Chen J et al (2006) Carbonate biomineralization induced by soil bacterium *Bacillus megaterium*. *Geochim Cosmochim Acta* 70:5522–5535
22. Mortensen BM, Haber MJ, DeJong JT et al (2011) Effects of environmental factors on microbial induced calcium carbonate precipitation. *J Appl Microbiol* 111:338–349
23. Natarajan KR (1995) Kinetic study of the enzyme urease from *Dolichos biflorus*. *J Chem Educ* 72:556
24. Paul F, Morin A, Monsan P (1986) Microbial polysaccharides with actual potential industrial applications. *Biotechnol Adv* 4:245–259
25. Pei R, Liu J, Wang S, Yang M (2013) Use of bacterial cell walls to improve the mechanical performance of concrete. *Cem Concr Compos* 39:122–130
26. Rittmann BE, Crawford L, Tuck CK, Namkung E (1986) In situ determination of kinetic parameters for biofilms: isolation and characterization of oligotrophic biofilms. *Biotechnol Bioeng* 28:1753–1760
27. Sarda D, Choonia HS, Sarode DD, Lele SS (2009) Biocalcification by *Bacillus pasteurii* urease: a novel application. *J Ind Microbiol Biotechnol* 36(8):1111–1115
28. Siddique R, Chahal NK (2011) Effect of ureolytic bacteria on concrete properties. *Constr Build Mater* 25:3791–3801
29. Soon NW, Lee LM, Khun TC, Ling HS (2013) Improvements in engineering properties of soils through microbial-induced calcite precipitation. *KSCE J Civ Eng* 17:718–728

30. Tamura K, Stecher G, Peterson D et al (2013) MEGA6: molecular evolutionary genetics analysis version 6.0. *Mol Biol Evol* 30:2725–2729
31. Tsuru D, Fukumoto J, Yamamoto T (1974) Process for producing detergent resisting alkaline protease. U.S. Patent No. 3,838,009
32. Uppal HL, Chadda LR (1967) Physico-chemical changes in the lime stabilization of black cotton soil (India). *Eng Geol* 2:179–189
33. Wang JY, Soens H, Verstraete W, De Belie N (2014) Self-healing concrete by use of microencapsulated bacterial spores. *Cem Concr Res* 56:139–152
34. Wingender J, Neu TR, Flemming H-C (1999) What are bacterial extracellular polymeric substances? In: Wingender J, Neu TR, Flemming H-C (eds) *Microbial extracellular polymeric substances: characterization, structure and function*. Springer, Berlin, Heidelberg, pp 1–19
35. Zhu T, Dittrich M (2016) Carbonate precipitation through microbial activities in natural environment, and their potential in biotechnology: a review. *Front Bioeng Biotechnol* 4:4. <https://doi.org/10.3389/fbioe.2016.00004>

Mitigation of Soil Liquefaction Under Strip Footing by Densification: A Numerical Investigation



N. Dinesh, Subhadeep Banerjee and K. Rajagopal

Abstract Simple procedures are available to capture the characteristic response of loose sand under cyclic loading in free field conditions. However, the applicability of these procedures to evaluate the performance of the geotechnical structures overlying the saturated granular soil remains as a concern since the responses exhibited by the soil are very complex in these cases. One such case involving the strip foundation on top of liquefiable sand is numerically studied. The constitutive behavior of the sand is modeled using PM4Sand. In addition to the basic case, soil densification which has been a traditional remediation measure against liquefaction of saturated loose sand deposits is considered to mitigate the deformations of the strip footing. The depth of densified column below the footing is varied in order to assess its influence on the performance of the footing during seismic shaking. The settlement and excess pore water pressure corresponding to the five different cases of numerical model including an untreated model and four other models with different vertical extent are presented and its implications on the response of the footing are discussed.

Keywords Liquefaction · PM4Sand · Densification · Numerical model · Strip footing

1 Introduction

The numerical simulation of cyclic behavior of sands and the associated effects such as liquefaction are continuously explored by the researchers across the globe. The programs like LEAP serves as the evidence of such efforts. Besides it, the

N. Dinesh (✉) · S. Banerjee · K. Rajagopal
Indian Institute of Technology Madras, Chennai, India
e-mail: dineshn500@gmail.com

S. Banerjee
e-mail: subhadeep@iitm.ac.in

K. Rajagopal
e-mail: gopalkr@iitm.ac.in

mitigation of liquefaction has also been studied using different numerical codes and complex soil constitutive models [1, 6, 8, 9, 12]. These studies had focused on mitigating the liquefaction induced deformations in the structures such as embankments, earth, dam, and soil slopes. Dimitriadi et al. [7] investigated the seismic response of the footing placed on the soil deposit consisting of two layers in which a saturated non-liquefiable crust is underlain by a loose sand layer. They used FLAC 2D to perform the numerical simulations while soil skeleton response was represented by user-defined critical state concept based bounding surface model called NTUA-SAND. The present study considers two objectives such as (1) evaluation of the effect of the thickness of dense sand layers in mitigating the deformations of strip footing which was constructed over the liquefiable sand (2) investigation of effect of vertical stresses on cyclic resistance of sand. The latter objective was chosen since the author's experience on using the PM4Sand model to simulate the seismic response of earth embankment founded on liquefiable soil deposit. Despite the higher overburden stress on soil under the embankment, the numerical model predicted the excess pore pressure to attain very high value and this contradicts the experimental findings of various centrifuge studies like Adalier et al. [2], Liu and Dobry [10], and Rollins and Seed [11]. The beneficial effects of the increased confining pressure resulting from the normal stress exerted by the loading from the structure on the loose sand deposit did not get reflected in the numerical analysis as expected. It was believed that the softening of the loose sand below the embankment which was predicted by the numerical simulations could be due to the inhibition of drainage in the numerical model whereas the cracks in centrifuge model of embankment had let off the excess pore pressure. It is not clear whether the problem is associated with the numerical model regarding its capabilities to approximate the effect of confining stress on cyclic resistance of sand or the discrepancies can be attributed to physical reason (cracks). So, the present study intends to provide clarity on the same but instead with a shallow foundation because such cracks are not possible in this case.

2 Numerical Methodology

Among the available data on the seismic performance of the shallow foundation placed on liquefiable soil, the centrifuge test results reported by Liu and Dobry [10] are considered to be well documented and it has also explored the effect of spatially limited compaction underneath and around the circular rigid foundation to mitigate the seismic settlement of the foundation. Width of the compacted zone is maintained constant across all the tests whereas the depth was varied ($D_{1\text{imp}}$, $D_{2\text{imp}}$, $D_{3\text{imp}}$, and $D_{4\text{imp}}$) ranging from zero to the full-depth of the liquefiable layer of Nevada sand. The geometric configuration of the soil models studied here, which is illustrated in Fig. 1, is essentially same as that of these centrifuge tests but the strip footing is analyzed in the present study as opposed to the isolated circular footing in the centrifuge tests since the constitutive model chosen for the present study,

PM4Sand ver. 3 is implemented in FLAC 2D 7.0 for only plane strain applications. This soil constitutive model has been chosen based on its credibility in incorporating the stress–strain relations that are generally deemed as essential for addressing the cyclic behavior of sand. The features of critical state concept are invoked in this model to simulate distinctive, dilative, and contractive behavior of the soil that is associated with cyclic loading. Extensive discussion on the default calibration and implementation of the PM4Sand in FLAC 2D can be found in Boulanger and Ziotopoulou [5]. Explicit comparisons cannot be made between the computed results of present study and the measurements from centrifuge tests since circular footing which is essentially a 3D problem. Because the numerical methodology adopted in this study can only idealize it as a plane strain case and hence the present study intends only to simulate the key aspects of deformations of foundation resulting from liquefaction of loose sand which were observed from the centrifuge tests.

The validity of the numerical model (PM4S and FLAC 2D) and the soil model parameters for Nevada sand was already studied by authors based on the simulations of the centrifuge tests of Adalier et al. [2] and Adalier and Sharp [3]. These centrifuge tests have explored the effectiveness of liquefaction mitigation measures including that of the soil densification.

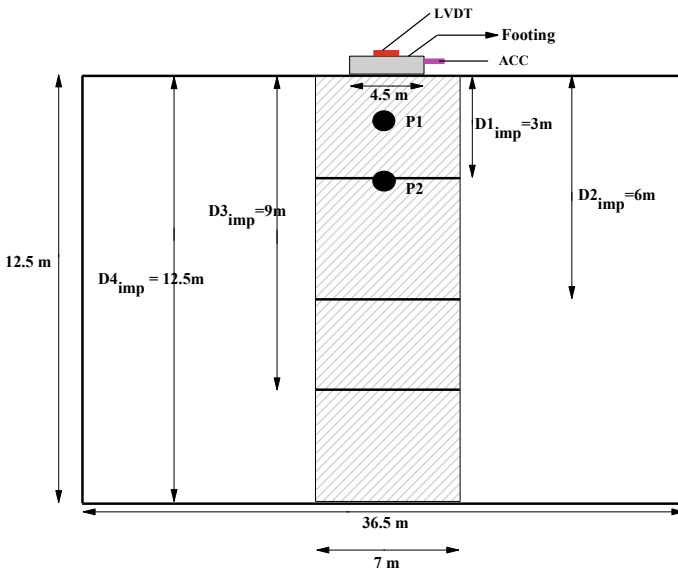


Fig. 1 Schematic sketch of the strip foundation laid on the varying thickness of dense sand layer

3 Development of Numerical Model

The geometry of the model is 36.5 m wide and 12.5 m deep. The model is discretized into a grid of quadrilateral zones. Initially, the zones were assigned with Mohr-Coulomb model and the model was run to static equilibrium thereby establishing the initial stress state associated with soil deposit by assigning the material properties summarized in Table 1. The hydrostatic pore water pressure distribution is established with reference to the presence of the water table at the top surface of the soil. A strip footing of width 4.5 m is considered in the present study. A surcharge loading was assumed to act on the foundation such that the bearing pressure on soil below the footing is 100 kPa. The foundation was modeled using beam element. The beam element connects the nodes in the grid which corresponds to the base of footing. The stresses exerted on the soil due to the foundation and the surcharge is simulated by applying the normal stress on these nodes in an incremental manner and the model is run to equilibrium for every such increment. The stress state that prevails in the model at the static phase is illustrated in Fig. 2. Boundary conditions of the numerical model were specified such that it roughly approximates the end conditions of the rigid centrifuge container. The 1-D input motion is applied at all the nodes forming the lateral and base boundaries. Bottom boundary is constrained in vertical direction while the lateral boundaries in horizontal direction. The sinusoidal input x-acceleration (frequency 1.5 Hz, PGA 0.2 g, and 10cycles) used for the simulation of seismic shaking in all the five models analyzed here. During seismic loading simulation, constitutive model of soil is switched to PM4Sand. The detailed characterization of Nevada 120 sand based on the monotonic and cyclic loading is described in Arulmoli et al. [4] and it served as the basis for calibration of PM4Sand model. The calibrated soil model constants are also included in Table 1. The density and bulk modulus of water used in the analyses is 1000 kg/m^3 and $4e5 \text{ kPa}$ (for assumed saturation of 99%), respectively.

Table 1 Properties of Nevada 120 sand used in the present analysis

Relative density (%)	40	90
<i>Basic properties of Nevada 120 sand [4]</i>		
G_{\max} (MPa)	65	100
Dry density (kN/m^3)	15.08	16.91
Permeability (m/s)	6.60E-05	2.30E-05
e_{\max}	0.887	
e_{\min}	0.511	
<i>Model parameters of PM4Sand</i>		
G0	726	950
hp0	0.1	0.005
h0	0.3	0.6
Q	9.5	
R	0.7	

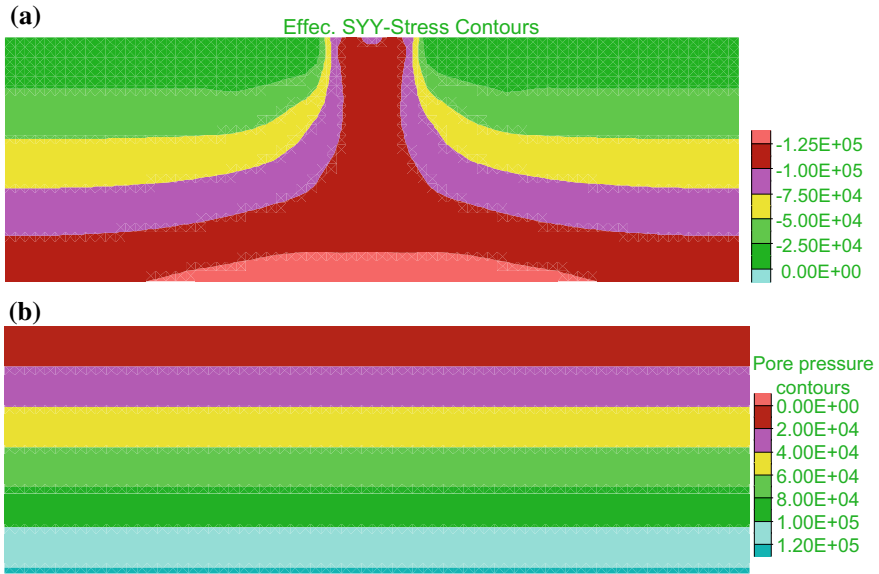


Fig. 2 a Initial effective stress distribution, b hydrostatic pore water pressure distribution

4 Results and Discussions

The effect of the various depth of compaction under the footing is evaluated in terms of the footing acceleration and the settlement. The settlement time history of footing for the untreated model and that involving different vertical compaction depth during the seismic loading is illustrated in Fig. 3. The compaction of soil under the footing drastically reduced the settlement of footing, particularly the first two depths of improvement $D1_{imp}$ and $D2_{imp}$. Despite the reduction in the rate of settlement, a little improvement was predicted for the full-depth of densification $D4_{imp}$ as compared to the partial depth of densification $D3_{imp}$.

The computed footing acceleration for the five cases of analysis is shown in Fig. 4. Attenuation and amplification of the acceleration indicate the influence of soil compaction. First two cases (D_{imp1} and D_{imp2}) exhibits the attenuation which manifests the loss of strength and stiffness of soil due to the soil liquefaction caused by seismic shaking. On the other hand the compacted soil column extending to full-depth (D_{imp4}) of the model ensures the preservation of stiffness of soil and hence it helps transmitting the soil acceleration to the footing.

The computed time history of excess pore water pressure build-up from five different cases analyzed are plotted in Fig. 5 corresponding to the two different vertical locations (**P1** and **P2** shown in Fig. 1) below the center of footing. The variation in the rate of excess pore pressure build-up between the models clearly denotes the effect of soil compaction.

Fig. 3 Settlement of footing due to the seismic loading

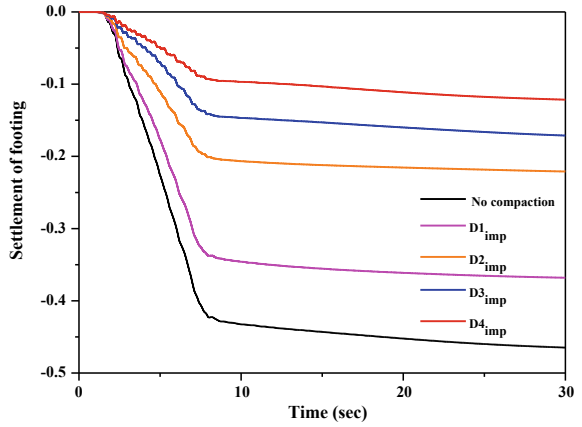


Fig. 4 Acceleration response of footing for the non-treated and treated sand models

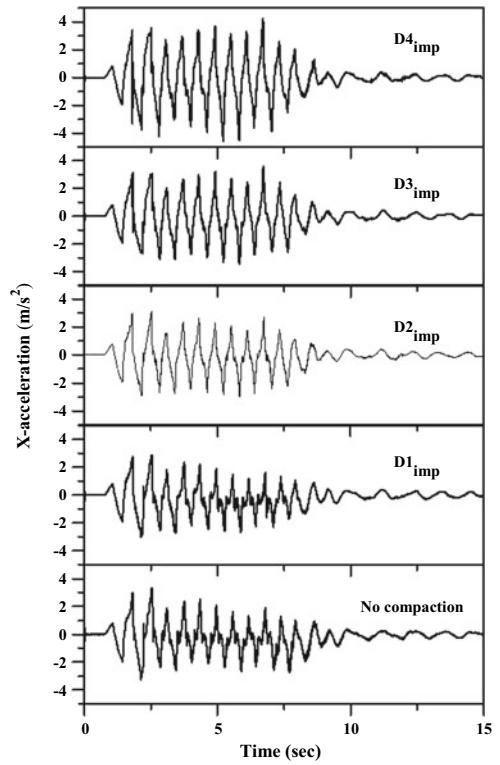
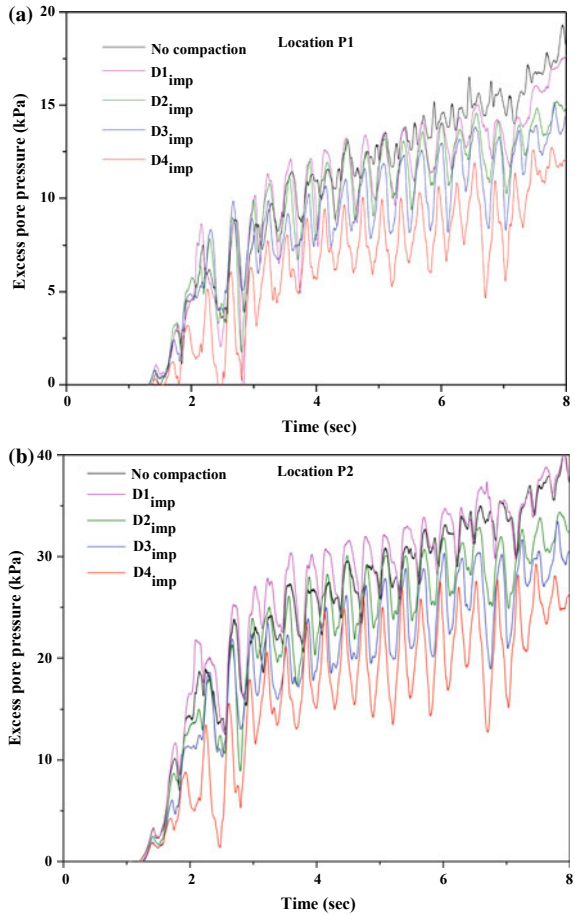


Fig. 5 Numerically computed excess pore pressure of the unimproved and improved sand models



The excess pore pressure ratio contours in Fig. 6 shows the complete liquefaction of the free field. Band of low excess pore pressure region that appears below the foundation is attributed to the higher cyclic resistance of the sand offered by the vertical stresses from the foundation. The computed excess pore pressure ratio under the footing which is eventually very low is consistent with the trends reported by Adalier et al. [2], Liu and Dobry [10] based on their centrifuge experiments.

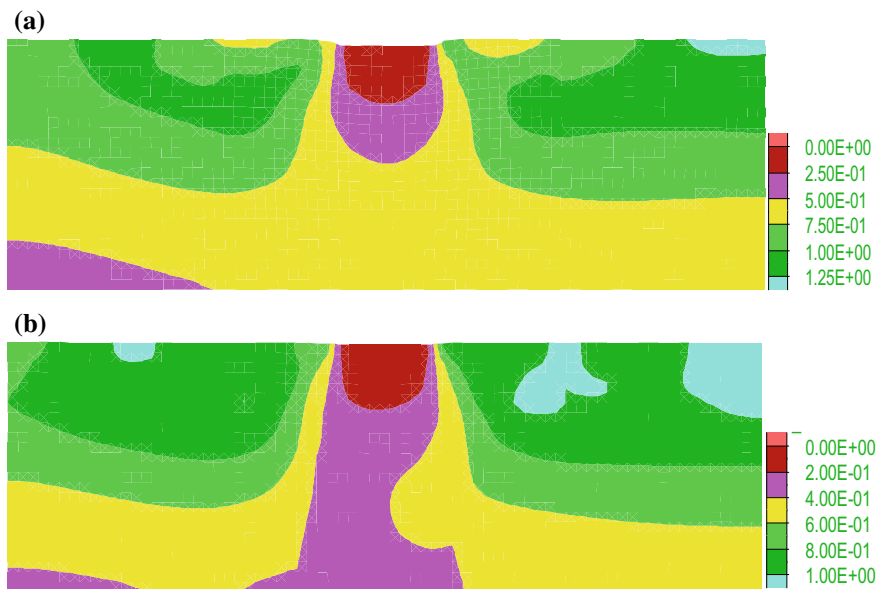


Fig. 6 Excess pore pressure ratio **a** untreated model, **b** full-depth compacted model (D_{4,imp})

5 Conclusions

The seismic response of the footing was assessed and the mitigation of soil liquefaction with various levels of the limited densified zone was presented. The results of the numerical simulations presented have demonstrated the effectiveness of the numerical model in accounting the key aspects of the response of mitigated soil that was reported in the literature based on centrifuge tests. This includes (1) the increase in footing acceleration as a result of soil densification (2) the drop in cyclic shearing-induced pore pressure due to compaction of soil, and (3) significantly lower pore water pressure under the foundation.

References

1. Adalier K, Aydingun O (2003) Numerical analysis of seismically induced liquefaction in earth embankment foundations. Part II Application of remedial measures. *Can Geotech J* 40:766–779
2. Adalier K, Elgamal AW, Martin GR (1998) Foundation liquefaction countermeasures for earth embankments. *J Geotech Geoenviron Eng* 124(6):500–517 (ASCE)
3. Adalier K, Sharp MK (2004) Embankment dam on liquefiable foundation-dynamic behaviour and densification remediation. *J Geotech Geoenviron Eng* 130(11):1214–1224 (ASCE)

4. Arulmoli K, Muraleetharan KK, Hossain MM, Fruth LS (1992) Verification of liquefaction analysis by centrifuge studies laboratory testing program soil data, Irvine, CA, Earth Technology Corporation
5. Boulanger RW, Zioutopoulou K (2015) PM4Sand model version 3 a sand plasticity model for earthquake engineering applications, Department of Civil and Environmental Engineering, UC Davis, Centre for Geotechnical Modeling, Report No. UCD/CGM-15-01
6. Boulanger RW, Khosravi M, Khosravi A, Wilson DW (2018) Remediation of liquefaction effects for an embankment using soil-cement walls: centrifuge and numerical modeling. *Soil Dyn Earthq Eng* 114:38–50 (Elsevier Ltd)
7. Dimitriadi VE, Bouckovalas GD, Chaloulos YK, Aggelis AS (2018) Seismic liquefaction performance of strip foundations: effect of ground improvement dimensions. *Soil Dyn Earthq Eng* 106:298–307
8. Elgamal A, Parra E, Yang Z, Adalier K (2002) Numerical analysis of embankment foundation liquefaction countermeasures. *J Earthq Eng* 6(4):447–471
9. Li P, Dashti S, Badanagki M, Kirkwood P (2018) Evaluating 2D numerical simulations of granular columns in level and gently sloping liquefiable sites using centrifuge experiments. *Soil Dyn Earthq Eng* 110:232–243 (Elsevier Ltd)
10. Liu L, Dobry R (1997) Seismic response of shallow foundation on liquefiable sand. *J Geotech Geoenviron Eng* 123(6):557–567 (ASCE)
11. Rollins KM, Seed HB (1990) Influence of buildings on potential liquefaction damage. *J Geotech Eng* 116(2):165–185 (ASCE)
12. Yang Z, Elgamal A, Adalier K, Sharp MK (2004) Earth dam on liquefiable foundation and remediation: numerical simulation of centrifuge experiments. *J Eng Mech* 130(11):1168–1176 (ASCE)

Effect of Strain Rate on Strength Behaviour of Cohesionless Soil



Amit Singh and Manash Chakraborty

Abstract The objective of this article is to present, qualitatively, the impact of strain rate on the strength behaviour of dry cohesionless sands. The strength behaviour was studied from the aspect of friction angle and dilation angle. A significant number of tests were performed in the direct shear test apparatus for different combinations of normal stresses and shearing strain rates. Shearing strain seems to have a noticeable impact on both the measured strength parameters. For a constant normal load, it is observed that as the shearing rate increases, shear strength increases up to a certain level and then it decreases. The rate of this decrement with respect to the strain level is also a function of the applied normal load. Insightful observations were made for the dilation angle as well. These laboratory observations and interpretations would be further helpful in designing the geotechnical structures in practice.

Keywords Sands · Direct shear test · Friction angle · Dilation angle · Strain rate

1 Introduction

Determination of strength and stiffness parameters are a major concern in soil mechanics. Strength parameters are used for stability analysis, and stiffness parameters are used for predicting the deformational aspects. The strength in the soil mass at failure is a critical combination of both normal and shear stresses. Reynold [16] concluded that failure of soil could not be treated as the failure of rigid material because, on shearing, there is a volumetric change (dilation or contraction) which influences immensely on the shear strength behaviour. In 1948, Taylor hypothesized that shear strength of granular sand is a summation of the resistance due to internal friction (rolling and sliding) and interlocking of particles and it is not an intrinsic property of sand. The total shear resistance is related to the

A. Singh · M. Chakraborty (✉)
Indian Institute of Technology (Banaras Hindu University), Varanasi 221005, India
e-mail: manashchakra.civ@itbhu.ac.in

normal force which pushes the particles together. At very large strain, any sand irrespective of its initial density attains a condition where there is a complete breakage of the interlocking effect and the shear stress and volume deformation remains to be constant. This condition is referred to as critical state condition. During the mid of the previous century and subsequent decades thereafter the geotechnical group in Cambridge [19], developed the critical state concept wherein the plastic dilatancy ratio is being formulated considering the energy dissipative function. This expression has an origin in the work of Taylor [25] who studied the interlocking behaviour of sand and the boundary energy correction for shear in the direct shear apparatus. There was a contemporary work at the University of Manchester where Rowe (1996, [20]) had extensively worked on the stress–dilatancy relationship. The stress–dilatancy relation proposed by Roscoe’s Cambridge group modelled the behaviour of NC clay and loose sand whereas, Rowe’s dilatancy relation [20] is more appropriate in the case of dense sand. By simple analogy of saw-tooth, it is clearly shown that the peak friction angle is a summation of critical state friction angle and angle of dilation.

Bolton [6] performed a number of experiments to show the effect of confining pressure and relative density on the angle of friction and angle of dilation. However, in his work critical state friction angle was considered to be the same for both the axisymmetric and plane strain test and lower confining stresses were not taken into account. Chakraborty and Salgado [8] modified the Bolton’s equation by considering the effect of lower confining stresses. Simoni and Housbly [24] showed that the gradation of soil also affects the strength parameter. Hamidi et al. [10] experimentally proved that the critical friction angle increases with an increase in relative density.

From the previous literature, it can be firmly concluded that the shearing strength of soils does not depend only on its structure and composition but also on geometrical configuration of the sample (e.g., size and shape of the sample), loading conditions (e.g., type of loading, magnitude, orientation of loading, and rate of loading, etc.), and environmental factors (e.g., drainage conditions and temperature) as well. Out of all these factors, the present manuscript focuses on the effect of shearing strain rate.

Seed et al. [23] performed drained and undrained triaxial tests on the saturated sand at high density and observed that on high strain rate pore water did not have much time to drain and hence, the testing eventually approaches towards the undrained condition. However, it was observed that the impact of normal strain rate on the magnitude of undrained strength is not so significant. Yamamuro [26] also observed that with increasing strain rates there is an appreciable improvement in elastoplastic stiffness and the failure shear strength. This study also suggested that the volumetric strains became more dilatant with an increasing rate of shear strain. Mamo and Dey [15] reported that the peak and critical angle of internal friction are significantly affected by the variation in applied strain rate and relative density of the sample.

In the present manuscript, an effort has been made to establish the effect of strain rate on the frictional and dilatational behaviour of sand. Quite a number of direct shear tests are performed for observing the impact of shearing rate of strain. It is

noticed that owing to the optimum interlocking of sand particles the peak and critical state friction angle are found to be maximum at an intermediate strain rate. The laboratory test results provide an impression that the impact of strain rate on the strength characteristics of soil is more profound for the deeper soil.

2 Friction Angle and Dilation Angle

The angle of friction (ϕ) is the maximum obliquity angle in Mohr's circle of stress (as shown in Fig. 1a). It is an indicator of highest principal stress ratio (that is the ratio of maximum and minimum principal stresses). There are two friction angles mentioned by Jewell and Wroth [12] for the plane strain coaxial deformation of granular soil, namely, (i) plane strain angle of friction (ϕ_{ps}) and (ii) direct shear angle of friction (ϕ_{ds}); ϕ_{ps} is defined as the slope of the Mohr-Coulomb failure envelope and ϕ_{ds} denotes the shearing resistance mobilized on a plane in the soil along which there is no linear incremental strain.

The friction angle (ϕ), which is being referred to in the present work, is precisely the direct shear angle of friction (ϕ_{ds}). It is obtained by the following relationship:

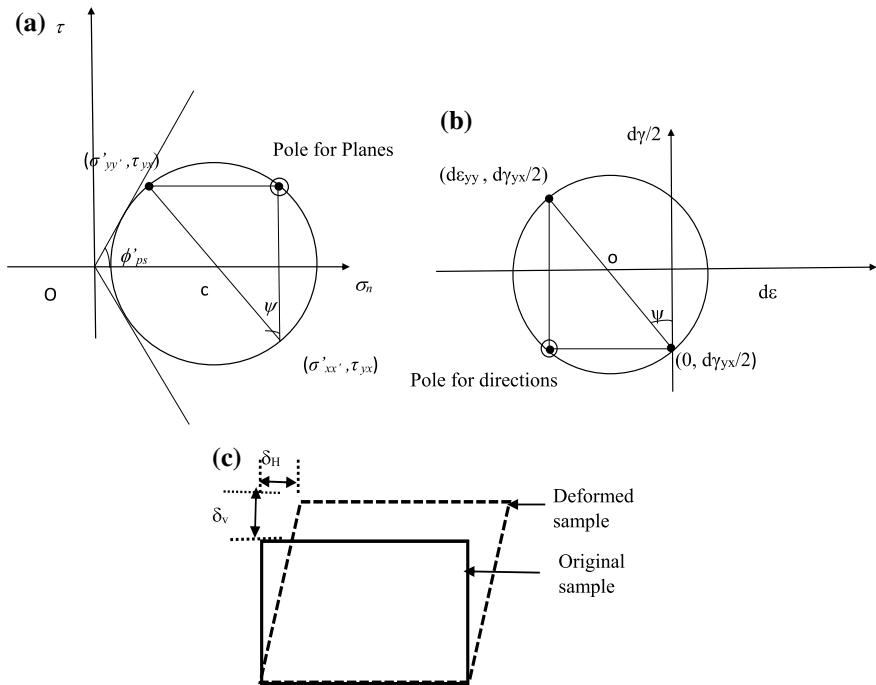


Fig. 1 Schematic representation of **a** Mohr circle of stress, **b** Mohr circle of incremental strain and **c** dilation angle during shear (Ref. [14])

$$\tan\phi_{ds} = \frac{\tau_{xy}}{\sigma_n} \quad (1)$$

where σ_n = vertical normal stress and τ_{xy} refers to the horizontal shear stress.

For a certain applied vertical stress (σ_n) on the direct shear test apparatus, the horizontal shear stress (τ_{xy}) is measured by using the proving ring along the boundary. While talking about the cardinal parameters, Lings and Dietz [14], Jewell and Wroth [12, 13] have also suggested that the ϕ_{ds} is obtained from boundary measurements of average horizontal shear stress (τ_{xy}) and average vertical normal stress (σ_n).

The angle of dilation or dilatancy angle (ψ) is the ratio of vertical (δv) and horizontal displacement (δu).

$$\sin\psi = \frac{\delta v}{\delta u} \quad (2)$$

Dilatancy is a fundamental deformation characteristic in soils. It differentiates the plastic behaviour of soil from that of metal. It indicates the amount of increase in the volume of soil when a shear force is applied. The angle of dilation controls an amount of plastic volumetric strain developed during plastic shearing. The aspect of dilatancy cannot properly model by the classical plasticity theory that was developed for metals. Dilatancy angle at any point is being represented in Mohr circle of strain (as shown in Fig. 1b).

3 Materials and Experimental Design

In the present study, Allahabad sand is used for studying the kinematics of the soil. A typical particle size distribution curve for the sand along with its properties is shown in Fig. 2. The values indicate that the chosen sand is poorly graded. The range between the maximum and the minimum friction angle is very narrow. Hence, there was not much scope to vary the relative density in the experimental programme. The entire sets of tests were carried out by keeping the sample at maximum dry density. A total number of 45 direct shear tests were performed to capture the influence of strain rate on strength and dilation of soil. The tests were carried out for five different normal stresses, namely, 5, 10, 25, 50, and 100 kPa; corresponding to each normal stress nine different strain rates (viz., 0.5, 0.75, 1.00, 1.25, 1.50, 2.00, 3.00, 4.00, and 5.00 mm/min) were applied.

The size of the shear box was 60 mm \times 60 mm \times 3.5 mm. Two dial gauges having least count of 0.01 mm were used for measuring the vertical and horizontal displacement and proving ring of least count 10 N was used to record the horizontal force applied on the specimen. The direct shear box used for the testing is shown in Fig. 3.

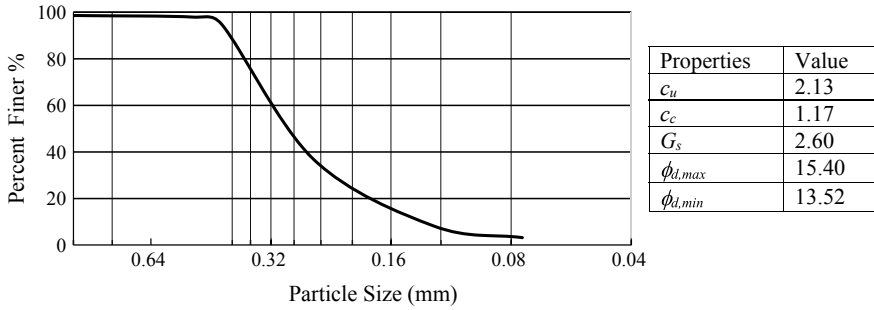
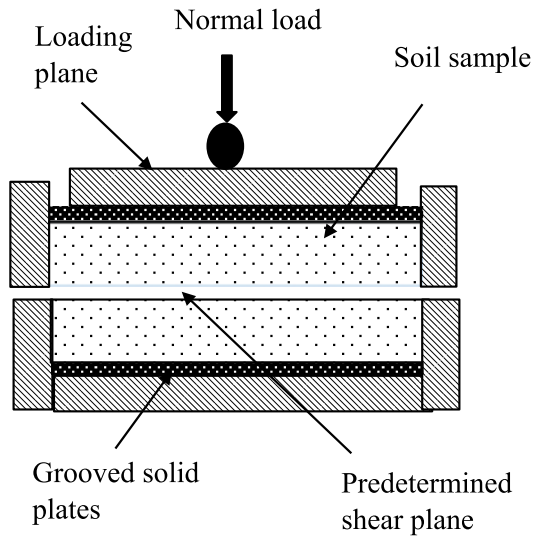


Fig. 2 Grain size distribution curve and geotechnical properties of Allahabad sand

Fig. 3 Cross section of direct shear box



4 Results

For each test, corresponding to certain horizontal displacement, shearing load and vertical displacement is recorded through the proving ring and dial gauge. These recorded data are further mathematically operated for obtaining developed shearing stress and vertical strain. By using Eqs. 1 and 2, ϕ and ψ are obtained for different shear strain corresponding to different σ_n and strain rate.

4.1 Variation of ϕ and ψ with Shear Strain

Figure 4 depicts the variation of friction angle ϕ and dilation angle ψ with shear strain γ for a different combination of normal stress σ_n . The graphs are plotted for three different strain rates—(a) minimum strain rate, (b) the strain rate at which friction angle is maximum, and the (c) maximum strain rate.

The ϕ lines in the graphs show to have a pronounced peak and strain softening, thereafter; this is supposed to be the case for the dense sands. In most of the cases, the value of maximum dilation angle and maximum friction angle are found at the same shear strain but in some cases shear strain is different.

The ψ lines display a very interesting picture. The undulating trend of the ψ lines reduces as the applied normal stress increases. It is observed that when the normal stress is lower, the mechanism of dilatancy starts at very early stage of shearing. As normal stress increases the occurrence of dilation takes place at a delayed shear strain. This phenomenon is highly prominent when the rate of applied shearing

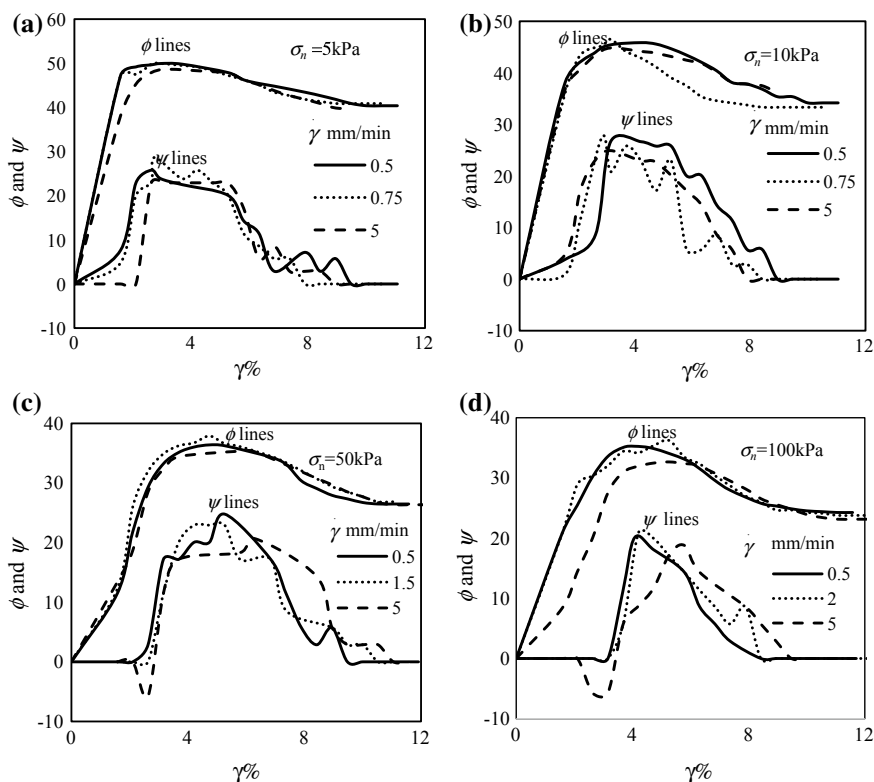


Fig. 4 Variation of ϕ and ψ with γ % for different values of $\dot{\gamma}$ and σ_n : **a** $\sigma_n = 5 \text{ kPa}$; **b** $\sigma_n = 10 \text{ kPa}$; **c** $\sigma_n = 50 \text{ kPa}$; **d** $\sigma_n = 100 \text{ kPa}$

strain is quite lower (e.g., 0.5 mm/min). Application of higher normal stresses not only delays the beginning of dilation but also makes the process to cease earlier. Hence, the window of shear strain, within which the phenomenon of dilation remains to be present reduces with high normal stresses. However, the reduction of shearing strain zone for active dilation does not seem to be significant when the soil sample undergoes high rate of shearing strain (5 mm/min). It is also observed that for high shearing strain rate, there is an appreciable amount of compression of the sample especially for high normal stresses; this compression part was never being observed for lower strain rate. These observations eventually prove the fact that the shearing strain rate influences the dilatancy characteristics of soil sample and hence need to be incorporated in the strength–dilatancy relationship.

4.2 Variation of Peak Friction Angle with Strain Rate

It is observed that the value of ϕ_p is also significantly influenced by the strain rate ($\dot{\gamma}$). Figure 5 illustrates the variation of ϕ_p with $\dot{\gamma}$ for different normal stresses. It can be observed that initially ϕ_p increases with $\dot{\gamma}$ and there is a reversal in the trend of the curve, thereafter. Similar behaviour is observed for different normal stresses. The strain rate at which the change of the trend of the curve takes place is termed as “critical strain rate”. Figure 6 shows the variation of the critical strain rate with applied normal stresses. The curve depicts that the critical strain rate increases linearly with the increment of normal stresses.

Figure 5 indicates that the difference of strain rate, at which the maximum and minimum peak friction angle occurs, decreases as the value of normal stress increases. The difference of $\phi_{p,max}$ and $\phi_{p,min}$ is normalised with respect to the required strain rate difference (as shown in Fig. 5). This is being displayed in Fig. 7. It clearly shows that the rate of decrement of peak friction angle increases

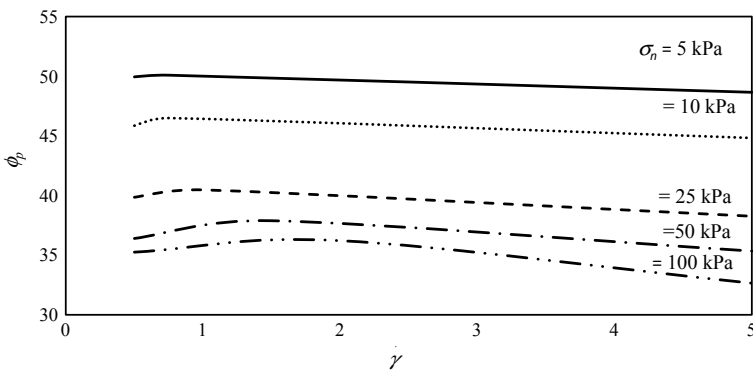


Fig. 5 Variation of ϕ_p with $\dot{\gamma}$ corresponding to different σ_n

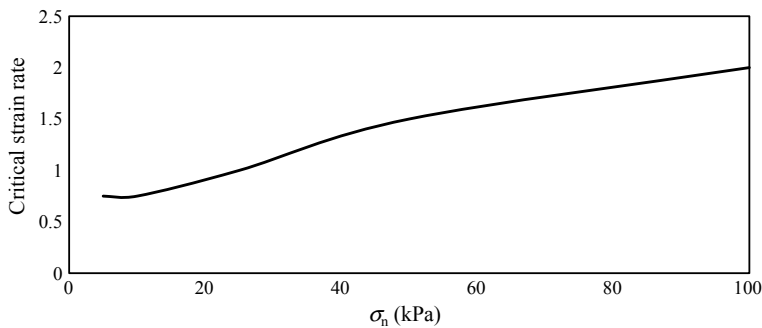


Fig. 6 Variation of critical strain rate ($\dot{\gamma}$ critical) with σ_n

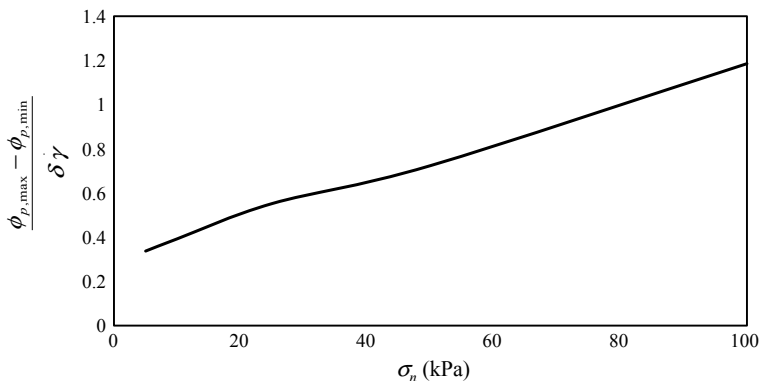


Fig. 7 Variation of the rate of change of ϕ_p with change of $\dot{\gamma}$ and versus σ_n

almost linearly with increasing normal stress. It reveals the fact that the influence of strain rate on the prediction of strength characteristics predominates as we move deeper from the ground surface. This observation seems to have a severe impact on stability analysis of geotechnical problems.

Figure 8 displays the variation of ϕ_p with normal stress for two different strain rates and it can be concluded that ϕ_p decreases rapidly in the lower range of normal stress and then maintains almost a constant value in the zone of higher normal stress; this nature is quite evident and observed by many researchers [6]. The graph shows that irrespective of the normal stress, the value of ϕ_p always remains higher for $\dot{\gamma} = 0.5$ mm/min in comparison to the sample sheared at a shearing strain rate of 5 mm/min.

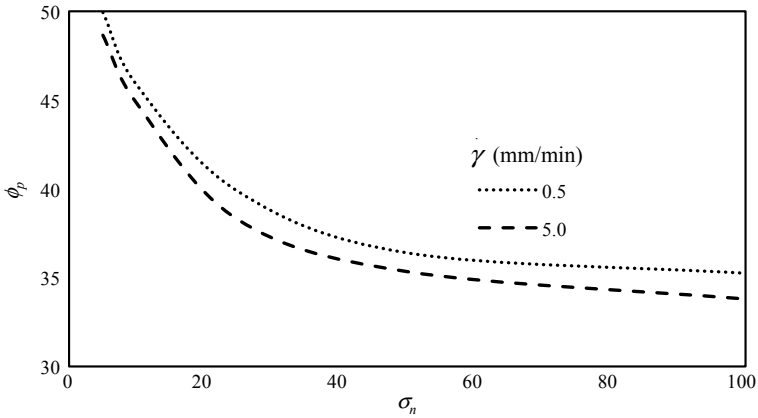


Fig. 8 Variation of ϕ_p with σ_n for two different values of $\dot{\gamma}$

4.3 Variation of Peak Dilation Angle with Strain Rate

Figure 9 shows the variation of peak dilation angle with a strain rate corresponding to different normal stresses. Note that the values of the dilation angle are substantially lower than the friction angle. Similar to the friction angle, dilation angle also decreases with strain rate after a certain strain rate. Unlike the friction angle curves presented in Fig. 5, here the curves intersect with each other and have certain anomalies. The reason behind these anomalies can be attributed to the fact that there might be certain inaccuracies in predicting the magnitude of dilatancy due to the error in the apparatus.

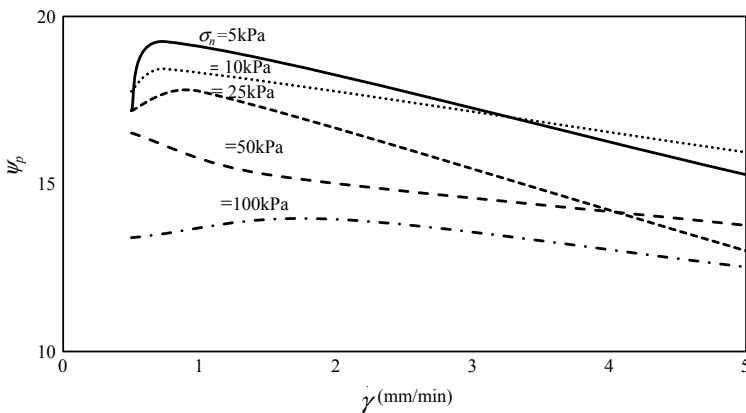


Fig. 9 Variation of ψ_p with $\dot{\gamma}$ at different σ_n

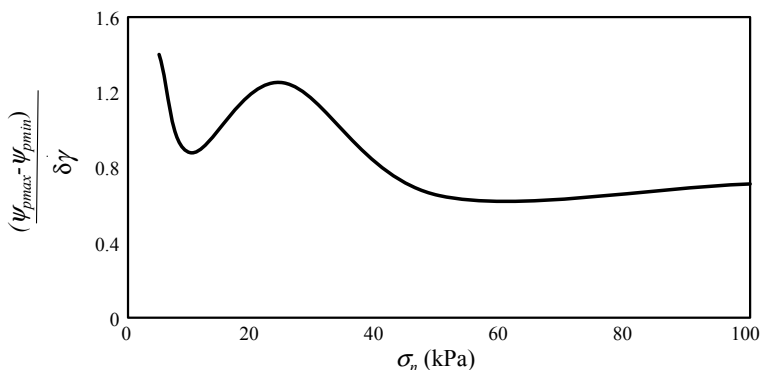


Fig. 10 Variation of the rate of change of ψ_p with change of $\dot{\gamma}$ versus σ_n

However, the trend itself is quite informative. An effort has been made to plot the rate of reduction in dilatancy rate with normal stress. Figure 10 depicts such a plot where the ordinate indicates the difference of $\psi_{p,\max}$ and $\psi_{p,\min}$ normalised with reference to the essential strain rate difference and the abscissa shows the normal stress. An entirely different trend was observed in comparison to Fig. 7. Although the peak friction angle and the dilation angle both reduce with the increasing shear strain rate, however, the rate of decrement is different for ψ_p and ϕ_p .

Figure 11 shows the variation of peak dilation angle with normal stress for two different strain rates. It can be concluded that similar to the graph displayed in Fig. 8 the curve for the smaller strain rate (0.5 mm/min) is lying above the curve corresponds to the higher strain rate (5 mm/min). Although there is a certain amount of hump and depression in the curve, especially for higher strain rate, however, it can be concluded that the peak dilation angle reduces with increasing normal stress.

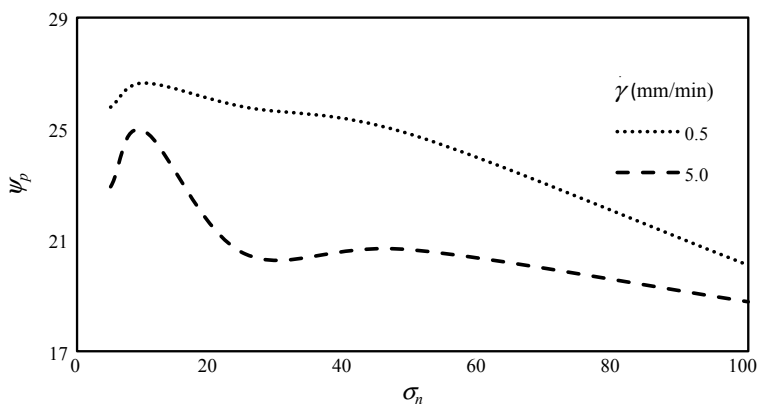


Fig. 11 Variation of ψ_p with σ_n for two different values of $\dot{\gamma}$

5 Conclusion

In the present work, it is intended to observe the influence of shear strain rate on the strength behaviour of sands. The direct shear tests were performed for different combinations of normal stresses and shearing strain rates. For a certain rate of shearing strain, friction angle decreases nonlinearly with the increasing normal stress. This decrement is significantly prominent in the region of lower normal stresses. There exists a certain shear strain rate at which the peak friction angle is always maximum. This particular strain rate is being termed as the “critical strain rate”. The magnitude of the critical strain rate increases with normal stress. Beyond the critical strain rate, the peak friction angle decreases. The rate of decrement of peak friction angle is higher for the high value of normal stress. Similar to the friction angle curve, the magnitude of the dilation angle decreases as the normal stress increases. However, the rate of change of peak dilation angle with respect to the strain rate decreases as the normal stress increases.

Acknowledgements The corresponding author acknowledges the support of “Department of Science and Technology (DST), Government of India” under grant number DST/INSPIRE/04/2016/001692.

References

1. Abrantes AE, Yamamuro JA (2002) Experimental and data analysis techniques used for high strain rate tests on the cohesionless soil. *Geotech Test J* 25(2):128–141
2. Abrantes AE, Yamamuro JA (2003) Effect of strain rates in cohesionless soil. In: *Constitutive modelling of geomaterials*, pp 188–194
3. Barden L, Amir JK (1966) Incremental strain rate ratios and strength of sand in the triaxial test. *Geotechnique* 16(4):338–357
4. Bishop AW, Blight GE (1963) Some aspects of effective stress in saturated and partially saturated soils. *Geotechnique* 13(3):177–197
5. Bishop AW, Green GE (1965) The influence of end restraint on the compression strength of a cohesionless soil. *Geotechnique* 15(3):243–266
6. Bolton MD (1986) The strength and dilatancy of sands. *Geotechnique* 36(1):65–78
7. Casagrande A (1936) Characteristics of cohesionless soils affecting the stability of slopes and earth fill. *J Boston Soc Civil Eng* 23(1):13–32
8. Chakraborty T, Salgado R (2010) Dilatancy and shear strength of sand at low confining pressures. *J Geotech Geoenviron Eng* 136(3):527–532
9. Darwin GH (1883) On the horizontal thrust of a mass of sand. In: *Minutes of the proceedings of the institution of civil engineers*, vol 71, no 1883. Thomas Telford-ICE Virtual Library, pp 350–378
10. Hamidi A, Azini E, Masoudi B (2012) Impact of gradation on the shear strength-dilatation behavior of well graded sand-gravel mixtures. *Sci Iran* 19(3):393–402
11. Housley GT (1991) How the dilatancy of soils affects their behaviour. The University of Oxford, Oxford, Department of Engineering Science, pp 1189–1202
12. Jewell RA, Wroth CP (1987) Direct shear tests on reinforced sand. *Geotechnique* 37(1):53–68
13. Jewell RA (1989) Direct shear tests on sand. *Geotechnique* 39(2):309–322

14. Lings ML, Dietz MS (2004) An improved direct shear apparatus for sand. *Geotechnique* 54 (4):245–256
15. Mamo GB, Dey A (2014) Critical overview of the effect of strain rate on direct shear test results. In: North East students geo-congress on advances in geotechnical engineering-2014, pp 1–6, Oct 2014
16. Reynolds O (1885) LVII. On the dilatancy of media composed of rigid particles in contact. With experimental illustrations. *The Lond Edinb Dublin Phil Mag J Sci* 20(127):469–481
17. Roscoe K, Burland JB (1968) On the generalized stress-strain behaviour of wet clay
18. Roscoe KH (1963) Mechanical behaviour of an idealized ‘wet’ clay. In: Proceedings of 3rd European conference on soil mechanics, Wiesbaden, 1963, vol 1, pp 47–54
19. Roscoe KH, Schofield A, Wroth AP (1958) On the yielding of soils. *Geotechnique* 8(1): 22–53
20. Rowe PW (1962) The stress-dilatancy relations for static equilibrium of an assembly of particles in contact. *Proc R Soc Lond Ser A* 269:117–141
21. Salgado R, Bandini P, Karim A (2000) Shear strength and stiffness of silty sand. *J Geotech Geoenviron Eng* 126(5):451–462
22. Schanz T, Vermeer PA (1996) Angles of friction and dilatancy of sand. *Géotechnique* 46 (1):145–152
23. Seed HB, Lundgren R, Chan CK (1954) Effect of compaction method on stability and swell pressure of soils. *Highw Res Board Bull* (93)
24. Simoni A, Houlsby GT (2006) The direct shear strength and dilatancy of sand–gravel mixtures. *Geotech Geol Eng* 24(3):523
25. Taylor DW (1948) *Fundamentals of soil mechanics*. Wiley, Inc., New York, N.Y.
26. Yamamuro JA, Lade PV (1993) Effects of strain rate on the instability of granular soils. *Geotech Test J* 16(3):304–313

Compaction and Strength Characteristics of Bentonite Rock-Quarry Dust Mixtures



Hemanga Das, Tinku Kalita and Malaya Chetia

Abstract The paper investigates the compaction and unconfined compressive strength (UCS) of bentonite-rock quarry dust (B-Q) mixtures for assessing the suitability of a cost-effective material for landfill liner. There is a criterion that the UCS of greater than 200 kPa is desirable for liner material for landfill applications to account for the load placed above (Younus and Sreedeeep in *J Test Eval* 40:357–362). The bentonite–sand mixtures are commonly used as a liner material in landfills. As the sand is a scarce material, it is important to find suitable substitutes against the sand. The rock quarry dust is a waste material which can substitute sand to improve the geotechnical properties of soil. In this study, four different B-Q mixtures have been used to determine their compaction and UCS characteristics. The rock quarry dust content varied from 60 to 90%. The UCS values of the mixtures were obtained using the unconfined compression testing machine under two different deformation rates. The results indicated that the maximum dry density (MDD) and UCS value increased significantly when the rock quarry dust content was increased from 60 to 70%. But, the MDD value remained almost constant and the UCS value decreased significantly when the rock quarry dust content was increased from 70 to 90%. The results further revealed that the deformation rate considered has minimum influence on the UCS of the mixtures. Based on the MDD and UCS values obtained, the study recommends an optimum rock quarry dust content of 70% to be added with bentonite to create a cost-effective liner material, especially for landfill applications.

Keywords Bentonite · Rock quarry dust · Mixtures · Compaction · UCS

H. Das · T. Kalita · M. Chetia (✉)
Assam Engineering College, Guwahati, India
e-mail: mchetia.ce@aec.ac.in

© Springer Nature Singapore Pte Ltd. 2020
A. Prashant et al. (eds.), *Advances in Computer Methods and Geomechanics*, Lecture Notes in Civil Engineering 56,
https://doi.org/10.1007/978-981-15-0890-5_11

1 Introduction

Bentonite–sand mixtures have been utilized as a liner material in several engineering applications. These engineering applications include waste containments such as landfill, cutoff walls, cores of earth dams, etc. The use of sand is not only limited to geotechnical and geoenvironmental applications, it is also used in the construction industries and hence, sand is becoming a valuable and scarce material day by day. So, it is important to find suitable substitutes for sand. The rock quarry dust which is obtained as solid wastes during crushing of stones to obtain aggregates can be used as a substitute for sand to improve the geotechnical properties of soil [14]. In the initial phase of a waste containment project, it is very essential to know the suitability of available materials as landfill liners. Permeability, compressibility, and strength are the important properties of bentonite–sand mixtures and are often required to evaluate for the design of the liner of the containments. There is a criterion available in the literature for assessing the suitability of the material for liner construction based on UCS and a UCS greater than 200 kPa is desirable for liner material to account for the load placed above [15]. Therefore, this study investigates the compaction characteristics and UCS of bentonite rock quarry dust mixtures and suggests a particular bentonite rock quarry dust mixture suitable as landfill liner.

The effect of deformation rate on the UCS of bentonite–sand mixtures have been studied by many researchers. Awolaye [2] have studied the effect of deformation rate on UCS of remoulded and undisturbed samples. The tests were conducted for three different rates of deformation 0.5, 1, and 2 mm/min. It was found that the UCS increases as the deformation rate increases. Casagrande and Shannon [3] also studied the effect of deformation rate on UCS of Cambridge clay and found that the UCS increases with an increase in deformation rate. Seed et al. [13] reported the effects of duration and rate of loading on the UCS of compacted clay. The strength was found to decrease initially and thereafter increase with time. Hampton [6] also studied the effect of the rate of deformation on the UCS of clay and silty clay. It was observed that the UCS increases with the increase in the deformation rate. Goldstein and Ter-Stepanian [5] reported that the UCS of compacted or undisturbed soil reduces as the rate of loading increases. There are limited studies on the effect of deformation rate on the UCS of soil mixtures. Moreover, there are contrasting observations on the effect of the deformation rate on the UCS. Therefore, this study also investigates the effect of deformation rate on the UCS of bentonite rock quarry dust mixtures.

2 Experimental Investigations

2.1 Materials and Properties

The bentonite used in this study is commercially available and the origin of this bentonite was in the state of Gujarat. The rock quarry dust was collected from the rock quarry site in Patharkuchi village, Meghalaya, India. The grain size distribution as per IS 2720 (part 4)-1973 [8], specific gravity, and Atterberg limits of rock quarry dust and bentonite were obtained according to the respective Indian standard (IS) guidelines. Tables 1 and 2 present the physical characteristics of the rock quarry dust and bentonite, respectively. The mineral constituents of the rock quarry dust sample were determined using the Petrographic images taken with the Electron microscope (25×) as shown in Fig. 1. The images also provide an idea of the particle shapes of the minerals present in the rock quarry dust. The major constituent in rock quarry dust is quartz; which has 85% quartz mineral having rounded to subrounded shape.

The mineralogical composition of the bentonite was determined by using the X-ray diffraction (XRD) method and the XRD image is shown in Fig. 2. From the XRD analysis and the free swell test results, the bentonite used in this study was found to be sodium bentonite. Table 3 represents the designations of the mixtures used in this study.

Table 1 Physical properties and classification of Q

Sl. No.	Property	Q
1	Effective diameter (D_{10}) (mm)	0.095
2	D_{30} (mm)	0.23
3	D_{60} (mm)	0.85
4	Coefficient of uniformity, C_u	8.95
5	Coefficient of curvature, C_c	0.655
6	Classification as per IS (1970)	SP

Table 2 Classification of B

Sl. No.	Property	B
1	Liquid limit (%)	207
2	Plastic limit (%)	56
3	Plasticity index (%)	151
4	Classification as per IS (1970)	CH

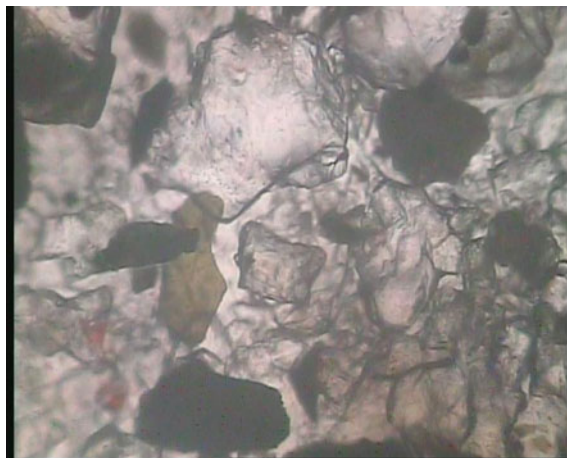


Fig. 1 Petrographic image of rock quarry dust (25 \times)

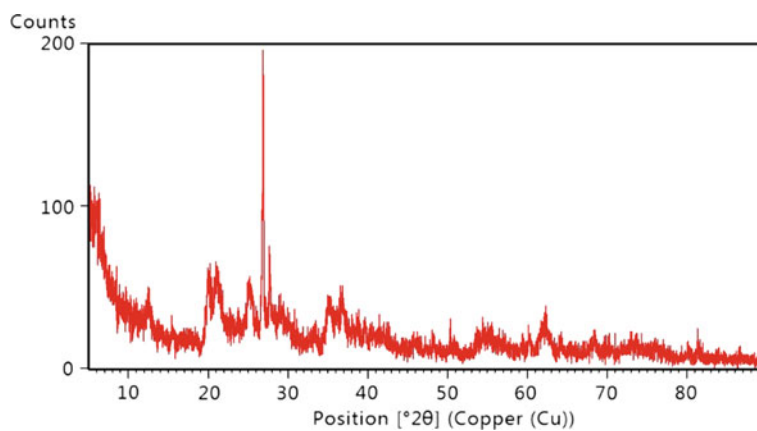


Fig. 2 XRD image of bentonite used in this study

Table 3 Designations of B-Q mixtures used in the study

Sl. No.	B content (%)	Q content (%)	Designation
1	10	90	B10-Q90
2	20	80	B20-Q80
3	30	70	B30-Q70
4	40	60	B40-Q60

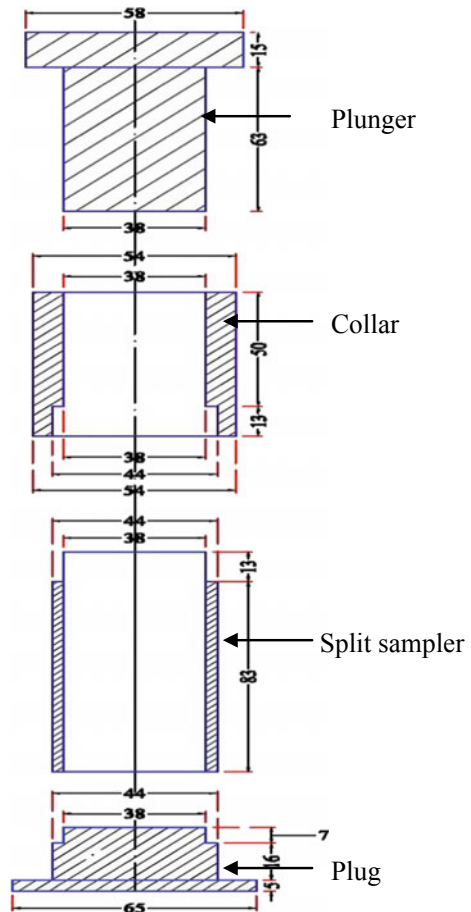
2.2 Compaction Test

The compaction properties of the B-Q mixtures were determined by the standard Proctor test according to the IS: 2720 (Part 7)-1980 [10] guidelines.

2.3 Unconfined Compressive Strength (UCS) Test

The UCS tests were conducted according to IS 2720 (Part 10)-1991 [11] guidelines. The UCS tests were conducted on the remoulded B-Q mixture samples that were prepared at MDD and OMC of the respective mixtures obtained from the compaction tests. The size of the sample was of 38 mm diameter and 76 mm height. The mass of sample was calculated from the MDD value and was mixed with the required amount of water-based on the OMC value. Then the known amount of the mass of sample was inserted into the mould of the setup (Fig. 3) prepared and

Fig. 3 Schematic view of the setup used to prepare samples for UCS test



compacted at a constant rate to prepare the sample. The sample was then removed carefully from the split sampler and tested. The UCS tests were performed under a particular rate of deformation. The UCS was determined for varying deformation rates of 1.5 and 2 mm/min. It must be mentioned that the UCS testing machine that was used in this study has the capacity of applying only three deformation rates and out of these three deformation rates the higher two rates were considered.

2.4 Details of the Setup Used to Prepare the Samples for the UCS Test

A setup was prepared from the hard plastic material to prepare the samples for the UCS test. The different parts of the setup along with their dimensions (in mm) are shown in Fig. 3.

3 Results and Discussion

3.1 Compaction Characteristics

Figure 4 shows the compaction characteristics of all the four B-Q mixtures. Table 4 shows the values of the MDD and OMC values of these mixtures. The highest MDD was achieved for the mixture B20-Q80 and the MDD decreased with further increase in the rock quarry dust content to 90%. This trend agrees with the findings as observed by Abdelrahman and Shahien [1], Dixon et al. [4], Howell et al. [7], etc., for bentonite–sand mixtures.

Fig. 4 Standard Proctor test results for the various B-Q mixtures

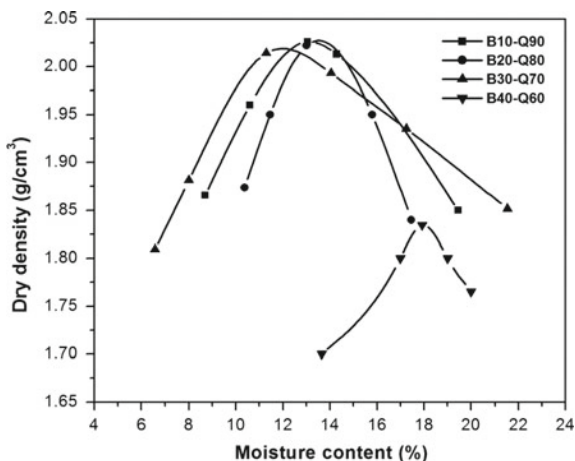


Table 4 MDD and OMC of different of B-Q mixtures

Designation	MDD (g/cm ³)	OMC (%)
B10-Q90	2.01	13.2
B20-Q80	2.03	13.7
B30-Q70	2.02	12.5
B40-Q60	1.835	17.92

Fig. 5 Variation of MDD with rock quarry dust content

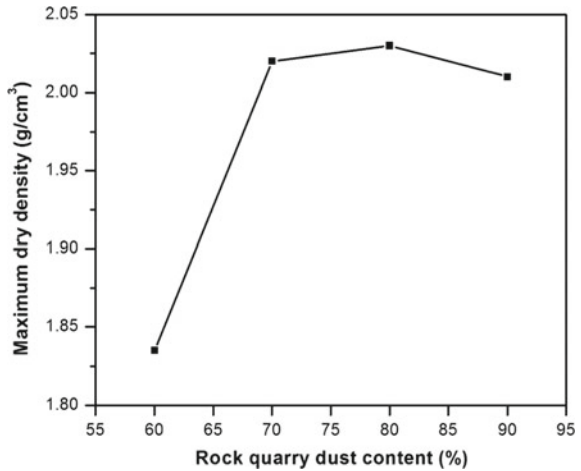


Figure 5 highlights the variation of the MDD with the rock quarry dust content. It can be seen from Fig. 5 that with the increase in the rock quarry dust content from 60 to 80%, the MDD increases significantly and thereafter, the MDD decreases with further increase in the rock quarry dust content from 80 to 90%. Hence, the optimum mixture considering the MDD is B20-Q80. The change in the MDD value is very less when the rock quarry dust was increased from 60 to 80%. At low bentonite content, the pore spaces in the rock quarry dust are being filled up by the bentonite, resulting in higher density. Also, at lower bentonite content, the swelling is not enough to disturb the soil structure. At higher bentonite content the high swelling of bentonite will destruct the structure resulting in reduction of the density.

3.2 Unconfined Compressive Strength Characteristics

Figure 6 shows the stress–strain plots of the different B-Q mixtures at deformation rates of 1.5 and 2.0 mm/min. The compaction density and water content of the UCS samples tested were their MDD and OMC values obtained from the compaction tests of the mixtures. Table 5 shows the values of the UCS and failure axial strains of various B-Q mixtures tested.

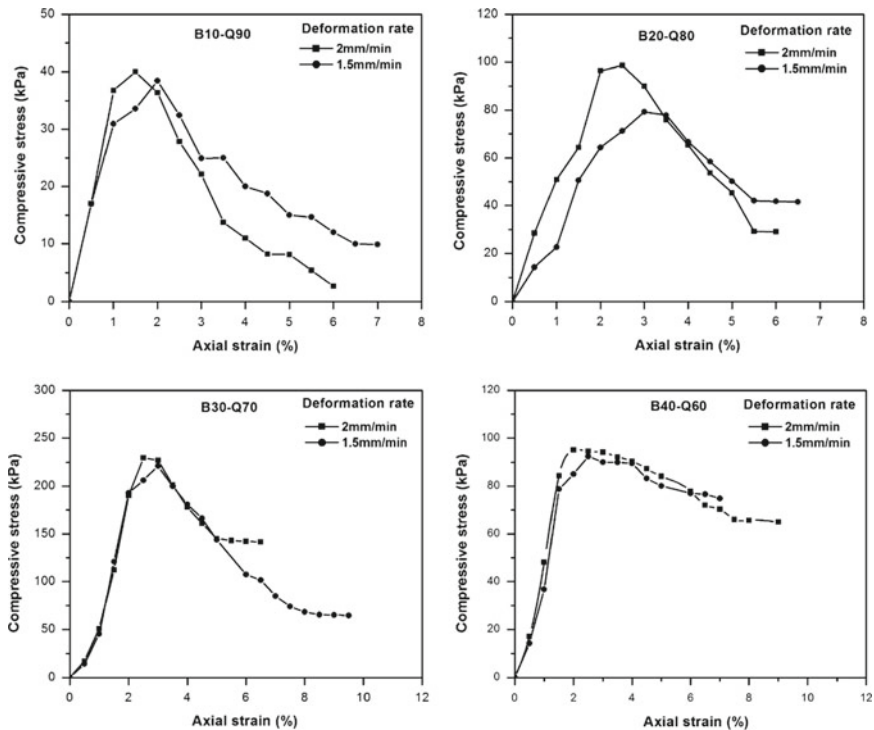


Fig. 6 Compressive stress–strain plots of B: Q mixtures at varying deformation rates

Table 5 UCS test results of B:Q mixtures for different deformation rates

Designation	Deformation rate (mm/min)			
	2		1.5	
	UCS (kPa)	Failure axial strain (%)	UCS (kPa)	Failure axial strain (%)
B10-Q90	40.01	1.5	38.45	2
B20-Q80	98.66	2.5	79.25	3
B30-Q70	229.63	2.5	221.05	3
B40-Q60	95.12	2	92.42	2.5

From Fig. 6, it can be seen that the peak of the stress–strain plots rises and shifts towards left with the increase in the deformation rate. The shifting of the peaks towards left indicates the brittle behaviour exhibited by the mixtures due to the increase in the deformation rate. Similarly, the rising of the peak of the stress–strain plots indicates the increase in the UCS of the B-Q mixtures with the deformation rate.

3.3 Variation of UCS and Failure Axial Strain with Deformation Rates

Figure 7 shows the variation of the UCS with a deformation rate of the B-Q mixtures used in this study. It has been observed that the UCS increases with the increase in the deformation rate. This finding is similar to the one as observed by Casagrande and Shannon [3] and Richardson and Whitman [12]. Figure 8 highlights the variation of failure axial strain with the deformation rate for the B-Q mixtures. It is clearly observed from Fig. 8 that the failure axial strain decreases with the increase in the deformation rate.

3.4 Variation of UCS with Rock Quarry Dust Content

Figure 9 shows the variation of the UCS of B-Q mixtures with the rock quarry dust content for two different deformation rates. It was observed that the UCS increases significantly when the rock quarry dust content was increased from 60 to 70%. But, the UCS decreases significantly on further increase in the rock quarry dust content from 70 to 90%.

When the Q content is 70% in the mixture, the interaction between the rock quarry dust and bentonite may be more and hence, there is the maximum mobilization of strength from bentonite in the form of cohesion, and in the form of friction from rock quarry dust. This combination of strength will be less with further increase in the Q content because of loss of rock quarry dust grains from the sides of the sample during shearing. The optimum Q content considering the UCS for

Fig. 7 Variation of UCS with deformation rate

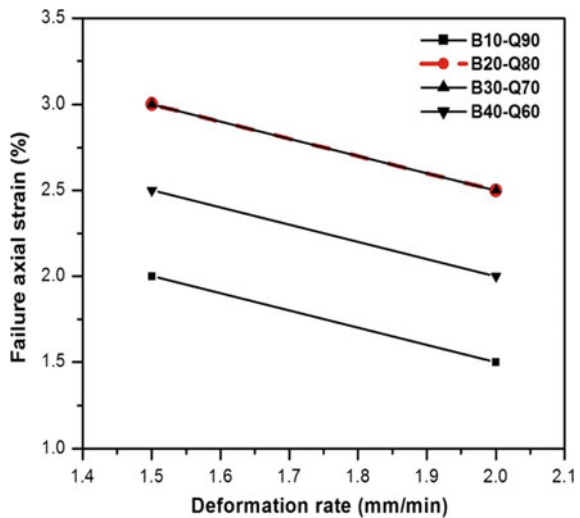


Fig. 8 Variation of failure axial strain with deformation rate

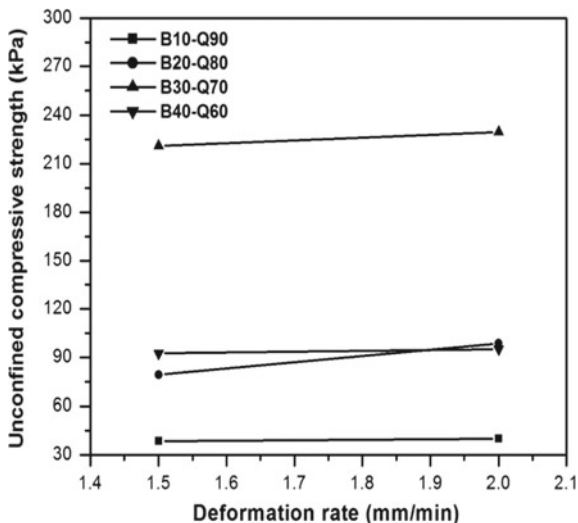
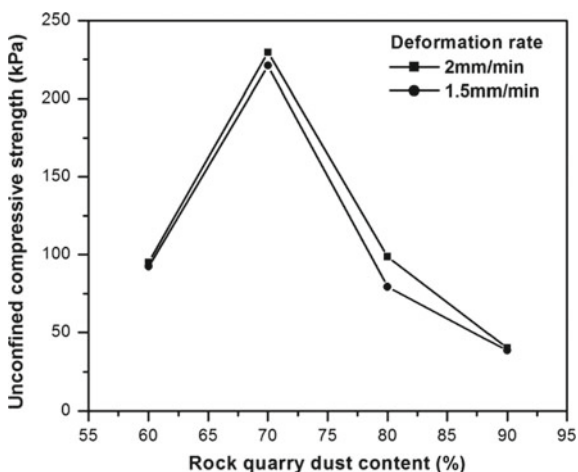


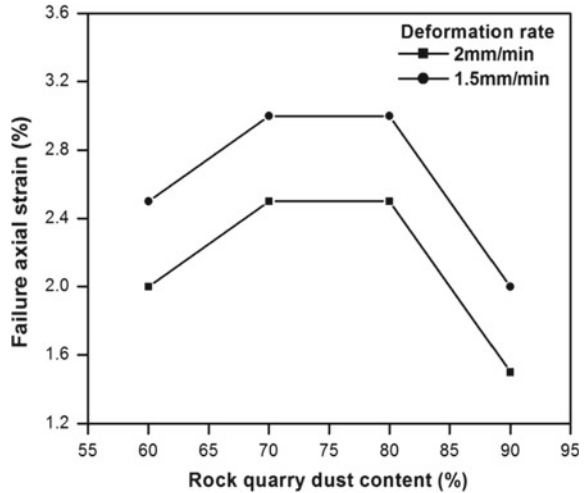
Fig. 9 Variation of UCS with rock quarry dust content at varying deformation rates



both the cases of deformation rates was found to be 70%. Therefore, based on the UCS value obtained, the B30-Q70 mixture can be considered as the optimum one.

Figure 10 shows the variation of the failure axial strain with the rock quarry dust content for varying deformation rates. The failure axial strain increases with the increase in the rock quarry dust content from 60 to 70% and then remained constant up to 80%. On further increase in the rock quarry dust content to 90%, the failure axial strain decreases. For Q = 70 and 80%, the B-Q mixtures show less brittle behaviour than the other two mixtures. Therefore, based on the highest MDD, maximum UCS and failure axial strain, the optimum Q content is found to be 70% and the optimum B-Q mixture is B30-Q70. The UCS value obtained for the

Fig. 10 Variation of failure axial strain with rock quarry dust content at varying deformation rates



optimum mixture is greater than 200 kPa and hence, it is suggested that the B30-Q70 mixture will be a suitable cost-effective material for the construction of liner landfill in place of bentonite–sand mixture.

4 Conclusions

The following are the conclusions made from this study.

1. The MDD of the B-Q mixtures increases significantly from Q = 60 to 80%, and then it decreases. Therefore, based on the MDD value, the optimum mixture is found to be B20-Q80.
2. The UCS of the B-Q mixtures increases with the increase in the deformation rate. This highlights that the UCS value specified for assessing the suitability of liner material for landfill should be deformation rate specific.
3. The failure axial strain of the B-Q mixtures decreases with the increase in the deformation rate.
4. The failure axial strain of the mixtures increases from Q = 60 to 70% and then remains constant up to Q = 80%. However, the failure axial strain decreases with further increase in the Q content.
5. Irrespective of the deformation rate, with an increase in the Q content from 60 to 70%, the UCS increases, and then decreases on further increase in the Q content from 70% to 90% and hence, the optimum mixture considering the UCS value is found to be B30-Q70. Therefore, based on the MDD and UCS values obtained, the study recommends an optimum Q content of 70% to be added with bentonite to create a cost-effective liner material which may be suitable for landfill applications.

References

1. Abdelrahman GE, Shahien MM (2004) Swelling treatment using sand for Tamia swelling soil. In: Fourth international engineering conference, Egypt
2. Awoloye OA (1991) Time effects on the unconfined compressive strength and sensitivity of a clay. *Geotech Test J* 20(4):345–351
3. Casagrande A, Shannon WL (1949) Strength of soil under dynamic loads. *Trans Am Soc Civil Eng ASCE*
4. Dixon DA, Gray MN, Thomas AW (1985) A study of the compaction properties of potential clay-sand buffer mixtures for use in nuclear fuel waste disposal. *Eng Geol* 21:247–255
5. Goldstein M, Ter-Stepanian (1957) The long term strength on clays. *Soil Mech Found Eng* 2 (4):311–314
6. Hampton D (1958) Effect of rate of strain on the strength of remoulded soil. Joint Highway Research Project, No. 17, Purdue University, Lafayette, Indiana, USA
7. Howell JL, Shackeford CD, Amer NH, Stern RT (1997) Compaction of sand processed clay soil mixtures. *Geotech Test J* 20(4):443–458
8. IS: 2720 (Part 4) (1973) Grain size analysis. Indian standard methods of tests for soils, Bureau of Indian Standards, New Delhi
9. IS: 2720 (Part 5) (1985) Determination of liquid and plastic limit. Indian standard methods of tests for soils, Bureau of Indian Standards, New Delhi
10. IS: 2720 (Part 7) (1980) Determination of water content-dry density relation using light compaction. Indian standard methods of tests for soils, Bureau of Indian Standards, New Delhi
11. IS: 2720 (Part 10) (1991) Determination of unconfined compressive strength. Indian standard methods of tests for soils, Bureau of Indian Standards, New Delhi
12. Richardson AM, Whitman RV (1964) Effect of strain-rate upon undrained shear resistance of saturated remolded fat clay. *Geotechnique* 12:310–324
13. Seed HB, Mitchell JK, Chan CK (1960) The strength of compacted cohesive soil. Research conference on the shear strength of cohesive soils, Boulder, Colombia, USA
14. Sridharan A, Soosan TG, Jose BT, Abraham BM (2006) Shear strength studies on soil-quarry dust mixtures. *Geotech Geol Eng* 24:1163–1179
15. Younus MM, Sreedeeep S (2012) Evaluation of bentonite-fly ash mix for its application in landfill liners. *J Test Eval* 40(3):357–362

Synthesis of Bentonite Clay-Based Geopolymer and Its Application in the Treatment of Expansive Soil



Kaling Taki and Sudhanshu Sharma

Abstract Geopolymer technology is gaining a lot of interests in research and development because they act as a ‘versatile admixture’ for different purposes. The focus of the present work was: (1) To investigate the suitability of Bentonite soil for the synthesis of Geopolymer (2) To investigate the effect of Bentonite soil-based Geopolymer for potential improvement in swelling–shrinkage behaviour of expansive soil. The source material for Geopolymer synthesis was commercially available Bentonite cohesive soil. The presence of montmorillonite mineral causes high water absorption response and swelling–shrinkage behaviour, which makes it extremely difficult to use for civil engineering construction purposes. The critical soil parameters of Bentonite soil such as Liquid Limit (LL), Plastic Limit (PL), Differential Free Swell Index (DFSI), Plasticity index (PI) and Flow index (I_f) were found to be very high (LL = 609%, PL = 51%, DFSI = 662%, PI = 558% and I_f = 0.55) due to the presence of Montmorillonite mineral. Remarkable improvement in the properties was observed after treating Bentonite soil with 4% of synthesized Geopolymer. The sample was prepared on weight basis and were cured for a period of seven days, after the end of curing period the test was conducted. A drastic reduction in the studied parameter was observed, after the seventh day, the LL, PL, DFSI, PI and I_f values were observed to be decreased; 509%, 40%, 329%, 469% and 0.28, respectively. Thus, the study revealed that Geopolymer can be effectively used for treating expansive soil.

Keywords Bentonite • Geopolymer • Energy-dispersive X-ray spectroscopy (EDX) • Expansive soil • Montmorillonite

K. Taki (✉)

Civil Engineering, Indian Institute of Technology Gandhinagar, Gandhinagar, India
e-mail: kaling.taki@iitgn.ac.in

S. Sharma

Chemistry, Indian Institute of Technology Gandhinagar, Gandhinagar, India
e-mail: ssharma@iitgn.ac.in

© Springer Nature Singapore Pte Ltd. 2020

A. Prashant et al. (eds.), *Advances in Computer Methods and Geomechanics*, Lecture Notes in Civil Engineering 56,
https://doi.org/10.1007/978-981-15-0890-5_12

133

1 Introduction

In the present time, Geopolymer technology is gaining a lot of interest in research and development, because they act as a 'versatile admixture' for different purposes. Being a versatile material, most engineering technologies, inorganic chemistry, geology, physical chemistry, analytical chemistry and mineralogy utilizes its properties for resourceful applications [6]. Joseph Davidovits introduced the concept of geopolymers for the first time [9]. The inorganic polymeric material was found to be at par in applications with the traditional geopolymer [13].

Geopolymers are inorganic aluminosilicate polymers, with 3-dimensional network and aluminosilicate as the building blocks [8]. Research in the field of Geopolymers has anciently been application-driven. The brittle characteristics of geopolymer are a major drawback in its extensive applications. However, significant commercial and technological applications are discovered to overcome such shortcomings [16]. Some of the areas utilizing the potency of Geopolymers include construction industry (as cement, concrete and binders), catalysis, separation processes (in filtering), medical applications (as biomaterials), heat transfer equipment (as thermal insulators and thermal shock refractory) and polymer industry (as resins, composites for infrastructure repair and aircraft interior) [10, 16].

Geopolymers comprises of three classes of inorganic polymer that contain the following three basic units: ($-\text{Si}-\text{O}-\text{Al}-\text{O}-$), polysialate (PS), $\text{SiO}_2/\text{Al}_2\text{O}_3=2$; ($-\text{Si}-\text{O}-\text{Al}-\text{O}-\text{Si}-\text{O}-$), polysialatesiloxo (PSS), $\text{SiO}_2/\text{Al}_2\text{O}_3=4$; ($-\text{Si}-\text{O}-\text{Al}-\text{O}-\text{Si}-\text{O}-\text{Si}-\text{O}-$), polysialatedisiloxo (PSDS), $\text{SiO}_2/\text{Al}_2\text{O}_3=6$ which depends on the Si/Al ratio [5]. The synthesis of geopolymers cement and concretes in most researches are by waste sources, viz blast furnace slag (GGBFS) [24, 27], fly ash [22, 31], coal and petroleum coke [1, 26]. Geopolymers can exhibit a huge variety of characteristics, including fireproof ability, less shrink capacity, swift and relaxed setting, acid resistivity, high compressive strength and low thermal conductivity which solely depends on the source material and physical parameters [11]. Higher compressive strength geopolymers are synthesized from calcined sources (metakaolin) in comparison to materials synthesized by non-calcined sources (kaolin clay). Alkali bonded ceramic, hydroceramic, alkali activated cement, low-temperature aluminosilicate glass and geocement are some of the types of geopolymeric gels and composites [23].

Geopolymerisation includes an exothermic chemical reaction under atmospheric pressure yielding polymeric structures with Si-O-Al linkage. The reactants involved in geopolymerisation reaction are metal silicate solutions (alkaline) and oxides of alumina silicate resulting in amorphous to semi 3D crystals of polymers [6]. Optimum temperature (below 100 °C) and pressure lead geopolymerisation reaction with setting and hardening of geopolymers. The exact mechanism of geopolymer setting is still a matter of research but the general geopolymerisation mechanism comprises of the following five steps occurring collaterally: (a) Dissolution (b) oligomer formation (c) polycondensation (d) filler material bonding and (e) hardening of polymer. Despite the fact, geopolymer has amorphous structure it's

chemical composition has similarities with natural zeolite material. Alkaline activators widely used are in the form of $\text{Na/K}_2\text{SiO}_3$ and Na/KOH [24].

Ordinary portland cement (OPC) is the material used as an effective binder in building materials especially in concrete. According to International Energy Agency, the production of OPC has a major contribution (around 7% of the total CO_2 emissions) in emission of the greenhouse gases [21]. Geopolymers, on the other hand, have the advantage of comparative decline in greenhouse emission while used in concrete applications. OPC consumes a substantial amount of energy and releases high volumes of gases associated with greenhouse effect which certainly is a threat to the environment [4]. Significantly, geopolymer is a more environment friendly approach as FA based concretes (geopolymeric) emit approximately 90% lesser CO_2 in comparison to its OPC analogue [12, 30].

Zeolites and geopolymers both have been used extensively for heavy metal removal from wastewaters [15, 19, 28]. On a contrary basis synthesis of geopolymer is reported to be very simple and feasible than zeolite production [25]. Porous metakaolin geopolymer is efficient in the optimal adsorption of lead from wastewater under discrete experimental parameters [3]. Successful column tests proved that geopolymer being low-cost and eco-friendly is a promising emerging method for wastewater metal removal [14] to replace the common costly adsorbents of lead like silica, activated carbon and alumina from wastewater, first time a geopolymeric monolith was synthesized for this application. The maximum lead uptake (about 6.34 mg) by the porous biomass FA-containing geopolymer and its easy collection after exhaustion ensures its position in better metal removal technologies from wastewater [20].

Though Geopolymer has diverse applications in a different field, its use as a soil stabilizing agent has not been explored and also the synthesis of Geopolymer using Bentonite clay has not been reported elsewhere to the best of our knowledge. The objectives with which the present study was carried out can be subdivided into two folds: (1) To assess the suitability of Bentonite soil for the synthesis of Geopolymer. (2) To investigate the effect of Bentonite soil-based Geopolymer for potential improvement in swelling–shrinkage behaviour of expansive soil.

2 Experimental Programme

2.1 *Material Properties and Preparation of Geopolymer*

Geopolymer is synthesized using materials which are rich sources of alumina and silica. In the present study the source material taken was commercially available Bentonite cohesive soil. Bentonite soil is aluminium phyllosilicate clay consisting mostly of montmorillonite mineral, and the building blocks are alumina and silica.

Table 1 Basic properties of Bentonite soil

Particulars	Specifications
Material used	Bentonite (Brown colour)
Liquid limit (%)	609
Plastic limit (%)	51
Plasticity index (%)	558
Flow index (I_f)	0.55
Soil classified	CH type
Differential free swell index (DFSI) (%)	662

The presence of alumina and silica makes it as a potential source for Geopolymer synthesis. Basic geotechnical properties of the Bentonite soil are given in Table 1.

2.2 *Synthesis of Bentonite Soil-Based Geopolymer*

A schematic representation of the testing procedure for the synthesis of Bentonite soil-based Geopolymer is shown in Fig. 1. Initially the 10 g of Bentonite soil was calcined by preheating up to 700 °C in a muffle furnace for 10 h. Potassium silicate solution was prepared by dissolving an appropriate amount of KOH pellets (14 g) in deionized water in a polypropylene cup. Fumed silica (15.43 g) was then added into the KOH solution and the mixture was stirred for 30 min at 800 rpm to give a clear solution of 8 M. The geopolymer resins were then prepared by mechanically mixing preheated Bentonite into the potassium silicate solution to form a homogenous solution. The solution was further cured in oven at 60 °C for 24 h to obtain a solid crystalline phase, after the curing the solid crystalline resins was broken into small pieces and washing was done by cold distilled water.

The pH of the resins was about 14 (highly alkaline) during the initial stage of washing. To make it neutral the resin samples were further washed with distilled water. After every wash, the pH of the sample was monitored, with continuous washing there was a reduction in pH value as shown in Fig. 2. The washing continued for many days till the pH reached almost 7. After the pH was dropped to 7 the extra water was decanted, and the leftover sediment was collected in a crucible. The wet collected sediment was kept inside the muffle furnace for 24 h at 60 °C for the removal for moisture. After 24 h, it was found that 10 g of Bentonite Yielded 3.7 g of Geopolymer. The dried samples were used to perform characterization test. Also, its applicability as an effective admixture to control the swell–shrink behaviour of expansive soil was explored by performing the geotechnical tests.

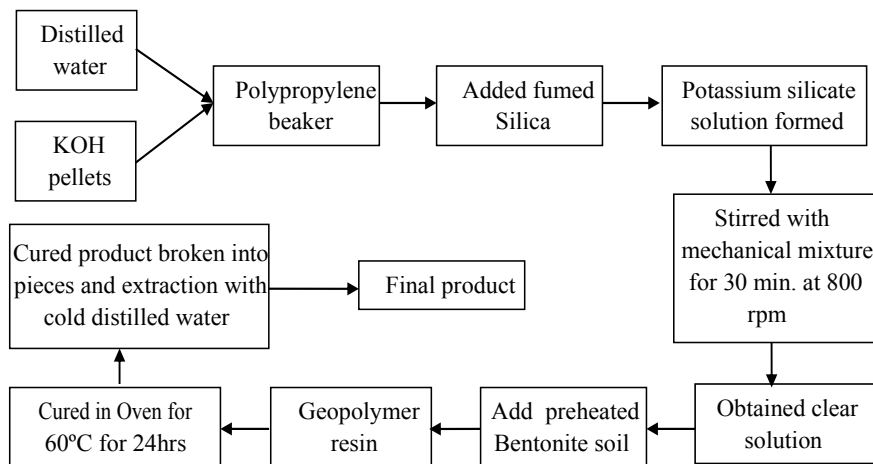


Fig. 1 Procedure adopted for the synthesis of the Bentonite soil-based Geopolymer

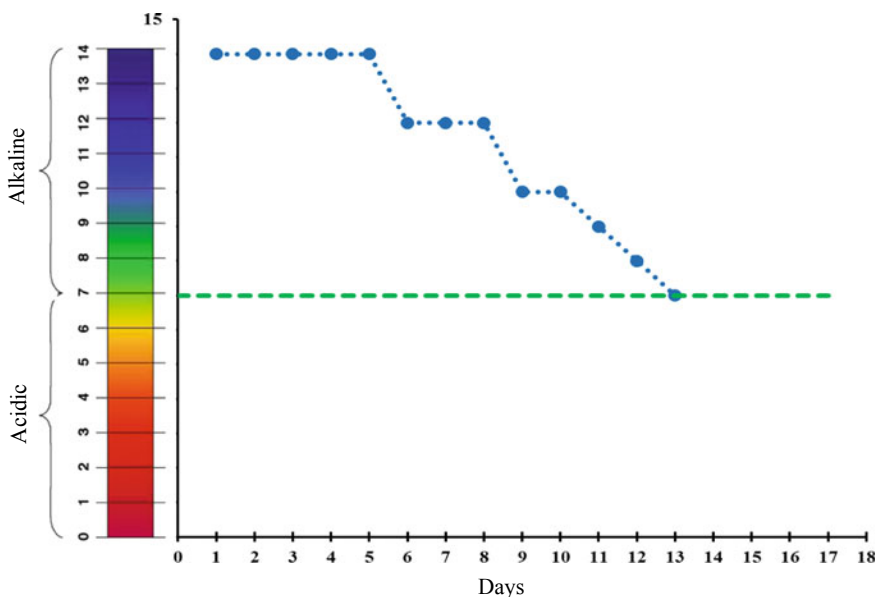


Fig. 2 Change in pH of the crystalline resins with days of washing

2.3 Characterization of Synthesized Geopolymer

Scanning Electron Microscopy (SEM) and Energy-Dispersive Spectroscopy (EDS) elemental analysis was carried out for characterization of the synthesized Geopolymer. It was observed that when the Bentonite soil translated into Geopolymer, structural modification took place. From Fig. 3 it can be seen that for pure Bentonite soil the structure was stable with no rupture and foliation. When the Bentonite soil was further heated to 700 °C, the structure got deteriorated. It can also be observed that, during the conversion from virgin clay soil to Geopolymer major amount of modification occurred, lots of small granulated particle got attached on the surface of the larger particles as shown in Fig. 3.

EDS analysis (Fig. 4) shows that the presence of CaCO_3 {C} as the Bentonite soil gets converted into Geopolymer. The presence of CaCO_3 signifies that if Geopolymer is used as an admixture, it might improve the properties of expansive soil because it will act as a source of Ca^{2+} ions. The Ca^{2+} ions will further help in modifying the clay structure thereby changing its plasticity characteristic and controls the swell–shrink behaviour.

2.4 Testing Procedure

The applicability of Geopolymer to bring about modification in the critical properties of Bentonite soil was further explored by incorporating it as an admixture.

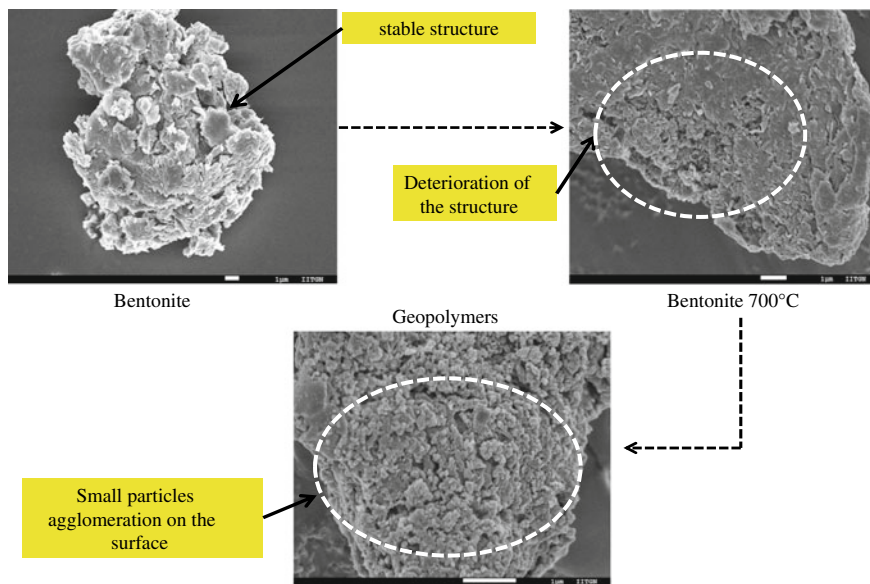


Fig. 3 SEM micrograph of Bentonite soil-based Geopolymer

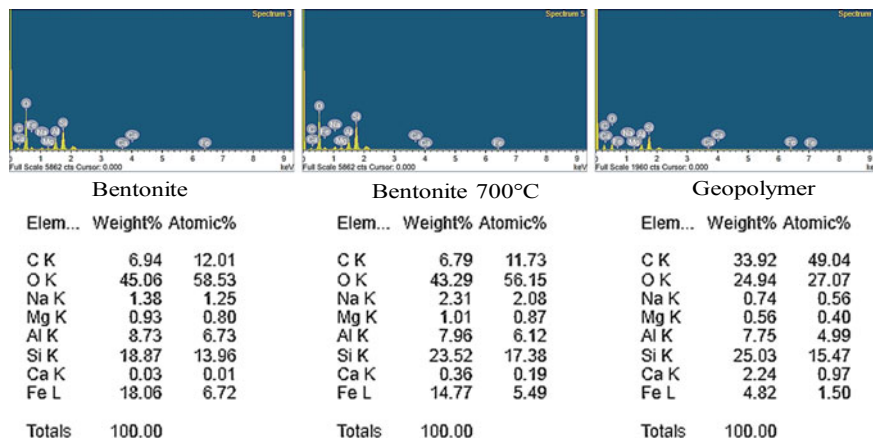


Fig. 4 EDS analysis of Bentonite, Preheated Bentonite and Geopolymer

The Geopolymer was added to the same Bentonite soil from which it was synthesized to control its swell–shrink behaviour.

2.4.1 Sample Preparation

For the test, the dry geopolymer powder was added to the Bentonite soil in weight basis. 4% of Geopolymer by weight of the Bentonite soil was taken and dry mixed. For mixing the total soil mass was divided into four parts, and to each part, the Geopolymer was added and mixed for at least 5 min. After 5 min, each part was mixed together to form two parts for another 5 min. In the end, the remaining two parts were mixed together for another 5 min to give the final mixture. The mixing was done in steps to achieve homogeneity throughout, and the mixing was done by using mechanical mixture.

2.4.2 Liquid Limit Test (IS: 2720 (Part 5)-1985)

For the test 150 g Bentonite soil passing through 425 μ sieve was mixed with 4% Geopolymer in a dry state and then water was added to make slurry. In order to ensure the uniform distribution of moisture in the Bentonite soil due to its clayey nature and high water absorption properties. The prepared soil slurry was sealed in a plastic bag and kept inside the desiccator for seven days. After seven days the plastic bag was opened and the soil slurry was spread over the plastic sheet, and using Casagrande apparatus the liquid limit test was conducted as shown in Fig. 5.

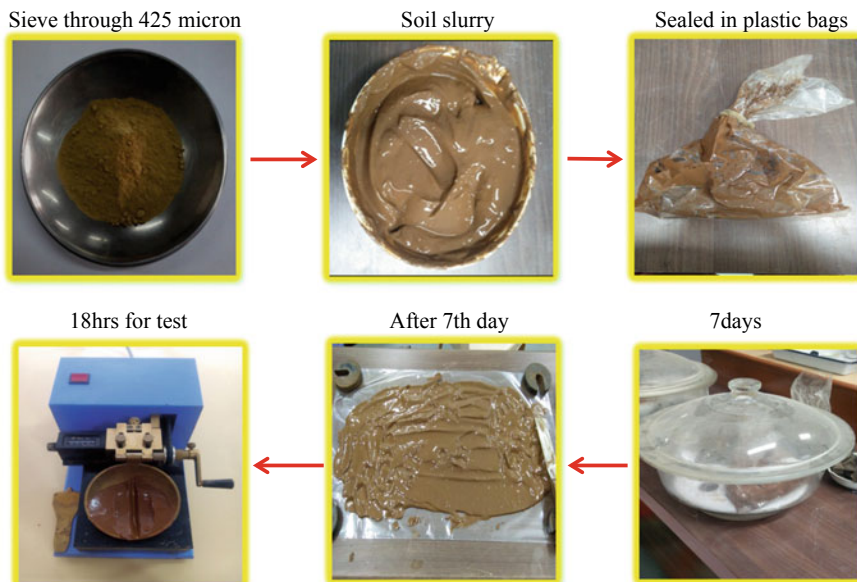


Fig. 5 Liquid limit test stage

2.4.3 Plastic Limit Test (IS: 2720 (Part 5)-1985)

Once the Liquid Limit test was done plastic limit was done on the soil that was left after the Liquid Limit test. By rolling the clay paste into a thread of 3 mm on a glass plate.

2.5 *Differential Free Swell Index (DFSI) Test (IS: 2720 (Part 40)-1977)*

This is one of the basic tests to see the degree of expansiveness of the expansive soil. For the test initially, untreated Bentonite soil weighing 5 g was taken in 100 ml cylinder and it was mixed with distilled water. As a control, another cylinder was taken wherein 100 ml kerosene was taken with 5 g of Bentonite soil and mixed with 4% Geopolymer, both the setup was kept for 24 h. After 24 h the change in volume was computed, which gives the DFSI of the corresponding soil in percentage.

Table 2 Comparison of Geopolymer treated and untreated Bentonite soil after seven days curing

Particulars	Untreated	Treated	Percentage reduction (%)
Liquid limit (%)	609	509	20
Plastic limit (%)	51	40	28
Plasticity index (%)	558	469	19
Flow index (I_f)	0.55	0.28	96
Differential free swell index (DFSI) (%)	662	329	51

3 Results and Discussion

After treating the Bentonite soil with Geopolymer, it was found that there was 20% and 28% reduction in Liquid Limit and Plastic Limit value as shown in Table 2. Also, 50 and 96% reduction in DFSI and I_f was observed. There was an overall reduction in the plasticity characteristics of the Bentonite soil, this reduction could be attributed to the generation of calcium carbonate during the transformation of the virgin Bentonite soil to Geopolymer. The reduction in plasticity characteristic of the Geopolymer treated Bentonite soil can be attributed to the modification in the diffuse double layer of clay particle by the Ca^{2+} ions released from calcite. The Ca^{2+} ion from calcite is released into the pores of soil and as a result divalent Ca^{2+} ions replace the monovalent Na^+ ions present in Bentonite soil. This replacement of ions causes an increase in electrolytic concentration, which may reduce the thickness of 'diffuse double layer' (an ionic layer found around the clay particle). Reduction in thickness of diffuse double layer will lessen water absorption, retention and swelling properties of soil leading to decrease in LL, PL and DFSI [7]. In addition, CaCO_3 forms an aggregated structure (0.02–0.05 mm in diameter), which is larger than the size of clay particle (0.002 mm in diameter). These particles behave as silt sealing the pores and further enhance the clay properties [2, 29].

4 Conclusions

- Bentonite clay-based Geopolymers has been successfully synthesized.
- The SEM showed structural modification as the Bentonite soil gets converted into Geopolymer.
- After treatment 20, 28, 51 and 96% reduction in the value of Liquid Limit, Plastic Limit, DFSI and flow index was observed.
- The study revealed that Geopolymer can be effectively used for treating expansive soil.

Acknowledgements Financial Support from IIT Gandhinagar is gratefully acknowledged. Any opinions, findings, and conclusions or recommendations expressed in this material are those of authors and do not necessarily reflect the views of IIT Gandhinagar.

References

1. Álvarez-Ayuso E, Querol X, Plana F, Alastuey A, Moreno N, Izquierdo M, Font O, Moreno T, Diez S, Vázquez E, Barra M (2008) Environmental physical and structural characterisation of geopolymer matrixes synthesised from coal (co-) combustion fly ashes. *J Hazard Mater* 154(1–3):175–183
2. Bell FG (1996) Lime stabilization of clay minerals and soils. *J Eng Geol* 42:223–237
3. Cheng TW, Lee ML, Ko MS, Ueng TH, Yang SF (2012) The heavy metal adsorption characteristics on metakaolin-based geopolymer. *J Appl Clay Sci* 56:90–96
4. Chotetanorm C, Chindaprasirt P, Sata V, Rukzon S, Sathonsaowaphak A (2012) High-calcium bottom ash geopolymer: sorptivity, pore size, and resistance to sodium sulfate attack. *J Mater Civ Eng* 25(1):105–111
5. Cioffi R, Maffucci L, Santoro L (2003) Optimization of geopolymer synthesis by calcination and polycondensation of a kaolinitic residue. *Resour Conserv Recycl* 40(1):27–38
6. Damilola OM (2013) Syntheses, characterization and binding strength of geopolymers: a review. *Int J Mater Sci Appl* 2(6):185–193
7. Dash S, Hussain M (2011) Lime stabilization of soils: reappraisal. *J Mater Civ Eng* 24:707–714
8. Davidovits J (1976) Solid phase synthesis of a mineral blockpolymer by low temperature polycondensation of aluminosilicate polymers. In: IUPAC international symposium on macromolecules, Stockholm
9. Davidovits J (1991) Geopolymers: inorganic polymeric new materials. *J Therm Anal Calorim* 37(8):1633–1656
10. Davidovits J (2008) Geopolymer chemistry and applications. Geopolymer Institute
11. Duxson P, Fernández-Jiménez A, Provis JL, Lukey GC, Palomo A, van Deventer JS (2007) Geopolymer technology: the current state of the art. *J Mater Sci* 42(9):2917–2933
12. Gao T, Shen L, Shen M, Liu L, Chen F, Gao L (2017) Evolution and projection of CO₂ emissions for China's cement industry from 1980 to 2020. *Renew Sustain Energy Rev* 74:522–537
13. Gartner E (2004) Industrially interesting approaches to “low-CO₂” cements. *Cem Concr Res* 34(9):1489–1498
14. Ge Y, Cui X, Kong Y, Li Z, He Y, Zhou Q (2015) Porous geopolymeric spheres for removal of Cu (II) from aqueous solution: synthesis and evaluation. *J Hazard Mater* 283:244–251
15. Hernandez-Ramirez O, Holmes SM (2008) Novel and modified materials for wastewater treatment applications. *J Mater Chem* 18(24):2751–2761
16. Huseien GF, Mirza J, Ismail M, Ghoshal SK, Hussein AA (2017) Geopolymer mortars as sustainable repair material: a comprehensive review. *Renew Sustain Energy Rev* 80(1):54–74
17. IS: 2720 (Part 40) (1977) Determination of free swell index of soils
18. IS: 2720 (Part 5) (1985) Determination of liquid and plastic limit (second revision)
19. Naseem R, Tahir SS (2001) Removal of Pb (II) from aqueous/acidic solutions by using bentonite as an adsorbent. *J Water Res* 35(16):3982–3986
20. Novais RM, Buruberrri LH, Seabra MP, Labrincha JA (2016) Novel porous fly-ash containing geopolymer monoliths for lead adsorption from wastewaters. *J Hazard Mater* 318:631–640
21. Palomo Á, Fernández-Jiménez A, López Hombrados C, Lleyda JL (2007) Railway sleepers made of alkali activated fly ash concrete
22. Palomo A, Grutzeck MW, Blanco MT (1999) Alkali-activated fly ashes: a cement for the future. *Cem Concr Res* 29(8):1323–1329

23. Petermann JC, Saeed A, Hammons, MI (2010) Alkali-activated geopolymers: a literature review. Applied Research Associates Inc Panama City, FL
24. Poojidha M, Nirmalkumar K (2016) Review paper on geopolymer concrete by using GGBS
25. Rees CA, Provis JL, Lukey GC, Van Deventer JS (2008) The mechanism of geopolymer gel formation investigated through seeded nucleation. *Colloids Surf A Physicochemical Eng Asp* 318(1–3):97–105
26. Scott AN, Thomas MD (2007) Evaluation of fly ash from co-combustion of coal and petroleum coke for use in concrete. *ACI Mater J* 104(1):62
27. Shi C, Jiménez AF, Palomo A (2011) New cements for the 21st century: the pursuit of an alternative to Portland cement. *Cem Concr Res* 41(7):750–763
28. Tahir SS, Rauf N (2004) Removal of Fe (II) from the wastewater of a galvanized pipe manufacturing industry by adsorption onto bentonite clay. *J Environ Manag* 73(4):285–292
29. Uppal HL, Chadda LR (1967) Physico-chemical changes in the lime stabilization of black cotton soil (India). *J Eng Geol* 2:179–189
30. Wang JC, Wang YC, Ko L, Wang JH (2017) Greenhouse gas emissions of amusement parks in Taiwan. *Renew Sustain Energy Rev* 74:581–589
31. Zhang Z, Provis JL, Reid A, Wang H (2014) Geopolymer foam concrete: an emerging material for sustainable construction. *Constr Build Mater* 56(15):113–127

A Micromechanical Study on the Effect of Initial Static Shear Stress on Cyclic Shearing Response



R. Kolapalli, M. M. Rahman, M. R. Karim and H. B. K. Nguyen

Abstract The cyclic shearing response of granular materials is highly influenced by various parameters such as void ratio (e), confining stress (p'), initial static shear stress (q_s), cyclic deviatoric stress (q_{cyc}), stress reversal and non-stress reversal conditions. Traditionally, most liquefaction studies evaluated the influence of e , p' , q_{cyc} and reversals on isotropically consolidated specimens where q_s is zero. However, a soil element in a level ground is normally or K_0 consolidated and hence subjected to a q_s . Extensive studies have suggested that q_s may dramatically alter the pore water pressure generation (Δu), deviatoric strain (ε_d) and soil fabric for same e , p' and q_{cyc} . In order to evaluate the effect of q_s alone, it is required to produce replicated specimens through different consolidation paths to achieve different q_s . Since, it is hard to replicate specimens and assess soil fabric in laboratory, this study used an alternative approach, discrete element method (DEM), which has reproducibility and trace micromechanical parameters such as coordination number, CN and fabric. It is found that Δu , CN and fabric were significantly affected by consolidation path and corresponding q_s conditions. This study provides a good understanding on the effect of q_s on cyclic response of soils.

Keywords Initial static shear stress · Cyclic shear stress · Pore water pressure · von Mises fabric · Coordination number

1 Introduction

The cyclic liquefaction behaviour has gained significant research interest after the Niigata and Alaska earthquakes in 1964, where wide spread soil liquefaction was observed. Since then liquefaction phenomenon and respective devastating effects were brought to the attention of engineers and seismologists [1–3]. To understand the cyclic liquefaction resistance of soil in laboratory condition, traditionally, an

R. Kolapalli (✉) · M. M. Rahman · M. R. Karim · H. B. K. Nguyen
School of Natural and Built Environments, University of South Australia, Adelaide, Australia
e-mail: rohini.kolapalli@mymail.unisa.edu.au

equal amplitude of cyclic shear stress (q_{cyc}) is applied in compression and extension side of effective stress space on an isotropically consolidated soil element, where q = deviatoric stress = $\sigma'_1 - \sigma'_3$, σ'_3 and σ'_1 are minor and major principal stresses, respectively. Since $\sigma'_1 = \sigma'_3$ at the end of isotropic consolidation, the static shear stress (q_s) is zero. However, a soil element in level ground is K_0 consolidated ($\sigma'_1 \neq \sigma'_3$) and hence subjected to initial static shear stress (q_s). Some researchers have observed that the cyclic liquefaction resistance is significantly affected by q_s [4–6]. Hyodo et al. [7] conducted a series of laboratory cyclic triaxial tests with q_s and suggested that the axial strain accumulated gradually on the compression side and mean effective stress (p') decreased monotonically for higher q_s , where $p' = (\sigma'_1 + 2\sigma'_3)/3$. Therefore, it is worth evaluating the effect of consolidation paths and corresponding q_s on cyclic response of soils.

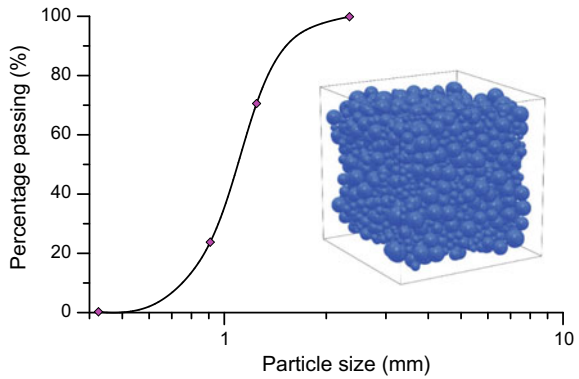
Cyclic triaxial test commonly adopted for defining the liquefaction resistance of sands under laboratory condition. However, a specimen under triaxial test can be affected by non-uniform stresses and strains distribution, end restraint, membrane penetration, etc. It is also difficult to produce replicated specimens to compare their behaviour. In addition, DEM also allows us to capture the micromechanical quantities (e.g. fabric, particle contacts) of granular materials, which affects the overall observed behaviour. Hence an alternative approach, discrete element method (DEM) has been widely used to simulate granular material behaviour. DEM, proposed by Cundall and Strack [8], was adopted in the current study for conducting triaxial simulation. Many researchers also used DEM for evaluation of the cyclic liquefaction behaviour in the past [9–11]. However, most of those studies focused on evaluating the cyclic liquefaction behaviour for isotropically consolidated specimens. The effect of K_0 consolidation has not been thoroughly investigated. Therefore, in the current study similar soil samples with same e_0 and p'_0 were prepared under different consolidation paths to achieve different q_s . This allowed us to evaluate the effect of q_s and corresponding fabric on cyclic liquefaction behaviour on a specimen with same e_0 , p'_0 and q_{cyc} , where subscript '0' denotes the state after consolidation.

2 Test Preparation

2.1 Assembly Generation

OVAl, an open-source program, is used for DEM simulation. The numerical program in OVAl which was implemented by Kuhn [12] and has been used in some other studies of granular material [13–15]. The particle size distribution (PSD) and the initial assembly of three-dimensional spherical particles used in this study are shown in Fig. 1. Initially, 2744 spherical particles were produced using a random generator function with respect to the grain size distribution as presented in Fig. 1. These particles were then distributed over predefined cubical cells in space

Fig. 1 Grain size distribution



without any overlaps. Then, this assembly was compressed to an initial compressive stress of 10 kPa and the specimen dimension was $13.43 \times 13.43 \times 13.43 \text{ mm}^3$ at this stage. The specimen was then further compressed or consolidated to a desired stress state through isotropic ($K = 1$) or anisotropic ($K \neq 1$) or K_0 ($K = K_0$) path. In isotropic consolidation, specimen was compressed by applying $\sigma'_1 = \sigma'_3$, i.e. ($K = \sigma'_3/\sigma'_1 = 1$) and in anisotropic consolidation, specimen was compressed by applying $\sigma'_1 \neq \sigma'_3$, i.e. $K = \sigma'_3/\sigma'_1 \neq 1$. However, in K_0 consolidation, specimen was compressed by applying σ'_1 and restricting lateral movement, i.e. $\varepsilon_1 = 0$, which is a form of anisotropic consolidation, i.e. $K = K_0$. In this study, specimens were consolidated through three different consolidation paths so that they have same state at the end of consolidation, i.e. $e_0 = 0.593$ and $p'_0 = 120 \text{ kPa}$, but different initial static shear stress q_s of 0 ($K = 1$), 18 kPa ($K = 0.74$) and 28 kPa ($K = K_0 = 0.64$). Then, to evaluate the effect of q_s on cyclic loading, these specimens were sheared under different magnitudes of cyclic shear stress (q_{cyc}). This allows the evaluation of the effect of q_{cyc} and q_s on the behaviour of granular materials in this study.

2.2 Model Parameters

Nguyen et al. [16], by conducting a large number of DEM simulations in OVAL suggested a set of DEM parameters for numerical stability and reliability. Same parameters were used in this study and were provided in Table 1. Following other

Table 1 Numerical parameters for DEM simulations

Parameter	Value
Coefficient of friction between particles and wall	0
Coefficient of friction at particle contacts	0.5
Normal contact stiffness, k_n	10^8 N/m
Ratio between normal and tangential contact stiffness (k_t), k_n/k_t	1
Particle mass density	$9.76 \times 10^8 \text{ kg/m}^3$

studies, e.g. Thornton [17] and Ng [18], the particle density was scaled up to $9.76 \times 10^8 \text{ kg/m}^3$ to reduce computational effort. In addition, a linear contact model was used for the current DEM simulations due to its simplicity and reduced computational time.

3 Test Procedure

A series of cyclic triaxial simulations were conducted through different consolidation paths so that different q_s was achieved at the end of consolidation. Therefore, at this stage each specimen had different static stress ratio, $SSR = q_s/(2p'_0)$. Then, different magnitudes of cyclic shear stress (q_{cyc}) were applied to evaluate cyclic response. The cyclic shear stress is presented in terms of cyclic stress ratio, $CSR = q_{cyc}/(2p'_0)$. A summary of testing program was presented in Table 2.

4 Test Results

The behaviours of an isotropically consolidated specimen (T1) with SSR of 0 and CSR of 0.25 in $q-p'$, $q-\varepsilon_d$, $\Delta u-N$ and ε_d-N spaces are presented in Fig. 2a, b, c and d, respectively, where Δu is the excess pore water pressure and N is the number of cycles. Note, Δu was not measured directly but was assumed to be the difference between p' for drained and undrained paths as suggested in Sitharam et al. [19]. This behaviour is typical cyclic mobility, *CM*, where effective stress path forms a butterfly shape in compression and extension side in $q-p'$ space (Fig. 2a) and p' transiently reaches zero effective stress without plastic strain accumulation. Figure 2c shows gradual increase in Δu with N and Fig. 2d and b shows strain accumulation in both sides of stress space with increase in N .

Table 2 Details of the cyclic triaxial simulations

Test ID	$K(\sigma'_3/\sigma'_1)$	e_0	p'_0 (kPa)	SSR	CSR	Mode of failure	N_L
T1	1	0.593	60	0	0.25	CM	18
T2	0.74	0.593	60	0.15	0.25	CM	9
T3	0.74	0.593	60	0.15	0.17	PSA	93
T4	0.64	0.593	60	0.23	0.25	PSA	18
T5	0.74	0.593	60	0.15	0.17	PSA	93
T6	0.74	0.593	60	0.15	0.33	CM	4
T7	1	0.593	60	0	0.33	CM	10
T8	1	0.593	60	0	0.42	CM	4
T9	0.64	0.593	60	0.23	0.33	CM	6
T10	0.64	0.593	60	0.23	0.42	CM	3

CM Cyclic Mobility, *PSA* Plastic Strain Accumulation

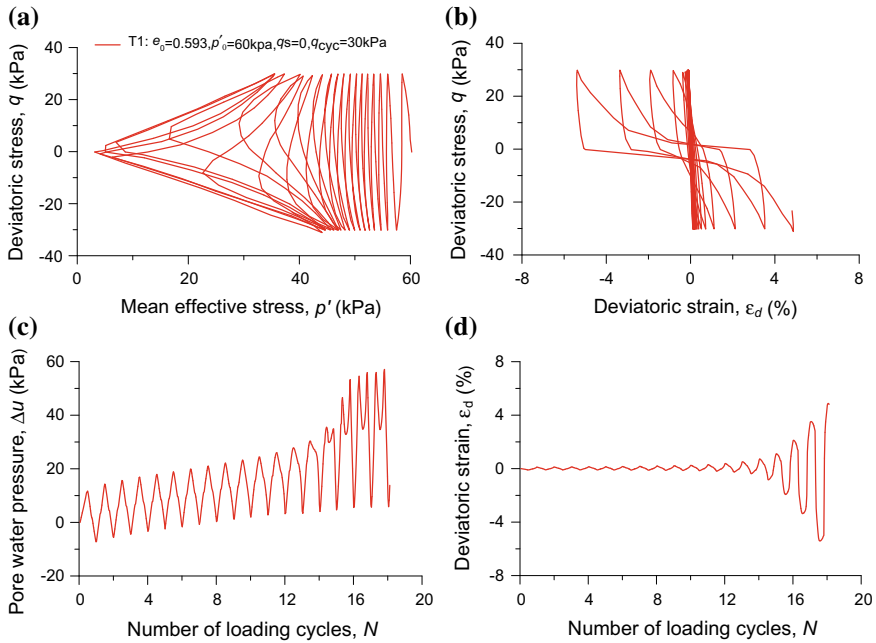


Fig. 2 Undrained cyclic response ($e_0 = 0.593, p'_0 = 60$ kPa, $q_s = 0$ kPa, $q_{cyc} = 30$ kPa) in **a** $q-p'$, **b** $q-\epsilon_d$, **c** $\Delta u-N$ and **d** ϵ_d-N spaces

The behaviours of an anisotropically consolidated specimen (T2) with *SSR* of 0.15 and *CSR* of 0.25 in $q-p'$, $q-\epsilon_d$, $\Delta u-N$ and ϵ_d-N spaces are presented in Fig. 3a, b, c and d, respectively. Both T1 and T2 have same initial state after consolidation, i.e. $e_0 = 0.593$ and $p'_0 = 120$ kPa. Therefore, a comparison of the two simulations demonstrated the effect of q_s or *SSR*. It is evident that gradual strain accumulation in compression side increased with increasing *SSR* from 0 to 0.15. The specimen T3 had exactly same initial condition as T2, i.e. $e_0 = 0.593, p'_0 = 120$ kPa and *SSR* of 0.15, but different magnitudes of cyclic shear stress (q_{cyc}), i.e. different $CSR = q_{cyc}/(2p'_0)$. T3 and T2 had *CSR* of 0.25 and 0.17, respectively, which allowed in evaluating the effect of *CSR* in cyclic loading response. The cyclic loading behaviours of T3 in $q-p'$ and $q-\epsilon_d$ spaces are presented in Fig. 4a and b, respectively. It is found that N required to initial liquefaction increased with the reductions *CSR*; however, *PSA* dominated the failure behaviour. The results were inline with the experimental results of Pan and Yang [4], Yang and Sze [20], Ishihara [21], Rahman et al. [22].

To observe the effect of K_0 consolidation, T4 was K_0 -consolidated ($K = K_0 = 0.64$), which had the same initial state after consolidation as T1, T2 and T3, i.e. $e_0 = 0.593$ and $p'_0 = 120$ kPa, but different q_s of 28 kPa, i.e. *SSR* of 0.23. T2 and T4 had same *CSR* of 0.25. This allowed for comparing the influence of *SRR* between T1, T2 and T4. The behaviours of T4 in $q-p'$, $q-\epsilon_d$, $\Delta u-N$ and ϵ_d-N spaces

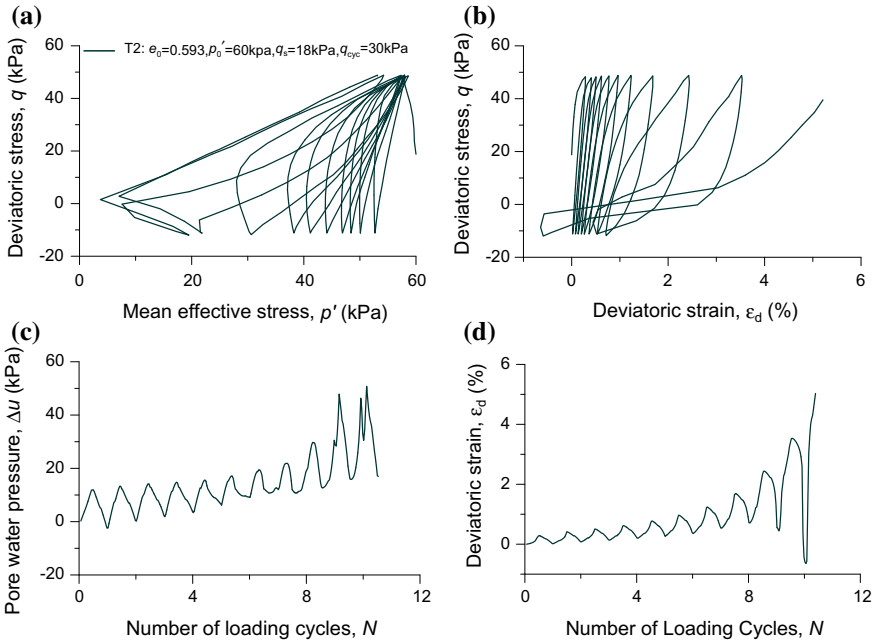


Fig. 3 Undrained cyclic response ($e_0 = 0.593, p'_0 = 60 \text{ kPa}, q_s = 18 \text{ kPa}, q_{cyc} = 30 \text{ kPa}$) in **a** q - p' , **b** q - ϵ_d , **c** Δu - N and **d** ϵ_d - N spaces

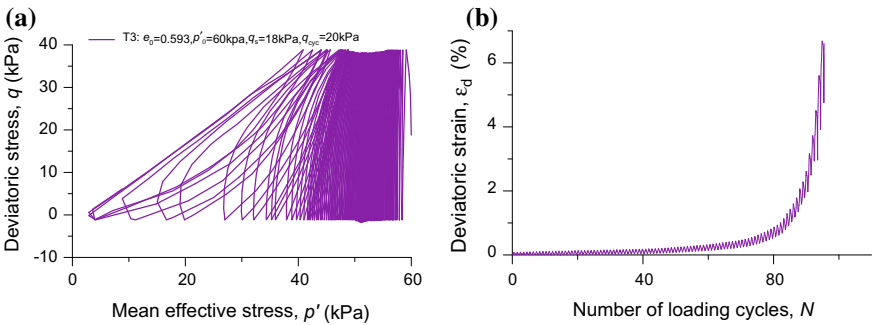


Fig. 4 Undrained cyclic response ($e_0 = 0.593, p'_0 = 60 \text{ kPa}, q_s = 18 \text{ kPa}, q_{cyc} = 20 \text{ kPa}$) in **a** q - p' , **b** ϵ_d - N spaces

are presented in Fig. 5a, b, c and d, respectively. In the absence of SSR, i.e. $SSR = 0$ in T1, Δu was built gradually during early stages of shearing and later increased suddenly when it reached approximately close to p' (see Fig. 2c) and as a result p' reached initial liquefaction ($p' \approx 0$). Whilst SSR for T2 and T4 are 0.15 and 0.23, respectively, Δu was steady during initial stages of shearing and then increased gradually with N (Figs. 3c and 5c). Also noticed that when $q_s = 0 \text{ kPa}$, ϵ_d

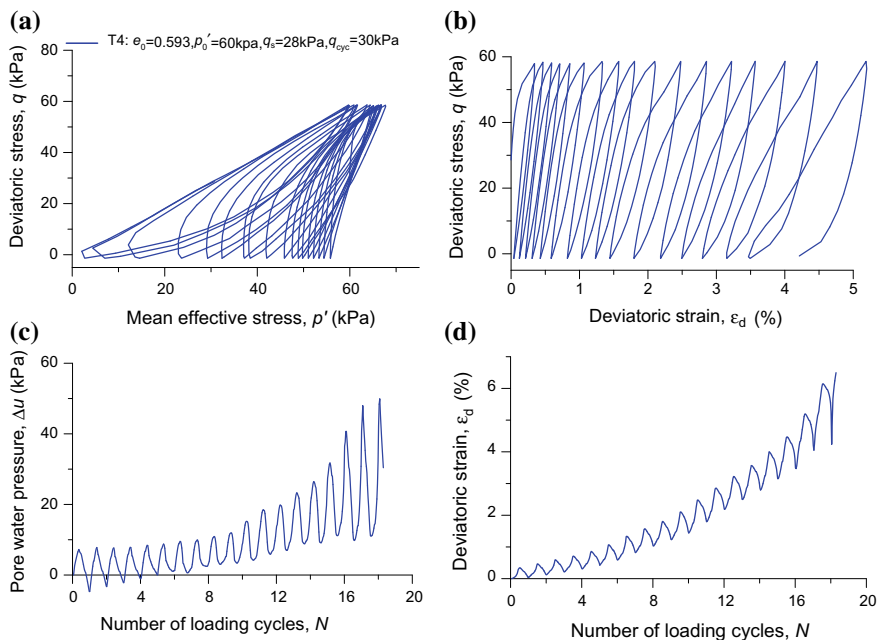


Fig. 5 Undrained cyclic response ($e_0 = 0.593$, $p'_0 = 60$ kPa, $q_s = 28$ kPa, $q_{cyc} = 30$ kPa) in **a** q - p' , **b** q - ϵ_d , **c** Δu - N and **d** ϵ_d - N spaces

remains considerably small till 14th loading cycle but as soon as the Δu started approaching p' accumulation of deviatoric strain (ϵ_d) increased drastically and thereafter increased to 3% in the consecutive three cycles and reached its initial liquefaction point as shown in Fig. 2d and b. But strain accumulated continuously on the compression side for SSR of 0.15 and 0.23 as shown in Figs. 3d and 5d, respectively. Stress reversal is the governing/key factor, which differentiated the failure patterns of granular materials under cyclic loading. Cyclic mobility behaviour was captured under stress reversal condition and plastic strain accumulation under non/partial stress reversal. Yang and Sze [20] found similar observation from his experimental studies.

5 Micromechanics Behind Liquefaction

Coordination number, CN and Fabric, F were the two parameters that allowed us to capture the micromechanical quantities of granular material which affected the behaviour of sand under cyclic triaxial loading conditions. Rothenburg and Bathurst [23] defined $CN = (C \times 2)/N$; where C is the total number of contacts and N is number of particles in the specimen. CN is often correlated to stability of a soil

specimen. Fabric is another micromechanical parameter where structural anisotropy can be captured. Satake [24], first proposed the following equation for the structural anisotropy and is given below in Eq. (1).

$$F = F_{ij} \frac{1}{N} \sum_{k=1}^N n_i^k n_j^k \quad (1)$$

where n^k is the direction of the k th contact and N is the number of contacts in the specimen. In the current study, von Mises fabric, F_{vM} was used for measuring the scalar quantity, which is equal to $(3F_{J2D})^{\frac{1}{2}}$, where F_{J2D} is the invariant of the second invariant of the deviatoric fabric tensor and is given below in Eq. (2).

$$F_{J2D} = \frac{1}{6} \left[(F_{11} - F_{22})^2 + (F_{11} - F_{33})^2 + (F_{22} - F_{33})^2 \right] + F_{12}^2 + F_{13}^2 + F_{23}^2 \quad (2)$$

where F_{11} , F_{22} and F_{33} are the fabric in the principal directions and F_{12} , F_{13} and F_{23} are the fabric in the shear directoins.

Figure 6a, c exhibited the evolution of von Mises fabric, F_{vM} and CN for isotropic (T1), Anisotropic (T2) and K_0 (T4) consolidated specimens. Figure 6b represents the evolution of stress ratio ($\eta = q/p'$) with N . It is found that η increased gradually with the increase in the number of loading cycles for isotropically consolidated specimen (T1). But on the other hand, due to the presence of q_s for T3 and T4, magnitude of η was high in the first loading cycle and hence η increased at a very slow rate during shearing process and hence the F_{vM} . Whenever there was a change in F_{vM} , reorientation of particles occurred and hence there was change in the contacts (see Fig. 6b). CN decreased gradually throughout shearing for isotropically consolidated specimen whereas CN for anisotropically and K_0 consolidated specimen decreased significantly at initial stages of shearing and later reduced at a very slow rate. However, by the end of shearing or at point of initial liquefaction, CN almost have a constant value of approximately 3.2 for all the specimens irrespective of presence/absence of q_s as shown in Fig. 6c.

6 Effect of Consolidation Path on Cyclic Liquefaction Resistance

CSR and the number of cycles required for initial liquefaction (N_L) data points formed a unique line for same initial state of the soil (see Fig. 7a). Similar behaviour was observed by Ishihara [21]. Irrespective of initial state of the soil, N_L increased with the reduction of CSR as shown in Fig. 7a. DEM simulations of the current study was very well in agreement with the laboratory studies conducted by Rahman et al. [22]. Figure 7a demonstrated the effect of magnitude of static stress ratio in $CSR-N_L$ space. The cyclic resistance ratio (CRR) is the resistance of a

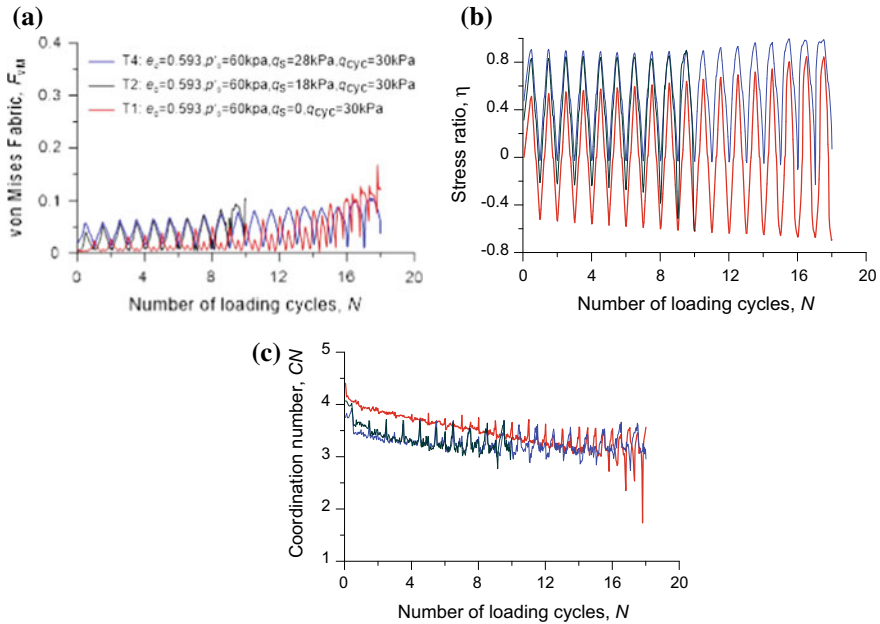


Fig. 6 Undrained cyclic response of sand at micro level

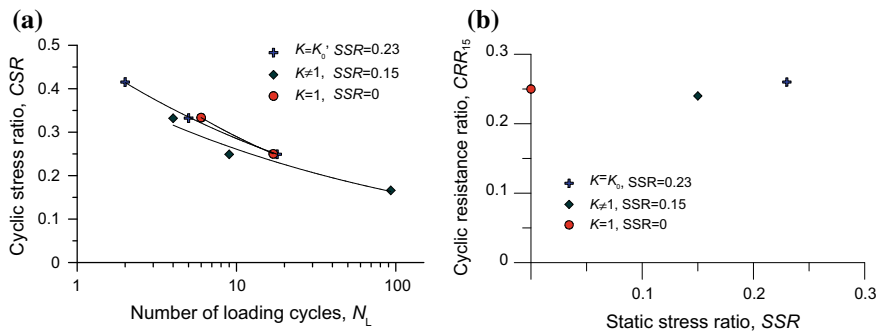


Fig. 7 Effect of cyclic resistance on consolidation path in **a** $CSR-N_L$ and **b** $CRR_{15}-SSR$ spaces

specimen to liquefaction and can be found from the cyclic resistance curves, CSR curves (Fig. 7a) for an expected number of cycles, N_L from an earthquake. Seed and Idriss [25] suggested 10, 20 and 30 cycles for magnitude of earthquake, M_w of 7, 7.5 and 8, respectively. In the current study expected number of equivalent cycles from an earthquake was assumed as 15. $CSR-N_L$ curve in Fig. 7a gives a corresponding value of CSR for 15 cycles for the same e_0 and p'_0 and is represented as CRR_{15} . Figure 7b demonstrated the effect of SSR on CRR . CRR_{15} defined from

Fig. 6a for SSR of 0, 0.15 and 0.23 was 0.25, 0.24 and 0.26, respectively. Cyclic resistance for K_0 consolidated specimen ($SSR = 0.23$) demonstrated higher cyclic resistance when compared with that of isotropically and anisotropically consolidated samples. At higher static shear stress levels, the increase of cyclic resistance tends to be more promising than at lower static shear stress levels. Yang and Sze [20] found similar observation from his experimental study where higher cyclic resistance encountered for $SSR > 0.4$ than at lower SSR (0–0.1). However, further investigation on huge data set from various tests on same soil samples consolidated at higher static shear stress levels is highly recommended.

7 Conclusions

The following inferences were made from the current cyclic triaxial DEM simulations:

- DEM demonstrated the capability of capturing the behaviour of granular materials under cyclic loading at different static shear stress levels. Cyclic mobility, CM was observed for the specimen consolidated isotropically ($K = 1$) in the presence of stress reversal whilst plastic strain accumulation (PSA) was captured under no stress reversal for K_0 consolidated specimen.
- Also noticed that when $q_s = 0$ kPa, deviatoric strain, ε_d remains considerably small till 12th loading cycle, but as soon as the Δu started approaching p'_0 accumulation of ε_d increased drastically and thereafter increased to 3% in the consecutive three cycles and reached its initial liquefaction point.
- In the presence of q_s , ε_d accumulated gradually with the increase in the number of loading cycles but Δu was notable to reach p'_0 .
- Similar specimens with same SSR , when applied with different magnitudes of cyclic shear stress demonstrated significant influence on the liquefaction susceptibility. It was found that N required to initial liquefaction increased with the reduction of CSR .
- Although the CRR values for K_0 and isotropic consolidation are quite similar, the CRR value for anisotropic ($K = 0.15$) is a bit smaller. Moreover, the presence of SSR changed the failure criteria for liquefaction. For instance, K_0 specimen exhibited strain accumulation whereas isotropic specimen demonstrated cyclic mobility. There was a net decrease in the coordination number, CN with the reduction of p' or increase in pore water pressure.
- Presence of high static shear stress level ($SSR = 0.23$) was found to be beneficial from the specimen used in this study.

Acknowledgements The authors would like to acknowledge Professor Matthew R. Kuhn of University of Portland, USA for his DEM software OVAL. The first author, Rohini Kolapalli, would like to acknowledge the Australian Department of Education's Australian Postgraduate Award (APA) which facilitated her to conduct research on her Ph.D. dissertation at the University of South Australia.

References

1. Shibata T, Yukimoto H, Miyoshi M (1972) Liquefaction process of sand during cyclic loading of sand. *Soils Found* 12(1):1–16
2. Seed HB, Lee KL (1966) Liquefaction of saturated sands during cyclic loading. *J Soil Mech Found Div (ASCE)* 92(SM6):105–134
3. Ishihara K, Tatsuoka F, Yasuda S (1975) Undrained deformation and liquefaction of sand under cyclic stresses. *Soils Found* 15(1):29–44
4. Pan K, Yang ZX (2018) Effect of initial static shear on cyclic resistance and pore pressure generation of sand. *Acta Geotech* 473–487
5. Yang ZX, Pan K (2017) Flow deformation and cyclic resistance of saturated loose sand considering initial static shear effect. *Soil Dyn Earthq Eng* 92:68–78
6. Lee KL, Seed HB (1967) Dynamic strength of anisotropically consolidated sand. *J Soil Mech Found Div (ASCE)* 93(5):169–190
7. Hyodo H et al (1994) Undrained cyclic and monotonic triaxial behaviour of saturated loose sand. *Soils Found* 34(1):19–32
8. Cundall PA, Strack ODL (1979) A discrete numerical model for granular assemblies. *Géotechnique* 29(1):47–65
9. Sitharam TG (2003) Discrete element modelling of cyclic behaviour of granular materials. *Geotech Geol Eng* 21(4):297–329
10. Kuhn M et al (2014) Investigation of cyclic liquefaction with discrete element simulations. *J Geotech Geoenviron Eng* 140(12):04014075
11. Huang X et al (2017) Exploring the undrained cyclic behaviour of sand using DEM. In: Feng X, Li Y, Mustoe G (eds) *Proceedings of the 7th international conference on discrete element methods*. Springer, Singapore, pp 757–765
12. Kuhn MR (2006) *Oval and OvalPlot: programs for analyzing dense particle assemblies with the discrete element method*. Department of Civil Engineering, University of Portland, 5000 N. Willamette Blvd., Portland, OR 97203 USA
13. Nguyen HBK, Rahman MM, Fourie AB (2018) Characteristic behaviour of drained and undrained triaxial tests: a DEM study. *J Geotech Geoenviron Eng* (2018) (In press)
14. Rahman MM, Nguyen HBK, Rabbi ATMZ (2018) The effect of consolidation on undrained behaviour of granular materials: experiment and DEM simulation. *Geotech Res* 5(3):1–19
15. Nguyen HBK, Rahman MM, Fourie AB (2017) Undrained behaviour of granular material and the role of fabric in isotropic and K_0 consolidations: DEM approach. *Géotechnique* 67(2):153–167
16. Nguyen H, Rahman MM, Cameron D (2015) Undrained behavior of sand by DEM study. In: *IFCEE 2015, GSP 256*. ASCE, San Antonio, USA, pp 182–191
17. Thornton C (2000) Numerical simulations of deviatoric shear deformation of granular media. *Géotechnique* 50(1):43–53
18. Ng T (2006) Input parameters of discrete element methods. *J Eng Mech* 132(7):723–729
19. Sitharam TG, Vinod JS, Ravishankar BV (2008) Evaluation of undrained response from drained triaxial shear tests: DEM simulations and experiments. *Geotechnique* 58(7):605–608
20. Yang J, Sze HY (2011) Cyclic behaviour and resistance of saturated sand under non-symmetrical loading conditions. *Géotechnique* 61(1):59–73
21. Ishihara K (1993) Liquefaction and flow failure during earthquakes. *Géotechnique* 43(3):351–415
22. Rahman M, Baki M, Lo S (2014) Prediction of undrained monotonic and cyclic liquefaction behavior of sand with fines based on the equivalent granular state parameter. *Int J Geomech* 14(2):254–266
23. Rothenburg L, Bathurst RJ (1989) Analytical study of induced anisotropy in idealized granular materials. *Géotechnique* 39(4):601–614

24. Satake M (1982) Fabric tensor in granular materials. In: Vermeer PA, Luger HJ (eds) Proceedings of the IUTAM symposium on deformations and failure of granular materials 1982, Delft, the Netherlands, pp 63–68
25. Seed HB, Idriss IM (1971) Simplified procedure for evaluating soil liquefaction potential. *J Soil Mech Found Div (ASCE)* 97(9):1249–1273

Study on the Behaviour of NATM Tunnel Face During Seismic Activities



R. B. Jishnu, Ramanathan Ayothiraman and Raghvendra Sahu

Abstract Tunnelling in mountainous terrain using sequential excavation activities like New Austrian Tunnelling Methods (NATM) methods has been on the rise due to increased haulage and transportation demands. These structures are normally constructed in stages, where exposed tunnel face will be supported by some additional measures. However, in tectonically active places, like in the Himalayas, it is highly possible to have failure at the tunnel face due to seismic activities. In this study, such an excavation is considered using three-dimensional finite element methods. Face stability of such a system is ensured using certain face deformation criteria. Further efficacy of such measures during seismic activities is monitored using pseudo-static methods. For such an analysis, Peak Ground Acceleration (PGA) of a typical earthquake of Himalayan origin is considered. It was observed that proposed face support systems should be enhanced for such excavations in seismically active zones.

Keywords Seismic analysis · NATM tunnel face · Dynamic tunnel face stability · Tunnel face reinforcement · Three-dimensional pseudo-static analysis

1 Introduction

Travelling by roads in mountainous terrain requires higher resource demands like time and fuel costs as the shortest distances between start and destination could not be directly met. Also, most of such routes need high maintenance demands due to climate, instability of slope cuts (for highways), etc. With the available advanced construction techniques and methodologies, it is possible to construct tunnels in these locations, as they reduce transit distances. Also, they have less maintenance requirements and are safer to travel. Like highways, construction of tunnels takes time and it happens in gradual stages. In this study, such a tunnel construction

R. B. Jishnu · R. Ayothiraman (✉) · R. Sahu
Department of Civil Engineering, Indian Institute of Technology Delhi, New Delhi, India
e-mail: araman@civil.iitd.ac.in

performed by New Austrian Tunnelling Method (NATM) will be studied where construction happens by 'Build as you go' [1]. For such tunnels, its face will be supported by certain face support systems (like fibreglass elements) as a temporary stability measure. Later on, excavation proceeds to complete the tunnel trajectory. However, in seismic active zones, like in the Himalayas (where tremors or even earthquakes are frequent), it is highly possible to have sudden tunnel face collapses due to earthquake activities. In this study, tunnels of different weak rock types [2] have been considered (for a specific tunnel geometry) to appreciate such needs using three-dimensional pseudo-static methods. It has been found that for zones of high tectonic activities, face support systems should be enhanced incorporating such seismic demands.

2 Tunnel and Geotechnical Parameters

2.1 Tunnel Profile and Structural Properties

The finite element analysis is carried out using three-dimensional approach using PLAXIS 3D. A model domain of 100 m (Width) *100 m (Length) *50 m (Height) is prepared. The tunnel axis has been assumed along the 'length' dimension. The model comprises 10 node tetrahedral elements (93450 in number with 134987 nodes). Interface elements are adopted to model soil-tunnel interaction. Such elements have been modelled around the tunnel periphery and face reinforcing elements. The excavated face (where stability of the face is ascertained) is assumed at a distance of 50 m (at mid-domain) along the tunnel axis to have the least boundary effects. The typical FE mesh is shown in Fig. 1. More details on numerical modelling can be found in Jishnu et al. [6]. Detailed excavation sequence of this tunnel profile is already explained in the same literature. The scope of the current study is to ascertain the stability at the exposed tunnel face.

For this study, reinforced concrete liner has been used as the final tunnel support. M45 concrete is used as liner material. 400 mm thick liner material has been used as the final support after checking its sufficiency against cracking and serviceability. Modulus of concrete liner (E) is computed as per IS 456 [5] where ' f_{ck} ' represents characteristic compressive strength of concrete in N/mm^2 (28 days cube strength of concrete, where 5% test results are allowed to fail). Details regarding this tunnel's primary support systems are already reported in the literature [6]. Hence, the structural parameters (' A ' represents area of resisting cross section per 'm', ' I ' section modulus of resisting cross section per 'm') used for the tunnel liner is shown in Table 1.

Another important structural element which ensures a stable tunnel face is the face reinforcement system. A stable tunnel face could be ensured by using fibreglass elements which could be further excavated easily. These elements could be

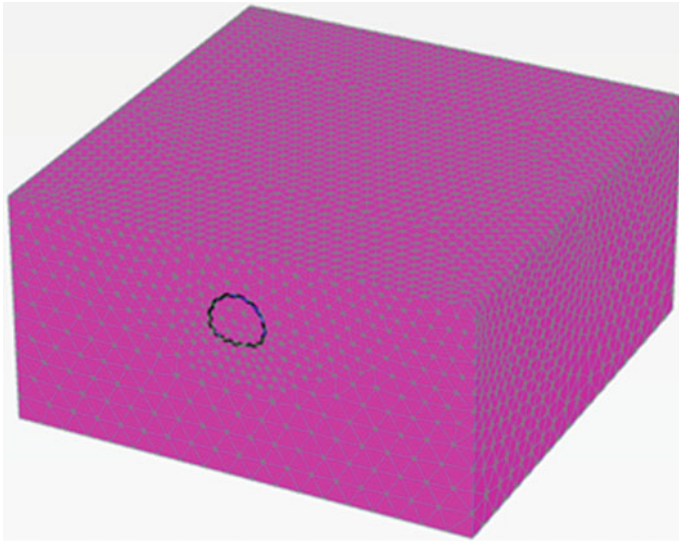


Fig. 1 Typical FE mesh of tunnel

Table 1 Structural parameters used for tunnel lining

Liner thickness (t-m)	Modulus (E-MPa)	A (m ² /m)	EA (kN/m)	EI (kNm ² /m)
0.4	33,541	0.4	1.34E + 07	1.79E + 05

Table 2 Structural parameters used for face reinforcement (fibreglass elements)

Diameter (D-m)	Area (A-m ²)	Modulus E(MPa)	Yield tensile stress (σ_t -MPa)
0.15	0.0177	40,000	400

modelled as tension members (Table 2) with the following parameters as per the literature (Table 2, [7]). The length of these members could be arrived by using three-dimensional FE analyses as described later.

2.2 Geotechnical Parameters

It is known [3, 4] that tunnels constructed in weak deposits are highly prone to seismic activities. Most of the tunnels in mountainous terrain are constructed in rock masses and hence in this study, mean rock mass parameters of grade *R0* (Extremely weak) and *R1* (Very weak) (as per Hoek [2]) have been considered. For these rock types, a mean Uniaxial Compressive Strength (*UCS*) value of 0.5 MPa is used for ‘*R0*’ rocks where for representative ‘*R1*’ rocks *UCS* magnitudes of 1 MPa

and 2.5 MPa have been used. A Geological Strength Index (*GSI*) of 40 has been used for these rocks (representing poor to fair disturbed mass). To incorporate the construction techniques of tunnelling a disturbance factor is introduced. Possible squeezing for these rock masses could result in a disturbance factor (*D*) of 0.5 where poor quality blasting could result in an upper bound disturbance factor of 0.8. In this study, a mean disturbance factor of 0.65 is adopted. For igneous plutonic rocks in Himalayas a ‘mi’ value (Hoek–brown constant) of 25 and Modulus Ratio (*MR*) of 325 is adopted. For all these rocks, a weight density (γ) of 23kN/m³ is adopted. For these analyses, Mohr–Coulomb constitutive model is used and these parameters have been derived from Hoek–Brown parameters as per reported correlations [2]. The equivalent Mohr–Coulomb fit for all these rock masses is shown in Fig. 2. The equivalent cohesion (*c*), friction angle (ϕ) and rock mass deformation modulus (*E*) thus derived is shown in Table 3. For all these analyses, tunnel depth is assumed to be 10 m from ground surface.

3 Stability Analysis at Tunnel Face

Stability of exposed tunnel face during static and seismic conditions will be addressed in detail in this study. Such an issue has been repeatedly reported in the literature as a limited equilibrium problem [8–10] where active wedge formation happens at the tunnel face with a chimney formation in the silo area. The support elements (here fibreglass elements) should sufficiently arrest such a face

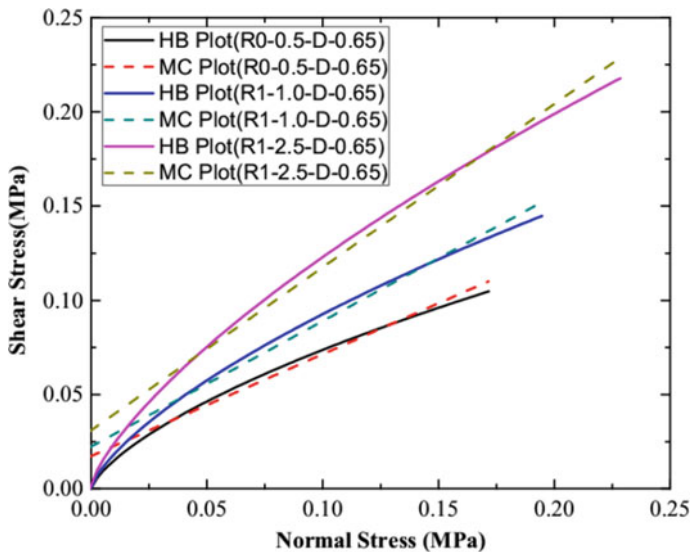


Fig. 2 Comparison of Mohr–Coulomb and Hoek–Brown envelopes for considered rock masses

Table 3 Equivalent Mohr–Coulomb Parameters for rock masses considered

GSI = 40	$m_i = 25$	$D = 0.65$	$MR = 325$	$\gamma = 23\text{kN/m}^3$
Rock grade	UCS (MPa)	c (KPa)	ϕ (deg)	E (KPa)
<i>R0</i>	0.5	17	28.39	10,130
<i>R1</i>	1.0	22	33.69	20,260
<i>R1</i>	1.5	31	40.89	50,640

deformation pattern. For all the three rock types described in Sect. 2 (*R0*, $UCS = 0.5$ MPa, *R1*, $UCS = 1.0$ MPa, *R1*, $UCS = 2.5$ MPa) three-dimensional F.E models were prepared in PLAXIS 3D. The minimum dimensions for the model geometry, around the tunnel for static analysis have been adhered as per literature [11]. At first, it is required to understand the deformation pattern at the tunnel face without any reinforcement. This is necessary to understand the need to any face reinforcement. It is clear from Fig. 3, that without face reinforcement, the maximum face deformation ranges from 27 mm to 450 mm for rock of ‘*R1*’ grade with UCS of 2.5 MPa to rock of ‘*R0*’ grade of UCS 0.5 MPa. This makes it clear that face reinforcement measures are indeed required for these types of rocks.

Now, since high deformations were observed at the tunnel face, it is required to reinforce the tunnel face to avoid any such instability. Fibreglass elements with structural properties (mentioned in Sect. 2.1) need to be provided. The length of these fibreglass elements was decided based on the deformation behaviour at the unreinforced tunnel face in the axial direction. Such a deformation pattern for all the rock masses considered is shown in Fig. 4. In this study, length of these elements

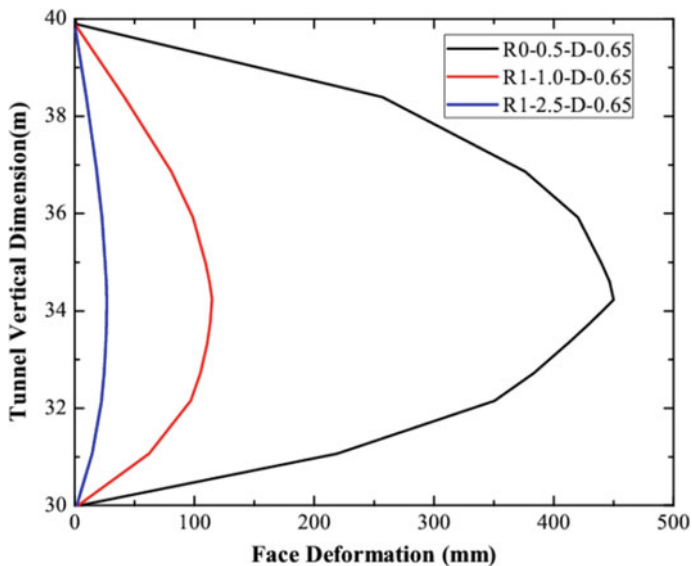


Fig. 3 Behaviour of unreinforced tunnel face for various rock masses considered

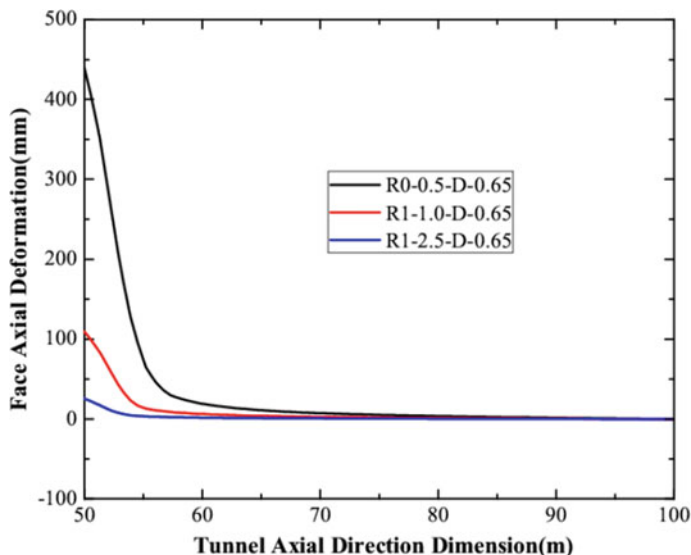


Fig. 4 Face deformation in the axial direction for different rock masses in unreinforced condition

have been provided till the point where axial face displacements reduce to 10 mm (i.e. 0.1% of tunnel height of 10 m) for unreinforced condition. It was found that, abiding this criterion a length of 3 m is required for ‘R1’ rock of $UCS = 2.5$ MPa. Similarly, for ‘R1’ rock of $UCS = 1.0$ MPa and for ‘R0’ rock of $UCS = 0.5$ MPa, a length of 7 m and 16 m is required.

Now since the length of fibreglass elements and the need of them are decided, it is required to understand their pattern (spacing) at the tunnel face in order to avoid any instabilities. It is clear that for such high deformations (observed in ‘R0’ rock with $UCS = 0.5$ MPa and ‘R1’ rock with $UCS = 1.0$ MPa), along with fibreglass elements shotcrete spraying could be required at the surface. Using three-dimensional finite element methods, shotcrete and fibreglass elements were modelled at the tunnel face to limit face deformation. The maximum permissible face displacement is limited to 0.25% of tunnel height = 25 mm in this study (to ensure a sufficiently stable tunnel face). After several trials, in order to have a stable face the following support measure (Table 4) is arrived. Also, maximum deformation behaviour at the tunnel face for different shotcrete thickness is shown in Fig. 5.

Thus, once the requirement of face support system is arrived for static conditions, it needs to be checked whether such a system suffices well against seismic condition. By such an approach efficacy of the support system against any tectonic activity could be quantified during construction stage in seismically active areas. Since a full three-dimensional dynamic analysis takes high computational resources and time, in this study, pseudo-static analysis (IS 1893. Criteria for earthquake resistant design of structures [12]) applicable for underground structures have been performed.

Table 4 Face reinforcement scheme for different rock types

Rock type	Face bolting scheme	Spacing (m)
R0-0.5-UCS-0.5MPa	Len (16 m) + SCT (310 mm)	1.0 m c/c
R0-1.0-UCS-0.5MPa	Len (7 m) + SCT (225 mm)	1.5 m c/c
R0-2.5-UCS-0.5MPa	Len (3 m)	2.0 m c/c

(‘SCT’ = shotcrete thickness, ‘Len’ = fibreglass element length)

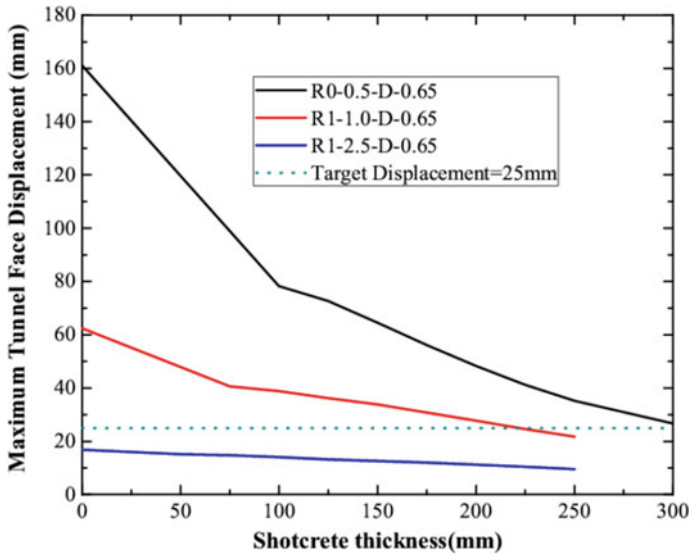


Fig. 5 Variation of maximum tunnel face displacement with shotcrete thickness

4 Performance of Face Support System Against Seismic Events

In this study, performance of tunnel face support systems have been appreciated using pseudo-static analysis applicable for underground structures. For a three-dimensional pseudo-static analysis first, seismic coefficients pertaining to this area have to be quantified. For this purpose, an earthquake of Himalayan origin (Chamba Earthquake, March 24, 1995, $M_w = 4.9$, Fig. 6) has been considered. It could be observed that the maximum Peak Ground Acceleration (*PGA*) of this earthquake is 0.125 g.

Now, three-dimensional pseudo-static analyses have to be performed to ascertain the safety of designed support systems as mentioned in Sect. 3. For the same, pseudo-static coefficients have to be arrived. The horizontal seismic coefficient (A_h) could be computed IS 1893 (2002). Further for underground structures (in this case tunnel depth = 10 m), these horizontal coefficients could be reduced (IS 1893 2002). The vertical seismic coefficient is taken as $2/3^{rd}$ of horizontal seismic

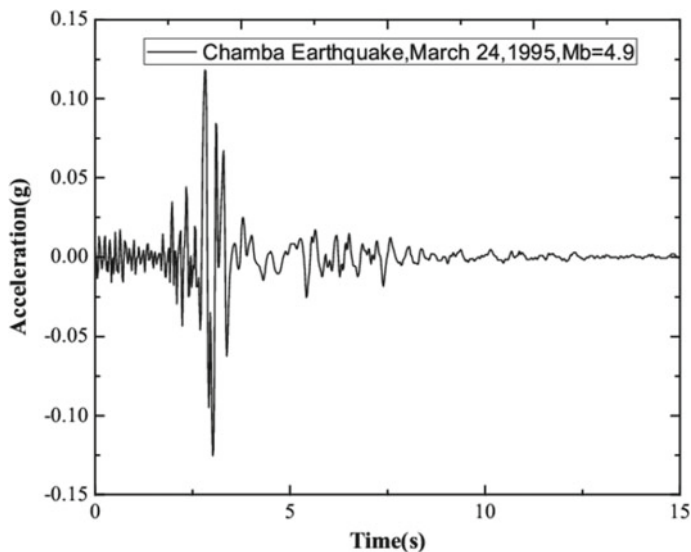


Fig. 6 Earthquake time history for Chamba earthquake (March 24, 1995, Mb = 4.9) (after [13])

coefficient. The Zonal factor (Z) is taken as 0.125 g (PGA for Chamba Earthquake), I , the importance factor as 1.5 (for important structures), R , the response reduction factor as 3.0 (for ordinary moment-resisting frame) and Sa/g , spectral acceleration coefficient as 2.5 (maximum possible coefficient for varying soils encountered). The computed seismic coefficients in vertical and horizontal directions ($A_h = 0.052$ g, $A_v = 0.035$ g) is applied in eight different directions (horizontal coefficients to right and left side, horizontal seismic coefficients into/out of the tunnel face and vertical coefficients in the up and down direction). All these combinations were considered to compute the displacements at the tunnel face which is already reinforced (as mentioned in Sect. 3).

After performing the analysis, it was found that direction of horizontal seismic coefficients, in the transverse direction (perpendicular to the tunnel axis) would not have any implication on the tunnel face displacements. Hence, the eight combinations reduce to four different possibilities for a face stability problem (i.e. vertical coefficients in the upward/downward direction and horizontal coefficients in the direction in/out of the tunnel face). The main effect as expected will be caused by the horizontal coefficients in the outward direction from tunnel face where minor differences have been found on the tunnel face with direction of vertical seismic coefficients (Fig. 7). From these analyses it has been found that for all the rock types considered (Figs. 7, 8, and 9) reinforced tunnel face deforms beyond permissible limits (0.25% tunnel height = 25 mm in these cases). Also, maximum effect on face displacements happens for weakest rock mass ('R0' grade with $UCS = 0.5$ MPa) as expected (Fig. 10). Thus, it is clear from these analyses that some additional provisions may be required at the tunnel face to limit face

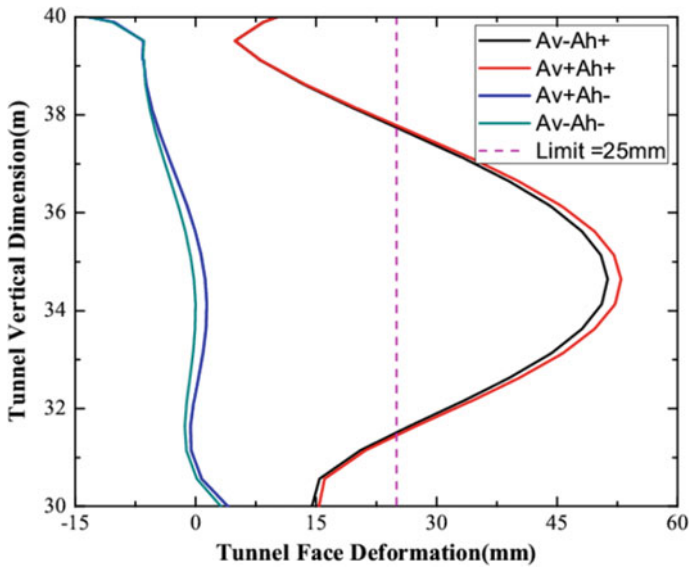


Fig. 7 Tunnel face deformation trends for rock type, R0-0.5MPa-D-0.65 (A_{h+} represents horizontal coefficient out of the tunnel face, A_{v+} represents upward excitation and vice versa)

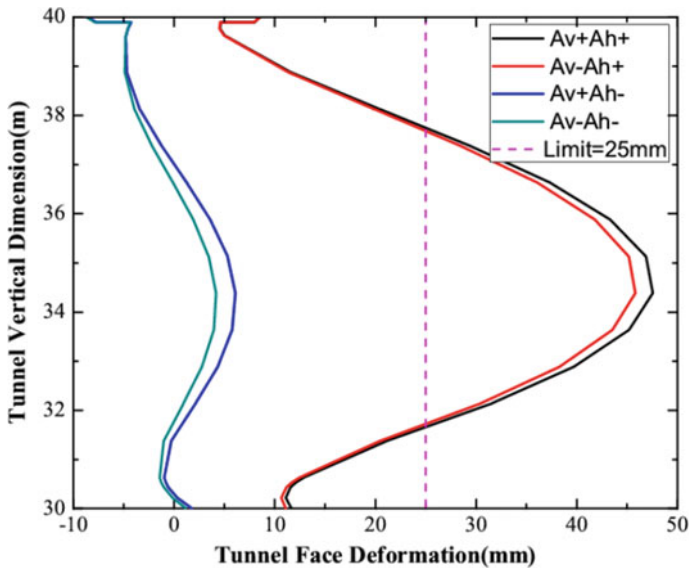


Fig. 8 Tunnel face deformation trends for rock type, R1-1.0MPa-D-0.65 (A_{h+} represents horizontal coefficient out of the tunnel face, A_{v+} represents upward excitation and vice versa)

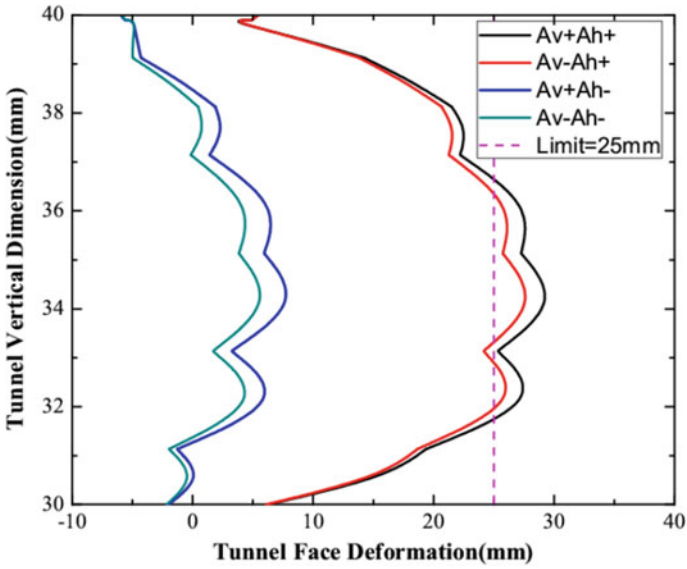


Fig. 9 Tunnel face deformation trends for rock type, R1-2.5MPa-D-0.65 (A_{h+} represents horizontal coefficient out of the tunnel face, A_{v+} represents upward excitation and vice versa)

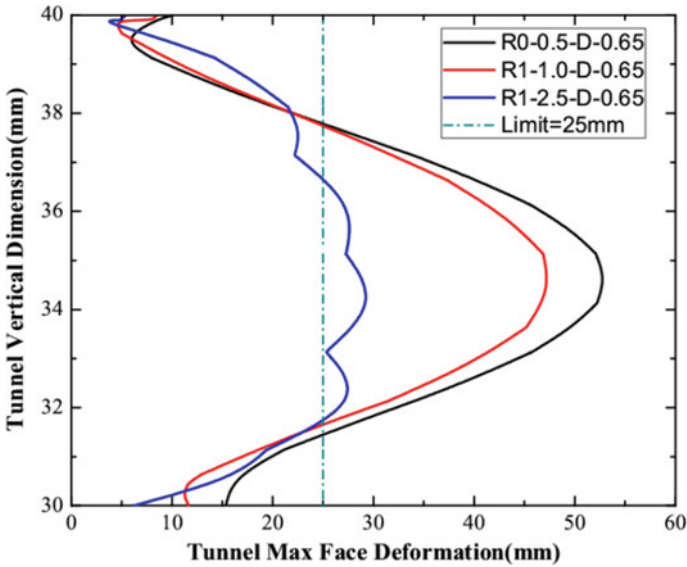


Fig. 10 Maximum tunnel face deformation for different rock masses under the worst case pseudo force combination (A_{v+} , A_{h+})

displacements as static design could not suffice the required needs (For all the figures ‘+’ direction for horizontal coefficients represents out of face forces, where ‘+’ direction for vertical coefficients represents upward excitation).

5 Conclusions

- (1) Face stability for NATM tunnels (constructed in stages) in seismically active zones is an issue which needs some attention.
- (2) For weak rock masses, such instabilities could be very high resulting in sudden collapses. In such cases, face stability provisions for static condition will not suffice as reinforced system as a whole could fail.
- (3) In these conditions, earthquake in the direction of tunnel axis or closer direction (closer incident angle) could have more detrimental effect. Similarly, seismic excitation perpendicular to tunnel axis will have negligible effect.
- (4) A more detailed dynamic analysis with site-specific ground motion (and its direction with respect to tunnel axis) could result in more accurate estimates.

References

1. Singh B, Goel RK (2006) *Tunnelling in weak rocks*, vol 5. Elsevier Science, India
2. Hoek E (2001) Rock mass properties for underground mines. In: Hustrulid WA, Bullock RL (eds) *Underground mining methods: engineering fundamentals and international case studies*. Society for Mining, Metallurgy, and Exploration (SME), Colorado
3. Pakbaz MC, Yareevand A (2005) 2-D analysis of circular tunnel against earthquake loading. *J Tunn Undergr Space Technol* 20:411–417. <https://doi.org/10.1016/j.tust.2005.01.006>
4. Wang JN (1993) *Seismic design of tunnels*. Parsons Brinckerhoff Inc., New York
5. Indian Standard IS 456-2000 (2000) Indian standard for plain and reinforced concrete- code of practice (fourth revision). Bureau of Indian Standards, New Delhi
6. Jishnu RB, Ayothiraman R, Ahmed S, Ghosh S, Patra C (2016) Performance of primary tunnel support systems under seismic loads in weak rock masses. In: *Proceedings of recent advances in rock engineering*, 16–18 Nov 2016, Atlantis Press. <https://doi.org/10.2991/rare-16.2016.33>
7. Oreste P, Dias D (2012) Stabilisation of the excavation face in shallow tunnels using fibreglass dowels. *J Roc Mech Roc Eng* 45(4):499–517. <https://doi.org/10.1007/s00603-012-0234-1>
8. Anagnostou G, Kovari K (1994) The face stability of slurry shield driven tunnels. *J Tunn Undergr Space Technol* 9:165–174. [https://doi.org/10.1016/0886-7798\(94\)90028-0](https://doi.org/10.1016/0886-7798(94)90028-0)
9. Broere W (2001) Tunnel face stability and new CPT applications. Doctoral thesis, TU Delft
10. Leca E, Dormieux L (1990) Upper and lower bound solutions for the face stability of shallow circular tunnels in frictional material. *Geotechn* 40:581–606. <https://doi.org/10.1680/geot.1990.40.4.581>
11. Moeller S (2006) Tunnel induced settlements and structural forces in linings. Doctoral thesis, University of Stuttgart

12. Indian Standard IS 1893-2002 (2002) Criteria for earthquake resistant design of structures (fifth revision). Bureau of Indian Standards, New Delhi
13. Jishnu RB, Naik SP, Patra NR, Malik JN (2013) Ground response analysis of Kanpur soil along Indo-Gangetic Plains. *Soil Dyn Earthq Eng* 51:47–57. <https://doi.org/10.1016/j.soildyn.2013.04.001>

A PSO-Based Estimation of Dynamic Earth Pressure Coefficients of a Rigid Retaining Wall



Swarnima Subhadarsini, Sushree Paritwasha Pradhan,
Jayanti Munda and Pradip Kumar Pradhan

Abstract Earth retaining walls are the alleviating structures used to avert downward slope movement of earth masses and provide sustenance for vertical or near vertical grade changes. For designing these structures, it is necessary to regulate the earth pressure exerted by the soil behind the wall. But in seismic prone areas, retaining structures experience maximum devastation as dynamic loads are repetitive in nature. Mononobe–Okabe method based on pseudo-static approach gives an approximate value for the linear distribution of seismic earth pressure by considering the parameters like wall friction angle, soil friction angle, horizontal, and vertical seismic coefficients. The present work includes the determination of dynamic earth pressure coefficients by using Particle Swarm Optimization (PSO) technique. The effects of wide range of parameters like shear wave velocity, primary wave velocity, time effects, and phase difference on earth pressure coefficients have been studied. A comparison has been made between the pseudo-static and pseudo-dynamic earth pressure coefficients to highlight the realistic and non-linearity nature of seismic active earth pressures. It is found that the horizontal and vertical seismic accelerations are more significant for the computation of dynamic earth pressure, which is highly sensitive to soil friction angle and less sensitive to wall friction angle. The results obtained in the proposed method are also compared with reported results, which show a good agreement.

Keywords Retaining wall · Pseudo-dynamic earth pressure coefficients · PSO · Shear wave velocity · Primary wave velocity

S. Subhadarsini (✉) · S. P. Pradhan · J. Munda · P. K. Pradhan
Department of Civil Engineering, VSSUT, Burla, India
e-mail: swarnima1993subha@gmail.com

© Springer Nature Singapore Pte Ltd. 2020
A. Prashant et al. (eds.), *Advances in Computer Methods
and Geomechanics*, Lecture Notes in Civil Engineering 56,
https://doi.org/10.1007/978-981-15-0890-5_15

1 Introduction

Planning and designing of retaining structures in both static and dynamic conditions is one of the most critical phases as the damage of such structures may prompt to catastrophic failure. Estimation of earth pressure in both static and dynamic conditions behind the retaining wall using coulomb's theory and pseudo-static methods, respectively, can be found in most of the textbooks (e.g., [1]; [2]). The pseudo-static method of estimation of dynamic earth pressure is an extension of coulomb's sliding wedge theory in which the transient earthquake force on the soil backfill are represented by an equivalent static force. This method is popularly called as Mononobe-Okabe method [3, 4]. In this approach, the dynamic nature of the earthquake loading is considered in a very approximate manner without taking the effect of time and phase difference. Later time and phase deference due to finite shear wave propagation behind a retaining wall were considered by using a simple and more realistic way of pseudo-dynamic method, proposed by [5]. But this method gives less focus on the effects of wall friction angle. Again, this method was studied and analyzed by [6]. They determined the seismic active earth pressure in a more general way by considering time effect and phase difference. For the analysis they considered a vertical rigid retaining wall supported by backfill having a particular value of soil friction angle ϕ and wall friction angle δ with particular value of horizontal and vertical seismic acceleration ($k_h g$ and $k_v g$, respectively, where g is the acceleration due to gravity) along with shear wave velocity $V_s = \sqrt{G/\rho}$, primary wave velocity $V_p = \sqrt{\frac{2G(1-\mu)}{\rho(1-2\mu)}}$, whereas ρ = density, G = specific gravity of the backfill material, and μ = Poisson's ratio of the backfill which was assumed to be act within the soil media. It has considered the ratio of V_p/V_s ($\cong 1.87$) as proposed by Das [1] and the period of lateral shaking, $T = \frac{2\pi}{\omega} = \frac{4H}{V_s}$, whereas ω = angular frequency. A planer rupture surface inclined at an angle α with the horizontal was optimizing along with t/T ratio (t = time period) to determine the dynamic active earth pressure coefficients. From their analysis, they concluded that the nonlinearity of the active earth pressure distribution increases with seismicity, which leads to the shifting of the point of application of total active thrust which is the most important factor for designing retaining structures. Hence, an attempt has been taken in this paper to obtain complete and more accurate values of pseudo-dynamic earth pressure coefficients using one of the recent advanced techniques, i.e., Particle Swarm Optimization (PSO).

2 Problem Formulation

Failure wedge for both active and passive conditions and associated forces are presented in Fig. 1a, b.

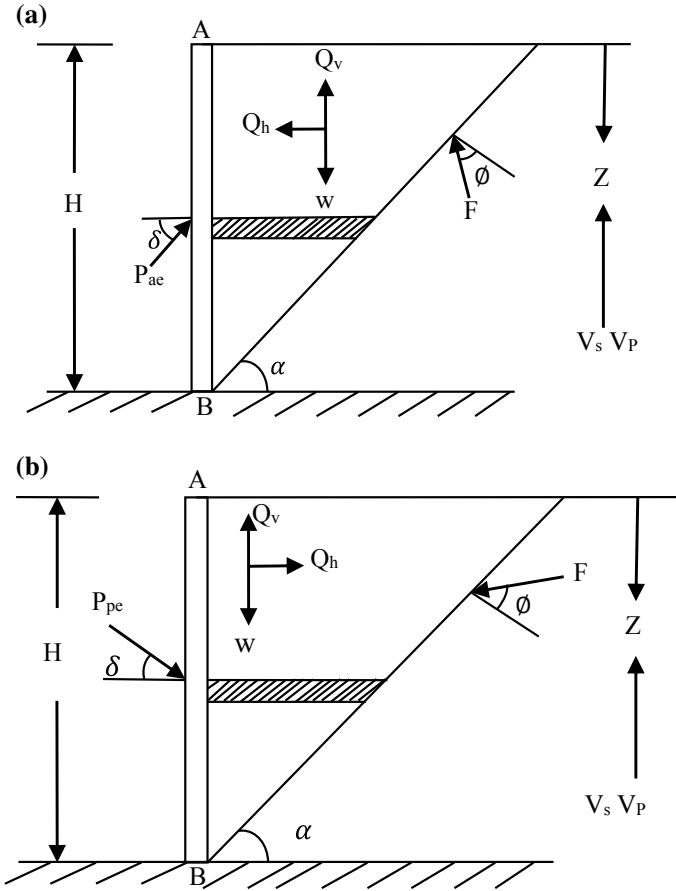


Fig. 1 a Failure wedge for pseudo-dynamic active condition and associate forces. b Failure wedge for pseudo-dynamic passive condition and associate forces

The theory proposed by [6] has been considered, where he considered a cantilever type of retaining wall supporting a cohesionless backfill with horizontal ground surface. The shear modulus G and poisson's ratio ν for the backfill are considered constant throughout the depth of the retaining wall and shear wave velocity and primary wave velocity act within the soil media. Thus, the pseudo-dynamic earth pressure coefficients and total active thrust are given as follows:

$$K_{ae} = \frac{1}{\tan \alpha \cos(\delta + \theta - \alpha)} + \frac{k_h}{2\pi^2 \tan \alpha} \frac{TV_s}{H} \frac{\cos(\alpha - \theta)}{\cos(\delta + \theta - \alpha)} C_1 - \frac{k_v}{2\pi^2 \tan \alpha} \frac{TV_p}{H} \frac{\sin(\alpha - \theta)}{\cos(\delta + \theta - \alpha)} C_2 \tag{1}$$

whereas $C_2 = 2\pi \cos 2\pi \left(\frac{t}{T} - \frac{H}{TV_s} \right) + \frac{TV_s}{H} \left(\sin 2\pi \left(\frac{t}{T} - \frac{H}{TV_s} \right) - \sin 2\pi \left(\frac{t}{T} \right) \right)$
 and $C_2 = 2\pi \cos 2\pi \left(\frac{t}{T} - \frac{H}{TV_p} \right) + \frac{TV_p}{H} \left(\sin 2\pi \left(\frac{t}{T} - \frac{H}{TV_p} \right) - \sin 2\pi \left(\frac{t}{T} \right) \right)$

$$p_{ae}(t) = \frac{\partial P_{ae}(t)}{\partial z} = \frac{yz}{\tan \alpha \cos(\delta + \emptyset - \alpha)} \frac{\sin(\alpha - \emptyset)}{\cos(\delta + \emptyset - \alpha)} + \frac{k_h yz}{\tan \alpha \cos(\delta + \emptyset - \alpha)} \frac{\cos(\alpha - \emptyset)}{\cos(\delta + \emptyset - \alpha)} \sin \omega \left(t - \frac{z}{V_s} \right) - \frac{k_v yz}{\tan \alpha \cos(\delta + \emptyset - \alpha)} \frac{\sin(\alpha - \emptyset)}{\cos(\delta + \emptyset - \alpha)} \sin \omega \left(t - \frac{z}{V_p} \right) \quad (2)$$

The pseudo-dynamic passive earth pressure coefficient and total passive thrust are given as

$$K_{pe} = \frac{1}{\tan \alpha \cos(\delta + \emptyset + \alpha)} \frac{\sin(\alpha + \emptyset)}{\cos(\delta + \emptyset + \alpha)} + \frac{k_h}{2\pi^2 \tan \alpha} \frac{TV_s}{H} \frac{\cos(\alpha + \emptyset)}{\cos(\delta + \emptyset + \alpha)} C_1 - \frac{k_v}{2\pi^2 \tan \alpha} \frac{TV_p}{H} \frac{\sin(\alpha + \emptyset)}{\cos(\delta + \emptyset + \alpha)} C_2 \quad (3)$$

whereas $C_1 = 2\pi \cos 2\pi \left(\frac{t}{T} - \frac{H}{TV_s} \right) + \frac{TV_s}{H} \left(\sin 2\pi \left(\frac{t}{T} - \frac{H}{TV_s} \right) - \sin 2\pi \left(\frac{t}{T} \right) \right)$
 and $C_2 = 2\pi \cos 2\pi \left(\frac{t}{T} - \frac{H}{TV_p} \right) + \frac{TV_p}{H} \left(\sin 2\pi \left(\frac{t}{T} - \frac{H}{TV_p} \right) - \sin 2\pi \left(\frac{t}{T} \right) \right)$

$$p_{ae}(t) = \frac{\partial P_{ae}(t)}{\partial z} = \frac{yz}{\tan \alpha \cos(\delta + \emptyset + \alpha)} \frac{\sin(\alpha + \emptyset)}{\cos(\delta + \emptyset + \alpha)} + \frac{k_h yz}{\tan \alpha \cos(\delta + \emptyset + \alpha)} \frac{\cos(\alpha + \emptyset)}{\cos(\delta + \emptyset + \alpha)} \sin \omega \left(t - \frac{z}{V_s} \right) - \frac{k_v yz}{\tan \alpha \cos(\delta + \emptyset + \alpha)} \frac{\sin(\alpha + \emptyset)}{\cos(\delta + \emptyset + \alpha)} \sin \omega \left(t - \frac{z}{V_p} \right) \quad (4)$$

$p_{ae}(t)$ and $p_{pe}(t)$ are the pseudo-dynamic active thrust and the pseudo-dynamic passive thrust each having three sets of equations. The first term from each equation represents the static earth pressure acting on the wall, whereas second and third terms represent pressure due to horizontal inertia and vertical inertia of the soil wedge.

K_{ae} and K_{pe} are the pseudo-dynamic active earth pressure coefficient and pseudo-dynamic passive earth pressure coefficient, respectively, which are functions of the dimensionless parameters H/TV_s , H/TV_p , t/T , and the wedge angle α . The normalized values of H/TV_s and H/TV_p are used in particle swarm optimization to arrive at more accurate values of earth pressure coefficients.

2.1 Optimization Steps

The normalized value of the two nondimensional parameters has considered for both K_{ae} and K_{pe} . Here, the K_{ae} value is maximized and K_{pe} is minimized by objective functions each having velocity and swarm constraints. According to Nanda et al. [7] velocity of the particle at t th iteration can be represented by

$$v_i(t) = (v_{i1}, v_{i2}, v_{i3}, v_{i4} \dots \dots \dots v_{is}) \tag{5}$$

Then, the velocity of the particle for $(t + 1)$ th iteration is updated according to the equation

$$v_{ij}^{t+1} = w^t v_{ij}^t + c_1 r_1 (p_i - x_i^t) + c_2 r_2 (p_i - x_i^t) \tag{6}$$

The term w^t denotes the inertia weight at t th iteration and its value is calculated using the equation

$$w^t = w_{\max} - \frac{(w_{\max} - w_{\min})t}{t_{\max}} \tag{7}$$

whereas w_{\max} = maximum value for inertia weight and considered as 0.9 for this study.

w_{\min} = minimum value for inertia weight and taken as 0.4,

t = the current iteration number, and

t_{\max} = the maximum number of iterations to be carried out.

r_1 and r_2 = random numbers (uniformly distributed between [0, 1]).

c_1 and c_2 = acceleration coefficients.

The second term of the Eq. (6) represents the cognition part and is responsible for exploiting its own experience, whereas the third term of the Eq. (6) represents the social part, which is responsible for sharing information and mutual cooperation among the particles.

Velocity of the particles determines the fineness and helps to search the target in between the search area. The particle is constrained within the range $[-v_{\max}, v_{\max}]$. The value of v_{\max} can be expressed as follows:

$$v_{\max} = 0.1 \times (x_{\max} - x_{\min}) \tag{8}$$

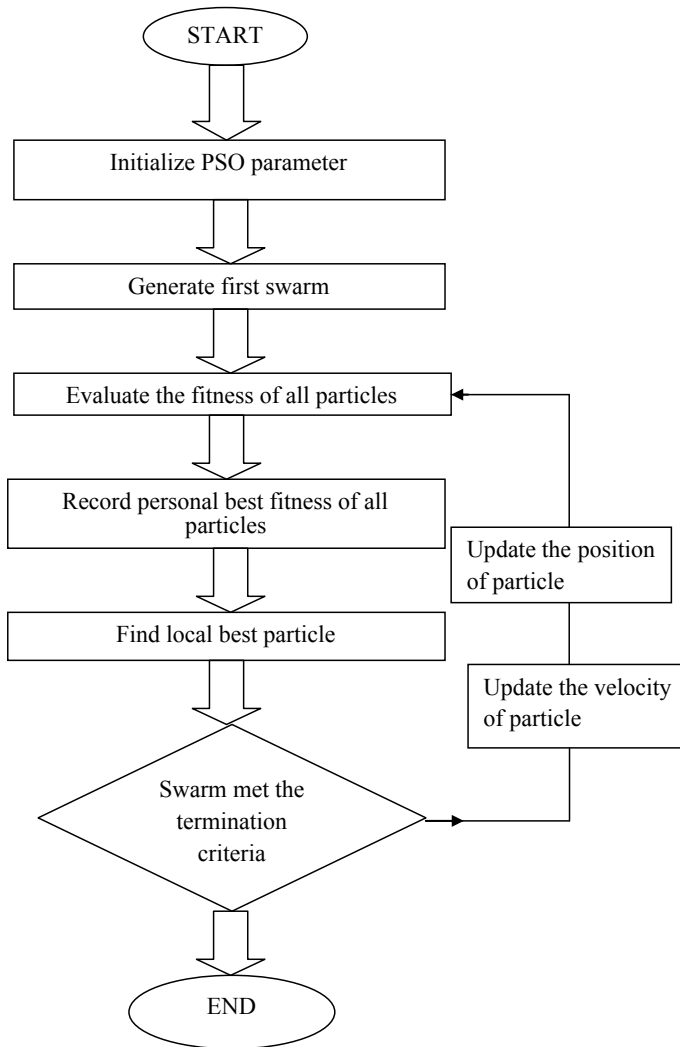


Fig. 2 Flow chart of PSO

whereas x_{\max} and x_{\min} denote the dynamic range of the variable on each dimension (Fig. 2). Finally, using the updated velocity, the updated position of the i th particle in $(t + 1)$ th iteration is given by

$$x_{ij}^{t+1} = x_{ij}^t + v_{ij}^{t+1} \quad (9)$$

3 Results and Discussions

Dynamic earth pressure coefficients obtained by using particle swarm optimization techniques are presented in Tables 1 and 2 and Figs. 3 and 4 for deferent values of k_h and k_v . The failure wedge angles for various values of k_h and k_v are presented in Table 3. The following parameter values are considered.

$$\emptyset = 20^\circ, 30^\circ, 40^\circ$$

$$\delta = 0, 0.5\emptyset, \emptyset$$

$$k_h = 0, 0.1, \text{ and } 0.2$$

$$k_v = 0, 0.5k_h, \text{ and } k_h$$

From Tables 1 and 2 it is observed that for given values of \emptyset and δ , K_{ae} increases and K_{pe} decreases with increase in k_h value. For example at $\emptyset = 20^\circ$ and $\delta = 0$ with the increase in k_h from 0 to 0.2, K_{ae} increases by 26.30%, whereas K_{pe} decreases by 5.6%. With the increase in δ value, K_{ae} decreases and K_{pe} increases as shown in Fig. 4a, b. At $k_h = k_v$ the values of K_{ae} increases and at $k_v = 0.5k_h$ it decreases as compared to $k_v = 0$. However, K_{pe} decreases with the increase in k_v values from 0 to k_h by 30%.

From Table 3 it was observed that it is decreased by 23% when k_h varies from 0 to 0.2 in active condition and by 47% in passive condition. With the increase of value \emptyset from 0 to 20° at $\delta = 20^\circ$ values is decreased by 24% in active condition and 27% in passive condition.

Table 1 Values of K_{ae}

\emptyset	δ	$k_v = 0$			$k_v = 0.5k_h$			$k_v = k_h$		
		$k_h = 0$	$k_h = 0.1$	$k_h = 0.2$	$k_h = 0$	$k_h = 0.1$	$k_h = 0.2$	$k_h = 0$	$k_h = 0.1$	$k_h = 0.2$
20	0	0.4903	0.5778	0.6653	0.4903	0.5178	0.5452	0.4903	0.6979	0.9055
	10	0.4431	0.5222	0.6013	0.4431	0.4680	0.4928	0.4431	0.6308	0.8185
	20	0.4158	0.4900	0.5642	0.4158	0.4391	0.4624	0.4158	0.5919	0.7679
30	0	0.3333	0.4055	0.4777	0.3333	0.3647	0.3960	0.3333	0.4872	0.6410
	10	0.2989	0.3636	0.4283	0.2989	0.3270	0.3550	0.2989	0.4368	0.5747
	20	0.2887	0.3512	0.4137	0.2887	0.3158	0.3429	0.2887	0.4219	0.5551
40	0	0.2174	0.2757	0.3340	0.2174	0.2491	0.2807	0.2174	0.3024	0.3873
	10	0.1978	0.2508	0.3039	0.1978	0.2266	0.2554	0.1978	0.2751	0.3523
	20	0.2040	0.2587	0.3134	0.2040	0.2337	0.2634	0.2040	0.2837	0.3634

Table 2 Values of K_{pe}

θ	$k_v = 0$			$k_v = 0.5k_h$			$k_v = k_h$		
	$k_h = 0$	$k_h = 0.1$	$k_h = 0.2$	$k_h = 0$	$k_h = 0.1$	$k_h = 0.2$	$k_h = 0$	$k_h = 0.1$	$k_h = 0.2$
20	1.5300	1.1937	1.1246	2.0239	1.9648	1.6789	2.0396	2.0150	1.9900
10	2.3671	2.0610	2.1524	2.7681	2.4934	1.9384	2.7681	2.6070	2.5510
20	4.2532	3.0960	3.0956	4.5268	3.0801	2.5217	4.5246	3.4562	3.3888
30	3.0000	3.0910	3.0102	3.0000	2.6710	2.4010	3.0000	2.5206	2.0210
10	4.9765	4.5615	4.1289	4.9765	4.3123	3.6267	4.9765	4.0631	3.1228
20	10.0591	4.0202	7.9211	10.0951	8.5149	6.9051	10.0951	8.0095	5.8867
40	4.5989	4.3803	4.1923	4.5089	4.1591	3.6901	4.5989	3.9199	3.2271
10	22.0031	11.2898	10.009	22.3001	10.3250	8.8631	22.3001	9.7360	7.6818
20	92.5855	83.2469	73.9023	92.5855	78.6342	64.6385	92.5855	73.9943	55.3731

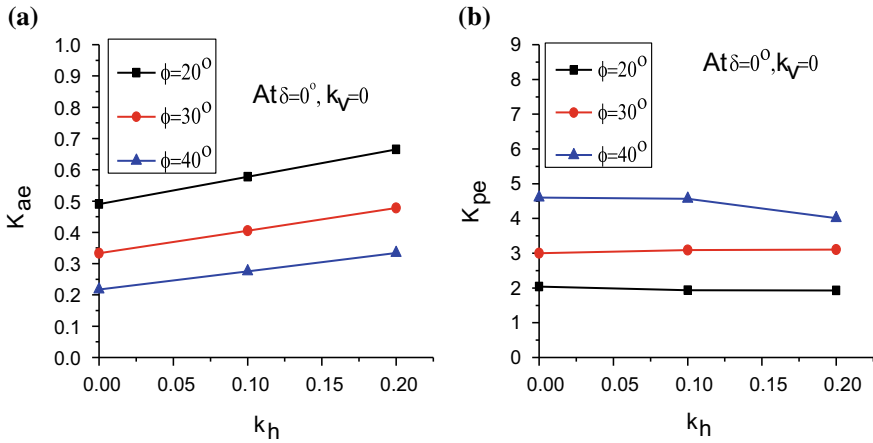


Fig. 3 a Pseudo-dynamic active earth pressure coefficients. b Pseudo-dynamic passive earth pressure coefficients

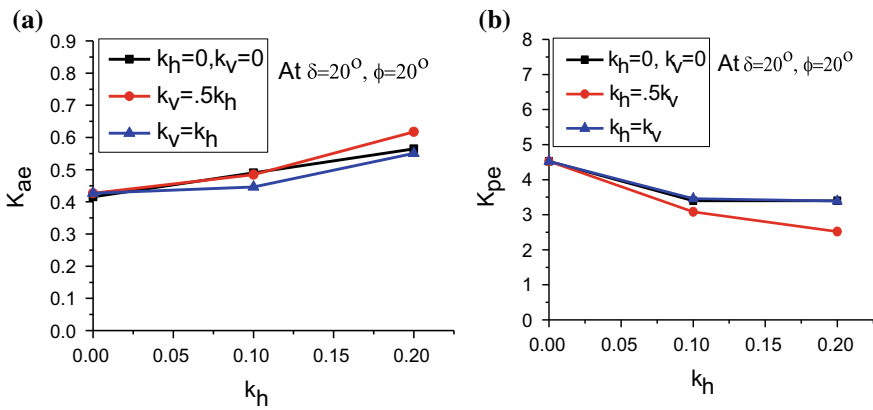


Fig. 4 a Pseudo-dynamic passive earth pressure coefficients. b Pseudo-dynamic passive earth pressure coefficients

3.1 Effect of Soil Friction Angle on the Coefficients of Dynamic Earth Pressure

The Fig. 3a, b shows the dynamic earth pressure coefficients for different values of k_h and k_v . The seismic passive earth pressure coefficients increase with increase in soil friction angle, whereas seismic active earth pressure coefficients decreases with increase in soil friction angle.

Table 3 Variation of failure wedge plane angle with the horizontal (°)

		For active condition			For passive condition		
\emptyset	δ	$k_h = 0$	$k_h = 0.1$	$k_h = 0.2$	$k_h = 0$	$k_h = 0.1$	$k_h = 0.2$
20	0	55.0000	47.2611	31.7273	25.5341	24.5330	21.0010
	10	51.1069	44.7343	27.2361	17.1890	22.3734	18.2310
	20	47.8995	39.0437	24.1047	12.1495	16.6334	15.1407
30	0	60.0000	53.4648	45.6478	20.6666	18.6486	10.7664
	10	56.8598	49.9674	41.0766	16.9841	10.5969	6.3214
	20	54.3429	46.4795	37.3566	14.4320	7.6711	–
40	0	65.0000	60.4621	53.8372	14.9859	9.2641	6.8735
	10	61.7813	55.3887	59.8452	12.1306	7.7889	9.8926
	20	59.9855	54.5057	45.9671	10.4551	6.5542	–

3.2 Effects of k_h and k_v on Dynamic Earth Pressure Coefficients

From Fig. 4a, b, it was observed that, with increasing k_h and k_v seismic active earth pressure increases and seismic passive earth pressure decreases. Figure 4a shows pseudo-dynamic active earth pressure coefficients.

3.3 Comparison Between Static and Dynamic Earth Pressure Coefficients

From Fig. 5a it is observed that active earth pressure coefficients decrease with increase in \emptyset value but increase with increase in k_h irrespective of finite value of \emptyset . The earth pressure increases with increase in k_h value due to time effect and

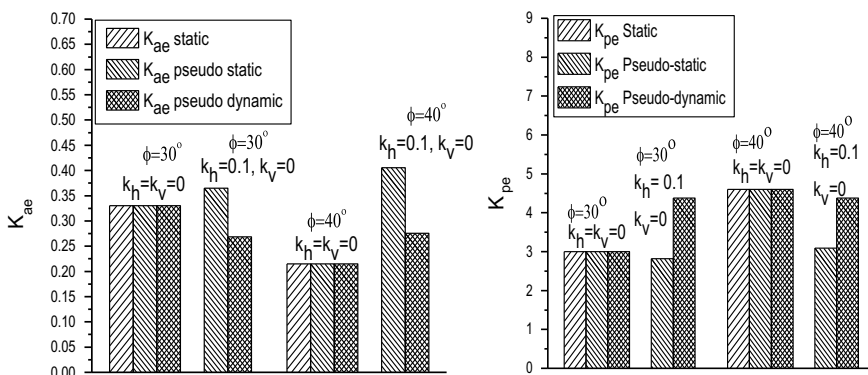


Fig. 5 Active earth pressure coefficients for static, pseudo-static and pseudo-dynamic conditions

phase difference. From Fig. 5b reverse trend is observed in case of passive earth pressure. For $k_h = k_v = 0$ earth pressure coefficients remain same for all the three conditions, i.e., static, pseudo-static, and pseudo-dynamic.

3.4 Comparison of Results Between Present Method and Previously Proposed Methods

Table 4 shows the K_{ae} values obtained by PSO technique are compared by Kapila [8], Choudhury [6, 9], and Ghosh (2010). And it can be seen that the results obtained from present technique compares well with the existing methods. Table 5 shows the K_{pe} values obtained by PSO technique which are compared by [10], Ghosh (2010), and [11]. The present technique is well contrast with previously proposed methods.

Table 4 Comparison of values at $k_h = k_v = 0$

	K_{ae} (present method)		K_{ae} (Kapila Method [8])		K_{ae} (Choudhury [6, 9])		K_{ae} (Ghosh 2010)	
	δ/\emptyset		δ/\emptyset		δ/\emptyset		δ/\emptyset	
$\emptyset(\circ)$	0.0	0.5	0.0	0.5	0.0	0.5	0.0	0.5
20	0.4903	0.4431	0.49	0.45	0.49	0.45	0.491	0.447
30	0.3333	0.2989	0.33	0.30	0.33	0.30	0.33	0.301
40	0.2174	0.1978	0.22	0.20	0.22	0.20	0.217	0.199

Table 5 Comparison of values at $k_h = k_v = 0.0$

	K_{pe} (present method)		K_{pe} (M-O Method [10])		K_{pe} (Ghosh 2010)		K_{pe} [11]	
	δ/\emptyset		δ/\emptyset		δ/\emptyset		δ/\emptyset	
$\emptyset(\circ)$	0.0	0.5	0.0	0.5	0.0	0.5	0.0	0.5
20	1.5300	2.3671	1.79	2.25	1.18	2.29	1.964	2.49
30	3.0000	4.9765	2.33	3.63	3.78	2.40	2.40	3.78
40	4.5989	22.031	3.69	8.88	3.79	9.89	3.95	10.10

4 Conclusion

Dynamic earth pressure coefficient charts have been evaluated using PSO technique and presented in the graphical form charts, which can be readily used by practicing engineers. The results have been compared with those obtained by static and pseudo-static condition. The following are some of the conclusions drawn from the present work:

1. As the pseudo-dynamic methods of analysis considers time effects and phase difference in shear wave velocity and primary wave velocity propagating in the backfill behind the rigid retaining wall, gives more realistic nonlinear earth pressure distribution as compared to the Mononobe-Okabe method using pseudo-static approach.
2. It was found that the horizontal and vertical seismic accelerations are more significant for the computations of dynamic earth pressure.
3. It is found that seismic earth pressure is highly sensitive to friction angle whereas less sensitive to wall friction angle.
4. The results obtained in the PSO technique, when compared with reported results, show a good agreement.

Acknowledgements The work is a complete contribution of all the authors along with the corresponding author. This work is technically and financially supported by VSSUT, Burla, India.

References

1. Das BM (1992) Principles of soil dynamics. PWS-Kent, Boston. Das BM (1993)
2. Taylor DW (1948) Fundamentals of Soil Mechanics. Wiley, New York, 700
3. Okabe S (1926) General theory on earth pressure and seismic stability of retaining walls and dams. J Jpn Soc Civil Eng 12–311
4. Mononobe N (1929) Earthquake proof construction of masonry dams. In: Proceedings of world engineering congress, international association of earthquake engineering, Tokyo, pp 9–275
5. Steedman RS, Zeng X (1990) The influence of phase on the calculation of pseudo-static earth pressure on a retaining wall. Géotechnique 40(1):103–112
6. Choudhury D, Nimbalka S (2006) Seismic passive resistance by pseudo-dynamic method. Geotechnique 55(9):699–702
7. Nanda B, Maity D, Maiti D (2013) Crack assessment in frame structures using modal data and unified particle swarm optimization technique. Adv Struct Eng 17(5):747–766
8. Kapila IP (1962) Earthquake resistance design of retaining walls 2nd earthquake symposium, University of Roorkee, India
9. Choudhury D, Nimbalka S (2006) Pseudo-dynamic approach of seismic active earth pressure behind retaining wall. Geotech Geol Eng 24:1103–1113
10. Mononobe N, Matsuo H (1929) On the determination of earth pressures during earthquakes. In: Proceedings of the World Engineering Conference, vol 9, Pp176
11. Giri D (2014) Pseudo-dynamic methods for seismic passive earth pressure behind a cantilever retaining wall with inclined backfill. Geomech Geoeng 9(1):72–78

Analytical Study on the Influence of Rigidity of Foundation and Modulus of Subgrade Reaction on Behaviour of Raft Foundation



Sujay Teli, Palak Kundhani, Virag Choksi, Pritam Sinha and Kannan K. R. Iyer

Abstract Shallow foundations are commonly used for supporting structures unless soil, loading and serviceability requirements necessitate deep foundations. Shallow foundations may be designed as rigid or flexible foundations depending on loading conditions as well as relative stiffness of foundation and supporting soil subgrade. For design of flexible foundations, soil is modelled as per Winkler approach or as a continuum. For analysis of most foundations, Winkler approach is found acceptable, wherein modulus of subgrade reaction is evaluated and applied as soil springs. The different factors which affect design of foundation include superstructure geometry and stiffness; type, magnitude and location of loading; rigidity of foundation and modulus of subgrade reaction. The current study attempts to understand the influence of rigidity of foundation and modulus of subgrade reaction on behaviour of raft foundation. A multistoreyed structure is analysed in Staad Pro V8i software for different combinations of foundation rigidity and modulus of subgrade reaction; and parameters such as base pressure, settlement, shear stress and bending moment have been compared. It is concluded from the study that modulus of subgrade reaction has higher influence on variation in foundation base pressure as compared to rigidity of foundation. It is also noted that impact of variation in modulus of subgrade reaction on structural design of foundation is negligible. However, the rigidity of foundation influences the shear stress and bending moment in foundation. It is opined that such studies would help in developing decision matrix to account for various parameters in optimization of foundation design.

Keywords Modulus of subgrade reaction · Rigidity · Flexible · Raft foundation · Staad pro

S. Teli · P. Kundhani · V. Choksi · P. Sinha · K. K. R. Iyer (✉)

Department of Civil Engineering, Institute of Infrastructure Technology Research and Management, Near Khokhra Circle, Maninagar (East), Ahmedabad 380026, India
e-mail: kannaniyer@iitram.ac.in

1 Introduction

Shallow foundations are commonly used for transferring superstructure (viz., building, water tanks, industrial structures, etc.) loads to soil, unless the bearing capacity of soil is inadequate or expected settlement (total and differential settlement) are higher than permissible values. Shallow foundation includes isolated foundations with or without tie beams, combined foundations and raft (mat) foundations. For multistoreyed structures, Raft foundation is generally preferred when columns are closely spaced, intensity of loading is higher, and higher total/differential settlement of soil is anticipated. Raft foundation is economical compared to isolated foundation when the area of foundation covers more than half of structure base area [1].

Analysis approach for raft foundation depends on soil–structure interaction. Depending on the relative stiffness of the foundation superstructure system and subgrade soil, the foundation can be designed as rigid foundation or flexible foundation [2]. Rigid foundation can be analysed as a plate undergoing rigid body settlement, whereas flexible foundation needs to account for the flexural effects on load distribution and soil–structure interaction. Winkler model is one of the popular models for analysis of flexible raft foundation. In this model, the subgrade soil is replaced by number of linear elastic uncoupled springs. The modulus of subgrade reaction obtained from plate load test or correlations with field/laboratory tests is usually assigned as stiffness value of the springs after considering the effect of foundation size, depth of foundation and other site-specific geotechnical aspects. However, modulus of subgrade reaction is a complex interface parameter [3] and is also dependent on other factors such as geometry and stiffness of superstructure, foundation shape and rigidity as well as location and magnitude of loading [4]. Modulus of subgrade reaction is defined as the contact pressure required to cause unit settlement of foundation and is an important parameter for foundation design. A clear understanding of the behaviour of raft foundation in relation to the supporting subgrade is mandatory to ensure the economy and safety in design, and hence a clear understanding of factors affecting foundation design is necessary.

Earlier studies have reported that the factors affecting modulus of subgrade reaction includes foundation size, shape and rigidity, type and stiffness of soil as well as loading conditions. It has also been reported that the inability to account for these factors could result in about 50% error in estimation of modulus of subgrade reaction [4]. Mondal et al. [5] studied the influence of superstructure modelling on behaviour of raft foundation. The study concluded that modelling of superstructure reduces the design stresses and moment for foundation significantly, and hence results in economical design. The study also noted that modelling of horizontal stiffness of raft does not have much influence on the behaviour of raft foundation. Marto et al. [6] studied the relationship between modulus of subgrade reaction (K_s) and the footing dimensions through an analytical study in PLAXIS 2D software, with and without considering the effect of water. The study suggested that K_s is inversely proportional to width of the foundation but the relationship is non-linear.

The study also highlighted that water decreases the internal contact pressure of soil particles, which leads to reduction in the value of K_s due to lower resistance to stress and higher tendency to settle under loading. With increase in the size of the footing the reduction in internal contact pressure due to saturation of soil decreases, and for foundation size larger than 4 m, the variation in values of K_s for saturated and unsaturated soil is less than 25%.

Hany and Mohammed [7] studied the effect of footing-clayey soil system rigidity on the modulus of subgrade reaction (K_s) and suggested that footing rigidity has significant influence on the distribution of K_s beneath the footing. The study also noted that K_s distribution based on linear elastic and elastic perfect plastic models are quite different. It was also stated that at the edges of the footing, K_s distribution is not appropriate as per the linear elastic model, as this model does not account for the plasticity of soil. It was noted that an unrealistic tension in elastic soil model may be generated at the edge of the footings. Further, the study suggests that a new modification factor is required to take into account the rigidity of footing, while computing K_s from plate load test. The study concluded that K_s is uniformly distributed under the flexible footing; however, K_s is concentrated near edges and has low values at the centre of footing for the semi-rigid or rigid footings. Lemman et al. [8] carried out centrifuge test studies to understand the influence of foundation stiffness on strip foundation supported on sand. The study noted that relative stiffness of foundation and soil affects the contact pressure and settlement distribution below foundation. It was also noted that reduction in foundation stiffness results in reduction in contact pressure at edges. The study also observed that initially stiff foundation upon cracking behaves as more flexible foundation.

The review of literature suggests that not many studies have reported the influence foundation rigidity and modulus of subgrade reaction on different parameters for foundation design such as base pressure, settlement, bending moment and shear stress in foundation. It is opined that such studies would enhance the understanding of foundation behaviour due to variation of different factors and would help to arrive at a decision matrix for optimum design of foundation. With this perspective, the present study evaluates the influence of foundation rigidity and modulus of subgrade reaction on different parameters governing the foundation design.

2 Theoretical Background and Methodology

2.1 Theoretical Background: Winkler's Approach

Winkler's model represents the soil subgrade as a system of identical but mutually independent (discrete), closely spaced and linear elastic springs. Winkler's model of an elastic foundation assumes that the deflection y at any point on the surface of the foundation is proportional to the stress σ at that point, i.e. $\sigma = K_s \cdot y$, where K_s is

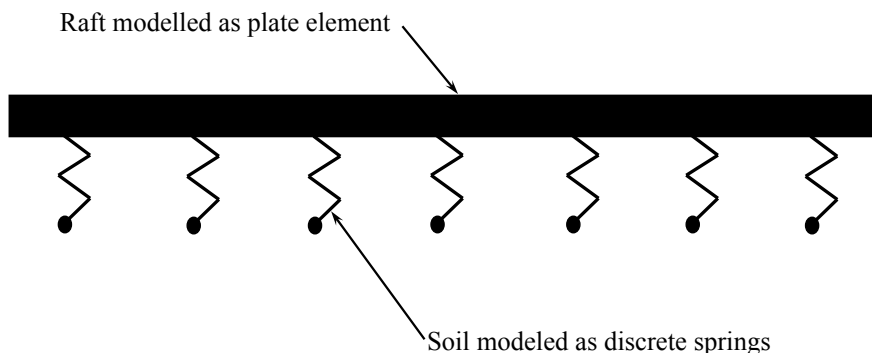


Fig. 1 Conceptual representation of Winkler soil springs connected with raft

called modulus of subgrade reaction of the foundation system. The modelling of foundation supported on discrete springs is based on modified Winkler's approach where the discrete soil springs are connected by continuous raft (plate), which distributes the load to different springs based on its rigidity and loading conditions. Figure 1 depicts the schematic view of Winkler soil springs connected with raft.

2.2 Methodology

STAAD Pro V8i software [9] is the one of the most popular finite element-based software in practice for analysis and design of structures including foundation, wherein the foundation and superstructure can be modelled together to understand the combined effects for simple as well complex structures. It is preferable to model foundation in Staad Pro along with superstructure if the foundation is expected to behave as flexible foundation. In Staad Pro, the flexible foundation can be modelled using plate elements. In the present study, a 10-storey reinforced concrete building frame with five bays each of 5 m span in both directions and 4 m as storey height is modelled in Staad Pro. The foundation raft is modelled as a mesh of four-noded plate elements, with each plate element of size $0.5 \text{ m} \times 0.5 \text{ m}$. The plate size is selected based on the authors past experience.

Figure 2 shows the plan view with dimensions and Fig. 3 shows typical three-dimensional view of the model. Further, Fig. 4 shows that local axes for plate element are different that the global axes for the overall model. A clockwise modelling of plate starting from top-left node results in local axes as shown in the figure. As per the foundation modelling procedure considered in the study, positive value of moment indicates tension at bottom (sagging moment), i.e., local z -direction. It may be noted that change in modelling procedure of plate element would result in different orientation of local axes and would result in different interpretation of results

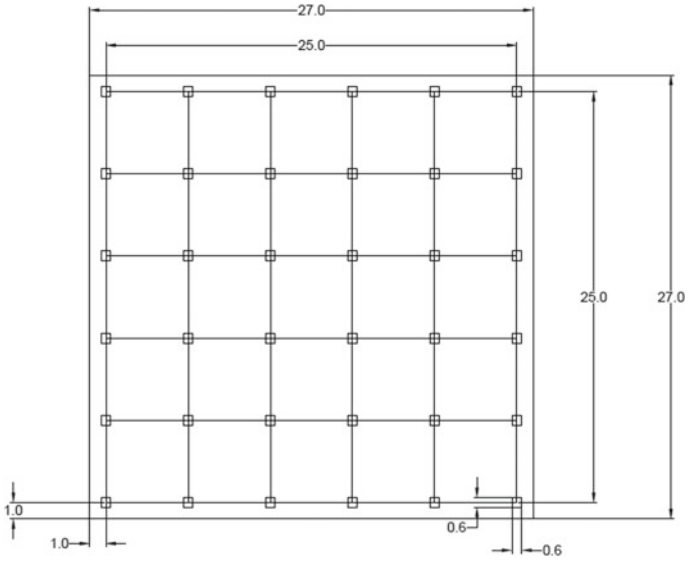
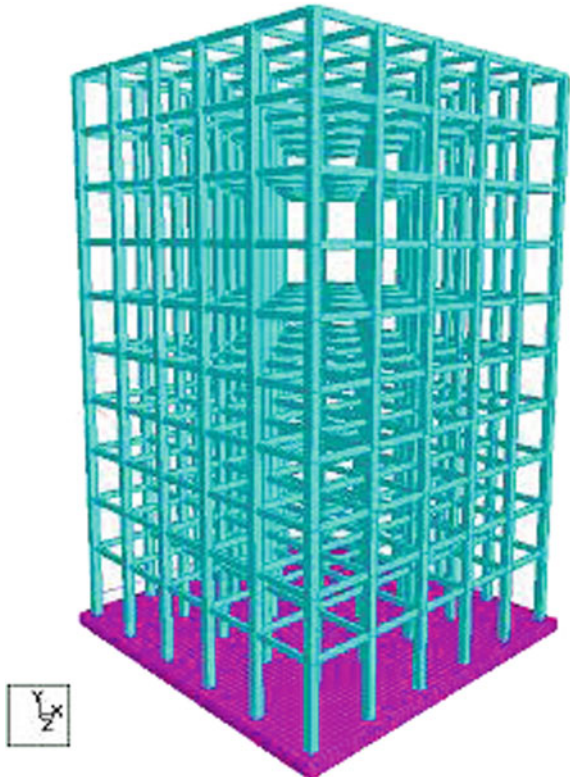


Fig. 2 Plan dimensions of building and foundation considered in the study (in metres)

Fig. 3 Three-dimensional view of multistoreyed building with raft foundation



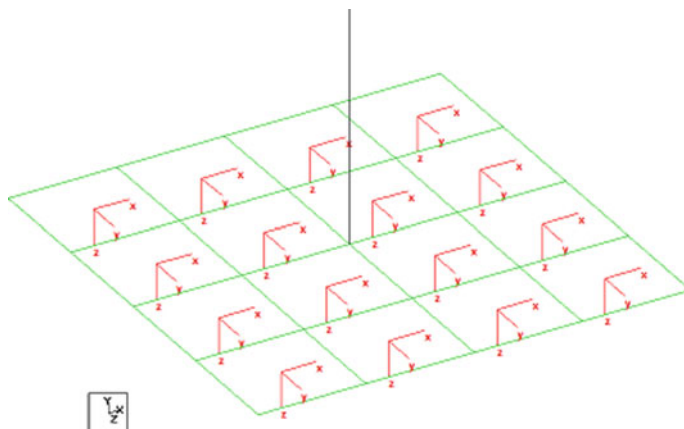


Fig. 4 Local and global axes in Staad Model

(shear stress and bending moment). The size of foundation raft is considered as $27\text{ m} \times 27\text{ m}$ in the present study, with edge of raft having an offset of 1 m from centre of edge columns.

2.3 Method of Analysis

STAAD Pro uses the finite element method for analysis of any structure. A ten-storeyed symmetric building was analysed as a three-dimensional frame with appropriate dimensions of the beams ($0.23\text{ m} \times 0.45\text{ m}$) and columns ($0.6\text{ m} \times 0.6\text{ m}$) under the combined impact of vertical dead load and live load. The 230 mm thick wall (not modelled) load was applied as uniformly distributed load on beams in the model. For the live load, the building was assumed to be an institutional building and the live load of 4 kN/m^2 was applied as per Indian Standard IS-875 Part-II [10]. The parameters and their values used in the study are summarized in Table 1.

At each node of the foundation raft (plate elements), vertical spring stiffness values were assigned with Staad command as depicted in Fig. 5. For the same building, considering five different values of modulus of subgrade reaction (K_s) and five different values of raft thickness (t_r), total 25 cases were analysed and the change in the foundation analysis parameters like base pressure, settlement, shear stress and bending moment were compared and explained in the next section.

Table 1 Parameters and values used in the study

Parameter	Values used in study					Units
Modulus of elasticity of concrete (E)	2.17×10^7					kN/m^2
Dimensions of raft	27 × 27 (For ten-storey building with five bays in both direction, each bay with 5 m centre to centre span and storey height of 4 m)					m
Modulus of subgrade reaction (K_s)	2000	4000	6000	8000	12000	kN/m^3
Thickness of raft	0.5	0.6	0.7	0.8	0.9	m
Flexural rigidity of raft (EI)	6103125	10546200	16746975	24998400	35593425	kN-m^2

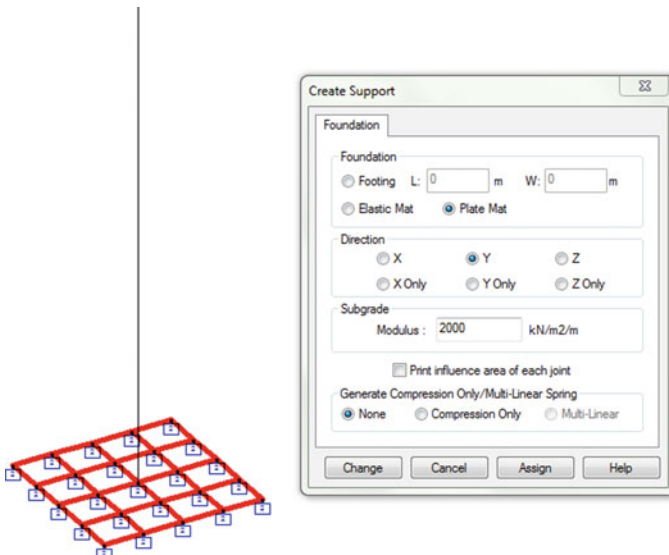


Fig. 5 Soil spring definition for raft foundation in Staad Pro

3 Results and Discussion

Total 25 cases have been analysed in the study. The raft foundation thickness (t_r) have been varied as 0.5 m, 0.6 m, 0.7 m, 0.8 m and 0.9 m. The values of modulus of subgrade reaction (K_s) have been varied as 2000 kN/m^3 , 4000 kN/m^3 , 6000 kN/m^3 , 8000 kN/m^3 and 12000 kN/m^3 . Figure 6 shows the maximum and minimum base pressure for different values of raft thickness, t_r , and modulus of subgrade reaction, K_s .

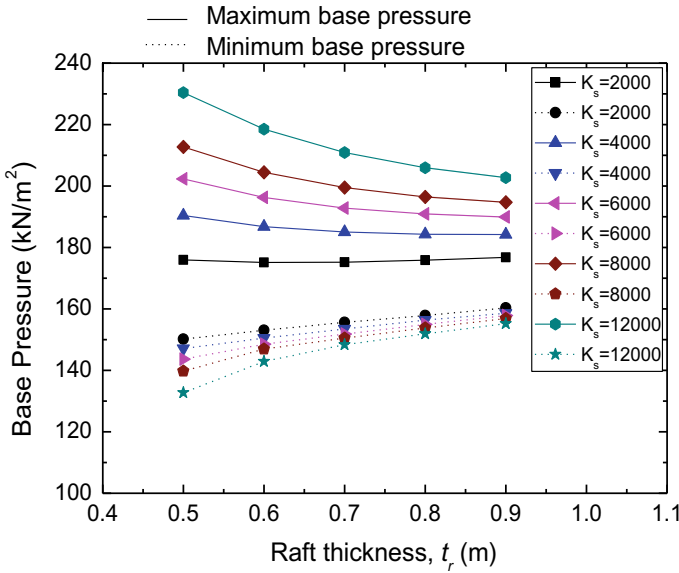


Fig. 6 Maximum and minimum base pressure of raft foundation for different values of ' t_r ' and ' K_s '

It can be observed from the figure that with increase in t_r and K_s , the maximum base pressure reduces and minimum base pressure increases. In order to understand the influence of t_r and K_s on variation in base pressure within foundation, the percentage variation between maximum and minimum foundation base pressure is plotted for different values of t_r and K_s as depicted in Fig. 7. The influence of K_s on base pressure is observed to be higher as compared to t_r . It can be observed from the figure that at higher values of K_s (12000 kN/m³) and lower value of t_r (0.5 m), the base pressure variation is found to be maximum (42.4%). Further, minimum base pressure variation in foundation is observed for lower value of K_s (2000 kN/m³) and higher value of t_r (0.9 m). This indicates that for lower values of K_s , the base pressure tends to be more uniform as compared to higher values of K_s . Moreover, increase in rigidity of foundation tends to make base pressure distribution more uniform. Hence, the rigidity of foundation and its relative stiffness with respect to soil affects base pressure distribution. Further, it can be noted from Fig. 8 that settlement of foundation is inversely proportional to K_s as expected. It can also be seen that settlement is not significantly influenced by thickness of raft (t_r). However, it can be clearly observed that the difference between maximum and minimum settlement (differential settlement) within foundation raft reduces with increase in t_r .

In order to quantify this, Fig. 9 shows the variation of differential settlement for different values of K_s and t_r . It can be observed from the figure that differential settlement is maximum (12.9 mm) for lower values of K_s (2000 kN/m³) and t_r (0.5 m) and is minimum (3.95 mm) for higher values of K_s (12000 kN/m³) and t_r (0.9 m). However, a comparison for Figs. 8 and 9 indicates that the differential

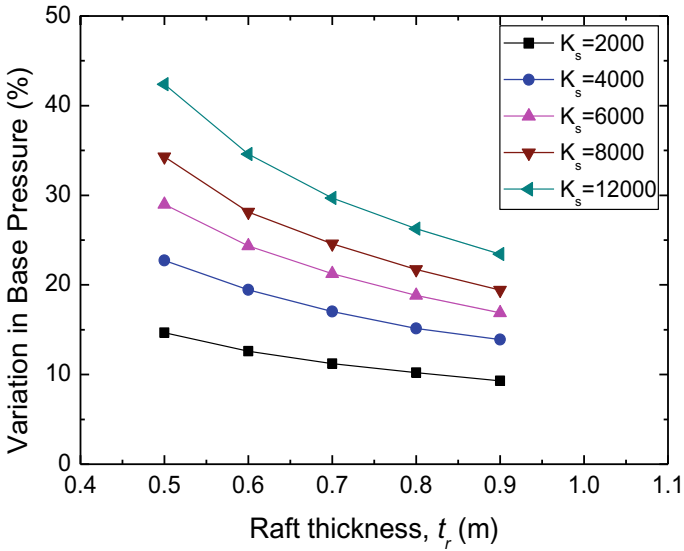


Fig. 7 Variation in base pressure of raft foundation for different values of ' t_r ' and ' K_s '

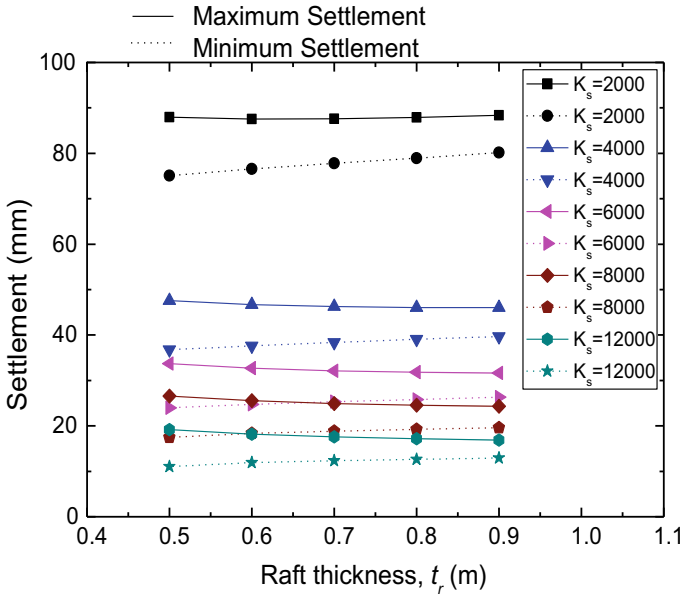


Fig. 8 Maximum and minimum settlement of raft foundation for different values of ' t_r ' and ' K_s '

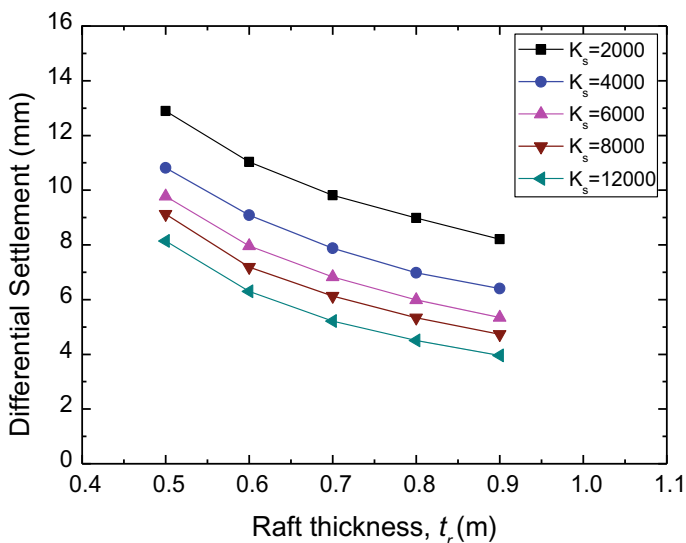


Fig. 9 Differential settlement of raft foundation for different values of ' t_r ' and ' K_s '

settlement expressed as percentage of maximum settlement for case with $K_s = 2000 \text{ kN/m}^3$ and $t_r = 0.5 \text{ m}$ is 14.65%, whereas for case with $K_s = 12000 \text{ kN/m}^3$ and $t_r = 0.9 \text{ m}$, differential settlement is about 23.44% of maximum settlement. This indicates that for foundation with low rigidity supported on soft soil, the settlement distribution is relatively uniform as compared to foundation with higher rigidity on stiff soil. Further, for case with $K_s = 12000 \text{ kN/m}^3$ and $t_r = 0.5 \text{ m}$, the differential settlement is observed to be about 42.4% of maximum settlement in foundation. This suggests that for foundation with low rigidity on stiff soil, settlement is non-uniform due to non-uniformity in base pressure distribution (flexural effects) as seen from Fig. 7. It may be noted that the maximum settlement is generally observed at corner of the foundation and minimum settlement is observed between column locations on the raft foundation. The typical variation of base pressure for two cases ($K_s = 2000 \text{ kN/m}^3$ and $t_r = 0.5 \text{ m}$; $K_s = 12000 \text{ kN/m}^3$ and $t_r = 0.9 \text{ m}$) is depicted in Fig. 10.

In order to further compare the influence of K_s and foundation flexural rigidity, EI (refer Table 1) on percentage variation in foundation base pressure (percentage variation between maximum and minimum base pressure within foundation), the ratio of K_s and EI values with respect to their corresponding base values in the study ($K_s = 2000 \text{ kN/m}^3$; EI = $6.10 \times 10^6 \text{ kN-m}^2$, flexural rigidity for foundation of size $27 \text{ m} \times 27 \text{ m}$ and 0.5 m thickness) are presented with respect to percentage variation in base pressure in Table 2. These ratios are designated as K_{sn} and EI_n , respectively. It can be clearly seen that increase in K_s values by six times increase the variation in base pressure by about 189%. However, an increase in EI by about 5.83 times results in reduction in variation in base pressure by about 36.59%. This clearly indicates that the

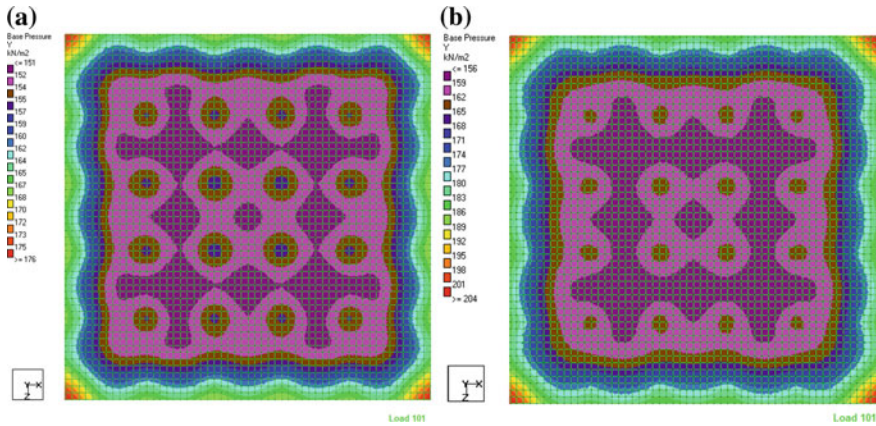


Fig. 10 Variation of base pressure diagram of raft foundation for (a) $K_s = 2000 \text{ kN/m}^3$ and $t_r = 0.5 \text{ m}$, (b) $K_s = 12000 \text{ kN/m}^3$ and $t_r = 0.9 \text{ m}$

Table 2 Influence of variation in K_s and EI values on percentage variation in base pressure

EI _n	Ks _n				
	1	2	3	4	6
1.00	14.65	22.72	29.00	34.31	42.40
1.73	12.59	19.46	24.34	28.13	34.60
2.74	11.20	17.03	21.24	24.57	29.68
4.10	10.22	15.14	18.82	21.73	26.26
5.83	9.29	13.91	16.88	19.43	23.43

influence of K_s on base pressure distribution is more prominent as compared to rigidity of foundation. Further, it can also be inferred that base pressure variation can be expected to be larger for soil after ground improvement (higher K_s) as compared to unimproved ground (lower K_s). However, lower values of total settlement and differential settlement for stiffer soil (after ground improvement) would result in higher allowable base pressure and would compensate for this effect. It may be inferred from the study that K_s influences the dimensioning of the raft foundation (based on its effect on base pressure and corresponding settlement). Hence, it is an important parameter of foundation design.

To understand the influence of K_s and t_r on the bending moment and shear stress in foundation, values of these parameters (Bending Moment, M_x along global x-direction) and Shear stress (SQ_x) perpendicular to global x-y plane are plotted as depicted in Figs. 11 and 12. It can be concluded from these figures that K_s has negligible influence on variation in M_x and SQ_x . However, it is observed that M_x increases marginally and SQ_x reduces with increase in t_r .

It may be noted that the increase in thickness of raft foundation is expected to result in better load distribution from raft to soil. This distribution is expected to reduce the total settlement, differential settlement variation below the raft and the bending

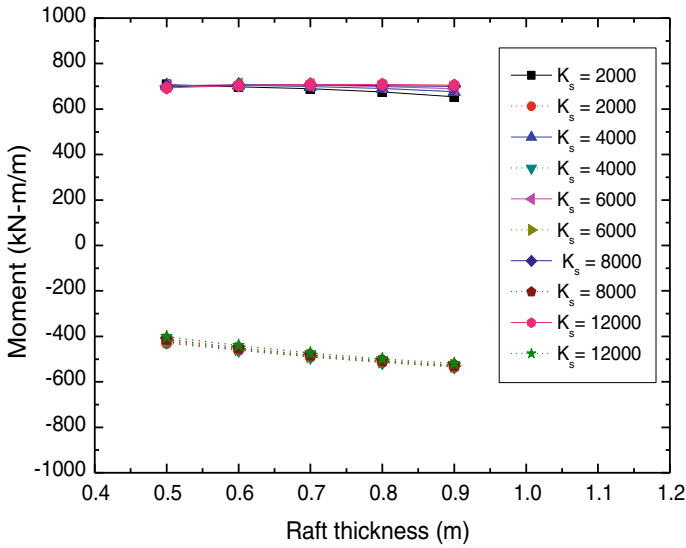


Fig. 11 Bending moment (M_x) in raft foundation for different values of ' t_r ' and ' K_s '

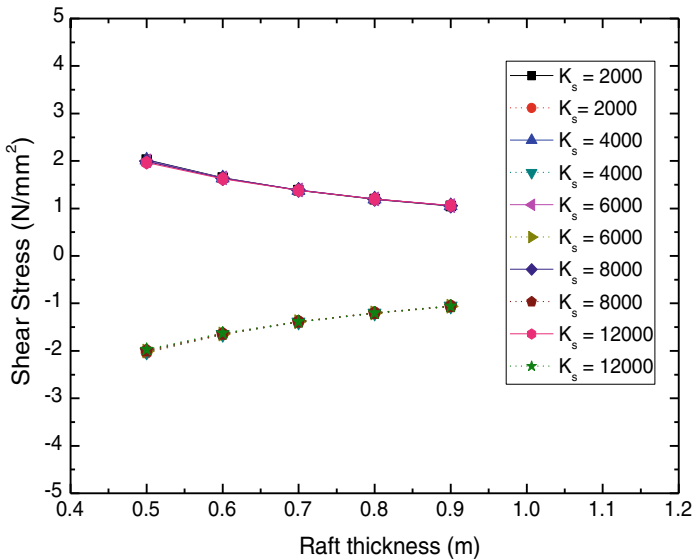


Fig. 12 Shear stress (SQ) in raft foundation for different values of ' t_r ' and ' K_s '

moment in raft. However, increase in thickness of raft would cause additional self-weight induced bending moment. It appears that the combined effect of both these aspects partly nullifies each other and hence the changes in bending moment appears to

less with increase in foundation raft thickness. The reduction in shear stresses with increase in raft thickness can be attributed to increase in the shear resisting area with increase in raft thickness. Further, for design of raft foundation, as shear reinforcement is usually avoided, the thickness would also be governed by the limiting value of shear stress on foundation mainly based on the grade of concrete. Appropriate reinforcement design is usually provided to resist the bending moment in raft.

In spite of the findings, the current study has some limitations. The soil springs defined in Staad Pro are discrete springs, which are not inter-coupled. The distribution of stresses due to soil continuum cannot be accounted for in Staad Pro software. However, load distribution to different springs due to continuity of raft partially overcome this limitation especially under loaded area; however, the same cannot be concluded in unloaded areas under raft. Interestingly, a recent study by Lee et al. [11] suggested comparable foundation base pressure versus settlement response of foundation when soil is modelled as Winkler spring (no coupling) as compared to soil model which accounts for inter-coupling. Further, this study does not consider the effect of change in rigidity of foundation due to its cracking [12]. The study also does not account for variation in modulus of subgrade reaction at centre and edges of foundation depending of the type of soil. The present study also does not account for wind load and seismic load effects, which is part of extended study by the authors. However, in spite of these limitations, the study attempts to present a clear understanding of the influence of foundation thickness and modulus of subgrade reaction on base pressure, settlement, shear stress and bending moment in raft foundation. It is believed that such studies would be useful to arrive at a decision matrix for optimum foundation design in practice.

4 Conclusions

The present study evaluates the influence of change in foundation rigidity and modulus of subgrade reaction on the base pressure, settlement of foundation as well as shear stress and bending moment within the foundation. The following conclusions can be derived from the study:

1. The influence of modulus of subgrade reaction, K_s is more prominent on foundation base pressure distribution as compared to the influence of rigidity of foundation. It is concluded from the study that increase in K_s values results in higher variation in base pressure distribution, whereas increase in rigidity of foundation results in more uniform base pressure distribution.
2. It is observed that differential settlement is lower for stiff soil (higher K_s) as compared to soft soil (lower K_s). This is mainly due to significant reduction in total settlement of foundation. However, the percentage variation in maximum and minimum settlement is higher for stiff soil as compared to soft soil, which can be attributed to larger variation of base pressure in stiff soil. Further, differential settlement reduces with increase in rigidity of foundation.

3. It is noted from the study that maximum base pressure is higher for stiff soil as compared to soft soil. Hence, it can be inferred that soil after ground improvement (stiff soil) would experience higher maximum base pressure as compared to unimproved ground (softer soil) for the same foundation and loading conditions. However, higher allowable base pressure due to lower total/differential settlement and higher bearing capacity (shear criteria) for improved ground would compensate this effect.
4. The variation in modulus of subgrade reaction, K_s is observed to have negligible influence on bending moment and shear stress in raft foundation. However, increase in rigidity of foundation results in slightly higher bending moment and lower values of shear stress.

References

1. Kame GS, Ukarande SK (2008) A parametric study on raft foundation. In: 12th International Conference of International Association for Computer Methods and Advances in Geomechanics (IACMAG). Goa, India, pp 1–6
2. ACI 336.2R-88 (2002) suggested analysis and design procedures for combined footings and mats, Report by ACI Committee 336
3. Teodoru IB, Toma IO (2009) Numerical analyses of plate loading test. The Bulletin of the Polytechnic Institute of Jassy, Construction. Architecture Section, Romaina, Section LV (LIX), 57–65
4. Terzaghi K (1955) Evaluation of coefficient of subgrade reaction. *Geotechnique* 5(4):297–326
5. Mondal A, Singh AK, Roy R, Verma USP, Warudkar AS (2003) Effect of modeling of super-structure on the behaviour of reactor building raft. In: Transactions of the 17th International Conference on Structural Mechanics in Reactor Technology (SMiRT 17). Prague, Czech Republic, pp 17–22
6. Marto A, Latifi N, Janbaz M, Kholghifard M, Khari M, Alimohammadi P, Banadaki AD (2012) Foundation size effect on modulus of subgrade reaction on sandy soils. *Electron J Geotech Eng* 17:2523–2530
7. Hany F, Mohammed F (2014) Calculation of subgrade reaction modulus considering the footing-soil system rigidity, vulnerability, uncertainty, and risk, ASCE
8. Lemman HE, Jacobsz SW, Kearsley EP (2017) The influence of foundation stiffness on the behaviour of surface strip foundations on sand. *J South Afr Inst Civ Eng* 59(2):19–27
9. Staad Pro V8i (2012) Technical reference manual Bentley, USA
10. IS 875 Part II (1987) Code of practice for design loads (other than earthquake) for buildings and structures. Part 2: Imposed loads, Bureau of Indian Standards, New Delhi
11. Lee J, Jeong S, Lee JK (2015) 3D analytical method for mat foundations considering coupled soil springs. *Geomech Eng* 8(6):845–857
12. Skorpen S, Dekker N (2014) The application and interpretation of linear finite element analysis results in the design and detailing of hogging moment regions in reinforced concrete flat plates. *J South Afr Inst Civ Eng* 56(1):77–92

Numerical Study on the Undrained Response of Silty Sands Under Static Triaxial Loading



M. Akhila, K. Rangaswamy and N. Sankar

Abstract The silty soils are more susceptible to liquefaction, even under static loading, than the coarse sands. Pore pressure developed during dynamic events may not dissipate easily due to the presence of more number of small voids. Hence, the rate of pore pressure build-up under static/dynamic loading conditions is much faster in silty sands, which lead to a reduction in the soil strength. This phenomenon may be assessed in terms of either contraction or dilation behaviour under triaxial loading. Therefore, it is necessary to analyse the undrained response of silty sands under triaxial loading so that the damages occurring during future dynamic events may be predicted. The present study involves both the experimental and numerical simulations on various silty sands, which contain 0, 10, 20, 30 and 40% silt fines. Initially, experimental static triaxial testing was performed to determine the undrained response of silty sands moulded to cylindrical specimens at medium relative density. The saturated samples are isotropically consolidated at 100 kPa pressure before shearing. Further, numerical simulations were performed on silty sands by inputting the material parameters into the hypoplastic model. This model requires eight material constants as input including critical friction angle, hardness coefficients, limited void ratios, peak state and stiffness coefficients. These constants were determined for each silty sand combination after conducting basic laboratory tests according to the formulations build in the hypoplastic model program. The experimental trends were compared with numerical model simulations under triaxial testing. The effect of the initial state of soil and the amount of silt fines on the undrained response of fine sands is discussed in detail. The liquefaction susceptibility of silty sand is described based on steady state line concept. The results indicate that the silt sands behave as highly contractive, i.e. more liquefiable when compared with sands.

M. Akhila (✉)

Department of Civil Engineering, SCMS School of Engineering and Technology,
Ernakulam, Kerala, India
e-mail: akhila144@gmail.com

K. Rangaswamy · N. Sankar

Department of Civil Engineering, NIT Calicut, Calicut, India

© Springer Nature Singapore Pte Ltd. 2020

A. Prashant et al. (eds.), *Advances in Computer Methods and Geomechanics*, Lecture Notes in Civil Engineering 56,
https://doi.org/10.1007/978-981-15-0890-5_17

195

Keywords Hypoplastic modelling · Sand · Silt · Undrained response

1 Introduction

The liquefaction may occur in fully saturated sands, silts and low plastic clays. When the saturated soil is subjected to seismic or dynamic loads, there is a sudden build-up of pore water within a short duration, and it could not dissipate which leads to reduction of the effective shear strength of soil mass. In this state, the soil mass behaves like a liquid and causes large deformations, settlements, flow failures, etc. This phenomenon is called soil liquefaction. As a result, the ability of soil to support the foundations of buildings, bridges, dams, etc., are reduced. Liquefiable soil also exerts a higher pressure on retaining walls, which can cause them to tilt or slide. The lateral movement could cause settlement of the retained soil and distraction of structures constructed on various soil deposits. A sudden build-up of pore water pressure during earthquake also triggers landslides and cause the collapse of dams. Liquefaction effects on damages of structures are commonly observed in low-lying areas near the bodies of water such as rivers, lakes and oceans.

An experimental study by Vaid and Sivathayalan [1] indicate that for a given initial state, the liquefaction potential depends on the stress path during loading. Yamamuro and Lade [2] have conducted drained tests at confining pressure between 25 and 1000 kPa and suggested that void ratio fails to provide a unifying parameter for evaluation of liquefaction potential in silty sands; volumetric compressibility is proposed to provide a better measure for separation between liquefaction and non-liquefaction behaviour. Monotonic undrained tests by Yamamuro and Covert [3] indicated that static liquefaction occurred at low confining pressures and dilatancy increases with confining pressure. The study by Yang et al. [4] showed that the steady-state line (SSL) could be represented by one line in tests under drained conditions if the fines contents are less (0–30%) than the transition fines content and the corrected intergranular void ratios are used.

The present paper initially discusses the experimental triaxial studies performed to analyse the undrained response of silty sands and then attempts to use the hypoplastic model simulations to analyses the liquefaction susceptibility of silty sands under static triaxial loading using steady-state line. Details of the materials used a small introduction to the hypoplastic model and hypoplastic parameter determination is discussed in the following sections.

2 Materials Used

The silty sands used in this study were processed by mixing quarry dust into the fine sand at different percentages. The fine sand is collected from Cherthala, Kerala and quarry dust is procured from Blue Diamond M-sand manufacturers, Kattangal, Kerala. For preparing the soil combination, the ingredients were put into a container and mixed thoroughly to have a homogeneous soil mix until there was no noticeable colour difference and segregation. All the basic properties tests were performed on the soil combinations, and the properties are listed in Table 1. A combined dry sieve and hydrometer analysis were carried out to obtain the particle size distribution. The gradation curves are shown in Fig. 1. Relative density tests were performed as per the IS test procedure to arrive at the maximum density

Table 1 Basic properties of silty sands

Notation	FS	SS10	SS20	SS30	SS40
Fines content %	0	10	20	30	40
Sand, %	100	90	80	70	60
Silt, %	0	10	20	30	40
Specific gravity	2.62	2.66	2.71	2.72	2.69
D_{50} , mm	0.28	0.26	0.23	0.2	0.15
Uniformity coefficient, C_u	2.36	4.00	4.67	6.25	7.33
Coefficient of curvature, C_c	0.87	1.28	1.17	0.72	0.74
Maximum dry density (g/cc)	1.66	1.71	1.81	1.86	1.89
Minimum dry density (g/cc)	1.41	1.44	1.48	1.52	1.53

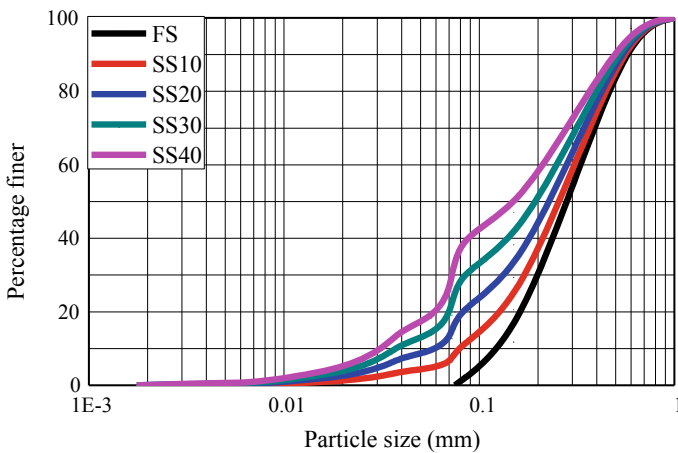


Fig. 1 Particle size distribution curves of silty sands [8]

of all soil combinations. The minimum density of soil sample was obtained after placing the material steadily with zero height using paper cone into the CBR mould of 150 mm size in thrice as per the IS code procedure. Based on limited densities, the maximum and minimum void ratios are estimated by using the empirical equations.

3 Hypoplastic Model

The hypoplastic constitutive law describes the deformation behaviour of cohesionless soils up to certain fines, including the nonlinearity and inelasticity. The first version of the hypoplastic constitutive law was proposed by Kolymbas [5]. It was used as a single-state variable, the current Cauchy stress T_s . Later another state variable the void ratio e was added. The hypoplastic constitutive equation in general form is given by

$$\dot{T}_s = F(T_s, e, D) \quad (1)$$

Herein, \dot{T}_s represents the objective stress rate tensor as a function of the current void ratio e , the Cauchy granulate stress tensor T_s and the stretching tensor of the granular skeleton D .

4 Determination of Model Parameters

The standard routine laboratory tests were conducted on the non-plastic silty sands to determine the model parameters. The limited eight numbers of hypoplastic model parameters (φ_c , h_s , n , e_{i0} , e_{d0} , e_{c0} , β and α) are determined based on the detailed procedure for the determination of model parameters explained by Herle and Gudehus [6].

Critical State Friction Angle: The critical friction angle φ_c can be obtained from the angle of repose of dry granular material from cone pluviation tests. If the portion of grains with diameter <0.1 mm is too large, conventional shear tests are recommended for determination of φ_c . Hence, for the present study, direct shear box tests were conducted on loose soil at different consolidation pressures to determine the critical friction angle φ_c . A series of direct shear box tests were conducted on silty sand samples of loosest and densest possible conditions at different normal stresses.

Minimum, maximum and critical void ratios at zero pressure state: Based on limited densities, the maximum and minimum void ratios were estimated by using the empirical equations. Three limit void ratios at zero pressures, i.e. e_{i0} (during isotropic compression at the minimum density), e_{c0} (critical void ratio) and e_{d0} (maximum density) were estimated.

Table 2 Model parameters

Sample	Critical state friction angle	Limiting void ratios			α	h_s (MPa)	n	β
		e_{d0}	e_{c0}	e_{i0}				
FS	30.54	0.578	0.858	1.030	0.374	169	0.394	0.41
SS10	30.96	0.554	0.847	1.016	0.303	140	0.375	0.39
SS20	31.38	0.497	0.831	0.997	0.332	78	0.420	0.25
SS30	32.45	0.462	0.789	0.947	0.330	59	0.440	0.21
SS40	33.20	0.503	0.758	0.910	0.345	43	0.509	0.19

Peak state coefficient: The exponential coefficient of peak state was determined after conducting a series of direct shear box tests on the silty sand in densest possible condition at different normal stresses. The peak friction angles of each sample are determined from the slope of linear failure envelope in densest possible state and they used to estimate the peak state exponent coefficient of model parameter (α).

Hardness coefficient and exponent ‘n’: A series of oedometer compression tests were carried out on the silty sand in loosest possible condition to arrive the hardness parameters. From this experimental e -log p curve and by using mathematical formulations the hardness parameters of all silty sands were determined.

Stiffness Parameter: A series of oedometric compression tests were carried out on the silty sand in loosest and densest possible conditions to arrive the stiffness parameter. From the experimental e -log σ curves and by using mathematical formulations the stiffness parameter can be found. The parameters of all the soil combinations are listed in Table 2.

5 Validation of the Model

The element test program has been prepared by Herle [7] using mathematical formulations involved in Hypoplastic soil model. The test program requires three input files, namely, material parameters, initial state parameters and test conditions.

Initially, the hypoplastic model simulations were performed on oedometric compression of both the loose and dense silt soil samples and the obtained numerical e -log σ curves are compared with the experimental e -log σ curves for validation of the model. The overlapped curves of both the experimental and model simulated tests are presented to check the validity of the model. Fig. 2 shows the combined overlapped e -log p curves under oedometric loading in both loose and dense conditions. It can be seen that the model simulation results well coincide with experimental curves (only the curves for the SS40 sample are shown because of the space limitations).

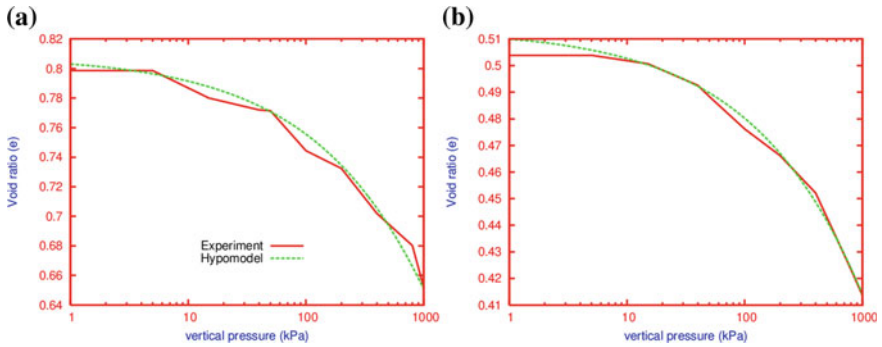


Fig. 2 Combined e -log p curves on the silty sand with 40% silt fines under oedometric compression loading **a** loose state **b** dense state

6 Results and Discussions

To determine the effect of the amount of non-plastic fines on the undrained behaviour of clean fine sands, static triaxial tests were performed on soil samples at 50% relative density and 50, 100 and 150 kPa consolidation pressures. (Due to space limitations, only the graphs obtained for 100 kPa consolidation pressure are shown in this paper).

It is clear that the non-plastic fines have a major influence on the behaviour of fine sand. The effect on non-plastic fines on stress-strain and pore pressure response at 100 kPa consolidation pressure is shown in Fig. 3. From Fig. 3a, it is clear that the fine sand is more dilative compared to the sand–silt mixtures. The dilation tendency decreases with the addition of fines. It is also observed that there is no peak stress even if the samples were sheared over a large axial strain. This may be

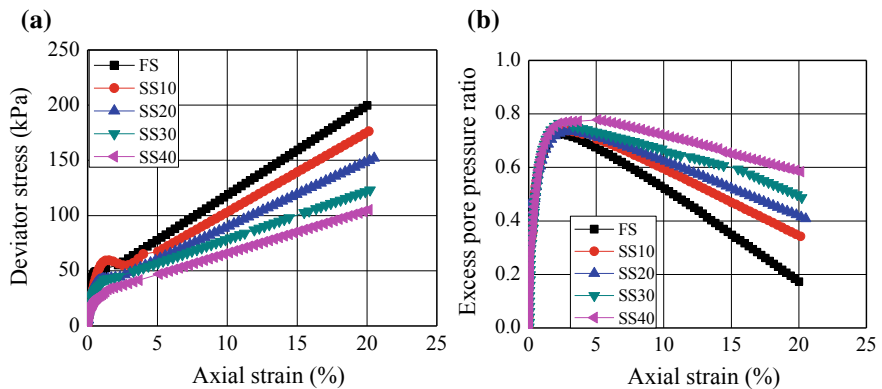


Fig. 3 Effect of fines at a consolidation pressure of 100 kPa **a** stress-strain response **b** pore pressure response (medium dense state)

due to the dilation behaviour. But in the case of silt–sand mixtures with high silt content (30 or 40%), peak stress is observed within a small strain range, and there is not much increase in the deviator stress after that. It is clear from Fig. 3b that, initially, there is an increase in the pore pressure ratio due to initial contraction; but afterwards the pore pressure ratio decreases. The decrease is rapid in the case of fine sand when compared to the silty–sand combinations. The slower reduction indicates the contractive nature, and it results in the reduction of undrained strength. From the figure, it is clear that, in the starting stage of shearing, i.e. at a small strain of 1–2%, the pore pressure generation is nearly the same for all the soil combinations tested. After this strain, the pore pressure ratio increases with the addition of silt content at any constant value of strain.

After the experimental studies, numerical simulations were performed to study the effect of density and consolidation pressure on the undrained response of silty sands (Only results of SS40 are discussed in this paper). Further, SSL of silty sands were developed after predicting the stress paths at different consolidation pressures and void ratios.

6.1 Effect of Density Using Hypoplastic Model Simulations

To study the effect of density (or void ratio) on the undrained response of silty sands (SS40), static triaxial test simulations were performed on silty sand (reconstituted at various densities) at different consolidation pressures.

The effect of density on the undrained response of silty sand consolidated at 100 kPa is shown in Fig. 4. The dense silty sands ($e_c = 0.5$ to 0.58) experience the dilation behaviour by indicating a continuous increase in deviator stress to higher values and decrease in pore water pressure towards negative values. However, loose silty sands ($e_c = 0.804$ and 0.98) show a contractive nature by the continuous increase in pore water pressures and a decrease in deviator stress. It can be seen from Fig. 4a that, at same strain, the deviator stress increases with decrease in void ratios. Sharp peak stress was observed for loose silty sands ($e_c = 0.98 \sim 0.804$) at the low strain levels of 2.5–4% and then further decreases towards residual stress levels. For dense and medium dense silty sands ($e_c = 0.5 \sim 0.65$), the continuous increase in deviator stress was observed up to the failure strain level of 25%. Figure 4b presents the pore pressure ratios developed during shearing of silty sand at different void ratios consolidated at 100 kPa. It is clear that the loose silty sands ($e_c = 0.98 \sim 0.804$) exhibit contractive nature, i.e. positive high pore pressure ratios. However, the dilative behaviour, i.e. small or negative pore pressure ratios increase with decrease in the void ratios from 0.65 to 0.5 representing the state of soil changes from medium dense to very dense state. The quantitative values of shear strength and reduction on pore pressure ratios are increasing with increase the applied consolidation pressures.

Figure 4c shows the effect of void ratio on effective stress paths of silty sand consolidated at 100 kPa. The figure indicates that the stress paths are moving

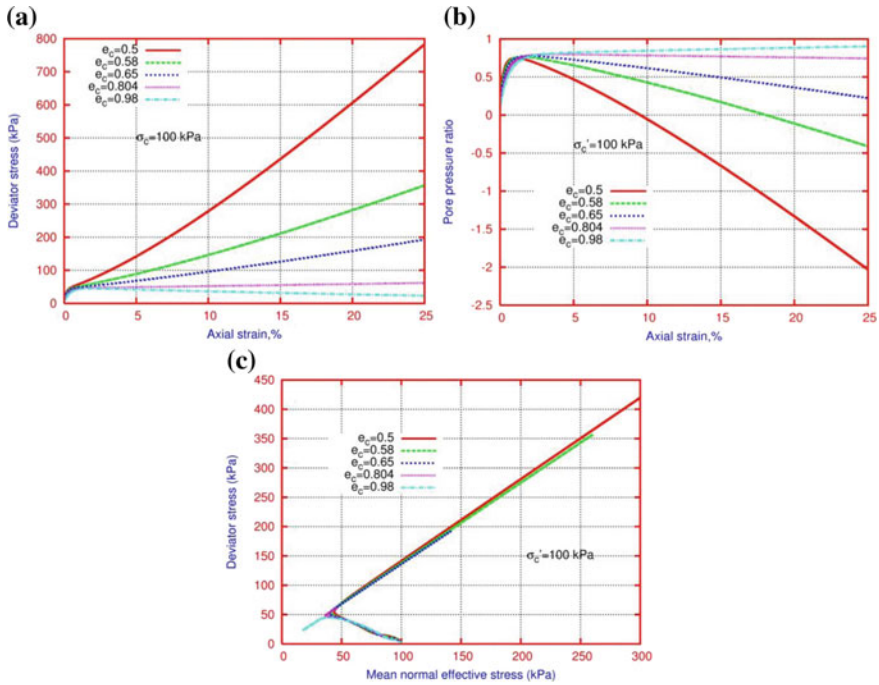


Fig. 4 a Stress–strain characteristics b pore pressure response c effective stress path of SS40 for different densities at $\sigma_3 = 100$

towards the lesser mean effective stress and deviator stress levels in the case of loose silty sands, but the reverse trend of increasing stress path moving towards the higher effective and deviator stress levels is observed in the medium and dense silty sands. It indicates that the loose silty sands possess the contraction state and susceptible to liquefaction and no liquefaction (dilation) state is observed in medium dense and dense silty sands. However, the amount of increase or decrease in deviator stresses depends on the applied confining pressure and the density of samples.

6.2 Effect of Consolidation Pressure Using Hypoplastic Model Simulations

To study the effect of effective confining pressure on the triaxial undrained response of silty sands (SS40), simulations were performed at different pressures. The effect of consolidation pressure on the undrained response is assessed at the loose state of silty sands and the responses are shown in Fig. 5. The dilation tendency decreases with an increase in consolidation pressures in loose and dense silty sands. The silty

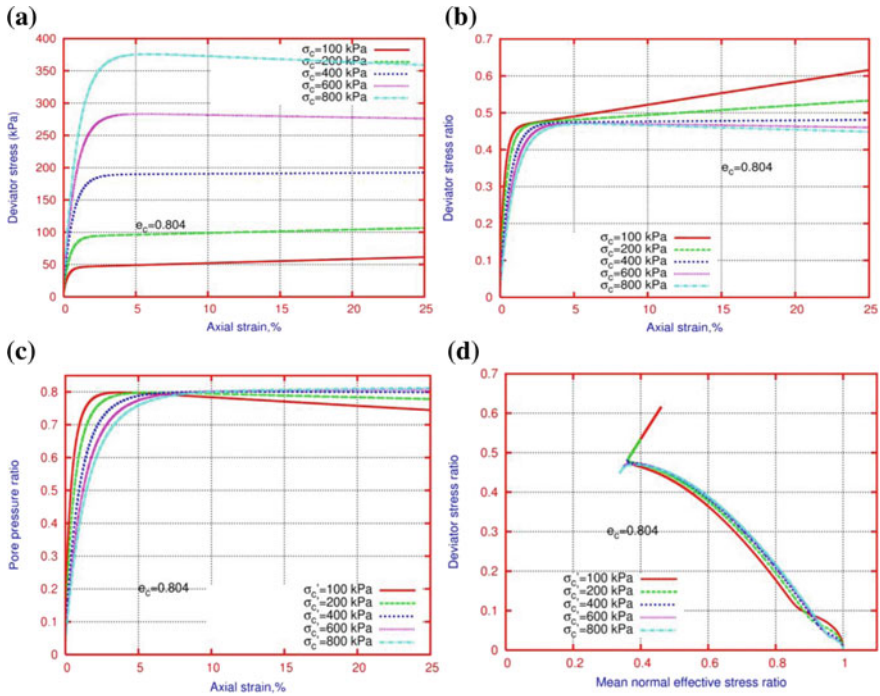


Fig. 5 a Stress–strain characteristics b stress ratio characteristics c pore pressure response d normalized effective stress ratio path for different pressures of loose ($e = 0.804$) SS40

sands consolidated at high consolidation pressures behave as contractive and vice versa. At a particular density of silty sand, while increasing the consolidation pressures, the state of soil changes from dilative to contraction nature.

Figure 5a shows the stress–strain characteristics of silty sand consolidated at different pressures. The deviator stress values are normalized with the corresponding applied consolidation pressures to obtain static stress ratios as shown in Fig. 5b. It can be seen from Fig. 5b that the stress ratios decrease at the failure strain level of 25% with an increase in applied consolidation pressures. The increase in stress ratios at low consolidated silty sands is due to a slight decrease in build-up of pore pressure ratios as shown in Fig. 5c. It demonstrates that the loose silty sands consolidated to pressures of 100–200 kPa possess the state of dilation and then changes to contraction state at high pressures those susceptible to liquefaction due to increase in the positive pore water pressures. The undrained response on effective stress paths of silty sands moulded is shown in Fig. 5d. The stress paths show that the mean normal effective stress ratios are decreasing due to increase the pore pressure which leads to contraction. It is also observed that the reduction in mean effective normal stress ratio is large at small confining pressures.

6.3 Steady-State Line

The effective stress paths show the transition of soil behaviour from dilative to contraction state while increasing the effective pressures and at some certain pressure, a steady-state point (SSP) is reached where the soil just become contractive. The strength at that steady-state point is called steady-state strength. The line connecting the steady-state strength at each dense state of soil is called the steady-state line (SSL). SSL acts as the boundary to separate the state of no liquefaction and liquefaction. The steady-state strength values corresponding to each density void ratio are derived from effective stress paths and SSL is established in $e-s_u$ plane.

The effective stress paths of SS40 are shown in Fig. 6 for reference. The SSL in $e-s_u$ plane is given in Fig. 7a. As the range of the consolidation pressures is very large, for better representation, a log scale is required to make the linear relation between steady-state pressures and void ratios as shown in Fig. 7b. Until now, no

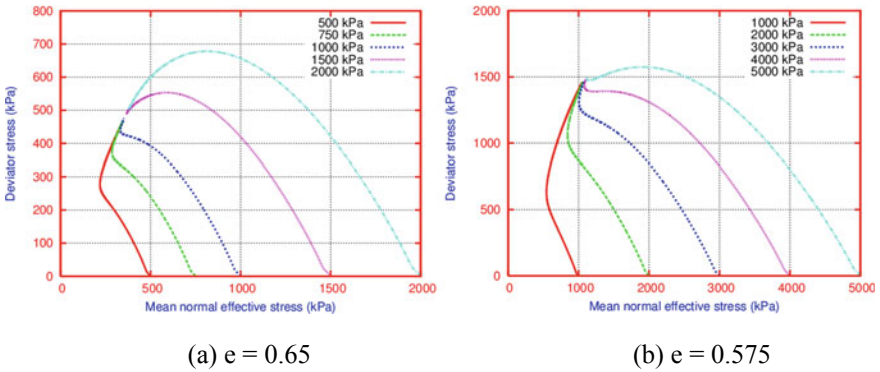


Fig. 6 Effective stress path of SS40 sample at different void ratios

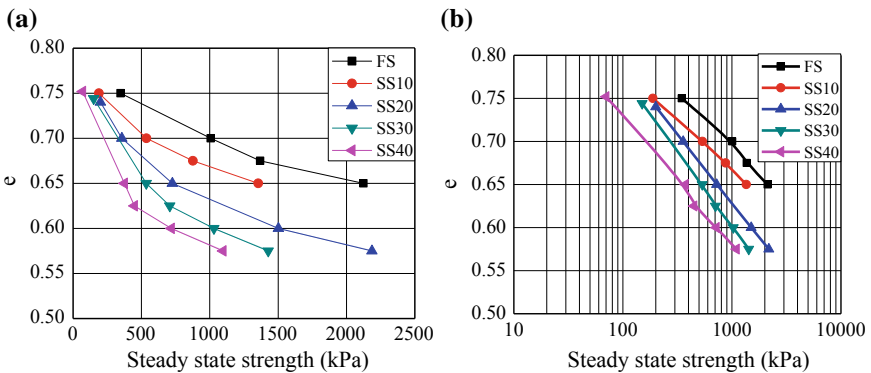


Fig. 7 Identification of liquefaction susceptibility based on SSL

research has been done to establish the SSL based on undrained triaxial test simulations by using a hypoplastic model. The SSL of silty sands lies below that of fine sand. It implies that the liquefaction susceptibility of silty sands is more when compared to fine sand. As the fines content increases, the SSL shifts downwards which indicate higher liquefaction susceptibility (Fig. 7).

7 Conclusions

The paper presents the results of undrained static triaxial tests and hypoplastic model studies done on silty sand samples. The non-plastic fines have a major influence on the behaviour of fine sand. The dilation tendency decreases with the addition of fines. It is also observed that there is no peak stress even if the samples were sheared over a large axial strain. This may be due to the dilation behaviour. But in the case of silt–sand mixtures with high silt content (30 or 40%), peak stress is observed within a small strain range, and there is not much increase in the deviator stress after that. While examining the pore pressure response, initially, there is an increase in the pore pressure ratio due to initial contraction but afterwards the pore pressure ratio decreases. The decrease is rapid in the case of fine sand when compared to the silty–sand combinations. The slower reduction indicates the contractive nature, and it results in the reduction of undrained strength.

From the hypoplastic simulations of SS40 sample it is clear that the stress paths are moving towards the lesser mean effective stress and deviator stress levels in the case of loose silty sands, but the reverse trend of increasing stress path moving towards the higher effective and deviator stress levels is observed in the medium and dense silty sands. In very loose silty sands, both the deviator stresses and stress ratios are increasing with the increase in applied consolidation pressures. Lesser deviator stress ratios at low consolidation pressures are due to large build-up of pore pressure ratios. It indicated that very loose silty sands are more liquefiable at low consolidated pressures.

The SSL was developed from the triaxial undrained response of silty sands. SSL acts as the boundary to separate the state of no liquefaction and liquefaction regions. As the fines content increases, the SSL shifts downwards which indicates that the silty sands are more susceptible to liquefaction than the fine sand.

References

1. Vaid YP, Sivathayalan S (1996) Static and cyclic liquefaction potential of fraser delta sand in simple shear and triaxial tests. *Can Geotech J* 33:281–289
2. Yamamuro JA, Lade PV (1998) Steady-state concepts and static liquefaction of silty sands. *J Geotech Geoenvironmental Eng* 124(9):868–877
3. Yamamuro JA, Covert KM (2001) Monotonic and cyclic liquefaction of very loose sands with high silt content. *J Geotech Geoenvironmental Eng* 127(4):314–324

4. Yang SL, Sandven R, Grande L (2006) Steady-state line of sand-silt mixtures. *Can Geotech J* 43:1213–1219
5. Kolymbas D (1985) A generalized hypoelastic constitutive law. In: *Proceedings of the eleventh international conference on soil mechanics and foundation engineering*, vol 5
6. Herle I, Gudehus G (1999) Determination of parameters of a hypoplastic constitutive model from properties of grain assemblies. *Mech Cohesive-Frict Mater* 4:461–486
7. Herle I (1997) *Hypoplasticität und Granulometrie einfacher Korngerüste*. PhD thesis, Insitut für Boden- und Felsmechanik der Universität Karlsruhe
8. Akhila M, Rangaswamy K, Sankar N (2018) Undrained response and liquefaction resistance of sand-silt mixtures. *Geotech Geol Eng*. <https://doi.org/10.1007/s10706-018-00790-0>

Seismic Hazard Estimation for Southwest India



C. Shreyasvi and Katta Venkataramana

Abstract The objective of the study is to understand the seismicity of the Western coast and its adjoining regions whose seismic potential has not been evaluated so far. The study area encompasses a major portion of Karnataka and Northern part of Kerala and Goa. The approach incorporated in the study is probabilistic in nature and attempts to capture the uncertainty involved in various phases of hazard estimation. The seismic sources in the study region are mostly diffused in nature and are modeled as areal sources with uniform seismicity within a source zone. Regionally, adaptable ground motion prediction equation constitutes the ground motion modeling. The epistemic uncertainty involved in the selection of ground motion models is addressed by adopting a logic tree approach. The seismic source model and the ground motion model are combined together to produce hazard curves for the study region. Most of the ground motion prediction equations are developed for hard rock conditions ($V_s > 800 \text{ ms}^{-1}$). However, most of the built environment rests on the soil and there is a necessity to estimate the hazard values at the surface level. Based on the site topography, it was observed that majority of the study area belongs to NEHRP site class *C* and *D*. The hazard values were estimated for the boundary site condition CD ($310 < V_{S(30)} < 520 \text{ ms}^{-1}$) using a nonlinear site amplification model. Seismic hazard maps produced from this study are believed to be of immense use for building planners and designers.

Keywords Regional earthquake catalog · Gutenberg–Richter parameters · Areal seismic sources · Nonlinear site amplification · Hazard maps

C. Shreyasvi (✉) · K. Venkataramana
Department of Civil Engineering, National Institute of Technology Karnataka, Surathkal,
India
e-mail: shreyasvic@gmail.com

C. Shreyasvi
Department of Civil Engineering, BMS College of Engineering, Bangalore, India

1 Introduction

The seismic potential of Stable Continental Regions (SCR) is the most sought-after issue in recent times. The rare occurrences of intraplate earthquakes in SCR adds complexity to the existing mysterious nature of earthquakes posing a challenging task to research groups all over the world. The repercussions of an earthquake are usually disastrous with the extent of damage depending on the magnitude of ground shaking. It forms an essential part of the engineering community to create a seismic resilient built environment. The previous earthquake experiences have been crucial in drafting the seismic provisions for earthquake resistant design of structures. The Indian seismic code has been revising the seismic zoning map for the country based on the epicenters of past earthquakes and their spatial impact. Each of these seismic zones has a zone factor (in terms of PGA) and is further used in estimating seismic loads on the structure. In reality, this practice may have found huge acceptance in the case of structures of low to moderate building height located in the low seismic zone. However, the aforementioned practice must be discouraged in the case of important structures such as hospitals, structures of architectural, historical, and mythological importance. In addition, buildings located in severe seismic zones and resting on liquefiable soils require site-specific studies in order to reduce the seismic damage and the resulting loss of lives.

The present study is an attempt to understand the seismicity of the West coast of India and its adjoining regions, whose seismic potential has been neglected over the years. The study region encompasses the complete coastal stretch of Karnataka, Goa, and North Kerala along with its adjacent Western Ghats and surrounding areas. The seismic zoning map (BIS 1893) categorizes the study region as seismic zone II and III with a potential for moderate-sized earthquakes. The region houses a bunch of petrochemical industries, ports of commercial interest, dams, mining area, hospitals, and academic institutions. The study region has varied interests in terms of commercial, historical, social, mythological, and educational, which necessitates the present study.

The seismic hazard is a quantitative estimation of the ground shaking at a particular chosen site of interest by considering various contributing factors. The estimation can be made probabilistically or deterministically depending on the importance level of the project. Deterministic methods find application in the case of nuclear power plants, bridges, and dams located in a severe seismic zone. Based on the regional infrastructure and demographics, the probabilistic approach was chosen for estimating the seismic hazard. The probabilistic approach also termed as Probabilistic Seismic Hazard Analysis (PSHA) delivers the probability of an intensity measure exceeding a certain level in a given time frame by considering all the potential contributing seismic sources. Cornell [1] was a pioneer in formulating the framework for PSHA and later many researchers have improvised the former's methodology. Earlier attempts to estimate the seismic hazard for the whole of India was started by Khattri et al. [2] and later by Bhatia et al. [3] under the Global Seismic Hazard Assessment Program (GSHAP). Over the years, seismic hazard

estimation has been independently carried out for many regions such as in Delhi [4], Gujarat [5], North East India [6], and West Bengal [7].

The seismic potential of the study region is assessed with the aid of existing regional tectonic evidence coupled with the macroseismic observations. The methodology incorporates a wide range of magnitude flagged by a lower and upper bound value chosen based on the observed seismicity. The distance from the epicenter also plays a major role in deciding the intensity of ground shaking at a particular site. The earthquake source and the wave propagation characteristics along with the possible site effects are presented by ground motion prediction equations. All these parameters are combined together using total probability theorem to present probabilistic estimation of seismic hazard. The outcome of the computation is expressed in terms of hazard curve and Uniform Hazard Spectrum (UHS). The estimation so far is projected on the engineering bedrock layer located at a depth from the surface. Conceptually, the seismic waves travel through various layers of soil deposit undergoing significant amplification or attenuation before reaching the surface. Hence, a significant difference is observed between the ground motion characteristics recorded at depth and on the surface. The concept of ground motion propagation through soil medium is captured by amplification equations. The hazard values are refined to provide the estimation at the surface level by considering the dynamic characteristic (V_{S30}) of the local soil using suitable amplification equations. The final outcome of the study presents seismic hazard contour maps at the surface level benefitting the engineering community in building earthquake-resistant infrastructure.

2 Seismic Characteristics of the Study Region

Peninsular India constitutes one of the most prominent and largest Precambrian shield areas of the world. The PI is composed of three major tectonic domains, viz., the Dharwar craton, Eastern Ghat mobile belt, and the Southern Granulite terrain which are separated by rifts. During the orogenic activity, the western and eastern edges of the peninsular transformed into Western and Eastern Ghats, respectively. The Western Ghats stretch between 15°N and 21°N and runs parallel to the West coast and is considered to be seismically active. Many hot springs and parallel faults are believed to exist under the Deccan traps in this zone. An east-west trending ridge passing from Mulki on the West coast to Pulicat Lake on the East coast is a major drainage divide and is characterized by relatively thinner crust and micro-seismicity. The coastal zone consists of a series of beach ridges and swales indicating uplift of land [8]. It was also observed that numerous low to moderate earthquakes occur in the vicinity of 13°N.

The collision of the Indo–Australian Plate against the Eurasian plate in the North has led to significant depression in the South and hence, the region is under compression. The destruction of the Indian crust due to the collision near the plate boundary is compensated by the continuous seafloor spreading near the West coast.

The West coast is a transition zone and lies close to major shear zone, as a result, the stresses are released in small amounts instead of steady accumulation. The frequent release of small amounts of stress is believed to be the reason behind the occurrence of a large number of small magnitude earthquakes along the coastal stretch.

Geological features such as faults, shear zones, and lineaments can be geomorphic or structural by nature. In general, lineaments refer to a linear feature whose parts align in a straight line or a slightly curving manner and distinctly differs from the adjacent features. Active faults are those that were responsible for the seismic activity in the recent period and have the potential for reactivation in near future. Mapping and analysis of prominent tectonic features such as active faults, fractures, shear zones, and other structural deformations facilitate in understanding the underlying tectonics and seismicity of the area. In this regard, the Geological Survey of India has published seismotectonic atlas mapping the active tectonic features across the country.

Mangalore has been chosen as the center of the study region and all the tectonic features in the area under the circumference of 350 km radius from Mangalore has been considered for the study. The tectonic features have been georeferenced and digitized from the seismotectonic atlas on the ArcGISplatform. Most of the lineaments are trending either parallel (NNW) or perpendicular (ENE) to the West coast as evident from Fig. 1. Few lineaments like Chapora, Bennihalla, and the Chandragutti–Kurnool lineaments aligned in ENE-WSW direction; transverse to the coastal line are few significant ones. There are a few offshore faults, parallel to the coast in the Western offshore basin. Gravimetric and bathymetric studies on continental margin have confirmed the extension of ENE-WSW and E-W lineaments over a considerable distance into the offshore region [9]. A total of five active shear zones, 111 minor lineaments, 10 major lineaments, 15 gravity faults, and around 40 other faults were mapped. Lineaments of length varying from 20 km to 475 km were observed.

3 Regional Seismicity and Seismogenic Sources

The past earthquake records play a major role in understanding the seismicity associated with a study area and its seismic hazard quantification. In this regard, a catalog of past seismic events reported by various researchers [10–14] and recorded by various global (ISC, NEIC, IRIS) and local agencies (IMD, GSI, ASC) was collected and compiled. The data was acquired for a period of over 186 years from about 12 sources consisting of historical and instrumental earthquakes along with meager Paleo earthquakes. These datasets consisting of a geographical location of the epicenter, date and time of occurrence, focal depth, and its magnitude/intensity were compiled together and multiple reporting of the same event by different sources were being removed manually. The data collected from various sources describe the magnitude of events on different scales such as M_w , M_s , m_B , and M_L .

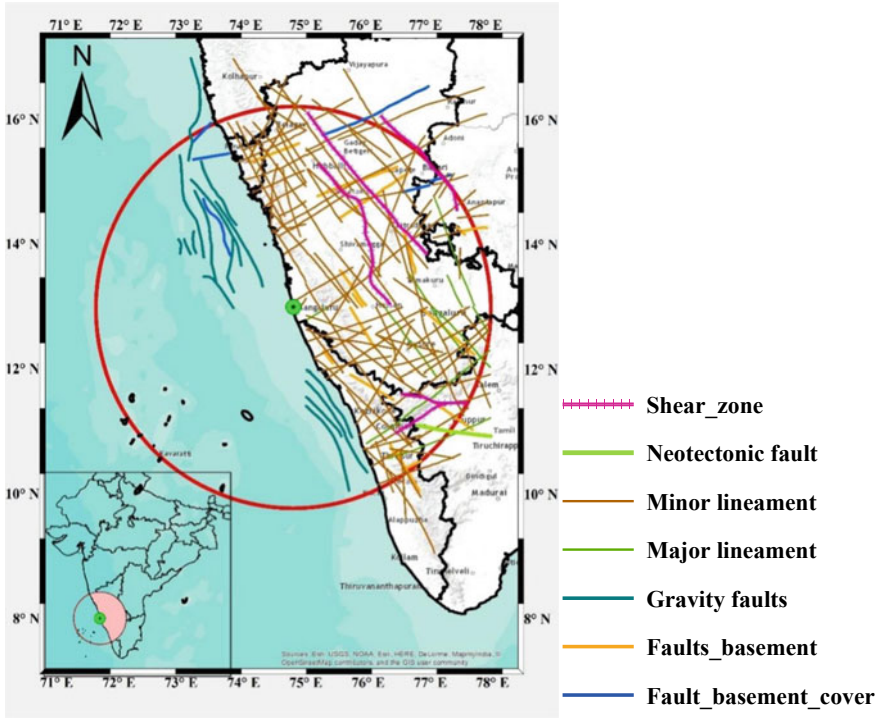


Fig. 1 Map showing the georeferenced and digitized tectonic features in the study region

and historical data on various Intensity scales (MMI, MSK, EMS–98). All the data collected from various sources were homogenized to M_w scale using the region-specific correlation proposed by [15] for events reported on the magnitude scale. The events reported on different intensity scales were unified to MMI (I_0) using the correlation proposed by Musson et al. [16]. Further, these events are converted to M_w using Eq. 1.

$$M_w = \frac{2}{3} I_0 + 1 \tag{1}$$

The epicenters of the previous earthquakes have been mapped as shown in Fig. 2. The seismic activity is found to be quite dense along the coastal stretch and certain parts of the study region.

Figure 3 represents the temporal variation of the compiled catalog and demonstrates the technological advancement in seismic monitoring post-1960. The period between 1916 and 1934 has not witnessed a single event and can be considered a period of quiescence. The compiled catalog consists of dependent events such as aftershocks and foreshocks along with independent events, i.e., mainshocks. These dependent events need to be removed from the catalog in order to fit the Poissonian

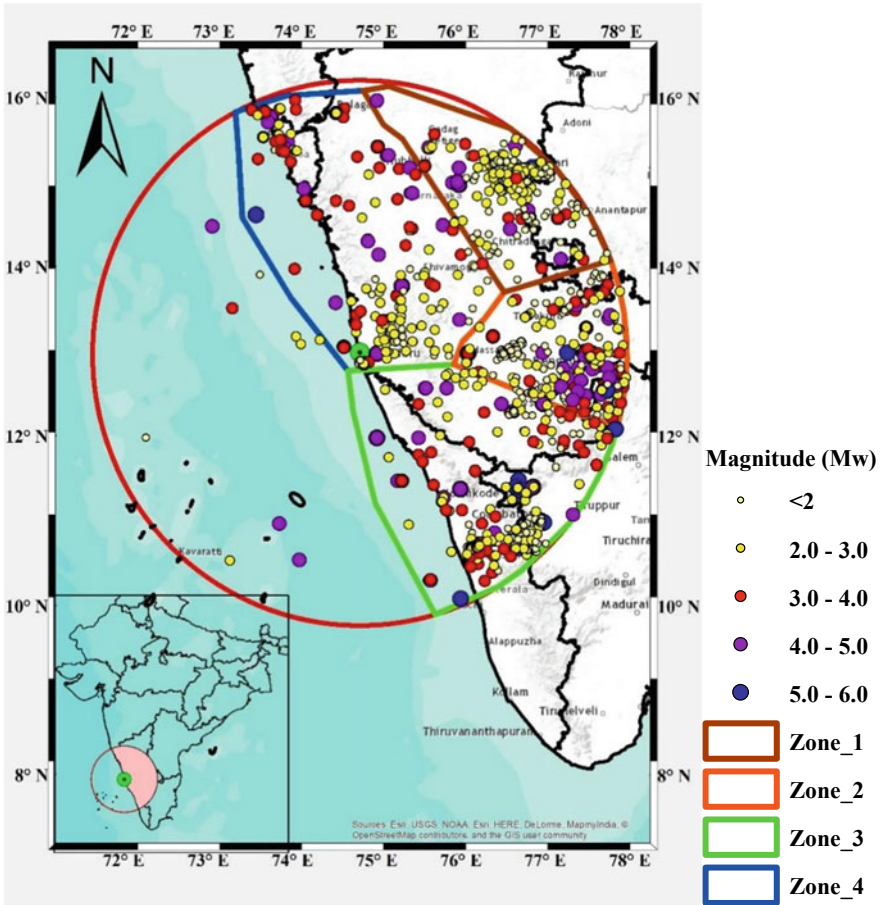


Fig. 2 Map showing the epicentral location of the previous earthquakes and the seismogenic zones identified in the study region

distribution for earthquake occurrences. The process of removal of aftershocks and foreshocks from the sequence of mainshocks is known as Declustering. Numerous Declustering algorithms are available capturing the dynamic window method. This method refers to the identification of the dependent events in a given span of time (T) within a certain radius (D) from the mainshock. Gardner and Knopoff [17] suggested a Declustering algorithm (Eq. 2) and the same has been incorporated in the study.

The algorithm of Gardner and Knopoff is given as

$$D = 10^{0.1238 * M + 0.983} \text{ (km)} \quad T = \begin{cases} 10^{0.032 * M + 2.7389} & \text{if } M \geq 6.5 \\ 10^{0.5409 * M - 0.547} & \text{else} \end{cases} \text{ (days)} \quad (2)$$

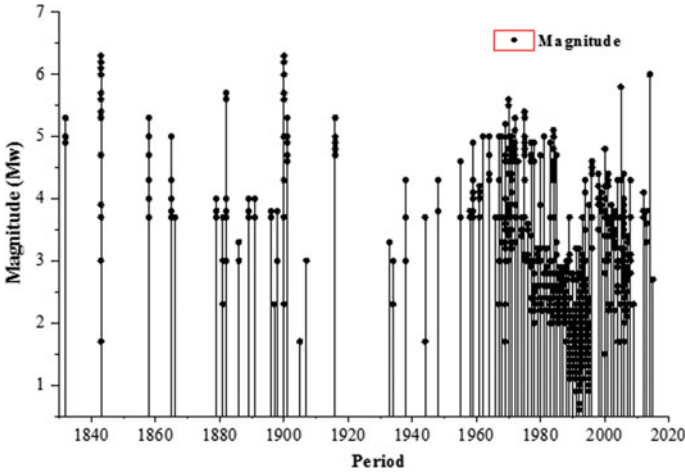
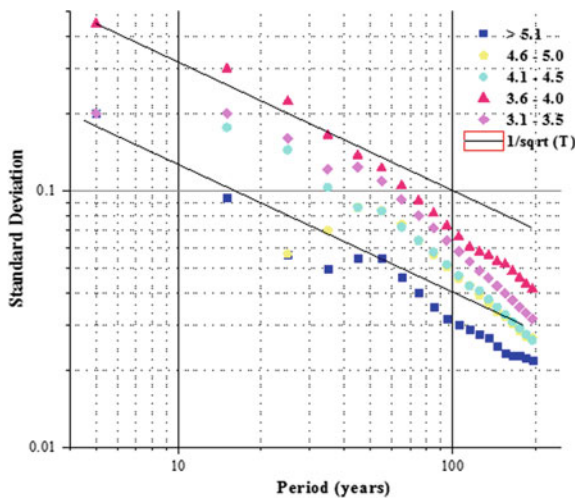


Fig. 3 Temporal variation of the compiled catalog

The compiled catalog was not found to be complete for an entire magnitude range. In other words, lower magnitude events say in the range of 3–4 (M_w) was found to be complete only in the post-1960 period and larger events with $M_w > 6$ throughout the catalog period. In order to estimate the recurrence rate of these earthquakes, it is essential to determine the completeness period of various magnitude ranges. In this regards, Stepp [18] proposed an empirical and statistically simple method based on the stability of magnitude recurrence rate as shown in Fig. 4. The completeness period for magnitude classes 3.1–3.5, 3.6–4.0, 4.1–4.5, 4.5–5.0, and >5.0 are found to be 40, 60, 70, 80, and 160 years, respectively.

Fig. 4 Completeness test for the declustered catalog using Stepp’s method



The recurrence rate (λ) for each of the independent magnitude classes can be determined by the relation proposed by Gutenberg and Richter (G-R) [19] as presented in Eq. 3. The coefficients “ a ” and “ b ” represent regional seismic characteristics for events greater than or equal to M .

$$\log \lambda_M = a - bM \text{ or } \ln \lambda_M = \alpha - \beta M \tag{3}$$

The G-R law bounded by a minimum magnitude (m_{\min}) and maximum magnitude (m_{\max}) (Eq. 4) was adopted to capture the regional potential for earthquake recurrences.

$$\lambda_m = v * \frac{\exp[-\beta(m - m_{\min}) - \exp(-\beta(m_{\max} - m_{\min}))]}{1 - \exp[-\beta(m_{\max} - m_{\min})]} m_{\min} \leq m \leq m_{\max} \tag{4}$$

where $\alpha = 2.303*a$, $\beta = 2.303*b$, $v = \exp(\alpha - \beta * m_{\min})$.

The frequency magnitude distribution based on Eq. 4 was obtained using maximum likelihood approach proposed by Aki [20] (Eq. 5) and implemented using a MATLAB based computer program (Ha.3) developed by Kijko and Smit [21]. The term \bar{m} represents the average magnitude, m_{\min} represents the minimum magnitude, and β is the value of b on a logarithmic scale.

$$\beta = \frac{1}{\bar{m} - m_{\min}} \tag{5}$$

The rate of occurrence for each individual magnitude is presented in Fig. 5. The curve shows a decreasing trend with an increase in the magnitude.

Based on the observed seismic activity with respect to its Epicentral location and alignment of the tectonic features, the entire study region is divided into four potential seismogenic zones as shown in Fig. 2. The seismicity parameters are

Fig. 5 Frequency–Magnitude distribution of the compiled catalog

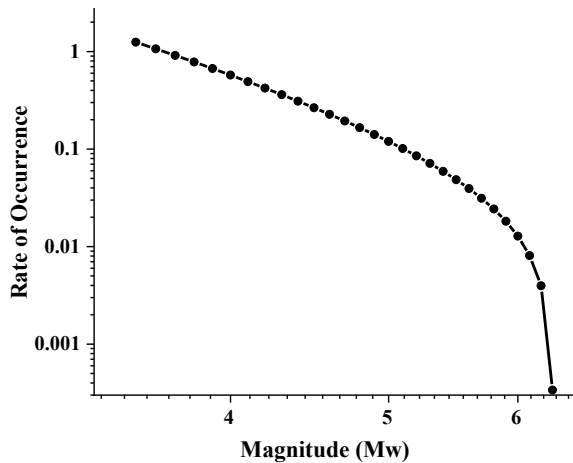


Table 1 Comparison of seismicity parameters

Authors	b value	M_{\max}
Bhatia et al. [3]	0.598	6.5
Jaiswal and Sinha [32]	0.92 (\pm 0.052)	6.5
Iyengar et al. [26]	0.76 (\pm 0.07)	6.8
Kolathayar and Sitharam [33]	0.57	6
Ashish et al. [34]	0.85	6.5
Present study	0.74 (\pm 0.08)	6.3(\pm 0.5)

estimated for each of these individual zones [22] and that includes M_{\min} , λ , b value, and M_{\max} . The seismicity parameters available from most of the studies for comparison are b and M_{\max} and hence, only these two parameters have been presented in Table 1 to maintain uniformity. The data used in the study, as well as the methodology incorporated in estimating the parameters, are found to be in good agreement with other studies.

4 Selection of Ground Motion Prediction Equations and Hazard Analysis

The estimated seismicity parameters provide an insight into the seismic potential of the study region. However, the source mechanism, wave propagation and path effects, near-site effects can be captured only with the use of Ground Motion Prediction Equations (GMPEs). GMPEs provides ground motion parameter (such as PGA and PSA) as a function of magnitude, distance, and other controlling parameters at a chosen site of interest. The GMPEs are developed based on statistical tests performed on a large database of recorded or simulated ground motions. In the Indian scenario, the lack of ground motion records especially for Southern India necessitates the use of GMPEs developed for other countries but for a similar tectonic regime. The studies on the aftershocks of Bhuj earthquake (2001) by Cramer and Kumar [23] revealed that the regional tectonics of Peninsular India (PI) is similar to that of Eastern North America (ENA) and the GMPEs developed for ENA is comparable with PI. In this regard, a number of GMPEs developed for stable continental region all over the world were investigated and qualitative tests were performed for shortlisting the candidate GMPEs. However, due to space constraint, the details of the selection process has not been enclosed. The GMPEs developed by [24–27] were used in the study. ND10 was developed for PI while the rest have been incorporated from ENA. The epistemic uncertainty involved in the choice of GMPEs is addressed by using a logic tree approach. The choice of GMPEs was based on the recommendations by Bommer et al. [28] and the choice

Table 2 Comparison of the hazard values for different regions

Intensity levels	Bangalore	Mangalore	Bellary	Authors
10% probability of exceedance	0.12	0.09	0.195	Present study
	0.131	0.044	0.064	Sitharam et al. [35]
	0.024	0.023	0.038	Iyengar et al. [26]
	0.05	0.08	0.05	BIS (2016)
	0.11	0.08	0.12	Nath and Thingbaijam [36]
	0.10	–	–	Jaiswal and Sinha [32]
	0.06	0.1	0.08	Sitharam and Kolathayar [37]
	0.057	0.06	0.10	Ashish et al. [34]

of weights for each of these GMPEs have been based on qualitative testing [29]. A weighting factor of 0.3 has been chosen for AB06 and ND10 and 0.2 for CA03 and TR02 and the overall combination sums up to 1.

The seismicity parameters and the ground motion models are combined together to perform hazard analysis in CRISIS software. The hazard computation in CRISIS adopts a spatial integration approach by dividing the entire study region into numerous triangles. This disintegration is based on the recursive functions [30]. The hazard values computed in the present study are compared with that of the previous studies as shown in Table 2 and the results are found to be in good agreement. The hazard values can be predicted for different return periods and in the present study, the same has been estimated for a return period of 475 years (10% probability of exceedance in 50 years) and 2475 years (2% probability of exceedance in 50 years).

The contour plots for the study region have been plotted for two spectral periods, i.e., 0.01 and 0.5 s. The contour values in Fig. 6 presents the hazard values at the bedrock level corresponding to a return period of 475 years. It is evident from these contour plots that the study area is subjected to the higher intensity of ground shaking at a lower time period when compared to the higher time period.

5 Estimation of Seismic Hazard at the Surface Level

The seismic hazard predicted at the bedrock level is halfway between the source and the surface. The seismic waves undergo significant modification on its way from the focus to the surface and this modulation needs to be captured for effective estimation of seismic hazard. Numerous studies have been conducted to understand the dynamic behavior of soils and capture its amplification characteristics. In this regard, an attempt was made by [31] to develop empirical relationships in

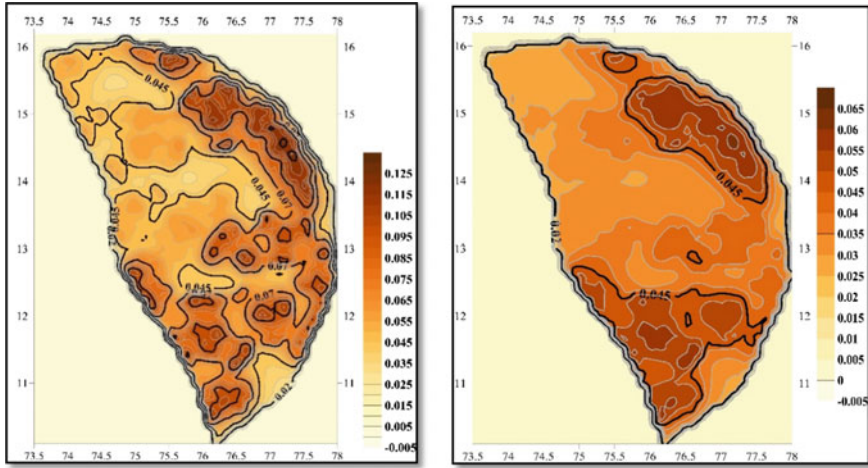


Fig. 6 Contour plots depicting the hazard values estimated at the bedrock level for $T = 0.01$ s (left) and $T = 0.5$ s (right)

predicting nonlinear amplification as a function of shear velocity in the upper 30 m (V_{S30}). Based on the topography of the region, it was observed that majority of the study region can be classified as NEHRP site C ($V_{S(30)} = 360\text{--}760 \text{ ms}^{-1}$) and D ($V_{S(30)} = 180\text{--}360 \text{ ms}^{-1}$). Hence, in the present study, the hazard values have been estimated for the site category (CD) with V_{S30} in the range of $310\text{--}520 \text{ ms}^{-1}$. The amplification is estimated from a unified model that depends on V_{S30} as well as the input bedrock motion PHA_r from the hazard analysis. The model is expressed in Eq. 5. F_{ij} represents the amplification factor for a site i with respect to a particular ground motion j ; c , b , and V_{ref} are the regression parameters; η_i is a random effect for an earthquake event i ; and ε_{ij} represents the intraevent model residual for motion j in event i .

$$\ln(F_{ij}) = c \ln\left(\frac{V_{s-30}}{V_{\text{ref}}}\right) + b \ln\left(\frac{\text{PHA}_{r_{ij}}}{0.1}\right) + \eta_i + \varepsilon_{ij} \tag{6}$$

The contour plots for the similar spectral period, i.e., 0.01 and 0.5 s corresponding to a return period of 2475 years has been presented in Fig. 7. Higher hazard values are encountered in seismogenic source zone 1.

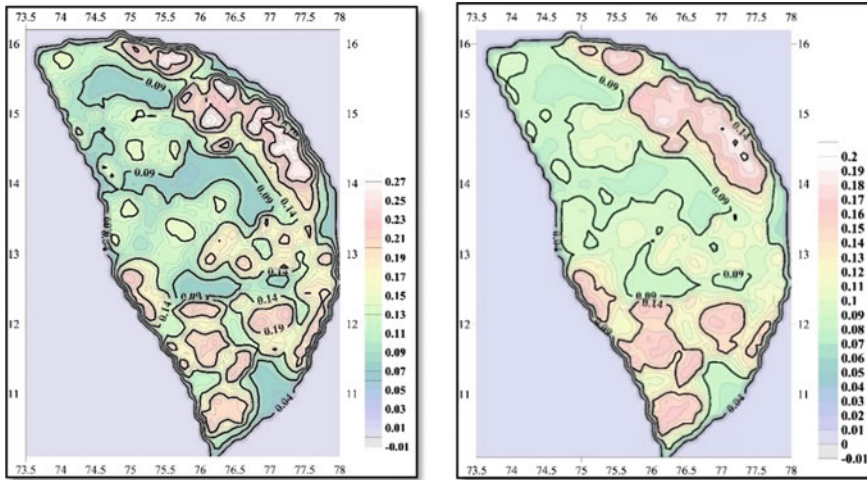


Fig. 7 Contour plots depicting the hazard values estimated at the surface level for $T = 0.01$ s (left) and $T = 0.5$ s (right)

6 Conclusions

The seismic hazard analysis was performed in a probabilistic manner by considering all the possible magnitude and distance combinations along with the local site effects. The earthquake data compiled in the catalog spans between 1820 and 2015 with few events in the early 1500 s. While identifying the potential seismogenic source zones for the study, it was observed that few dormant faults have been reactivated and one such example is that of Shimoga earthquake (May 12, 1975). Based on the compiled catalog, this region had no evidence of past seismic activity. It is interesting to note that some of the earthquake events have been reported away from the shore. The seismic zoning map of India categorizes Bangalore as Seismic zone II and the present study recommends appraisal to seismic zone III as the region is frequently visited by low to moderate-sized earthquakes. In addition, Bangalore lies within the influence area of Coimbatore (1900) and Bellary earthquake (1843). Most of the previous hazard studies have undermined the seismic potential of Bellary and its surrounding area, even though the region has witnessed an earthquake of magnitude 6.3 (M_w) in the past. In addition to that, numerous low-magnitude earthquakes in the region are suspected to be the outcome of ongoing mining activity. Selection of GMPEs required utmost attention as they alter the overall hazard estimation. The GMPEs developed for the stable tectonic regime was incorporated and the epistemic uncertainty involved in the selection was addressed using a logic tree approach. AB10 provides a lower bound estimate whereas CA03 provides a higher bound estimate. ND 10 and TR 02 forms the median estimate and hence, the choice of the weighting factor for logic tree computation was based on these observations. The hazard has been predicted at the

bedrock level as well the surface level. The hazard values are high for seismic zone 1 in the range of 0.27 g ($T = 0.01\text{ s}$)– 0.2 g ($T = 0.5\text{ s}$) and are low in the range of 0.07 g ($T = 0.01\text{ s}$)– 0.09 g ($T = 0.5\text{ s}$) at certain parts of the study region. Site amplification was found to be prominent in the coastal area when compared to the rest of the study region. The present study attempts to provide a reasonable estimate of ground motion parameters (PGA and S_a at 0.5 s) benefitting engineers and policymakers in building a sustainable environment.

References

1. Cornell CA (1968) Engineering seismic risk analysis. *Bull Seismol Soc Am* 58:1583–1606
2. Khattri KN, Rogers AM, Perkins DM, Algermissen ST (1984) A seismic hazard map of India and adjacent areas. *Tectonophysics* 108(1–2):93111–108134
3. Bhatia SC, Kumar MR, Gupta HK (1999) A probabilistic seismic hazard map of India and adjoining regions. *Ann Geophys* 42(6)
4. Iyengar RN, Ghosh S (2004) Microzonation of earthquake hazard in greater Delhi area. *Curr Sci* 87(9):1193–1202
5. Chopra S, Kumar D, Rastogi BK, Choudhury P, Yadav RBS (2013) Estimation of seismic hazard in Gujarat region. *India Nat Hazards* 65(2):1157–1178
6. Das R, Sharma ML, Wason HR (2016) Probabilistic seismic hazard assessment for northeast India region. *Pure appl Geophys* 173(8):2653–2670
7. Maiti SK, Nath SK, Adhikari MD, Srivastava N, Sengupta P, Gupta AK (2017) Probabilistic seismic hazard model of West Bengal. *India J of Earthq Eng* 21(7):1113–1157
8. Subrahmanya KR (1996) Active intraplate deformation in south India. *Tectonophysics* 262(1–4):231–241
9. Dasgupta S, Narula PL, Acharyya SK, Banerjee J (2000) Seismotectonic Atlas of India and its environs. *Geological Survey of India*
10. Oldham TA (1883) Catalogue of Indian Earthquakes from the earliest time to the end of AD 1869, *Memoirs of the Geological Survey of India* 19 Part 3
11. Chandra U (1977) Earthquakes of peninsular India—a seismotectonic study. *Bull Seismol Soc Am* 67(5):1387–1413
12. Rao BR, Rao PS (1984) Historical seismicity of peninsular India. *Bull Seismol Soc Am* 74(6):2519–2533
13. Martin S, Szeliga W (2010) A catalog of felt intensity data for 570 earthquakes in India from 1636 to 2009. *Bull Seismol Soc Am* 100(2):562–569
14. Rastogi BK (2016) Seismicity of Indian stable continental region. *J Earthq Sci Eng* 3:57–93
15. Kolathayar S, Sitharam TG, Vipin KS (2012) Spatial variation of seismicity parameters across India and adjoining areas. *Nat Hazards* 60:1365. <https://doi.org/10.1007/s11069-011-9898-1>
16. Musson RM, Grünthal G, Stucchi M (2010) The comparison of macroseismic intensity scales. *J Seismolog* 14(2):413–428
17. Gardner JK, Knopoff L (1974) Is the sequence of earthquakes in Southern California, with aftershocks removed, Poissonian? *Bull Seismol Soc Am* 64(5):1363–1367
18. Stepp JC (1973) Analysis of completeness of the earthquake sample in the Puget Sound area. *Seismic zoning edited by ST Harding NOAA Tech. Report ERL*
19. Gutenberg B, Richter CF (1944) Frequency of earthquakes in California. *Bull Seismol Soc Am* 34(4):185–188
20. Aki K (1965) Maximum likelihood estimate of b in the formula $\log N = a - bM$ and its confidence limits

21. Kijko A, Smit A (2012) Extension of the Aki-Utsu b -value estimator for incomplete catalogues. *Bull Seismol Soc Am* 102(3):1283–1287
22. Shreyasvi C, Venkataramana K, Chopra S, Rout MM (2019) Probabilistic seismic hazard assessment of Mangalore and its adjoining regions, a part of Indian Peninsular: an intraplate region. *Pure Appl Geophys* 176(6):2263–2297
23. Cramer CH, Kumar A (2003) 2001 Bhuj, India, earthquake engineering seismoscope recordings and Eastern North America ground-motion attenuation relations. *Bull Seismol Soc Am* 93(3):1390–1394
24. Atkinson GM, Boore DM (2006) Earthquake ground-motion prediction equations for eastern North America. *Bull Seismol Soc Am* 96(6):2181–2205
25. Campbell KW (2003) Prediction of strong ground motion using the hybrid empirical method and its use in the development of ground-motion (attenuation) relations in eastern North America. *Bull Seismol Soc Am* 93(3):1012–1033
26. Iyengar RN, Chadha RK, Balaji Rao K, Raghukanth STG (2010) Development of probabilistic seismic hazard map of India. The National Disaster Management Authority, 86
27. Toro GR (2002) Modification of the Toro et al. (1997) attenuation equations for large magnitudes and short distances. Risk Engineering Technical Report
28. Bommer JJ, Douglas J, Scherbaum F, Cotton F, Bungum H, Fäh D (2010) On the selection of ground-motion prediction equations for seismic hazard analysis. *Seismol Res Lett* 81(5):783–793
29. Danciu L, Kale Ö, Akkar S (2016) The 2014 earthquake model of the Middle East: ground motion model and uncertainties. *Bull Earthq Eng* 1–37
30. Aguilar-Meléndez A, Schroeder MGO, De la Puente J, González-Rocha SN, Rodríguez-Lozoya HE, Córdova-Ceballos A, Campos-Rios A (2017) Development and validation of software CRISIS to perform probabilistic seismic hazard assessment with emphasis on the recent CRISIS2015. *Computación y Sistemas* 21(1):67–90
31. Choi Y, Stewart JP (2005) Nonlinear site amplification as function of 30 m shear wave velocity. *Earthq Spectra* 21(1):1–30
32. Jaiswal K, Sinha R (2007) Probabilistic seismic hazard estimation for peninsular India. *Bull Seismol Soc Am* 97(1B):318–330
33. Kolathayar S, Sitharam TG (2012) Characterization of regional seismic source zones in and around India. *Seismol Res Lett* 83(1):77–85
34. Ashish Lindholm C, Parvez IA, Kühn D (2016) Probabilistic earthquake hazard assessment for peninsular India. *J Seismolog* 20(2):629–653. <https://doi.org/10.1007/s10950-015-9548-2>
35. Sitharam TG, James N, Vipin KS, Raj KG (2012) A study on seismicity and seismic hazard for Karnataka State. *J Earth Syst Sci* 1–16
36. Nath SK, Thingbaijam KKS (2012) Probabilistic seismic hazard assessment of India. *Seismol Res Lett* 83(1):135–149
37. Sitharam TG, Kolathayar S (2013) Seismic hazard analysis of India using areal sources. *J Asian Earth Sci* 62:647–653
38. Amateur Seismic Centre, <http://www.asc-india.org/>, Pune, India (last accessed 31st March 2017)
39. Incorporated Research Institutions for Seismology, Earthquake browser, <http://www.iris.edu/hq/> (last accessed 26th October 2016)
40. Indian Meteorological Department (IMD), www.imd.gov.in/, New Delhi, India (Through Personal communication)
41. International Seismological Centre, Online Bulletin, <http://www.isc.ac.uk>, Internatl. Seismol. Cent., Thatcham, United Kingdom, 2014 (last accessed on 31st October 2016)
42. IS1893(Part 1)- 2016, Indian standard, criteria for earthquake resistant design of structures, sixth revision, Part-I. Bureau of Indian Standards, New Delhi
43. National Earthquake Information Center 2003 USA PDE reportings <http://neic.usgs.gov/neis/epic/> (last accessed on 28th November 2016)

Assessment of Bond Strength on Geosynthetic Interlayered Asphalt Overlays Using FEM



S. Shiyamalaa and K. Rajagopal

Abstract Reflective cracking is the major issue in hot mix asphalt overlays. Many methods are developed to retard these reflective cracking; among them, the most suitable method is the usage of interlayers. Geosynthetics has good tensile strength and can act as a stress reliever thus making these suitable as an interlayer for reducing the propagation of reflective cracking in hot mix asphalt overlay. The inclusion of geosynthetics in HMA overlays affect the bond between the overlay and existing pavement. The reduction in bond strength between the overlay and existing pavement will lead to delamination of the overlay. This study is going to explain how the bond strength is going to vary for different geosynthetics namely, coir, jute and synthetic interlayered asphalt overlays using finite element analysis. Prony parameters are going to be used to define HMA Property. The cohesive zone model is adopted to define the interface properties in the numerical model. The bond strength of geosynthetic interlayered asphalt overlays at three different temperatures as 10, 20 and 30 °C are going to be evaluated using finite element analysis.

Keywords Reflective cracking · Hot mix asphalt overlays · Geosynthetics · Finite element analysis

1 Introduction

Hot mix asphalt (HMA) overlays are the best method widely used to restore deteriorated pavements. The common problem in HMA overlays is the occurrence of reflective cracks. The development of crack from the old pavement to the new overlay is termed as reflective cracking. The main cause of reflective cracking is the stress concentration at the tip of an existing crack due to traffic loading and temperature change in the old pavement [1]. As per Button and Lytton [2], the methods

S. Shiyamalaa (✉) · K. Rajagopal
Civil Engineering Department, Indian Institute of Technology Madras, Chennai, India
e-mail: ce15d010@smail.iitm.ac.in; Shiyamu.selvaraj@gmail.com

available to prohibit the growth of reflective cracks are reinforcing the overlays, providing stress-relieving interlayers and by re-strengthening the existing pavement before laying HMA overlay. Among all types of reflective crack prohibition methods, geosynthetic interlayers are widely used nowadays, because of its ease of application. Various experimental and numerical studies have been conducted to understand the performance of the interlayer system in mitigating reflective crack growth [2–8]. Geosynthetics made of natural fibres such as jute and coir are also found to be effective and economical in mitigating crack growth [9, 10]. One of the issues in using interlayers in between the existing pavement and HMA overlays is bonding, which has been addressed in few studies [11–13]. The reduction in bond strength causes slippage, delamination and tearing of pavement layers [14, 15]. The interlayered pavement undergoes shear failure when vehicles travel in a curved section or breaks are applied, leading to shoving, crescent-shaped and parabolic crack development in the overlay [16]. Study on the reflective crack growth by using natural geosynthetic as interlayers and their influence on the bonding strength was carried out by Nithin et al. [17].

Ozer et al. [18] conducted a numerical study to understand the mechanism of de-bonding. The separation due to bond failure between the layers occurs in three different failure modes namely, shear separation (mode A), tensile separation (mode B) and mixed shear and tensile separation (mode C) as shown in Fig. 1. Mode A failure is caused due to traffic- or temperature-induced horizontal or transverse stress in the field when the pavement is subjected to forces due to braking, acceleration or deceleration of vehicles. Mode B failure is known to occur due to the expansion of gases by bacterial action between the interface or due to the suction by the tyre. Mixed-mode failure is not commonly observed in the pavement.

Numerical studies may provide a better understanding of the failure mechanism of the reflective crack growth. In the present study, the effect of bond strength of three different interlayers namely jute, coir and Synthetic are studied by using the

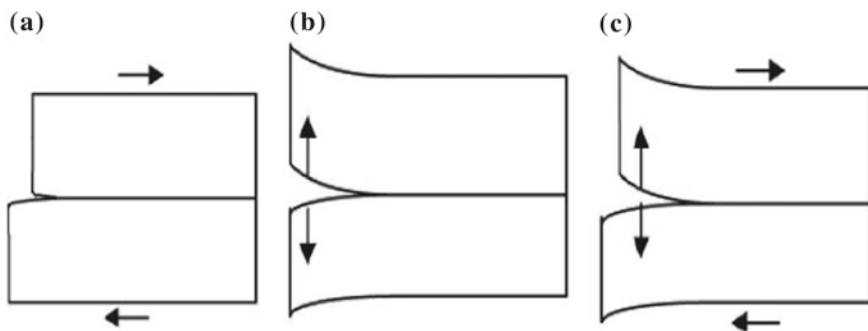


Fig. 1 Modes of bond failure: **a** shear separation, **b** tensile separation and **c** mixed shear and tensile separation (from Nithin et al. [17])

finite element software “ABAQUS”. The numerical model adopted has been validated using the interface properties obtained from the experimental tests. Also, the effect of three different temperatures 10, 20 and 30 °C are captured numerically.

2 Methodology

HMA and interlayers are the key materials to be modelled in this paper. HMA behaves both as an elastic solid and viscous fluid. Therefore it is modelled as a viscoelastic material. Some of the commonly adopted constitutive models for HMA material are the Maxwell model, Kelvin–Voigt model, Burger model and Generalized Maxwell model. The generalized Maxwell model is found to give a more realistic response for HMA material [4]. Constitutive law for an isotropic linear viscoelastic material is defined as an integration of shear and bulk parts with respect to time as shown in the equation below [19].

$$\sigma(t) = \int_0^t 2G(t-t')e' dt' + \int_0^t K(t-t')\varphi' dt' \tag{1}$$

where $G(t)$ and $K(t)$ are shear and bulk moduli with respect to relaxation time t' . e' and φ' are mechanical deviatoric strain and volumetric strain, respectively. Prony parameters that are indirectly representing the linear springs and dashpots are used to get $G(t)$ and $K(t)$ as follows:

$$G(t) = G_0 \left[1 - \sum_{i=1}^N g_i \left(1 - e^{-t/t_i} \right) \right] \tag{2}$$

$$K(t) = K_0 \left[1 - \sum_{i=1}^N k_i \left(1 - e^{-t/t_i} \right) \right] \tag{3}$$

where, g_i , k_i and t_i are the Prony parameters. Prony parameters required to model the viscoelastic material are derived based on the equation stated below,

$$G'(\omega) = G_0 \left(1 - \sum_{i=1}^N g_i \right) + G_0 \left(\sum_{i=1}^N \frac{g_i \tau_i^2 \omega^2}{1 + \tau_i^2 \omega^2} \right) = |G^*(\omega)| \cos \emptyset \tag{4}$$

$$G''(\omega) = G_0 \left(\sum_{i=1}^N \frac{g_i \tau_i \omega}{1 + \tau_i^2 \omega^2} \right) = |G^*(\omega)| \sin \emptyset \tag{5}$$

where $G'(\omega)$ and $G''(\omega)$ are storage and loss modulus at an angular frequency of $\omega = 2\pi f$ and \emptyset is the phase angle. g_i and τ_i are Prony parameters and N denotes the number of spring and dashpot elements. A non-linear least square regression

analysis is performed by MATLAB to get the Prony parameters from Eqs. 4 and 5 for the present paper. The parameters g_i and k_i are assumed to be equal with respect to the reference from Baek [4].

The pavement layers are similar to layered composite materials in which the delamination effect is modelled using cohesive zone model (CZM) [20, 21]. Hence the interface used in pavements can also be modelled using CZM. The model was developed by Hillerborg et al. [22] who combined the work of Dugdale [23] and Barenbatt [24]. This model explains the post-peak softening behaviour for quasi-brittle materials having a fracture process zone which is also suitable for this paper. The interface uses cohesive elements of zero thickness or very negligible thickness which are similar to that of zero thickness interface element formulated by Goodman et al. [25]. The cohesive elements are inserted between the continuum elements and their behaviour is shown in Fig. 2.

The constitutive behaviour of cohesive element follows the traction–separation law (TSL) concept. Typical traction–separation law behaviour is shown in Fig. 3, where T_n and T_s denotes maximum traction in normal and shear direction, respectively, δ_m^0 is the separation at maximum traction in mixed mode condition, δ_m^{\max} denotes the maximum relative displacement after the material undergoes degradation, δ_m^f denotes the relative displacement when the element is completely degraded, K_p is the initial stiffness in the liner zone and D is the damage variable. But the issue in using cohesive elements as interface elements is the artificial compliance problem which occurs where the overall stiffness of the material gets reduced. This can be countered by using bilinear cohesive zone model suggested by Geubelle and Baylor [26].

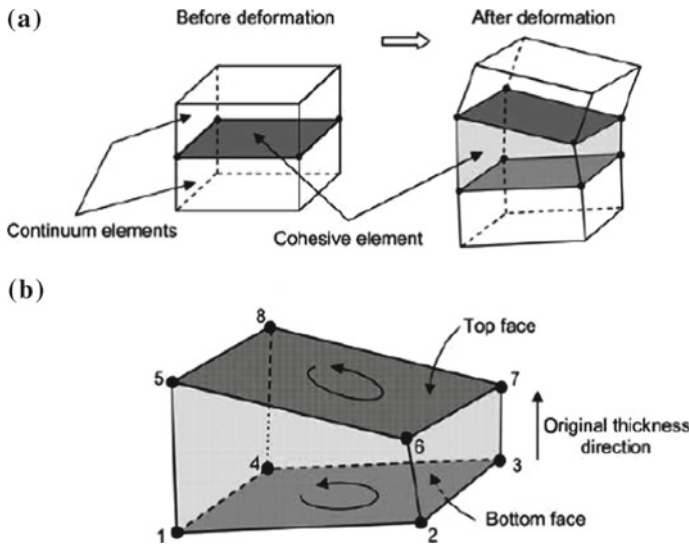


Fig. 2 a Cohesive element before and after deformation sandwiched between the continuum elements and b deformed cohesive element (from Baek [4])

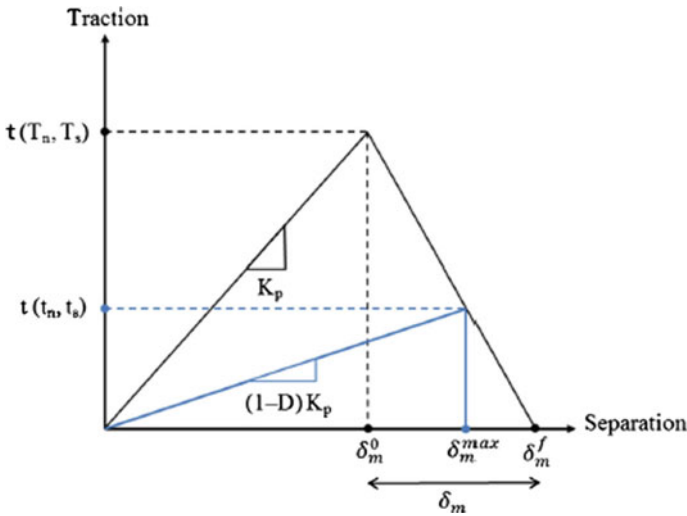


Fig. 3 Traction–separation law (from Sivakumar and Maji [27])

In the present paper, the interface layer is modelled in ABAQUS by adopting the CZM that follows traction–separation law. The initial linear portion of traction law is defined either by coupled traction or uncoupled traction. Since traction in the adopted experiment is predominant only in the direction of shear, uncoupled traction is assumed in the numerical model. The traction force developed by the uncoupled traction is given as follows:

$$\begin{Bmatrix} t_n \\ t_s \\ t_t \end{Bmatrix} = \begin{bmatrix} K_{nn} & 0 & 0 \\ 0 & K_{ss} & 0 \\ 0 & 0 & K_{tt} \end{bmatrix} \begin{Bmatrix} \varepsilon_n \\ \varepsilon_s \\ \varepsilon_t \end{Bmatrix} \tag{6}$$

where t denotes traction, K denotes stiffness and ε denotes strain. The subscript n denotes normal direction, s denotes in-plane shear direction and t denotes out-plane shear direction. The strain is calculated as the ratio of relative displacement with respect to the initial thickness of the cohesive element in the corresponding direction,

$$\left(\varepsilon = \frac{\delta}{T_0} \right) \tag{7}$$

Once the interface property crosses its threshold value, the degradation of the material triggers the delamination process. To model the degradation of the interface, damage initiation and its evolution are to be defined in the numerical model. There are various damage initiation criteria available in ABAQUS which are maximum nominal stress, maximum nominal strain, quadratic nominal stress and

quadratic nominal strain criterion. Among them, the maximum nominal stress criterion which is popular and also adopted in this study is given by

$$\max\left(\frac{t_n}{t_n^0}, \frac{t_s}{t_s^0}, \frac{t_t}{t_t^0}\right) = 1 \quad (8)$$

where t_n^0 , t_s^0 and t_t^0 are peak nominal stresses corresponding to normal, in-plane and out-plane shear directions. Once the traction present in the interface reaches this limit, the delamination begins. The damage evolution is defined by the damage variable D that describes the rate at which the material stiffness degrades once the damage initiation starts. The value of D varies from 0 to 1, where $D = 0$ denotes the starting stage of damage and $D = 1$, the full damage attained. The traction values with respect to the damage evolution are given as

$$t_n = \begin{cases} (1 - D)\bar{t}_n, & \bar{t}_n \geq 0 \\ \bar{t}_n & \end{cases}, \quad (9)$$

$$t_s = (1 - D)\bar{t}_s \quad (10)$$

$$t_t = (1 - D)\bar{t}_t \quad (11)$$

The term D can be defined either by using relative displacement or fracture energy. In this study, fracture energy (which is the area under the traction–separation curve) is used for describing the damage evolution. The post softening behaviour is followed by exponential variation.

3 Numerical Modelling

In the present paper, the interface properties obtained from Leutner shear experiment by Prashanthi [28] is validated by adopting CZM in ABAQUS for all three different temperatures and geosynthetic types mentioned above. The geometry of Leutner shear model is a cylindrical specimen of 150 mm diameter and 100 mm high, consisting of geosynthetic sandwiched between the hot mix asphalt (HMA) layers. The specimen is divided longitudinally into three parts as the top 29 mm HMA layer, intermediate 2 mm interface layer and bottom 69 mm HMA layer. The material properties adopted in the numerical model are mentioned in Tables 1 and 2. The HMA material properties such as Young's modulus and Prony parameters are determined by conducting dynamic modulus test as per AASHTO TP: 79-13 [29]. The Poisson's ratio of HMA is assumed based on the recommendation given in the Mechanistic-Empirical Pavement Design Guide. According to Nithin et al. [10], coir and jute fabrics satisfy the conditions required for paving fabrics; hence they are adopted in this present study. The Young's modulus of 36 MPa for coir, 71.3 MPa for jute and 121.1 MPa for synthetic, obtained from

Table 1 Hot mix asphalt properties

Temperature	10 °C		20 °C		30 °C	
Young's modulus (MPa)	13527.58		13800		14403.93	
Poisson's ratio	0.2		0.2		0.25	
Prony parameters	g_i	τ_i	g_i	τ_i	g_i	τ_i
	0.10271	2.96E+01	0.13829	4.91E-04	0.15167	9.49E-05
	0.16749	3.34E-01	0.06919	9.76E-08	0.16033	1.03E-05
	0.09167	2.37E-04	0.14243	6.77E-05	0.10289	4.76E-07
	0.04318	7.44E-07	0.13615	1.75E-01	0.08351	1.33E-08
	0.16434	3.78E-03	0.14841	3.55E-03	0.15897	7.79E-04
	0.06535	1.66E-05	0.10170	3.19E-06	0.13916	6.04E-03
	0.15458	3.21E+00	0.14088	2.39E-02	0.11358	4.09E-02
	0.15832	3.74E-02	0.08143	1.50E+00	0.06210	3.60E-01
	0.05017	4.91E+02	0.03982	2.10E+01	0.02672	4.50E+00

Table 2 Interface properties (28)

Temperature	Properties	Control specimen	Synthetic	Jute	Coir
10 °C	Bond strength (MPa)	1.9015	1.6206	1.3133	0.9948
	Stiffness (MPa/mm)	0.2607	0.2191	0.1644	0.1328
	Fracture energy (mJ/mm ²)	8.135	6.1431	4.2218	4.0445
20 °C	Bond strength (MPa)	1.2867	0.86	0.75	0.59
	Stiffness (MPa/mm)	0.199172	0.13	0.17	0.1
	Fracture energy (mJ/mm ²)	11.02	5.16	2.39	4
30 °C	Bond strength (MPa)	0.3671	0.2822	0.2531	0.2205
	Stiffness (MPa/mm)	0.05472	0.0476	0.0428	0.0395
	Fracture energy (mJ/mm ²)	3.2014	2.1932	1.9087	1.612

wide width tensile test is adopted in the model. Poisson's ratio of 0.25 is assumed for all geosynthetics.

The hot mix asphalt is modelled as a solid section with linear hexahedral elements of type C3D8. The geosynthetic along with the tack coat is modelled as a cohesive section with linear hexahedral elements of type COH3D8. The boundary

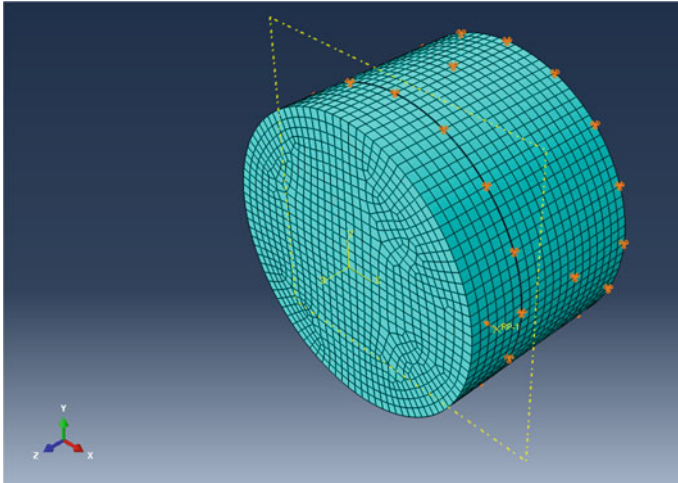


Fig. 4 Abaqus model showing the boundary, loading and mesh pattern

condition for the present model is given in accordance with the experiment, where the bottom portion of the HMA is restricted in all X , Y and Z directions. The loading is applied to the top portion of HMA in the X direction at a rate of 50 mm/min until the material delaminates. The meshing of the model is shown in Fig. 4, and a dynamic implicit step analysis is carried out.

4 Results and Discussion

The adopted CZM model predicts the interface properties obtained from experimental values with reasonable accuracy. Figure 5 compares the experimentally obtained bond strength with that predicted using the model studies, for the different types of geosynthetics and control specimen (i.e. specimen without geosynthetic). The threshold bond strength obtained from the numerical model is found to be comparable with the experimental results for specimens with and without interlayers. There is a slight deviation observed in the predicted post-peak behaviour from the experimental value. This may be due to the frictional effect between the interface and HMAs. The under prediction of the softening behaviour by the numerical model gives a conservative estimate of bond strength which will provide a safe pavement design. The reduction in bond strength with respect to control specimen falls in the range of 24–35% for Synthetic, 30–41% for Jute and 39–55% for coir for the range of temperatures considered. The reduction rate is comparably more for natural geosynthetics. Hence while designing the HMA overlay with the inclusion of natural geosynthetics, the tack coat must be of good quality and quantity in such a way it provides more bond strength.

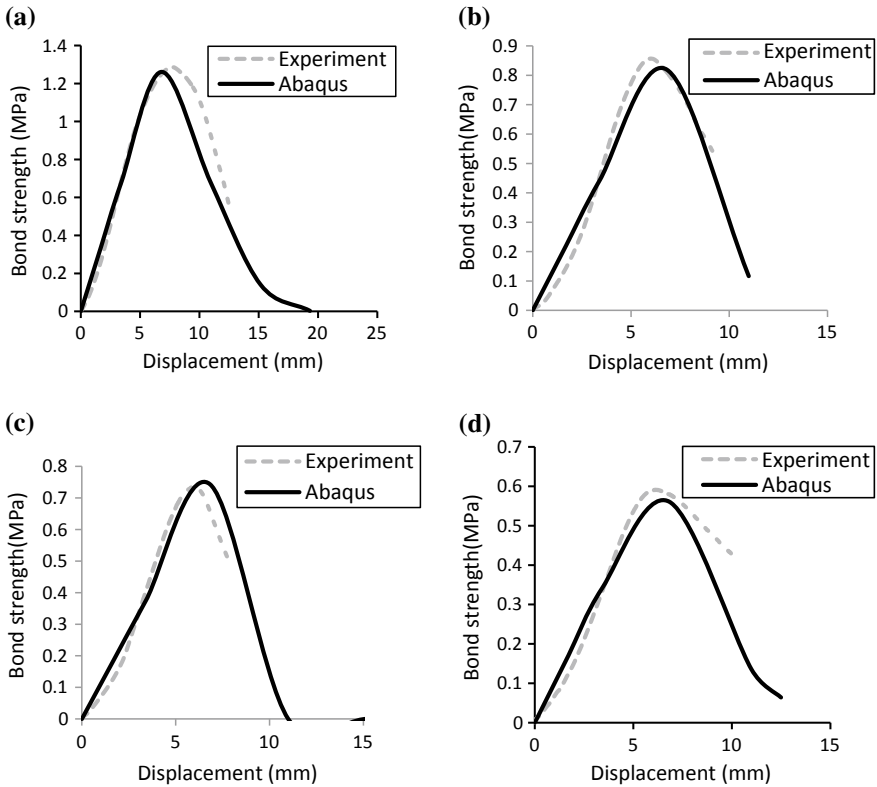


Fig. 5 Validation of numerical values with experiment for a typical temperature of 20 °C: **a** control specimen, **b** synthetic, **c** jute and **d** coir

HMA is a material that shows a transition of solid to viscous state as temperature increases. This change in viscosity affects the bond strength noticeably. Figure 6 gives a comparison of the bond strength at temperatures 10, 20 and 30 °C for the control specimen and with the inclusion of different geosynthetics.

The bond strength value reduces by 35% for control specimen, 44% for synthetic, 39% for jute and 43% for coir at temperature 20 °C with respect to 10 °C. Similarly, at temperature 30 °C, the reduction is of about 81% for control specimen, 81% for synthetic, 80% for jute and 78% for coir with respect to 10 °C. Natural geosynthetics shows a lesser reduction in bond strength when compared to control specimen and synthetic (synthetic) as temperature increases.

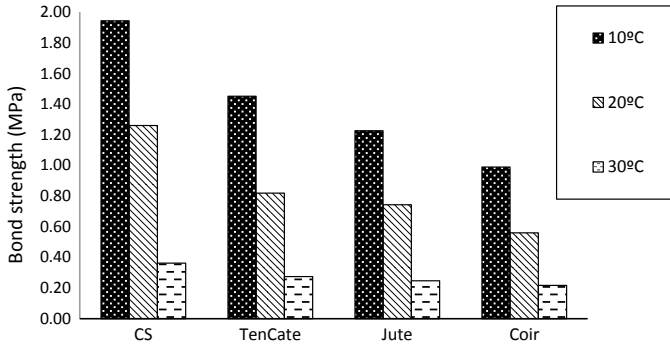


Fig. 6 Comparison of bond strength at temperatures 10, 20 and 30 °C

5 Summary

The adopted numerical model is able to predict the experimental results. The procedure for the determination of properties of HMA as well as interface parameters to be used as input for the numerical model is explained in detail. The adopted CZM predicts the behaviour of the interface between the pavement layers with reasonable accuracy by performing back analysis. Therefore, CZM can be adopted as an interface model in pavement analysis where the HMA overlay consists of natural geosynthetic interlayers. Bond strength reduces while geosynthetics are used as interlayers. The reduction in bond strength is more for coir, as its modulus is lesser compared to synthetic interlayer. Thus while using natural geosynthetics in the field, the tack coat must be used at the appropriate level and applied properly such that it enhances the bond strength. There is a considerable reduction in bond strength as temperature increases. But this effect is lesser in natural geosynthetics when compared to control specimen and synthetic.

References

1. Kim J, Buttlar WG (2002) Analysis of reflective crack control system involving reinforcing grid over base-isolating interlayer mixture. *J Transp Eng ASCE* 128(4):375–384
2. Button J, Lytton R (2007) Guidelines for using geosynthetics with hot mix asphalt overlays to reduce reflective cracking. *Transp Res Rec J Transp Res Board* 20(2):20–35
3. Khodaii A, Fallah S, Nejad FM (2009) Effects of geosynthetics on the reduction of reflection cracking in asphalt overlays. *Geotext Geomembr Elsevier* 27(1):1–8
4. Baek J (2010) Modelling reflective cracking development in hot-mix asphalt overlays and quantification of control techniques, PhD thesis, Department of Civil Engineering, University of Illinois, Urbana
5. Nithin S, Rajagopal K, Veeraragavan A (2014) Reflection cracking: a review on the potential of interlayer system with reference to natural fibres. In: 10th International conference on Geosynthetics, Berlin, Germany

6. Nithin S, Rajagopal K, Veeraragavan A (2015a) State-of-the-art summary of geosynthetic interlayer systems for retarding the reflective cracking. *Indian Geotech J Springer* 45(4):472–487
7. Fallah S, Khodaii A (2015) Evaluation of parameters affecting reflection cracking in geogrid-reinforced overlay. *J Cent South Univ Springer* 22(3):1016–1025
8. Nejad F, Asadi S, Fallah S, Vadood M (2016) Statistical-experimental study of geosynthetics performance on reflection cracking phenomenon. *Geotext Geomembr Elsevier* 44(2):178–187
9. Ghosh M, Banerjee PK, Rao GV (2010) Development of asphalt overlay fabric from jute. *J Text Inst, Taylor and Francis* 101(5):431–442
10. Nithin S, Mohapatra SR, Rajagopal K, Veeraragavan A (2017) Use of natural geotextiles to retard reflection cracking in highway pavements. *J Mater Civ Eng ASCE* 30(4):1–18
11. Prieto JN, Gallego J, Perez I (2007) Application of the wheel reflective cracking test for assessing geosynthetics in anti-reflection pavement cracking systems. *Geosynth Int ICE* 14 (5):287–297
12. Vinay Kumar V, Saride S, Pranav RT Peddinti (2017) Interfacial shear properties of geosynthetics interlayered asphalt overlays. *Geotech Front 2017 ASCE* 442–451
13. Noory A, Nejad FM, Khodaii A (2017) Effective parameters on interface failure in a geocomposite reinforced multilayered asphalt system. *Road Mater Pavement Des* 19(6):1458–1475
14. Brown SF, Thom NH, Sanders PJ (2001) A study of grid reinforced asphalt to combat reflection cracking. *Annual Meeting of Association of Asphalt Paving Technologists*, 543–569
15. Canestrani F, Grilli A, Santagata FA, Virgili A (2006) Interlayer shear effects of geosynthetic reinforcements. In: *A 10th international conference on asphalt pavements-august 12 TO 17, Quebec City, Canada*
16. Canestrari F, Belogi L, Ferrotti G, Graziani A (2015) Shear and flexural characterization of grid reinforced asphalt pavements and relation with field distress evolution. *Mater Struct Springer* 48(4):959–975
17. Nithin S, Rajagopal K, Veeraragavan A (2015b) Critical review on the bond strength of geosynthetic interlayer systems in asphalt overlays. In: *The 15th Asian regional conference on soil mechanics and geotechnical engineering, geotechnical society special publication, Japanese*, 67(2):2296–2301
18. Ozer H, Al-Qadi I, Leng Z (2008) Fracture-based friction model for pavement interface characterization. *J Transp Res Board* 54–63
19. Christensen R (2012) *Theory of viscoelasticity: an introduction*, Elsevier
20. Schellekens JCJ, De Borst R (1993) A non-linear finite element approach for the analysis of mode-I free edge delamination in composites. *Int J Solids Struct Elsevier* 30:1239–1253
21. Allix O, Corigliano A (1999) Geometrical and interfacial non-linearities in the analysis of delamination in composites. *Int J Solids Struct Elsevier* 36:2189–2216
22. Hillerborg A, Modeer M, Petersson PE (1976) Analysis of crack formation and crack growth in concrete by means of fracture mechanics and finite elements. *Cem Concr Res* 6:773–782
23. Dugdale D (1960) Yielding of steel sheets containing slits. *J Mech Phys Solids Elsevier* 8 (2):100–104
24. Barenbatt GI (1962) The mathematical theory of equilibrium cracks in brittle fracture. *Adv Appl Mech Elsevier* 7(1):55–129
25. Goodman RE, Taylor RL, Brekke TL (1968) A model for the mechanics of jointed rock. *J Soil Mech Found Div ASCE* 10(7):25–35

26. Geubelle PH, Baylor JS (1998) Impact-induced delamination of composites: a 2d simulation. *Compos B Eng* 29(5):589–602
27. Sivakumar G, Maji VB (2018) A study on crack initiation and propagation in rock with pre-existing flaw under uniaxial compression. *Indian Geotech J Springer*. <https://doi.org/10.1007/s40098-018-0304-8>
28. Prashanthi P (2016) Numerical modeling of reflective cracking in flexible pavements with geosynthetic overlays. M. Tech thesis, Indian Institute of Technology
29. AASHTO TP 79 (2013) Determining the dynamic modulus and flow number for Hot mix asphalt (HMA) using the Asphalt Performance Tester (AMPT), American Association of State and Highway Transportation Officials

Influence of Variabilities of Input Parameters on Seismic Site Response Analysis



C. Shreyasvi, N. Badira Rahmath and Katta Venkataramana

Abstract The seismic waves originating from an earthquake source undergoes significant amplification on its way toward the surface. The dynamic properties of the soil such as shear modulus/stiffness degradation and damping play a major role in amplifying the seismic waves. In the present study, two sample bore logs from Calicut have been taken for one-dimensional equivalent linear ground response studies. The bore logs represent clayey and sandy deposits and the shear wave velocity (V_s (30)) of these sites are in the range of 300–360 ms^{-1} (NEHRP C). The uncertainty in the soil properties has been addressed by randomizing the soil profile using Monte Carlo simulation on STRATA. Similarly, the influence of the number of ground motions on the site response has been analyzed by considering different ground motion suites. The regional seismic hazard consistent ground motions have been considered for the analysis. The variation of Peak Ground Acceleration (PGA) along the depth of the soil profile is studied to understand the influence of local soil profile in modifying the wave properties. The influence of variability associated with the input parameters has been assessed through numerical experiments considering multiple numbers of realizations (V_s profile) and ground motions. The study reveals the variability associated with the ground motions to be high when compared to soil property. It can be concluded that the uncertainty in the input motion has a significant impact on the overall outcome of site response analysis.

Keywords Equivalent linear method · Monte carlo simulation · Spectral matching · Site amplification · Response spectrum

C. Shreyasvi (✉) · N. Badira Rahmath · K. Venkataramana
Department of Civil Engineering, National Institute of Technology Karnataka,
Surathkal, India
e-mail: shreyasvic@gmail.com

C. Shreyasvi
Department of Civil Engineering, B M S College of Engineering, Bangalore, India

1 Introduction

The ground motion from the source on reaching the bedrock level undergoes amplification and in some cases, attenuation when propagated through various soil layers to the surface. The local soil deposits play a crucial role in altering the characteristics of the ground motion as it passes through different soil layers before reaching the surface. The soil underlying a site has a major impact on amplitude, frequency content, and duration of ground shaking. The gradient in the impedance between the bedrock condition and the soil medium, the trapped energy between the surface and the bedrock leading to resonance effect, and increased damping are the primary physical phenomena that affect the amplitude of ground motions at the site. The ground motion expected at a site (surface) is predicted by performing site response analysis that involves the application of multiple ground motion time histories at the elastic rock half-space and transfer of these ground motions through various soil layers to the surface.

The site effects responsible for amplification of ground motion is dependent on dynamic properties of the soil such as shear modulus and damping associated with each of the subsurface layers, in addition to the characteristics of the ground motion being transmitted. The shear wave velocity plays a major role in determining the dynamic shear modulus of the underlying soil. There are various in situ methods available for determining the shear wave velocity profile of a soil stratum such as cone penetration test, seismic cross-hole test, Multichannel Analysis of Surface Waves (MASW), and Spectral Analysis of Surface Waves (SASW). However, these methods require skilled labor apart from being expensive and time-consuming. Hence, these methods are not feasible under all circumstances. A more feasible solution in seismic site characterization will be the utilization of the widely practiced and abundantly available SPT data in establishing the shear wave velocity profile. The shear wave velocity corresponding to each soil layer can be indirectly estimated from “N” values of the SPT bore logs through various empirical correlations. The correlation developed for sand and clay type was used in this study to estimate the shear wave velocity at each soil layer. A typical soil profile consisting of depth, unit weight, shear wave velocity, and damping associated with each layer serves as an input in evaluating the geotechnical site response. The soil profile of our study area can be characterized as hard laterite and sandy soil (Fig. 1). The influence of local site effects in earthquake ground shaking is evaluated by performing site response analysis.

In order to understand the amplification characteristics of the already modeled soil profile, an input motion is applied at the bedrock level to all the soil profiles individually and the variation in the response of ground motion parameters at every soil layer is measured and the dynamic characteristics such as shear stress and strain and response spectrum at the surface level is studied. During the selection of ground motion, more stress was laid on choosing the earthquake records with source mechanism, source depth, tectonic regime, soil profile, magnitude, and source distance similar to the study area. The equivalent linear ground/site response

analysis in time domain evaluates vertical propagation of the shear waves through soil layers lying on an elastic layer of the rock. The transfer function for different soil layers is developed from its inherent properties, which aids in determining the amplification of the amplitude and other response parameters such as displacement, shear stress, and strain ratio at the interface of each soil type in the considered soil profile.

The present study attempts to understand the influence of input parameters on the site response analysis. The variability associated with these input parameters is assessed individually and the influence of these parameters on the final outcome of the site response analysis is quantified.

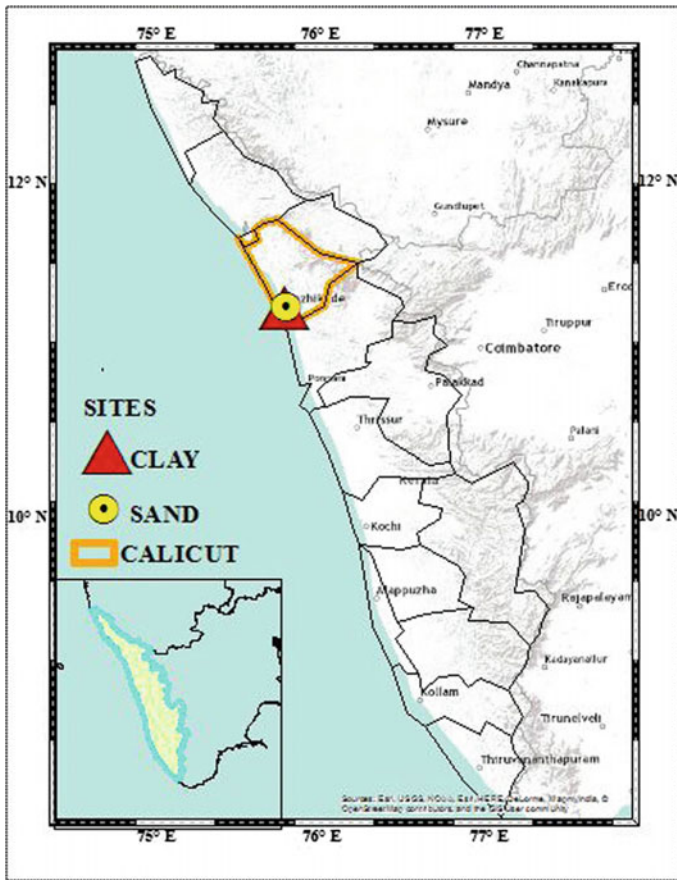


Fig. 1 The geographical locations of the boreholes used in the study

2 Estimation of Shear Wave Velocity Profile

The dynamic characteristics of the soil layer form an inherent parameter in estimating the amplification characteristics of a given site. The information on the local site was procured from the consultancy cell of Dept. of Civil Engineering, NIT Calicut. The bore logs consisted of information about the soil type, unit weight, water content, and the SPT “N” value. Various literature are available on correlations between SPT “N” value and the shear wave velocity “ V_s ”. In this regard, 11 correlations were investigated for estimating V_s and more details about these correlations has been provided in Table 1. A sample estimation of the V_s profile along the depth of the borehole is shown in Fig. 2. It can be inferred from Fig. 2 that the standard deviation in the estimated V_s values increases with depth.

One of the major issues while using SPT bore logs is the realization of engineering bedrock. Most of the in situ tests find it difficult to reach the bedrock with $V_s > 760 \text{ ms}^{-1}$ and hence, this is accomplished by geophysical methods. In the present study, the groundwater information reports, findings from an electrical resistivity survey along with the available literature for the Calicut region was

Table 1 V_s —N correlations used in the study

Sl. no	Author	Soil type	Correlation	Region	Nomenclature
1	Dikmen [5]	Clay	$V_s = 44 N^{0.48}$	Turkey	UD(09)
		Sand	$V_s = 73 N^{0.33}$		
2	Anbazhagan et al. [1]	Clay	$V_s = 89.31 N^{0.358}$	Lucknow	KAS(10)
		Sand	$V_s = 100.53 N^{0.265}$		
3	Tsiambaos and Sabtakakis [15]	Clay	$V_s = 140.1 N^{0.29}$	Greece	TS(11)
		Sand	$V_s = 92 N^{0.341}$		
4	Chatterjee and Chaudhury [4]	Clay	$V_s = 77.11 N^{0.3925}$	Kolkata	CC(13)
		Sand	$V_s = 54.82 N^{0.5255}$		
5	Kirar et al. [12]	Clay	$V_s = 94.4 N^{0.379}$	Roorkee	TS(11)
		Sand	$V_s = 100.3 N^{0.348}$		
6	Uma Maheswari et al. [16]	Clay	$V_s = 89.31 N^{0.358}$	Chennai	UM(10)
		Sand	$V_s = 100.53 N^{0.265}$		
7	Lee [11]	Clay	$V_s = 114 N^{0.31}$	Usa	LEE(90)
		Sand	$V_s = 57 N^{0.49}$		
8	Pitilakis et al. [13]	Clay	$V_s = 114 N^{0.31}$	Greece	P(92)
		Sand	$V_s = 57 N^{0.49}$		
9	Jafari et al. [10]	Clay	$V_s = 27 N^{0.73}$	South of Tehran	J(02)
		Sand	$V_s = 80 N^{0.33}$		
10	Imai [9]	Clay	$V_s = 80.2 N^{0.292}$	Japan	IM(07)
		Sand	$V_s = 80.6 N^{0.331}$		
11	Hasancebi and Ulusay [7]	Clay	$V_s = 97.9 N^{0.269}$	Turkey	HU(07)
		Sand	$V_s = 90.8 N^{0.319}$		

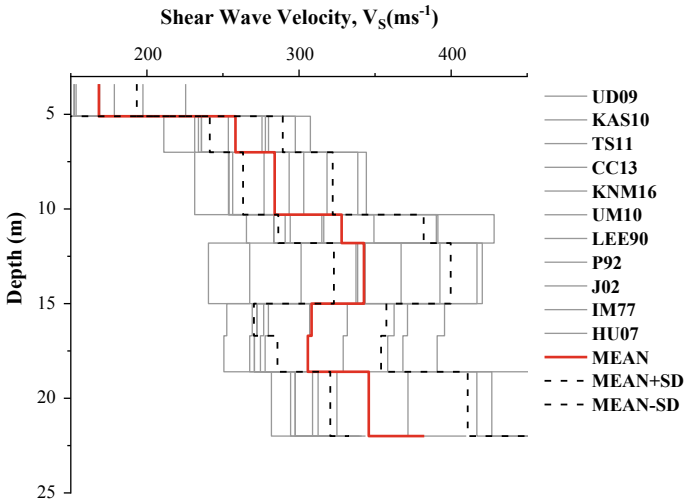


Fig. 2 Shear wave velocity profile estimated using all the correlations along with the mean and the boundary values

studied to estimate the depth to bedrock. Upon a thorough literature survey, it was found that the bedrock is usually met at a depth of 20–35 m from the surface. Hence, engineering bedrock is assumed to exist from 40 m below the surface.

In the present study, a total of two bore logs with one being clayey and the other being sandy deposit have been considered. The estimated shear wave velocity profile for both the deposits has been shown in Figs. 3 and 4. The soil stratigraphy mainly consists of sandy, laterite, weathered rock, and fractured rock. The shear wave velocity of both the deposits is in the same range and both the sites belong to NEHRP class C. The dynamic characteristics of the soil have high variability due to geologic processes and the method used in the measurement of V_s . The variability in the soil property is incorporated by Monte Carlo simulation using the STRATA program. The approach considers “n” number of soil profiles within a user-specified lower and upper bounds of the V_s values. The upper and lower bound for the V_s profile is estimated as shown in Fig. 2. The modulus reduction curve and damping curve proposed by Idriss [8] was used for modeling clayey and sandy soil and the base of the soil profile was modeled as a weathered rock [6].

One of the major concern in the randomization of soil properties is the number of realizations that need to be generated for obtaining an accurate estimate of the soil response. The numerical experiments were conducted by considering various number of realizations such as 5, 10, 15, 20, 22, 25, and 30. The plot of median responses was unable to depict the variation among a different number of realizations in estimating spectral amplification. Hence, a plot of median + 1 standard deviation for the estimated spectral amplification has been shown in Fig. 5a. In addition to these realizations, a baseline soil profile (median V_s profile) was

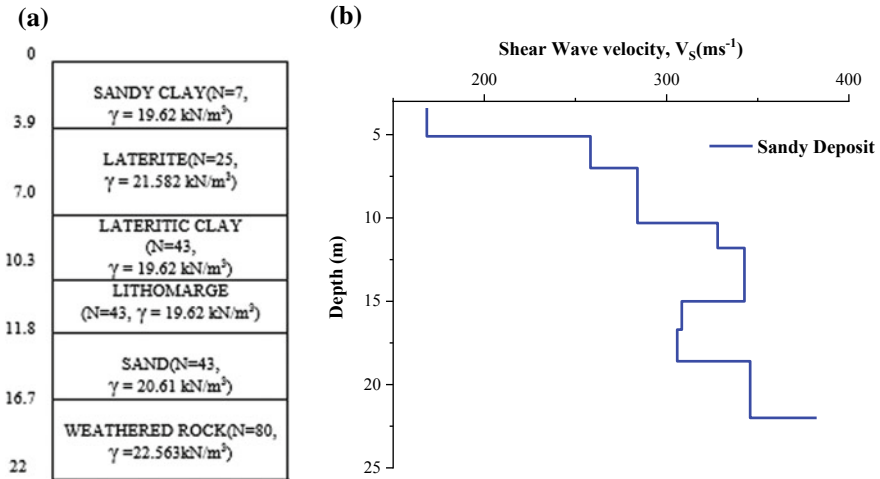


Fig. 3 a Soil stratigraphy. b Shear wave velocity profile of the sandy deposit

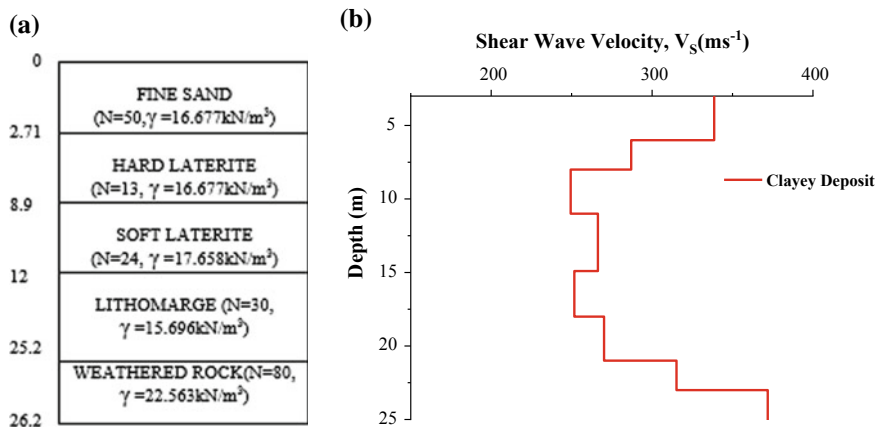


Fig. 4 a Soil stratigraphy. b Shear wave velocity profile of the clayey deposit

compared to highlight the necessity for considering multiple realizations of a shear wave velocity profile. The difference in the soil response was found to be minimal for various realizations but significantly higher with respect to the baseline soil profile. However, based on close observation, it can be inferred that realization more than 15 provides a reasonable estimate. Additionally, the microlevel difference was observed between the median response spectra for realizations exceeding 22. Hence, it can be concluded that 22 realizations are usually sufficient in estimating the dynamic site response and any number higher than this may lead to a minute reduction in the spectral parameter. The standard deviation was observed to

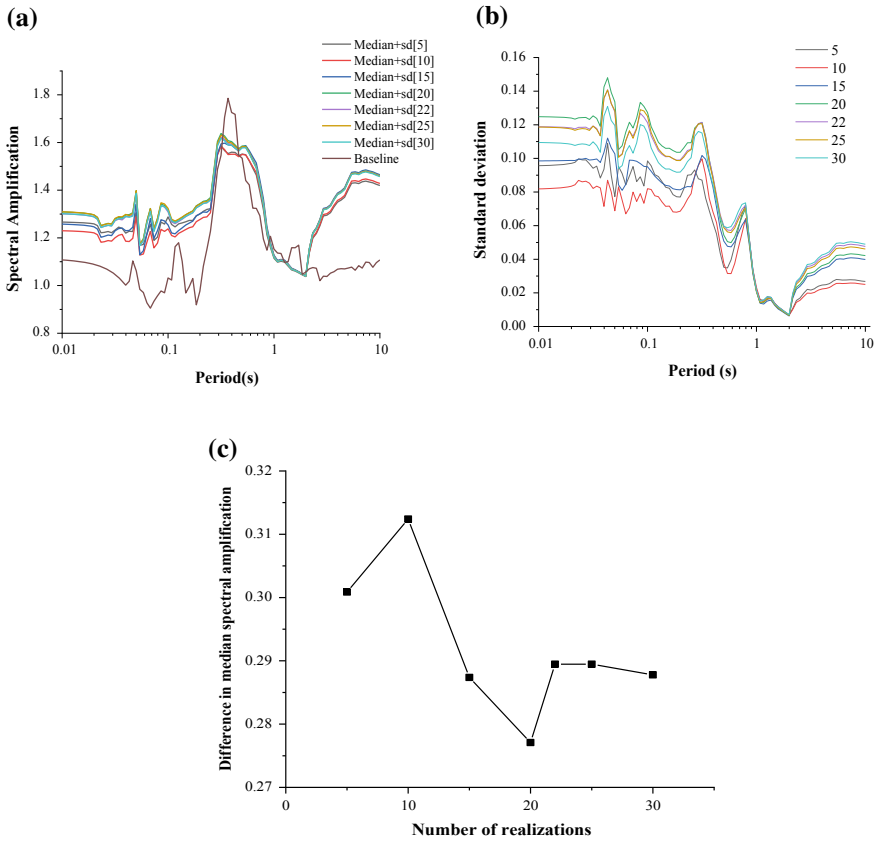


Fig. 5 The **a** median and the **b** standard deviation of the estimated spectral amplification for the different realization of the shear wave velocity profile. **c** Gradient in median spectral acceleration between different realizations

be quite high for periods below the site period ($T < 0.3$ s) as evident from Fig. 5b. However, the insignificant difference in the computed standard deviation was observed for realizations greater than 20 (Fig. 5c).

3 Selection of Input Ground Motion

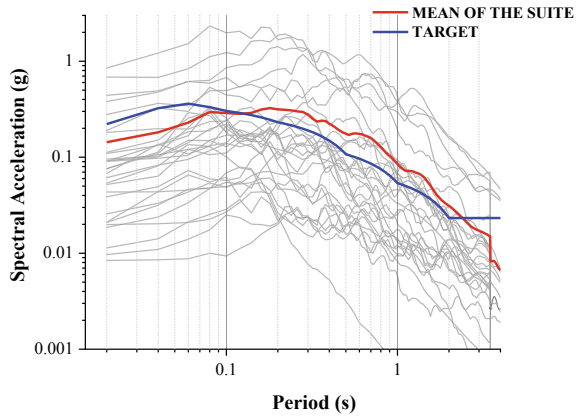
The input motion to a soil profile demonstrates the wave propagation from the bedrock to the surface level undergoing significant modification along its path. The soil layers modify the characteristics of the ground motion based on their inherent dynamic properties such as dynamic shear modulus and damping. The choice of input motion for a site response analysis is a crucial step in obtaining a statistically

stable estimate of the surface motion. However, there are no definite guidelines for the selection of ground motion through ASCE—07 [2] suggests a minimum of 5–7 motions to be used in the analysis. In the present study, an experiment was conducted to determine the number of ground motion required to obtain a good estimate of soil response. In this regard, ground motions suites with records of 5, 7, 10, 15, 18, 20, 22, 25, and 30 were analyzed and compared. The details of the ground motions used in the study are presented in Table 2. The ground motions were selected from a region with a similar tectonic regime as the study region, i.e., Calicut. The hazard consistent ground motions were selected for scaling. In other

Table 2 Details of the ground motion used in the study

Sl no.	Earthquake name	Nomenclature	Date	M _w	Epicentral Distance (km)	PGA(g)	Scale factor
1	Bovec	RF.SVAL	12-04-1988	5.7	23.5	0.0254	5
2		3A.MZ21	26-10-2016	5.9	30.7	0.1827	2.5
3		3A.MZ19_5	26-10-2016	5.9	30.4	0.0957	0.7
4		3A.MZ14	26-10-2016	5.9	36.6	0.0515	2.8
5		3A.MZ11	26-10-2016	5.9	31	0.0441	5
6		IV.T1212	26-10-2016	5.9	18.8	0.0680	2
7		IV.T1211_25	26-10-2016	5.9	47.4	0.0180	4.5
8		IV.T1215	26-10-2016	5.9	24.4	0.0209	5
9		IT.ACC_17	26-10-2016	5.9	25.4	0.0901	2.5
10		IT.SLO	26-10-2016	5.9	14.4	0.0587	3
11		IT.LSS 18	26-10-2016	5.9	41.1	0.0113	3
12		IT.TER_9	26-10-2016	5.9	53.8	0.0379	1
13	Central Italy	IT.TOD	26-10-2016	5.9	63.5	0.0085	5
14		IT.MMO	30-10-2016	6.5	19.2	0.1890	0.75
15		IV.1215_12	30-10-2016	6.5	20.1	0.0749	2.3
16		IT.TER	30-10-2016	6.5	51.3	0.0753	4.5
17		IT.ACC_7	30-10-2016	6.5	18.6	0.4343	0.6
18		IV_T1213	30-10-2016	6.5	12	0.7946	0.2
19		IV.T1212_10	30-10-2016	6.5	10.5	0.2798	1
20		3A_MZ19-14	30-10-2016	6.5	22.6	0.3631	0.9
21		3A_MZ29	30-10-2016	6.5	26.9	0.6890	0.7
22		IV.RM13	07-04-2009	5.5	15.6	0.0898	2.3
23		IV.RM03	07-04-2009	5.5	3.4	0.0927	2.2
24	IT.SUL	07-04-2009	5.5	44	0.0199	2	
25	Sicily	IT.SRT	13-12-1990	5.6	36.9	0.1074	1
26		IT.NOT	13-12-1990	5.6	48.3	0.0904	3
27	L_Aquila	IT.LSS	06-04-2009	6.1	41.5	0.0098	4.5
28		IT.ANT	06-04-2009	6.1	26.2	0.0201	3
29	Northwestern	CR.A306	03-04-1999	4.8(M _L)	22	0.1108	1
30	Balkan_Peninsula	SI.CEY	22-05-1955	4.2(M _L)	21.3	0.0510	1.2

Fig. 6 Response spectra of the ground motion suite and the target uniform hazard spectrum



words, ground motion records with PGA in the range obtained from the probabilistic seismic hazard assessment was used. The target uniform hazard spectrum was obtained from Shreyasvi et al. [14]. The response spectrum of the chosen ground motions has been compared with the target spectrum and has been presented in Fig. 6.

The ground motions are chosen in such a way that the values of the ground motion parameter such as spectral acceleration covers the upper and the lower bound of the specified target spectrum.

The influence of the choice of the input ground motions has been demonstrated in the form of response spectrum at the surface as shown in Fig. 7a. The median spectral parameter for a suite of 5–10 ground motions predicts a higher value when compared to the other suites. However, this inherent difference between the predicted spectral parameters is negligible for suites with ground motions exceeding 10.

The variability in the ground motions was found to be very high when compared with the site properties as shown in Fig. 7b. The variability was found to be higher for suites with ground motion records 5–10. However, this variability tends to reduce and implies the possibility of a stable estimate when ground motions more than 15 are considered in site response analysis. The variation of standard deviation tends to stabilize for ground motions exceeding 20. Hence, it can be inferred that the variability in input motion is more crucial than that of the site properties. A similar observation has been made by Bazzurro and Cornell [3]. In order to demonstrate the performance associated with the number of ground motions, amplification spectrum has been plotted for two suites with ground motions 5 and 30, respectively. Figure 8a represents higher values of standard deviation for a ground motion suite with 5 records. Supporting the earlier claim, the standard deviation has reduced in ground motion suite with 30 records. A lesser standard deviation was observed in the case of a suite consisting of 30 ground motions.

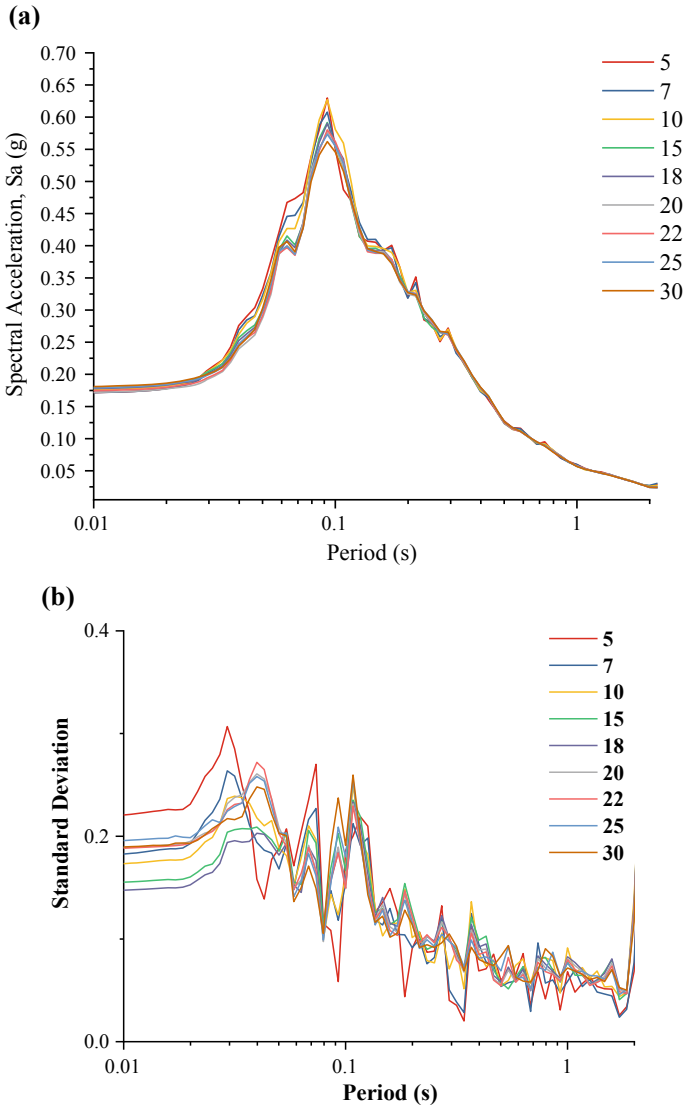


Fig. 7 **a** Median response spectrum at the surface for different suites of ground motions. **b** Standard deviation in the predicted spectral response for different suites of ground motions

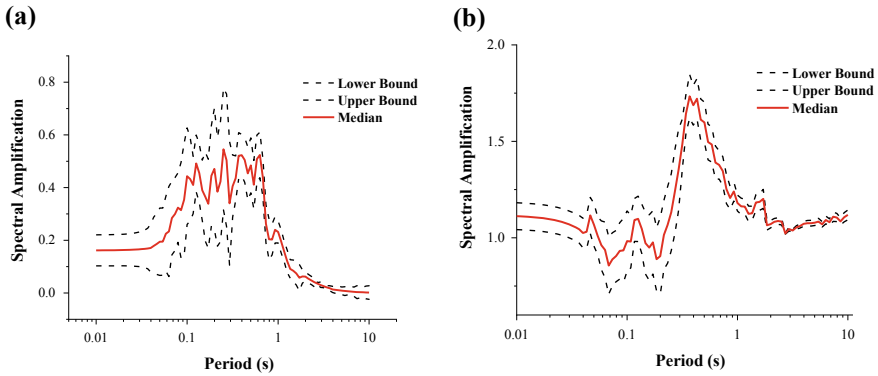


Fig. 8 **a** Amplification spectrum for a suite of 5 motions and **b**, for a suite of 30 motions

4 Conclusion

The present study is an investigation to understand the sensitivity of the site response analysis to various input parameters. The input parameters studied are the shear wave velocity profile and input ground motions. The discussion focusses on the variability in the soil property by simulating numerous shear wave velocity profiles. The number of realizations required to provide an unbiased estimate plays a major role in predicting the dynamic response of the local site. The study suggests 22 realizations to produce a rational estimate of the soil response. In addition, no significant variation was observed for realizations exceeding 20. A similar analysis was performed with a number of ground motion records. The standard deviation in the estimated spectral acceleration for different suites of ground motions reveals higher variability at periods less than 0.3 s which is very close to the site period. The variation of peak ground acceleration along the depth of the soil profile suggests that the top 6 m plays a significant role in amplifying the ground motion by more than 50%. A comparison of the standard deviation in the estimated response parameters by varying the soil property as well as the input motions suggests higher variability in the latter. It is concluded that the variability associated with the ground motion selection needs utmost attention when compared to the site property variability.

Acknowledgements The authors would like to sincerely acknowledge Prof. S Chandrakaran, Mr. Mohanlal, Ms. Shreya and staff of the Geotechnical Division of NIT Calicut for their support and assistance in procuring the soil data.

References

1. Anbazhagan P, Thingbaijam KKS, Nath SK, Narendara Kumar JN, Sitharam TG (2010) Multi criteria seismic hazard evaluation for Bangalore City, India. *J Asian Earth Sci* 38:186–198
2. ASCE Standard (2016) Minimum design loads for buildings and other structures, ASCE/SEI 7-05
3. Bazzurro P, Cornell CA (2004) Ground-motion amplification in nonlinear soil sites with uncertain properties. *Bull Seismol Soc Am* 94(6):2090–2109
4. Chatterjee K, Choudhury D (2013) Variations in and soil site class in Kolkata city using regression and sensitivity analysis. *Nat Hazards*, 2057–2082
5. Dikmen U (2009) Statistical correlations of and penetration resistance for soils. *J Geophys Eng* 6:61–72
6. EPRI (1993) Guidelines for determining design ground motions. EPRI TR-102293
7. Hasancebi N, Ulusay R (2007) Empirical correlations between and penetration resistance for ground shaking assessments. *Bull Eng Geol Environ* 66:203–213
8. Idriss IM (1990) Response of soft soil sites during earthquakes. In: *Proceedings of the HB seed memorial symposium*, vol 2, pp 273–289
9. Imai T (1977) P- and S-wave velocities of the ground in Japan. In: *Proceedings of the 9th international conference on soil mechanics and foundation Engineering* 2:127–132
10. Jafari MK, Asghari A, Rahmani I (1997) Empirical correlation between (V_s) and SPT-N value for south of Tehran soils. In: *Proceedings of the 4th international conference on civil engineering*, Tehran, Iran (in Persian)
11. Lee SHH (1990) Regression models of shear wave velocities. *J Chin Inst Eng* 13:519–532
12. Kirar B, Maheshwari BK, Muley P (2016) Correlation between shear wave velocity (v_s) and SPT resistance (N) for Roorkee region. *Int J Geosynt Ground Eng* 2(1):9
13. Ptilakis KD, Anastasiadis A, Raptakis D (1992) Field and laboratory determination of dynamic properties of natural soil deposits. In: *Proceedings of the 10th world conference on earthquake engineering*, Rotterdam, pp 1275–1280
14. Shreyasvi C, Venkataramana K, Chopra S, Rout MM (2019) Probabilistic seismic hazard assessment of mangalore and Its adjoining regions. A part of indian peninsular: an intraplate region. *Pure Appl Geophys* 176(6):2263–2297
15. Tsiambaos G, Sabatakakis N (2010) Empirical estimation of from in situ tests on soil formations in Greece. *Bull Eng Geol Environ* 291–297
16. Uma Maheswari R, Boominathan D, Dodagoudar GR (2010) Use of surface waves in statistical correlations of and penetration resistance of Chennai soils. *Geotech Geol Eng* 28:119–137

3D-Continuum Numerical Analysis of Offshore Driven Pipe Pile Using Finite Difference Method



D. S. Murthy, Ramesh Gedela, Rajagopal Karpurapu
and R. G. Robinson

Abstract This paper presents the results from three-dimensional analysis of offshore driven pipe piles using FLAC3D (Fast Lagrangian Analysis of Continua in three Dimensions) program. The numerical model was developed with solid elements for both the pile and the surrounding soil. Interfaces are created both on the inside and outside surfaces of the pipe pile along the length as well as at the bottom of the annular area of the pile. The pile driving was simulated by giving hammer impact force of one blow which was measured during offshore pile installation. Parametric studies were performed with different soil properties until the signals from the numerical analyses matched with the measured force–velocity data of the pile installed in offshore South East Asia region. The results include the soil plug behaviour under continuous driving and with a delay time of 12 h.

Keywords Pile driving · Numerical analysis · Soil plug · FLAC3D · Interface surfaces

1 Introduction

Open-ended steel pipe piles are commonly used for the foundations of fixed offshore platforms, mooring piles, offshore wind turbines, coastal structures, etc. as they offer relatively low driving resistance compared to closed-ended piles. The drivability of the open-ended piles is influenced significantly by the formation of soil plug inside the pile during driving particularly in granular soils. Most of the piles driven as a part of the foundations for the offshore structures were instrumented and tested dynamically to control the pile drivability as well as for estimating the pile capacity. The analysis of the data from the dynamic testing of piles

D. S. Murthy (✉) · R. Gedela · R. Karpurapu · R. G. Robinson
Indian Institute of Technology Madras, Chennai, India
e-mail: durbakula@gmail.com

© Springer Nature Singapore Pte Ltd. 2020
A. Prashant et al. (eds.), *Advances in Computer Methods
and Geomechanics*, Lecture Notes in Civil Engineering 56,
https://doi.org/10.1007/978-981-15-0890-5_21

are mostly done using the one-dimensional wave equation methods initially developed by Smith [6], in which the pile is divided into a number of masses attached to each other by elastic springs and soil is replaced by spring and dashpot to simulate the pile driving. The most popular method adopted to estimate the soil resistance during driving for the driven piles tested dynamically is signal matching analysis program CAPWAP (Case Pile Wave Analysis Program) developed by PDI (Pile Dynamics Inc.). This method provides a good estimate of the soil resistance during driving. However, it is not possible to thoroughly understand the behaviour of the soil plug or stresses in the soil during the pile driving using the existing methods. By using the continuum numerical model, it is possible to understand the behaviour of the soil as well as the soil resistance during the driving.

Continuum method can be used for an accurate analysis of the pile driving problem, as this method is based on a more realistic modelling of the actual physics of the pile driving than the wave equation Nath [4]. Consideration of the physics of the pile driving problem shows that stress waves generated in a pile due to hammer impact would propagate along its length and also depending upon the properties of the pile, soil and how the pile–soil interface behaves as a result of hammer blow, a proportion of the impact wave energy will also be transmitted to the surrounding soil, to carry some portion of impact energy away from the source when the extent of the soil medium is semi-infinite. A finite-difference based continuum numerical model (axisymmetric model) for displacement pile (solid pile) developed by Masouleh and Fakharian [3] was used to calculate the bearing capacity of the driven pile as well as to study the effect of the radiation damping.

During the pile driving operations, the plug formation in the soil can be understood by the sudden increase in the number of blows. However, the same during the numerical analyses can only be understood indirectly by the nature of stresses developed in the soil. The plug formation in the numerical analysis is indicated by increased soil stresses inside the pile compared to those in the outside soil. Further, the horizontal stresses increase rapidly compared to vertical stresses after the plug formation both inside and outside the pile. These aspects are clearly brought out through the results of this paper.

The objective of the present study is to model the driving of the pipe pile driven in offshore conditions in 3D by matching the measured instrumented data with computed data from the numerical model which enables the understanding of the soil behaviour both inside as well as outside the pile. Also, the behaviour of the soil plug during the end of the continuous driving (EOD) as well as at the beginning of driving after a delay (BOD) was studied using the continuum model. The numerical analysis is carried out using the FLAC3D (Fast Lagrangian Analysis of Continua in Three Dimensions) software version 6.0. The approach and preliminary verification of the model are similar to the approach followed by Masouleh and Fakharian [3] and hence not explained here.

2 Case Study Pile

The case study pile selected for the analysis was installed in offshore South East Asia as part of the foundation for a fixed offshore platform. The pile geometry, material properties and penetration details are given in Table 1, and the soil properties are given in Table 2. The soil properties given in Table 2 are arrived based on the soil boring done with sampling and PCPT (Piezocone penetration tests). The selected pile was driven to its final penetration of 25 m below the seabed and a restrrike test after a delay of 12 h was conducted. One hammer blow at the end of continuous driving, as well as one at the beginning of the drive, were analysed to understand the behaviour of the soil plug and effect of the delay on the soil plug.

Table 1 Pile geometry and material properties

Parameters	Value
Length, m	43.0
Outer diameter, m	1.067
Wall thickness, mm	38
Penetration, m	25
Elastic Modulus (E)	206,000 MPa
Poisson's ratio (ν)	0.3
Unit weight	77 kN/m ³
Impact wave speed	5120 m/s

Table 2 Soil properties at the location

Layer	Depth, m		Soil description	Submerged unit weight, kN/m ³	Angle of internal friction, ϕ°
	from	to			
1	0.0	5.3	Loose siliceous sand	9.5	20
2	5.3	12.2	Medium dense silty silica sand	11.0	33
3	12.2	13.2	Medium dense sand	11.0	30
4	13.2	18.8	Very dense very silty silica sand	11.3	40
5	18.8	36.0	Very dense silty silica sand	11.3	40

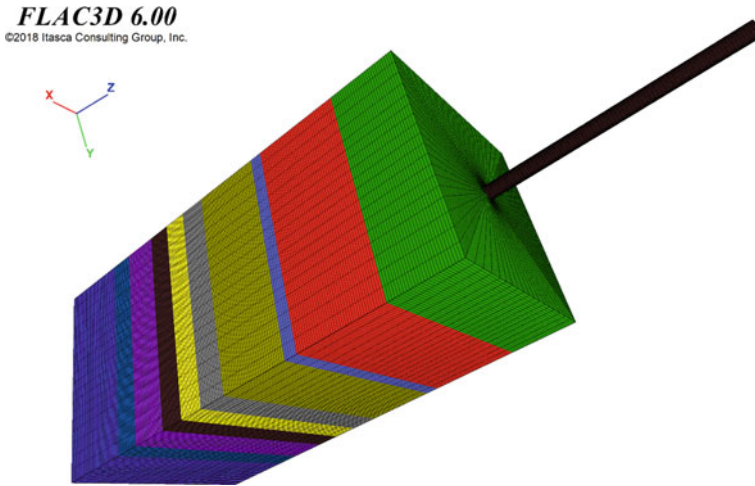


Fig. 1 Pile–soil model created in the FLAC3D

3 Numerical Modelling

The numerical analysis of the driven pile using FLAC3D is an iterative process and consists of two stages. The first stage of the analysis is the initial equilibrium analysis. During this stage, the soil layers are allowed to reach the equilibrium under static conditions using overburden pressure and self-weight stresses, and then the resulting deformations were set to zero. The second stage of the analysis is dynamic analysis by applying the impact load of one selected hammer blow on the top of the pile. The pile properties listed in Table 1 are used in the numerical model. The soil around the pile was modelled as a square block with layered soil as shown in Fig. 1. The size of the square block is 16 m \times 16 m. The depth of the soil model is 36 m. The pile was driven with Menck MHU500T hammer which has rated energy of 550 kN-m.

4 Material Properties

Pile is modelled as an elastic material, and the soil is modelled using elastoplastic constitutive model with Mohr–Coulomb failure criterion. The soil parameters are given in Table 2, which were selected based on both laboratory and in situ testings. The material properties of the soil for the first iteration of the signal matching analysis were arrived based on common correlations Bowles [1] available and FLAC3D manual. The parameters used in the first iteration of the signal matching analysis for both EOD and BOD are presented in Table 3.

Table 3 Material properties of the soil for the first iteration for EOD and BOD analysis

Layer	Depth, m		Friction angle ϕ°	Young's modulus, E, kPa, final values	Poisson's ratio
	from	to			
1	0	5.3	18	10,000	0.3
2	5.3	12.2	32.5	20,000	0.3
3	12.2	13.2	30	25,000	0.3
4	13.2	18.8	40	40,000	0.3
5	18.8	21	40	50,000	0.3
6	21	23	40	50,000	0.3
7	23	25	40	50,000	0.3
8	25	28	40	50,000	0.3
9	28	30	40	50,000	0.3
10	30	36	40	50,000	0.3

5 Interfaces Between Pile and Soil

Interfaces between pile and soil along the shaft of the pile were provided on both the inside as well as outside of the pipe pile to facilitate the relative displacement between the two. The interfaces were defined using the Mohr–Coulomb failure criterion. These interfaces along the shaft represent the skin friction capacity of the piles and also one interface provided at the bottom of the annular area of the pile represents the end bearing force. The total number of interface surfaces between the pile and soil in each case is equal to twice the number of soil layers modelled between the zero penetration and final pile penetration depths. For the present cases, a total of seven soil layers were modelled from zero penetration to 25 m penetration, which resulted in a total of 15 interface surfaces (14 in the vertical plane and one in the horizontal plane).

6 Numerical Model with the Signal Matching Technique

During the first stage of the analysis (static equilibrium analysis) of the system, fixity was applied at all the four sides of the model. The purpose of the equilibrium analysis is to allow all soil layers to reach equilibrium under self-weight (overburden pressure) and the resulting deformations were set to zero.

During the first stage of the analysis, the strength of the interface elements was set to zero. During the second stage of the analysis (dynamic analysis), properties of the interface elements were defined for the first iteration as described in the FLAC3D manual (version 6). Viscous or quiet boundaries were created for the numerical system for the dynamic analysis [2].

The case study pile was instrumented in the field during the pile installation with strain gages and accelerometers installed at the pile top, and hammer impact in the form of force (obtained from the strain measurements) and velocity (obtained from the acceleration measurement) was acquired using the pile driving analyser (PDA). The dynamic analysis has been carried out by applying the impact of the single hammer blow and resulting velocity from the numerical analysis and compared with the measured velocity in the field. The downward travelling wave of the hammer impact is calculated by using the measured force and velocity of the hammer impact by using Eq. 1

$$F_d = \frac{(F + ZV)}{2} \tag{1}$$

where F_d is the downward travelling force of the hammer impact, F is the measured force of the hammer impact at the sensor location, V is the velocity of the hammer impact measured at the sensor location and Z is the pile impedance. The input to the dynamic analysis for the EOD analysis as well as BOD analysis is shown in Figs. 2 and 3 (blue curve) along with the measured force and velocity data. The properties of the interfaces were changed in each iteration along with the material properties (below the pile tip as well as around the pile tip) until the computed velocity data from the numerical analysis matched with measured velocity data as the numerical analysis was carried out iteratively. The elastic modulus of the soil, particularly below the pile tip and soil layers near the pile tip, increased during the dynamic analysis which is necessary to match the computed data with the measured force–velocity data. As the pile-driving progresses, the soil below the pile tip and also

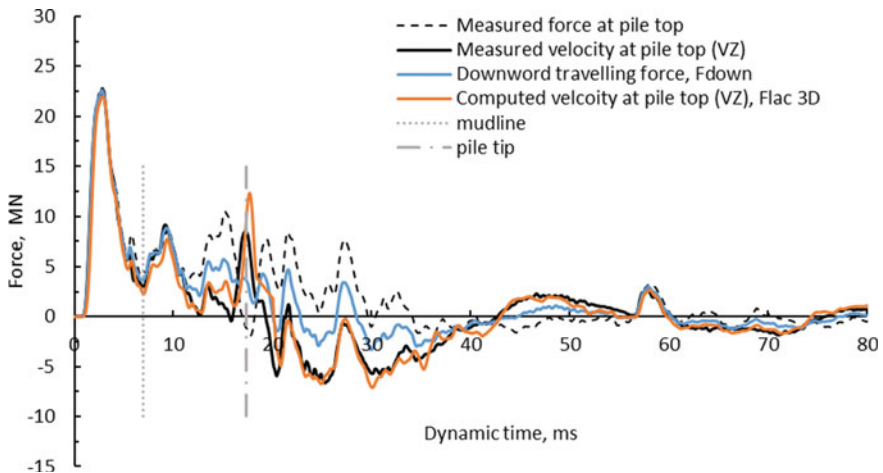


Fig. 2 Measured and computed data for the EOD case

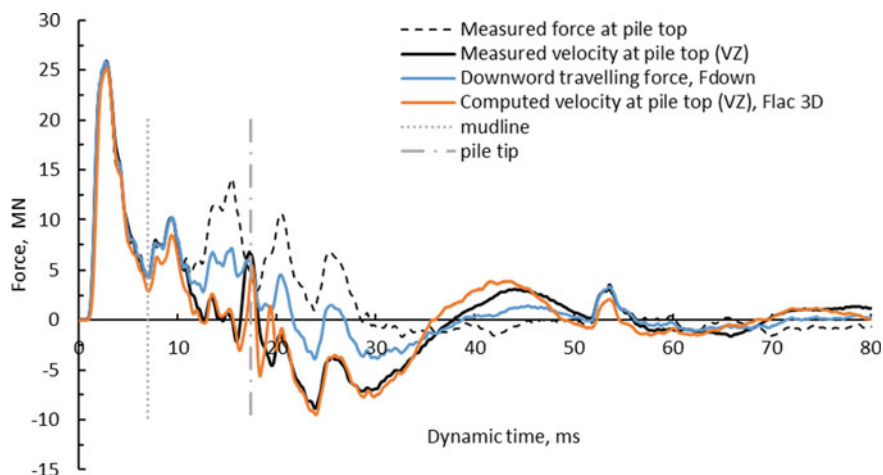


Fig. 3 Measured and computed data for the BOD case

Table 4 Material properties of the soil at the end of analysis for EOD and BOD

Layer	Depth, m		Angle of internal friction, ϕ°	Young's Modulus, E, kPa, Final Values	Poisson's ratio
	from	to		EOD/BOD	
1	0	5.3	18	10,000/10,000	0.3
2	5.3	12.2	32.5	20,000/20,000	0.3
3	12.2	13.2	30	25,000/25,000	0.3
4	13.2	18.8	40	40,000/40,000	0.3
5	18.8	21	40	50,000/50,000	0.3
6	21	23	40	150,000/450,000	0.3
7	23	25	40	350,000/450,000	0.3
8 ^a	25	28	45	500,000/500,000	0.3
9	28	30	40	300,000/400,000	0.3
10	30	36	40	50,000/50,000	0.3

^aLayer just below the pile tip, end bearing layer

around the pile tip just above densifies due to the driving and stiffness of the soil changes. The increase in the elastic modulus during the hammer impact was also presented by Feizee Masouleh and Fakharian [3], and Pinto and Grazina [5]. The material properties at the end of the analysis are presented in Table 4 while the interface properties arrived at the end of the analysis are given in Table 5 for both EOD and BOD analysis.

Table 5 Interface properties at the end of the signal matching analysis

Interface element Number	Depth, m		Cohesion, c, kPa	Friction angle, ϕ°	Normal stiffness, k_n (kN/m ³)	Shear stiffness, k_s (kN/m ³)
	from	to	EOD/BOD	EOD/BOD	EOD/BOD	EOD/BOD
1	0	5.3	0	10/10	7E + 04/ 7E + 04	7E + 04/ 7E + 04
3	5.3	12.2	0	20/25	1E + 05/ 1E + 05	1E + 05/ 1E + 05
5	12.2	13.2	0	25/25	1E + 06/ 1E + 06	1E + 06/ 1E + 06
7	13.2	18.8	0	40/35	5E + 06/ 5E + 06	5E + 06/ 5E + 06
9	18.8	21	0	40/40	5E + 06/ 5E + 07	5E + 06/ 5E + 06
11	21	23	5	40/40	5E + 09/ 5E + 08	5E + 08/ 5E + 07
13	23	25	10	45/45	5E + 09/ 5E + 09	5E + 09/ 5E + 08
2	0	5.25	0	5/10	7E + 04/ 7E + 04	7E + 04/ 7E + 04
4	5.3	12.2	0	10/15	1E + 05/ 1E + 05	1E + 05/ 1E + 05
6	12.2	13.2	0	15/15	1E + 06/ 1E + 05	1E + 06/ 1E + 05
8	13.2	18.8	0	15/20	3E + 06/ 3E + 06	3E + 06/ 3E + 06
10	18.8	21	0	25/35	5E + 06/ 5E + 07	5E + 06/ 5E + 06
12	21	23	0	40/40	5E + 08/ 5E + 09	5E + 08/ 5E + 07
14	23	25	10	45/45	5E + 09/ 5E + 10	5E + 08/ 5E + 08
15	25	25	15	45/45	5E + 09/ 5E + 09	5E + 09/ 5E + 09

6.1 Damping in the Dynamic Analysis

Local damping of 2% (2% of π , which is 0.0628) was considered for the pile material. Local damping is also assigned for the soil inside the pile as well as soil below the pile tip. For the outside soil in the shaft friction region initially, Rayleigh damping has been considered by using the Rayleigh damping parameters, frequency (ζ_{\min}) in Hertz and minimum damping ratio (f_{\min}) available in FLAC3D. The Rayleigh damping factors used in the final iteration resulted in a decent

Table 6 Damping factors at the end of the signal matching analysis for both EOD and BOD

Elements	Damping	Value (EOD/BOD)
Pile	Local damping	0.0618/0.0618
Soil outside the pile in the shaft friction region	Rayleigh damping	6 and 38 (ζ_{\min} and f_{\min})/5 and 38
	Artificial viscosity	1, 1 (a_n and a_t)/1, 1
Soil inside the pile (soil plug)	Local damping	0.124/0.094
Soil below the pile tip (tip soil)	Local damping	0.628/0.57

comparison with measured data in the field. In order to have a better match and no further change in the soil stiffness and interface properties, artificial viscosity damping option (a_n and a_t are factors of artificial viscosity in FLAC3D) has been used for the soil outside the pile in the shaft resistance region which resulted in a better correlation between measured and computed data. Artificial viscosity option improved the match between measured and computed data significantly in the latter part of the curve, which cannot be matched easily by changing the soil stiffness and strength parameters. The damping factors used in the dynamic analysis in the final iteration are presented in Table 6. Apart from the damping parameters, the viscous nature of the pile–soil movement in the interface elements has been considered by allowing the pile–soil slip in the interface elements. Both measured data as well as computed velocity data from the FLAC3D continuum numerical analysis are compared in Figs. 3 and 4 which show relatively good agreement between the measured and computed velocities. The data presented in the figures are with the artificial viscosity damping option.

7 Results and Discussions

The objective of the study is to develop a continuum numerical model by conducting the signal matching analysis and observe the behaviour of the soil plug inside the pipe pile during the EOD and BOD. The stresses developed in the soil due to hammer impact along the pile wall both inside the pile and outside the pile are compared in Fig. 4 while the stresses at the centre of the soil plug are compared in Fig. 5. It can be seen from the results presented in Fig. 4 that both horizontal and vertical stresses are increased after delay. The stresses inside the pile are higher near the pile tip compared to the stresses outside during EOD, which indicate the formation of the soil plug. The increase in stresses seen during BOD in these cases is more due to the increase in the soil strength due to the delay. The results presented in Fig. 5 indicate that the stresses in soil plug are also increased after the delay,

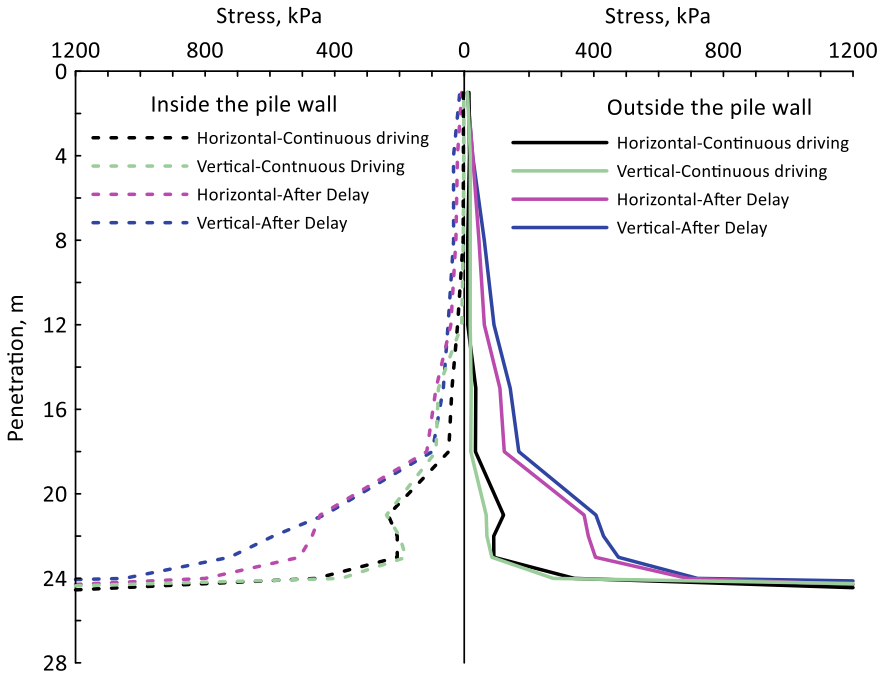


Fig. 4 Stresses in the soil along the pile wall

mainly the horizontal stresses are higher compared to vertical stresses near the pile tip which indicates the formation stronger soil plug near the pile tip.

From the results presented in Figs. 4 and 5, it can be seen that the soil plug formation has started during the EOD. The stresses increased not only in the soil plug but also in the soil around the pile during the driving after delay. This increase in stresses may be due to the soil setup. The formation of the soil plug during continuous driving causes an increase of strength of the soil inside the pile whereas the delay in the pile driving increases not only the strength of the soil plug but also the strength of the soil around the pile. This increase in soil strength leads to an increase of soil stresses during driving.

The stresses in the soil will come back to the state of continuous driving as the driving progresses continuously. The increased strength of the soil/soil plug after a delay in the pile driving is temporary and will reduce as the driving progresses unlike the strength of the soil plug which is formed during the continuous driving which will increase the driving resistance tremendously.

The results shown in Figs. 4 and 5 have clearly brought out the implication of the plug formation on the soil stresses and also the effect of delay time on the increase in soil stresses. The increase in soil strength (and stresses) leads to higher resistance in pile driving (larger number of blows). For example, the number of

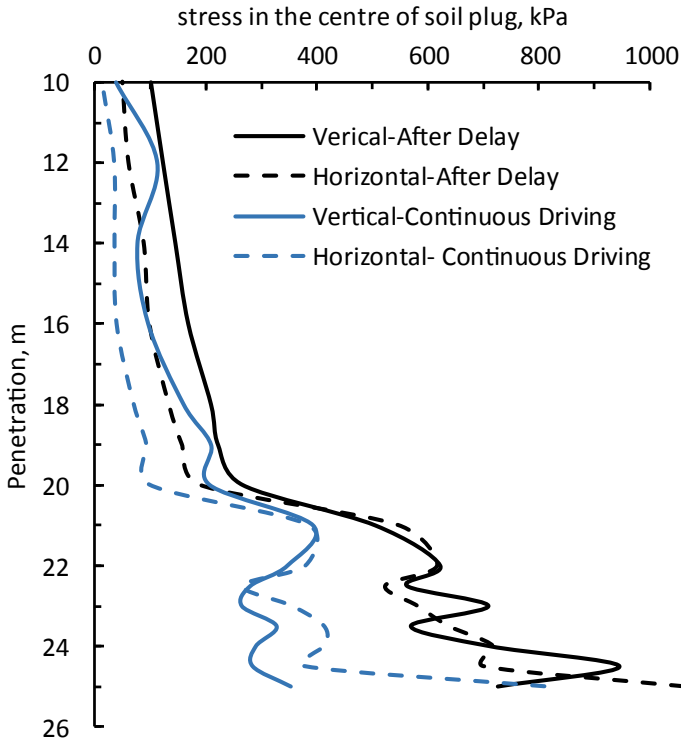


Fig. 5 Stresses at the centre of the soil plug

blows required for 250 mm penetration at EOD was around 28 blows while this number of blows has increased to around 100 blows at similar energy after the delay.

Acknowledgements The authors wish to thank M/s Somehsa Geosciences Pte. Ltd. for providing the field test data.

References

1. Bowles JE (1996) Foundation analysis and design. McGraw-Hill
2. FLAC3D v6.00 Manual (2017) Fast lagrangian analysis of continua, Itasca Consulting Group Inc., USA
3. Masouleh SF, Fakharian K (2008) Application of a continuum numerical model for pile driving analysis and comparison with a real case. *Comput Geotech* 35(3):406–418
4. Nath B (1990) A continuum method of pile driving analysis: comparison with the wave equation method. *Comput Geotech* 10(4):265–285

5. Pinto PL, Grazina JC (2008) Evaluation of 1D and 2D numerical modelling techniques of dynamic pile testing. In: Proceedings of the 8th international conference on the application of the stress-wave theory to piles, Lisbon, Portugal, Sept 8–10
6. Smith EAL (1960). Pile-driving analysis by the wave equation. *J Soil Mech Found Div* 86(EM 4): 35–61

A Study on the Seismic Behaviour of Embankments with Pile Supports and Basal Geogrid



Radhika M. Patel, B. R. Jayalekshmi and R. Shivashankar

Abstract For constructing the roads on soft grounds, basal geogrid-reinforced pile-supported embankments are a suitable solution over other conventional ground improvement techniques like preloading, embankment slope flattening, removing and replacing the soft soil, etc. Many studies are available on these basal geogrid-reinforced piled embankments to understand their behaviour under static loading conditions. But it is necessary to understand the behaviour of these geogrid-reinforced piled embankments under seismic excitations. Hence, finite element analysis of three-dimensional models of embankment having crest width of 20 m, height above ground of 6 m, with side slopes of 1V:1.5H consisting of pulverized fuel ash, overlying soft marine clay of 28 m thickness is carried out under seismic excitations corresponding to Zone III (IS:1893). Soft marine clay layer is improved by the addition of piles arranged in square grid pattern with 5.75% area replacement ratio. Geogrid with a tensile modulus of 4600 kN/m is used as the basal reinforcement. Initially, the embankment is analyzed without geogrid reinforcement and pile supports. Then, it is analyzed with (i) Basal geogrid (ii) With pile supports (iii) With basal geogrid and pile supports. The influence of various parameters of the embankment on maximum crest displacements, differential settlements at crest, toe horizontal displacements, stresses at pile head and foundation soil between piles and pile bending moment along the depth at peak acceleration are studied. Analysis of results shows that the embankment supported over piles with basal geogrid reinforcement will experience less crest settlements, differential settlements at crest and toe horizontal displacements due to earthquake load.

Keywords Embankment · Seismic excitations · Pile foundations · Geogrid reinforcement · Finite element method

R. M. Patel (✉) · B. R. Jayalekshmi · R. Shivashankar
National Institute of Technology Karnataka, Surathkal, Karnataka, India
e-mail: radikagmpatel@gmail.com

© Springer Nature Singapore Pte Ltd. 2020
A. Prashant et al. (eds.), *Advances in Computer Methods and Geomechanics*, Lecture Notes in Civil Engineering 56,
https://doi.org/10.1007/978-981-15-0890-5_22

1 Introduction

Population increase demands for the construction of buildings, bridges, embankments and roads in soft unfavourable grounds also. It is well known that for the construction of roads in these soft grounds, basal geogrid-reinforced pile-supported embankments are a suitable solution over the conventional ground improvement techniques like preloading, embankment slope flattening, removing and replacing the soft soil with good bearing soil, use of vertical drains, etc.

Liu et al. [18], Zhao et al. [30], Yu and Bathurst [28], Bhasi and Rajagopal [6], Ariyaratne and Liyanapathirana [2], Bhasi and Rajagopal [5], Han et al. [11], Wachman et al. [23], Yoo and Kim [27], Smith and Filz [20], Han and Gabr [10] and many others did numerical analysis to understand the load transfer mechanism, time-dependent behaviour and settlements at different parts of geogrid-reinforced piled embankments subjected to static loading conditions. Shen et al. [21], Wang et al. [24, 25], Briançon and Simon [4] conducted experiments and Liu et al. [17] and Zhang et al. [29] reported case studies on these geogrid-reinforced piled embankments to understand their behaviour subjected to static loads with consolidation.

Han et al. [12] and Thach et al. [21, 22] analyzed geogrid-reinforced piled embankments subjected to cyclic loading. Panah et al. [19] and Wang et al. [24, 25] studied the seismic performance of reinforced rigid retaining walls using large-scale shaking table tests. Armstrong et al. [1] performed dynamic centrifuge model tests to investigate pile-pinning effects for the embankment resting over piles. Yet there is a need to understand the behaviour of geogrid-reinforced piled embankments subjected to seismic excitations better because these embankments should stand safe during disaster situations like earthquakes also.

This paper investigates the effect of addition of (i) Basal geogrid (ii) Piles (iii) Basal geogrid and piles for the embankment supported over soft marine clay under seismic excitations in terms of maximum crest displacements, differential settlements at crest, toe horizontal displacements, stresses at pile head and foundation soil between piles and pile bending moment.

2 Methodology

2.1 Numerical Analysis

A 6 m high embankment made of pulverized fuel ash (PFA) with 20 m crest width constructed over 28 m thick soft marine clay has been considered for the time history analysis. Hard stratum exists below the clay layer. Soft marine clay is improved with (i) Basal geogrid (ii) Piles (iii) Basal geogrid and piles and the different cases are shown in Fig. 1.

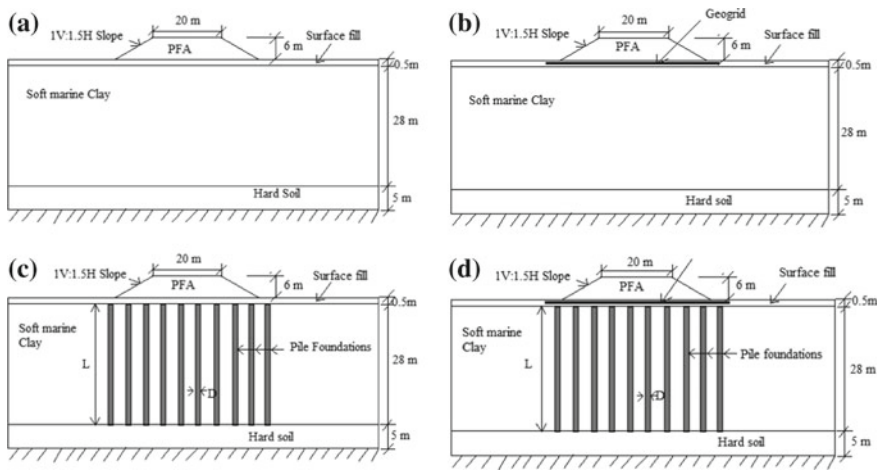


Fig. 1 Different cases of soft marine clay improvement considered for the study (i) Without geogrid and piles (ii) With Geogrid (iii) With Piles (iv) With geogrid and piles

2.2 Idealization of Soil

All the soils for the finite element analysis are modelled as Mohr–coulomb material model. Because Mohr–coulomb model is one of the simple and basic soil models and it can be able to give good results. The properties of PFA, surface fill [17], soft marine clay having same properties of clay as in Cochin region [13] and hard soil considered for the analysis are listed in Table 1. Since the soft marine clay considered is having very less permeability, the effect of pore pressure is not considered in the analysis.

Table 1 Soil properties

Soil type	Density (kN/m ³)	Young’s modulus (MN/m ²)	Poisson’s ratio	Angle of internal friction	Cohesion (kN/m ²)
PFA	18.5	20	0.3	30°	10
Surface fill	18.5	7	0.3	28°	15
Soft Marine clay	13.8	4	0.45	2°	12.5
Hard soil	20.6	250	0.3	40°	50

2.3 Idealization of Pile Foundation

End bearing piles of length (L) 28 m having 300 mm diameter (D) arranged in a square grid pattern are considered. The piles are designed according to BS8006 and the designed area replacement ratio (Ratio of the area shared by piles to the total area. [10] is 5.75%. The piles will behave as linear elastic at an acceleration of 0.1 g. Hence, piles were modelled as linear elastic isotropic material with modulus of elasticity corresponding to M20 grade concrete, density 25 kN/m³ and Poisson's ratio 0.15.

2.4 Idealization of Reinforcement

For the 6 m high embankment considered, tensile strength design for the basal geogrid reinforcement is done according to BS8006. Based on the design, geogrid with a tensile modulus of 4600 kN/m and Poisson's ratio of 0.3 with linear elastic isotropic material property is used as basal geogrid.

2.5 Modelling

Three-dimensional finite element modelling is performed using general-purpose finite element software ANSYS because this software is capable of modelling the soil–pile interaction and time history analysis. Both soil and piles are modelled using SOLID65 element. It is an eight-noded element with three degrees of freedom at each node: translations in the nodal x, y and z directions. Geogrid is modelled using SHELL181 element with membrane effect. It is a four-noded element with three translational degrees of freedom at each node. Soil–pile interaction is achieved by sharing the common nodes at the interface between soil and pile with soil having angle of internal friction properties (Table 1). Three-dimensional finite element model of embankment, pile and geogrid are shown in Fig. 2.

2.6 Boundary Conditions

For time history analysis, lateral boundary is taken as four times the base width of the embankment so that the waves propagated from the soil cannot reflect back

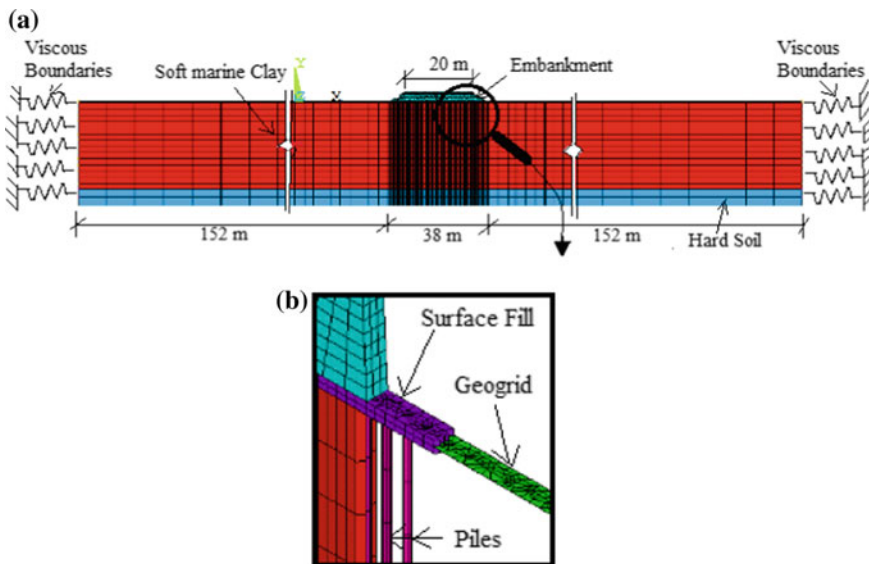


Fig. 2 a Finite element model of embankment. b Enlarged view of geogrid-reinforced pile-supported embankment

Ghosh and Wilson [9]. Viscous boundaries are applied for the lateral boundaries using spring-damper element to simulate the infinite soil medium [7]. The equation of motion with additional damping matrix C^* can be written as follows when the viscous boundaries are taken into account.

$$[M]\{\ddot{u}(t)\} + [C]\{\dot{u}(t)\} + [C^*]\{\dot{u}(t)\} + [K]\{u(t)\} = -[M]\{\ddot{u}_g(t)\}. \quad (1)$$

where $[M]$ is the structural mass matrix, $[C]$ is the structural damping matrix, $[K]$ is the structural stiffness matrix, $\{\ddot{u}_g(t)\}$ is the ground acceleration vector, $\{\ddot{u}(t)\}$ is the nodal acceleration vector, $\{\dot{u}(t)\}$ is the nodal velocity vector, $\{u(t)\}$ is the nodal displacement vector and $[C^*]$ is the special damping matrix that is considered as follows:

$$[C^*] = \begin{bmatrix} A_n \rho v_p & 0 & 0 \\ 0 & A_{t1} \rho v_s & 0 \\ 0 & 0 & A_{t2} \rho v_s \end{bmatrix}$$

where v_p and v_s are the dilatational and shear wave velocity of the considered medium, ρ is the density of soil medium, A_n , A_{t1} and A_{t2} are the fields controlling

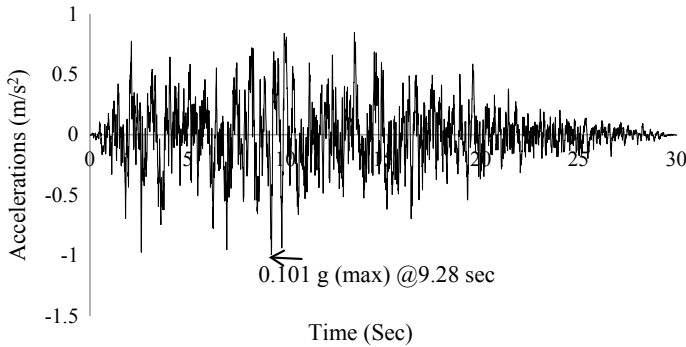


Fig. 3 Time history of IS-1893 ground motion for Zone III spectrum

the viscous dampers and the subscripts n and t represent normal and tangential directions in the boundary.

2.7 Loading

The present study considers embankments situated at sites classified as earthquake zone III under seismic zoning of India. Hence, the embankment is subjected to time history of accelerations corresponding to Indian Standard (IS-1893) code spectrum for Zone III. The time history plot of IS code Zone III spectrum is shown in Fig. 3. The macro developed by Sahin, 2010; was used accordingly in ANSYS software for time history loading.

3 Results and Discussions

3.1 Crest Displacements

Figure 4 shows the time history of embankment vertical displacements at crest centre and crest edge for all the four cases considered. Table 2 shows the maximum vertical displacements at embankment crest due to earthquake loading. From Fig. 4 and Table 2, it is observed that the crest centre and crest edge vertical displacements are very large for the embankment resting over soft clay without basal geogrid and piles. Since the depth of soft clay is very large, the addition of basal geogrid could reduce only 0.3% vertical displacements.

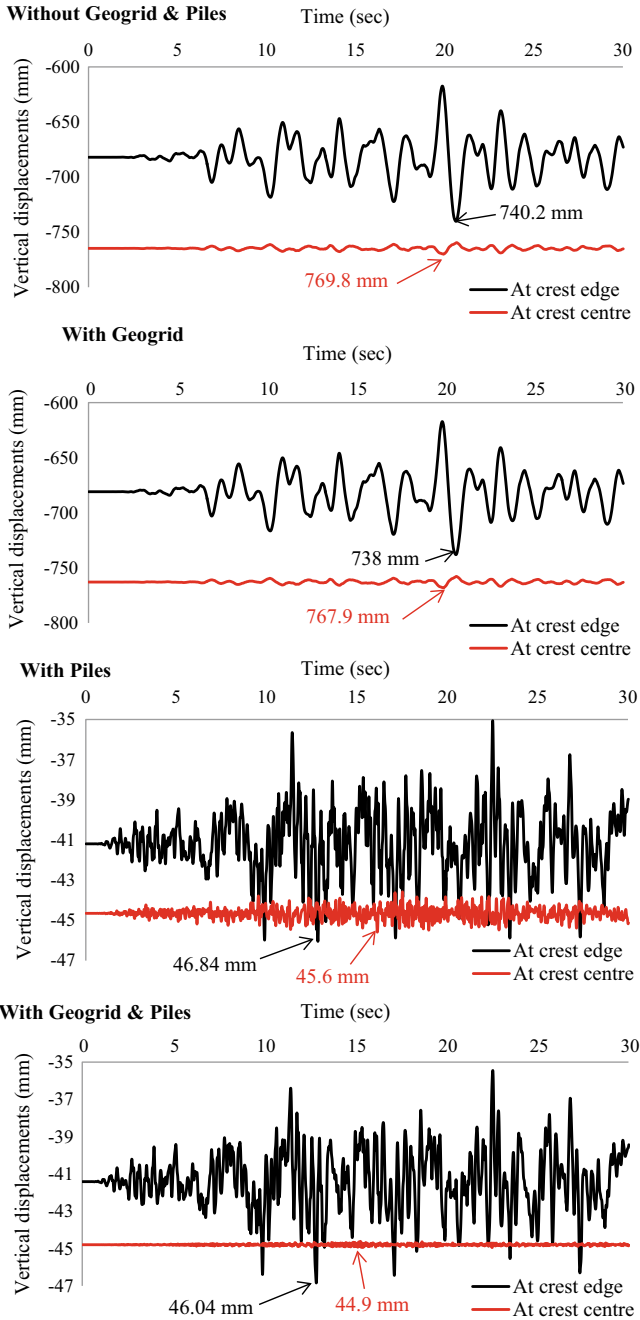


Fig. 4 Time history of embankment vertical displacements at crest centre and edge

Table 2 Maximum vertical displacement and differential settlement at embankment crest

Embankment support condition	Maximum vertical displacement (mm)		Maximum differential settlement (mm)
	At crest centre	At crest edge	
Without geogrid & Piles	769.8	740.2	152.34
With geogrid	767.9	738	150.66
With piles	45.6	46.84	9.6
With geogrid and piles	44.9	46.04	9.31

But the addition of piles could reduce 93.67 and 94% of crest edge and crest centre displacements. Addition of basal geogrid and piles also reduces 93.7 and 94.2% of crest edge and crest centre displacements.

3.2 Differential Settlements at Crest

Table 2 shows the differential settlements at embankment crest (Difference in settlement between crest centre and edge at every time interval) subjected to earthquake loading. It is observed from Fig. 4 and Table 2 that embankment without basal geogrid and piles experiences more differential settlement. Very less reduction in the differential settlement is observed by adding the basal geogrid. Similar to vertical displacements, addition of piles reduces more than 90% of differential settlements. But further reduction in differential settlements is seen by the addition of geogrid and piles. This is due to the fact that the basal geogrid acts as flexible raft above piles and transfers embankment loads to the piles more effectively.

3.3 Toe Horizontal Displacements

Figure 5 shows the time history of embankment toe horizontal displacements for all the four cases of ground improvement considered. It is seen from Fig. 5 that embankment without geogrid and pile supports undergo more toe horizontal displacements. It is also observed from Fig. 5 that the addition of geogrid could able to reduce about 0.8% of toe horizontal displacements. But the addition of piles reduces the toe horizontal displacements up to 15.5%.

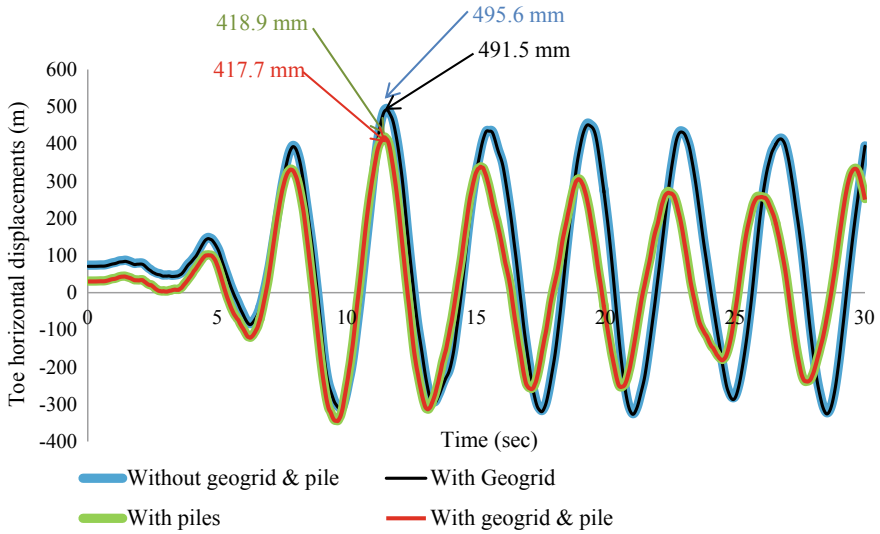


Fig. 5 Time history of embankment toe horizontal displacements

3.4 Stresses at Pile Head and Foundation Soil Between Piles

Figure 6 shows the time history of stresses at pile head and foundation soil between piles measured at peak ground accelerations. From Fig. 6 it is observed that the addition of basal geogrid above pile supports further reduces the stresses in the foundation soil when compared to the addition of only piles. This reduces the risk of foundation soil failure by maximum stresses.

3.5 Pile Bending Moment

Figure 7 shows the bending moment along the depth of the pile measured at peak ground acceleration (PGA). The piles considered for the study are end bearing piles and just bearing on the hard stratum, hence the bending moment at the bottom tip of the pile is very high. A similar variation of bending moment is observed from Dezi et al. [8]. It is observed from Fig. 7 that the addition of basal geogrid along with piles increases the bending moment in piles.

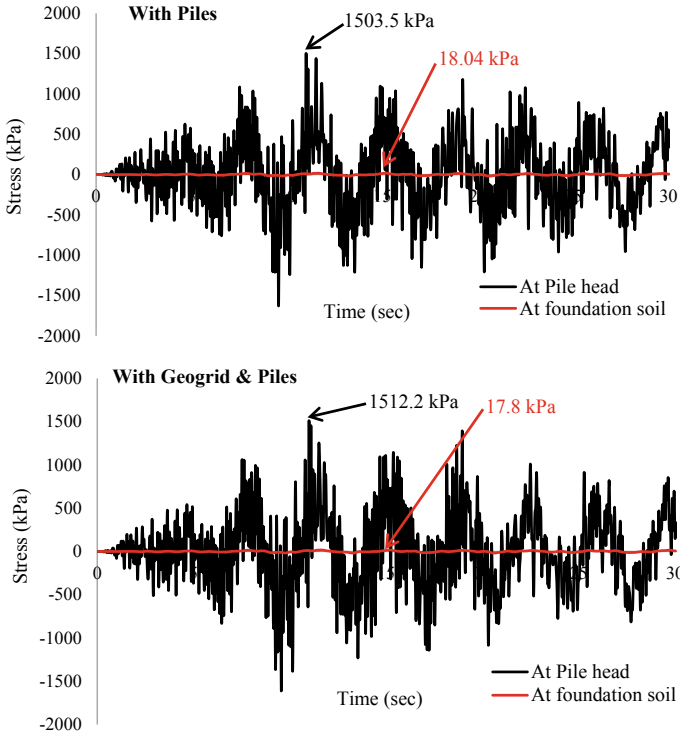
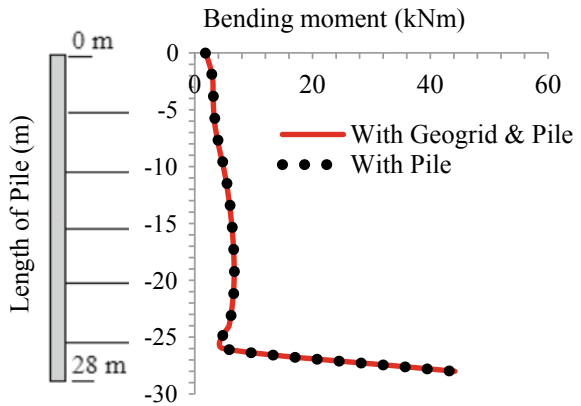


Fig. 6 Time history of stresses at the pile head and foundation soil between piles

Fig. 7 Bending moment along the depth of the pile at PGA



4 Conclusions

Time history analysis was conducted for a three-dimensional finite element model of embankment supported over soft marine clay improved with or without basal geogrid and pile supports.

Analysis of results revealed that the addition of pile supports reduces more than 90% of vertical displacements at embankment crest. Also, due to the large depth of soft marine clay, addition of basal geogrid alone could able to reduce very little vertical displacements.

The differential settlement at crest was also considerably reduced by the addition of pile supports. Further reduction in differential settlements is observed by the addition of geogrid along with the piles.

Addition of piles reduces the toe horizontal displacements up to 15.5%. But the addition of basal geogrid reduces only 0.8% of toe horizontal displacements.

Foundation soil between piles experienced less stress by the addition of basal geogrid. This reduces the risk of foundation soil failure by maximum stresses. Also, the addition of basal geogrid increases the bending moment in piles.

References

1. Armstrong RJ, Boulanger RW, Beaty MH (2013) Liquefaction effects on piled bridge abutments: centrifuge tests and numerical analyses. *J Geotech Geoenvironmental Eng ASCE* 139(3):433–443
2. Ariyaratne P, Liyanapathirana DS (2015) Review of existing design methods for geosynthetic-reinforced pile-supported embankments. *J Soils Found* 55:17–34
3. BS 8006:2010. Code of practice for strengthened/reinforced soils and other fills. British Standard Institution, UK
4. Briançon L, Simon B (2011) Performance of pile-supported embankment over soft soil: full-scale experiment. *J Geotech Geoenvironmental Eng* 138(4):551–561
5. Bhasi A, Rajagopal K (2014) Geosynthetic-reinforced piled embankments: comparison of numerical and analytical methods. *Int J Geomech ASCE*. 15(5):04014074
6. Bhasi A, Rajagopal K (2015) Numerical study of basal reinforced embankments supported on floating/end bearing piles considering pile-soil interaction. *Geotext Geomembr* 43:524–536
7. Cakir T (2013) Evaluation of the effect of earthquake frequency content on seismic behavior of cantilever retaining wall including soil–structure interaction. *Soil Dyn Earthq Eng* 45: 96–111
8. Dezi F, Carbonari S, Leoni G (2010) Kinematic bending moments in pile foundations. *Soil Dyn Earthq Eng* 30(3):119–132
9. Ghosh S, Wilson EL (1969) Analysis of axi-symmetric structures under arbitrary loading, no. 69–10, EERC Report
10. Han J, Gabr MA (2002) A numerical study of load transfer mechanisms in geosynthetic reinforced and pile supported embankments over soft soil. *J Geotech Geoenvironmental Eng ASCE* 128(1):44–53

11. Han J, Bhandari A, Wang F (2011) DEM analysis of stresses and deformations of geogrid-reinforced embankments over piles. *Int J Geomech* 12(4):340–350
12. Han GX, Gong QM, Zhou SH (2014) Soil arching in a piled embankment under dynamic load. *Int J Geomech* 15(6):04014094
13. IRC:113-2013 Guidelines for the design and construction of geosynthetic reinforced embankments on soft subsoils
14. IS 1893(Part 1):2016. Criteria for earthquake resistant design of structures
15. Jose BT, Sridharan A, Abraham BM (1988) A study of geotechnical properties of Cochin marine clays. *Mar Georesour Geotechnol* 7(3):189–209
16. Kianoush MR, Ghaemmaghami AR (2011) The effect of earthquake frequency content on the seismic behavior of concrete rectangular liquid tanks using the finite element method incorporating soil–structure interaction. *Eng Struct* 33(7):2186–2200
17. Liu HL, Ng CWW, Fei K (2007) Performance of a geogrid-reinforced and pile-supported highway embankment over soft clay: case study. *J Geotech Geoenvironmental Eng ASCE* 133(12):1483–1493
18. Liu KW, Rowe RK, Su Q, Liu B, Yang Z (2017) Long-term reinforcement strains for column supported embankments with viscous reinforcement by FEM. *Geotext Geomembr* 45(4): 307–319
19. Panah AK, Yazdi M, Ghalandarzadeh A (2015) Shaking table tests on soil retaining walls reinforced by polymeric strips. *Geotext Geomembr* 43(2):148–161
20. Smith M, Filz G (2007) Axisymmetric numerical modeling of a unit cell in geosynthetic-reinforced, column-supported embankments. *Geosynth Int* 14(1):13–22
21. Shen P, Xu C, Han J (2017) Model tests investigating spatial tensile behavior of simulated geosynthetic reinforcement material over rigid supports. *J Mater Civ Eng* 30(2):04017288
22. Thach PN, Liu HL, Kong GQ (2013) Evaluation of PCC pile method in mitigating embankment vibrations from a high-speed train. *J Geotech Geoenvironmental Eng* 139(12): 2225–2228
23. Thach PN, Liu HL, Kong GQ (2013) Vibration analysis of pile-supported embankments under high-speed train passage. *Soil Dyn Earthq Eng* 55:92–99
24. Wachman GS, Biolzi L, Labuz JF (2009) Structural behavior of a pile-supported embankment. *J Geotech Geoenvironmental Eng* 136(1):26–34
25. Wang C, Wang B, Guo P, Zhou S (2015) Experimental analysis on settlement controlling of geogrid-reinforced pile-raft-supported embankments in high-speed railway. *Acta Geotech* 10 (2):231–242
26. Wang L, Chen G, Chen S (2015) Experimental study on seismic response of geogrid reinforced rigid retaining walls with saturated backfill sand. *Geotext Geomembr* 43(1):35–45
27. Yoo C, Kim SB (2009) Numerical modeling of geosynthetic-encased stone column-reinforced ground. *Geosynth Int* 16(3):116–126
28. Yu Y, Bathurst RJ (2017) Modelling of geosynthetic-reinforced column-supported embankments using 2D full-width model and modified unit cell approach. *Geotext Geomembr* 45(2): 103–120
29. Zhang C, Jiang G, Liu X, Buzzi O (2016) Arching in geogrid-reinforced pile-supported embankments over silty clay of medium compressibility: field data and analytical solution. *Comput Geotech* 77:11–25
30. Zhao LS, Zhou WH, Yuen KV (2017) A simplified axisymmetric model for column supported embankment systems. *Comput Geotech* 92:96–107

Parametric Investigation of Bridge Piers Reinforced with Shape-Memory Alloys in Plastic Hinge Regions



Kanan Thakkar and Anant Parghi

Abstract Bridge piers are one of the most vulnerable structural elements in a bridge system. The past earthquake reconnaissance report showed that the bridge structures with high residual displacements were unserviceable for the future use after a seismic event. Subsequently, post-disaster rescue and relief operations were rigorously affected. Generally, it is presumed that the utmost seismic demand in a bridge will focus in a small zone, which has a maximum inelastic curvature called as its plastic hinge length. As the bridge pier's plastic hinge zone governs the load carrying and deformation capabilities of the entire pier, hence it has achieved remarkable focus to structural designers for the last decades to improve the ductility of a pier. Shape memory alloy (SMA) is distinctive class of smart materials, which can sustain the enormous amount of inelastic deformations and reappear to its parental shape after removal of stress or loading. Substituting the typical steel reinforcement in the plastic hinge region of a bridge pier with super-elastic SMA could diminish the damages of a pier. The present research is focused on the numerical investigation on circular concrete bridge piers reinforced with SMA rebars in plastic hinge region and rest part of a pier reinforced with conventional steel under the effect of monotonic static loads. The parameters considered in this study are plastic hinge length and material properties of SMA. Nonlinear static pushover analysis is performed to compare the behavior of steel-RC and SMA-RC bridge piers under the effect of monotonic load. The results are presented in terms of base shear, displacement, ductility and limit state performance criteria of bridge piers.

Keywords Shape-Memory Alloy · Plastic hinge length · Bridge piers · Static pushover analysis

K. Thakkar (✉) · A. Parghi
Department of Applied Mechanics, S. V. National Institute of Technology,
Gujarat 395 007 Surat, India
e-mail: kananrthakkar@gmail.com

A. Parghi
e-mail: amp@amd.svnit.ac.in

1 Introduction

Highway bridges possess a considerable role in the transportation system of any country. The failure of bridge piers is devastating for the entire bridge structure, as they are one of the most susceptible structural elements in a bridge system. The bridges located in the high seismic region and designed according to current seismic design guidelines are liable to major damages during large earthquakes causing huge residual displacements [29]. Subsequently, post-disaster respite and release operations were rigorously affected. Thus, it shows a consensus of the structural engineer that residual displacement is the vital parameter in the performance of structures during seismic events. The reinforced concrete (RC) bridges longitudinally reinforced with steel bars undergo large plastic deformations to dissipate the seismic energy under the action of seismic load. This results in significant residual displacement which could make a bridge structure unstable [9, 23]. In order to address these issues, novel smart material such as super-elastic shape-memory alloy (SMA) is being explored since last decade, which could be used as an alternative of conventional steel rebar and which is capable to re-center after a seismic event [12]. SMAs are metallic alloys that can undergo large strains, while recovering their initial configuration after unloading (super-elastic effect) or by heating (shape-memory effect), without any permanent deformation [11]. Alam et al. [2] investigated various compositions and properties of SMA, such as Ni-Ti, Cu-Zn, Cu-Zn-Al, Cu-Al-Ni, Fe-Mn, Mn-Cu, Fe-Pd, and Ti-Ni-Cu. Among these, Ni-Ti-based SMA found to be the most appropriate SMA for structural applications because of its large recoverable strain, super-elasticity and exceptionally good resistance to corrosion [2]. The re-centering phenomenon of SMA-RC structure is unique and interesting feature for the structural applications [1]. Subsequently, to reduce the residual displacement in bridge piers after major earthquakes, many innovative methods were explored in the last decade, i.e., providing SMA-based base isolation systems, dampers, energy dissipation devices, replacing SMA rebars with conventional steel rebars, Providing SMA connectors, etc. [2, 15, 29]. For instance, one of the innovative methods is to replace the conventional longitudinal steel reinforcement in the plastic hinge region of bridge piers with super-elastic SMA-based reinforcements [29].

2 The Scope of Previous Research

SMA is emerging as a viable solution in context of the performance of structures under seismic load [22]. By replacing steel rebar with SMA rebar in the plastic hinge area of a bridge pier, many issues of safety and stability can be resolved. Since last decade, researchers have conducted extensive investigations exploring different structural applications and developing innovative devices making use of the distinctive characteristics of smart materials [4, 7, 22]. SMA offers numerous

structural applications, namely reinforcement in reinforced concrete, connectors in steel and concrete structures, damping devices, base isolation devices [22], seismic retrofit and serving as an active or passive confinement techniques in terms of pre-stressing and post-tensioning [2]. Over the last decade, a number of different applications of SMA in bridges have been investigated to improve the seismic performance of structures. Researchers have suggested inventive structural systems, such as SMA-RC bridge piers and decks with pre-stressed SMA wires, with the aim of reducing the residual/permanent displacement of bridge piers [27–29]. The reduction in the vulnerability of SMA-RC bridge piers was reported by Billah and Alam [8], owing to the high re-centering ability of SMA.

The literature shows that SMA-based smart RC structures are advantageous to reduce the large residual deformation after seismic events. The super-elastic SMA could be used as the most suitable reinforcements in plastic hinge area of RC structures. Furthermore, there is a limited research available on the parametric study of bridge piers utilizing SMA as an alternate of steel reinforcement in plastic hinge region to assess the seismic performance of bridge piers. Recently, there are no codes/guidelines available in the existing literature for the use of super-elastic SMA as an alternative reinforcement with conventional steel. Therefore, it is necessary to conduct a parametric investigation using the SMA in the plastic hinge region to improve the ductility of bridge piers.

3 Numerical Investigation of Bridge Piers

This research focuses on the seismic performance of bridge piers with super-elastic SMA reinforcement in the plastic hinge region and other part reinforced with conventional steel under nonlinear static load. The behavior of super-elastic SMA reinforced piers under nonlinear monotonic load has been investigated and compared with conventional steel-reinforced piers using finite element program (SeismoStruct 2018). A parametric study has been performed for the bridge piers reinforced with SMA in the plastic hinge region. Based on existing literature on plastic hinge length of SMA-RC bridge piers, three plastic hinge lengths have been selected for this study: $0.5 L_p/d$, $0.75 L_p/d$, and $1.0L_p/d$ along with three different yield strengths of the SMA. Following parameters are considered for the numerical modeling of the bridge piers as shown in Table 1.

Table 1 Parameters of Steel-RC and SMA-RC bridge piers

Parameters	Values
Diameter (D) (m)	1.22
Height (H) (m)	7.32
Aspect ratio (H/D)	6.0
Axial load ratio P (%)	5.3
Longitudinal reinforcement ratio (ρ_l) (%)	1.55
Yield strength of SMA rebar (f_y -SMA) (MPa)	210, 401, 750
Plastic hinge length (L_p) (%)	10, 15, 20

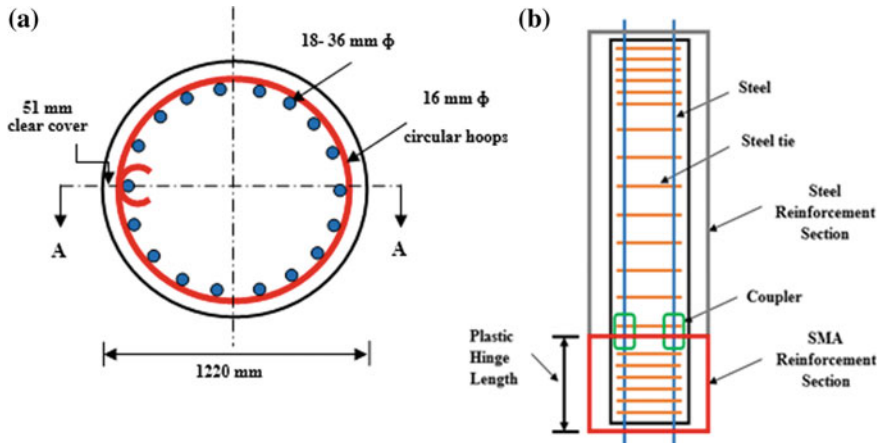


Fig. 1 Geometry and reinforcement details of SMA-RC bridge pier

In this study, a circular bridge pier has been considered for the nonlinear analysis of the bridge piers [27]. Diameter and height of the pier are considered as 1.22 m and 7.32 m, respectively as depicted in Fig. 1. The axial load is used as 5.3% of the axial capacity of a pier, and longitudinal reinforcement ratio (ρ_l) is used as 1.55%. Figure 1a illustrates the geometry of a pier through section A-A, and Fig. 1b shows the longitudinal and lateral reinforcement details of a bridge pier. It defines the steel rebar, SMA rebar, and their connection through a coupler; incorporated for this study.

3.1 Model Validation

The precision of the proposed model has been validated through experimental results by various researchers [3, 26, 30]. However, the proposed analytical model using nonlinear FE program (SeismoStruct) has been compared with the experimental results for the exactness of modeling techniques. The model has been compared with the experimental data proposed by [30] under the Highway Idea Project, University of Nevada, Reno. They conducted an experimental program on 0.2 scaled circular columns using Shape-Memory Alloys in plastic hinge zone. Three columns RSC (conventional concrete and steel reinforcement), RNC (shape-memory alloy longitudinal reinforcement in plastic hinge region) and RNE (engineered cementitious composites in plastic hinge region) were tested under the effects of dynamic loads. The RNC model was validated analytically for this study. The height and diameter of the RNC column were selected as 1143 mm and 254 mm, respectively. The aspect ratio was taken as 4.5. The lateral load was applied at the center of 508 mm cubic loading head on the top of the column. Each

column was reinforced with evenly spaced longitudinal bars in a circular pattern corresponding to 2% longitudinal reinforcement ratio. The column was reinforced with 12.7 mm diameter Ni–Ti rods in the plastic hinge zone and #5 ($\varnothing 15.9$ mm) Grade 60 (414 MPa) steel through the remaining of the column length. Plastic hinge length of 205.7 mm was calculated according to [25] equation and based on the SMA's specified yield strength of 413.7 MPa. The structural displacement of RNC column from the experimental data and analytical data was 114 mm and 122 mm, respectively. The proposed model has been validated with the experimental data with an error of 6.56%. Thus, it can be clinched that the local responses of SMA-RC bridge piers under the effect of dynamic loads can be determined satisfactorily with the adopted nonlinear FE modeling technique.

3.2 *Finite Element Modeling*

To study the seismic performance of super-elastic SMA-RC and steel-RC bridge piers, a finite element (FE) program (SeismoStruct) is adopted in this study. To model a pier, force-based nonlinear beam-column element has been chosen. The fiber section is used to discretize a pier into three parts: core fiber for confined concrete, cover fiber for unconfined concrete, and steel/SMA fiber for reinforcements. These piers are modeled using force-based inelastic system owing to its accuracy [10]. As shown in Fig. 2a, b, there are 5 integration sections and 302 fibers considered across the section for mesh refinement. It has been discretized into 11 FE frames (Fig. 2a) [10]. The pier length is divided into total 11 sections, among which 3 sections represent SMA-reinforced plastic hinge length and remaining sections represent steel-reinforced part of a pier. To model the slippage of super-elastic SMA rebar inside the coupler, a multilinear element is used to incorporate the behavior of the bond-slip model of SMA reinforced bridge piers [5], which was numerically validated by [8].

Takeda hysteresis curve is adopted to define the link element, which can represent a bond-slip model of the bridge pier [21]. At the bottom of a pier, the rotational spring was provided. Figure 2b describes the FE model of a bridge pier. As shown in Fig. 2b, zero-length rotational spring is provided in the bottom of a pier, which represents a mechanical coupler used to connect steel and SMA rebar. An axial load has been applied on the top of a pier as lumped mass, and the footing is assumed as a fixed support [10].

To represent the Ni–Ti reinforcement in FE model, [14] model is adopted. The stress-strain model proposed by [16] succeeding the constitutive behavior developed by [18], and the cyclic rules proposed by [17] with [19] are employed for the confined (i.e., core) concrete and unconfined (i.e., cover) concrete constitutive models. To simulate the behavior of steel reinforcement under cyclic load,

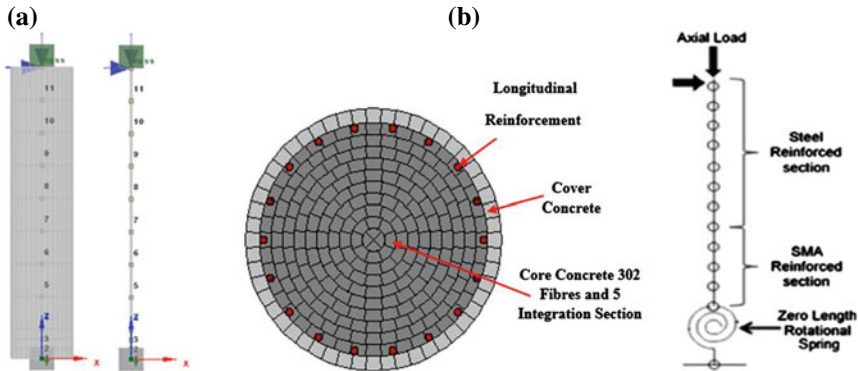


Fig. 2 a Idealized numerical model, b fiber discretization of cross section and finite element modeling of SMA-RC and steel-RC bridge pier [10]

[20] steel model with [31] isotropic strain hardening property is adopted as the constitutive model, which can be expressed as a bilinear kinematic hardening model.

4 Parametric Investigation of the Bridge Piers

In the previous section, a numerical FE model was generated for steel and SMA-reinforced RC bridge pier using a fiber modeling approach [10]. Three different materials properties of SMA (the yield strength of $re_{y} = 210$ MPa, $f_y = 401$ MPa and $f_y = 750$ MPa) and three different plastic hinge lengths (10, 15, and 20% of total length of the pier) have been considered. These total ten numerical models using different plastic hinge lengths and different yield strengths of SMA have been analyzed. The plastic length of the piers was estimated using [25] equation, as it provides a reasonable estimation of plastic hinge length for SMA-reinforced concrete elements [10].

$$L_p = 0.08L + 0.22f_y \cdot d_b \quad (1)$$

where L_p is the plastic hinge length, L is the total height of a pier, f_y is the yield strength of rebar, and d_b is the diameter of rebar. Table 2 depicts the material properties used for the numerical investigation of steel-RC and SMA-RC bridge piers.

For the length (L) of a pier of 7.32 m, rebar size (d_b) of 36 mm, and steel rebar yield strength (f_y) of 518.5 MPa; the potential plastic hinge length is estimated as 749.29 mm [25]. The plastic hinge length depends on axial load, aspect ratio,

Table 2 Materials properties used for Steel-RC and SMA-RC piers

Material	Property	Value
Confined concrete [27]	Compressive strength (MPa)	27.6
	Corresponding strain	0.0029
	Tensile strength (MPa)	3.5
	Elastic Modulus (GPa)	22.9
Longitudinal steel [27]	Elastic Modulus (GPa)	200
	Yield stress (MPa)	519
	Ultimate stress (MPa)	707
	Ultimate strain	0.14
Super-elastic SMA [8]	Yield strength- f_y (MPa)	410
	Modulus of elasticity- E (GPa)	62.5
	Super-elastic plateau strain length- ϵ_s (%)	6
	Austenite to martensite starting stress- f_y (MPa)	401
	Austenite to martensite finishing stress- f_{P1} (MPa)	510
	Martensite to austenite starting stress- f_{T1} (MPa)	370
	Martensite to austenite finishing stress- f_{T2} (MPa)	130

properties of SMA, longitudinal and transverse reinforcements, and strength of confined concrete [10]. Table 3 shows the detail of parameters used for steel-RC and SMA-RC bridge pier for the numerical model.

L_p is the plastic hinge length and $f_y\text{-SMA}$ is the yield strength of SMA rebar.

4.1 Static Pushover Analysis

As shown in the previous sections, bridge piers have been modeled incorporating SMA rebars in the plastic hinge region. A nonlinear static pushover analysis has been done to compare the performances of a conventional pier and a pier reinforced SMA in the plastic hinge region. Figure 3 shows the schematic of a typical pushover analysis of the pier. The bridge piers are modeled with the data mentioned in previous sections with three different plastic hinge lengths: 10, 15, and 20% of the total height of a pier (0.732, 1.098 and 1.464 m), and three different yield strengths of SMA ($f_y = 210$ MPa, $f_y = 401$ MPa and $f_y = 750$ MPa). This study has been performed to investigate the behavior of bridge piers by varying the plastic hinge lengths and the yield strengths of SMA.

Table 3 Details of parameters used for steel-RC and SMA-RC bridge piers

Pier-ID	P00-000	P10-210	P10-401	P10-750	P15-210	P15-401	P15-750	P20-210	P20-401	P20-750
L_p (%)	–	10	10	10	15	15	15	20	20	20
f_y -SMA (MPa)	–	210	401	750	210	401	750	210	401	750

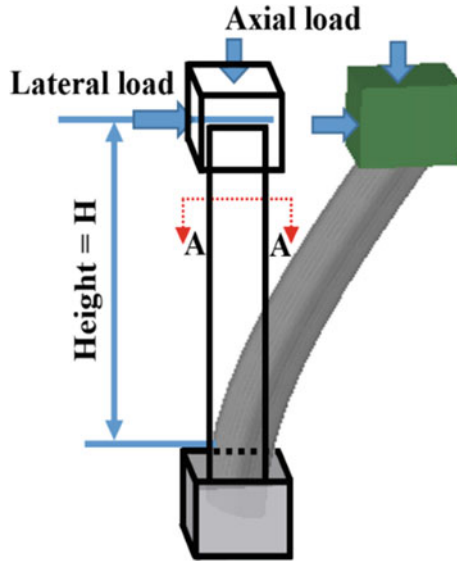


Fig. 3 Schematic of typical pushover analysis of a pier: deformed and undeformed shape [24]

5 Results and Discussion

Figures 4, 5 and 6 demonstrate the comparison of maximum base shear (capacity) versus displacement of the piers with 10, 15, and 20% of plastic hinge lengths, respectively. As seen from these figures, different plastic hinge lengths with the different yield strengths of SMA have different values of base shear and

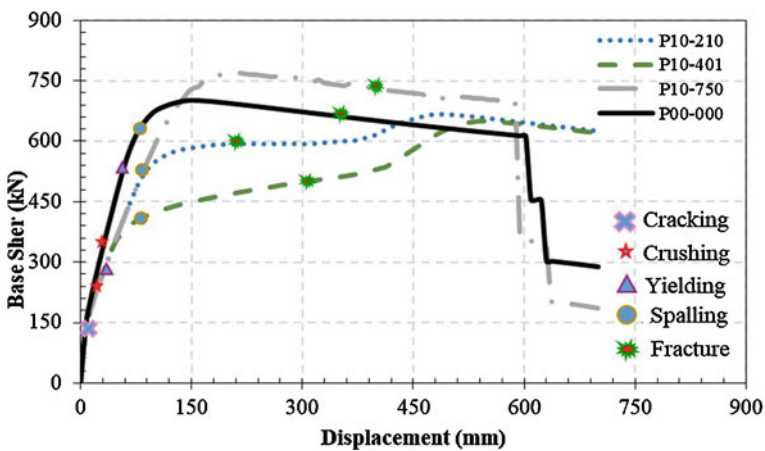


Fig. 4 Capacity curve for piers with 10% plastic hinge length reinforced with SMA ($f_y = 210$ MPa, $f_y = 401$ MPa and $f_y = 750$ MPa)

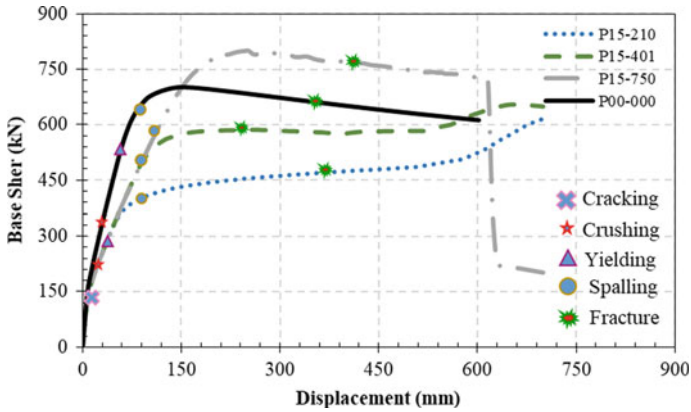


Fig. 5 Capacity curve for piers with 15% plastic hinge length reinforced with SMA ($f_y = 210$ MPa, $f_y = 401$ MPa and $f_y = 750$ MPa)

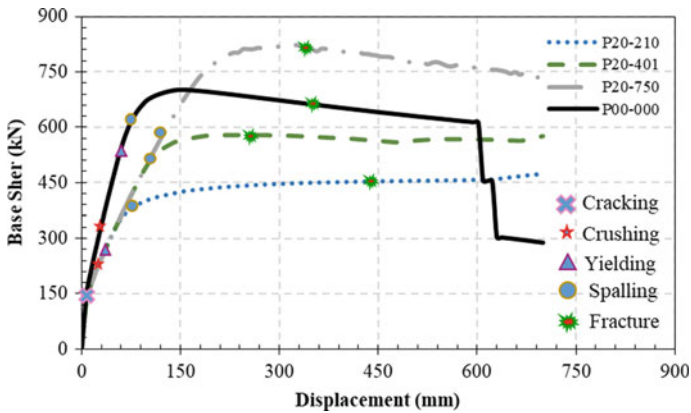


Fig. 6 Capacity curve for piers with 20% plastic hinge length reinforced with SMA ($f_y = 210$ MPa, $f_y = 401$ MPa and $f_y = 750$ MPa)

displacement. Steel-RC and SMA-RC bridge piers act similarly until the unconfined concrete is cracked. They start to behave differently after the cracking of unconfined concrete takes place. For a pier with 10% plastic hinge length reinforced with SMA rebar, an increase in the yield strength of SMA diminishes the capacity of a pier to attract the base shear. A further surge in the yield strength of SMA escalates the capacity of a pier to attract the base shear even more than a pier reinforced with conventional steel rebar as shown in Fig. 4. For the piers with 15 and 20% plastic hinge lengths reinforced with SMA rebar, an increase in the yield strength of SMA proliferates the capacity of a pier to attract the base shear (Figs. 5 and 6).

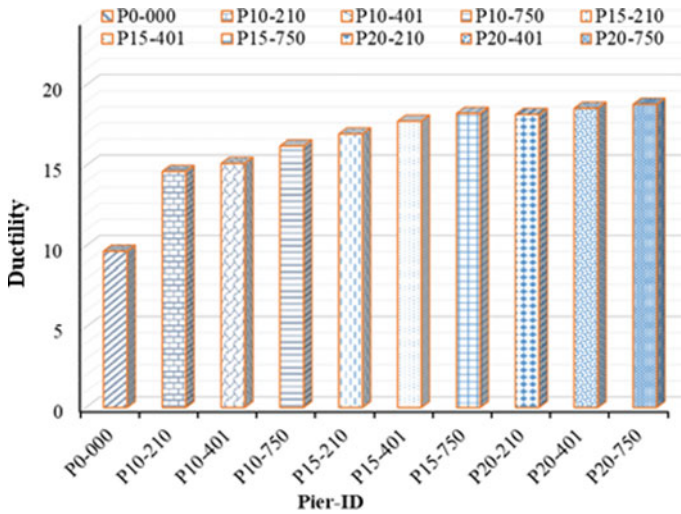


Fig. 7 The displacement ductility of piers with different plastic hinge lengths, and yield strengths of SMA rebar

Ductility is the ability of a material to undergo large inelastic deformation through elongation or bending, without permanent fracturing. The displacement ductility is defined as the ratio of ultimate displacement to yield displacement; $\mu_{\Delta} = \Delta_u/\Delta_y$ [24]. Figure 7 defines a displacement ductility for the ten piers with 10, 15, and 20% plastic hinge lengths reinforced with SMA reinforcement. It is evident from Fig. 7 that the application of SMA contributes more displacement ductility in comparison with the conventional model of a bridge pier. Higher yield strength of SMA leads to the greater ductility of a pier. The similar study has also been done by [6, 13] and they reported the improvement of ductility capacity of the bridge piers. Further, they revealed that the shape-memory effect of SMA increases the ductility, and decreases the residual displacement of the piers during a seismic event.

6 Summary and Limitation of the Use of SMA in Infrastructures

Based on the nonlinear static analysis of circular bridge piers for three different plastic hinge lengths and three different yield strengths of SMA, the following conclusions can be drawn:

- SMA-RC pier spectacles less stiffness due to the lower modulus of elasticity of SMA compared to the conventional steel-reinforced bridge piers.
- Both the steel-RC and SMA-RC bridge piers act similarly until the crack occurs; they start to behave differently afterwards.

- With an increment in SMA rebar length, the capacity of a pier to attract base shear gets decreased. Similarly, an increment in SMA rebar length decreases the stiffness of a pier.
- For 10% plastic hinge length, an increment in the yield strength of SMA decreases the capacity of a pier to attract base shear until certain limits, Further surge in the yield strength of SMA increases the capacity of a pier to attract base shear. Additionally, for 15 and 20% plastic hinge lengths, an increment in yield strength of SMA increases the capacity of a pier to attract base shear.
- An increment in SMA rebar length increases the ductility of a pier. The pier becomes more ductile, and it can sustain larger values of deformation when the conventional steel rebar is replaced with super-elastic SMA rebar in the plastic hinge region of a pier.

There is a considerable potential for the utilization of super-elastic SMA in civil infrastructures; however, the cost of SMA is a main concealing factor. Because of the large size of structural elements, higher forces need remarkable amount of the materials; hence, it is a big issue for the application of expensive super-elastic SMA in civil infrastructures. Thus, in order to initiate the large-scale applications, the development of low-cost SMA is mandatory for a reduction of global cost. Although, researchers have found a significant reduction in the cost of Ni–Ti over the last decade. Moreover, the researchers have initiated to utilize low-cost iron-based SMA in civil infrastructures.

References

1. Abdulridha A, Palermo D, Foo S, Vecchio FJ (2013) Behavior and modeling of superelastic shape memory alloy reinforced concrete beams. *Eng Struct* 49:893–904. <https://doi.org/10.1016/j.engstruct.2012.12.041>
2. Alam MS, Nehdi M, Youssef MA (2008) Shape memory alloy-based smart RC bridges: overview of state-of-the-art. *Smart Struct Syst* 4(3):367–389. <https://doi.org/10.12989/sss.2008.4.3.367>
3. Alam MS, Nehdi M, Youssef MA (2009) Seismic performance of concrete frame structures reinforced with superelastic shape memory alloys. *Smart Struct Syst* 5:565–585
4. Alam MS, Youssef MA, Nehdi M (2007) Utilizing shape memory alloys to enhance the performance and safety of civil infrastructure: a review. *Can J Civ Eng* 34(9):1075–1086. <https://doi.org/10.1139/l07-038>
5. Alam MS, Youssef MA, Nehdi ML (2010) Exploratory investigation on mechanical anchors for connecting SMA bars to steel or FRP bars. *Mater Struct* 43:91–107. <https://doi.org/10.1617/s11527-010-9601-0>
6. Andrawes B, Shin M (2008) Seismic retrofitting of bridge columns using shape memory alloys. In: *SPIE—the international society for optical engineering*, vol 6928, pp 69281K–1–9. <https://doi.org/10.1117/12.775480>
7. Bajoria KM, Kaduskar S (2016) A review on: shape memory alloy and its application in civil structures. *Int J Eng Res* 5(3):721–724
8. Billah M, Alam MS (2012) Seismic performance of concrete columns reinforced with hybrid shape memory alloy (SMA) and fiber reinforced polymer (FRP) bars. *Constr Build Mater* 28 (1):730–742. <https://doi.org/10.1016/j.conbuildmat.2011.10.020>

9. Billah M, Alam MS (2015) Seismic fragility assessment of concrete bridge pier reinforced with superelastic shape memory alloy. *Earthq Spectra* 31(3):1515–1541. <https://doi.org/10.1193/1.12512EQS337M>
10. Billah M, Alam MS (2016) Plastic hinge length of shape memory alloy (SMA) reinforced concrete bridge pier. *Eng Struct* 117:321–331. <https://doi.org/10.1016/j.engstruct.2016.02.050>
11. Boroschek RL, Farias G, Moroni O, Sarrazin M (2007) Effect of SMA braces in a steel frame building. *J Earthq Eng* 11(3):326–342. <https://doi.org/10.1080/13632460601125763>
12. Cai CS, Wu W, Chen S, Voyiadjis G (2003) Applications of smart materials in structural engineering. Department of Civil Engineering Louisiana State University Baton Rouge, Louisiana 70803 LTRC Project No. 02-4TIRE State Project No. 736-99-1055
13. Dong J, Cai CS, Okeil AM (2011) Overview of potential and existing applications of shape memory alloys in bridges. *J Bridge Eng* 16(2):305–315. [https://doi.org/10.1061/\(ASCE\)BE.1943-5592.0000145](https://doi.org/10.1061/(ASCE)BE.1943-5592.0000145)
14. Fugazza D (2003) Shape-memory alloy devices in earthquake engineering: mechanical properties, constitutive modelling and numerical simulations. European school of advanced studies in reduction of seismic risk, pp 1–141
15. Hedayati-Dezfuli F, Alam MS (2015) Seismic vulnerability assessment of a multi-span continuous steel-girder bridge isolated by SMA wire-based natural rubber bearings (SMA-NRB). In: Structures congress 2015—proceedings of the 2015 structures congress. <https://doi.org/10.1061/9780784479117.052>
16. Madas P (1993) Advanced modelling of composite frames subjected to earthquake loading. Ph.D. Thesis, Imperial College, University of London, London (UK)
17. Madas P, Elnashai AS (1992) A new passive confinement model for the analysis of concrete structures subjected to cyclic and transient dynamic loading. *Earthq Eng Struct Dynam* 21(5):409–431
18. Mander JB, Priestley MJN, Park R (1988) Theoretical stress-strain model for confined concrete. *J Struct Eng-ASCE* 114(8):1804–1825
19. Martinez-Rueda JE, Elnashai AS (1997) Confined concrete model under cyclic load. *Mater Struct* 30(3):139–147
20. Menegotto M, Pinto PE (1973) Method of analysis for cyclically loaded R.C. plane frames including changes in geometry and non-elastic behaviour of elements under combined normal force and bending. Zurich, Switzerland
21. Otani S (1974) SAKI: a computer program for inelastic response of R/C frames to earthquakes. University of Illinois Engineering Experiment Station. College of Engineering, University of Illinois at Urbana-Champaign
22. Ozbulut OE, Hurllebaus S, Desroches R (2011) Seismic response control using shape memory alloys: a review. *J Intell Mater Syst Struct* 22(14):1531–1549. <https://doi.org/10.1177/1045389X11411220>
23. Palermo D (2011) Super elastic SMA reinforced concrete elements: applicability and practicability. In: Fib symposium PRAGUE, concrete engineering for excellence and efficiency
24. Parghi A (2016) Seismic performance evaluation of circular reinforced concrete bridge piers retrofitted with fibre reinforced polymer. PhD. Thesis, University of British Columbia, Canada
25. Paule T, Prislley MNJ (1992) Seismic design of reinforced concrete and masonry buildings. 2nd ed. Wiley
26. Saiidi MS, Wang H (2006) An exploratory study of seismic response of concrete columns with shape memory alloys reinforcement. *ACI Struct J* 103(3):436–443
27. Schoettler MJ, Restrepo JI, Guerrini G, Duck DE (2015) A full-scale, single-column bridge bent tested by shake-table excitation. Pacific earthquake engineering research center (PEER), Berkeley
28. SeismoStruct (2018) SeismoStruct- a computer program for static and dynamic nonlinear analysis of framed structures, Italy. www.Seismosoft.com

29. Shrestha B, Hao H (2014) Comparison of performance of shape memory alloy reinforced bridge piers with conventional bridge piers using incremental dynamic analysis. In: Smith ST (ed.) 23rd Australasian conference on the mechanics of structures and materials, vol I, pp 375–380, Byron Bay, Australia
30. Zadeh MS, Brien MO, Saiidi MS (2007) A study of concrete bridge columns using innovative materials subjected to cyclic loading: a report by University of Nevada Reno and National Cooperative Highway Research Program (NCHRP)
31. Zulfikar N, Filippou FC (1990) Models of critical regions in reinforced concrete frames under earthquake excitations. Report No. EERC 90-06, University of California, Berkeley, USA

Response of Single Pile to Lateral Load with Constant Uplift



Poulami Ghosh, Sibapriya Mukherjee, Narayan Roy
and Subhadeep Banerjee

Abstract Model tests and the corresponding three dimensional FE analyses using PLAXIS 3D have been carried out to study the behavior of a single pile under combined action of lateral loading and uplift. Cast-iron model piles of 25 mm diameter and slenderness ratios (L/d) of 20, 25, and 30 have been chosen for the study. The variation of ultimate lateral load with pile head deflection with and without different values of uplift load has been obtained to examine the effect of relative density (R.D) of sand, and L/d ratio of pile on the ultimate pile capacity in both homogeneous and layered deposits of sand. Results indicate that the load–deflection behavior is nonlinear for independent lateral and uplift load, as well as in case of combined loading. It has been also found that independent lateral and uplift capacities of piles obtained from numerical analysis agree well with available theoretical and experimental results for the respective cases. Also, under combined action of lateral load and uplift, increase in lateral load capacity has been found to occur with increase in uplift load for a given L/d ratio, both in homogeneous and layered soil. It has also been observed that for any given L/d ratio, the ultimate lateral capacity decreases for a particular uplift in case of layered deposits when the thickness of topsoil layer (of lower R.D) increases.

Keywords Pile · Sand · Lateral load · Uplift · Numerical analysis · PLAXIS 3D

1 Introduction

Tall structures like high-rise buildings, transmission towers, offshore structures, etc. supported on pile foundations are subjected to large lateral loads and overturning moments due to wind, waves, or both, in addition to vertical compressive load,

P. Ghosh (✉) · S. Mukherjee · N. Roy
Jadavpur University, Kolkata, India
e-mail: poulamig04@gmail.com

S. Banerjee
Indian Institute of Technology, Madras, India

© Springer Nature Singapore Pte Ltd. 2020
A. Prashant et al. (eds.), *Advances in Computer Methods and Geomechanics*, Lecture Notes in Civil Engineering 56,
https://doi.org/10.1007/978-981-15-0890-5_24

which, act on piles simultaneously. Therefore, the safe design and performance of pile foundations under combined action of lateral loading and uplift have become the key concern of design engineers. Many well-established theoretical methods are available to evaluate the pile behavior under different types of independent loadings, viz, vertical, uplift, and lateral loadings. There are, however, limited studies, which reported pile behavior under combined loading: compressive-lateral [8, 11] and compressive-uplift [5]. Studies on pile behavior under combined lateral–uplift loading or inclined pullout load were carried out by only a few researchers [1]. Most recently, Reddy and Ayothiraman [15] carried out an experimental study to investigate the behavior of a single pile in homogenous sand (relative density, R.D = 70%) under combined uplift and lateral load. Based on literature mentioned above, it is observed that the study of the pile behavior under combined lateral–uplift loading is not well addressed for layered soil. Therefore, an attempt has been made in the present research to study the response of model piles to lateral loading with varying constant uplift in both homogeneous and layered deposits using finite element software PLAXIS 3D along with experimental validation.

2 Motivation and Objective

It is quite evident from the present scenario that it is important to study the pile response under combined action of lateral loading and uplift. Therefore, the objective of this study is to investigate the behavior of a single pile embedded in both homogeneous and layered deposits of non-cohesive soil of varying relative densities when subjected to combined uplift and lateral loading for different slenderness ratios of pile.

3 Experimental Investigation

3.1 Methodology

Model tests have been carried out in the laboratory on a single model pile embedded in locally available sand made uniform by sieving in appropriate way, to measure the pile behavior under independent lateral loads, independent uplift loads, and combined loads (uplift plus static lateral load). Details of experiments conducted have been discussed in the following sections.

3.2 Materials Used

3.2.1 Sand

In the present investigation, locally available sand has been used to prepare reconstituted foundation bed. It has been sieved through 1.18 and 0.425 mm sieve to simulate the gradation of Ennore sand as far as possible. The engineering properties of the materials passing through 1.18 mm sieve and retained on 0.425 mm sieve has been determined through laboratory tests as per the standard procedures recommended by the IS: 2720-Part 8. The gradation curve is shown in Fig. 1 and the summary of engineering properties of sand, obtained from routine laboratory tests, is presented in Table 1.

Also, pilot tests have been carried out to determine density of sand by pouring sand in a wooden box of specific dimension from a prefixed height of fall (for a particular R.D.) using rainfall technique. Calibration of shear strength parameters and elastic properties has been done by performing undrained triaxial tests on sand specimen of appropriate density. The values of angle of internal friction corresponding to different densities have been found out from the Mohr circle drawn

Fig. 1 The gradation curve of the sand

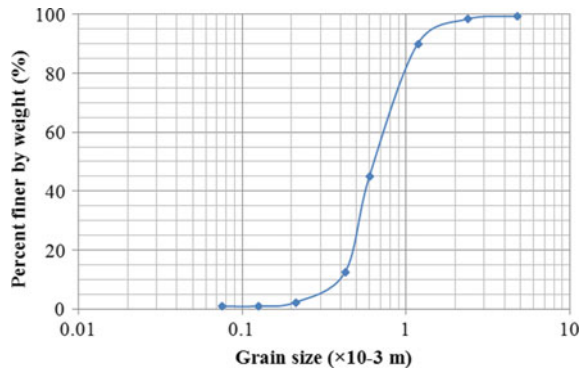


Table 1 Summary of properties of sand

Properties	Value
Maximum dry density, ρ_{max} (kN/m ³)	15.71
Minimum dry density, ρ_{min} (kN/m ³)	13.47
Specific gravity, G_s	2.63
Void ratio (loosest), e_{max}	0.915
Void ratio (densest), e_{min}	0.641
Uniformity coefficient, C_u	1.8
Coefficient of curvature, C_c	0.939
Effective size, D_{10} (mm)	0.4

Table 2 Shear parameters and elastic properties of sand at different densities

Properties	Relative density (%)		
	45%	70%	75%
Angle of internal friction, ϕ	23.6°	30.8°	32.2°
Unit weight, γ (kN/m ³)	14.39	14.97	15.08
Elasticity modulus, E (kN/m ²)	1.01×10^3	1.035×10^3	1.05×10^3
Poisson's ratio, μ	0.38	0.38	0.38

from the triaxial test results. The values of elastic modulus have been obtained by estimating Secant modulus (E_{50}) from the stress–strain curves generated from the triaxial test results, for different densities. The summary of relevant shear strength parameters and elastic properties of sand, obtained at different densities, is presented in Table 2.

3.2.2 Model Pile

In the present investigation, hollow cast-iron pipes having an outer diameter of 25 mm and thickness of 2.5 mm with L/d ratios of 20, 25, and 30 have been used to simulate both short/rigid and long/flexible piles for conducting model tests. It has been found that piles having L/d ratio more than 23 behave as long flexible pile under lateral loading [3] at 70% relative density of sand. Biswas et al. [2] have also reiterated that piles with L/d ratio 25 and 30 will behave as long flexible pile in both homogenous (R.D. = 70%) and layered (Top layer—45%, Bottom layer—75%) sand bed. Also, a cast-iron pile cap of dimensions 100 mm \times 100 mm \times 10 mm has been fabricated to attach it with the pile head to simulate the static vertical load on the pile. The total pile length includes the embedment depth required for a particular L/d ratio, plus a clearance of 50 mm for avoiding contact of the pile cap with the soil ensuring that the behavior measured from the experiments is only due to interaction of pile and soil throughout the pile length. The summary of properties of cast-iron piles is presented in Table 3.

Table 3 Properties of cast-iron pile

Properties	Value
Density (kN/m ³)	92.3
Young's modulus (kN/m ²)	6.52×10^7
Shear modulus, (N/mm ²)	2.71×10^5
Poisson's ratio	0.22

3.3 Experimental Setup

3.3.1 Test Tank

The dimensions of the model test tank have been decided based on the effective stressed zone of soil mass from the edge of the foundation so as to avoid the boundary effects while testing the model pile under lateral and uplift loads. Matlock [12] and Rao et al. [13, 14] have concluded that the boundary effect is more predominant within 10 times the pile diameter from the pile periphery, for a laterally loaded single pile. In the present study, the model pile diameter is 25 mm, and hence the size of the tank in the plan should be larger than 250 mm for a single pile. For piles subjected to uplift load, Kishida [10] observed that the zone of influence is about 3–8 times pile diameter from the edge of the pile at ground surface. Hence, the minimum size of the tank should be 425 mm ($8D + 8D + D = 17D$). Accordingly, the dimensions of the model test tank have been fixed as $1.0 \times 1.0 \times 2.25$ m (height).

3.3.2 Loading Arrangement

The static uplift load and static lateral load have been applied by means of dead weights placed on a hanger connected to a flexible steel rope, strung over a pulley supported by a loading platform. The lateral load has been applied at the pile head (center of pile cap). A pulley just above the pile and another pulley in the direction perpendicular to the point of application of lateral load, together help in applying the uplift load on the pile. Two dial gauges have been fixed diagonally on top of the pile cap to measure the pile head movement under uplift loading. One dial gauge has been used to measure pile head deflection under lateral loading. The experimental test set up is shown in Fig. 2.

Fig. 2 Experimental setup
(Note Image has been taken by the authors during the experiment at the laboratory of the Institute)



3.3.3 Sand Bed Preparation and Pile Installation

Model tests have been carried out in homogenous bed as well as layered medium. The test tank has been filled with sand by using rainfall/pluviation technique with a prefixed height of fall to achieve a homogenous sand bed with a relative density of 70%. Initially, the sand has been filled up to the pile tip, and then the pile has been kept in its position vertically. After that, sand has been filled again. During this process, it has been ensured that the pile remains vertical. This procedure of pile installation simulates the stress conditions around piles cast in situ. To carry out tests in layered medium, the sand bed has been prepared in similar manner by adjusting the height of fall to achieve the required density in a particular layer. One such layered medium has been prepared, having relative density of 45% in top layer, and 75% in bottom layer with the ratio of top layer thickness to bottom layer thickness (a:b) of 1:3, 1:2, and 2:1. The details of sand bed layers are presented in Fig. 3.

3.4 Test Procedure

3.4.1 Static Lateral Load Tests

The static lateral load tests have been conducted on piles as per the procedure recommended by IS: 2911 (Part 4)–1985. The initial reading in the dial gauges has been noted down before applying the load. The static lateral load has been applied in increments by adding dead weights through the loading arrangement. For each

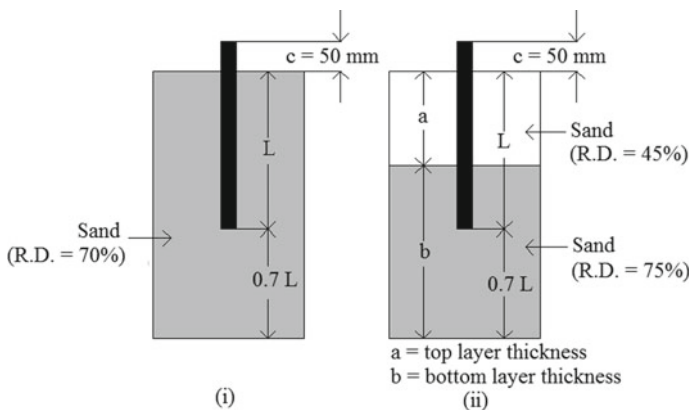


Fig. 3 Details of sand layer (*Note* Image has been taken by the authors during the experiment at the laboratory of the Institute)

Table 4 Test program

Type of sand bed	Relative density of sand (%)	a:b	L/d	Static uplift load tests	Static lateral load tests	Static lateral load tests with uplift load (P/P_u)	
Homogenous	70	N.A	20	Total 12	Total 12	0.4, 0.6, 0.8	
			25			0.4, 0.6, 0.8	
			30			0.4, 0.6, 0.8	
Layered	Top—45 Bottom—75	1:3	20	Total 12	Total 12	0.4, 0.6, 0.8	
			25			0.4, 0.6, 0.8	
			30			0.4, 0.6, 0.8	
		1:2	20			0.4, 0.6, 0.8	
			25			0.4, 0.6, 0.8	
			30			0.4, 0.6, 0.8	
		2:1	20			0.4, 0.6, 0.8	
			25			0.4, 0.6, 0.8	
			30			0.4, 0.6, 0.8	

increment of loading, the horizontal deflection of the pile head has been measured. When the deflection of the pile head ceases, the next load increment has been applied. This procedure has been repeated until failure or the specified maximum deflection value of $3b/80$, where b = diameter of the pile (in inch), i.e., 0.9 mm [16] is reached. A total of 12 tests will be conducted as per Table 4.

3.4.2 Static Uplift Load Tests

The static uplift load tests have been conducted on piles as per the procedure recommended by IS: 2911 (Part 4)–1985. Before applying the load, the initial reading in the dial gauges has been noted down. The static uplift load has been applied in several increments by adding dead weights through a loading arrangement. For each increment of loading, the pile head movement has been measured. When the pile head movement ceases, the next load increment has been applied. This procedure is repeated until the failure takes place. Since the load displacement behavior under uplift is continuously curvilinear, the double tangent method has been used to find the ultimate uplift load at the point of maximum curvature. A total of 12 tests will be conducted as per Table 4.

3.4.3 Tests Under Combined Loading

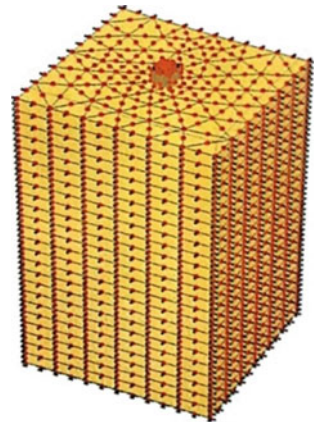
Static lateral load tests have been conducted under constant uplift to obtain the maximum pile capacity and corresponding pile head displacement. The constant

uplift has been applied as a certain percentage of ultimate uplift load, P ($=0.4P_u$, $0.6P_u$, $0.8P_u$). The failure criterion is considered to be same as given in Sect. 3.4.1. A total of 36 tests will be conducted and the overall test program is given in Table 4.

4 Numerical Study

A finite element analysis using PLAXIS 3D has been carried out to compare the results obtained from the experimental study. The pile has been modeled as a linear elastic element following Hooke's law. The whole soil continuum has been divided into a number of 15-noded elements to form the 3D finite element mesh (Fig. 4). The depth of soil continuum has been taken as 1.7 times the length of the pile [9] for numerical modeling same as that of experimental investigation. The domain so chosen has been found to be adequate to eliminate the boundary effects on the performance of pile. The finite element mesh has been investigated based on the four global levels of coarseness (relative element size), namely very coarse, coarse, medium and fine. It has been found that the medium mesh size optimizes the mesh to give comparable results in a sufficiently accurate manner without too much computational effort. The soil–pile interface has been discretized using 15-noded interface elements. Interfaces have been defined on both sides and underneath the pile with material properties from adjacent soil, with strength reduction factor, $R_{inter} = 1$. Sand bed has been modeled as an elastoplastic material using the Mohr-Coulomb failure criteria. The side boundaries have been constrained against horizontal direction and the bottom boundaries have been constrained against both horizontal and vertical directions. From the numerical analyses, the variation of ultimate lateral load with pile head deflection with and without different values of

Fig. 4 Discretized soil–pile model



uplift load has been obtained for various slenderness ratios of pile in both homogeneous and layered deposits. A total of 60 (12 + 12 + 36 = 60) models have been developed and analyzed for every case described as per Table 4.

5 Results and Discussion

5.1 Pile Behavior Under Uplift Load

The variation of uplift load with pile head movement has been found to be non-linear (Fig. 5). The ultimate uplift load has been obtained by double tangent method. The values of ultimate uplift capacity of piles with no lateral load for all L/d ratios, obtained from experimental results and numerical analysis have been presented in Table 5 along with the gross uplift capacity of piles estimated using limit equilibrium method proposed by Chattopadhyay and Pise [4]. It has been observed from Table 5 that the ultimate uplift capacity increases with increase in L/d ratio for a particular sand bed. It has also been observed that the results of experimental investigation are in close proximity with those obtained from numerical analysis and the theoretical ultimate uplift capacity.

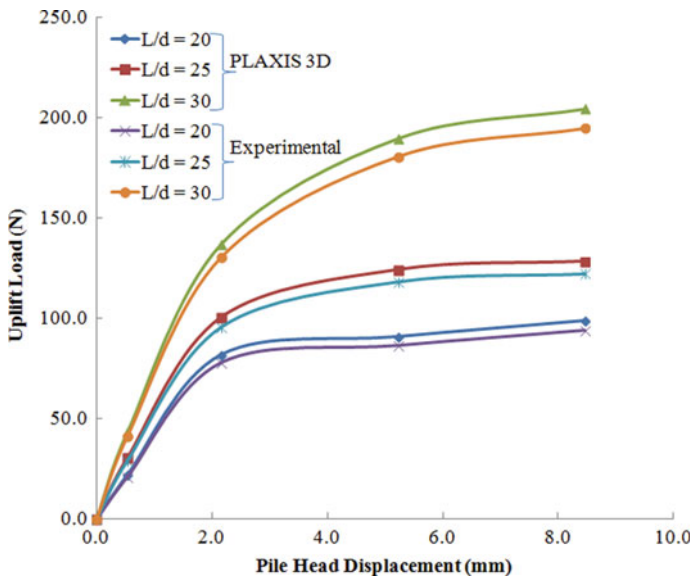


Fig. 5 Variation of uplift load with pile head movement for layered sand bed (a:b = 1:2)

Table 5 Ultimate uplift load

Type of sand bed	<i>a</i> : <i>b</i>	<i>L</i> / <i>d</i>	Ultimate uplift load, P_u ($\times 10^{-3}$ kN)			% deviation from experimental results	
			Experimental	PLAXIS 3D	^a Theoretical	PLAXIS 3D	^a Theoretical
Homogenous (R.D = 70%)	N. A	20	44.80	50.10	53.72	-11.83	-19.91
		25	79.10	82.90	83.94	-4.80	-6.12
		30	113.50	115.60	120.87	-1.85	-6.49
Layered (R.D = Top layer—45%, Bottom layer—75%)	1:3	20	90.20	94.20	97.00	-4.43	-7.54
		25	143.40	150.10	151.53	-4.67	-5.67
		30	209.20	215.40	218.27	-2.96	-4.34
	1:2	20	80.40	84.80	85.23	-5.47	-6.00
		25	125.80	128.60	133.13	-2.23	-5.83
		30	181.20	188.40	197.67	-3.97	-9.09
	2:1	20	69.20	76.40	78.80	-10.40	-13.87
		25	110.60	120.00	123.10	-8.50	-11.30
		30	160.80	169.00	177.24	-5.09	-10.22

^aChattopadhyay and Pise [4]

5.2 Pile Behavior Under Lateral Load

The variation of lateral load with pile head deflection has also been found to be nonlinear (Fig. 6). The ultimate lateral capacity obtained from the experimental investigation and numerical analysis, under no uplift condition ($P = 0$) for all L/d ratios has been presented in Table 6. It has been found that the ultimate lateral capacity increases with an increase in L/d ratio for a particular sand bed. This could be due to the increase of the passive resistance with the increase in pile length. Also, for any given L/d ratio, the ultimate lateral capacity decreases in case of layered deposits, when the thickness of topsoil layer (of lower R.D) increases. It has been also observed that the obtained ultimate lateral capacity from experimental investigation is comparable with those obtained from numerical analysis and theoretical ultimate lateral capacity.

5.3 Pile Behavior Under Combined Load

The variation of lateral load with pile head deflection under constant uplift load has been also found to be nonlinear (Fig. 7). Also, the variation of ultimate lateral capacity with L/d ratio with and without constant uplift load for a typical case has been shown in Fig. 8. It has been observed that for the same deflection, the presence of uplift load increases the lateral capacity of pile, which is in agreement with

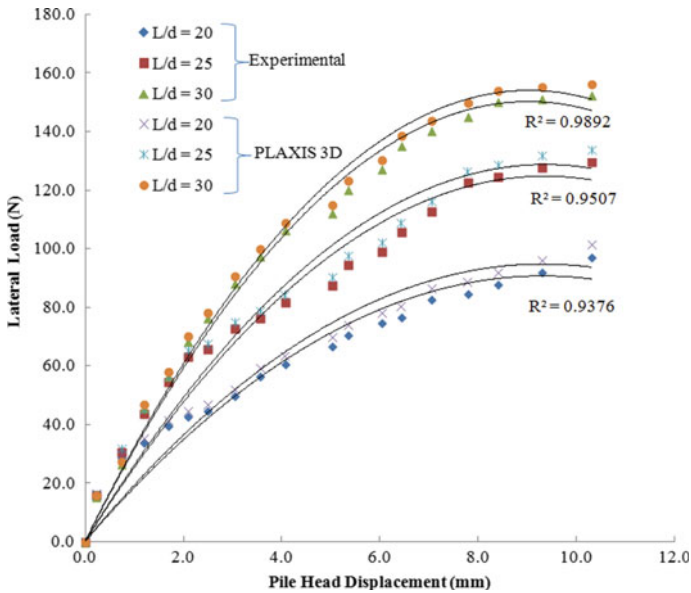


Fig. 6 Variation of lateral load with pile head movement for layered sand bed (a:b = 1:2)

the work of Reddy and Ayothiraman [15]. Similar behavior has been observed for all pile lengths ($L/d = 20, 25, 30$). This may be attributed to the fact that the pile–soil grip becomes loosened with increase of uplift load and hence, lateral displacement will be more at same lateral load. So, for a specified lateral displacement (the failure criterion), lateral capacity increases. The ultimate lateral capacity of pile under the effect of constant uplift ($P = 0.4P_u, 0.6P_u, 0.8P_u$) has been presented in Table 7.

It has been noticed from Table 7 that for the same L/d ratio, the ultimate lateral capacity decreases for a particular uplift in the case of layered sand bed when the a: b ratio increases. This is due to the fact that the thickness of weaker soil of lower R.D increases. It has been also observed that the thickness of top layer influences the lateral behavior throughout the length of the pile. Also, the obtained ultimate lateral capacity from experimental investigation has been found to be in close agreement with those obtained from numerical analysis. The failure plane at the surface has been found to be unsymmetrical, which extends more in the direction of lateral force and less on the other side. However, the study of the mechanics of the development of failure surface is beyond the scope of this paper. The variation of ultimate lateral capacity with P/P_u ratio with and without constant uplift load for a typical case has been shown in Fig. 9. It has been observed that at low constant uplift load ($P = 0.4P_u$), the effect of combined loading on lateral capacity of the pile is not significant. However, at high constant uplift load ($P = 0.8P_u$), the effect of combined loading is considerable.

Table 6 Ultimate lateral load

Type of sand bed	a:b	L/d	Ultimate lateral load ($\times 10^{-3}$ kN)			% Deviation from experimental results
			Experimental	PLAXIS 3D	^a Theoretical	PLAXIS 3D
Homogenous (R.D = 70%)	N. A	20	11.72	13.19	13.00	-12.54
		25	14.99	16.41	43.49	-9.47
		30	22.39	23.74	43.49	-6.03
Layered (R.D = Top layer - 45%, Bottom layer - 75%)	1:3	20	20.03	20.73	12.59	-3.49
		25	27.41	28.10	57.71	-2.52
		30	34.24	34.75	57.71	-1.49
	1:2	20	16.69	17.44	12.20	-4.49
		25	22.84	23.57	57.40	-3.20
		30	28.53	29.22	57.40	-2.42
	2:1	20	15.03	16.47	10.72	-9.58
		25	21.18	23.02	56.51	-8.69
		30	26.85	28.89	56.51	-7.60

^aBroms [3]

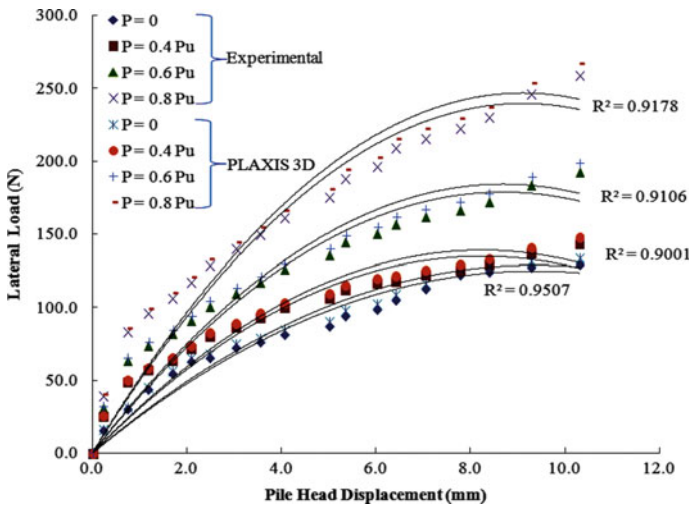


Fig. 7 Variation of lateral load with pile head movement for layered sand bed (a:b = 1:2, L/d = 25) under constant uplift

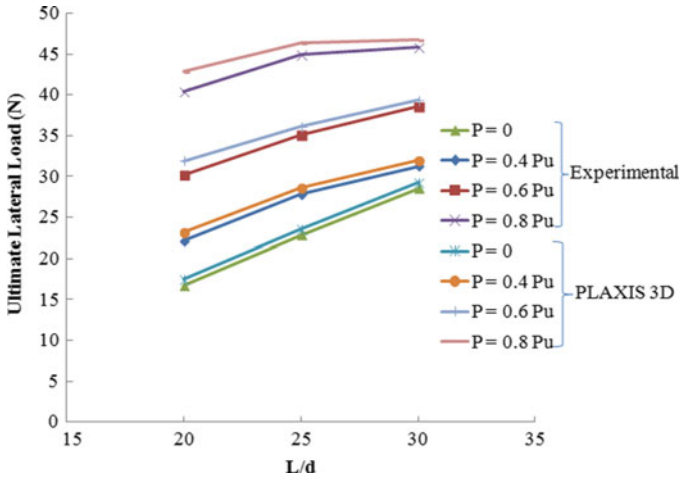


Fig. 8 Variation of lateral load with L/d ratio for layered sand bed (a:b = 1:2, L/d = 25) under constant uplift

From the experimental results, for homogenous sand bed, the ultimate lateral capacity of piles under constant uplift increases by an average of 18.69% at low constant uplift load ($0.4P_u$); however, it increases considerably by an average of 69.6% at high constant uplift load ($0.8P_u$), when compared with the ultimate lateral capacity of piles under no uplift. In case of layered sand bed (a:b = 1:3), the ultimate lateral capacity of piles under combined loading increases by an average of 14.7% and 98.23% at low constant uplift load ($0.4P_u$) and at high constant uplift load ($0.8P_u$), respectively. Similarly, for layered sand bed (a:b = 1:2), it increases by an average of 21.24% and 99.83% at low constant uplift load ($0.4P_u$) and at high constant uplift load ($0.8P_u$), respectively. For layered sand bed (a:b = 2:1), it increases by an average of 13.6% and 63.3% at low constant uplift load ($0.4P_u$) and at high constant uplift load ($0.8P_u$), respectively. It has been also observed that in case of layered sand bed, for any given L/d ratio, the ultimate lateral capacity decreases for a particular uplift when the a:b ratio increases from 1:3 to 2:1. The ultimate lateral capacity decreases by 23.5–25.63% at low constant uplift load ($0.4P_u$) and 35.02%–37.89% at high constant uplift load ($0.8P_u$). This is due to the fact that the thickness of weaker soil (top layer) of lower R.D increases. Similar results have been found from numerical analysis, which is in reasonably close agreement to that of experimental results. Due to the limitations of simulating the in situ behavior of pile in the laboratory, it is to be noted here that the above results, based on model tests carried out in the laboratory, may not be conclusive despite being further validated by numerical analysis. Therefore, these results may need to be verified if full-scale model test data or field data are made available.

Table 7 Ultimate lateral load under constant uplift

Type of Sand Bed	<i>a:b</i>	<i>L/d</i>	Ultimate lateral load ($\times 10^{-3}$ kN)						% Deviation from experimental results					
			Experimental			PLAXIS 3D								
			$P = 0.4P_u$	$P = 0.6P_u$	$P = 0.8P_u$	$P = 0.4P_u$	$P = 0.6P_u$	$P = 0.8P_u$	$P = 0.4P_u$	$P = 0.6P_u$	$P = 0.8P_u$	$P = 0.4P_u$	$P = 0.6P_u$	$P = 0.8P_u$
Homogenous (R.D = 70%)	N.A	20	13.46	18.65	23.82	15.16	20.98	26.79	-12.63	-12.49	-12.47			
		25	19.65	22.94	26.22	21.52	25.12	28.71	-9.52	-9.50	-9.50			
		30	24.66	26.95	29.25	26.09	28.54	30.88	-5.80	-5.90	-5.56			
Layered (R.D = Top layer—45%, Bottom layer—75%)	1:3	20	24.11	36.29	48.47	24.83	37.45	49.98	-2.99	-3.20	-3.11			
		25	31.28	42.11	52.68	32.01	43.00	53.73	-2.33	-2.11	-1.99			
		30	37.53	46.25	54.96	37.98	46.71	55.51	-1.20	-0.99	-1.00			
	1:2	20	22.10	30.24	40.40	23.21	31.91	42.82	-5.02	-5.52	-5.99			
		25	27.80	35.09	44.97	28.67	36.16	46.32	-3.13	-3.05	-3.00			
		30	31.27	38.54	45.80	31.99	39.35	46.72	-2.30	-2.10	-2.01			
2:1	20	18.44	23.59	30.42	20.18	25.76	33.16	-9.44	-9.20	-9.00				
	25	24.18	28.45	32.72	26.23	30.81	35.33	-8.48	-8.29	-7.98				
	30	27.91	31.81	35.71	29.98	34.10	38.21	-7.42	-7.20	-7.00				

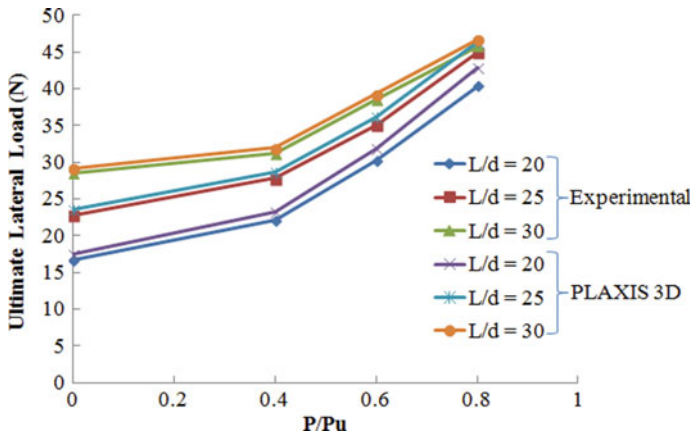


Fig. 9 Variation of lateral load with P/P_u ratio for layered sand bed (a:b = 1:2)

6 Conclusions

Based on the results obtained from the experimental investigation and numerical analysis, the following conclusions have been drawn:

- i. Pile behavior under independent uplift load and independent lateral load are nonlinear. Also, the ultimate uplift capacity as well as lateral capacity increases with increase in L/d ratio.
- ii. Results from numerical analysis closely follow the experimental results. Hence, PLAXIS 3D can be used satisfactorily for analysis of pile foundations.
- iii. Under combined action of lateral load and uplift, increase in lateral load capacity occurs with increase in uplift load for a given L/d ratio both in homogenous and layered soil. For homogenous sand bed, percent increase in lateral load is 18.69% (for $P = 0.4P_u$) and 69.6% (for $P = 0.8P_u$) on an average. In case of layered sand bed, the corresponding values are 14.7 and 98.23% (for a:b = 1:3), 21.24 and 99.83% (for a:b = 1:2) and 13.6% and 63.3% (for a:b = 2:1).
- iv. In case of layered sand bed, for any given L/d ratio, the ultimate lateral capacity decreases for a particular uplift when ratio of the thickness of topsoil layer (of lower R.D) to the thickness of bottom soil layer increases from 1:3 to 2:1. The ultimate lateral capacity decreases by 23.5–25.63% at low constant uplift load ($0.4P_u$) and 35.02–37.89% at high constant uplift load ($0.8P_u$).

References

1. Achmus M, Abdel-Rahman K, Thieken K (2009) Behavior of piles in sand subjected to inclined loads. In: Proceedings of the 1st international symposium on computational geomechanics (ComGeo I), IC2E, Greece, pp 763–774
2. Biswas SK, Mukherjee S, Chakrabarti S, De M (2015) Experimental investigation of free head model piles under lateral load in homogenous and layered sand. *Int J Geotech Eng* 9(4):363–378
3. Broms B (1964) Lateral resistance of piles in cohesionless soils. *J Soil Mech Found Div* 90 (SM3):123–156
4. Chattopadhyay, B. C. and Pise, P. J. (1986) Uplift capacity of piles in sand, *J. Geotech. Eng.* [https://doi.org/10.1061/\(asce\)0733-9410\(1986\)112:9\(888\)](https://doi.org/10.1061/(asce)0733-9410(1986)112:9(888)), pp. 888–904
5. Dash PK, Pise PJ (2003) Effect of compressive load on uplift capacity of model piles. *J. Geotech. Geoenvironmental Eng.* [https://doi.org/10.1061/\(asce\)1090-0241\(2003\)129:11\(987\)](https://doi.org/10.1061/(asce)1090-0241(2003)129:11(987)), pp. 987–992
6. IS: 2720 (Part 8) (1983) Specifications for methods of test for soils—Code of practice
7. IS: 2911 (Part 4) (1985) Specifications for design and construction of pile foundations—Code of practice
8. Karthigeyan S, Ramakrishna VVGST, Rajagopal K (2007) Numerical investigation of the effect of vertical load on the lateral response of piles. *J Geotech Geoenvironmental Eng.* [https://doi.org/10.1061/\(ASCE\)1090-0241\(2007\)133:5\(512\)](https://doi.org/10.1061/(ASCE)1090-0241(2007)133:5(512)), 512–521
9. Kim Y, Jeong S (2011) Analysis of soil resistance on laterally loaded piles based on 3D soil–pile interaction. *Comput Geotech* 38:248–257
10. Kishida H (1963) Stress distribution by model piles in sand. *Soils Found* 4(1):1–23
11. Liang F, Yu F, Jie H (2013) A simplified analytical method for response of an axially loaded pile group subjected to lateral soil movement. *J Civ Eng* 17(2):368–376
12. Matlock H (1970) Correlations for design of laterally loaded piles in soft clay. In: Proceedings of the 2nd offshore technology Conference, vol 1, British Maritime Technology, Teddington, pp 577–594
13. Rao SN, Ramakrishna VVGST, Babu Rao M (1998) Influence of rigidity on laterally loaded pile groups in marine clay. *J Geotech Geoenvironmental Eng ASCE* 124(6):542–549
14. Rao SN, Ramakrishna VVGST, Balarama Raju G (1996) Behavior of pile supported dolphins in marine clay under lateral loading. *J Geotech Geoenvironmental Eng* 122(8):607–612
15. Reddy K, Ayothiraman R (2015) Experimental studies on behavior of single pile under combined uplift and lateral loading. *J Geotech Geoenvironmental Eng ASCE*, 141
16. Reese LC, Cox WR, Koop FD (1974) Analysis of laterally loaded piles in sand. In: Proceedings of the 6th annual offshore technology conference, Houston, pp 473–483

Correlation Between Shear Strength of Soils and Water Content Ratio as a Substitute for Liquidity Index



Harshdeep Singh and Ashok Kumar Gupta

Abstract Undrained shear strength of saturated clays is a vital property in geotechnical engineering practice. If any relationship between shear strength of soil and index properties of soil is developed, it would be exceptionally alluring. A few endeavors have been made in the past to associate shear strength with Liquidity Index. The Liquidity Index requires the estimation of plastic limit calculated by Casagrande [1] thread rolling method which does not provide the correct assurance of plastic limit of the soil particularly in less plastic soils. Shear strength variation with water content does not follow a regular trend, which makes the analysis difficult. It has been observed in the past researches that shear strength of soil correlates very well with the consistency limits of soils. The present paper develops the correlation between shear strength and Water Content Ratio (w_x) and between shear strength and Liquidity Index, to find out the better parameter to evaluate shear strength between Water Content Ratio (w_x) and Liquidity Index. The experimental results on three different highly compressible soils having water content ranging from 5% to 25% showed that the regression coefficient value of relation between undrained shear strength with Water Content Ratio came out to be closer to one compared with Regression coefficient value of relation between undrained shear strength with Liquidity Index, for the soils of same geological origin. Liquidity Index variation with Water Content Ratio suggests that there is a definite relation between Liquidity Index and Water Content Ratio and Liquidity Index can be substituted by Water Content Ratio. However, the results obtained from both are more or less same for the soils irrespective of their origin.

Keywords Shear strength · Water content ratio · Liquidity index · Plastic limit

H. Singh (✉)

Department of Civil Engineering, Delhi Technological University, Delhi 110042, India
e-mail: hashasija@gmail.com

A. K. Gupta

Department of Civil Engineering, Room: FW3-FF5, Delhi Technological University,
Delhi 110042, India
e-mail: akgupta@dtu.ac

© Springer Nature Singapore Pte Ltd. 2020

A. Prashant et al. (eds.), *Advances in Computer Methods and Geomechanics*, Lecture Notes in Civil Engineering 56,
https://doi.org/10.1007/978-981-15-0890-5_25

299

1 Introduction

In order to find the undrained shear strength of remolded clays in an economical way, Liquidity Index is not a stable parameter as it requires the plastic limit which is not an accurate method for fine-grained saturated soils and also, most of the representative samples collected are disturbed. Therefore, a parameter which would strongly relate with the shear strength would be much appreciated. One such parameter is w_X (Water Content Ratio) which is defined as

$$w_X = w_N/w_L \quad (1)$$

In earlier researches, Wroth and Wood [2] established the relationship between shear strength and Liquidity Index. Leroueil et al. [3] examined undrained cohesion relation with Liquidity Index in an inverse power form. Schofield and Wroth [4], from the vane shear data collected from Skempton and Northey [5] observed that Liquid limit corresponds well approximately to fixed strengths that are in the ratio of 1:100. Sharma and Bora [6] used this observation and developed a log-linear relationship between undrained shear strength and water content. Prakash et al. [7] examined the effect of size of the rolled thread of soil on the plastic limit of fine-grained soils and the dependency of operator on the results. Kuriakose et al [8] developed a logarithmic relation for shear strength and Water Content Ratio for Cochin marine clays having water content ranging from 98% to 119%. The shear strength of soil reduces with increase in water content for a particular soil, but at same water content, due to plastic behavior, different soil behaves differently and has different shear strengths. So, water content alone would not describe the relation with shear strength in an absolute manner. Also, water content increases with increase in liquid limit values. These two parameters combined correlates strongly with shear strength and shows definite trends. Therefore, a parameter w_X (Water Content Ratio) which is defined as $w_X = w_N/w_L$ is taken into analysis and discussed (Fig. 1).

Fig. 1 Soil 1



2 Experiments and Methodology

Three different soils from Gwalior (Railway station) (Soil 1), Bhopal (Jhabua) (Soil 2), and New Delhi (Rithala) (Soil 3) were collected and tested for their Atterberg limits and were classified according to Indian soil classification system ([9]:1970). Specific gravity was determined using Pycnometer method as per IS 2720 part 3-1-1980 [10]. The liquid limit was determined by Cassagrande percussion method according to IS: 2720 (Part 5)—1985 (Reaffirmed-2006) [11] with rotating the lever at approximate rate of two revolutions per second. Standard proctor test was performed as per IS 2720- part 7- 1980 [12] to find out the OMC and maximum dry density of soils and different water contents was determined by Oven drying method (IS 2720- part 2- 1980) [13]. Thread rolling method was used in accordance with IS: 2720 (Part 5)—1985 (Reaffirmed-2006) [11] to determine the Plastic limit of the soil. UU (Unconsolidated Undrained) triaxial tests were performed at different water contents for each soil to determine the shear strength of soils in accordance with IS:2720 (Part 11)-1993 [14]. 50 mm diameter cylindrical samples were used with $L/B = 2$ (L = length of sample, B = diameter of sample) and strain rate of 1.25 mm/min. up to 20% axial strain. Membrane effect was not considered in the analysis. Variation of shear strength with different water contents, w_x values and I_L values, for each soil was determined and results were analyzed to develop a relation, if any (Fig. 2).

3 Results and Discussion

3.1 Results

3.1.1 Soil Classification

All the soils tested were classified according to Indian Soil Classification System [9]. All samples were fine-grained soils, which can be classified as highly Compressible Clays (CH) ($w_L > 50$) (Fig. 3).

Fig. 2 Soil 2

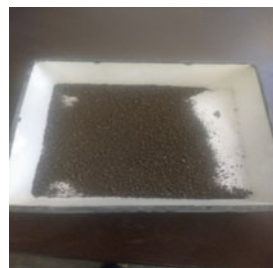


Fig. 3 Soil 3**Fig. 4** Soil 1 before test

3.1.2 Triaxial Test Sample Failure

The soil samples failed mostly under plastic failure and the failure was assumed when the axial strain reached 20% and some samples failed under brittle failure (Fig. 4).

4 Discussions

- Figure 6 suggests that shear strength is inversely proportional to water content, which relates to the earlier researches. However, no clear relation can be estimated if only water content is taken as basis (Table 1).
- Figure 7 shows the plot of three samples tested at different Liquidity Index values and for the combined values of all soils. Each soil follows binomial behavior. Plot suggests that shear strength can be related with Liquidity Index by equation:

$$C_u = a'I_L^2 - b'I_L + c' \quad (2)$$

Fig. 5 Soil 1 after test

where a' , b' , and c' are constants which depends on type of soil.

The above relation exists well for soil of similar geological origin as the regression coefficient is close to one but not for different geological origins, which has the regression coefficient not closer to one which is shown in combined values plot of Fig. 5. However, the above data contains only negative values of Liquidity indices which need to be verified with positive values of liquidity indices, which will occur at higher water content and would require Vane shear test for shear strength calculation.

- Figure 8 shows the plot of three samples tested at different w_x values and for the combined values of the all soils. It suggests that shear strength can be related with Water Content Ratio (w_x) by equation:

$$C_u = a w_x^2 + b w_x + c \quad (3)$$

Where a' , b' , and c' are constants which depend on type of soil.

The relation exists well for a soil of similar geological origin as the regression coefficient is close to one but not for different geological origins, which has the regression coefficient not close to one.

Figure 9 suggests that Liquidity Index varies linearly with w_x irrespective of the geological origin of soil. Therefore, w_x can be replaced by Liquidity Index to find out shear strength of soils, as it eliminates the determination of Plastic limit of soils.

It shall be noted that membrane effect was not considered during the triaxial testing and the samples may have subjected to water content change during testing in the hot month of May, which gave some values of ϕ in UU test.

The number of samples used for the tests in the present study was quite few and yet a good relation can be established. However, the above data needs to be verified with more test results on each soil to develop an accurate relation.

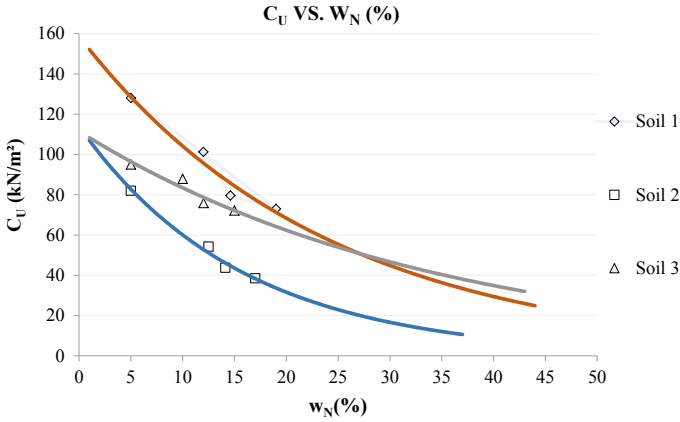


Fig. 6 Shear strength versus water content

Table 1 Physical properties and shear strength of three different clays

Properties	Soil 1	Soil 2	Soil 3
Soil classification	CH	CH	CH
Specific gravity	2.43	2.27	2.23
Liquid limit (w_L) (%)	55	62	58
Plastic limit (w_P) (%)	21	28	22.5
Shrinkage limit	18	21	20
Plasticity index (I_P)	34	34	35.5
OMC (%)	14.6	22.02	14.12
Dry unit weight, (γ_d)(kN/m^3)	17.06	17.46	18.02
Cohesion intercept, C (kN/m^2)	82.375	35.3	73.55
Angle of internal friction, ϕ ($^\circ$)	3.8	5.9	3.48
Undrained shear strength, C_U (kN/m^2)	95.22	43.75	80.795

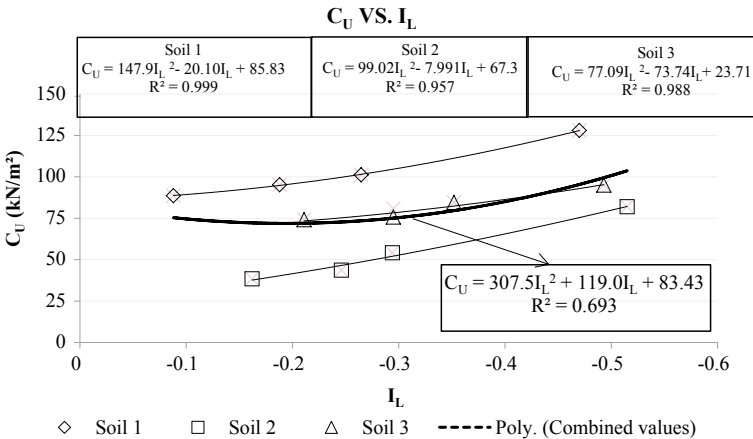


Fig. 7 Shear strength versus liquidity index

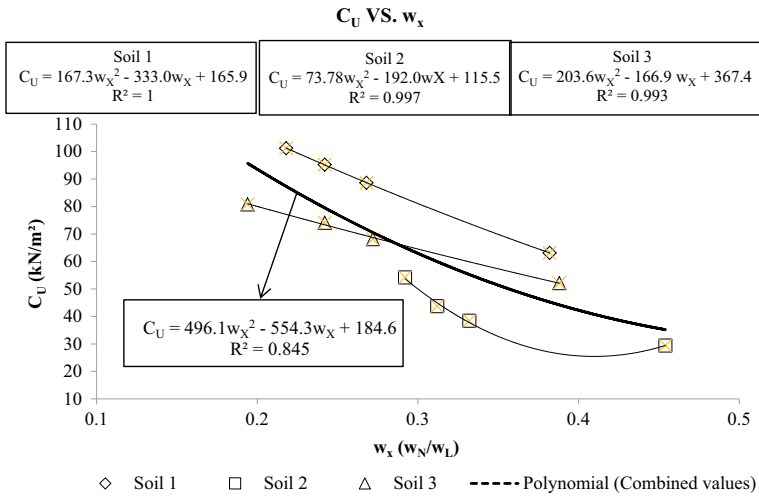


Fig. 8 Shear strength versus w_x

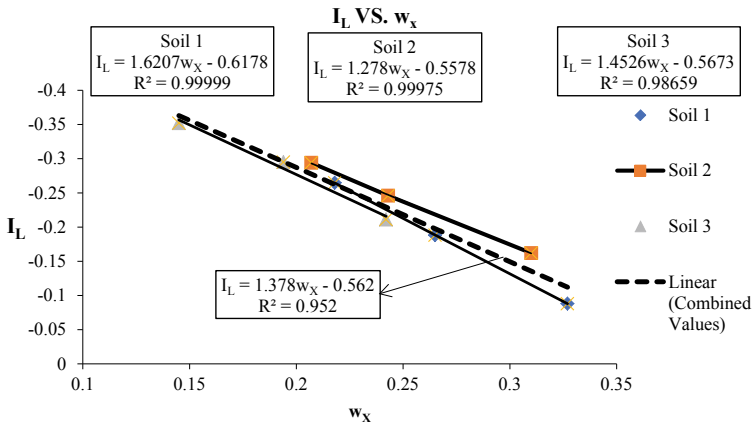


Fig. 9 Liquidity index versus w_x

5 Conclusions

Shear Strength correlates well with the I_L for the soils of same origin through binomial behavior but the combined I_L values do not correlate well with shear strength as discussed above. Shear strength correlates well with the w_x of soils of same origin but the combined w_x values do not correlate well with shear strength. Definite relationship exists between I_L and w_x irrespective of the geological origin of soil. From the above results, it can be inferred that fine-grained soils do

correspond to consistency limits and to develop a more accurate relation to predict shear strength of fine-grained soils, Liquidity Index can be replaced with the Water Content Ratio, which eliminates the determination of plastic limit. Also, Kuriakose et al [8] performed their tests on soils with positive I_L values only and in the present study, the tests were performed on negative I_L values and in both cases, w_x shows good linear relation with I_L values. Hence, the I_L can be replaced by w_x for all types of fine-grained soils.

References

1. Casagrande A (1932) Research on the atterberg limits of soils. *Public Roads* 13(3):121–130
2. Wroth CP, Wood DM (1978) The correlation of index properties with some basic engineering properties of soils. *Can Geotech J* 15(2):137–145
3. Leroueil S, Tavenas F, Leblond JP (1983) Properties characteristics des argiles lest du Canada. *Can Geotech J* 13:339–354
4. Schofield AN, Wroth CP (1968) *Critical state soil mechanics*. McGraw-Hill, London, UK
5. Skempton AW, Northey RD (1952) The sensitivity of clays. *Geotechnique* 3(1):30–53. <http://dx.doi.org/10.1680/geot.1952.3.1.30>
6. Sharma B, Bora PK (2003) Plastic limit, liquid limit and undrained shear strength of soil. Reappraisal. *J Geotech Geoenviron Eng ASCE* 129(8):774–777
7. Prakash K, Shridharan A, Prasanna HS (2009) A note on the determination of plastic limit of fine-grained soils. *Geotech Test J* 32(4):372–374
8. Kuriakose B, Abraham BM, Sridharan A, Jose BT (2017) Water content ratio: an effective substitute for liquidity index for prediction of shear strength of clays. *J Geotech Geol Eng* 35:1577–1586
9. IS 1498 (1970) Classification and identification of soils for general engineering purposes
10. IS 2720: Part 3 (1980) Method of test for soils: determination of specific gravity
11. IS 2720: Part 5 (1985) Method of test for soils: determination of liquid and plastic limit
12. IS 2720: Part 7 (1980) Method of test for soils: determination of water content-dry density relation using light compaction
13. IS 2720: Part 2 (1973) Method of test for soils: determination of water content
14. IS 2720: Part 11 (1993) Method of test for soils: determination of the shear strength parameters of a specimen tested in unconsolidated undrained triaxial compression without the measurement of pore water pressure

Numerical Study of Embankments Supported by Ordinary and Encased Granular Columns in Peat



J. Jayapal and K. Rajagopal

Abstract Highway and railway embankments form a major part of infrastructure in the transportation sector, but often these embankments rest on weak and problematic deposits with low load-bearing capacities and are prone to high settlements. An attempt has been made to study the performance of an embankment constructed over a weak organic deposit, namely, peat with granular columns as foundation elements. Granular columns have provided effective and promising solutions for flexible loading conditions, especially with soft soils. This ground improvement technique along with geosynthetic encasement is used in the numerical study in assessing and comparing the performance of the embankment in relation to stability. Some parametric studies are also conducted by varying the soil properties say cohesion of the in situ deposit, friction angle of granular column, spacing of granular column, etc., to understand the failure mechanism due to slope instability. The findings from the numerical study revealed the improved performance of embankments founded on geosynthetic encased granular columns.

Keywords Geosynthetics · Granular columns · Ground improvement · Embankment · Peat

1 Introduction

Soft clays, loose sands, collapsible soils, and organic soils are the potential class of problematic soils in geotechnical engineering. They are usually problematic for a geotechnical engineer due to their low bearing capacity leading to excessive

J. Jayapal (✉) · K. Rajagopal
Indian Institute of Technology Madras, Chennai, India
e-mail: jayapal.jp@gmail.com

K. Rajagopal
e-mail: gopalkr@iitm.ac.in

© Springer Nature Singapore Pte Ltd. 2020
A. Prashant et al. (eds.), *Advances in Computer Methods and Geomechanics*, Lecture Notes in Civil Engineering 56,
https://doi.org/10.1007/978-981-15-0890-5_26

settlements. If the thickness of these deposits is less than or equal to 1 m, they can be easily replaced. But if it is greater than 5 m a proper solution in the form of ground treatment has to be sorted out. In this paper, an attempt has been made to study numerically the stability response of an embankment constructed on an organic deposit, namely, peat with granular columns as foundation elements. Peat commonly occurs as an extremely soft, wet, unconsolidated superficial deposit normally as an integral part of wetland systems Huat et al. [5]. The term peat describes a naturally occurring highly organic substance derived primarily from plant materials. These conditions occur when organic matter is preserved below high water table, as in swamps or wetlands. To a geotechnical engineer, all soils with organic content greater than 20% are termed as organic soils. Peat is an organic soil with organic content greater than 75%. These deposits are extensively found in Canada, Russia, Germany, Finland, and Malaysia.

The Granular columns which are used as foundation elements in this study derive their capacity from the surrounding soil, as in this case the peat soil is very weak, a geosynthetic encasement has been provided to the ordinary granular columns (OGC) to study the stability response. The Geosynthetic Encased Granular columns (EGC) are recent innovations to enhance the overall performance of granular columns. This technique had been investigated by various researchers Van Impe [11], Raithel and Kempfert (2000), Malarvizhi and Ilamparuthi [6], Murugesan and Rajagopal [9], Almeida et al. [2], and Mohapatra and Rajagopal [8]. The vertical load on EGC generates radial outward stresses resulting in widening of the column. This radial widening provokes a counter pressure from the surrounding soil and a confining resistance from the geosynthetic encasement. This is the key difference between a granular column with and without geosynthetic encasement. Further, the mobilized hoop tension force in the geosynthetic encasement depends on its tensile stiffness modulus and strain levels.

Many researchers have studied the response of embankments resting on granular columns numerically Han et al. [4], Ambily and Gandhi [1], and Mohapatra and Rajagopal [8]. Except Mohapatra and Rajagopal [8], the other researchers have investigated the plane strain response of embankments on granular columns. Though the 2D approach is very simple it is unrealistic to model the granular columns in the form of a wall, which assumes a continuous support to the soil. Hence, this approach yields a high factor of safety. In the present analysis, an attempt has been made to investigate numerically the performance of a full-scale embankment resting on granular columns in Peat soils. PLAXIS 3D (2017) FE Program with 10 noded tetrahedral elements is used to conduct the stability analysis. A schematic representation of embankment loaded granular columns is shown in Fig. 1.

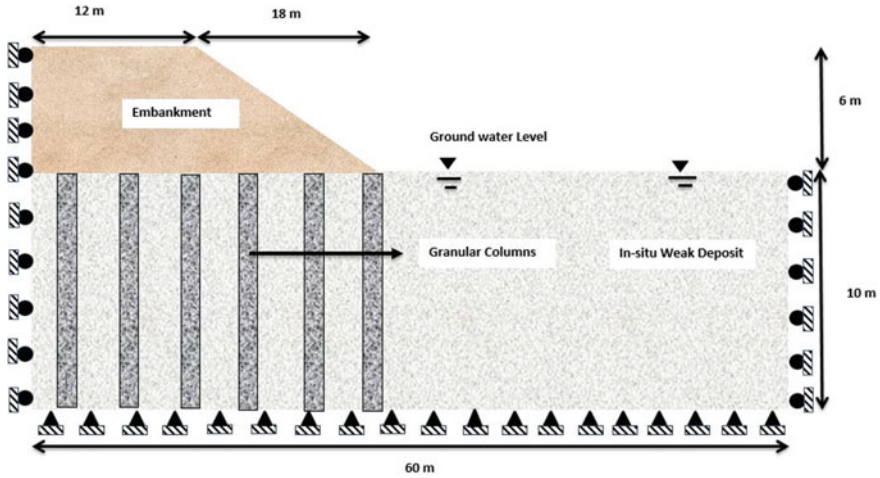


Fig. 1 Schematic of embankment resting on granular columns in Peat

2 Problem Statement and Modelling

Figure 2 FE Model of Embankment resting on Encased Granular Columns.

2.1 Modeling Embankment Loaded Ordinary and Encased Granular Columns

In general, the diameter of the granular columns adopted in the field ranges from 0.8 to 1.2 m. In the present analysis, 1 m Diameter (D) column is used with 2 m c/c spacing. Due to symmetry, only one-half of the embankment is modeled with a row

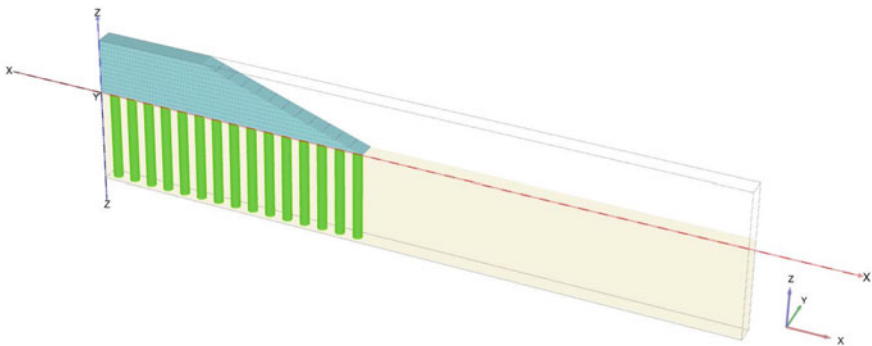


Fig. 2 FE Model of Embankment resting on Encased Granular Columns

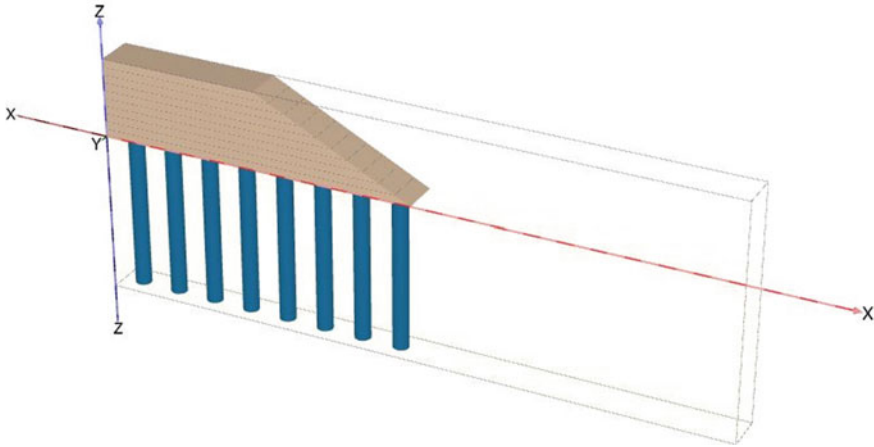


Fig. 3 FE model of an embankment on granular columns after Mohapatra and Rajagopal [8]

of granular columns. The extent of side boundary was chosen based on Navin [10], wherein which the distance from the toe should be more than twice the height of embankment to avoid boundary effects. The granular columns modeled are of end bearing type and assumed to rest on hard strata. Geosynthetic encasement of 500 kN/m secant modulus is used to encase the granular columns. The groundwater level was assumed close to ground level.

A uniform layer thickness of 0.5 m was adopted for constructing the 6 m height of embankment on a layer-by-layer basis using staged construction technique. A stability analysis was conducted to ensure the final safety after the last phase of construction. A square type layout of granular columns is used in the numerical modeling and the out of the plane thickness of the row was decided based on the spacing of granular columns. A medium fine type mesh was adopted as the numerical analysis with fine meshes yielded the same factor of safety. The granular columns and the surrounding peat soil were assumed to be intact, and hence no interface elements were used. As indicated in Fig. 1, the deformations were permitted only in vertical directions and the bottom boundary was completely fixed adopting standard fixities. The FE model of the embankment resting on EGC is shown in Fig. 2.

2.1.1 Factor of Safety Calculation Using FE Code

In finite element analysis, the factor of safety values is determined by performing the stability analysis with gradually increasing or decreasing factor of safety (FOS) values and plotting the deformations against the corresponding FOS values. The critical value is obtained when the deformations tend to increase drastically with small changes in FOS value. In the FE program, the factor of safety analysis

described above is performed by $C-\phi$ reduction or Strength reduction technique. The reduction of the strength parameters is directly controlled by the Total Multiplier (ΣMsf). This parameter is continuously changed in the analysis until reaching the limit state. Hence by plotting the variation of the Total Multiplier (ΣMsf) against Total deformation (u) the factor of safety can be directly found out. A typical result from the FE program is shown in Fig. 4.

2.1.2 Validation of the Numerical Model

The present numerical model is validated from the studies conducted by Mohapatra and Rajagopal [8]. The embankment model is shown below in Fig. 3. The results obtained from the current study and that of Mohapatra and Rajagopal [8] are summarized in Table 1. It can be seen that there is good agreement between the present study and the published results in terms of factor of safety with a variation of 5%.

2.1.3 Material Properties of the Present Numerical Model

The properties of various materials used in the numerical model are shown below in Table 2. The geosynthetic material was modeled as a linear elastic element with the tensile modulus as an input parameter.

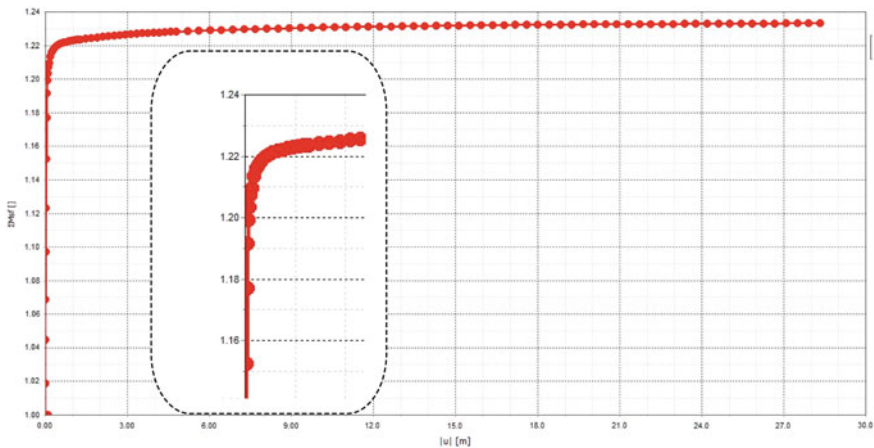


Fig. 4 ΣMsf with total deformation (u) m Mohapatra and Rajagopal [8]

Table 1 Validation of the numerical model in terms of FOS

S. No	Authors	Type of numerical analysis	FOS values
1	Mohapatra and Rajagopal [8]	Finite difference	1.17
2	Present study	Finite element	1.233

Table 2 Properties of various materials used for numerical modeling

S. No	Property	Embankment	Peat	Granular column
1	Bulk unit weight γ_b (kN/m ³)	16	8	18
2	Deformation modulus (kPa)	52000	6000	25500
3	Cohesion (Cu) kPa	3	3	1
4	Friction angle (ϕ)°	30	15	38
5	Constitutive model	Mohr–coulomb	Mohr–coulomb	Mohr–coulomb
6	Drainage	Drained	Undrained	Drained

2.1.4 Parametric Study

A detailed parametric study was conducted by varying the influencing parameters related to the stability of the embankment say friction angle of the granular column, cohesion value of the peat deposit, spacing of granular column, height of embankment for both ordinary and encased granular column. Additionally, the performance of the embankment when founded on encased granular columns with varying geosynthetic modulus was also investigated. Considerable improvement in the factor of safety was observed with encased granular columns when compared to ordinary granular columns. The range of values selected for parametric analysis was chosen based on the applicability of granular columns in the field.

Figure 5 shows the variation of friction angle of the granular column with the factor of safety. An increase in FOS is observed for both ordinary and encased granular columns but encased granular columns have mobilized higher FOS values due to the confining support provided and shear resistance offered by geosynthetic encapsulation. For higher values of friction angle, deep-seated failure surface was observed with embankment treated with OGC and a toe failure was observed with EGC.

The undrained shear strength of the peat ranges from 3 to 15 kPa, which is generally much lower than that of soft clays Huat et al. [5]. Nearly the same range has been adopted in the parametric study to evaluate the FOS for both OGC and EGC. From Fig. 6, it can be observed that with an increase in undrained shear strength of the foundation soil the embankment becomes more stable and higher factor of safety is mobilized. Encased granular columns exhibited higher FOS value when compared to OGC. The variation is especially high for the range of Cu values from 10 to 15 kPa.

Fig. 5 Variation of friction angle of granular column with FOS

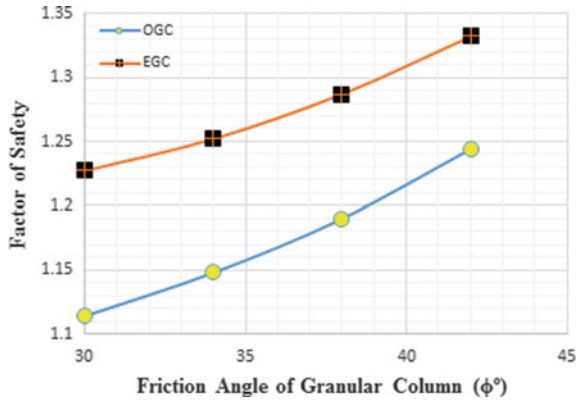
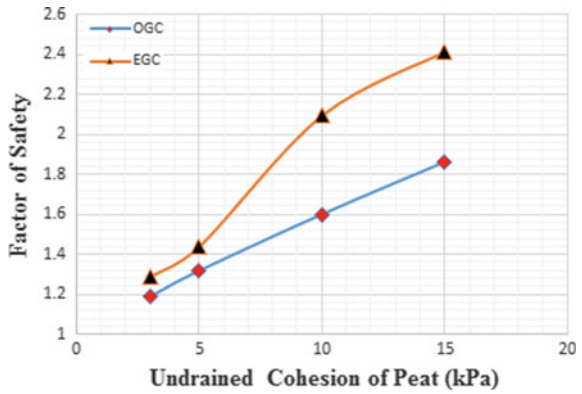


Fig. 6 Variation of cohesion of peat with FOS



Madhira and Rao [7] concluded from their laboratory studies that optimum spacing of granular columns ranges from 2 to 3 times the Diameter (D) of the granular column. The same range of spacing has been adopted in the present study. As indicated in Fig. 7, Granular columns with closer spacing (2D) yielded higher FOS. With the increase in spacing of columns, the group effect was lost and the granular columns started behaving individually indicating reduced FOS. However, the performance of granular columns in terms of FOS with geosynthetic encasement was considerably higher over ordinary columns due to confinement.

Figure 8 shows the variation of FOS values with area replacement ratio (ARR). ARR is defined as the area of the granular column to the total area within the unit cell or slice of the embankment currently considered for analysis. The ARR for the above-specified spacing of granular column ranges between 19.62% and 8.72% which is typically adopted in the field. The granular columns with higher replacement ratios (closer spacing) invariably yielded higher FOS values. For higher area replacement ratios of the EGC, the critical slip circles were contained within the embankment whereas a deep-seated failure was still observed for ordinary granular columns as they had undergone shear failure.

Fig. 7 Variation of granular column spacing with FOS

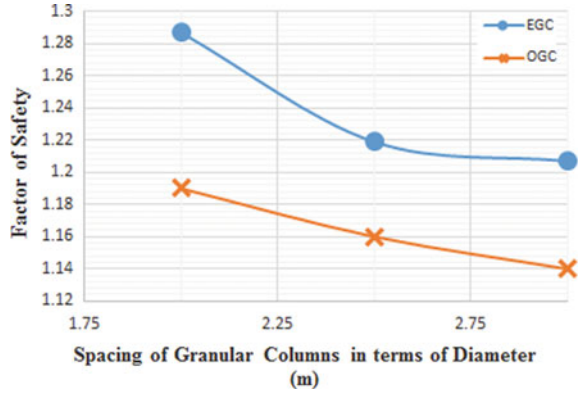
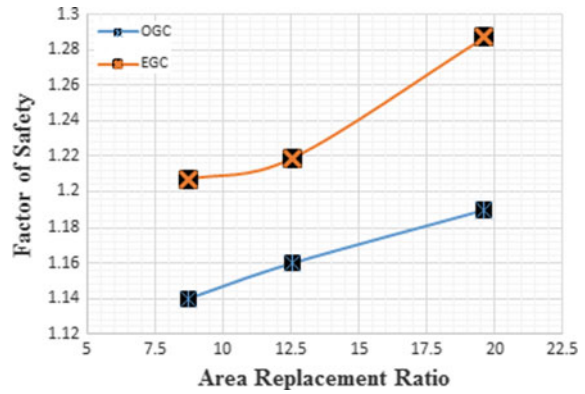
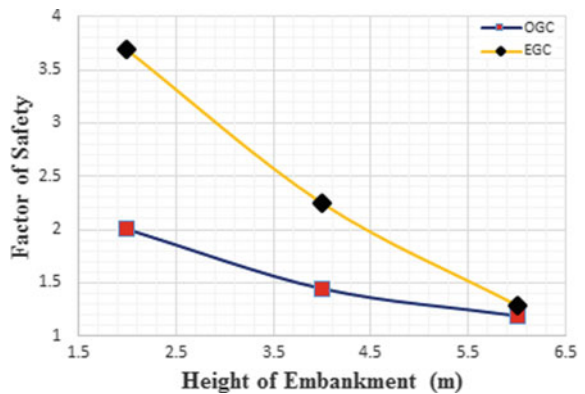


Fig. 8 Variation of Area Replacement Ratio with FOS



Variation of embankment height with FOS for both OGC and EGC cases is shown in Fig. 9. It can be easily noted that the FOS values reduce drastically with increase in height of embankment. Similar observations were reported by Abusharar and Han (2011) and Mohapatra and Rajagopal [8]. The encasement

Fig. 9 Variation of embankment height with FOS



provided to the granular columns is found to increase the FOS and the effect was more pronounced until embankment height of 4 m. With further increase in height, the effect of increase in FOS was nominal as the slip circles passed through the foundation soil.

The performance of the embankment with encased granular columns on par with ordinary granular columns is evaluated by varying the geosynthetic tensile modulus as shown in Fig. 10. The secant modulus (J) value was varied from 500 to 10000 kN/m. The tensile modulus value of zero indicates an ordinary granular column. The observations clearly indicate that with higher tensile modulus the FOS values increase drastically, i.e., from 1.19 to 1.60. This drastic improvement in FOS from geosynthetic encased granular columns is augmented from the change of failure pattern from deep-seated failure to toe failure. A typical incremental displacement plot from the numerical analysis showing the deep-seated mode of failure (OGC) to toe failure (EGC) is shown in Fig. 11.

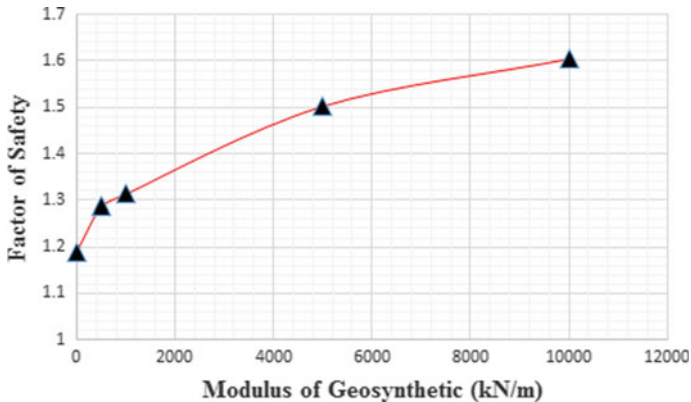


Fig. 10 Variation of tensile modulus of the geosynthetic with FOS

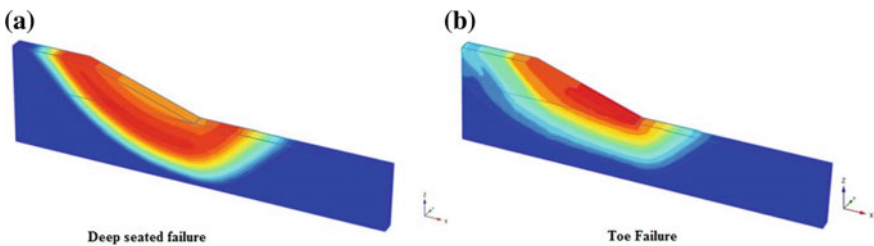


Fig. 11 Different failure modes of ordinary and encased granular columns

2.1.5 Additional Discussions on OGC and EGC Supported Embankments

The position of groundwater table is one of the important factors, which influence the stability of embankments. Normally, the groundwater levels are close to the ground surface in the case of wet marshy lands where peaty soils are predominant. Based on the numerical studies conducted by the authors, there is an improvement in FOS values with reduction in water table levels. The results of the analysis are not presented here for the want of space but still worth mentioning. Stability of the embankment alone is discussed in this paper and there are other factors say stress concentration ratios, method of installation of granular columns, type of loading which influence the performance of the embankment. The results from the present analysis have simply depicted the additional benefits that can be achieved by encapsulating the granular column with a suitable geosynthetic material, especially with peat deposit.

The case study reported by Alexiew and Raitel [3] on the applicability of encased granular columns in peat-like deposits for an Airbus construction at Hamburg has motivated the author to conduct a numerical analysis simulating the field conditions. The numerical analysis conducted by the authors needs support from full-scale field studies on encased granular columns to gain confidence and understanding of the load sharing technique, especially with peat deposits.

3 Conclusions

Based on the numerical investigations conducted on the embankments resting on both ordinary and encased granular columns in peat, some conclusions are drawn as indicated below.

1. Ordinary granular columns perform better only if appropriate support is provided from the surrounding soil and exhibit poor performance with lateral (shear) loading.
2. Geosynthetic encased columns have shown better performance in weak soils like peat in terms of stability and improvement irrespective of the poor lateral support provided.
3. The spacing of granular columns, quality infill material, and undrained cohesion of the soft deposit, area replacement ratio, height of embankment and modulus of the geosynthetic are the significant factors which affect the FOS values of embankment supported OGC and EGC's.

4. The performance improvement in the embankment is augmented from the deep-seated mode of failure with ordinary granular columns to a toe failure with encased granular columns for the cases analyzed in the study.
5. Additional full-scale instrumented field studies are required to further understand the behavior of embankments resting on geosynthetic encased granular columns in peat soils

References

1. Ambily AP, Gandhi SR (2007) Behavior of stone columns based on experimental and FEM analysis. *J Geotech Geoenviron Eng* 133(4):405–415
2. Almeida MSS, Hosseinpour I, Riccio M, Alexiew D (2015) Behaviour of Geotextile—encased granular column supporting test embankment on soft deposit. *J Geotechn Geoenviron Eng* 141:1–9
3. Alexiew D, Raithel M (2015) Geotextile—encased columns case studies over twenty years, Ground Improvement case histories: Embankments with special reference to consolidation and other physical methods. pp 451–475
4. Han J, Parsons RJ, Sheth AR, Huang J (2005) Factors of safety against deep-seated failure of embankments over deep mixed columns. In: *Proceedings of deep mixing conference*, vol 1.2. Sweden, pp 231–236
5. Huat BB, Prasad A, Asadi A, Kazemian S (2014) *Geotechnics of organic soils and peat*, 1st edn. CRC Press. The Netherlands
6. Malarvizhi SN, Ilamparuthi K (2004) Load versus settlement of clay bed stabilized with stone and reinforced stone columns. In: *Asian regional conference on geosynthetics*. GeoAsia, pp 322–329
7. Madhira M, Rao L (2010) Evaluation of optimum spacing of stone columns. In: *Indian geotechnical conference*. Geotrendz, Mumbai, pp 759–762
8. Mohapatra SR, Rajagopal K (2016) Analysis of failure of geosynthetic encased stone column supported embankments. In: *Proceedings of 3rd Pan-American conference on geosynthetic*. Miami Beach, USA
9. Murugesan S, Rajagopal K (2007) Model tests on geosynthetic encased stone columns. *Geosynth Int* 24(6):349–358
10. Navin MP (2005) Stability of embankment founded on soft soil improved with deep-mixing-method column. A PhD thesis submitted to Virginia Polytechnique Institute and State University, Virginia, USA
11. Van Impe WF (1989) *Soil improvement techniques and their evolution*. Balkema, Rotterdam, Netherlands, pp 63–66

Experimental Investigation for Damage Evaluation of Bridges Using Piezo-Transducers



Umesh T. Jagadale, Rutuja D. Kharade, Chittaranjan B. Nayak
and Wasudeo D. Deulkar

Abstract In recent years, there is a continuous rise in construction activities in the field of civil engineering. The life of a structure depends on the initial strength and the maintenance of construction. The effects on infrastructure due to aging, deterioration, and extreme events are associated with the realization of the need for advanced structural health monitoring (SHM) and damage detection tools. Civil engineering structures such as bridges have a long design life and, therefore, unavoidably come across physical aging and deterioration. Through this SHM technology, early detection of structural damage and examination of the structural integrity is possible with a resultant optimization of maintenance of bridges. The electro-mechanical impedance (EMI) technique is a recent method that is comfortable to implement complex structures with simple instrumentation and direct results. In this research work, a case study of bridge model is considered for SHM in determining damage severity and its location for moderate to severe damage. Also, the same technique applied to the existing bridge for structural health monitoring. From results, it was concluded that the presented methodology was capable of monitoring the existing bridges and also shows good efficiency in determining damage severity and its location. There are noticeable changes in frequencies for moderate to severe damage. Hence, this technique is suitable for the prediction of the presence of damage and its location.

U. T. Jagadale (✉)

JSPM'S Rajarshi Shahu College of Engineering, Tathwade, India

e-mail: umesh12jagadale@gmail.com

R. D. Kharade · C. B. Nayak

Civil Engineering Department, VPKBIET, Baramati, India

e-mail: rutujakharade611@gmail.com

C. B. Nayak

e-mail: cbnayak@gmail.com

W. D. Deulkar

Civil Engineering Department, Government College of Engineering and Research,

Avasari Khurd, Pune, India

e-mail: wasudeon@gmail.com

© Springer Nature Singapore Pte Ltd. 2020

A. Prashant et al. (eds.), *Advances in Computer Methods*

and Geomechanics, Lecture Notes in Civil Engineering 56,

https://doi.org/10.1007/978-981-15-0890-5_27

Keywords Structural Health Monitoring (SHM) · Nondestructive Evaluation (NDE) · PZT patches · Electro-Mechanical Impedance (EMI)

1 Introduction

The service life of civil structures depends on type and quality of construction, service loads, exposure conditions, aging, alterations, and maintenance. To get design life of any structure should be inspected for every 5 years from date of construction. Higher operational loads than design loads, multifaceted nature of design and longer life eras forced to common structure make it progressively critical to screen the wellbeing of these structures. Early detection of the damage or structural degradation prior to local failure can anticipate cataclysmic fall of those structures. The serviceability, security, and manageability of the bridges have gotten much consideration by regulatory specialists. Uses of EMI technique have been accounted by Adams et al. [1] for damage detection in composite materials using vibration technique. Dynamic system utilization for damage detection of the parameters like natural frequencies, damping ratio, and mode shapes due to vertical base motions to detect damage qualitatively and quantitatively have been studied by Bhalla and Soh [2]. Bhalla and Soh [3] also observed the natural frequencies and the mode shapes are directly related to the stiffness of the structure. The changes in natural frequencies and damping ratios can simply indicate the presence of damage or faults and its severity. The natural frequencies and the mode shapes are openly related to the stiffness of the structure. The change in natural frequencies and damping ratios can merely specify the occurrence of damage or faults and its severity. The formations can be appropriately hired to extract the mechanical impedance of any “unknown” structural system from the admittance signatures of a surface-attached PZT patch studied by Park et al. [4].

Two categories of PZT-based dynamic destruction identification techniques are available for study: (a) impedance-based technique and (b) Lamb wave-based technique. As for the impedance-based method, effective applications to damage detection for different kinds of structures have been reported in the last decade by Zagrai and Giurgiutiu [5]. Giurgiutiu et al. [6] utilize piezoelectric transducers, mainly made of piezoelectric ceramic as actuators and sensors. Because of the presence of the electro-mechanical coupling in the piezoelectric transducer, its electrical impedance is directly related to the mechanical properties of the host structure and is named the electro-mechanical impedance discussed by Park et al. [7]. The experimental and analytical results show the accuracy of the E/M impedance method for detecting damage in complex structures. The application of the EMI method ranges from the joints assessment to the civil and aerospace structures discussed in various literature, i.e., Providakis et al. [8], Kaur and Bhalla [9] and Moin et al. [10]. Nayak et al. [11] studied a nondestructive technique used to predict the residual life of reinforced concrete beams having different cracking levels. This paper presents the application of the EMI technique on a composite reinforced

concrete (RC) and steel girder bridge to observe vibration response on bridge due to various traffic conditions to find the efficiency of PZT patches in actual field structures like bridges. The bridge represented is two-lane road bridges over the railway with normal traffic conditions. The presented methodology was verified on truss bridge model. Using EMI technique frequency response for healthy and damaged state was observed using PZT patches. The change in natural frequencies and damping ratios can easily indicate the presence of damage or faults and its severity. Wang et al. [12] proposed a new damage detection method based on electromechanical admittances (inverse of impedance) of multiple PZT patches and a damage index, namely, cross-correlation coefficient (CC). Numerical and experimental studies on damage detection of a plain concrete beam based on the proposed method have also been reported. Narayanan and Kolluru [13] studied on PZT-based damage sensors consisting of piezo-electric patches, which are bonded to the surface of a concrete structure can be developed for assessing the damage progression of concrete members. Baptista et al. [14] presented an experimental study on the effect of temperature on the electrical impedance of the piezoelectric sensors used in the EMI technique. Allamraju and Srikanth [15] are demonstrating a novel piezoelectric vibration energy impact mass harvester (NPVEIMH) by using lead ball as impact mass for optimising the output power. Talakokula et al. [16] presented a new approach for detecting the onset and quantifying the level of carbonation induced rebar corrosion. The approach was based on the changes in the mechanical impedance parameters acquired using the electro-mechanical coupling of a piezoelectric lead zirconate titanate (PZT) ceramic patch bonded to the surface of the rebar. Demi et al. [17] studied the sensitivity of a new kind of embedded active PZT sensor in structural impact damage detection through theoretical and experimental analysis. A new embedded 2D electromechanical impedance model was formulated, in which the PZT patch can be protected from external impact or disturbance. Nayak et al. [18] experimentally and numerically studied non destructive techniques and accelerated corrosion process for prediction of residual life of structures. Jagadale et al. [19] experimentally studied to predict the strength of concrete cubes and aluminium plate using piezo-ceramic smart materials at various damage levels.

2 Experimental Work

2.1 Case Study I: Experimental Work on Truss Bridge Model

The presented methodology is broadly classified into two case studies, first one is on the steel truss bridge model and second one is on the existing bridge structure. Truss bridge model was selected for this study 400 mm long and 100 mm wide. The model was made up of mild steel members as 10 mm square bar and 6 mm

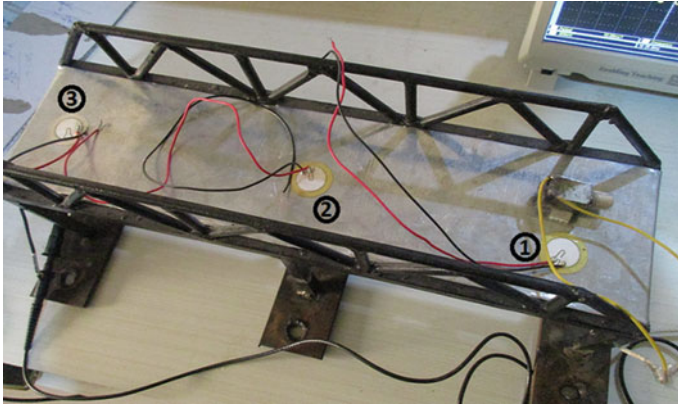


Fig. 1 Lab-scale truss bridge model

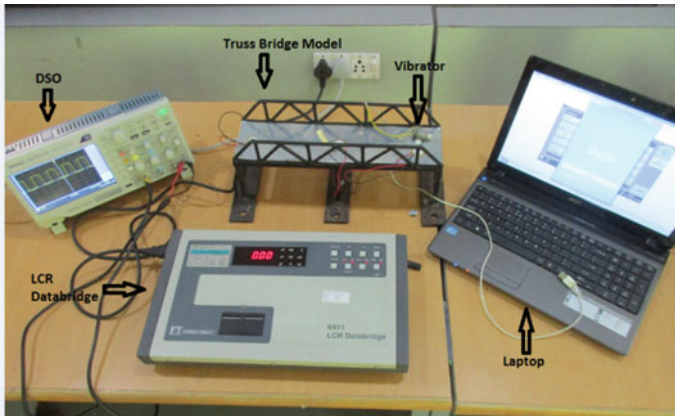


Fig. 2 Experimental setup along with bridge model

diameter bar. All joints are welded joints connected using arc weld. Platform for the bridge model is made up of aluminum sheet of 1 mm thickness as shown in Fig. 1. In modern years, the damage detection with EMI method has attained increased attraction. Surrounded by structural acoustics methods, the electro-mechanical impedance method is an innovative method that is easy to apply on complex structures with least instrumentation and direct results. The EMI technique uses PZT transducers for SHM. The PZT patches are prepared up of materials, which reveal the phenomenon of ‘piezoelectricity’.

The experimental setup as shown in Fig. 2 contains three PZT patches that were bonded on the platform of the model at 40, 150, and 330 mm from vibrator source. Then, the soldered PZT patches were wired to LCR Databridge and Digital Storage Oscilloscope (DSO).

2.1.1 Mechanical Impedance of Truss Bridge Model

In order to illustrate typical ranges of impedance measurements were made on a truss bridge model. The test setup is illustrated in Fig. 2. The vibration force generated and the magnitude of the impedance was calculated from the resistance and capacitance captured on LCR meter. The response was measured also with the force pickup in the resistance and capacitance head subjected to vibrations. Measurements were made on healthy state and damaged state of bridge model, respectively.

The concept of mechanical impedance of structures is similar to the concept of electrical impedance in electrical circuits. Using the 6411 LCR Databridge we can find out resistance and capacitance of structure. Generally, LCR meters in this class have an accuracy of $\pm 1\%$. Capacitive reactance is given by Eq. 1.

$$X_C = \frac{1}{2\pi fC} \tag{1}$$

where C is capacitance in Farad (f)

Figure 3 shows the impedance triangle, therefore by using Pythagoras theorem, the total impedance of a circuit is the square root of the sum of the squares of the resistance and reactance.

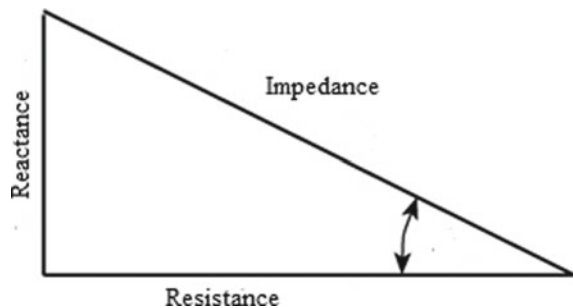
Therefore, impedance can be calculated by Eq. 2

$$Z = \sqrt{R^2 + X_C^2} \tag{2}$$

where,

- Z Impedance of structure
- R Resistance of structure
- X_C Capacitive Reactance of structure

Fig. 3 Impedance triangle



2.1.2 Frequency of Truss Bridge Model

In truss bridge model, change in frequencies before and after damage was observed at three different locations as 40, 150, and 330 mm from the vibrator source. In both cases, i.e., before damage and after damage, respectively, Bridge model is excited under the vibration from vibrator for 1 min. and there is pause of 2 min. in total, there are ten excited durations in which model is tested and examined and peak value from all these excitations were used as resultant value for that patch.

2.1.3 Mechanical Loss Factor for Truss Bridge Model

The concept of mechanical impedance can be easily extended to complicate multiple degree of freedom (MDOF) systems. This system is analogous to a series LCR circuit in classical electricity.

Therefore mechanical impedance (Z) = Damping coefficient (c)

The measurement, however, severely limits the frequency range over which continuous measurements may be made since the true driving point impedance of the compliant material increase with frequency.

The mechanical loss factor is given by Eq. 3.

$$\eta = \frac{c\omega}{k} \quad (3)$$

where

η Mechanical loss factor

$$\omega = 2\pi f$$

f frequency of vibration and stiffness factor k can be calculated as

$$k = \omega^2 m$$

m Mass of truss bridge model in kg

2.2 Case Study II: Study of Existing Bridge Structure

The selected bridge is a roadway bridge spanning 20 m. This is composite concrete-steel girder bridge is located over the railway and roadway in Baramati as shown in Fig. 4. It was constructed in 2014 and designed to be comprised of three straight simple spans supported on box piers.



Fig. 4 Existing bridge structure (TC college Baramati to Bhigwan Road, Baramati, Pune)

The bridge structure is composite steel-concrete girder bridge which is divided into three spans one long span with steel girder and under moving train. The other two spans are short spans with concrete deck spans and under roadway with normal traffic conditions. The bridge deck and the piers are made of reinforced concrete. Details of vehicles carried by the bridge and their frequencies illustrate that the bridge is experienced variable amplitude fatigue loading. In visual inspection, no visual cracks were observed in any component of the superstructure. The study includes the frequency response of the various parts of the bridge structure at various traffic conditions.

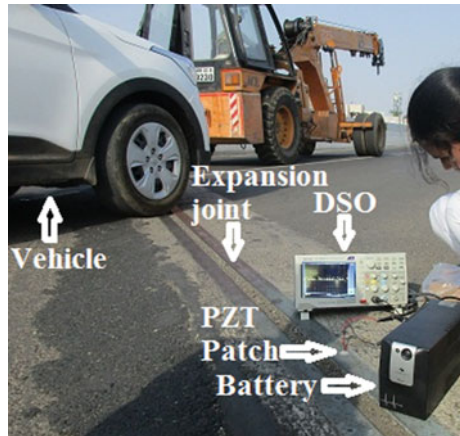
2.2.1 Observation of Under Moving Train Vibrations on Bridge Piers

In first case vibrations in columns of existing bridge structure were monitored for the moving train under bridge as shown in Fig. 5. The railway is not attached to the existing structure but train is moving under the structure, which transfers the vibrations in the ground which can come to the bottom of the bridge piers.

Fig. 5 Observations of vibration during moving train from below the bridge (TC college Baramati to Bhigwan Road, Baramati, Pune)



Fig. 6 Observation of vibrations at expansion joint due to moving traffic (TC college Baramati to Bhigwan Road, Baramati, Pune)



2.2.2 Observation of Vibrations at Expansion Joint Due to Moving Traffic

In next case, vibrations due to moving traffic were observed at the expansion joint as shown in Fig. 6. In this case vibrations due to car, bike was observed at normal traffic speed condition as shown in photo.

3 Experimental Results

This chapter presents the results obtained from a nondestructive technique to predict the damage in steel truss bridge model which was damaged artificially at three different locations, considering the impedance and frequencies response. With damage progression, the stiffness can be observed to reduce and the damping increase. The stiffness and self-weight of structure were reduced after the incipient damage.

3.1 Case Study I: Truss Bridge Model

The bridge model is artificially damaged at three different positions as shown in Fig. 7. At each position two holes were drilled of 5 mm diameter each.

The mechanical impedance of truss bridge model is increased by 5.62% after damaging model compared with healthy model. Also there is increase in vibration response due to stiffness reduction and weight loss in the structure. The frequency of all the observations measured for before and after damage case for the bridge model at three different locations from vibrator source.

Fig. 7 Damage locations on lab-scale truss bridge model

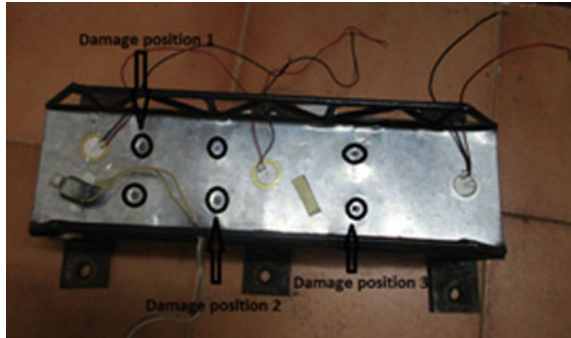


Table 1 Change in frequency for healthy and damaged state

Location of PZT patch From vibrator source (mm)	Frequency (Hz)		Increase in frequency (%)
	Healthy	Damaged	
40	926.0	1143.47	19
150	588.2	808.2	27.22
330	144.9	249.02	41.81

Table 1 shows that percentage increase in frequency for patch 1 is very much less as compared to remaining locations where damage is present in between vibrator and patch 2 and 3, by using this response we can detect location of damages and its severity in structures as shown in Fig. 8.

The Fig. 9 shows the change in frequencies observed at different locations after damage the bridge model.

The mechanical loss factor is a measure of mechanical damping and decrease in mechanical loss factor after damage as shown in Table 2.

3.2 Case Study II: Vibration Response of Existing Bridge Structure

The vibrations generated from moving train are transferred to the ground and large amount of vibrations are absorbed by ground and very less vibrations are occurred at column base near railway. The selected existing bridge structure contains normal traffic condition and the structural components of the bridge selected for observations are expansion joint and at side padadi. The frequencies observed for light and heavy vehicles like car, loaded truck, and bike are 12.7, 20.3, and 7.85 Hz, respectively, at an expansion joint. The observed values are taken as the maximum values at those points.

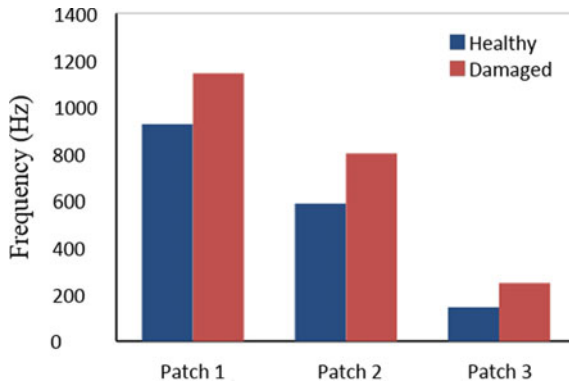


Fig. 8 Change if frequency response

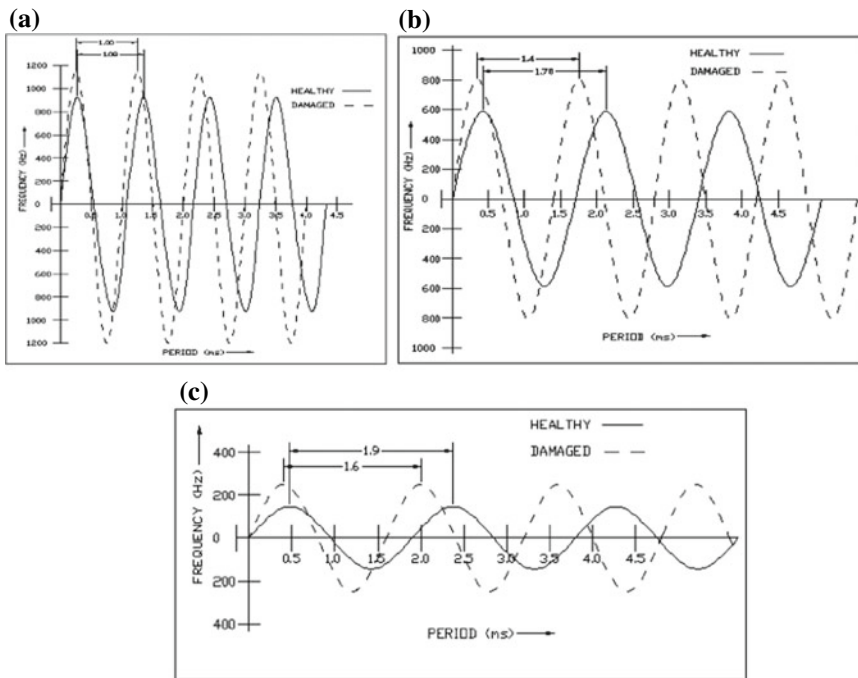


Fig. 9 Frequency response at different damage locations. a At distance of 40 mm from vibrator source b At distance of 150 mm from vibrator source c At distance of 330 mm from vibrator source

Table 2 Change in mechanical loss factor

Location of PZT patch From vibrator source (mm)	Mechanical loss factor η	
	Healthy	Damaged
40	0.19788	0.1693
150	0.3115	0.240
330	1.264	0.779

4 Discussion

Based on the above case studies, it is determined that the presented methodology is capable to monitor the existing structures like bridges and also shows good efficiency in determining damage severity and its location. It may be possible that frequency changes for the same level damage insame structure are different, depending upon how the damage originated in the structure. There are noticeable changes in frequencies for moderate to severe damage. Hence, this technique is suitable for prediction of presence of damage and its location.

5 Conclusion

The major novelty in the present research is that for the first time, proof-of-concept experimental demonstration has been provided to employ the same PZT patch for SHM on real-life bridge structure.

The following sections outline the major conclusions taking out from this research.

1. Using increased frequency response from moderate to severe damage locations on bridge model as well as increased mechanical impedance of the model after damage the severity and location of damage can be predicted with the desired accuracy.
2. With the help of frequency response and mechanical impedance, the mechanical loss factor was determined for healthy and damaged condition of truss bridge model.
3. In this work vibrations due to traffic on the existing bridge structure were used as input source hence there is no demand of any external source to charge PZT patch.
4. PZT patches proved very competent to sense low vibration response in nominal time on existing bridge structure with normal loading conditions.

References

1. Adams R, Walton D, Flitcroft J, Short D (1975) Vibration testing as a nondestructive test tool for composite materials. In: American society for testing and materials, composite reliability. ASMSMSP, Philadelphia. https://www.researchgate.net/publication/284071634_Vibration_testing_as_a_nondestructive_test_tool_for_composite_materials
2. Bhalla S, Soh C (2004) Structural health monitoring by piezo-impedance transducers. I: modeling. *J Aerosp Eng* 4(5). [https://doi.org/10.1061/\(ASCE\)0893-1321\(2004\)17:4\(154\)](https://doi.org/10.1061/(ASCE)0893-1321(2004)17:4(154))
3. Bhalla S, Soh C (2003) Structural impedance based damage diagnosis by piezo-transducers. *Earthq Eng Struct Dyn* 32:1897–1916. <https://doi.org/10.1002/eqe.307>
4. Park G, Sohn H, Farrar C (2003) Overview of piezoelectric impedance-based health monitoring and path forward. *Shock Vib* 6(35):451–463. <https://doi.org/10.1177/05831024030356001>
5. Zagrai A, Giurgiutiu V (2001) The electro-mechanical impedance method for damage identification in circular plates. In: 142nd meeting of the acoustical society of America. Fort Lauderdale, Florida. <https://pdfs.semanticscholar.org/2b24/1d61ba2337a50a05e1dd1474d907a8ee3cd4.pdf>
6. Giurgiutiu V, Reynolds A, Rogers C (2000) Experimental investigation of E/M Impedance health monitoring of spot-welded structural joints. *J. Intell Mater Syst Struct* 10(10):802–812. <https://doi.org/10.1106/N0J5-6UJ2-WIGV-Q8MC>
7. Park S, Yun C, Roh Y, Lee J (2006) PZT-based active damage detection techniques for steel bridge components. *Smart Mater Struct* 15:957–966. <https://doi.org/10.1088/0964-1726/15/4/009>
8. Providakis C, Angeli G, Favvata M, Papadopoulos N, Chalioris C, Karayannis C (2014) Detection of concrete reinforcement damage using piezoelectric materials—analytical and experimental study. *Int J Civil Environ Struct Constr Architect Eng* 8(2). https://www.researchgate.net/publication/261720891_Detection_of_concrete_reinforcement_damage_using_piezoelectric_materials_-_Analytical_and_experimental_study
9. Kaur N, Bhalla S (2016) Numerical investigations on energy harvesting potential of thin PZT patches adhesively bonded on RC structures. *Sens Actuators A: Phys* 2(02):44–59. <https://doi.org/10.1016/j.sna.2016.02.002>
10. Moin U, Bhalla S, Naqvi T (2017) Fatigue damage assessment of RC column using PZT sensor. *Proc Eng* 12(130):1223–1230. <https://doi.org/10.1016/j.proeng.2016.12.130>
11. Nayak C, Thorat N, Thakare S (2018) Corrosion impact analysis on residual life of structure using cathodic technique and algor simulation software. *Eng Struct Technol* 10:18–26. <https://doi.org/10.3846/est.2018.1468>
12. Wang D, Song H, Zhu H (2013) Numerical and experimental studies on damage detection of a concrete beam based on PZT admittances and correlation coefficient. *Constr Build Mater* 08 (74):564–574. <https://doi.org/10.1016/j.conbuildmat.2013.08.074>
13. Narayanan A, Kolluru V (2016) Damage assessment in concrete structures using PZT patches. <https://doi.org/10.21041/ra.v7i1.173>
14. Baptista F, Budoya D, Almeida V, Ulson J (2014) An experimental study on the effect of temperature on piezoelectric sensors for impedance-based structural health monitoring. *Sensors* 1424–8220. <https://doi.org/10.3390/s140101208>
15. Allamraju KV, Srikanth K (2016) Design and experimental study of novel piezoelectric vibration energy impact mass harvester. *Proc Eng* 5(4):560–567. <https://doi.org/10.1016/j.proeng.2016.05.042>
16. Talakokula V, Bhalla S, Ball R, Bowen C, Pesce G, Kurchania R, Bhattacharjee B, Gupta A, Paine K (2016) Diagnosis of carbonation induced corrosion initiation and progression in reinforced concrete structures using piezo-impedance transducers. *Sens Actuators* 02(33): 79–91. https://www.researchgate.net/publication/295699514_Diagnosis_of_carbonation_induced_corrosion_initiation_and_progression_in_reinforced_concrete_structures_using_piezo-impedance_transducers

17. Demi A, Hongping Z, Hui L (2016) Sensitivity of embedded active PZT sensor for concrete structural impact damage detection. *Constr Build Mater* 02(094):348–357. <https://doi.org/10.1016/j.conbuildmat.2016.02.094>
18. Nayak C, Thorat N, Thakare S (2018) Corrosion impact analysis on residual life of structure using cathodic technique and algor simulation software. *Eng Struct Technol* 10(1):18–26. <https://doi.org/10.3846/est.2018.1468>
19. Jagadale U, Nayak C, Narute G (2018) Structural health monitoring using piezo-ceramics smart material. In: 9th international conference on sustainable built environment 2018 (ICSBE), University of Peradeniya, Peradeniya, Sri Lanka. https://www.researchgate.net/publication/335321916_STRUCTURAL_HEALTH_MONITORING_USING_PIEZO-CERAMICS_SMART_MATERIAL
20. Markovic N, Nestorovic T, Stojic D (2015) Numerical modeling of damage detection in concrete beams using piezoelectric patches. *Mech Res Commun* 64:15–22. <https://doi.org/10.1016/j.mechrescom.2014.12.007>

Effect of Magnesium Incorporation in Enzyme-Induced Carbonate Precipitation (EICP) to Improve Shear Strength of Soil



Alok Chandra and K. Ravi

Abstract Enzyme-induced carbonate precipitation (EICP) is a novel, bioinspired soil stabilization technique in which calcium carbonate (CaCO_3) crystals are enzymatically precipitated to cement and link the soil grains, thereby improving the shear strength of the soil. This work aims to analyze the effect of incorporating Mg^{2+} ions on crystal morphology and their direct influence on the mechanical properties of the soil. A beaker experiment conducted by mixing urea, urease enzyme and $\text{MgCl}_2/\text{CaCl}_2$ in different molar ratios revealed that the increase in the $\text{Mg}^{2+}/\text{Ca}^{2+}$ molar ratio decreases the amount of precipitated mass. The soil specimens for unconfined compressive strength (UCS) test were prepared as per its maximum dry unit weight (γ_{dmax}), and an optimum solution content (w_{opt}) consisting of urea, urease enzyme and $\text{MgCl}_2/\text{CaCl}_2$ at various $\text{Mg}^{2+}/\text{Ca}^{2+}$ molar ratio. Field-emission scanning electron microscopy (FESEM) and X-ray powder diffraction (XRD) tests performed on precipitated mass verify the influence of Mg^{2+} ions on crystal morphology and the occurrence of other carbonates (dolomite) and polymorphs of CaCO_3 . The results of the UCS tests show that the lower molar ratio of $\text{Mg}^{2+}/\text{Ca}^{2+}$ can significantly improve the undrained shear strength of the soil.

Keywords EICP · Precipitation · Morphology · Shear strength

1 Introduction

Construction of civil engineering structures on weak or soft soil with poor mechanical properties requires adequate improvement in their strength and stiffness characteristics. Several existing ground improvement techniques are expensive and require substantial energy, and thus need to be replaced by innovative technologies

A. Chandra (✉) · K. Ravi
Indian Institute of Technology Guwahati, Guwahati, India
e-mail: alok.ce@alumni.iitg.ac.in

© Springer Nature Singapore Pte Ltd. 2020
A. Prashant et al. (eds.), *Advances in Computer Methods and Geomechanics*, Lecture Notes in Civil Engineering 56,
https://doi.org/10.1007/978-981-15-0890-5_28

that meet the environment-friendly and sustainable requirements of the society. In recent years, precipitation of calcium carbonate (CaCO_3) in granular soils by a biological process (such as biocalcification or biogrouting or biomineralization) has emerged as a promising soil stabilization technique and has been extensively studied in the last two decades [1, 2]. Most of the published works on this research include microbial-induced calcite precipitation (MICP), which includes incorporating bacteria (such as *Sporosarcina pasteurii*) to produce urease enzyme that helps in the hydrolysis of urea and leads to CaCO_3 precipitation in the presence of calcium ions at favorable condition (such as pH and temperature). These carbonate minerals fill within the soil pores, cementing and bridging the soil grains, thus providing an overall stability to the soil structure. However, bacteria's cultivation and its storage at a large scale is a complex process that challenges the use of MICP in real field application [3].

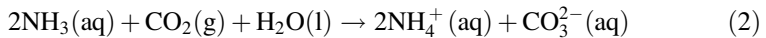
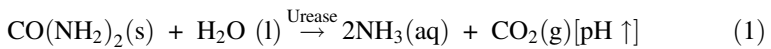
Alternatively, calcium carbonate can be precipitated through non-microbial means by using urease enzyme derived from the ureolytic agricultural sources, such as jack beans, watermelon seeds, etc., also known as enzyme-induced carbonate precipitation (EICP). In recent years, EICP has attracted various researchers who have successfully demonstrated its application through laboratory-scale experiments. These include injecting or percolating of EICP solution into the sand column to provide an improvement in the strength and reduction in permeability [4–8]. Also, EICP solution can provide more durable and substantial wind erosion stabilization in a very short period of time [9, 10].

Under the controlled laboratory condition, it has been observed that when CaCl_2 is the calcium source, CaCO_3 is precipitated as calcite (rhombohedral in shape), which is its most thermodynamically stable polymorph [11, 12]. Strength enhancement of soil due to the nucleation of calcite on soil grains has been well documented in various studies [13–15]. Al Thawadi [11] in his study observed that the strength of the CaCO_3 cemented column was caused mostly due to the point-to-point contacts of rhombohedral calcite crystals bridging adjacent sand grains. However, during real field application, unlike a controlled laboratory environment, there can be various in situ factors that can influence the morphology of calcium carbonate crystals [16]. So an understanding of the change in crystal morphology is important as it can directly affect the strength enhancement of soil.

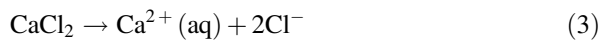
Magnesium is one such important modifier of CaCO_3 morphology and growth inhibitor found in the natural environment [17]. Magnesium is one of the ten most abundant metals in the earth's crust (2–3%) and is present in soil and water predominantly as Mg^{2+} [18]. It is evident that Mg^{2+} ions favor aragonite precipitation in marine environments [19]. Mortensen et al. [16] studied the bacterial growth in different aqueous environments (freshwater to seawater) and reported a large increase in shear wave velocity between the soil columns treated with seawater (salt) concentration up to 50%. This increase was attributed to alkalinity and additional cation present in the seawater that favored the microbial precipitation of calcium carbonate; however, no focus was given on the presence of Mg ions. While exploring MICP technology for providing biocementation in marine environments, Cheng et al. [20]

supported the contribution of the magnesium carbonate hydrate in the strength development of the sample treated with artificial seawater ($\text{MgCl}_2 \cdot 6\text{H}_2\text{O}$, 10.8 g/l). Fukue et al. [21] examined the cementation of sand due to MICP and observed that sand treated with calcite obtained due to the Mg/Ca ratio of 0.5 was stronger than calcite without magnesium. Putra et al. [8] substituted MgCl_2 in EICP solution and promoted aragonite precipitation which increased the unconfined compressive strength of treated sand specimens. Putra et al. [22], in his another study to increase the unconfined compressive strength of the sand, treated EICP solution by substituting MgSO_4 and promoted precipitation of aragonite and gypsum.

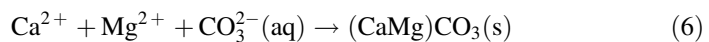
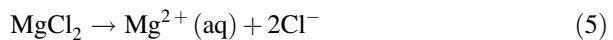
In contrast to many kinds of literature available in soil improvement by carbonate precipitation, no attention has been given to understand the effect of magnesium modified calcite crystals on the variation of the unconfined compressive strength of soil. Hence, in this paper, MgCl_2 is incorporated in the standard EICP solution consisting of urease enzyme, urea, and CaCl_2 such that it will lead to the possibilities of precipitating polymorphs of calcium carbonate (calcite, aragonite, and vaterite) and other carbonate minerals (dolomite). Carbonate mineral precipitation employing urease enzyme via the hydrolysis of urea is investigated in this work, which is described by the following reactions [1, 23].



At pH 7.0 and 38 °C, the urease catalyzes the hydrolysis of urea 10^{14} times faster [24]. With the increase in the pH value of the solution (Reaction 1), concentration of CO_3^{2-} increases (Reaction 2) and in the presence of calcium ions supplied by calcium chloride (Reaction 3), calcium carbonate is produced (Reaction 4) spontaneously [25].



Furthermore, under the presence of both Mg^{2+} and Ca^{2+} ions, carbonate precipitation may occur in a more complex manner and the product can be Mg-calcite, dolomite, and/or Ca-magnesite depending on the Mg/Ca ratio [21]. However, the reaction with an equal concentration of Mg^{2+} and Ca^{2+} ions are ideally described by the reactions 5 and 6 [26].



Considering the limitations in the previous understanding of magnesium-modified calcium carbonate precipitation for soil improvement, current work tried to evaluate the following parameters as discussed below by incorporating Mg^{2+} ions in the EICP solution at various Mg^{2+}/Ca^{2+} molar ratios from 0 to 1. The selected range of Mg/Ca resembles the Mg^{2+} ions concentration in the subsurface and terrestrial water varying from fresh to medium salinity [27].

- Evaluating the weight of the precipitated mass of carbonate obtained during the beaker experiment by mixing urea, urease enzyme and $MgCl_2/CaCl_2$ at various Mg^{2+}/Ca^{2+} molar ratio.
- Mineralogical and morphological characterization of carbonate minerals sample to understand the shape and texture by X-ray powder diffraction test (XRD) and field-emission scanning electron microscopy (FESEM).
- Finally, evaluating the unconfined compressive strength (UCS) of the soil specimens treated with EICP solution at various Mg^{2+}/Ca^{2+} molar ratios and the establishment of variation of undrained shear strength due to the occurrence of carbonates such dolomite and polymorphs of $CaCO_3$ (calcite, aragonite, and vaterite).

2 Materials and Methods

2.1 Characteristics of the Soil

The soil studied in this work was obtained from the campus premises of Indian Institute of Technology Guwahati, Guwahati, India and classified as clayey sand (SC) according to Unified Soil Classification System [28]. The compaction of the soil is characterized by a standard Proctor test [29], which provides a maximum dry unit weight (γ_{dmax}) and an optimum water content (w_{opt}), which are used to prepare the test specimens of the soils used in this work. Specific gravity (G) of the soil was determined by means of water pycnometer [30]. Liquid limit (w_L %), plastic limit (w_P %), and plastic index (PI%) of the soil were determined according to the standard procedure [31]. The pH value of the soil suspension was determined using a pH-sensitive electrode system [32]. The main characteristics of the soil are shown in Table 1.

Table 1 Main characteristics of the soil

Soil classification	Soil properties									
	Sand (%)	Silt (%)	Clay (%)	G	w_L (%)	w_P (%)	PI (%)	γ_{dmax} (g/cc)	w_{opt}	pH
SC	51	27.28	21.72	2.73	44	23.70	20.3	1.74	18	7.1

2.2 Cementation Reagents and Enzyme

The basic treatment solution for the EICP process comprises the mixture of urease enzyme, urea ($\text{CO}(\text{NH}_2)_2$), and calcium chloride dehydrate ($\text{CaCl}_2 \cdot 2\text{H}_2\text{O}$). In addition, magnesium chloride hexahydrate ($\text{MgCl}_2 \cdot 6\text{H}_2\text{O}$) was also used in this work to study the effect of magnesium ions (Mg^{2+}) incorporation in the EICP process. Urease enzyme EC 3.5.1.5 (Type III), which helps in the hydrolysis of urea, was derived from agricultural source, that is, *Canavalia ensiformis* (jack beans), and available in powder form which had an enzyme activity of 40150 U/g (One micromolar unit will liberate 1.0 μmole of NH_3 from urea per min at pH 7.0 at 25 °C). The enzyme was tightly packed and stored in a refrigerator at 4 °C throughout the experiment plan. All the reagents and enzyme were obtained from Sigma-Aldrich Chemical Company. Water was purified by using a Milli-RO plus system (Millipore) and used in all experiments.

2.3 Beaker Experiment

Under this test, the precipitation of carbonate minerals was directly evaluated in 100 ml transparent beaker. To prepare the cementation solution, urea concentration of 0.5 mol/L and $\text{MgCl}_2/\text{CaCl}_2$ of a total concentration of 0.5 mol/L were thoroughly mixed with purified water in various beakers to obtain a cementation solution of 10 ml. MgCl_2 was mixed with CaCl_2 to obtain various molar ratios varying from 0 to 1, as listed in Table 2. In a separate beaker, urease enzyme was also mixed with purified water to achieve a concentration of 8 kU/L (0.2 g/l as per the enzyme activity of 40,150 U/g). Then 10 ml of urea- $\text{MgCl}_2/\text{CaCl}_2$ solution and 10 ml of urease solution were mixed in the final beaker, resulting in a total solution volume of 20 ml and was allowed to cure for 14 days at the temperature (27 ± 3 °C). The beakers were sealed with a thin plastic sheet to prevent any evaporation loss or spill of the solution. Curing period of 14 days was adopted to allow complete precipitation of CaCO_3 [15, 33]. Later on, the amount of material precipitated was then evaluated by filtering the solution in the final beaker through the filter paper (11 μm) and drying the test beaker along with filter paper for 24 h at 60 °C [7]. Finally, the amount of carbonate precipitation was gravimetrically measured as the sum of the mass of the deposited on the filter paper and at the bottom of the beaker. Three samples of each condition were evaluated to check the reproducibility of the test.

Table 2 Testing program

Reagents	Urease = 8 kU/L			
Urea (mol/L)	0.5			
MgCl_2 (mol/L)	0	0.10	0.20	0.25
CaCl_2 (mol/L)	0.5	0.40	0.30	0.25
$\text{Mg}^{2+}/\text{Ca}^{2+}$	0	0.25	0.67	1.0

2.4 Field-Emission Scanning Electron Microscope and X-Ray Powder Diffraction Test

The morphological and mineralogical examination of the dried precipitated material obtained from the beaker experiment was characterized by field-emission scanning electron microscopy (FESEM) and X-ray powder diffraction test (XRD) test, respectively. Dried precipitated samples were mounted on aluminum stubs, sputtered with a gold coating (twice) and was imaged under (ZEISS Sigma 300) field-emission scanning electron microscope. The XRD patterns were recorded using (Bruker D8 Advance) X-ray diffractometer over the range of $10\text{--}60^\circ 2\theta$ at a step size = 0.05° and the scan speed of $0.2^\circ/\text{min}$. Phase identification was made by searching in the Inorganic Crystal Structure Database (ICSD), Powder Diffraction File database, and in the published literature.

2.5 Specimen Preparation and Unconfined Compressive Strength (UCS) Test

The soil specimens for unconfined compressive (UCS) test were prepared as per its maximum dry unit weight (γ_{dmax}), and an optimum water content (w_{opt}) is obtained from standard Proctor test. The optimum solution mixed with oven-dried soil consisted of urea, urease enzyme and $\text{MgCl}_2/\text{CaCl}_2$ at various $\text{Mg}^{2+}/\text{Ca}^{2+}$ molar ratios from 0 to 1, as shown in Table 2. A control soil sample was also prepared with only purified water. The sample preparation consisted of the following steps: (1) urea/ $\text{MgCl}_2/\text{CaCl}_2$ and urease solution were mixed together as per the required concentration and molar ratio and stirred for 5 min at 400 rpm; (2) the oven dried soil was mixed with the treatment solution as per the optimum water content to obtain a lump-free homogeneous paste; (3) the paste was then kept in a humidity chamber ($95 \pm 5\%$) for 24 h to ensure even distribution of solution through the soil [29]; (4) the paste was compacted to form the cylindrical test specimen of 38 mm diameter and 76 mm height; (5) after preparation, the specimens were carefully put inside a plastic bag and cured for 14 days inside a humidity chamber ($95 \pm 5\%$) and temperature ($27 \pm 3^\circ\text{C}$); (6) after the curing time, each sample was removed from the plastic bag and immediately tested for their unconfined compressive strength (UCS); (7) UCS tests were performed as per [34] under a constant strain rate of 1 mm/min and the data were recorded using an automatic data-acquisition system. All the UCS tests were repeated twice with three replicates of each soil specimen type in each test to guarantee the reliability of the results.

3 Results and Discussion

3.1 Beaker Experiment

While conducting the beaker experiment, it was observed that as soon as urease solution was mixed with the cementation solution of urea/MgCl₂/CaCl₂, the final solution turned milky white, indicating a quick start of urea hydrolysis. After completion of the 14 days curing period, on removing the plastic seal from the beaker, a pungent smell of ammonia (NH₃) was sensed. The mass of the precipitated minerals was represented in terms of the precipitation ratio (%) as in Eq. 7, which is the ratio of the actual mass of the precipitated minerals obtained to the maximum theoretical mass of CaCO₃ (Eq. 8).

$$\text{Precipitation ratio}(\%) = \frac{\text{The actual mass of the precipitated material}}{\text{Maximum theoretical mass of CaCO}_3} \tag{7}$$

$$\text{Maximum theoretical mass of CaCO}_3 = C \times V \times M \tag{8}$$

where

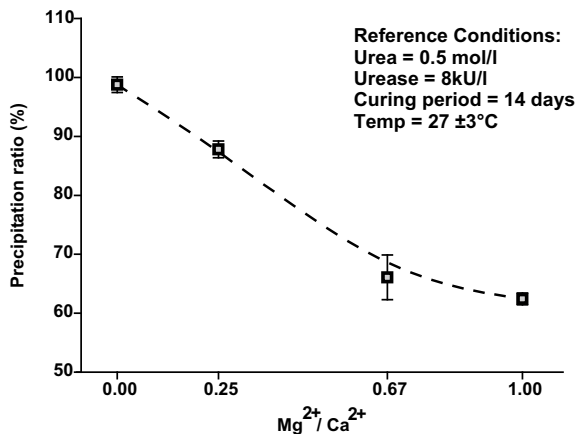
C is the final concentration of the solution (in mol/L)

V is the final solution volume in the beaker (in liters)

M is the molar mass of CaCO₃ (100.087 g/mol)

Based on the results of beaker experiments, Fig. 1 illustrates the effect of various Mg²⁺/Ca²⁺ molar ratios on the precipitation ratio (%) after a curing period of 14 days. The results show that as the Mg²⁺/Ca²⁺ molar ratio increases, there is a decrease in the precipitation ratio from 99.86 to 62.49% for the molar ratio from 0 to 1, respectively. The result is in accordance with the study done by Putra et al. [8] where an increase in MgCl₂ concentration decreased the precipitation ratio (%) up to 40% for the MgCl₂ ratio of 60%. In a similar study, Fukua et al. [21] observed

Fig. 1 Effect of Mg²⁺/Ca²⁺ ratio on precipitation ratio (%)



that with an increase in the $\text{Mg}^{2+}/\text{Ca}^{2+}$ molar ratio from 0 to 2.3, there is a change in the pH as well as transformation in carbonate mineral from calcite to dolomite through Mg-calcite. Under a pH change, the shape of carbonate changes goes through crystallization or re-crystallization until the most stable shape is obtained [21]. This re-crystallization can make the solution to lose energy by forming the improbable and difficult dolomite structure or by crystallizing the simpler calcite or aragonite structures [27], which may be one of the reasons for decreased precipitation mass. Fukue et al. [21] also reported an increase in the mass of the carbonate material beyond the $\text{Mg}^{2+}/\text{Ca}^{2+}$ molar ratio from 2.3, which is not in the scope of the present study.

3.2 Field-Emission Scanning Electron Microscopy (FESEM)

Although calcite (rhombohedral) is a stable phase of calcium carbonate at low temperature, its crystallization of the other two polymorphs, aragonite (orthorhombic) and vaterite (hexagonal), is also possible due to metastable nucleation [35]. The evolution of the different crystal shapes obtained from the FESEM analysis is shown in Fig. 2. The crystal structure image of calcite without the magnesium ($\text{Mg}^{2+}/\text{Ca}^{2+} = 0$) shows rhombohedral shape calcite (Fig. 2a). It has been reported that Mg^{2+} ions can be easily adsorbed onto the surface of calcite, thereby distorting the structure by inhibiting crystal growth [36]. Folk [27] reported that Mg^{2+} ion suppresses the crystal growth such that it grows along only one axis. Such unidirectional elongation of calcite crystals is evident in Fig. 2b, c. Struggling crystals can then be seen to form a dumbbell shape structure of dolomite (Fig. 2d). Low concentrations of Mg^{2+} ions in the solution are conducive to the formation of calcites, whereas high concentrations of Mg^{2+} ions promote the formation of aragonite [37]. A similar aragonite formation can be observed in Fig. 2d where crystals have taken fibrous shape just like bundle-like sheaf, whereas dumbbell shape crystals of dolomite were also presented. Fukue et al. [21] reported the presence of dolomite-like particles for the Mg/Ca molar ratios of 0.67 and 1.0. From the image, it could also be observed that the particle sizes became continuously smaller as Mg^{2+} concentrations increased in the solution, which could be due to the inhibiting effect of Mg^{2+} on the growth of calcite [21].

3.3 X-Ray Powder Diffraction (XRD) Test

The XRD results in Fig. 3 show the change in the mineralogy of the carbonate material due to magnesium addition. Diffraction peaks obtained at 2θ positions of 29.41, 36.02, 39.45, 43.21, 47.48, 48.52, and 57.48° confirm the presence of calcite

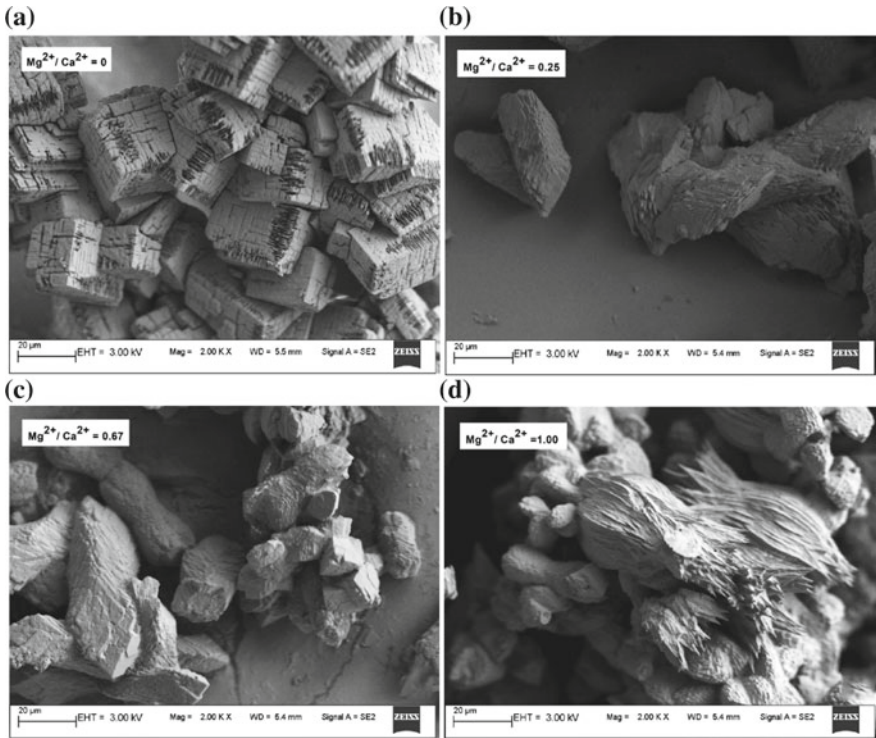


Fig. 2 Different crystal shape due to various Mg^{2+}/Ca^{2+} molar ratio

as the main material. However, substitution of magnesium decreased the intensity of the calcite peak, showing a mixture of other peaks corresponding to aragonite, vaterite, and dolomite. Subsequently, the peaks of calcite decreased gradually as the magnesium ratio increased even further. The lower intensity of diffraction peak meant the crystal structure of the mineral was destroyed and the degree of crystallinity decreased with the increasing Mg^{2+}/Ca^{2+} molar ratios. As the Mg^{2+}/Ca^{2+} ratio was increased, the mineralogical transformation is observed from calcite to various mixtures of aragonite, vaterite, and dolomite. Phase quantification study would further reveal their weight % distribution in the mixture of carbonate mineral.

3.4 Unconfined Compression Strength (UCS) Test

Figure 4 depicts the stress-strain curve obtained from UCS test results with specimens of soil treated with EICP solution incorporating various Mg^{2+}/Ca^{2+} molar ratios. The dotted line represents the control soil sample which was able to bear a

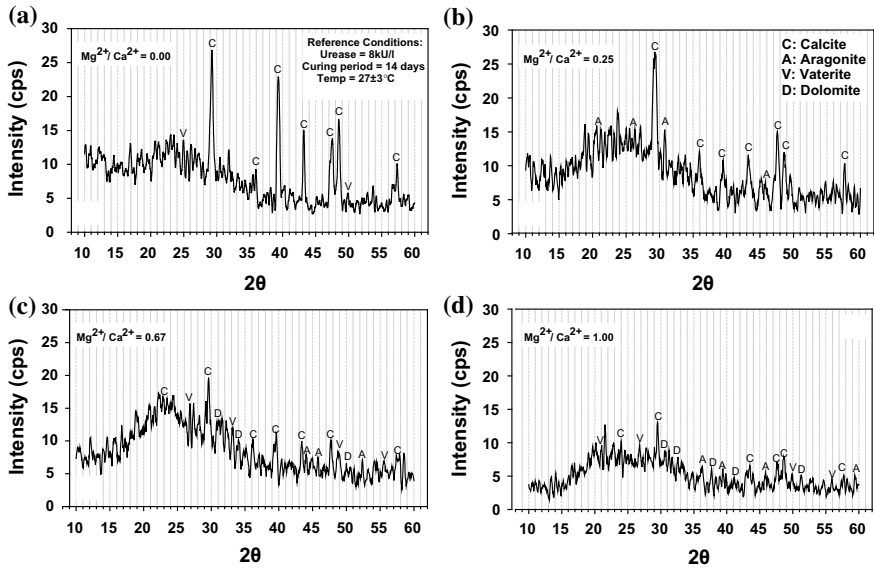


Fig. 3 X-ray diffraction pattern of the precipitated material at various Mg^{2+}/Ca^{2+} molar ratios

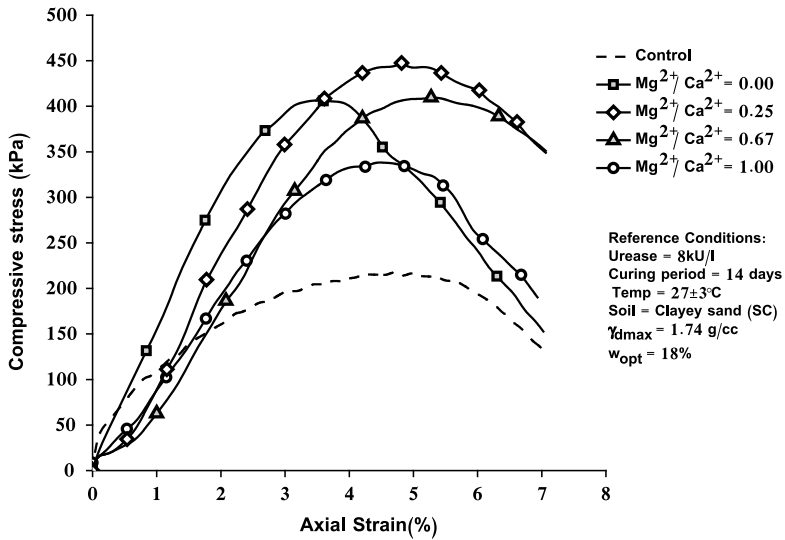


Fig. 4 Stress-strain response of clayey sand (SC) soil at various Mg^{2+}/Ca^{2+} molar ratios

UCS value of 220 kPa. The stress-strain curve obtained shows a linear elastic behavior before reaching to peak strength in all the cases of treatment. It also reveals the effectiveness of the carbonate precipitation, as it has shifted the stress-

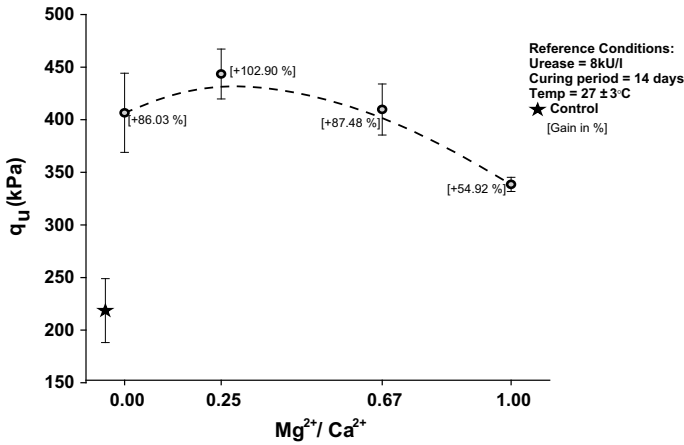


Fig. 5 Effect of various Mg^{2+} / Ca^{2+} molar ratios on q_u (kPa) of clayey sand (SC) soil

strain curve upward compared to the control sample. It is important to note that as the Mg^{2+} / Ca^{2+} molar ratio increases, the stress–strain curve shifts slightly upward and toward right, showing an increase in the value of UCS as well as the failure strain (%). This clearly reflects the presence of carbonate minerals in the void spaces and/or around the surfaces of the soil particles, thus increasing the contact points between the soil grains.

Figure 5 shows the variation in UCS of clayey sand (SC) at various Mg^{2+} / Ca^{2+} molar ratios. It can be seen that there is 86.03% gain in the unconfined compressive strength (q_u) value for the EICP treated sample without magnesium ($Mg^{2+} / Ca^{2+} = 0$). As the Mg^{2+} / Ca^{2+} ratio increases, there is a further improvement of 102.90% at $Mg^{2+} / Ca^{2+} = 0.25$, and after that the q_u value decreases. This increase can be attributed to the presence of more compact and rough crystals, which may have formed a more denser arrangement in the voids of soil. Addition of magnesium promoted precipitation of more angular and rough crystals of aragonite that could easily occupy the void space and thus resulted in greater particle contacts bonds to improve the shear strength of the soil. This can also be understood as the denser arrangement provided by the presence of fine-grained particles between coarse-grained particles, thus making more contact points to increase the shear strength of soil [38]. A further decrease in the q_u value is attributed to the decrease in the precipitating ratio (%) of carbonate material, showing a minimum gain of 54.82% for $Mg^{2+} / Ca^{2+} = 1$.

4 Conclusions

Considering the results of the beaker experiments and UCS tests performed to study the effect of incorporation of various Mg^{2+}/Ca^{2+} molar ratios in EICP solution, the following conclusions can be drawn:

- As the Mg^{2+}/Ca^{2+} molar ratio increases from 0 to 1, there is a decrease in the precipitation ratio from 99.86 to 62.49%, which may be due to simultaneous crystallization or re-crystallization of the crystal structure due to the change in the pH value.
- Addition of Mg ions produces progressive crystallization of carbonate material and shows the sequential appearance of various morphologies, starting from rhombohedral shape through elongated and dumbbell-like shape, and finally reaching to bundle-like fibrous morphology.
- As the Mg^{2+}/Ca^{2+} molar ratio was increased, the mineralogical transformation is observed from calcite to various mixtures of aragonite, vaterite, and dolomite.
- As the Mg^{2+}/Ca^{2+} molar ratio increases, the stress–strain curve shifted slightly upper and toward right, showing an increase in the UCS value as well as the failure strain (%).
- As the Mg^{2+}/Ca^{2+} ratio increases, there is a gain of 102.90% up to $Mg^{2+}/Ca^{2+} = 0.25$. A further increase in the ratio decreased the q_u value due to the decrease in the precipitating ratio (%) of carbonate material.
- Magnesium addition promoted precipitation of more angular and rough crystals that could easily occupy the void space, and thus resulted in denser and greater particle contacts bonds to improve the shear strength of the soil.

The above conclusions suggest that the enzyme-induced calcite precipitation (EICP) has the potential for strength improvement in cohesive soils. Addition of Mg^{2+} ions further increases the UCS value, reflecting the influence of crystals shape on the strength enhancement. However, high Mg concentration suppresses the carbonate precipitation and decreases the undrained shear stress. Hence, aqueous medium containing low magnesium ions can be beneficial for the EICP treatment; however, high magnesium-rich environment can decrease its efficiency.

References

1. Whiffin VS, van Paassen LA, Harkes MP (2007) Microbial carbonate precipitation as a soil improvement technique. *Geomicrobiol J* 24(5):417–423
2. van Paassen LA, Ghose R, van der Linden TJ, van der Star WR, van Loosdrecht MC (2010) Quantifying biomediated ground improvement by ureolysis: large-scale biogROUT experiment. *J Geotech Geoenviron Eng* 136(12):1721–1728
3. Zhu T, Dittrich M (2016) Carbonate precipitation through microbial activities in the natural environment, and their potential in biotechnology: a review. *Frontiers Bioeng Biotech* 4:4

4. Nemati M, Voordouw G (2003) Modification of porous media permeability, using calcium carbonate produced enzymatically in situ. *Enzyme Microbial Technol* 33(5):635–642
5. Dilrukshi RAN, Nakashima K, Kawasaki S (2018) Soil improvement using plant-derived urease-induced calcium carbonate precipitation. *Soils Found* 58(4):894–910
6. Yasuhara H, Neupane D, Hayashi K, Okamura M (2012) Experiments and predictions of physical properties of sand cemented by enzymatically-induced carbonate precipitation. *Soils Found* 52(3):539–549
7. Neupane D, Yasuhara H, Kinoshita N, Unno T (2013) Applicability of enzymatic calcium carbonate precipitation as a soil-strengthening technique. *J Geotech Geoenviron Eng* 139(12):2201–2211
8. Putra H, Yasuhara H, Kinoshita N, Neupane D, Lu CW (2016) Effect of magnesium as substitute material in enzyme-mediated calcite precipitation for soil-improvement technique. *Frontiers Bioeng Biotech* 4:37
9. Knorr B (2014) Enzyme-induced carbonate precipitation for the mitigation of fugitive dust. Arizona State University
10. Hamdan N, Kavazanjian E Jr (2016) Enzyme-induced carbonate mineral precipitation for fugitive dust control. *Géotechnique* 66(7):546–555
11. Al-Thawadi SM (2011) Ureolytic bacteria and calcium carbonate formation as a mechanism of strength enhancement of sand. *J Adv Sci Eng Res* 1(1):98–114
12. Sondi I, Škapin SD, Salopek-Sondi B (2007) Biomimetic precipitation of nanostructured colloidal calcite particles by enzyme-catalyzed reaction in the presence of magnesium ions. *Cryst Growth Des* 8(2):435–441
13. Almajed A, Khodadadi Tirkolaei H, Kavazanjian E Jr (2018) Baseline Investigation on Enzyme-Induced Calcium Carbonate Precipitation. *J Geotech Geoenviron Eng* 144(11):04018081
14. Hamdan N, Kavazanjian Jr, E, O'Donnell S (2013) Carbonate cementation via plant derived urease. In: *Proceedings of the 18th international conference on soil mechanics and geotechnical engineering*. Paris
15. Carmona JP, Venda Oliveira PJ, Lemos LJ, Pedro AM (2017) Improvement of a sandy soil by enzymatic calcium carbonate precipitation. *Proc Instit Civil Eng-Geotechn Eng* 171(1): 3–15
16. Mortensen BM, Haber MJ, DeJong JT, Caslake LF, Nelson DC (2011) Effects of environmental factors on microbial induced calcium carbonate precipitation. *J Appl Microbiol* 111(2):338–349
17. Davis KJ, Dove PM, De Yoreo JJ (2000) The role of Mg^{2+} as an impurity in calcite growth. *Science* 290(5494):1134–1137
18. Seiler H, Sigel A, Sigel H (eds) (1994) *Handbook on metals in clinical and analytical chemistry*. CRC Press
19. Oomori T, Kitano Y (1985) Catalytic effect of magnesium ions on polymorphic crystallization of calcium carbonate. *Bull Coll Sci Univ Ryukyus* 39:57–62
20. Cheng L, Shahin M, Cord-Ruwisch R (2014) Bio-cementation of sandy soil using microbially induced carbonate precipitation for marine environments. *Géotechnique* 64(12):1010–1013
21. Fukue M, Ono SI, Sato Y (2011) Cementation of sands due to microbiologically-induced carbonate precipitation. *Soils Found* 51(1):83–93
22. Putra H, Yasuhara H, Kinoshita N, Hirata A (2017) Optimization of enzyme-mediated calcite precipitation as a soil-improvement technique: the effect of aragonite and gypsum on the mechanical properties of treated sand. *Crystals* 7(2):59
23. De Muynek W, De Belie N, Verstraete W (2010) Microbial carbonate precipitation in construction materials: a review. *Ecol Eng* 36(2):118–136
24. Blakeley RL, Zerner B (1983) Jack bean urease: the first nickel enzyme. *InorganicaChimicaActa* 79:11
25. Stocks-Fischer S, Galinat JK, Bang SS (1999) Microbiological precipitation of $CaCO_3$. *Soil Biol Biochem* 31(11):1563–1571
26. Boyd V (2012) The effect of calcium and magnesium on carbonate mineral precipitation during reactive transport in a model subsurface pore structure

27. Folk RL, Land LS (1975) Mg/Ca ratio and salinity: two controls over crystallization of dolomite. *AAPG Bull* 59(1):60–68
28. ASTM D2487-17 Standard Practice for Classification of Soils for Engineering Purposes (Unified Soil Classification System), West Conshohocken, PA (2017). <https://doi.org/10.1520/D2487-17>
29. ASTM D698-12e2 Standard Test Methods for Laboratory Compaction Characteristics of Soil Using Standard Effort (12 400 ft-lbf/ft³ (600 kNm/m³)), West Conshohocken, PA (2012). <https://doi.org/10.1520/D0698-12E02>
30. ASTM D854-14 Standard Test Methods for Specific Gravity of Soil Solids by Water Pycnometer, West Conshohocken, PA (2014). <https://doi.org/10.1520/D0854-14>
31. ASTM D4318-17e1 Standard Test Methods for Liquid Limit, Plastic Limit, and Plasticity Index of Soils, ASTM International, West Conshohocken, PA (2017)
32. ASTM D4972-13 Standard Test Method for pH of Soils, ASTM International, West Conshohocken, PA, (2013). <https://doi.org/10.1520/D4972-13>
33. Carmona JP, Oliveira PJV, Lemos LJ (2016) Biostabilization of a sandy soil using enzymatic calcium carbonate precipitation. *Procedia Eng* 143:1301–1308
34. ASTM D2166/D2166M-16 Standard Test Method for Unconfined Compressive Strength of Cohesive Soil, ASTM International, West Conshohocken, PA (2016)
35. Fernandez-Diaz L, Putnis A, Prieto M, Putnis CV (1996) The role of magnesium in the crystallization of calcite and aragonite in a porous medium. *J Sediment Res* 66(3):482–491
36. Berner RA (1975) The role of magnesium in the crystal growth of calcite and aragonite from sea water. *Geochimica et Cosmochimica Acta* 39(4):489–504
37. Rushdi AI, Pytkowicz RM, Suess E, Chen CT (1992) The effects of magnesium-to-calcium ratios in artificial seawater, at different ionic products, upon the induction time, and the mineralogy of calcium carbonate: a laboratory study. *Geologische Rundschau* 81(2):571–578
38. Soon NW, Lee LM, Khun TC, Ling HS (2014) Factors affecting improvement in engineering properties of residual soil through microbial-induced calcite precipitation. *J Geotechn Geoenviron Eng* 140(5):04014006
39. De Yoreo JJ, Vekilov PG (2003) Principles of crystal nucleation and growth. *Rev Mineral Geochem* 54(1):57–93
40. Han M, Zhao Y, Zhao H, Han Z, Yan H, Sun B, ... Liu B (2018) A comparison of amorphous calcium carbonate crystallization in aqueous solutions of MgCl₂ and MgSO₄: implications for paleo-ocean chemistry. *Mineral Petrol* 112(2):229–244

Performance of Structural Concrete Using Recycled Plastics as Coarse Aggregate



P. R. Admile and P. D. Nemade

Abstract Nowadays due to rapid industrialization and urbanization the world facing massive problems such as shortage of natural construction material and increase in the plastic waste. It is essential to manage both problems as early as possible. The purpose of this investigation is to examine the custom of waste plastic as a coarse aggregate in the concrete mix of M20 grade concrete in a fractional way.

In this investigation, the seven mixes are prepared by using plastic waste as a coarse aggregate. In the present study, the natural coarse aggregate is exchanged by plastic coarse aggregates' in various percentages such as 0, 2, 3, 4, 5, 6, and 7%. Various concrete specimens are casted and tested by considering this percentage to find out the interpretation of recycled plastic as a replacement of coarse aggregate that would affect the development of strength in the concrete. It's observed that up to 5% replacement of ordinary coarse aggregate by plastic coarse aggregate the compressive strength of concrete will increases, after 5% it starts decreasing. Also, the tensile strength of concrete increases up to 4% and after that it starts decreasing. The additional tests are conducted to check the density of concrete and it is was observed that an increase in the percentage of plastic will decrease the density of concrete.

Keywords Alternative recycling method · Eco-friendly building material · Plastic waste · Density etc.

1 Introduction

The use of plastic for various domestic purposes is increasing with time, which causes an increase in plastic waste day by day. Every country has different composition of waste, because of socioeconomic characteristics, pattern of consumption, and excess management programs but generally the percentage of plastics composition in waste is

P. R. Admile (✉) · P. D. Nemade
S.B. Patil College of Engineering, Indapur, India
e-mail: Pushkrajadmile@gmail.com

© Springer Nature Singapore Pte Ltd. 2020
A. Prashant et al. (eds.), *Advances in Computer Methods and Geomechanics*, Lecture Notes in Civil Engineering 56,
https://doi.org/10.1007/978-981-15-0890-5_29

high studied by Murari et al. [7]. The main constituent of the plastic waste is namely polyethylene, followed by polypropylene, polyethylene, and polystyrene. As development is increasing, there is an increase in cost of construction and the maintenance of pavements. So, the Engineers and designer are looking for latest idea of using plastic wastes in cement concrete, Paver Blocks, and Solid Blocks. The formation of low biodegradable and non-decaying waste materials, combined with a rising population has resulted in waste dumping problems. One solution to this problem is recycling wastes into useful products. Many Government agencies, private organizations, and individuals are in the process of implementing a wide variety of studies and research projects regarding the feasibility and environmental suitability of plastic waste. Use of waste plastic in construction industry which may provide better cost-effective construction material and reduce environmental Pollution. Here for the preparation plastic coarse aggregates, Mathew and Paul [6] and Patil et al. [10] also presented that the recycled plastic waste was used and which provides an alternative option to deal with the plastic waste. Failure of concrete structures occurs due to the failure in concrete by crushing aggregates. Plastic coarse aggregates having low crushing values are not crushed easily as compared to natural aggregates. The density of natural coarse aggregate is more than plastic coarse aggregates. Total replacement of NCA was not possible, so partial replacement with varying percentage was done. About 500 billion plastic bags are used every year. In India the population is more than 1 billion and consumption of plastic is near about 4 million tones which causes increase in plastic waste.

Due to eating of discarded plastic, thousands of aquatic animals die every year similarly, on ground many animals suffer from similar fact in the direction of marine life. An additional environmental impact is produced due to gathering, hauling, and dumping of plastic bag. In a landfill or in environment, nearly 1000 years are required to degrade buried plastic. So there is a need to implement such innovative and environmental friendly technique to minimize the plastic waste at that point use of plastic aggregate in road construction is one of the effective technique to minimize the plastic waste Stayed on Subramani and Pugal [14]. The present study deals with the use of plastic as coarse aggregate in concrete mix in place of natural coarse aggregate and checking of tensile and compressive strength of concrete after using plastic as a coarse aggregate as compared to natural aggregates. Kumar and Baskar [5] presents an experimental investigation on structural concrete with partial replacement of coarse aggregate using electronic plastic waste (E-plastic). Most PET bottles used as beverage containers become waste after their usage, causing environmental problems. To address this issue, a method to recycle wasted PET bottles was presented by Kim et al. [4], in which short fibers made from recycled PET are used within structural concrete. Fraj et al. [2] examines the mechanical properties and the durability parameters of lightweight aggregate concretes (LWAC) incorporating rigid polyurethane (PUR) foam waste as coarse aggregates (8/20 mm). Saikia [3] discuss a review on the recycling plastic waste as aggregate in cement mortar and concrete productions. Nayak et al. [8] studied structural behaviour of beam and columns using various grades of concrete and GFRP circular bars.

2 Methodology

The main objective of this research is to use plastic recycled materials as a coarse aggregate for preparation of Concrete [12]. Nowadays disposal of plastic waste is a biggest problem and it creates adverse impact on the environment. Due to its biodegradability strain on environment get increase. Reclaim of plastic waste in concrete industry is measured as the most workable application [9, 10]. It reduces the pollution of environment as well as the cost of materials simultaneously.

The waste plastic is cut in size of natural coarse aggregates. The addition of plastic waste aggregate varied from 0 to 10% by weight. For compressive test samples are casted using cast iron molded cubes having standard size of $15 \times 15 \times 15$ cm. For flexural test samples are casted as a beam having standard size of $70 \times 15 \times 15$ cm mold. And for split tensile test cylinder are casted in standard size having length of 30 cm and diameter of 15 cm mold. For curing this specimen are placed in curing tank after 24 h for 7 and 28 days, respectively. For each given percentage of plastic aggregate three mold of each specimen are casted. According to IS 516-1959 and IS 1199-1959 the specimens were tested.

2.1 Collection of Waste Plastic

The plastic waste is collected from nearby places which include the polythene, (PVC), PET, etc.

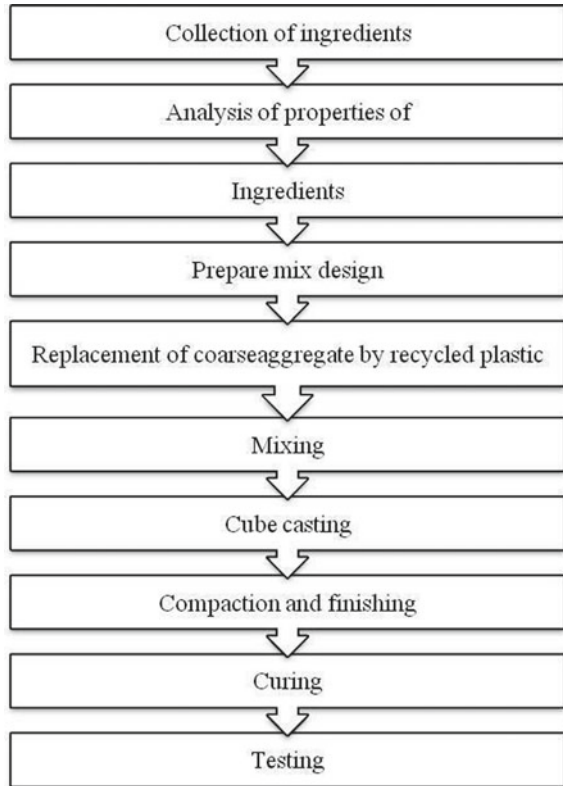
2.2 Preparation of Plastic Ingredients

Akcaozoglu et al. [1] proposed a technique for the preparation of plastic ingredients, the raw plastic is used as polythene, polyvinylchloride (PVC), PET Bottles, etc. the raw material is heated at standard temperature up to its melting point. After that this material is cooled. Due to this whole material is converted into homogeneous material. This material is crushed through a crusher. The size of the crushed material is fixed. The crushed material is of cylindrical shape of diameter 20 mm. This material is used in concrete as replacement of coarse aggregate.

2.3 Ingredients

Generally Concrete is a composite material consisting of following ingredients (a) Cement (b) Sand (c) Aggregate (d) Water.

Fig. 1 Methodology flow chart



Above are the ingredients of conventional concrete, but in this work recycled plastic are used as a coarse aggregate as replacement of natural coarse aggregate. So, this type of concrete consist of plastic coarse aggregate (PCA) and the remaining ingredients are same, i.e., cement, sand, and water as that of conventional concrete. Initially the ingredients are mixed properly in dry state and after that water is added to it by using proper water cement ratio. Flow chart of the methodology (Fig. 1).

2.4 Mix Design for M20

2.4.1 Design Parameters

- (1) Characteristic strength at 28 days 20 Mpa
- (2) Maximum nominal size of aggregate 20 mm

- (3) Type of aggregate—angular (crushed)
- (4) Degree of quality control—Good
- (5) Source of aggregate—natural
- (6) Degree of workability—slump 100 mm
- (7) Aggregate grading zone
 - (a) Coarse aggregate
 - (b) Fine aggregate

Target Strength for Mix Proportion

$$f_{ck} = f_{ck} + 1.65S \quad (1)$$

But for M20 grade standard deviation (s) = 4

$$f_{ck} = 20 + 1.65 \times 4, f_{ck} = 26.6 \text{ Mpa} \quad (2)$$

Selection of Water Cement Ratio

$$\text{Maximum free water cement ratio} = 0.5$$

Selection of Water Content, Slump = 100 mm

$$\begin{aligned} \text{Maximum water content} &= 186 + (186 \times 6)/100 \\ &= 197.16 \text{ L} \end{aligned} \quad (3)$$

Calculation of Cement Content

$$W/C = 0.5 \quad (4)$$

$$C = W/0.5, C = 197.16/0.5, C = 394.32 \text{ kg/m}^3$$

Proportion of Volume of Coarse Aggregate and Fine Aggregate for the Nominal Maximum Size of Aggregate 20 mm and Zone of Aggregate and Fine Aggregate of Zone 2 = 0.62

Approximate value for aggregate volume for water cement ratio is Volume of coarse aggregate per unit volume of total aggregate = 0.62

$$\text{Volume of fine aggregate per unit volume of total aggregate} = 1 - 0.62 = 0.38$$

Mix Calculation

The mix calculation per unit volume of concrete shall be as follows:

(a) Total volume of concrete = 1 m^3

$$\begin{aligned} \text{Volume of cement } (M_c/S_c) P \\ \text{(b)} \quad &= 394.32/3.15 \times 1000 \\ &= 0.125 \text{ m}^3 \end{aligned} \quad (5)$$

$$\begin{aligned} \text{Volume of water } (M_w/S_w) P \\ \text{(c)} \quad &= 197.16/1 \times 1000 = 0.19 \text{ m}^3 \end{aligned} \quad (6)$$

$$\begin{aligned} \text{Volume of all in aggregate} &= a - (b + c) \\ \text{(d)} \quad &= 1 - (0.12 + 0.197) \\ &= 1 - 0.32 = 0.67 \text{ m}^3 \end{aligned} \quad (7)$$

Mass of coarse aggregate =

$$\begin{aligned} \text{(e)} \quad &(\text{Volume of aggregate}) \times (\text{specific gravity of C.A}) \times (\text{volume of C.A}) \times 1000 \\ &= 0.67 \times 2.65 \times 0.62 \times 1000 = 1100.81 \text{ kg} \end{aligned} \quad (8)$$

Mass of fine aggregate =

$$\begin{aligned} \text{(f)} \quad &(\text{Volume of aggregate}) \times (\text{specific gravity of F.A}) \times (\text{volume of F.A}) \times 1000 \\ &= 0.67 \times 2.6 \times 0.38 \times 1000 = 661.96 \text{ kg} \end{aligned} \quad (9)$$

Mix proportion for Cement = 394.32 kg, Water = 197.16 L

$$\begin{aligned} \text{Fine aggregate} &= 661.96 \text{ kg} \\ \text{Coarse aggregate} &= 1100.81 \text{ kg} \\ \text{Water cement ratio} &= 0.5 \\ \text{Mix proportion} &= (1:1.68:2.79) \end{aligned}$$

After 1% replacement of fine aggregate with 1% plastic in mix design quantity for 1 M3 Volume of concrete Cement = 394.32 kg, Water = 197.16 L, Fine aggregate = 661.96 kg, Plastic = 11.00 kg, Coarse aggregate = 1089.80 kg, Water cement ratio = 0.5 2.6 Preparation of material.

2.4.2 For Cube (Replacement of Coarse Aggregate by 1% of Waste Plastic)

For the preparation of cube having standard size of 15 cm × 15 cm × 15 cm and the contents are used namely cement, fine aggregate, coarse aggregate, and water. In this study recycled plastic waste is used as a (i.e., plastic aggregate) coarse aggregate in place of natural aggregates. For replacement of coarse aggregate the mix design calculation is used. Natural Coarse aggregate is replaced by 1% of plastic material. In above mix design the calculated quantity of coarse aggregate excluding replacement of plastic coarse aggregate is equal to 1100.81 kg for 1 cub m of concrete. The quantity of material required for preparation of concrete cube is as shown in Table 1.

2.4.3 For Cylinder

The material used for the casting of the cylinder is same as that for cube. The cylinder was prepared to perform the split tensile strength of Concrete. The quantity of material required for preparation of concrete cylinder is as shown in Table 2.

Table 1 Quantity of material required for the preparation of concrete cube

Replacement of NCA (%)	Cement (kg)	F.A. (kg)	P.A. (kg)	C.A. (kg)	Water (L)
0	5.13	8.618	0.000	14.455	2.56
1	5.13	8.618	0.143	14.312	2.56
2	5.13	8.618	0.286	14.168	2.56
3	5.13	8.618	0.429	13.803	2.56
4	5.13	8.618	0.572	13.740	2.56
5	5.13	8.618	0.715	13.596	2.56
6	5.13	8.618	0.858	13.453	2.56

Table 2 Quantity of material taking for preparation of concrete cylinder

Replacement of NCA (%)	Cement (kg)	F.A. (kg)	P.A. (kg)	C.A. (kg)	Water (L)
0	4.2	6.9	0.00	11.400	2.10
1	4.2	6.9	0.114	11.280	2.10
2	4.2	6.9	0.228	11.170	2.10
3	4.2	6.9	0.342	11.050	2.10
4	4.2	6.9	0.456	10.900	2.10
5	4.2	6.9	0.570	10.830	2.10

2.4.4 For Beam

Similarly, the material used for the casting of the beam is same as that for casting of cube. The beam was prepared to perform the flexural strength of concrete. The quantity of material required for preparation of concrete beam is as shown in Table 3.

Plastic aggregates can be efficiently utilized to replace natural coarse aggregates. Use of plastic material in concrete as a fractional replacement of coarse aggregate shows the good characteristics. Use of plastic material in concrete shows the increase in compressive strength up to a certain percentage (i.e., up to 5%) and then it will start decreasing with an increases in the percentage of plastic coarse aggregate. The following table shows the compressive strength for conventional and plastic used concrete for 7 days, 14 days and 28 days, respectively. Also tensile strength of concrete gets increased up to 4% as well as flexural strength of concrete gets increased up to 5%, respectively. From result it was observed that the tensile strength, compressive strength, and flexural strength of concrete start decreases with an increases in the percentage of plastic.

2.5 Compressive Strength

Compressive strength of concrete depends on many factors such as water cement ratio, cement strength, quality of concrete material, and quality control during the production of concrete, etc. Table 4 shows the variation in compressive strength by replacing percentage of natural coarse aggregate by plastic coarse aggregate (PCA). The compressive strength of concrete is increased up to 5% then decreased after increasing the percentage of PCA (Fig. 2).

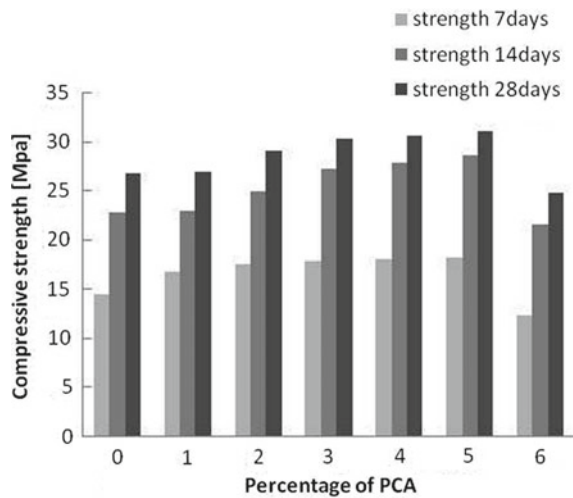
Table 3 Quantity of material required for preparation of concrete beam

Replacement of NCA (%)	Cement (kg)	F.A. (kg)	P.A. (kg)	C.A. (kg)	Water (L)
	4.2	6.9	0.00	11.400	2.10
1	4.2	6.9	0.114	11.280	2.10
2	4.2	6.9	0.228	11.170	2.10
3	4.2	6.9	0.342	11.050	2.10
4	4.2	6.9	0.456	10.900	2.10
5	4.2	6.9	0.570	10.830	2.10

Table 4 Results for compressive strength

Replacement of NCA (%)	Compressive strength after day's in Mpa		
	7 days	14 days	28 days
0	14.5	22.78	26.8
1	16.81	22.95	27
2	17.64	25.03	29.1
3	17.88	27.36	30.4
4	18.1	27.9	30.67
5	18.22	28.7	31.2
6	12.3	21.64	24.87

Fig. 2 Compressive strength of concrete versus PCA



2.6 Tensile Strength

The tensile strength of concrete is one of the basic and important properties. Splitting tensile strength test on the concrete cylinder is a method to determine the tensile strength of concrete [3]. Table 5 shows the variation in split tensile strength by replacing percentage of natural coarse aggregate by PA. The tensile strength of concrete is increased up to 3% then decreased after increasing the percentage of PCA.

Table 5 Result for split tensile strength

Replacement of aggregate (%)	Split tensile strength after days in Mpa
	28 days
0	3.4
1	4.26
2	3.55
3	3.53
4	3.15
5	3.05

Table 6 Results for flexural strength

Replacement of coarse aggregate (%)	Flexural tensile strength after days in Mpa
	28 days
0	53.3
1	67.4
2	65.4
3	60
4	54
5	50

2.7 Flexural Strength

Flexural strength is one of the important characteristics of concrete than the tensile strength of concrete. It is a measure of an unreinforced concrete beam or slab to resist failure in bending. It is measured by loading 6×6 -in. (150×150 -mm) concrete beams with a span length at least three times the depth. Table 6 shows the variation in Flexural strength by replacing percentage of natural coarse aggregate by PCA. The flexural strength of concrete is increased up to 4% the decreased after increasing the percentage of PCA (Fig. 3).

2.8 Density of Concrete

The density of the concrete differs from concrete to concrete, it enormously depends on the mix design and other characteristics like specific gravity of the aggregates, etc. But in general the density of normal concrete is taken as 2400 kg per cubic meter. Table 7 shows the variation in Density of Concrete by replacing percentage of natural coarse aggregate by PA. The density of Concrete is reduced by replacing natural coarse aggregate by PCA.

Fig. 3 Flexural strength of concrete versus PCA

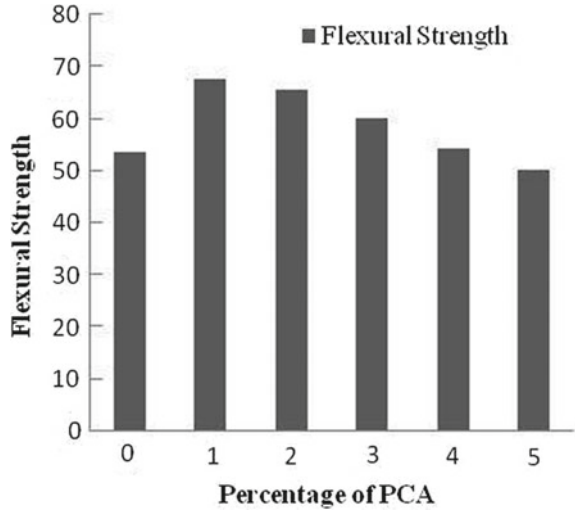


Table 7 Variation in density as per replacement of coarse aggregate by plastic

Replacement of coarse aggregate (%)	Density (Kg/m ³)
0	2400
1	2389
2	2372
3	2360
4	2349
5	2336
6	2327

3 Conclusion

From the above result the following observations are made:

1. The compressive strength of concrete is increased up to certain percentage (i.e., up to 5%) and then drastically decreases with an increase in the percentage of PCA.
2. Also, the split tensile strength and the flexural strength of concrete increases up to certain percentage (i.e., up to 4%) and then gradually decreases with the increase in the percentage of PCA.
3. As the percentage of plastic increases, the density of concrete goes on decreasing.
4. One of the important remarks perceived from the present study is that the concrete made of PCA gives intimation before failure (i.e., produce sound).

From the observation, it is concluded that the concrete mix containing plastic material tends to reduce its mechanical properties of concrete due to the poor bond

between the plastic and surrounding matrix. Since failure in concrete properties in tension, the poor bond around plastic particles leads to a reduced compressive and tensile strength. The utilization of plastic as an aggregate match to the size of the aggregate particles it replaces, and at a replacement of 4% by volume, gave the most promising overall performance. This material is furthermore cost-effective to produce and comes widely available as a waste material in many markets. This paper has shown that simply waste plastic material is sufficient processing to provide a viable alternative to aggregate testing different forms of plastic has demonstrated that the most efficient plastic aggregate used in a concrete mix should have a rough surface, be irregular in shape. The experiments result shows that through an appropriate mix design reductions in strength can be minimized to acceptable levels.

Acknowledgements The authors are thankful to Savitribai Phule Pune University, Pune (SPPU) for sponsoring and funding this research project by BCUD (Sanction No. 15ENG001210) and for providing academic support. The authors are also thankful to the laboratory staff of S.B. Patil College of Engineering, Indapur and for their full assistance during the experimental work.

References

1. Akcaozoglu S, Atis CD, Akcaozoglu K (2010) an investigation on the use of shredded pet waste bottles as aggregate in lightweight concrete. *Waste Manage* 32:285–290
2. Fraj AB, Kismi M, Mounanga P (2010) Valorization of coarse rigid polyurethane foam waste in lightweight aggregate concrete. *Constr Build Mater* 24:1069–1077. <https://doi.org/10.1016/j.conbuildmat.2009.11.010>
3. Juki MI, Awang M, Annas MMK, Boon KH, Othman N, Roslan MA, Khalid FS (2013) Relationship between compressive, splitting tensile and flexural strength of concrete containing granulated waste Polyethylene Terephthalate (PET) bottles as fine aggregate. *Adv Mater Res* 795(2013):356–359
4. Kim SB, Yi NH, Kim HY, Kim JHJ, Song YC (2010) Material and structural performance evaluation of recycled PET fibre reinforced concrete. *Cem Concr Compos* 32:232–240. <https://doi.org/10.1016/j.cemconcomp.2009.11.002>
5. Kumar KS, Baskar K (2015) Recycling of E-plastic waste as a construction material in developing countries. *J Mater Cycles Waste Manag* 17:718–724. <https://doi.org/10.1007/s10163-014-0303-5>
6. Mathew P, Paul T (2013) Recycled plastics as coarse aggregate for structural concrete. *IJRSET* 2(3):687–690. ISSN 2319-8753. http://www.ijrset.com/upload/march/26_Recycled%20Plastics.pdf
7. Murari K, Siddique R, Jain KK (2015) Use of waste copper slag, a sustainable material. *J Mater Cycles Waste Manage* 17(1):13–26
8. Nayak C, Tade M, Thakare S (2017) Strengthening of beams and columns using GFRP bars. *IOP Conf Ser: Mater Sci Eng* 225:012144. <https://doi.org/10.1088/1757-899X/225/1/012144>
9. Nithya Kurup S (2016) Use of waste plastic as fine aggregate substitute in concrete. *IJSER* 7(4):172–177. ISSN 2229-5518
10. Patil PS, Mali JR, Tapkire GV, Kumavat HR (2014) Innovative techniques of waste plastic used in concrete mixture. *IJRET* 1(9):29–32. eISSN: 2319-1163; Nabajyoti Saikia A, Jorge de Brito B (2012) Use of plastic waste as aggregate in cement mortar and concrete preparation. *Constr Build Mater* 34:385–401

11. Raghatare Atul M (2015) Use of plastic in a concrete to improve its properties. IJAERS 1(3): 109–111. E-ISSN 2249–8974. <https://www.technicaljournalonline.com/ijaers/VOL%20I/IJAERS%20VOL%20I%20ISSUE%20III%20APRIL%20JUNE%202012/137.pdf>
12. Saikia N (2009) Use of plastic waste as aggregate in cement mortar and concrete preparation: a review. Constr Build Mater 34:385–401
13. Saikia N, de Brito J (2012) Use of plastic waste as aggregate in cement mortar and concrete preparation: a review (Technical rep). Constr Build Mater 34(4):385–401. <https://doi.org/10.1016/j.conbuildmat.2012.02.066>
14. Subramani T, Pugal VK (2015) Experimental study on plastic waste as a coarse aggregate for structural concrete. IJAIEEM 4(5):144–152. ISSN 2319-4847

Effect of Ground Water Level and Seismic Intensity on Failure of a Slope



Sreyashi Dutta, R. K. Dubey, Sibapriya Mukherjee and Narayan Roy

Abstract Analysis of stability of a slope becomes important to predict the failure of a natural or manmade slope. Among several factors which trigger failure of a slope, earthquake in presence of groundwater may be quite significant. This paper studies the failure of embankment slopes under different seismic conditions with variable groundwater levels. Three embankments of different heights have been considered and their analyses have been performed by varying slope angle, embankment soil properties, and groundwater levels. The current study contains probabilistic approach of slope stability by assigning an uncertainty range of density and shear strength parameters of embankment soil. Thus the current study considers input variables like height and angle of slope along with three soil properties: bulk density, cohesion, and angle of internal friction of embankment soil. In each case three groundwater levels have been considered. Out of all these variables 50 numbers of random variables for each of bulk density, cohesion, and angle of internal friction of embankment soil have been generated within some specified uncertainty bound with the help of Monte Carlo simulation. Finally, results have been presented in the form of variation of factor of safety with slope geometry and seismic intensity levels for different positions of groundwater levels. The study finds different slope geometry and seismic conditions along with variable groundwater levels affecting the outcome of slope stability analysis quite substantially.

Keywords Slope stability · Seismic · Groundwater level · Factor of safety · Probability of failure · Monte Carlo simulation

S. Dutta (✉) · R. K. Dubey
Department of Applied Geology, IIT (ISM) Dhanbad, Dhanbad, India

S. Mukherjee · N. Roy
Department of Civil Engineering, Jadavpur University, Kolkata, India

1 Introduction

Landslides are natural phenomena which are very common in hilly regions, but still, it is difficult to predict due to uncertainties of its material properties. Even a variety of civil engineering projects such as the construction of embankments for road and railways, earth dams, trenches, and various other engineering structures require the consideration of slope stability in their geotechnical design. In mining, slopes of different gradients are provided while making the benches according to the height and type of depositions. Hence it is important to determine the stability of the slope against sliding and provide adequate safety against failure.

Slope stability is the resistance of an inclined surface to failure by sliding and collapsing [1]. Analysis of stability of the slope is performed to assess the safe design of a man-made or a natural slope. The main objective of slope stability analysis is the determination of slope sensitivity to different triggering effects and designing an optimal slope. So, to determine the failure of a slope, a combination of factors need to be considered. Height and angle of a slope along with the material properties of the slope primarily decide the stability of an embankment slope. Now, earthquake and groundwater condition act as triggering factors which accelerate the failure further. The inclusion of seismic force is mandatory if the study area falls in seismically active region, and also the fluctuations of groundwater levels are observed during different season, which makes the embankment slope from dry to partially saturated and further to fully saturated condition. A comprehensive study is quite mandatory by considering all the factors mentioned above in order to predict the failure of a slope accurately.

Deterministic method to assess the stability of a slope was primarily introduced with the method of slices [2] which is also known as the Swedish circle method. Further, the Friction circle method was proposed by Taylor [3] and then several other methods followed. In order to analyze a slope incorporating seismic forces, several methods are available. Pseudo-static [4], permanent displacement [5], and stress-deformation analyses [6] are mostly used for determination of seismic slope stability. Now, the outcome of a stability analysis may largely get influenced by the uncertainties associated with the soil properties of a slope. A slope stability analysis may exhibit significant sensitivity to the uncertainties present in the properties of embankment soil as well as foundation soil when the slip surface penetrates the base soil.

Variability in the soil properties in terms of strength parameters (c , ϕ , etc.) and physical properties (γ , etc.) can be combined in the pseudo-static slope stability analysis, and probabilistic methods are most suitable in this regard [7–9]. This probabilistic methods of analysis are increasingly being used with the advancement of computational resources and numerical methods [10]. Probabilistic analyses basically involve obtaining the probability distribution of dependent random variable from a set of independent input random variable with a particular assigned probability distribution. Monte Carlo Simulation (MCS) is one of the most popular

probabilistic methods of analysis which can incorporate the uncertainty of input random variable and is widely used in the reliability analysis of a geo-structure.

The current study aims to analyze an artificial embankment slope using pseudo-static slope stability analysis by varying the height, slope angle, and groundwater level. Probabilistic methods of analysis have been performed incorporating uncertainties in soil properties to find out the variation of factor of safety with different parameters. Uncertainty in embankment soil has been considered by assigning an uncertainty range with a particular probability distribution of density and shear strength parameters of the embankment soil in the probabilistic approach.

2 Methodology

An artificial embankment with three different slopes has been considered in the study. Embankment slopes of 1V:1H, 1V:1.5H, and 1V:2H have been considered and each slope has been analyzed for three different embankment heights of 8, 10, and 12 m. In order to account the fluctuations in groundwater levels, three different positions of water table have been considered in each case. The positions of water tables have been selected in such a way so that the slope can be analyzed for three different conditions of embankment soil, i.e., dry, partially saturated, and fully saturated conditions when the water table is at the base level, at the mid-height, and at the top of the embankment, respectively. Soil properties have been incorporated differently in the foundation and in the embankment soil. Analysis has been performed using Bishop's simplified method. Probabilistic approaches of analyses have been performed for each slope having different heights and slope angles with different position of groundwater tables to get the variations of factor of safety under seismic conditions. Probabilistic analysis has been performed using Monte Carlo simulation with soil parametric uncertainty of embankment soil for five different shaking levels. For probabilistic analysis, mean with standard deviation of three soil parameters cohesion (c), angle of internal friction (ϕ), and unit weight (γ) of embankment soil have been taken to create random variables for probabilistic distribution in Monte Carlo simulation.

2.1 *Bishop Simplified Method*

Basically, the slope stability analysis has been performed with Bishop's simplified method which is based on the assumption about the sliding surface shape and finding the potential slip surface within the soil slope. This method utilizes the Mohr-Coulomb expression in order to determine the shear strength along the sliding surface. The method involves dividing the sliding mass into a series of slices that are usually vertical so that their base can be comparable with a straight line. Once the sliding mass is divided into a number of slices, then the equilibrium condition is

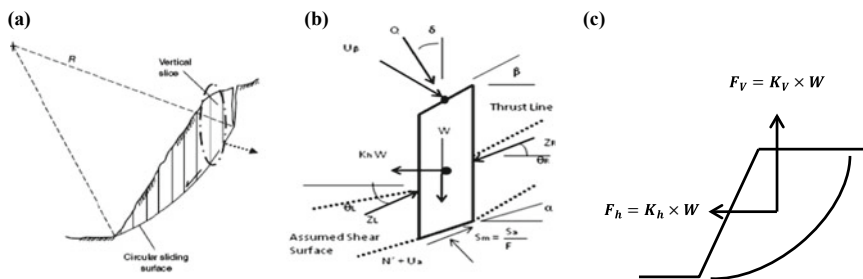


Fig. 1 a Assumed failure surface in Bishop's simplified method b forces considered in a slice and c concept of Pseudo-static slope stability analysis

examined and factor of safety is determined. Bishop's simplified method considers the inter-slice normal forces but neglects the inter-slice shear forces. For considering seismic forces, pseudo-static concept has been applied. The weight of each slice is multiplied by horizontal (K_h) and vertical (K_v) seismic coefficient in order to get the equivalent static horizontal and vertical seismic force. Five different levels of intensity in terms of horizontal seismic coefficient (K_h) have been considered in the analysis, whereas half of the K_h has been considered as vertical seismic coefficient (K_v). A range of K_h values from 0.01 to 0.5 have been considered for the analysis. Factor of safety is calculated comparing between resisting and driving forces. Figure 1 represents a sample failure surface (Fig. 1a), the forces acting on a slice (Fig. 1b) in Bishop's simplified method and the concept of pseudo-static slope stability analysis (Fig. 1c).

2.2 Monte Carlo Simulations

Monte Carlo simulation (MCS) technique is a reliable and famous method for probabilistic analysis of problems having large spatial variation. It is highly used when the analysis becomes too complex and can't be solved using simpler methods. In Monte Carlo simulations, each input random variable is represented by a probability density function and repeated "standard" system analyses are performed by changing the values of the random variables using a random number generator. In Monte Carlo simulations each random variable is represented by assigning a probability distribution. In most of the geotechnical engineering problems generally, four different probability distributions are used: 1. Uniform distribution, 2. Triangular distribution, 3. Normal distribution, and 4. Lognormal distribution. In the present study, embankment soil parameters such as cohesion, angle of internal friction, and unit weight have been assigned with a specified range of probability distribution. It is assumed that all the parameters follow a normal distribution and the samples are generated within $(\mu \pm 3\sigma)$ [where, μ = mean and σ = standard deviation] range. Variation of soil properties of the embankment and foundation

Table 1 Properties of embankment soil and foundation soil

Properties	Cohesion (t/m ²)	Friction angle (°)	Unit weight (saturated) (t/m ³)	Unit weight (bulk) (t/m ³)	Distributions	Standard deviation
Embankment soil	2	33	2.1	1.9	Normal	10%
Foundation soil	1.85	30	1.95	1.8	NA	NA

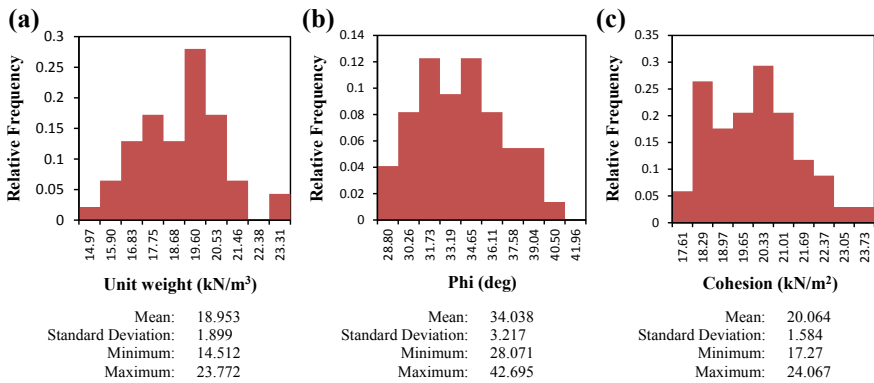


Fig. 2 Distribution of generated input variables: **a** unit weight **b** angle of internal friction and **c** cohesion

have been presented in Table 1. A standard deviation of 10% has been adopted for embankment soil parameters, whereas no uncertainty has been considered in the foundation soil. 50 numbers of samples of each parameter have been generated within the specified bound using Monte Carlo simulation. Figure 2 shows the distribution of generated random input variables after Monte Carlo simulation for unit weight (Fig. 2a), angle of internal friction (Fig. 2b), and cohesion (Fig. 2c).

3 Result and Discussion

The probabilistic analysis has been performed with three different assumed heights of the embankment (8, 10, and 12 m), and each embankment height is analyzed for three different values of slope angles (1V:1H, 1V:1.5H, and 1V:2H) under five different seismic conditions. For each case, water table at the base level, at the mid-height, and at the top of the embankment has been considered in the analysis to simulate the situation of dry, partially saturated, and fully saturated conditions,

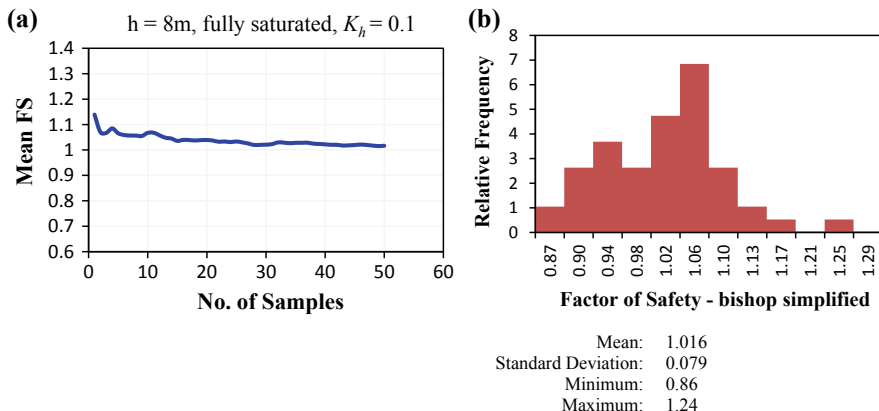


Fig. 3 Output of probabilistic slope stability analysis: **a** variation of mean factor of safety with no. of samples; **b** distribution of factor of safety

respectively. Five different K_h values of 0.01, 0.05, 0.10, 0.20, and 0.5 have been adopted for the analysis, and K_v has been taken as half of K_h values. Figure 3 presents a sample result of probabilistic slope stability analysis in terms of variation in mean factor of safety with number of samples (Fig. 3a) and distribution of FS (Fig. 3b) for embankment height 8 m, fully saturated embankment and $K_h = 0.1$. The plots clearly depict a little fluctuation, although convergence has nearly reached, in the mean FS with the number of samples (i.e., the convergence plot) as we have adopted a little lower number of samples (50 samples) and the intention here is to study the variation of mean FS for each case. So this shouldn't pose serious limitation in the current study, later, the work is going to be extended for increased number of samples.

3.1 Effect of Slope Geometry

Initially, analysis has been run to study the effect of slope geometry for different position of water table, keeping the constant value of K_h (0.1). To study the effect of embankment height on FS, analysis has been run for a constant slope angle (1H:1V) and the results have been presented in Table 2. The results clearly reflect that with the increase in embankment height FS reduces for all the degree of saturation. A percent reduction with respect to dry embankment case in FS values has been computed for partially and fully saturated embankment and the results show that average percent reduction is nearly doubled for the saturated condition of slope in comparison with partially saturated condition (Table 2). To study the effect of slope angle on FS variation, analysis has been run for different slope angle with constant height (12 m) and K_h value (0.1) under different degree of saturation of

Table 2 Variation of FOS with embankment height (constant slope gradient = 1H:1V, $K_h = 0.1$)

Embankment height (m)	FOS						
	Dry	Partially saturated	% reduction with respect to dry FS	Average % reduction	Fully saturated	% reduction with respect to dry FS	Average % reduction
8	1.71	1.35	21.05	22.04	1.001	41.46	43.74
10	1.55	1.22	21.29		0.874	43.61	
12	1.43	1.09	23.78		0.770	46.15	

Table 3 Variation of FOS with embankment gradient (constant height = 12 m, $K_h = 0.1$)

Slope	FOS						
	Dry	Partially saturated	% reduction with respect to dry FS	Average % reduction	Fully saturated	% reduction with respect to dry FS	Average % reduction
1H:1V	1.43	1.09	23.78	26.03	0.77	46.15	42.76
1.5H:1V	1.75	1.28	26.86		1.02	41.71	
2H:1V	1.93	1.40	27.46		1.15	40.41	

embankment slope and the results are presented in Table 3. Here also, FS is found to decrease when the slope angle gets steeper and fully saturated condition shows maximum reduction (average: 42.76%) in comparison with partially saturated condition of embankment soil (Table 3). A plot (Fig. 4) has been prepared for the same for better clarity, and it clearly depicts the variation of FS with slope geometry, i.e., embankment height and slope angle. Figure 5 depicts the variation in the percent reduction of FS with embankment height (Fig. 5a) and slope angle

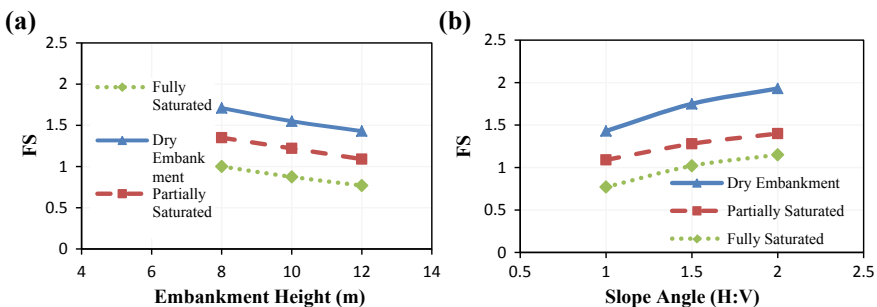


Fig. 4 Variation of factor of safety of a dry embankment: **a** with embankment height (at constant slope gradient = 1H:1V and $K_h = 0.1$); **b** with slope gradient (at constant embankment height = 12 m and $K_h = 0.1$)

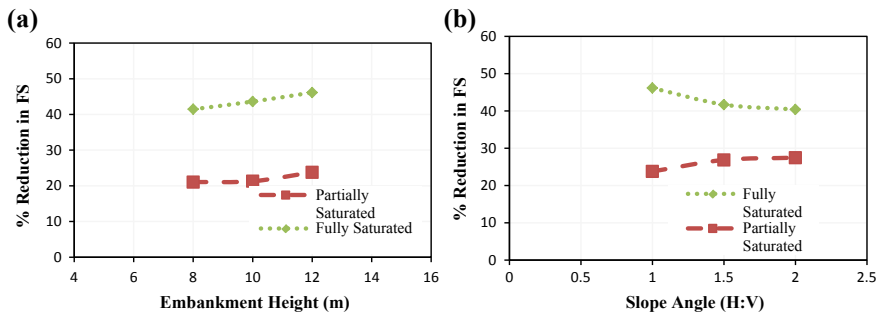


Fig. 5 Variation of percent reduction in FS with respect to dry soil embankment: **a** with embankment height (at constant slope = 1H:1V and $K_h = 0.1$); **b** with slope gradient (at constant height = 12 m and $K_h = 0.1$)

(Fig. 5b) for partially saturated and saturated conditions. The figure shows that the variation of percent reductions with embankment height and slopes are quite comparable and higher reduction is observed for fully saturated embankment.

3.2 Effect of Seismic Coefficient

Now the embankment slope has been analyzed to study the effect of seismic coefficients on slope failure for different saturation of embankment soil with a fixed combination of slope geometry. Two combinations of slope geometry have been selected for this purpose, one is the most stable combination of slope (Height = 8 m and Slope = 2H:1V) and the other is the most vulnerable combination of slope (Height = 12 m and Slope = 1V:1H). The objective here is to represent the variation in factor of safety for two fully different scenarios, one scenario is the most stable combination of slope and the other is the most vulnerable combination of slope under the influence of different position of water table and different seismic intensity levels.

After the analysis, it is found that the embankment with the most stable combination of slope geometry exhibited maximum factor of safety (2.635) under dry condition of embankment soil with minimum seismic intensity level ($K_h = 0.01$). The embankment with the most vulnerable geometry exhibited a minimum factor of safety (0.48) under fully saturated condition of embankment soil with maximum seismic intensity level ($K_h = 0.5$). Table 4 represents the variation of mean factor of safety for a constant embankment height 8 m and gradient 2H:1V, i.e., the most stable combination with different seismic intensity levels and water table positions, whereas Table 5 represents the variation of mean factor of safety for constant embankment height 12 m and gradient 1V:1H, i.e., most vulnerable combination with different seismic intensity levels and water table positions.

Table 4 Comparison of the mean value of factor of safety for the most stable combination of slope (embankment height = 8 m, gradient 2H:1V)

K_h	Factor of safety						
	Dry embankment	Partially saturated			Fully saturated		
		FS	% reduction with respect to dry FS	Average % reduction	FS	% reduction with respect to dry FS	Average % reduction
0.01	2.63	2.04	22.43	22.1	1.63	38.02	36.2
0.05	2.34	1.86	20.51		1.52	35.04	
0.10	2.16	1.68	22.22		1.38	36.11	
0.20	1.80	1.41	21.67		1.16	35.56	
0.50	1.27	0.97	23.62		0.81	36.22	

The most vulnerable combination of slope exhibits a lesser range of degradation in factor of safety values with the increase in seismic intensity in comparison with the most stable combination of slope (Tables 4 and 5). A percent reduction in factor of safety values has been calculated with respect to the factor of safety of dry embankment soil case, and finally an average value has been computed for different seismic intensity. Even though the most stable slope combination exhibit higher range of FS variation, but the average percent reduction of FS is comparatively lower (Table 4) than the most vulnerable combination of slope (Table 5) for both partially saturated and fully saturated conditions. The most stable and vulnerable slope show an average reduction in FS 22.1 and 22.9% for partially saturated condition and 36.2 and 45.7% for fully saturated condition, respectively (Table 4 and 5). So, the position of water table along with slope geometry may significantly affect the outcome of slope stability analysis under different seismic conditions. The percent reduction in FS is quite very substantial if the embankment soil changes from dry to partially saturated and then to fully saturated conditions.

Table 5 Comparison of the mean value of factor of safety for the most vulnerable combination of slope (embankment height = 12 m, gradient = 1H:1V)

K_h	Factor of safety						
	Dry embankment	Partially saturated			Fully saturated		
		FS	% reduction with respect to dry FS	Average % reduction	FS	% reduction with respect to dry FS	Average % reduction
0.01	1.598	1.25	21.53	22.9	0.88	44.62	45.7
0.05	1.549	1.18	24.02		0.86	44.48	
0.10	1.431	1.09	23.69		0.77	46.19	
0.20	1.241	0.95	23.21		0.65	47.62	
0.50	0.879	0.68	22.07		0.48	45.39	

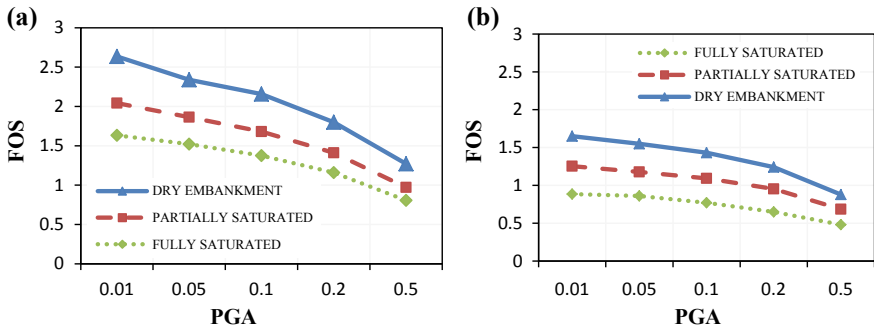


Fig. 6 Variation of factor of safety for different seismic intensity levels: **a** for the most stable combination of the slope; **b** for the most vulnerable combination of the slope

The same results for the two combinations of slope have been plotted in Fig. 6 for better clarity and representation. Figure 6a clearly depicts that the most stable slope combination exhibits more wide range of degradation in the factor of safety with the increase in seismic intensity level, whereas the degradation range is small for the vulnerable slope combination. Another plot has been prepared to present the percent reduction in FS with different seismic intensity levels (Fig. 7) for the above two combinations of the slope. The plots clearly exhibit that for partially saturated condition of embankment soil the variation of percent reduction is quite similar, but for fully saturated condition of embankment soil a remarkable difference is observed in the percent reduction of FS values, for vulnerable slope combination the reduction is higher than the stable combination (Fig. 7a, b).

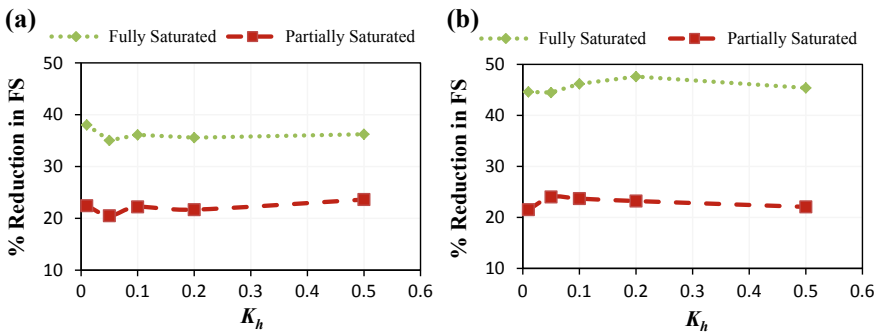


Fig. 7 % Reduction of FS in comparison with the dry soil case: **a** for the most stable combination of the slope; **b** for the most vulnerable combination of the slope

4 Conclusion

The article studies the failure of embankment slopes under different slope geometry and seismic conditions with variable groundwater levels using a probabilistic approach. The results have been presented in terms of variation in mean factor of safety (FS) values with slope geometry and seismic intensity levels in terms of K_h , i.e., horizontal seismic coefficient. The following conclusions can be drawn from the present study:

- Mean factor of safety of a slope is found to decrease with the increase in slope angle and an increase in slope height for all the considered position of groundwater levels. The maximum reduction in FS is observed for the fully saturated condition of embankment soil when the water table rises at the top of the embankment. For a variation in embankment height from 8 to 12 m, the average % reduction in FS is observed as 22.04 and 43.74 for partially saturated and saturated conditions, respectively.
- For the considered variations in slope geometry in terms of slope angles, the average percent reduction is observed as 26.03 and 42.76% for partially saturated and saturated conditions of embankment soil. So, not only the variation in slope geometry affects the FS of a slope but the position of groundwater levels also influences the FS variation quite significantly.
- Level of seismic intensity is found to influence the FS substantially, with the increase in seismic intensity mean values of FS show a significant reduction. Further reduction of factor of safety occurs when water table rises up to the top of the embankment, i.e., under full saturation condition leading to maximum reduction with highest intensity level. An average reduction in mean factor of safety values is observed as 22.1 and 36.2% for partially saturated and fully saturated conditions for the considered stable slope, whereas 22.9 and 45.7% average reductions are observed for the considered vulnerable slope.

Acknowledgements This work was supported by the Applied Geology department of IIT (ISM) Dhanbad and Civil Engineering department of Jadavpur University, Kolkata, which is gratefully acknowledged.

References

1. Wyllie DC, Mah CW (2004) Rock slope engineering. In: Civil and mining, 4th edn
2. Fellenius W (1936) Calculation of the stability of Earth dams. In: 2nd international congress on large darns. Washington, DC, pp 445–459
3. Taylor DW (1937) Stability of earth slopes. J Boston Soc Civ Eng 24(3):197–246
4. Kramer SL (1996) Geotechnical earthquake engineering. Prentice Hall, New Jersey
5. Newmark NM (1965) Effects of earthquakes on dams and embankments. J Geotech 15(2): 139–160

6. Griffiths DV, Prevost JH (1988) Two and three-dimensional finite element analyses of the Long Valley Dam. *J Geotech* 38(3):367–388
7. Reficea A, Capolongo D (2002) Probabilistic modeling of uncertainties in earthquake-induced landslide hazard assessment. *J Comput Geosci* 28:735–749
8. Jibson RW, Harp EL, Michael JA (2000) A method for producing digital probabilistic seismic landslide hazard maps. *J Eng Geol* 58:271–28
9. Kavvadas M, Karlatis M, Fortsakis P, Stylianidi E (2009) Probabilistic analysis in slope stability. In: 17th international conference on soil mechanics and geotechnical engineering
10. HASUS (1999) Earthquake loss estimation methodology by FEMA-NIBS, Washington DC

Stability of Two-Layered Earth Slope Under Varying Rainfall Intensity



Dooradarshi Chatterjee and A. Murali Krishna

Abstract Rainfall is one of the major causes of slope failures occurring in residual soils, which are of concern to geotechnical engineers. Naturally, soil is non-homogeneous in nature with different mechanical and hydraulic properties such as shear strength, soil–water characteristic curve, saturated permeability and unsaturated permeability functions. Negative pore-water pressure or matric suction plays an important role in the evaluation of stability of earth slopes. With rainfall infiltration, the pore-water pressure changes and hence affects its stability. A numerical model of a two-layered non-homogeneous slope is prepared with different hydraulic properties. An unsaturated seepage analysis with infiltration is performed in the finite element framework. With the pore pressures obtained from the seepage analysis, a finite slope stability analysis is performed in the limit equilibrium framework. The pore-water pressure profiles of the two-layered slope are studied with different rainfall intensities. The negative pore-water pressures are reduced to zero at a much shallow depth for higher rainfall intensity, thus reducing its safety factor rapidly. It is also observed that at high rainfall intensity, the two-layered slope suffers a shallow slope failure.

Keywords Non-homogeneous slope • SWCC • Pore-water pressure • Critical slip surface

1 Introduction

Slopes are non-homogeneous due to different mechanical properties and hydraulic properties like saturated permeability and unsaturated permeability function. Researchers have considered non-homogeneity in two ways, the first is lithological heterogeneity and the second is the spatial soil variability. Kim et al. [8] compared the stability of non-homogeneous slopes with different soil profiles using finite

D. Chatterjee (✉) · A. Murali Krishna
Indian Institute of Technology Guwahati, Guwahati, India
e-mail: dooradarshi@iitg.ac.in

element limit analysis and limit equilibrium method. Qian et al. [12] proposed stability charts for two-layered cohesive slopes with depth factors ranging from 1.5 to 5. Chatterjee and Krishna [2] performed stability analysis of two-layered slopes with different soil combinations and showed how slip surfaces change with fine-grained and coarse-grained soils.

Slopes can be considered non-homogeneous with respect to the saturation levels occurring within the slope. In the event of rainfall, the saturation and moisture content vary highly within the slope. Failure of slopes is attributed to rainfall events more than any other causes. Gasmo et al. [7] developed numerical models to study infiltration within a slope and its effect on stability of the slope. Cho and Lee [3] studied the effect of infiltration using a two-dimensional finite element flow-deformation coupled analysis program. Zhang et al. [18] explained how under certain conditions matric suction in a slope is maintained even under rainfall infiltration. Rahardjo et al. [13] conducted a series of parametric studies under various rainfall intensities to study the influence of soil properties, initial groundwater table location and slope geometry on the stability of a residual soil slope. They concluded that the primary causes of instability of the slope were soil properties and rainfall intensity while water table location and slope geometry played a secondary role. Cho [4] used a one-dimensional infiltration model with an infinite slope to formulate an approximate method for evaluating the surficial stability of two-layered slopes. Yubonchit et al. [17] performed parametric studies within the finite element framework to observe the effects of slope angle, antecedent rainfall and saturated permeability on the stability of a shallow slope. The effect of rainfall intensity on the stability of a homogeneous slope is well established. However, the studies on non-homogeneous slopes are scarce. Therefore, a two-layered non-homogeneous slope is modelled with different rainfall intensities applied on the surface. The results obtained are analysed and illustrated through pore-water pressure profiles, safety factors and critical slip surfaces.

2 Problem Statement and Theory

A two-layered slope model as shown in Fig. 1 is considered for the study. A layer of top soil of 2 m thickness, representing relatively less permeable (Soil-2) material due to weathering is adopted. The slope angle is 35° and the slope height is 10 m. The front extent is taken as 30 m in front of the toe while the portion behind the crest is taken as 45 m. The initial groundwater table exists at a height of 10 m on the right side from the bottom and 5 m on the left side.

Slope stability analysis is performed followed by a transient seepage analysis in SLIDE v.8 [14]. The pore pressures from the seepage analysis are used as the initial condition for the stability analysis. The slope stability analysis was performed using

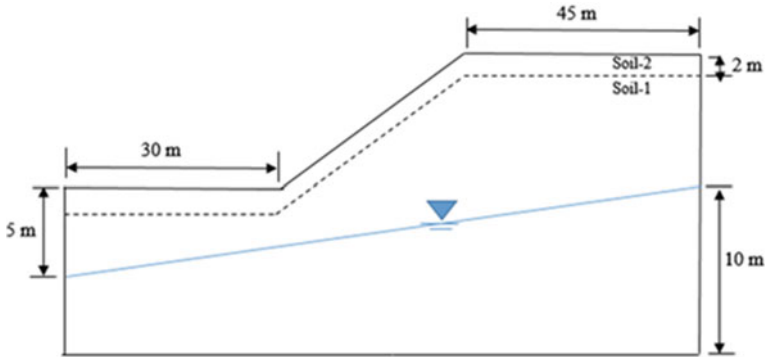


Fig. 1 Non-homogeneous two-layered slope model

the Morgenstern and Price [10] method with a half-sine function. A random search procedure [9] was used to obtain the minimum factor of safety of the slope.

The governing partial differential equation obtained from Darcy’s Law and the law of conservation of mass or continuity principle, for the flow of water through a two-dimensional unsaturated soil is represented by Eq. (1) [6]

$$\frac{\partial}{\partial x} \left(k_x \frac{\partial h}{\partial x} \right) + \frac{\partial}{\partial z} \left(k_z \frac{\partial h}{\partial z} \right) + q = \frac{\partial \theta}{\partial t} \tag{1}$$

where k_x and k_z are the hydraulic conductivities in the x- and z-directions, respectively, q is the applied flux and θ is the volumetric water content.

The soil–water characteristic curve (SWCC) or soil–water retention curve (SWRC) formulated by Van Genuchten [15] represents partially saturated soil behaviour in a very simple way as represented by Eq. (2).

$$\theta = \theta_r + \frac{\theta_s - \theta_r}{[1 + (\alpha h)^n]^m} \tag{2}$$

where θ is the volumetric water content; θ_s is the saturated water content; θ_r is the residual water content; h , the pressure head (matric suction) is positive; α is the inverse of the air entry value; n and $m = 1 - 1/n$ are curve fitting parameters. The hydraulic conductivity K is predicted using the statistical pore size distribution model of Mualem [11] illustrated by Eq. (3).

$$K = K_s S_e^{1/2} \left[1 - \left(1 - S_e^{1/m} \right)^m \right]^2 \tag{3}$$

$$S_e = \frac{\theta - \theta_r}{\theta_s - \theta_r} \tag{4}$$

The extended Mohr–Coulomb failure criterion uses effective cohesion, c' , net normal stress, $(\sigma - u_a)$, and matric suction, $(u_a - u_w)$ to represent shear strength in unsaturated soils. Fredlund et al. [5] proposed the extended model in the form of Eq. (5).

$$\tau = c' + \sigma' \tan \phi' + \psi \tan \phi^b \tag{5}$$

Where $\sigma' = \sigma - u_a$, $\psi = u_a - u_w$ and $\phi^b =$ parameter controlling increase in shear strength with suction.

3 Material Properties

To model the slope in this study, two different soils were selected. The soils were obtained from the field. From various laboratory tests, Soil-1 was classified as silty clay while Soil-2 as silty sand. Hydraulic conductivity of Soil-1 is less than Soil-2. The strength properties of the two soils are tabulated in Table 1.

Two experimental SWCC data were taken from Bordoloi et al. [1], corresponding to Soil-1, and Soil-2 in the present study. The Soil–water characteristic curves and unsaturated permeability functions of the two soils are represented by Van Genutchen function Van Genutchen [15] and Mualem [11]. The van Genutchen parameters (α, n, m, θ_s) were obtained (Table 2) using the optimization program RETC [16]. The Soil–water characteristic curves are shown in Fig. 2a and the permeability functions are shown in Fig. 2b.

Table 1 Mechanical Properties of soils used in study

Soil type	γ (kN/m ³)	c' (kPa)	ϕ' (°)	ϕ^b (°)
Soil-1	17.6	10	30	30
Soil-2	16.8	0	36	36

Table 2 Soil parameters used to evaluate SWCC and permeability functions

Soil type	a	n	m	θ_s	k_s (m/s)
Soil-1	0.005	1.26	0.21	0.43	8.38×10^{-6}
Soil-2	0.065	1.22	0.18	0.22	6.6×10^{-5}

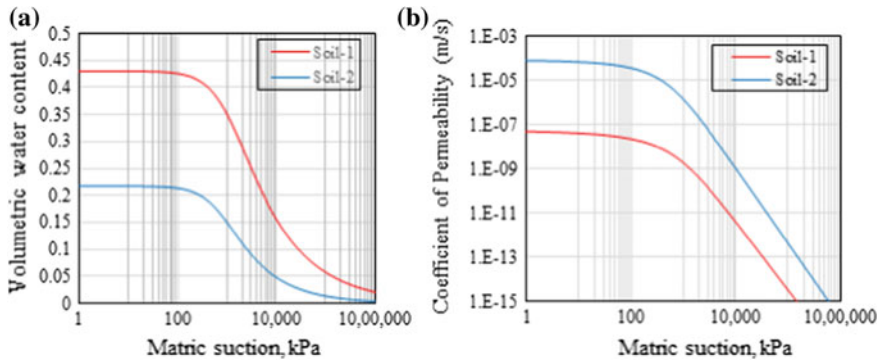


Fig. 2 a SWCC of the two soils used in the study and b permeability functions of the two soils used

4 Numerical Model

A numerical model of non-homogeneous slope (Fig. 3) has been prepared to study stability of slopes under rainfall infiltration. Finite element model was used in software SLIDE v8 [14] to perform the steady-state and transient seepage analysis. A constant head boundary condition was applied below the water table on both the sides of the slope. The portion of the boundary above the water table was specified as zero nodal flux boundary. To simulate rainfall, the slope surface was specified as flux equal to rainfall intensity. Five different rainfall intensities of 10, 30, 50, 100 and 200 mm/h were used. A short duration (24 h) rainfall was applied to the slope surface. To represent pore-water pressure profiles, section Y-Y at the middle of the slope is considered.

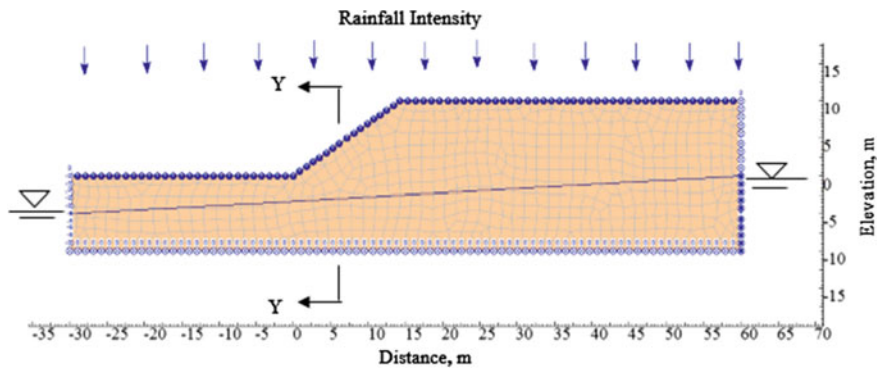


Fig. 3 Numerical model of slope

5 Results and Discussion

Figure 4 illustrates the pore pressure profiles of the two-layered slope at different rainfall intensities. The pressure profiles at the initial stage illustrate hydrostatic conditions within the slope mass. Figure 4a shows the pore pressure profile under 10 mm/h rainfall intensity. At the surface, the suction changes from 72 kPa at the initial stage to 42 kPa after 24 h and 59 kPa after 48 h. With rainfall infiltration, the profile shifts towards the right (positive pore pressures), i.e., suction decreases which results in a decrease in strength of the soil. As rainfall infiltration stops, the profile shifts left towards the initial position. Under 50 mm/h intensity (Fig. 4b), the 24th hour profile exhibit positive pore pressures throughout. There is no suction at all at this stage but with cessation of infiltration, the suction regains some of its value to 33 kPa after 48 h at the surface. Similarly, for 100 mm/h intensity (Fig. 4c), there is no suction after 24 h. The suction at the initial stage is 71 kPa at the surface, which becomes zero after 24 h but with stoppage of rainfall, it increases to 28 kPa. Figure 5 represents the pore pressure profiles of the mid-slope section after 24 h for different rainfall intensities. It is observed that the lowest rainfall intensity possess the maximum suction at the surface. As the intensity increases, the surface suction begins to reduce rapidly. The top 2 m of the pressure profiles indicates gradual reduction of suction but at more depth, the drop is almost vertical until the water level. Under 50 mm/h rainfall intensity, the pressure is positive throughout the depth. The pressure profiles for 100 and 200 mm/h follow the same path depicting that the soil has reached saturation.

Figure 5 depicts the pore-water pressure profiles of the two-layered slope under various rainfall intensities. As the rainfall intensity increases, the surface suction begins to reduce rapidly. Figure 6 represents the pore-water pressure contours within the two-layered slope. The negative pore pressure is maximum for rainfall intensity 10 mm/h whose factor of safety is also the maximum at 2.183. The water

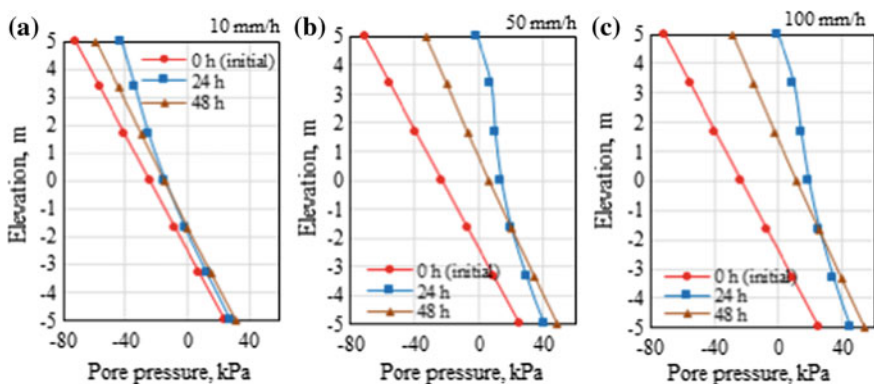
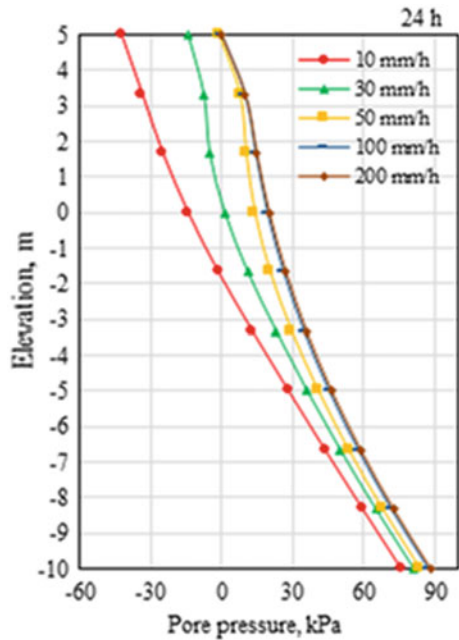


Fig. 4 Pore-water pressure profiles for the slope at different times under different intensities: **a** 10 mm/h, **b** 50 mm/h and **c** 100 mm/h

Fig. 5 Pore-water pressure profiles under different rainfall intensity after 24 h



just passes under the toe of the slope. The water level touches the slope surface under 30 mm/h rainfall intensity bringing the safety factor down to 1.364. A perched water table is formed under the 50 mm/h rainfall intensity. With an increase in rainfall intensity, the suction in the slope decreases and with it the safety factor as well.

The suction is in the range of 29–6 kPa for 50 mm/h rainfall intensity when the safety factor recorded is 0.721. At 100 mm/h, the maximum suction is in the range of 6–0 kPa with a safety factor of 0.59. The water now passes through the slope surface as run-off indicating that the soil has reached its infiltration capacity. After this stage, with more rainfall intensity, there is no effect on the pore pressures and the safety factor is similar at 0.587. WT represents the water table within the slope. The variation of factor of safety with rainfall intensity is illustrated in Fig. 7. The curve for 10 mm/h represents that the stability of the slope is not much affected because now the intensity is low as compared to the permeability of the soils. Hence, there is not much infiltration occurring to reduce the suction within the slope. With the increase in rainfall intensity, at 30 mm/h (nearly equal to permeability of Soil-1), the safety factor reduces to 1.364 after 24 h and reaching failure conditions (FS-0.928) after 48 h. The slope reaches failure conditions (FS-0.801) under 50 mm/h rainfall intensity just after 20 h of rainfall. The slope fails (FS-0.828) just after 5 h of rainfall while the safety factor is 0.679 after 5 h under 200 mm/h rainfall. The minimum factors of safety under the 100 mm/h and 200 mm/h rainfall intensity are similar which indicates the attainment of threshold

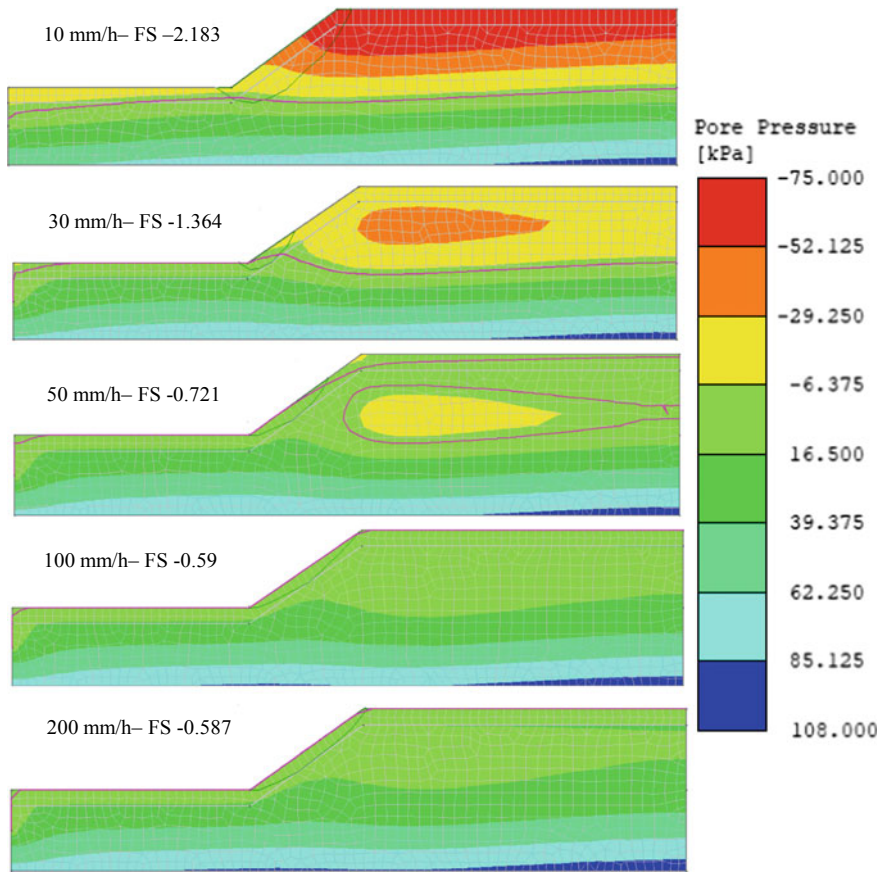


Fig. 6 Pore-water pressure contours under different rainfall intensity after 24 h

rainfall intensity. As rainfall stops, the slope recovers some safety factor with increase in suction.

Figure 8 depicts the critical slip surfaces for the slope at different rainfall intensities at initial stage, after 24 and 48 h. From Fig. 8a, it is observed that the slip surface at the initial stage and after 48 h follow same paths but the slip surface shifts towards the surface after 24 h due to water infiltrating during this time. The same phenomenon is observed under the 50 mm/h rainfall (Fig. 8b) when the slip surface after 24 h shifts towards the surface with a very shallow depth possessing a factor of safety of 0.721. With rainfall infiltration, the water reduces the effective cohesion within the soil and as a result, the critical surface becomes shallow with a reduced factor of safety. Under 100 mm/h intensity (Fig. 8c), the critical slip surface comes near the slope surface with a factor of safety of 0.59. At 200 mm/h rainfall intensity (Fig. 8d), similar slip surface is observed with a similar safety

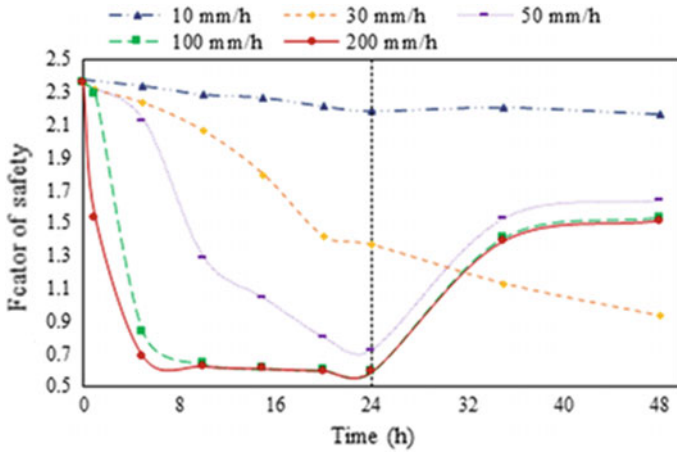


Fig. 7 Variation of safety factor with rainfall intensity

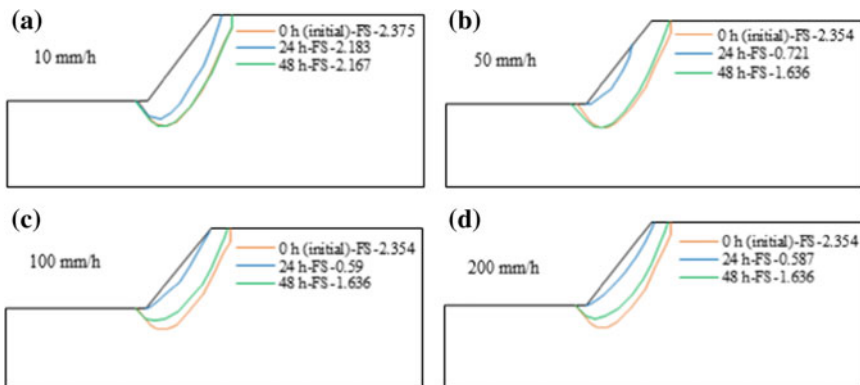


Fig. 8 Critical slip surfaces at different rainfall intensities 10, 50, 100 and 200 mm/h

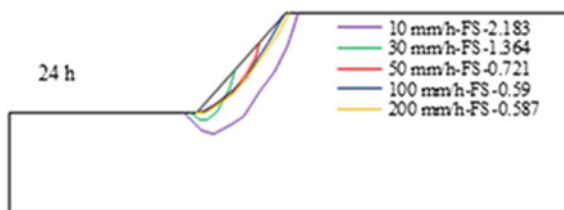


Fig. 9 Critical slip surfaces after 24 h for different rainfall intensities

factor denoting that the slope has reached its infiltration capacity where no effect will be observed with more increase in rainfall intensity.

Comparison of the critical slip surfaces under different rainfall intensities after 24 h is shown in Fig. 9. The slip surfaces for all the intensities represent shallow slope failure except the 10 mm/h intensity. The slip surfaces gradually extend towards the crest region with an increase in rainfall intensity from 30 to 200 mm/h.

6 Conclusions

Two-layered non-homogeneous slopes were modelled consisting of two soils of different saturated permeability and unsaturated permeability functions. From the results, it can be concluded that once the rainfall intensity exceeds the permeability of the soil, then only there is considerable change in suction, factor of safety and critical slip surface of the slope. With increase in rainfall intensity, the rate of decrease of suction increases and consequently the factor of safety. The critical slip surface starts moving towards the surface of the slope due to the decrease in effective cohesion of the soil. After the infiltration capacity of the soil is reached, run-off starts and there is no further change in the pore-water pressures within the slope.

References

1. Bordoloi S, Yamsani SK, Garg A, Sreedeeep S (2018) Critical Assessment of infiltration measurements for soils with varying fine content using a mini disk infiltrometer. *J ASTM Int* 47(2)
2. Chatterjee D, Krishna AM (2018) Stability analysis of two-layered non-homogeneous slopes. *Int J Geotech Eng* 5(1):1–7
3. Cho SE, Lee SR (2001) Instability of unsaturated soil slopes due to infiltration. *Comput Geotech* 28(3):185–208
4. Cho SE (2009) Infiltration analysis to evaluate the surficial stability of two-layered slopes considering rainfall characteristics. *Eng Geol* 105(3):32–43
5. Fredlund DG, Morgenstern NR, Widger RA (1978) The shear strength of unsaturated soils. *Can Geotech J* 15(3):313–321
6. Fredlund DG, Rahardjo H (1993) *Unsaturated soil mechanics*. Wiley, New York
7. Gasmoo JM, Rahardjo H, Leong EC (2000) Infiltration effects on stability of a residual soil slope. *Comput Geotech* 26(2):145–165
8. Kim J, Salgado R, Lee J (2002) Stability analysis of complex soil slopes using limit analysis. *J Geotech Geoenviron Eng* 128(7):546–557
9. Malkawi AIH, Hassan WF, Sarma SK (2001) Global search method for locating general slip surface using Monte Carlo techniques. *J Geotech Geoenviron Eng* 127(8):688–698
10. Morgenstern NR, Price VE (1965) The analysis of the stability of general slip surfaces. *Geotechnique* 15(1):79–93
11. Mualem Y (1976) Hysteretical models for prediction of the hydraulic conductivity of unsaturated porous media. *Water Resour Res* 12(6):1248–1254

12. Qian ZG, Li AJ, Merifield RS, Lyamin AV (2014) Slope stability charts for two-layered purely cohesive soils based on finite-element limit analysis methods. *Int J Geomech* 15(3):1–14
13. Rahardjo H, Ong TH, Rezaur RB, Leong EC (2007) Factors controlling instability of homogeneous soil slopes under rainfall. *J Geotech Geoenviron Eng* 133(12):1532–1543
14. Rocscience (2018) SLIDE (v8). Toronto, Canada: Rocscience Inc
15. Van Genuchten MT (1980) A closed-form equation for predicting the hydraulic conductivity of unsaturated soils. *Soil Sci Soc Am J* 44:892–898
16. Van Genuchten MT, Leij FJ, Yates SR (1991) The RETC code for quantifying the hydraulic functions of unsaturated soils. U.S. Environmental Protection Agency, Ada, Oklahoma
17. Yubonchit S, Chinkulkijniwat A, Horpibulsuk S, Jothityangkoon C, Arulrajah A, Suddeepong A (2017) Influence factors involving rainfall-induced shallow slope failure-numerical study. *Int J Geomech* 17(7):1–13
18. Zhang LL, Fredlund DG, Zhang LM, Tang WH (2004) Numerical study of soil conditions under which matric suction can be maintained. *Can Geotech J* 41(4):569–582

Studies on Embankment Foundations with Soft Soil Reinforced with Prestressed Geosynthetic Encapsulated in Thin Layer of Granular Soil



R. Anciya Fazal, J. Jayamohan and S. R. Soorya

Abstract This paper investigates the behavior of an embankment resting on soft clay reinforced with prestressed geogrid encapsulated in thin layer of granular soil. Over-excavation and replacement by geosynthetic reinforced granular soil is an effective technique to improve the load-settlement behavior of embankments resting on soft soil. The effectiveness of geosynthetic reinforcement embedded in clayey soil is very less due to poor interfacial strength and buildup of pore water pressure. But now the availability of granular soil is very less and it makes the reinforced soil technique uneconomical. It is also well established that geosynthetics demonstrate their beneficial effects only after considerable settlements. Thus, there is a need for a technique which will improve the bearing capacity without excessive settlement of reinforced granular soil. One technique yet to be comprehensively studied is prestressing the geosynthetic and encapsulating it in a thin layer of sand when used as reinforcement in clays. A series of finite element analyses are carried out using the FE software PLAXIS 2D to investigate the influence of prestressing the geogrid and encapsulating it in thin layer of sand on the load-settlement behavior of embankment foundations. The influence of prestress on the interaction between geogrid and granular soil is investigated by carrying out large-scale direct shear tests. It is observed that the load-settlement behavior and the interaction between geosynthetic and granular soil can be significantly improved by prestressing the geosynthetic reinforcement.

Keywords Geosynthetics · Finite element analyses · Embankment · Prestress · Bearing capacity

R. Anciya Fazal (✉) · S. R. Soorya
Marian Engineering College, Thiruvananthapuram, Kerala, India
e-mail: anciya786@gmail.com

J. Jayamohan
LBS Institute of Technology for Women, Thiruvananthapuram, Kerala, India

1 Introduction

Highways and Railways are essential components of development and are vital for the economic growth of the country. The growing economy requires expansion of existing carriageways into multilane expressways and development of new road/rail routes. However difficult subsoil conditions along with high economic and social costs and dearth of good construction material coupled with environmental constraints pose major challenges to the development of the road network. A typical road project has two major components; the embankment supporting the carriageway and the pavement/track. The design of high embankments on very soft soil normally requires the assessment of the following problems: bearing capacity failure, global slope failure, local instability, excessive lateral displacement, and intolerable total and/or differential settlements. A variety of techniques may be used to solve these problems, such as the use of lightweight fill, over-excavation and replacement by granular soil, vertical drains with preloading, horizontal reinforcement, and vertical reinforcement.

Over-excavation and replacement by geosynthetic reinforced granular soil is an effective technique to improve the bearing capacity of the soft soil. But now granular soils have become very scarce and costly, making reinforced soil technique uneconomical. One promising technique is to encapsulate/embed geosynthetics in thin layers of sand so that the quantity of granular soil can be minimized. The sand will act as a drainage layer and will assist in the dissipation of pore water pressure. Geosynthetics are extensible materials and will require some elongation to mobilize sufficient tensile stress in it. The strains occurring during initial settlements are insufficient to mobilize significant tensile load in the geosynthetic and hence the improvement in bearing capacity will occur only after considerable settlements. One technique yet to be comprehensively studied is prestressing the geosynthetic layers before implementing them as reinforcement in various engineering applications.

Nowadays, in order to increase stability of embankments geosynthetic materials are being used [2–4, 6, 10, 11]. Due to the addition of geosynthetics, the embankment stability can be increased by virtue of two primary functions: tensile reinforcement and pore pressure reducing drainage element. The effect of the tensile stiffness of the geosynthetics is considered in most of the analyses of reinforced embankments but mostly do not consider the drainage function of nonwoven geotextile reinforcement.

The scarcity of good-quality granular material limits the benefit of reinforcing soil [5]. The main concerns expressed about the use of marginal soils in soil reinforcement are buildup of pore water pressure, lower frictional strength, compactibility, and higher post-construction creep potential [8]. The use of geosynthetics that function not only as reinforcement but also as lateral drains is one of the potential solutions for reinforcing marginal soils [9, 13, 14]. In case of clayey soil, the interfacial strength between the soil and the reinforcement is low resulting in early failure of the interface before the full strength of reinforcement can be achieved [1].

Laboratory model studies and finite element analyses are conducted on a circular footing resting on reinforced sand with prestressed geotextile [7]. It was observed that the addition of prestress to reinforcement resulted in the load-bearing capacity improvement and settlement reduction of foundation [12].

The purpose of this paper is to investigate the improvement in bearing capacity of embankment foundation in clay by reinforcing with prestressed geogrid encapsulated in thin layers of sand. A series of finite element analyses are carried out using the FE software PLAXIS 2D to determine the influence of various parameters.

2 Experimental Studies

The interaction between the reinforcement and surrounding soil is a major data required for finite element analyses. Hence, the influence of prestress on the interaction between reinforcement and the surrounding soil was investigated by carrying out large-scale direct shear test.

2.1 Large-Scale Direct Shear Tests

Large-scale direct shear tests are carried out in a shear box of dimensions $300 \times 300 \times 200$ mm. The details of materials used and experimental setup are presented below.

A. Materials Used

Locally available clay and sand are used in this investigation. Biaxial geogrid is used as reinforcement. The properties of clay, sand, and geogrid are presented in Tables 1, 2, and 3, respectively.

Table 1 Properties of clay

Properties	Clay
Specific gravity	2.63
Optimum moisture content (%)	18
Dry unit weight (kN/m^3)	15.61
Liquid limit (%)	58
Plastic limit (%)	22
Plasticity index	36
IS classification	CH
Friction angle (ϕ°)	5
Cohesion (KPa)	25

Table 2 Properties of sand

Properties	Sand
Specific gravity	2.65
Friction angle (ϕ°)	31.2
Cohesion (kPa)	0
Effective grain size D10 (mm)	0.13
D60 (mm)	0.90
D30 (mm)	0.34
Coefficient of uniformity C_u	6.92
Coefficient of curvature C_c	1.00
Permeability (m/s)	1.07×10^{-4}
IS classification	SW

Table 3 Properties of geogrid

Property	Value
Color	Black
Type	Biaxial
Tensile strength (kN/m)	30
Aperture size (mm)	26×20
Mass per unit area (g/m^2)	225

B. Experimental Setup

As per ASTM D6243 (2013), a large-scale direct shear apparatus of shear box size $300 \times 300 \times 200$ mm, with facility for prestressing the geosynthetic reinforcement is designed and fabricated as shown in Fig. 1. ASTM procedure for direct shear tests is adopted to determine the shear parameters of reinforced clay, reinforced sand, and clay reinforced with geogrid encapsulated in thin layer of sand. The various cases studied are outlined in Table 4.

2.2 Finite Element Analyses

Finite element analyses are carried out using the commercially available finite element software *PLAXIS* 2D. For simulating the behavior of soil, different constitutive models are available in the FE software. In the present study, Mohr–Coulomb model is used to simulate soil behavior. This nonlinear model is based on the basic soil parameters that can be obtained from direct shear tests; internal friction angle and cohesion intercept. Since an embankment foundation is analyzed, a plane strain model is adopted in the analyses.

The displacement of the bottom boundary is restricted in all directions, while at the vertical sides; displacement is restricted only in the horizontal direction. The initial geostatic stress states for the analyses are set according to the unit weight of



Fig. 1 Modified direct shear apparatus

Table 4 Arrangement of soil layers and reinforcement for shear tests

Sl. no.	Figure	Description
1		Clay
2		Sand
3		Sand overlying clay
4		Reinforced clay
5		Reinforced sand
6		Geogrid at interface between sand and clay
7		Thin layer of sand at the plane of shear
8		Reinforced clay with geogrid encapsulated in thin layer of sand
9		Prestressed geogrid encapsulated in thin layer of sand

soil. The soil is modeled using 15 noded triangular elements. Mesh generation can be done automatically. Medium mesh size is adopted in all the simulations.

The reinforcement is modeled using the five-noded tension element available in the software. To simulate the interaction between the reinforcement and surrounding soil, an interface element is provided on both upper and lower surface of reinforcement. The interaction between soil and reinforcement is simulated by choosing an appropriate value for strength reduction factor R_{inter} at the interface. The interface shear parameters between the geogrid and sand is determined by carrying out large-scale direct shear tests using a shear box of size $300 \times 300 \times 200$ mm. The value of R_{inter} determined from shear tests is 0.81. The typical deformed shape after loading is shown in Fig. 2. The soil is modeled using 15-node triangular elements. Poisson’s ratio of the soil is taken as 0.25 for all cases.

In finite element analyses, embankment is modeled with top width 4 m, base width 20 m, side slope 1:2, and height 4 m. Basal reinforcement of woven geotextile is provided at the interface between embankment and the foundation. Geogrid reinforcement encapsulated in thin layer of sand is provided at a depth of $0.06 B$ from the bottom of embankment, where B is the base width of embankment. The thickness of thin layer of sand encapsulating the geogrid is $0.04 B$. The influence of prestress on the load–settlement behavior of embankment foundation is studied. Prestress is modeled by applying as a horizontal uniformly distributed load to the geogrid.

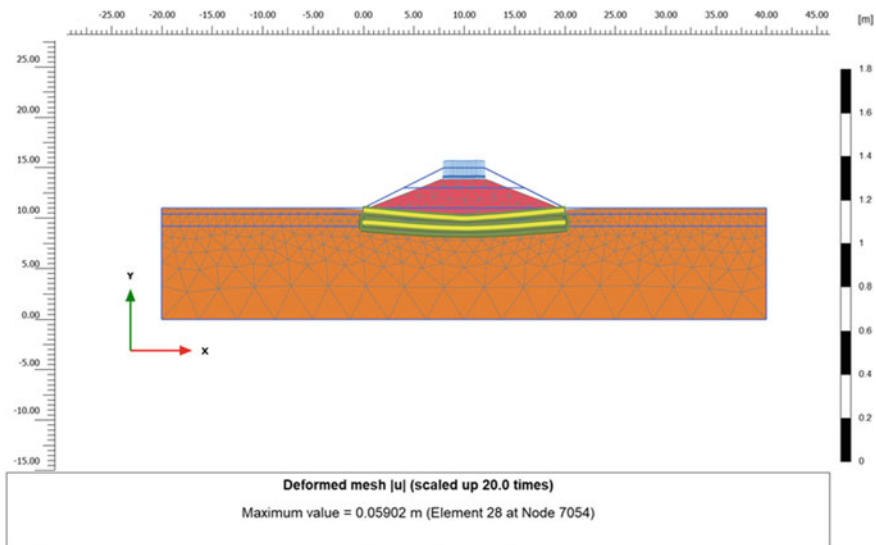


Fig. 2 Deformed shape after loading

In *PLAXIS 2D*, a staged construction procedure is adopted to simulate the various construction stages. At first, the excavation for embankment foundation is modeled. Then, sand up to the base of geogrid is modeled. Then, the geogrid is modeled and prestress is applied. In the subsequent stages, sand above geogrid, clay, basal reinforcement, and embankment are modeled. Analyses of the geometric models are carried out in the output module of the program. Analyses are carried out for a prestress of 0, 1, 2, and 3% of the tensile strength of geogrid.

2.3 Results and Discussions

The results of finite element analyses and large-scale direct shear tests are presented below

I. Results of Shear Tests

A. Influence of Encapsulated Geosynthetic with the Granular Layer

Shear stress versus shear displacement curves of various cases of reinforced and unreinforced soil are presented in Fig. 3. It is observed that maximum shear strength is mobilized when clay is reinforced with geogrid encapsulated in thin layer of sand. In reinforced clay, there is interaction between reinforcement and clay only, whereas when the reinforcement is encapsulated in thin layer of sand, there is shear interaction between sand and clay as well as reinforcement and sand. Hence, the mobilized shear strength is more when the clay is reinforced with geogrid encapsulated in thin layer of sand. The shear strength mobilized in reinforced clay was much lesser than that in geogrid is encased in thin layer of sand, due to buildup of pore water pressure.

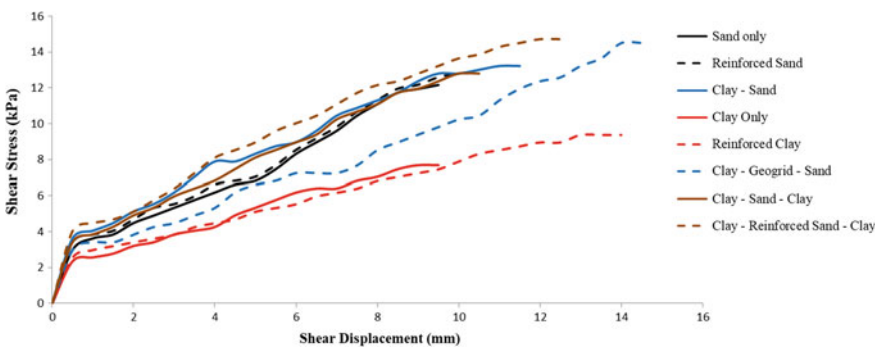
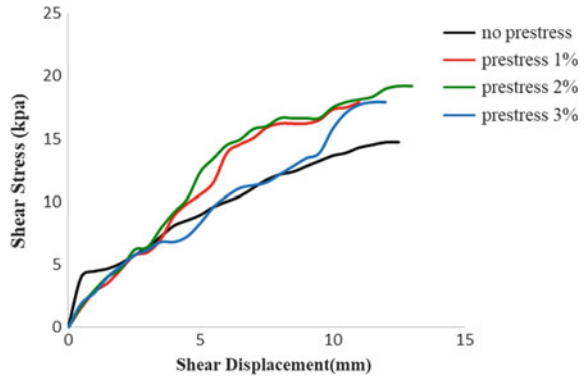


Fig. 3 Shear stress versus shear displacement curves for various cases of unreinforced soil and reinforced soil without prestress

Fig. 4 Shear stress versus shear displacement for prestressed reinforced soil



B. Influence of Prestress on Shear behavior

The influence of prestress on the shear behavior is presented in Fig. 4. It is seen that the mobilized shear stress increases with the magnitude of prestress up to 2%. Further increase in prestress did not show any improvement.

II. Results of Finite Element Analyses

A. Deformation at the Base of the Embankment

Figure 5 presents the influence of prestress on the deformation at the base of embankment. It is seen that the maximum deformation occurs below the midpoint of embankment and the deformation reduces with prestress. The minimum deformation occurs at 2% prestress, and a further increase in prestress is not beneficial.

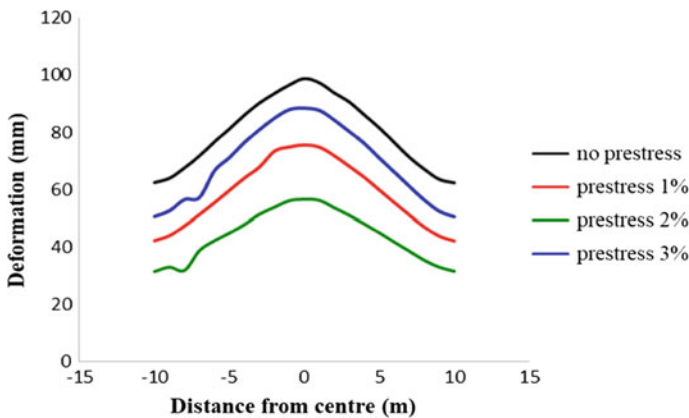


Fig. 5 Deformation at the base of embankment

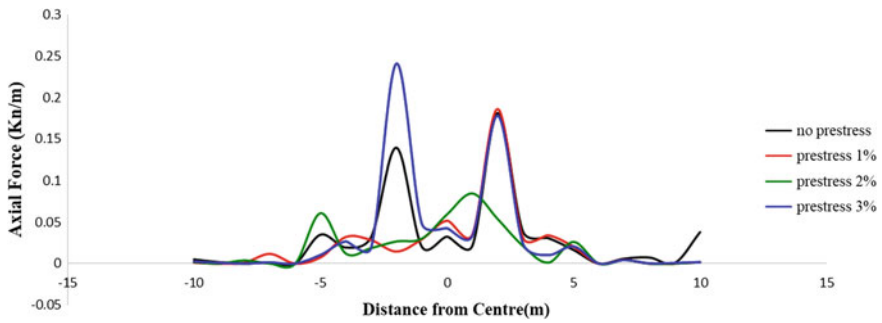


Fig. 6 Distribution of axial force in the basal reinforcement

B. Distribution of Axial force in basal reinforcement

Figure 6 presents the distribution of axial force in basal reinforcement. It is observed that for case of without prestress and with smaller magnitude of prestress, peak axial stress is seen below the edges of embankment. When the prestress is equal to 2%, the peak stress at the edges of embankment has come down, however at 3% prestress, the peak stress is high.

C. Load–Settlement Behavior of Embankment foundation

Figure 7 presents the vertical stress versus deformation curve of the embankment foundation from finite element analyses. It is observed that the load–settlement behavior considerably improves with application of prestress. Maximum improvement is attained when the magnitude of prestress is 2%. Further increase in magnitude of prestress is not beneficial.

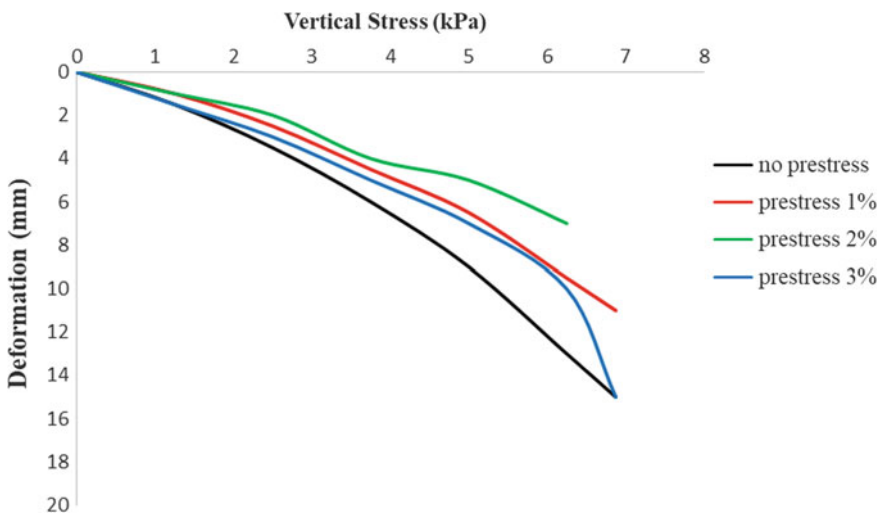


Fig. 7 Load-settlement behavior of embankment foundation

The improvement in bearing capacity of reinforced soil is influenced by the mobilized tensile force of reinforcement and the stress transfer between reinforcement and the surrounding soil. Even though increase in prestress improves the mobilized tensile force of reinforcement. It is inferred that it adversely affects the stress transfer between reinforcement and surrounding soil. Hence bearing capacity initially increases with increase in prestress and later reduces when the prestress increases beyond a particular value.

3 Conclusions

Based on the results obtained, the following conclusions are drawn on the influence of prestress on the embankment foundation with soft soil.

- Mobilized shear stress is maximum when the clay is reinforced with geogrid encapsulated in thin layer of granular soil.
- The load-settlement behavior of embankment foundation improves considerably with the addition of prestress and is dependent upon the magnitude of prestress.
- Optimum prestress is observed to be 2% of the tensile strength of the reinforcement.

References

1. Abdi MR, Sadrnejad A, Arjomand MA (2009) Strength enhancement of clay by encapsulating geogrids in thin layers of sand. *Geotext Geomembr* 27:447–455
2. Bergado DT, Teerawattanasuk C (2008) 2D and 3D numerical simulations of reinforced embankments on soft ground. *Geotext Geomembr* 26(1):39–55
3. Briançon L, Villard P (2008) Design of geosynthetic-reinforced platforms spanning localized sinkholes. *Geotext Geomembr* 26(5):416–428
4. Chen Y-M, Cao W-P, Chen R-P (2008) An experimental investigation of soil arching within basal reinforced and unreinforced piled embankments. *Geotext Geomembr* 26(2):164–174
5. Elias V, Christopher BB (1996) Mechanically stabilized earth walls and reinforced soil slopes, design and construction guidelines. Federal Highway Administration FHWA-Sa-96-071
7. Li AL, Rowe RK (2008) Effects of viscous behaviour of geosynthetic reinforcement and foundation soils on embankment performance. *Geotext Geomembr* 26(4):317–334
6. Lovisa J, Shukla SK, Sivakugan N (2010) Behaviour of prestressed geotextile-reinforced sand bed supporting a loaded circular footing. *Geotext Geomembr* 28(2010):23–32
8. Mitchell JK (1981) Soil improvement: state of the art. In: *Proceedings of tenth international conference on soil mechanics and foundation engineering*, Stockholm, Sweden, vol 4, pp 509–565
9. O’Kelly BC, Naughton PJ (2008) On the interface shear resistance of a novel geogrid with in-plane drainage capability. *Geotext Geomembr* 26:357–362
11. Rowe RK, Taechakumthorn C (2008) Combined effect of PVDs and reinforcement on embankments over rate-sensitive soils. *Geotext Geomembr* 26(3):239–249

12. Sarsby RS (2007) Use of 'Limited Life Geotextiles' (LLGs) for basal reinforcement of embankments built on soft clay. *Geotext Geomembr* 25(4–5):302–310
10. Shivashankar R, Jayaraj J (2013) Effects of prestressing the reinforcement on the behaviour of reinforced granular beds overlying weak soil. *Geotext Geomembr* 42(1):69–75
13. Tatsuoka F, Yamauchi H (1990) A reinforcing method for steep clay slopes using a non-woven geotextiles. *Geotext Geomembr* 4:241–268
14. Zornberg JG, Mitchell JK (1994) Reinforced soil structures with poorly drained backfills. Part I: reinforcement interactions and functions. *Geosynth Int* 1(2):103–148

Influence of Reinforcement Pattern on the Performance of Geotextile-Reinforced Slopes



Veerabhadra M. Rotte and Hardik V. Gajjar

Abstract Rapid development in infrastructure facilities in urban areas requires engineered slopes for various applications. Geotextile-reinforced slope is one of the engineered slopes that is being used more than three decades. Generally, geotextile-reinforced slopes are designed high and steep due to limited space available for the construction of slope in urban areas. Increase in height as well as slope inclination and other parameters influence the stability behavior of geotextile-reinforced slopes. In the present study, the stability of geotextile-reinforced slope ($\beta = 80^\circ$) was carried out to understand the influence of various parameters such as: cohesion (c), angle of internal friction (ϕ), vertical spacing of geotextiles (S_v), length of geotextiles (L_g), ultimate tensile capacity of geotextile materials (T_u) and loading conditions (F). In addition, three reinforcement patterns were studied. They are: (i) gradual increase in length of geotextile from top to bottom of the slope (P_i); (ii) gradual decrease in length of geotextile from top to bottom of the slope (P_d); and (iii) uniform length of geotextile from top to bottom of the slope (P_u). In all these three cases, the total length of geotextile layers was maintained the same. The stability analysis of geotextile-reinforced slopes was performed by limit equilibrium method using OASYS SLOPE software, and Bishop slip circle method was adopted for the same. It was observed that for various reinforcement patterns (P_d , P_i and P_u), identical factor of safety can be achieved by reducing total length of geotextile up to 14%. Moreover, to achieve alike factor of safety, angle of internal friction needs to be increased less as compared to cohesion of soil.

Keywords Slope stability · Geotextile · Reinforced slope · Placing pattern · Tensile capacity

V. M. Rotte (✉) · H. V. Gajjar
Institute of Infrastructure Technology Research and Management, Ahmedabad, India
e-mail: vmrotte@iitram.ac.in

© Springer Nature Singapore Pte Ltd. 2020
A. Prashant et al. (eds.), *Advances in Computer Methods and Geomechanics*, Lecture Notes in Civil Engineering 56,
https://doi.org/10.1007/978-981-15-0890-5_33

397

1 Introduction

Much steeper slope can be constructed for various applications, such as highway embankment, railway embankment and any manmade slopes with the help of geotextile (that acts as reinforcement) which enhances the stability of slope. Limit equilibrium is the most commonly used approach for stability analysis of slopes with and without reinforcements. In this method, failure plane is presumed along which failure occurs [1]. Available shearing strength of soil is compared with shearing resistance that is required to maintain limiting equilibrium [2]. In geotextile-reinforced slopes, first the failure plane is assumed and the length of geotextile beyond the failure plane is considered for resisting moment. Resisting moment depends upon the tensile capacity, interface friction developed between geotextile and soil and placing pattern of reinforcements. Hence, sequential modification is required in design until the required factor of safety is not achieved. Koerner [3] provided an analysis method of geotextile-reinforced slopes for $c-\phi$ soil using limit equilibrium concept. Mandal and Labhane [4] carried out studies on geotextile-reinforced slopes. The lengths of geotextiles at the top and bottom portion of the slope were varied for various slope inclinations and soil properties. It was noticed that for steeper slope the length of geotextile at the top layer was kept higher as compared to the bottom layer in order to enhance the stability of slope. Tolooiyan et al. [5] considered three parameters of geotextile for stability analysis in their study: hydraulic conductivity, elastic modulus and tensile strength. Rapid drawdown condition was analyzed for two cases: conventional method without considering drainage function and the proposed method of considering drainage function. It was noticed that drainage function of geotextile should be incorporated in computational study for realistic representation of deformation pattern of slope. Griffiths and Lane [6] explained the advantages of finite-element stability analysis over conventional method of calculation. Tandjiria et al. [7] studied the effect of reinforcement force distribution on the stability of reinforced embankment. Zornberg and Arriaga [8] conducted digital image analysis and centrifugal testing to understand the strain distribution in geotextile-reinforced slope. Onur et al. [9] conducted comparative study between geogrid and geotextile on experimental model under various slope inclinations. Duncan [10] showed the benefits of finite-element methods over limit equilibrium. The deformation observed in geotextile was much higher as compared to geogrid. The results obtained from two software packages based on finite-element analysis were compared by Maula and Zhang [11]. Gua and Hamada [12] considered geological structure and rock material along with slope geometry for natural slope stability. Digital elevation model was obtained using ArcGis software, and regression analysis was conducted for various parameters. Ranking of various slope reinforcements has been presented for seismic conditions. Song et al. [13] considered three cases of placing pattern of reinforcements. It was observed that reducing the vertical spacing at the bottom layer increases the factor of safety of slopes. Up till now, priorities were given to length of reinforcements, spacing between the reinforcements and tensile capacity

of reinforcements. Only few studies have been conducted on placing pattern of reinforcements. Moreover, very few studies related to placing patterns of geotextile with identical slope inclination along with identical total geotextile length (summation of geotextile length of each layer provided within the slope) are available. Further, studies related to influence of position of vertical loading (away from the crest of slope) on the stability of reinforced slopes are limited.

In the present study, stability analysis of slopes reinforced with geotextiles having slope inclination of 80° was carried out to understand the influence of placing pattern of geotextile layers and position of vertical loading on the behavior of geotextile-reinforced slopes. Effect of various soil and geotextile parameters on the stability of reinforced slopes was also considered in the present study.

2 Material Properties

2.1 Soil

Soil considered in the present study was clayey sand. Unit weight of soil considered above the ground water level is 16 kN/m^3 , and 18 kN/m^3 for below the ground water level. Cohesion and angle of internal friction were 9 kN/m^2 and 30° , respectively.

2.2 Geotextile

Ultimate tensile capacity (T_u) of geotextile was considered as 200 kN/m , to calculate the stability of slopes reinforced with geotextiles. The minimum reinforcement length required for the given soil parameters was taken as per the Jewell's charts recommended by BS:8006-2010. Here the minimum required reinforcement length satisfies both internal and overall stability requirements and prevent direct sliding through the reinforced block. Partial reduction factors according to BS:8006-2010 were considered for long-term design strength (LTDS).

3 Stability Analysis of Geotextile-Reinforced Slopes

Slopes having inclination of 80° with horizontal and reinforced with geotextiles were considered for stability analysis. The schematic diagram of geotextile-reinforced slope is shown in Fig. 1. Limit equilibrium SLOPE software was used to study the effect of various parameters on the performance of slope with and without reinforcements. To ensure the maximum factor of safety under various soil

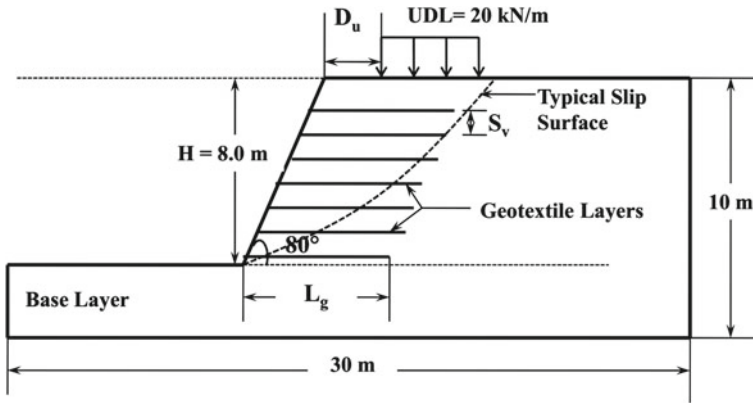


Fig. 1 Schematic diagram of geotextile-reinforced slope

properties and placing pattern of geotextiles, different combinations of parameters were considered in the present study. Bishop’s slip circle method was used for stability analysis. Parameters such as ultimate tensile strength of geotextiles, vertical spacing of geotextiles, properties of soil and phreatic surface can be modified in the software. Rectangular grid of centers was used to delineate circular slip surface. To find out the critical slip surface the grid’s coordinates were redefined after two to three initial iterations. Wherever center of slip circle was noticed on the outside of the defined grid, ‘extend grids’ option was used to calculate minimum factor of safety. Initial radius of slip surface was kept 1 m with an increment of 1 m. Table 1 shows the summary of geotextile parameters and patterns used in stability analysis. For all the three patterns of geotextile placing, initially stability was checked under gravity loading with no reinforcements. For long-term approach, tensile capacity of geotextile can be obtained by partial factor concept. Reduction factor is determined considering chemical and biological degradation as well as damage of polymer during installation.

Table 1 Geotextile parameters and patterns used in the analysis

Pattern	L_g (m)	S_v (m)	F (kN/m)	D_u (m)
P_u	4.8, 5.6, 6.4 and 7.2	0.6, 0.7, 0.8, 1.0 and 1.2	20	0, 2.5 and 5.0
P_i	5–7.76	0.6, 0.7, 0.8, 1.0 and 1.2	20	0, 2.5 and 5.0
P_d	7.76–5	0.6, 0.7, 0.8, 1.0 and 1.2	20	0, 2.5 and 5.0

P_u = uniform length of geotextile layer (Fig. 2a), P_i = gradual increase in length of geotextile from top to bottom of the slope (Fig. 2b), P_d = gradual decrease in length of geotextile from top to bottom of the slope (Fig. 2c), L_g = length of geotextile, S_v = vertical spacing between geotextile layers (Fig. 3a and b), F = vertical uniformly distributed loading, D_u = horizontal distance between starting point of uniformly distributed loading and crest of the slope (Fig. 1)

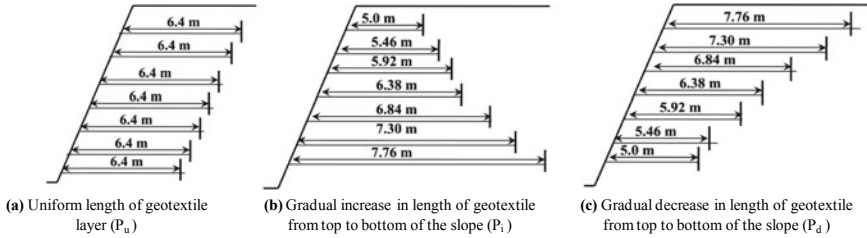


Fig. 2 Schematic diagram for placing pattern used in the stability analysis

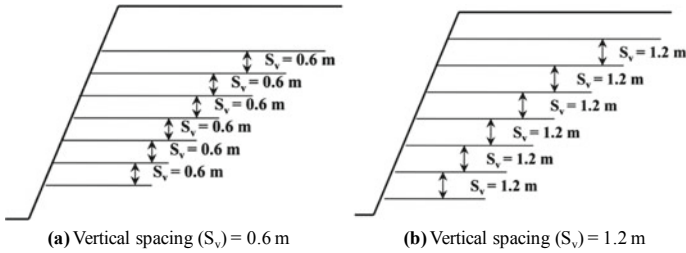


Fig. 3 Schematic diagram for vertical spacing of geotextile layers

Here, it should be noted that for each pattern the total number of geotextile layers remains the same irrespective of variation in spacing. Figs. 2 and 3 show the better visualization of the placing patterns and spacing selected for the study. From Fig. 2a and b it can be seen that for all the vertical spacing, number of geotextile layers (seven layers) is kept constant.

4 Results and Discussion

The results of stability analysis of geotextile-reinforced slopes performed using OASYS SLOPE are presented in terms of factor of safety. Stability analysis was carried out to study the influence of various parameters, such as length of geotextile (L_g), vertical spacing (S_v), position of vertical loading (D_u), cohesion of soil (c) and angle of internal friction of soil (ϕ). Tensile capacity of all geotextile reinforcements was kept constant. Moreover, spacing between any two reinforcements remains identical during stability analysis. For pattern P_i , length of all intermediate geotextile layers has an increment of 0.46 m from top to bottom of the slope. Same way for pattern P_d , length of geotextile layers has decrement of 0.46 m from top to bottom of the slope. A total of seven layers of geotextile reinforcement were kept constant for stability analysis of all slopes. It should be noted that for all geotextile placing patterns the total length of geotextiles was kept constant. For pattern P_u ,

individual geotextile length was 0.8 times height of the slope (i.e. $0.8 \times 8 = 6.4$ m) and the total length of geotextiles provided within the slope was $6.4 \times 7 = 44.7$ m). This total length of geotextiles was maintained for all the geotextile placing patterns (P_u , P_d and P_i). If the slope height is much higher than 8 to 10 m, it becomes mandatory to increase the tensile capacity of reinforcement, and modification of spacing is also needed. Based on the stability analysis, the effect of various parameters is discussed hereafter.

4.1 Effect of Geotextile Length (L_g)

Figure 4 shows the variation in factor of safety with vertical spacing of geotextiles for various length of geotextiles. Clear increase in factor of safety is observed with increase in length of geotextiles for pattern P_u . It was observed that for internal stability of slope, length of geotextile should be available beyond slip surface to achieve design pullout resistance. In all the observed cases, by keeping the spacing 0.6 or 0.7 m, the least factor of safety was captured irrespective of length of geotextile as the slip circle passes above the top layer of reinforcement without intersecting with intermediate as well as bottom geotextile layers. Maximum axial force develops at the bottom-most geotextile layer. It was noticed that for a slip circle with identical radius, increase in vertical spacing of geotextiles ensures more length of geotextile beyond the slip circle at the bottom portion of the slope. Hence, increase in factor of safety was observed with increase in vertical spacing of geotextiles and it was in between (10–20%).

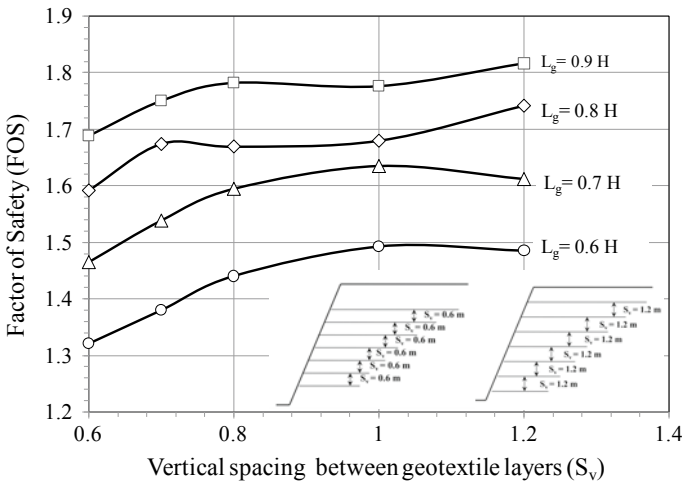


Fig. 4 Variation in FOS with vertical spacing of geotextiles for uniform length of geotextile layers

4.2 Effect of Horizontal Distance Between Starting Point of UDL and Crest of the Slope

A uniformly distributed load with 20 kN/m intensity and span of 10 m was considered for various vertical spacing of geotextiles in the stability analysis. To understand the effect of position of vertical loading from crest of the slope (D_u) and to find out its optimum value, various combinations were analyzed. Figure 5 depicts the variation in FOS with different positions of vertical loading for the pattern (P_i) of gradual increase in length of geotextile from top to bottom of the slope. It can be clearly seen from Fig. 5 that factor of safety increases with increase in horizontal distance of vertical loading from crest of the slope (D_u). However, no major variation in FOS can be noticed beyond $D_u = 2.75$ m distance from crest of the slope as the slip surface passes from the bottom four geotextiles only. The variation in FOS with different positions of vertical loading for the pattern (P_d) of gradually decrease in length of geotextile from top to bottom of the slope is presented in Fig. 6. It can be clearly observed from Figs. 5 and 6 that for identical vertical spacing of geotextiles ($S_v = 0.6, 0.7$ and 0.8 m), the pattern P_d experiences less variation in FOS as compared to the pattern P_i . For the pattern P_i , percentage increase in factor of safety for identical spacing ($S_v = 0.8$ m) was recorded as 38%. However, for pattern P_d , it was observed to be 24%.

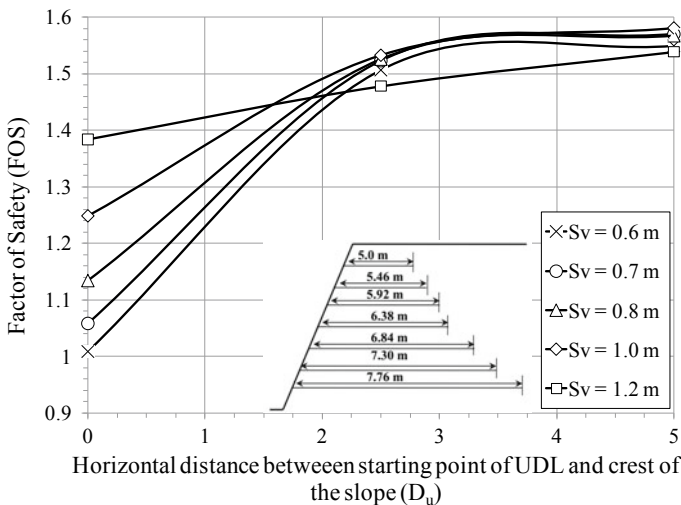


Fig. 5 Variation in FOS with horizontal distances between starting point of UDL and crest of the slope (gradual increase in length of geotextile from top to bottom of the slope)

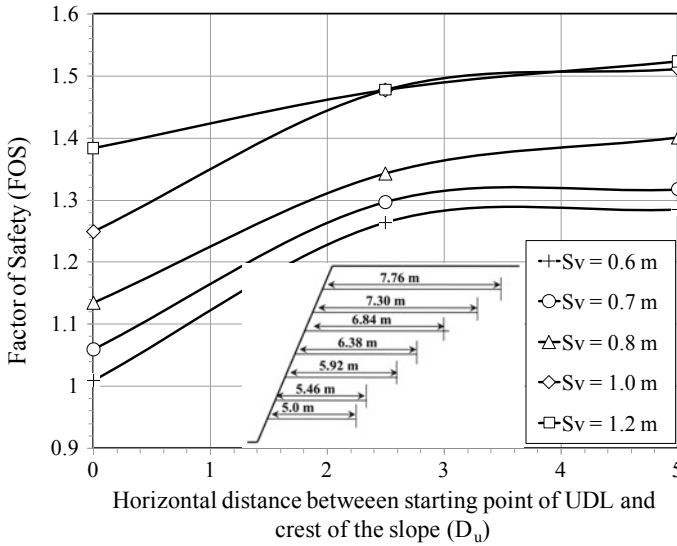


Fig. 6 Variation in FOS with horizontal distances between starting point of UDL and crest of the slope (gradual decrease in length of geotextiles from top to bottom of the slope)

4.3 Effect of Angle of Internal Friction (ϕ) and Cohesion (c)

Shear strength parameters play a critical role in stability of slopes with and without reinforcements. To have enough shearing resistance for developed stresses, it is important to have a brief understanding of soil parameters. Variation in the tensile capacity of geotextile can be done depending upon soil properties. Stability analysis of geotextile-reinforced slopes with various values of angle of internal friction and cohesion was carried out for different vertical spacing of geotextiles. In this analysis, uniform length of geotextiles (pattern P_u) and the position of vertical loading $D_u = 2.5$ were kept constant. Variations in FOS with various angles of internal friction and cohesion are plotted in Fig. 7 and Fig. 8, respectively. Angle of internal friction plays an important role to provide stability for geotextile-reinforced slopes. It can be clearly observed from Fig. 7 that increase in angle of internal friction by 100%, FOS increases nearly by 63%. However, when cohesion is increased by 100%, FOS was observed to increase by 28% only (Fig. 8). This trend in both the cases (for cohesion and angle of internal friction) was noticed to be similar for all the slopes reinforced with geotextiles having various vertical spacing.

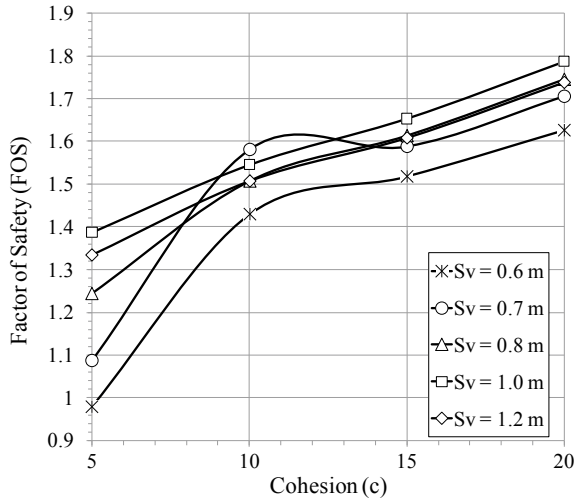


Fig. 7 Variation in FOS for various values of angle of internal friction of soil

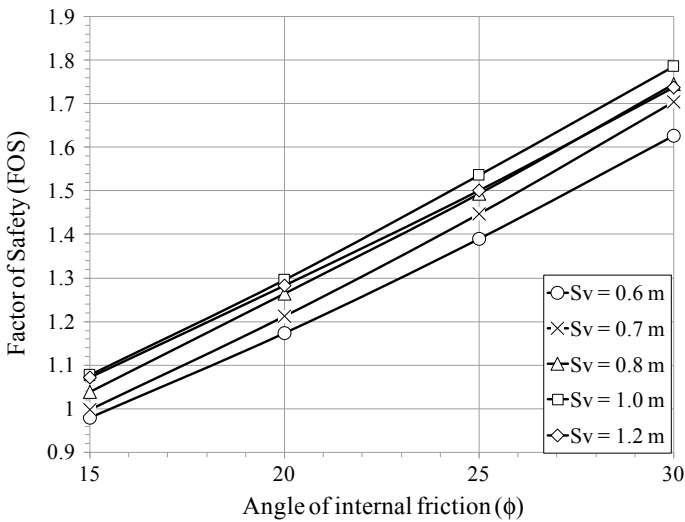


Fig. 8 Variation in FOS under various values of cohesion of soil

4.4 Influence of Placing Pattern of Geotextile Layers

In the present study, three reinforcement placing patterns were considered. They were (i) uniform length of geotextile layers (P_u), (ii) gradual increase in length of geotextiles from top to bottom of the slope (P_i) and (iii) gradual decrease in length

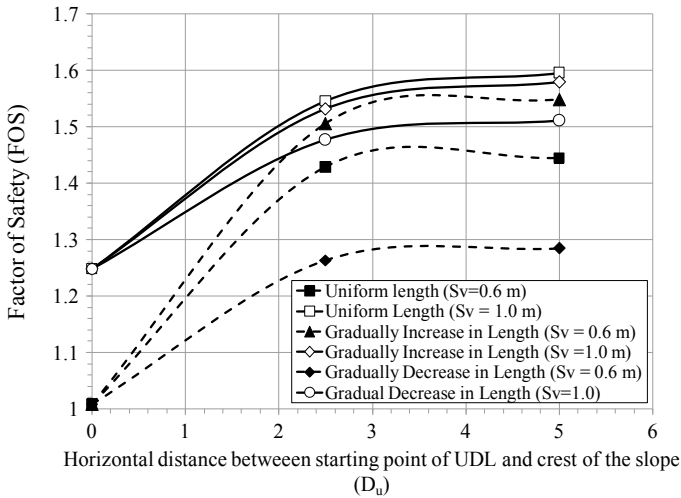


Fig. 9 Variation in FOS for various horizontal distances between starting point of UDL and crest of the slope

of geotextile from top to bottom of the slope (P_d). In all the three cases, number of geotextile layers [14] and overall (addition of all geotextile layers length) length of all geotextiles remained constant. To find out the effect of various geotextile placing pattern on the stability of reinforced slopes, a graph is plotted for vertical spacing of 0.6 and 1 m (Fig. 9). It can be clearly seen from Fig. 9 that performance of geotextile-reinforced slopes with uniform length of geotextiles (P_u) and with pattern P_i (gradual increase in length of geotextiles from top to bottom of the slope) is superior than a slope provided with geotextiles having gradual reduction in length from top to bottom of the slope (P_d).

5 Conclusions

Effect of geotextile parameters and soil properties on the stability of slopes reinforced with geotextiles has been studied for three different placing patterns of geotextile layers using limit equilibrium method. The following conclusions can be drawn based upon the results obtained:

1. Even though keeping the total length of geotextile same in all the patterns, large variation was obtained in factor of safety. Maximum value of factor of safety was obtained in pattern P_i and P_u as the critical circles for above two patterns passes through more number of geotextile layers compared to pattern P_d . Highest FOS was obtained for pattern P_i as failure plane narrows down near toe of the slope but the lengths of bottom four geotextile layers are available beyond it.

That means the total available length beyond the failure plane is more for gradual increase in length pattern compared to other two patterns.

2. Stability of geotextile-reinforced slopes is highly influenced by the angle of interface friction than adhesion between soil and geotextile. Angle of interface friction and adhesion between soil and geotextile mainly depend upon the angle of internal friction and cohesion of soil. It was noticed that when angle of internal friction was increased by 100%, FOS was improved nearly by 63%. However, increase in cohesion by 100% showed only 28% increase in FOS.
3. Based on the results obtained for influence of horizontal distances between starting point of UDL and crest of the slope (D_u) on stability of slope, it was observed that as the value of D_u increases beyond 2.75 m (i.e. 0.34 H) no change in slip circle was noticed. Hence, to maintain certain value of FOS and to optimize the distance of placing vertical load it become essential to have brief analysis related to various loading positions away from crest of the slope.

Along with the above concluded results many parameters can also be considered, such as rising of water table, variable tensile strength for all the three patterns to make design more economical and safe. Moreover, influence of slope and back slope inclination can also be considered under various placing patterns to have overall idea about variation in factor of safety.

References

1. Bishop AW (1955) The use of the slip circle in stability analysis of slope. *Geotechnique* 5(1): 7–17
2. Huang YH (2013) Slope stability analysis by limit equilibrium method. ASCE press
3. Koerner RM (2005) Designing with geosynthetics, 5th edn. Pearson Prentice Hall
4. Mandal JN, Labhane L (1992) A procedure for the design and analysis of geosynthetic reinforced soil slope. *Geotech Geol Eng* 10:291–319
5. Tolooiyan A, Abustan I, Selamat MR, Ghaffari SH (2009) A comprehensive method for analyzing the effect of geotextile layer on embankment stability. *Geotextile Geomembr* 27(5):399–405
6. Griffiths DV, Lane PA (1999) Slope stability analysis by finite element. *Geotechnique* 49(3): 423–443
7. Tandjiria V, Low BK, Teh CI (2002) Effect of reinforcement force distribution on stability of embankment. *Geotextile Geomembr* 20(6):423–443
8. Zornberg JG, Arriaga F (2003) Strain distribution within geosynthetic reinforced slope. *J Geotech Geoenvironmental Eng* 123(1):32–45
9. Onur MI, Tuncan M, Evirgen B, Ozdemir B, Tuncan A (2016) Behavior of soil reinforcement in slope. *Procedia Eng* 143:483–489
10. Duncan JM (1996) State of art: limit equilibrium and finite element analysis of slope. *J Geotech Eng ASCE* 122(7):577–596
11. Maula BH, Zhang L (2011) Assessment of embankment factor safety using two commercially available program in slope stability analysis. In: The twelfth East Asia Pacific conference on structural engineering and construction, vol 14, pp 559–566
12. Guo DP, Humada M (2012) Observed stability of natural and reinforced slope during the 2008 wenchuan earthquake. *J Jpn Soc Civ Eng* 29(2):481–494

13. Song F, Chen RY, Ma LQ, Zhco J (2018) Stability analysis of reinforced slope based on limit equilibrium method. *Tech Gaz* 25(1):224–229
14. Jewell RA, Paine N, Wood RI (1984) Design methods for steep reinforced embankments. In: *Proceedings of the polymer grid reinforcement conference*, London, pp 70–81
15. BS 8006-1:2006 Code of practice for strengthened/reinforced soil and other fills
16. Oasys (2011) Oasys slope version 19.1 stability analysis for geotechnical structure with or without reinforcement, Oasys, London, UK

Use of Polypropylene Fibres for Cohesive Soil Stabilization



Trudeep N. Dave, Dhavalkumar Patel, Gafur Saiyad and Nirmal Patolia

Abstract Rapidly increasing infrastructure demands more ground availability to transfer the stresses safely. Scarcity of good bearing soil at infrastructure site requires improvement/modification in the soil properties to allow further construction activity mainly in fine-grained soils. This paper presents application of polypropylene fibres (PPF) for stabilization of expansive soil procured from Bhestan near Surat, South Gujarat. During the study, PPF in proportion of 0.75, 1.5, 2.0, 2.25 and 2.5% have been mixed randomly with soil. Various tests were performed to study compaction characteristics, soaked California bearing ratio (CBR) and unconfined compression of virgin soil samples and soil samples with above-mentioned PPF contents. Results showed that addition of PPF reduced maximum dry density in the range of 3–6.5% and increased optimum moisture content in the range of 2.3–5.25%. Also, mixing of PPF (10 mm fibre length) up to 2.25% increased soil CBR from 1.54 to 5.75%, which decreased on further addition of PPF. Increase in PPF fibre length from 10 to 30 mm further increased CBR from 5.75 to 7.06% for same PPF content. In addition, the unconfined compressive strength of the soil was observed to increase by 56.9% at 2.25% PPF. Results highlighted that soil stabilization using PPF is quite useful for modifying properties of cohesive soil.

Keywords Polypropylene fibres · Soil stabilization · Cohesive soil · Experimental study

T. N. Dave (✉) · D. Patel · G. Saiyad · N. Patolia
Department of Civil Engineering, Institute of Infrastructure Technology Research and Management (IITRAM), Ahmedabad, India
e-mail: trudeepdave@iitram.ac.in

© Springer Nature Singapore Pte Ltd. 2020
A. Prashant et al. (eds.), *Advances in Computer Methods and Geomechanics*, Lecture Notes in Civil Engineering 56,
https://doi.org/10.1007/978-981-15-0890-5_34

1 Introduction

Earlier studies related to soil reinforcement were primarily focused on the use of metallic and polymeric strips and geosynthetic elements. Effectiveness of these reinforcements was observed in various forms such as strips, bars, discs and mesh. In past three decades, the engineering behaviour of randomly distributed, discrete, flexible and fibre-reinforced soils has been studied in significant detail by many researchers worldwide. Most of these studies are based on the laboratory and small-scale tests such as direct shear tests, triaxial compression tests, unconfined compression tests, compaction tests, California bearing ratio (CBR) tests and plate load tests. McGown et al. [1] investigated polymeric mesh reinforcement in coarse-grained soil and observed the improvement in strength of the soil at all strain levels. Experimental findings by Fletcher and Humphries [2] indicated that there is an optimum fibre dosage as well as an optimum configuration for improving a CBR value of compacted soil. Puppala and Musenda [3] recommended the use of polypropylene fibre in civil engineering because it causes significant improvement in the compressive and shear strength of the soil. Babu and Vasudevan [4] conducted triaxial compression test on soils reinforced with coir fibres. It was observed that deviator stress at failure increases up to 3.5 times compared to unreinforced soil and maximum stress increase was observed for fibres of length between 15 and 25 mm. Further, soil stiffness increased considerably due to fibre inclusion which may reduce immediate settlement of soil.

Malekzadeh and Bilsel [5] concluded that for enhancing physical and mechanical properties of subsoils of roads and light buildings on expansive soils, the use of polypropylene fibres might be an effective method. Pradhan et al. [6] studied the effectiveness of polypropylene fibres for stabilization of black cotton soil. Experiments were performed to study swelling characteristics, Atterberg's limits and unconfined compressive strength. It was concluded that for fibre-reinforced soil, optimum moisture content and maximum dry density of soil are significantly affected due to addition of polypropylene fibre. Zaimoglu and Yetimoglu [7] conducted a series of unconfined compression tests to investigate the effects of randomly distributed polypropylene (PP) fibre reinforcement (length 12 mm and diameter 0.05 mm) on the unconfined compressive strength (UCS) of a fine-grained (MH) soil. The study observed an increase of 85% in unconfined compressive strength of reinforced soil, which might be due to the bridging effect of fibre which can efficiently impede the further development of failure planes and deformation of the soil. The strength characteristics of fibre-reinforced soil is significantly governed by interfacial shear resistance of the fibre–soil interface, which is primarily affected by friction, bonding force, matrix suction and interface morphologies [8]. Shukla [9] listed soil characteristics, fibre characteristics, fibre concentration, type of admixtures, fibre mixing method, type and amount of compaction and test conditions as factors affecting engineering behaviour of fibre-reinforced soils.

Past studies have highlighted the effectiveness of PP fibres to improve properties of cohesive soils. Keeping in view the importance of use of fibre reinforcement, this

study is aimed at studying the effects of fibre length and its concentration on compaction characteristics, CBR and unconfined compressive strength of fibre-reinforced soil compared to unreinforced soil.

2 Experimental Program

In this study, the soil sample was collected from dedicated freight corridor (DFC) project site at Bhestan village near Surat, South Gujarat. Experiments were performed to evaluate various properties of the soil as listed in Table 1. As per unified soil classification system (USCS), the soil was classified as CH.

Commercially available polypropylene fibres (Fig. 1) were used in this study and properties are listed in Table 2. The fibres were mixed manually with soils to ensure homogeneous mixture of soil and fibres.

Table 1 Properties of soil used in this study

Property	Value
Specific Gravity (G_s)	2.74
Free swell index	60%
Degree of expansiveness	Very high
Liquid limit	59.82%
Plasticity index	28.83%
Shrinkage limit	16.7%
Maximum dry density	15.1 kN/m ³
Optimum moisture content	21%
Soil Type (as per USCS)	CH

Fig. 1 Polypropylene fibres used in this study



Table 2 Properties of PP fibres used in this study

Property	Value
Density	0.91 gm/cc
Diameter	0.05 mm
Tensile strength ^a	280 MPa
Tensile modulus ^a	3.3 GPa
Tensile elongation ^a	350%
Molar mass ^a	42.08/mol

^aObtained from manufacturer

A series of tests were conducted to obtain the effect of fibre concentration on the properties of fibre-reinforced soil. Tests to observe compaction characteristics, penetration resistance through California bearing ratio (CBR) test and unconfined compression strength were performed at fibre concentration of 0, 0.75, 1.5, 2.0, 2.25 and 2.5%. Second series of experiments were performed to analyze effect of length of fibre on the above-mentioned properties of soil at optimum fibre concentration. Third series of experiments were conducted to investigate effectiveness of fibres on stress–strain behaviour of fibre-reinforced soil.

3 Results and Discussion

Effect of fibre concentration on compaction characteristics of fibre-reinforced soil is shown in Fig. 2. It is observed that as the percentage of fibre content increases, the maximum dry density decreases and optimum moisture content increases. The maximum dry density reduced from 15.1 to 14.57 g/cc with addition of fibres in range of 0–2.5% and optimum moisture content increased from 21 to 22.1%. The

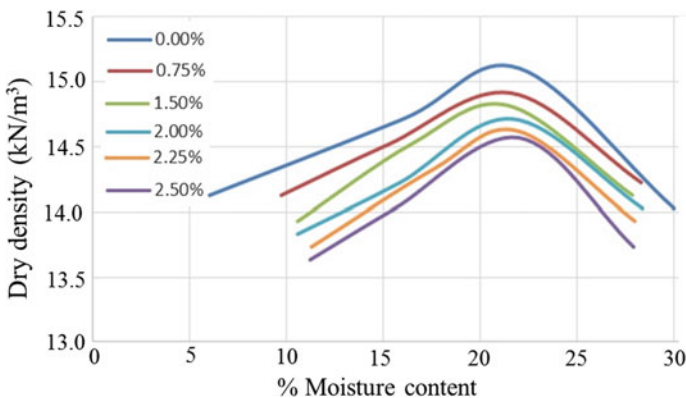


Fig. 2 OMC and MDD comparison of unreinforced and reinforced soil

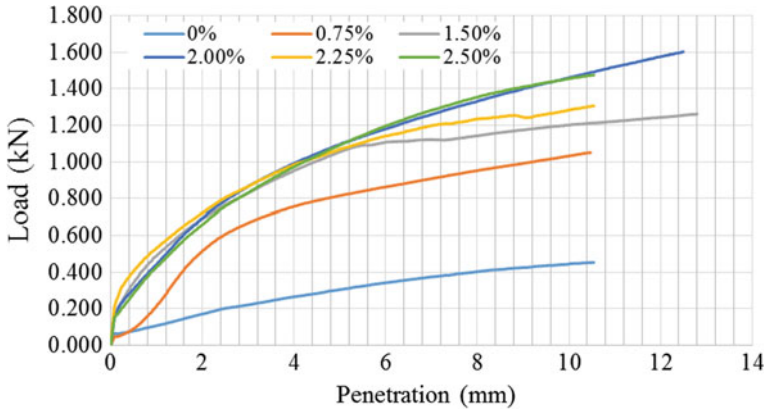


Fig. 3 CBR results for varying % of PP fibres

reduction in maximum dry density may be due to the reduction in unit weight of soil due to addition of fibres and creation of additional pore space by fibre addition. The increase in the optimum moisture content may also be due to creation of additional pore spaces and/or due to additional specific surface area available in fibre-reinforced soil as compared to unreinforced soil.

Soaked CBR tests were performed to observe the effect of fibre reinforcement on penetration resistance offered by the soil by using 10 mm long fibres. As presented in Fig. 3, CBR corresponding to unreinforced soil was found as 1.54% for 2.5 mm penetration and the maximum penetration resistance of 6.1% for 2.5 mm penetration was corresponding to 2.25% fibre concentration. The increase in the CBR value by about 300% may be due to the increase in the interfacial shear strength due to the addition of fibres. Further, it can be observed that by increasing the percentage of fibre content up to 1.5%, the CBR value increases by 289% while further increase in fibre content from 1.5 to 2.25%, the increment in CBR value is 5% only. Considering the cost aspect, addition of 1.5% PP fibres by weight is optimum for improvement in penetration resistance. CBR tests were also performed at 2.25% fibre content corresponding to OMC-MDD, i.e., 2.25% by varying the length of the fibres as shown in Fig. 4. The results pointed out that on increasing the length of PP fibre from 10 mm length to 20 mm, CBR increases from 6.1 to 6.88% and CBR value for 30 mm fibre length is 7.08%. It can be concluded that as the length of fibre increases from 10 to 30 mm, the CBR value increased by 14% only revealing limited change in CBR by increasing the length of fibre.

Results of unconfined compression tests are shown in Fig. 5. Unconfined compressive strength of reinforced soil sample was observed to increase from 20.8 to 48.4 kPa by addition of 10 mm PP fibres at 2.25% concentration. It indicates that unconfined compressive strength increases by 132% by the addition of 2.25% polypropylene fibre of 10 mm length. Further increase in fibre content reduced the unconfined compressive strength of soil. It indicates that addition of 2.25%

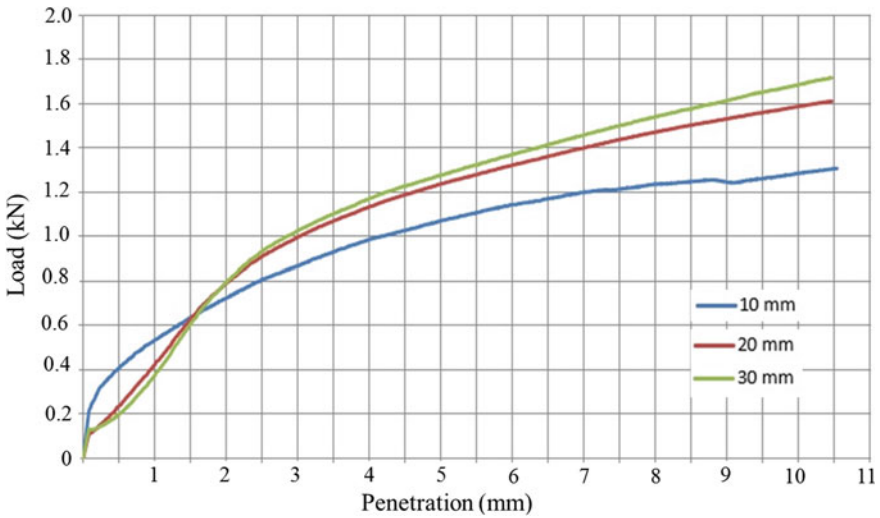


Fig. 4 CBR results for varying length of 2.25% PP fibre-reinforced soil

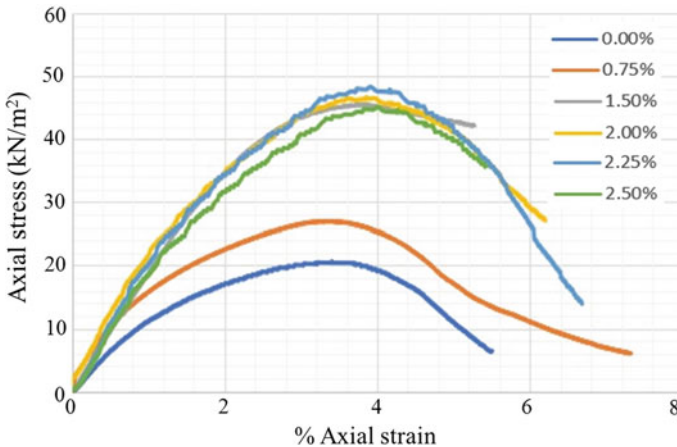


Fig. 5 Stress–strain behaviour of UCS sample for varying % of PP fibres

polypropylene fibre of 10 mm length gives maximum unconfined compressive strength. However, the addition of fibre content from 0 to 1.5% increased unconfined compressive strength by 119% while for increase in fibre content from 1.5 to 2.25%, addition of polypropylene fibre strength increase only by 10%, so 1.5% addition of polypropylene fibre by weight is optimum with respect to cost. In addition, it can be observed that addition of fibre content increased the % axial strain corresponding to failure, which indicates an increase in the ductility of fibre-reinforced soil.

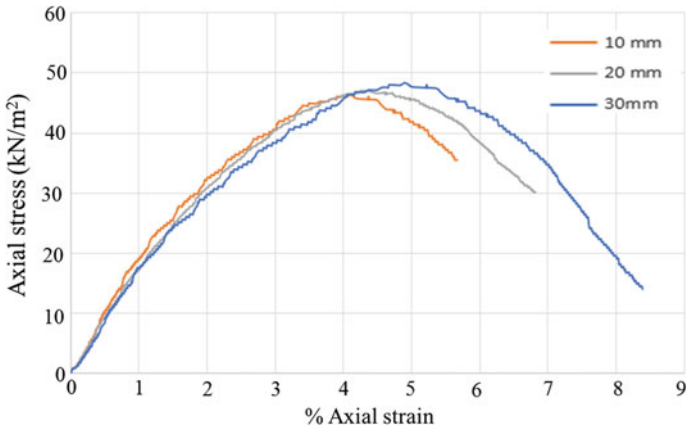


Fig. 6 Stress–strain behaviour of UCS sample for varying fibre length

Tests were also performed at 2.25% fibre content by varying length of the fibres to observe the effect of length of fibres on unconfined compressive strength of the soil specimen as shown in Fig. 6. It can be observed that with increase in the length of fibre from 10 to 30 mm, the unconfined compression strength increased by 6% only. The study highlights limited significance of increase in length of fibres on unconfined compression strength.

In addition, unconsolidated undrained triaxial tests were performed on unreinforced soil samples and soil sample reinforced at 2.25% fibre content. Mohr’s circle obtained for both the cases are presented in Figs. 7 and 8. It has been observed that the addition of fibres increases the cohesion (c) of soil from 26 to 35 kPa while the angle of internal friction (ϕ) increases from 5° (nominal value of friction angle) to

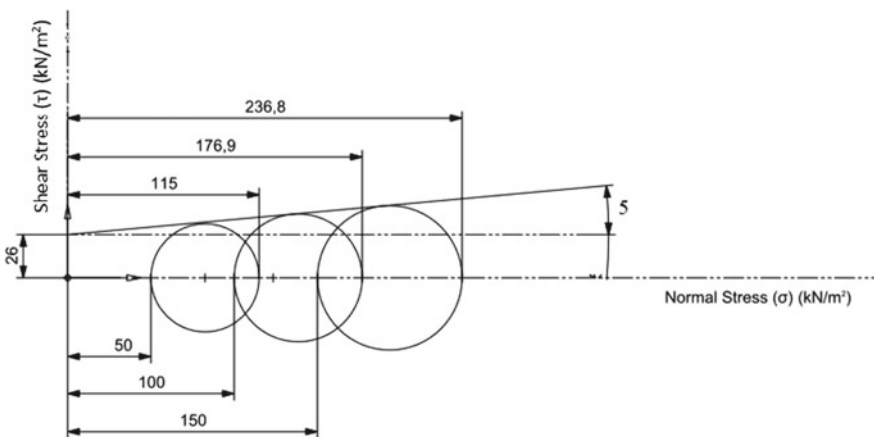


Fig. 7 Mohr’s circles corresponding to unreinforced soil

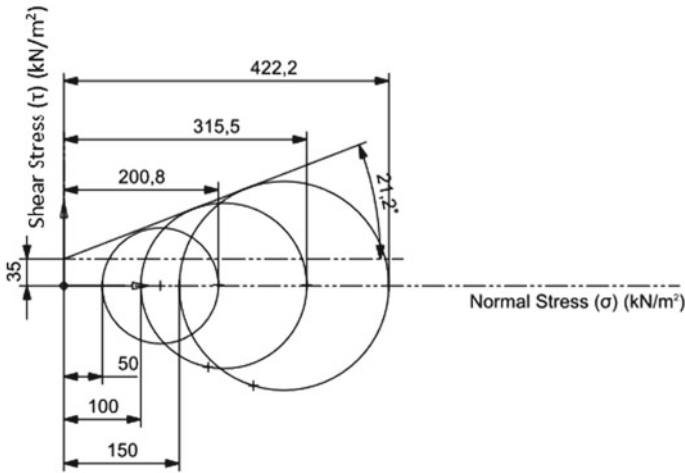


Fig. 8 Mohr's circles corresponding to 2.25% PP fibre-reinforced soil

21.2°. Hence, the addition of 2.25% of fibre content results in an increase in cohesion by 34.61% and friction angle by 15.2°. The increase in friction angle for PP fibre-reinforced soil may be attributed to the interlocking friction effect induced by the fibres. However, further studies are required to understand the associated mechanism. Hence, it can be concluded that use of fibres to reinforce the soil improves both shear strength parameters c and ϕ .

4 Conclusions

- Use of polypropylene fibres reduced maximum dry density in the range of 3–6.5% and increased optimum moisture content in the range of 2.3–5.25%.
- Addition of PP fibres increased CBR corresponding to 2.5 mm penetration by up to 300%. At optimum fibre content of 1.5%, the increase in CBR was about 289%.
- The unconfined compressive strength increased by 119% due to the addition of 1.5% PP fibres. Further, increase in fibre content from 1.5 to 2.25% increased UCS by only 10%.
- As the length of fibre increases from 10 to 30 mm, the unconfined compressive strength increases by 6%.
- Addition of fibre content increased the % axial strain corresponding to failure thereby enhances the ductile behaviour of soil and is expected to reduce the shrinkage settlement during desiccation which would help in reducing the detrimental damages to supported structure. Results pointed out limited

significance of increase in length of fibres on CBR values. Based on this study, 1.5% PP fibre is observed to be optimum for improving soil properties.

- With the addition of 2.25% of polypropylene fibres in the soil, an increase in the value of cohesion was 34.61% and angle of friction increases from 15.2°.

References

1. McGown A, Andrawes KZ, Hytiris N, Mercer FB (1985) Soil strengthening using randomly distributed mesh elements. In: Proceedings of the 11th international conference on soil mechanics and foundation engineering, San Francisco, California, 1735–1738
2. Fletcher CS, Humphries WK (1991) California bearing ratio improvement of remoulded soils by the addition of polypropylene fibre reinforcement. Transp Res Rec 1295, Washington DC, 80–86
3. Puppala AJ, Musenda C (2002) Effect of fibre reinforcement on strength and volume change in expansive soils. Transp Res Rec 0716, Washington DC, 134–140
4. Babu GLS, Vasudevan AK (2008) Strength and stiffness response of coir fibre-reinforced tropical soil. J Mater Civ Eng ASCE 20(9):571–577
5. Malekzadeh M, Bilsel H (2012) Effect of polypropylene fibre on mechanical behaviour of expansive soils. Electron J Geotech Eng 3(7):725–733
6. Pradhan P, Karand R, Naik A (2012) Effect of random inclusion of polypropylene fibres on strength characteristics of cohesive soil. Geotech Geol Eng 30(1):15–25
7. Zaimoglu AS, Yetimoglu T (2012) Strength behavior of fine grained soil reinforced with randomly distributed polypropylene fibers. Geotech Geol Eng 30:197–203
8. Gelder C, Fowmes GJ (2016) Mixing and compaction of fibre- and lime-modified cohesive soil. Ground Improv 169(GI2):98–108
9. Shukla SK (2017) Fundamentals of fibre-reinforced soil engineering, developments in geotechnical engineering, Springer Nature, Singapore

Analytical Investigation on High and Low Seismic Response of Zero Liquid Discharge Steel Structure



B. Nambiyanna, Mohammed Younus Salman and R. Prabhakara

Abstract Industrial steel structures supporting thermal Zero Liquid Discharge (ZLD) are subjected to great lateral forces due to wind and an earthquake. Industrial steel structures are made out of number of joints and structural members, this complicated structural system has to be designed carefully. Strength and performance of these structures for the various combinations of load, geometry, and boundary conditions have to be ascertained before erection. In the present investigation, analytical procedure has been carried out to know the response of various lateral force resisting systems such as “X”, “Inverted V”, “K”, and “Knee” bracings and “Moment Resisting Frame” under high (Zone 5) and low (Zone 2) seismic zones. Response spectrum method of seismic analysis has been used for the study using STAAD Pro V8i software. The various parameters such as fundamental time period, lateral displacement, and storey shear among various structural systems are compared. From the results, it was found that Inverted V bracings show better performance under both high (Zone 5) and low (Zone 2) seismic zone. Further Inverted V bracing is found to be the most efficient structural system for ZLD structure compared to other lateral force resisting systems.

Keywords Zero liquid discharge · Response spectrum method · Time period · Lateral displacement · Storey shear

B. Nambiyanna (✉) · M. Y. Salman
Civil Engineering Department, Ramaiah Institute of Technology, Bengaluru, Karnataka, India
e-mail: nambiyannab@msrit.edu

B. Nambiyanna · R. Prabhakara
Former Professor, Civil Engineering Department, Ramaiah Institute of Technology,
Bengaluru, Karnataka, India

1 Introduction

Strict environmental regulation in many countries has mandated true ZLD wastewater treatment in a large number of industries including power, manufacturing, refining, pulp and paper, mining, and chemical processing. ZLD is a new technology where all industrial wastewater at a site is reduced to dry solids and recycled or sent back to a landfill. Any useable water recovered from the wastewater treatment process is reused for various industrial purposes. Industrial steel structures supporting ZLD are subjected to heavy gravity load due to weight of various equipment resting on it. These weights attract large inertia force in the event of an earthquake creating large amount of lateral force. Also as the equipments are resting at different heights, the wind force acting on the equipments creates lateral force and overturning moment of substantial magnitude. This makes it necessary to use suitable lateral force resisting system which improves the performance of the structure and also decreases the overall cost. Siddiqi et al. [1] showed bracings increase the load-carrying capacity of structure laterally by increasing the stiffness and strength of the frame. The braced frame comprises of typical set of columns and beams configurations whose main drive is to resist the gravity load and bracings which are provided so that the entire system forms the vertical cantilever truss against lateral load.

Di Sarno and Elnashai [2] proved that bracings are primarily subjected to axial load; thus, providing the least size of members to satisfy lateral shear with respect to strength and stiffness. While bracing decreases shear force and bending moment of column and there was increase in axial load in column where bracings are connected to columns. Tajheem and Khusru [3] indicated that if concentric bracing increases the stiffness laterally in the frames, then there is increase in the natural frequency and reduction in time period. These characteristics result in favorable seismic response reducing the total lateral displacement. Khadiranaikar and Halli [4] showed that eccentric bracing improves the energy absorption capacity of frames but has comparatively less stiffness than concentric bracing system. Further, hollow tube or square sections perform better than any other section as bracing members. Lai and Mahin [5] indicated diamond brace configuration observed that the degradation of storey shear occurs quickly which formed cracks in bracings and bracings were laterally buckled through plastic hinges formed at mid-span and at gusset plate regions. Also, it was observed that even after the complete failure of braces, the frame is behaving like conventional moment frame. and continued to take the load.

Tajheem and Khusru [3] indicated that maximum lateral storey displacement was reduced up to 87% in case of concentric bracing and up to 48% in case of eccentric bracing compared to unbraced frame. The exterior column moment was high in unbraced frame compared to braced frame. Alibhat et al. [6] showed that the introduction bracing system in frames enhances the base shear resistance of frame and thereby reduction in roof displacement of the structure. The lateral displacement of frame reduced by using Inverted V brace over X bracing. Tande and

Sankpal [7] investigated that the plastic hinges were formed in bracing prior to compression members in eccentric bracings. Sangle et al. [8] showed that base shear has been increased by 38% in bracings with both directions. The roof deformation of frame with different brace systems is reduced from 43 to 60%. Choudhari and Nagaraj [9] showed that the drift ratios of each storey of frame in X direction is comparable with IS:1893:2002 and also X bracing showed nominal results over K bracing. Different lateral force resisting systems such as “ X ”, “Inverted V ”, “ K ”, and “Knee” bracings with “Moment Resisting Frame” are provided for the attained configuration of ZLD structure in order to study the response of various lateral force resisting systems under earthquake loading. In this investigation, the structures are analyzed for both high and low seismic zone to study the performance of structure.

2 Modeling and Inputs

Response spectrum method has been used for the study using STAAD Pro V8i software. A wind speed of 50 m/s as per IS 875 p3 for Chennai zone is taken for the analysis purpose. The main objectives of this investigation are to study seismic performance of various lateral force resisting systems for ZLD structure in terms of fundamental time period, lateral displacement, storey shear in both high and low seismic zone (Zone 5 and Zone 2). Based on the size of equipments, installation height, and functionality, the structural frame as shown in Fig. 1 is attained for 11 m³/h capacity ZLD. Table 1 shows the input used for modeling.

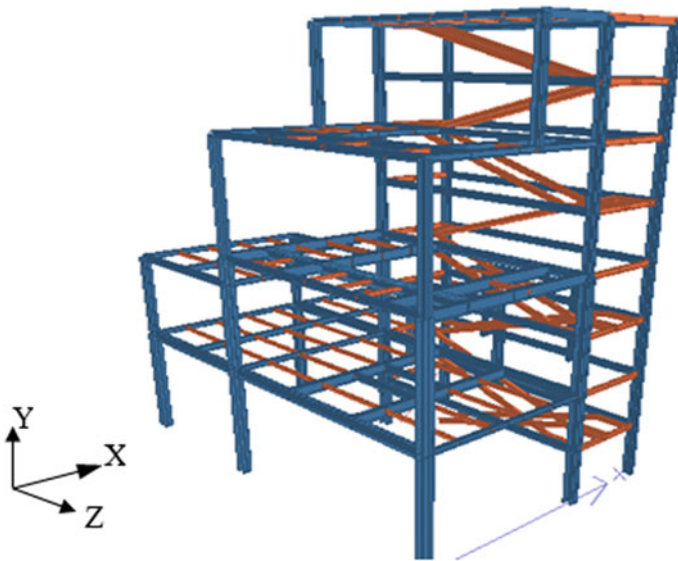


Fig. 1 Model frame for 11 m³/h capacity ZLD

Table 1 Input data

Model inputs		Staircase	ISMC200
Height of structure	17.3 m	Grating	40 mm FRP
Width of structure	11.85 m	Handrail	PIPE50L
Length of structure	14 m	Floor Load	
Average storey height	4.5 m	Dead load (Grating)	0.25 kN/m ²
Foundation type	Isolated footing	Live load	5 kN/m ²
Material properties		Equipment load	
Type of steel	Carbon steel conforming to IS 2062	Crystallizer	416 kN
Young's modulus	205 Gpa	Heat Exchanger	410 kN
Poisson ratio	0.3	Deaerator	8 kN
Density	78.33 kN/m ³	Condenser	34.8 kN
Yield strength	250 Mpa	Seismic data	
Ultimate strength	410 Mpa	Seismic zone	Zone V and Zone II
Member properties		Zone factor	0.36 and 0.1
Type of section	Jindal section	Importance factor	1
Beam	UC305, UC254, UC152	Response reduction factor	4
Column	UC305, UC254, UC152	Damping	2%
Bracing	Pipe 110 M	Soil type	Medium

2.1 Analytical Models

The analytical model of various lateral force resisting systems provided for 11 m³/h capacity ZLD structure to study the variation of seismic response under high and low seismic zones are shown in Fig. 2.

3 Results and Discussions

3.1 Fundamental Time Period

The time period of 11 m³/h capacity ZLD structure with different bracing systems for Zone 5 and Zone 2 is given in Table 2 and Table 3, respectively.

It has been observed from Figs. 3 and 4 that by providing bracing the time period reduces considerably compared to moment frame. This is because bracing system increases the overall stiffness of the structure which results in increase in frequency of vibration and decreasing the time period. Also, the time period given

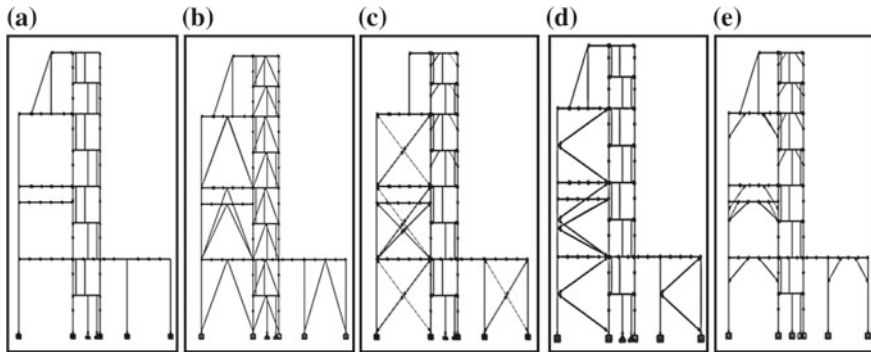


Fig. 2 Elevation of 11 m³/h capacity ZLD structure along X direction. **a** moment resisting frame **b** inverted V braced **c** X braced **d** K braced **e** knee braced

Table 2 Time period in X direction (Zone 5)

Structural frame	IS 1893 code	Analysis
Moment frame	0.721	0.717
Inverted V braced frame	0.721	0.293
X braced frame	0.721	0.267
K braced frame	0.721	0.347
Knee braced frame	0.721	0.65

Table 3 Time period in X direction (Zone 2)

Structural frame	IS 1893 code	Analysis
Moment frame	0.721	1.068
Inverted V braced frame	0.721	0.3
X braced frame	0.721	0.449
K braced frame	0.721	0.367
Knee braced frame	0.721	0.605

by the code differs from that obtained from analysis. The reduction in time period for different bracing systems compared to moment frame is presented in Table 4.

3.2 Lateral Displacement

The lateral displacement of 11 m³/h capacity ZLD structure with different bracing systems in Zone 5 and Zone 2 is given in Table 5 and Table 6, respectively.

It has been observed from Tables 5 and 6 that the lateral displacement of the structure decreases by providing bracing in comparison to moment frame for both high and low seismic zone. The least lateral displacement is obtained for Inverted

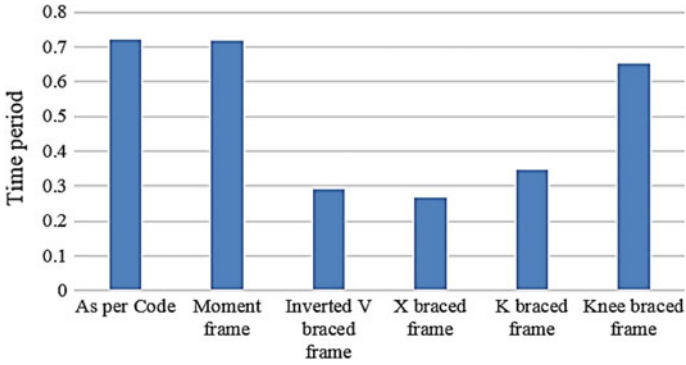


Fig. 3 Time period in X direction (Zone 5)

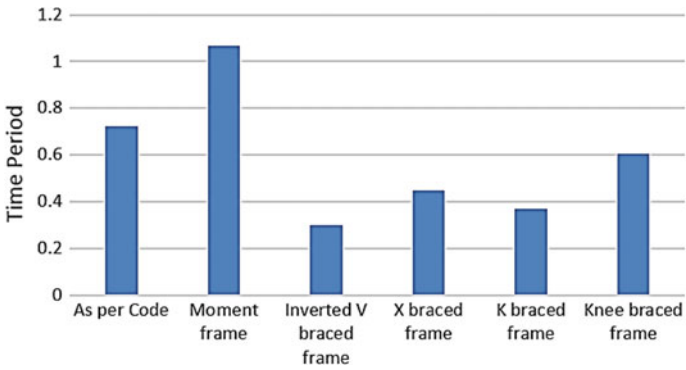


Fig. 4 Time period in X direction (Zone 2)

Table 4 Percentage reduction in time period in X direction

Capacity	Seismic zone	Bracing	Reduction of time period in X direction compared to Moment Frame (%)
11 m ³ /h	5	Inverted V bracing	59.10
		X bracing	62.70
		K bracing	51.60
		Knee bracing	9.34
11 m ³ /h	2	Inverted V bracing	71.90
		X bracing	57.90
		K bracing	65.60
		Knee bracing	43.30

Table 5 Lateral displacement in X direction (Zone 5)

Level in meter	IS 1893 code	Displacement in mm				
		Moment frame	Inverted V braced frame	X braced frame	K braced frame	Knee braced frame
0	0	0	0	0	0	0
4.5	18	23.52	6.12	6.58	7.15	12.08
8	31	41.78	10.94	27.67	52.27	28.7
13.5	54	63.25	11.5	30.06	57.14	30.2
17.3	69.2	67.23	19.9	33.27	62.5	34.5

Table 6 Lateral displacement in X direction (Zone 2)

Level in meter	IS 1893 code	Displacement in mm				
		Moment frame	Inverted V braced frame	X braced frame	K braced frame	Knee braced frame
0	0	0	0	0	0	0
4.5	18	26.13	5.66	7.5	7.36	10.1
8	31	54.2	8.93	37.61	25.28	23.74
13.5	54	73.15	11.04	38.35	43.75	34.06
17.3	69.2	75.04	20.4	49.8	50.32	34.22

V bracing compared to any other structural system. The decrease in lateral displacement for different bracing systems compared over moment frame is shown in Table 7.

3.3 Storey Shear Capacity

The storey shear capacity of 11 m³/h capacity ZLD structure with different bracing systems in Zone 5 and Zone 2 is shown in Fig. 5 and Fig. 6, respectively.

From Figs. 5 and 6, the storey shear capacity increases for braced frame in comparison to moment frame. This is because if there is increase in stiffness of the structure, then it can resist more seismic force. The increase or decrease of storey shear capacity for different bracing systems compared moment frame is given in Table 8.

Table 7 Percentage reduction in lateral displacement in X direction

Capacity	Seismic zone	Bracing	Reduction of lateral displacement in X direction compared to Moment Frame (%)
11 m ³ /h	5	Inverted V bracing	70.40
		X bracing	50.50
		K bracing	7.03
		Knee bracing	48.60
11 m ³ /h	2	Inverted V bracing	72.80
		X bracing	33.40
		K bracing	32.90
		Knee bracing	54.40

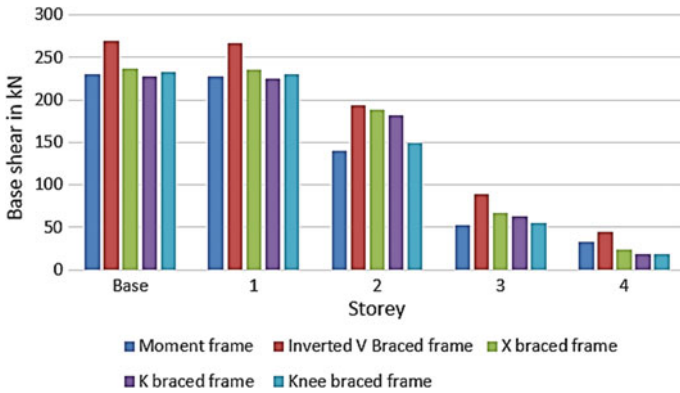


Fig. 5 Storey shear capacity in X direction (Zone 5)

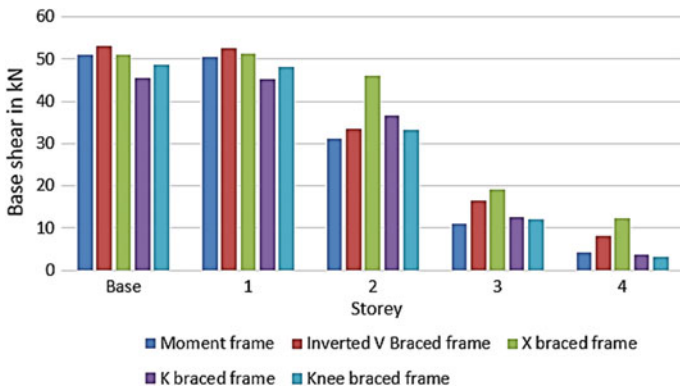


Fig. 6 Storey shear capacity in X direction (Zone 2)

Table 8 Increase or decrease of storey shear capacity compared over moment frame

Capacity	Seismic zone	Bracing	Increase or decrease of storey shear capacity at base in X direction compared to Moment Frame (%)
11 m ³ /h	5	Inverted V bracing	121.00
		X bracing	18.40
		K bracing	-6.30
		Knee bracing	-6.30
11 m ³ /h	2	Inverted V bracing	96.40
		X bracing	93.00
		K bracing	-9.00
		Knee bracing	-21.30

4 Conclusions

By comparing all the above analytical results, some of the important conclusions are drawn as follows:

- The natural time period of the structure was reduced by providing bracing compared to unbraced frame (Moment Frame).
- Maximum reduction in time period was observed in X bracing (up to 62%) in high seismic zone and Inverted V bracing (up to 71%) in low seismic zone compared to moment frame.
- By providing bracing, the lateral displacement of the structure got reduced compared to moment frame. The maximum reduction in lateral displacement was observed for Inverted V with a reduction up to 70% in high seismic zone and 72% in low seismic zone compared to moment frame.
- Because of the increase in global stiffness of the structure, the storey shear capacity of the frames increased compared over moment frame. The maximum increase in storey shear capacity at base was observed in Inverted V bracing with increase up to 121 and 96% in high and low seismic zone, respectively, compared to moment frame.

From the above results, it was found that Inverted V braced structure showed better performance with respect to time period, lateral displacements, and storey shear capacity under both high and low seismic zones. And also “Inverted V Bracing” creates less hindrance to the operation and maintenance work.

Acknowledgements We sincerely thank the management of RIT, General Electric Water and Process Technologies, HOD Civil engineering department, and Principal of RIT Affiliated to VTU Belagavi for their support extended to carry out this work.

References

1. Siddiqi ZA, Hameed R, Akmal U (2014) Comparison of different bracing systems for tall buildings. *Pak J Eng Appl Sci* 14:17–26
2. Di Sarno L, Elnashai AS (2004) Bracing systems for seismic retrofitting of steel frames. *J Constr Steel Res* 65:452–465
3. Tajheem Z, Khusru S (2013) Structural behaviour of steel building with concentric and eccentric bracing: a comparative study. *Int J Civ Struct Eng* 4(1):12–19
4. Khadiranaikar RB, Halli Y (2012) Seismic performance of RC steel frame with and without bracings. In: 15th World conference on earthquake engineering, Lisbon Port
5. Lai J-W, Mahin SA (2014) Steel concentrically braced frames using tubular structural sections as bracing members: design, full scale testing, numerical solution. *Int J Steel Struct* 14(1): 43–58
6. Alibhat MG, Kamath K, Prasad SK, Pai RR (2014) Seismic performance of concentric braced steelframes from pushover analysis. *IOSR J Mech Civ Eng* 67–73
7. Tande SN, Sankpal AA (2014) Study of inelastic behavior of eccentrically braced frames under non linear range. *Int J Latest Trends Eng Technol* 4(1)
8. Sangle K, Bajoria KM, Mhalungkar V (2012) Seismic analysis of high rise steel frame with and with without building and bracing without bracing. In: 15th World conference on earthquake engineering, Lisbon Port, no. AISC 2005
9. Choudhari VA, Nagaraj TK (2015) Analysis of moment resisting frame by knee bracing. *Int J Innov Eng Res Technol* 2(6):1–18

Chemical Compatibility of Fly Ash–Bentonite Based Hydraulic Barrier



G. Suneel Kumar, Kami Venkata Balaiah and Rabi Narayan Behera

Abstract To assess the durability of a liner material, it is important to study its chemical compatibility. In an attempt to define the hydraulic conductivity characteristics of clay liners, use of normal water is far from being representative of the in situ conditions. Therefore, the influence of chemical solutions (inorganic) of different concentrations on hydraulic conductivity of fly ash–bentonite mixtures used as hydraulic barriers was examined. The bentonite content in the fly ash–bentonite mixture was taken up to 15% @ 5% increment starting from 5%. The permeant solutions used include NaCl, NaOH and HCl, at different concentrations, i.e. 0, 0.01, 0.1, 0.5 and 1 M (where ‘M’ represents Molarity), which were chosen to best represent the acidic, basic and neutral nature of the landfill leachate as well as to better portray the effect of monovalent cations present in the in situ landfill leachate. Based on the test results, NaCl proved to have more effect on hydraulic conductivity than NaOH and HCl, considering an overall increase in hydraulic conductivity. Irrespective of the nature of the permeant solution (acidic/basic/neutral), the hydraulic conductivity of all the fly ash–bentonite mixtures increased with the increase in chemical concentrations. Thus, hydraulic conductivity of fly ash–bentonite liner material proved to be more sensitive to the permeant solution.

Keywords Chemical compatibility · Hydraulic barrier · Hydraulic conductivity · Bentonite · Salt solution

G. S. Kumar · K. V. Balaiah · R. N. Behera (✉)
Department of Civil Engineering, National Institute of Technology Rourkela,
Rourkela 769008, Odisha, India
e-mail: rbhehera82@gmail.com

G. S. Kumar
e-mail: sunilicon9@gmail.com

K. V. Balaiah
e-mail: 217ce1024@nitrrkl.ac.in

1 Introduction

Hydraulic barriers are a part of lining systems which are responsible for preventing a potential pollutant present in the waste containment from migrating to surface water, groundwater and thus polluting them. Natural clays, calcium or sodium-based bentonite mixed with specific geo-materials are widely used in the construction of hydraulic barriers such as liners and covers due to their low hydraulic conductivity (i.e. $k \leq 10^{-7}$ cm/s).

Although bentonite alone satisfies the permeability criteria of a liner material, being highly plastic in nature, with the variation of water content, it shows a high change in volume and possesses low strength. Hence, cohesionless soils (sands) were mixed with bentonite clay in the right proportions to increase the strength and enhance the volume change characteristics without compromising the overall hydraulic conductivity. Due to the depletion of natural resources, practising engineers are looking for an alternate material. Nowadays, large quantities of fly ash are generated from thermal power plants, disposal of which is a problem. Therefore, fly ash can be used along with bentonite as a replacement for sand, thus addressing the problem of effective disposal of fly ash and conserving natural resources.

In the present study, sodium bentonite (low sodium content) is used instead of calcium bentonite as the hydraulic conductivity of Na-bentonite is approximately five times lower than that of the Ca-bentonite at similar void ratios [11]. Chlorides and Sulphates are widely distributed in nature and are common constituents in the leachate [3, 17], the chemical properties of the landfill leachate listed by Kayabali et al. [9] also showed larger amounts of Cl^- , Na^+ and K^+ ions which are exchangeable. Therefore, chlorides and sulphates of different cations such as sodium, calcium and iron are chosen for the permeation process, which best represents the in situ conditions in the laboratory. Also, the leachate may be acidic, basic or neutral in nature. These acidic, basic and neutral natures of the leachate in the field were represented by hydrochloric acid (HCl), sodium hydroxide (NaOH) and sodium chloride (NaCl), respectively, in the laboratory test where all of them were chosen based on the chemical properties of the landfill leachate assessed by Kayabali et al. [9]. The preference for replacement is the lyotropic series, which is Li^+ , Na^+ , K^+ , Rb^+ , Cs^+ , Mg^{2+} , Ca^{2+} , Ba^{2+} , Cu^{2+} , Al^{3+} and Fe^{3+} [10, 16]. Because Na^+ is at the lower end of the lyotropic series, Na-bentonites are more prone to cation exchange when permeated with solutions containing divalent or trivalent ions, Sposito [16].

Therefore in the present study, bentonite mixed with fly ash was permeated with different chemical solutions and their chemical compatibility as a liner material was assessed

2 Materials and Methodology

2.1 Materials

Cohesionless material includes fly ash collected from Aditya Alumina Ltd. situated in Lapanga town of Sambalpur district, Odisha. Cohesive material includes commercially available sodium-based bentonite in the local market.

2.2 Methodology

The basic geotechnical characteristics of the materials were found out by performing different laboratory tests which include specific gravity test by density bottle method [4], particle size analysis (both sieve and hydrometer analysis) [6], differential free swell index [7] and water content–dry density relation by light compaction [5]. In order to assess the chemical characteristics, permeability tests [8] were carried out on different trial mixes of fly ash and bentonite with different chemicals such as NaCl, NaOH and HCl as permeants.

Although permeability by falling head method is recommended for fly ash and bentonite being fine-grained materials but due to time constraint and liner material being exposed to very high heads in site which is not practically possible to be created experimentally using falling head, pressure permeameter is adopted which is capable enough of producing very high heads using pressure.

Hydraulic conductivity tests are carried out using a pressure permeameter, under different heads of 15, 25, 35 and 45 m of water respectively. The working principle of the pressure permeameter is as follows:

- The permeant solution (different concentrations of NaCl, NaOH and HCl) by which the sample is to be permeated with, is filled into the cylindrical chamber of the permeameter.
- A pressure corresponding to the required head is created in the cylindrical chamber of the pressure permeameter with the help of an air compressor.
- Once the required head is reached, both the inlet and the outlet valves of the permeability mould are turned open.
- A cylindrical measuring jar is placed at the outlet of the permeability mould in order to collect the effluent and so as to measure its volume.

Table 1 Geotechnical properties of fly ash and bentonite

Property	Fly ash	Bentonite
Specific gravity	2.08	2.74
Liquid limit, <i>LL</i> (%)	–	268
Plastic limit, <i>PL</i> (%)	–	54
Linear shrinkage, <i>L_s</i>	–	29
Plasticity index, <i>PI</i> (%)	–	214
Differential free swell index, <i>DFSI</i> (%)	0	400

3 Results and Discussions

3.1 Geotechnical Properties

The geotechnical properties of fly ash and bentonite were determined as per the IS code and are shown in Table 1.

From the particle size analysis of fly ash, it can be observed that the particles range from fine sand to silt as shown in Fig. 1. So it may be concluded that most of the particles present in the fly ash are silty. The percentage of fly ash passing through 75 μ IS sieve was found to be 84%, which indicates uniform gradation of fly ash. Similarly, from the particle size distribution curve of bentonite, it may be concluded that more than 50% of the soil particles present in bentonite are clayey type particles.

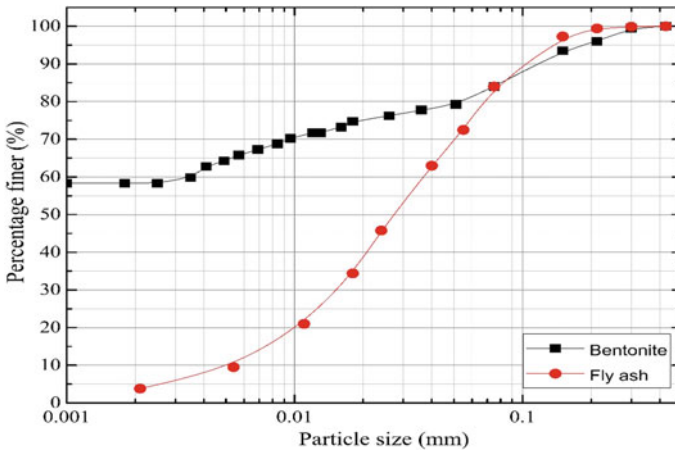


Fig. 1 Particle size distribution curves of bentonite and fly ash

3.2 Compaction Characteristics of Fly Ash

Fly ash and bentonite mixtures were compacted by Standard Proctor method of compaction. Compaction effort or energy achieved by this method is 592 kJ/m^3 . The fly ash–bentonite mixture with 15% bentonite had the maximum dry density (Fig. 2).

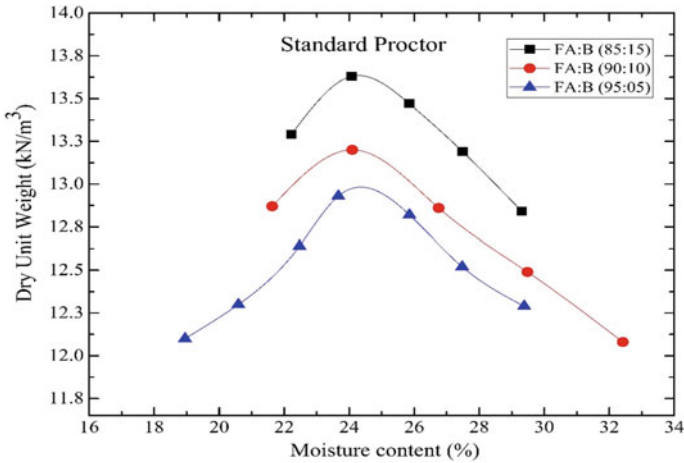


Fig. 2 Water content–dry density relation for FA: B mixtures from Standard Proctor method

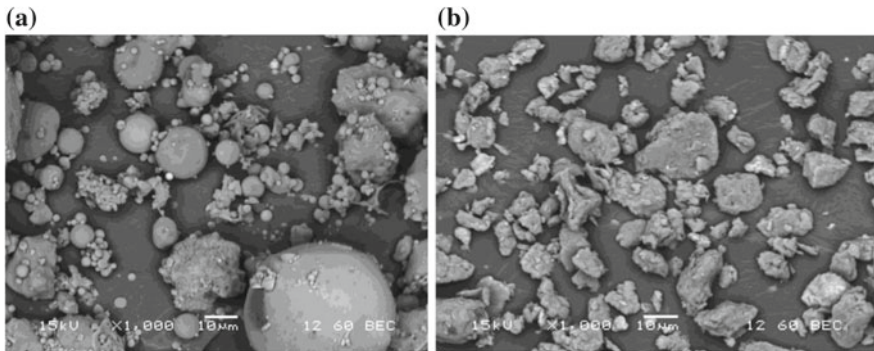


Fig. 3 SEM images of a fly ash and b bentonite

3.3 Morphology of Fly Ash and Bentonite

From the SEM images of fly ash and bentonite (Fig. 3), it can be observed that most of the fly ash particles are spherical in shape. This spherically shaped particle shows the presence of cenosphere in huge amounts. Whereas most of the bentonite particles were found to be flaky in shape.

3.4 Geotechnical Properties of Fly Ash and Bentonite Mixtures

Fly ash and bentonite are blended with varying bentonite content, i.e. 5, 10 and 15% by dry weight of fly ash and different geotechnical characteristics are determined for these samples. The maximum percentage of bentonite is restricted to 15% only, as the hydraulic conductivity criteria to be satisfied by a clay liner is attained, Alla et al. [1].

3.4.1 Consistency Limits

Liquid limit, plastic limit and shrinkage limit tests are conducted for fly ash and bentonite mixtures and the variation in consistency limits with increasing bentonite content is observed (Table 2).

3.5 Effect of Chemicals on Hydraulic Conductivity Characteristics of Fly Ash–Bentonite Mixture

Hydraulic conductivity tests were conducted on different fly ash–bentonite trial mixtures. Since both fly ash and bentonite consists of fine-grained particles (Fig. 1), they have low permeability. Therefore, pressure permeameter was used to estimate the hydraulic conductivity of these trial mixtures (Table 3).

Different trial mixes of fly ash–bentonite are permeated with these chemicals at different concentrations, which include 0, 0.01, 0.1, 0.5 and 1 M (where ‘M’ represents Molarity). Prehydration of the samples was done prior to actual testing to temper the sensitivity of hydraulic conductivity to the salt solution.

Table 2 Consistency limits of fly ash–bentonite mixtures

FA + B mixture (FA: B)	Liquid limit, <i>LL</i> (%)	Plastic limit, <i>PL</i> (%)	Plasticity index, <i>PI</i> (%)
85:15	62.15	31.68	30.47
90:10	56.44	27.37	29.07
95:05	40.84	15.79	25.05

Table 3 Hydraulic conductivity of fly ash and bentonite mixtures with water as permeant

Sl. no.	Trial mix	Type of compaction	Permeability, k (cm/s)	Average permeability, k (cm/s)
1.	FA + B (95:05)	Standard proctor	2.58×10^{-6}	1.87×10^{-6}
			1.85×10^{-6}	
			1.60×10^{-6}	
			1.46×10^{-6}	
2.	FA + B (90:10)	Standard proctor	0.90×10^{-6}	0.70×10^{-6}
			0.63×10^{-6}	
			0.77×10^{-6}	
			0.50×10^{-6}	
3.	FA + B (85:15)	Standard proctor	4.12×10^{-8}	3.64×10^{-8}
			3.16×10^{-8}	
			3.60×10^{-8}	
			3.68×10^{-8}	

Hydraulic conductivity is determined with varying concentrations of these solutions in fly ash–bentonite mixtures. The relation between hydraulic conductivity, bentonite percentage and chemical concentrations were also determined and analysed.

The hydraulic conductivity decreased with the increase in bentonite content while it increased with the increase in chemical concentration, which is in acceptance with the findings of Mishra et al. [12] and Arasan [2] as shown in Fig. 4. The bentonite used being rich in sodium, there might not be any possible reaction to occur between the NaCl salt solution and the mixture with the increasing bentonite percentage.

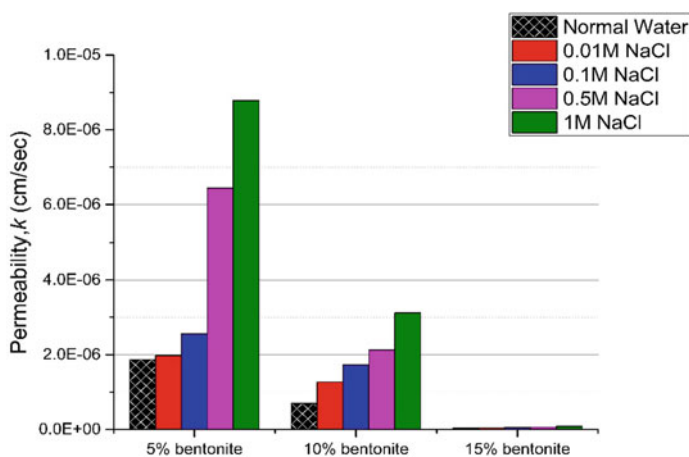


Fig. 4 Effect of bentonite content and NaCl concentration on the permeability of FA: B mixture

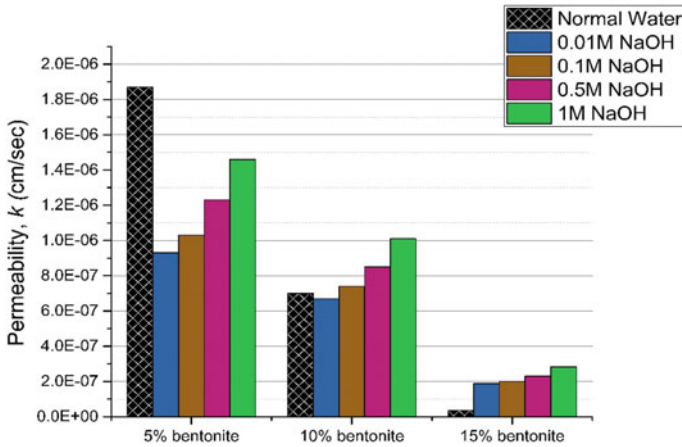


Fig. 5 Effect of bentonite content and NaOH concentration on the permeability of FA-B mixture

The effect of a basic solution containing monovalent cation, i.e. NaOH solution is minimum for a bentonite content of 5% and 10% but showed a significant increase in the permeability for a bentonite content of 15% (Fig. 5). This increase in hydraulic conductivity may be attributed to the decrease in the thickness of DDL (Diffused Double Layer), resulting in flocculation of the clay particles [14].

HCl solution proved to show more effect on permeability at lower concentrations than at higher concentrations as observed from Fig. 6. This may be due to several parameters such as the dielectric constant and cation valence [13, 15].

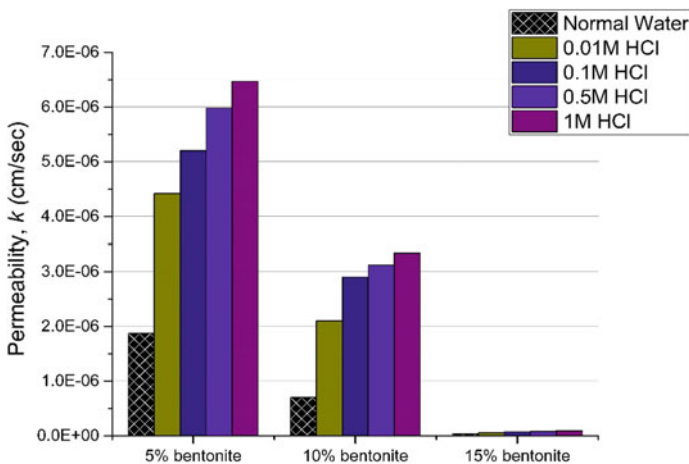


Fig. 6 Effect of bentonite content and HCl concentration on the permeability of FA-B mixture

Figures 7, 8 and 9 show that at lower bentonite content (i.e. at 5% and 10%), NaCl and HCl solutions are found to be more effective in increasing the hydraulic conductivity of fly ash and bentonite mixtures whereas at higher bentonite content (i.e. at 15%), NaOH solution was found to be more effective. In addition, irrespective of the nature of the permeant solution (acidic/basic/neutral), the hydraulic conductivity of all the fly ash–bentonite mixtures increased with an increase in chemical concentrations.

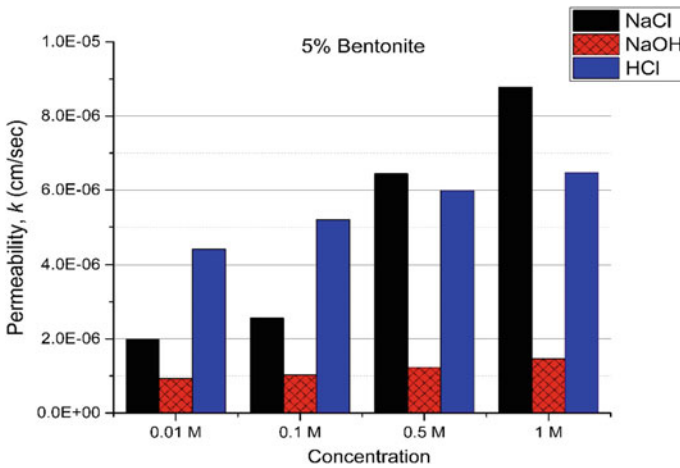


Fig. 7 Effect of concentration and type of permeant solution on the permeability of FA: B (95:05) mixture

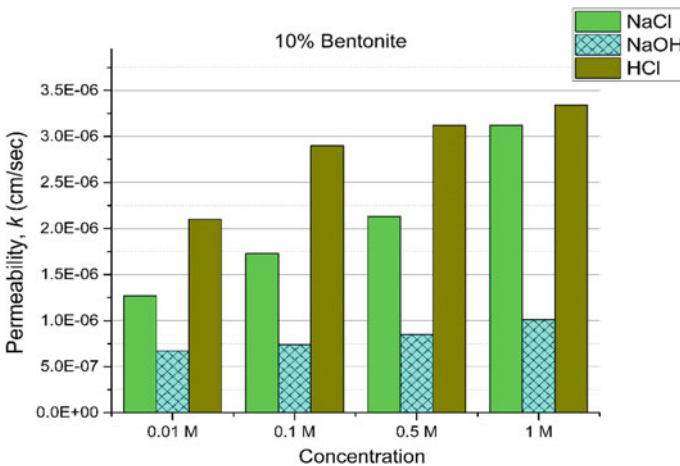


Fig. 8 Effect of concentration and type of permeant solution on the permeability of FA: B (90:10) mixture

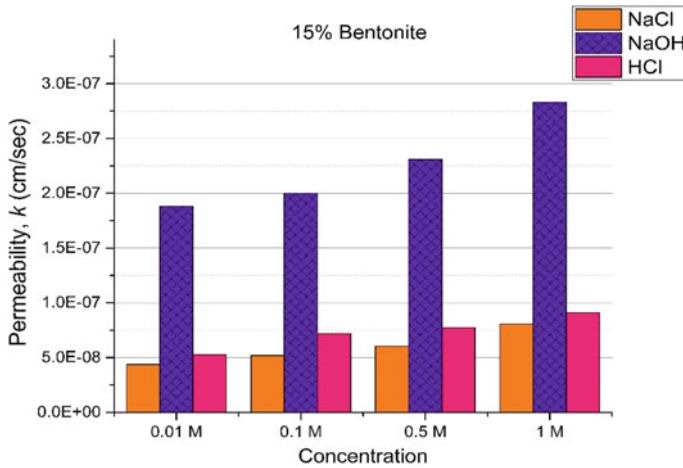


Fig. 9 Effect of concentration and type of permeant solution on the permeability of FA: B (85:15) mixture

4 Conclusions

Based on the test results of fly ash and bentonite mixtures (i.e. 85:15, 90:10 and 95:05) with three types of permeating solutions (i.e. NaOH, NaCl and HCl) of five different concentrations (i.e. 0, 0.01, 0.1, 0.5 and 1 M), the following major inferences were drawn:

- Irrespective of the nature of the permeant solution (acidic/basic/neutral), the hydraulic conductivity of all the fly ash–bentonite mixtures increased with an increase in chemical concentrations.
- NaCl and HCl solutions proved to have more effect on permeability at lower concentrations and at lower bentonite content. Whereas the effect of basic solution, i.e. NaOH solution is minimum for a bentonite content of 5% and 10% but showed a significant increase in permeability for a bentonite content of 15%.

References

1. Alla V, Sasmal SK, Behera RN, Patra CR Development of alternate liner material by blending fly ash, local soil and bentonite. In: Proceedings of Indian geotechnical conference GeoNEst, 14–16 December 2017, IIT Guwahati, India, p 95
2. Arasan S (2010) Effect of chemicals on geotechnical properties of clay liners: a review. Res J Appl Sci, Eng Technol 2(8):765–775
3. Arasan S, Yetimoglu T (2006) Effect of leachate components on the consistency limits of clay liners. In: 11th National soil mechanic and foundation engineering congress, Trabzon, Turkey, pp 439–445

4. IS 2720: (1980 Part 3/sec 1) Method of test for soil, Determination of specific gravity
5. IS 2720: (1980 Part 7) Determination of water content-dry density relation using light compaction
6. IS 2720: (1985 Part 4) Method of test for soil, Grain size analysis
7. IS 2720: (1985 Part 40) Method of test for soil, Determination of free swell index of soils
8. IS 2720: (1986 Part 17) Method of test for soil, Laboratory determination of permeability
9. Kayabali K, Kezer H (1998) Testing the ability of bentonite-amended natural zeolite (clinoptinolite) to remove heavy metals from liquid waste. *Environ Geol* 34(2–3):95–102
10. McBride MB (1994) *Environmental chemistry of soils*. Oxford University Press, New York
11. Mesri G, Olson RE (1971) Mechanisms controlling the permeability of clays. *Clays Clay Miner* 19:151–158
12. Mishra AK, Ohtsubo M, Li L, Higashi T (2005) Effect of salt concentrations on the permeability and compressibility of soil-bentonite mixtures. *J-Fac Agric Kyushu Univ* 50 (2):837
13. Mitchell JK (1993) *Fundamentals of soil behavior*. Wiley, New York; *Fundamentals of soil behavior*, 2nd edn Wiley, New York
14. Quigley RM (1993) Clay minerals against contaminant migration. *Geotech News* 11(4):44–46
15. Sharma HD, Lewis SP (1994) *Waste containment systems, waste stabilization, and landfills: design and evaluation*. Wiley
16. Sposito G (1981) *The thermodynamics of soil solutions*. Oxford University Press
17. Yilmaz G, Yetimoglu T, Arasan S (2008) Hydraulic conductivity of compacted clay liners permeated with inorganic salt solutions. *Waste Manage Res* 26(5):464–473

Retrofitting of Beam–Column Joint Under Seismic Excitation



Marimuthu Sumathi and Sivasankarapillai Greeshma

Abstract The objective of this paper is to compare the experimental and analytical behavior of exterior beam–column joint sub-assemblages with transverse reinforcements detailed as per IS 456. Eight-storied reinforced concrete building located in Chennai (Zone III) has been modeled and analyzed in STADD Pro software. The earthquake analysis and design has been carried out as per IS 1893 and critical exterior beam–column joints were taken for study. A one-third scaled model, detailed as per IS 456 and SP 34 was taken for analyzing the effect of lateral force and axial load on the behavior of beam–column joints. A numerical study was carried for scaled model using the finite element software ABAQUS to study the real physical behavior of beam–column joint structure. A concrete damage plastic model is assigned for the finite element model in ABAQUS. Seismic type loading is applied at the end of the beam in order to develop moments at the beam–column joint region. The specimens are retrofitted with the addition of new concrete at the joint region and tested for its load-carrying capacity.

Keywords Beam–column joint · Retrofitting · Forging slag · Styrene–butadiene rubber and epoxy

1 Introduction

In recent days, structures are more susceptible to earthquake which causes severe damage to reinforced concrete structures. These were more prominent for buildings constructed without seismic provisions and were studied by several researchers [1, 2]. Past three decades, extensive research has been carried out on the behavior of

M. Sumathi · S. Greeshma (✉)
Department of Civil Engineering, College of Engineering Guindy, Anna University,
Chennai, India
e-mail: greeshmas@annauniv.edu; greeshmasspillai@yahoo.co.in

M. Sumathi
e-mail: sumathimarimuthu20@gmail.com

joints under seismic conditions through experimental and analytical studies [3]. Being the lateral and vertical load resisting members, in reinforced concrete structures, beam–column joints are vulnerable due to reversal of forces causing distress during earthquakes. ABAQUS is a very complex nonlinear finite element analysis program introduced with huge material characteristics and parameters to reproduce high accuracy in calculations. Numerical investigations are conducted recently by many researchers [4–7] to validate the above software.

2 Modeling of Building (STAAD.Pro)

In the present study, an exterior beam–column joint of a seven-storey reinforced concrete frame building for the seismic Zone-II has been modeled Fig. 1a and analyzed using STAAD Pro. The columns designed were 3 m long with 600×600 mm cross section and beams with 300×450 mm cross section. The thicknesses of the peripheral and internal walls were taken as 230 mm. The M30 grade concrete and Fe415 steel grade were used for the design. The building is analyzed, and the force resultants for various load combinations (IS1893:2002 [8]) were estimated. The exterior beam-column joint marked “A” in Fig. 1a, b was considered for the design and the short frame beam corresponding to the joint “A” was taken for testing. The exterior column was designed for an axial load of

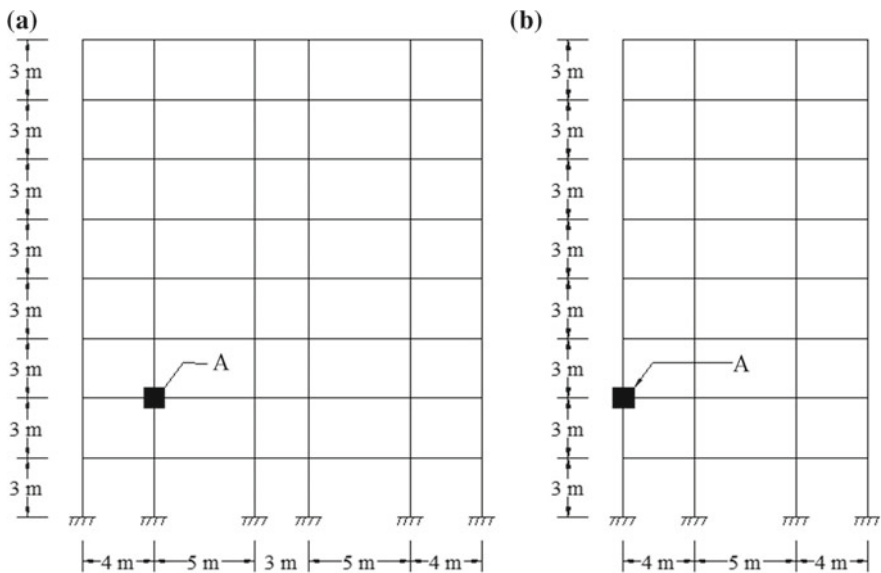
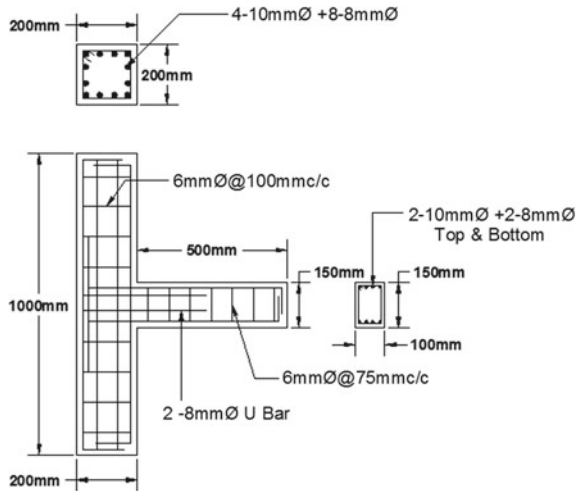


Fig. 1 Details of the building: **a** Elevation of the longitudinal frame. **b** Elevation of the transverse frame

Fig. 2 Details of reinforcement as per IS456 and SP34



4325 kN and moment of 475 kN-m, which were the critical values obtained from 13 different load combinations. The design moment and shear force obtained from the critical load combinations for the beam were 484 kN-m and 322 kN, respectively.

The model analyzed has been reduced to one-third dimension consisting of a beam of 100 mm × 150 mm × 500 mm and column of 200 mm × 200 mm 1000 mm. M30 and Fe415 are the grades of concrete and steel, respectively, and the reinforcement detailing was done as per IS 456 [9] and SP 34 [10] are shown in Fig. 2. The specimen with a pinned support in its upper column end and a roller support in its lower end was subjected to reverse cyclic loading and tested until failure up to 3.5% drift.

3 Finite Element Modeling

The concrete was modeled with Solid 3D elements eight-node brick (C3D8), with three degrees of freedom at each node, i.e., translation in the nodal *x*, *y*, and *z* directions. The element is capable of plastic deformation, cracking in three orthogonal directions, and crushing. The steel reinforcement was modeled with two-node linear 3D truss element (T3D2) which also has three degrees of freedom, as in the case of the concrete element. A concrete damaged plasticity model (CDP) was used to define the concrete in plastic range.

4 Material Properties

In the case of concrete, ABAQUS requires an input data for material properties such as elastic modulus (E_c), ultimate uniaxial compressive strength (f_c), ultimate uniaxial tensile strength (modulus of rupture, f_r), and Poisson's ratio (ν). The modulus of elasticity of concrete was determined as 32250 MPa in accordance with IS 456:2002 and the Poisson's ratio for concrete was assumed to be 0.2.

The concrete used was of M30 and the compressive strength of 39 MPa was adopted (Laboratory Results) in the finite element model. The behavior of steel in the finite element models is assumed to be an elastic-perfectly plastic and identical in tension and compression. Poisson ratio is assumed as 0.3 and elastic modulus, E_s as 200 GPa

5 Material Parameters for ABAQUS

All other material properties are assigned as per the literature [11]. The tensile damage in concrete under dynamic condition is simulated by the plasticity model proposed by Lubliner et al. [12], Lee and Fenves [13] and incorporated in ABAQUS.

The numerical expressions to investigate the compression stress–strain relation for nonlinear behavior of concrete as suggested by Hognestad are Eqs. (1) and (2)

$$\frac{\sigma}{\sigma_{cu}} = 2 \frac{\epsilon}{\epsilon_0} \left[1 - \frac{\epsilon}{2 \epsilon_0} \right] \quad 0 < \epsilon < \epsilon_0 \quad (1)$$

$$\frac{\sigma}{\sigma_{cu}} = 1 - 0.15 \left[\frac{\epsilon - \epsilon_0}{\epsilon_{cu} - \epsilon_0} \right] \quad \epsilon_0 < \epsilon < \epsilon_{cu} \quad (2)$$

$$\epsilon_{cu} = 3.5\%$$

The tension stiffening curve suggested by Schnobrich [14] used where the average tensile stress (f_t) and strain normal (ϵ_t) to the crack direction (θ) is measured in degrees counterclockwise from the steel direction to the crack direction.

$$f_t = \frac{f_t'}{1 + (1000 \times \epsilon_t \times \theta / 90)^{1.5}} \quad (3)$$

From the above Eqs. (1)–(3) and parameters, a linear elastic stress–strain relationship is obtained. The concrete behavior under uniaxial tension is linear only up to the formation of micro cracks in concrete (failure stress) beyond which the curve softens. In the case of uniaxial compression, the response is linear up to its initial

yield. The response in the plastic region is characterized by stress hardening followed by strain softening beyond the ultimate stress. When the concrete specimen is unloaded from any point on the strain softening branch of the stress–strain curve, the response is weakened and the elastic stiffness of the material is damaged.

6 Behavior Under Cyclic Load

The curves represented in Fig. 3 shows the behavior of the concrete element under cyclic loading. The element subjected to tension exceeds the tensile strength. Thereby causing cracks and partial damage to the material, which is defined using the parameter d_t . The modulus of elasticity changes to $(1 - d_t) E_0$ in the process of unloading the element. If the element is then compressed, its elastic behavior is determined using the parameter w_c and the elasticity modulus in compression as $(1 - d_t + w_c d_t) E_0$. Assuming that the cracks do not influence the stiffness in compression, the parameter w_c is defined as 1. When the value of the parameter w_c equals zero (full degradation), the stiffness in compression is identical to the tension stiffness. The crushed section loses its initial properties in compression, defined by the parameter d_c , and initial properties in tension, defined by the parameter d_t .

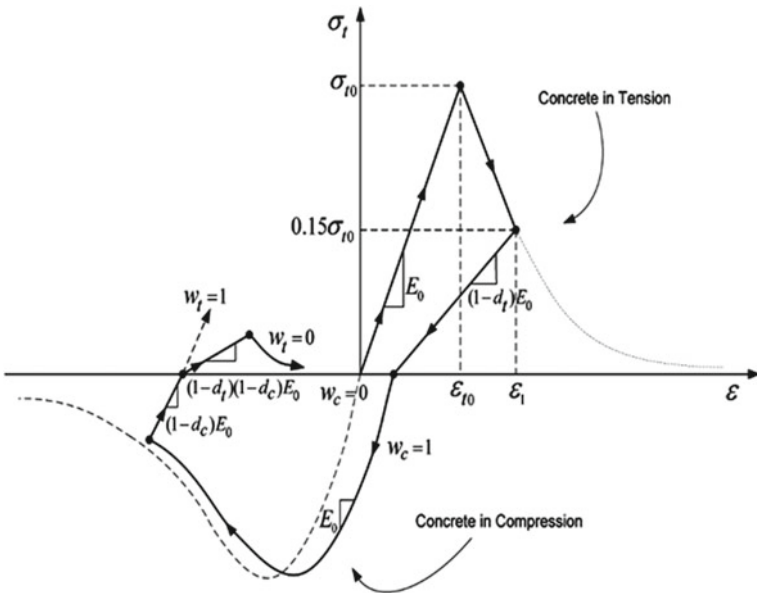


Fig. 3 Stress–strain curve of concrete damaged plasticity model used in ABAQUS [13]

7 Experimental Investigation

7.1 Material Details

The specimens were cast with 53 grade Ordinary Portland Cement (OPC) conforming to IS 12269 (BIS [15]). Medium river sand passing through 4.75 mm IS sieve with a fineness modulus of 2.94 was used as the fine aggregate. The crushed granite stone of maximum size not exceeding 10 mm having a fineness modulus of 3.58 was used as the coarse aggregate. M30 grade of concrete is adopted.

7.2 Retrofitting Materials

Retrofitting the exterior beam–column joint is done by the removal and replacement of concrete in regions of damaged joints. Special attention is given to ensure a good bond between the new and the existing concrete in the process of retrofitting. The damaged region is replaced by new concrete of grade of concrete with mix proportion for M30 grade concrete, 1:1.51:2.53 and water–cement ratio 0.45. Forging slag is used (20%) as partial replacement of fine aggregate and a polymer material SBR (styrene–butadiene rubber) is used in dosages (20%) by volume of water that improves bonding with cement paste. Super-plasticizer (1%) is also used as a water reducing agent. The concrete which is used to retrofit the affected area attained compressive strength of 39 MPa in 7 days. Epoxy resin (1:3) is used as a bonding layer between existing concrete and new concrete and also ensures that most of the cracks were fully filled with epoxy resin.

8 Test Setup

To investigate the seismic performance experimentally, a scaled model (1/3) was adopted. The exterior beam–column joint was subjected to reverse cyclic loading. A schematic diagram of the test setup is shown in Fig. 4.

The specimen was tested in an upright position with hinged support at the top end and pinned support at the bottom. These boundary conditions were provided in the setup to simulate the actual working situation of the beam–column joint and loading protocol was adopted as shown in Fig. 5.

A constant column axial load of 5T was applied by means of a 50T hydraulic jack mounted vertically to the 100T loading frame to simulate the gravity load on the column. The cyclic loading was applied by two 100 kN (10T) hydraulic jacks, one fixed to the loading frame at the top and another to the strong reaction floor. The reverse cyclic load was applied at 50 mm from the free end of the beam. The

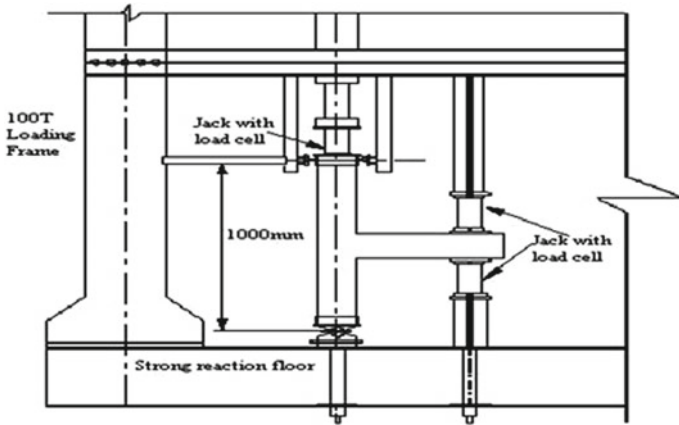


Fig. 4 Schematic diagram of the test setup

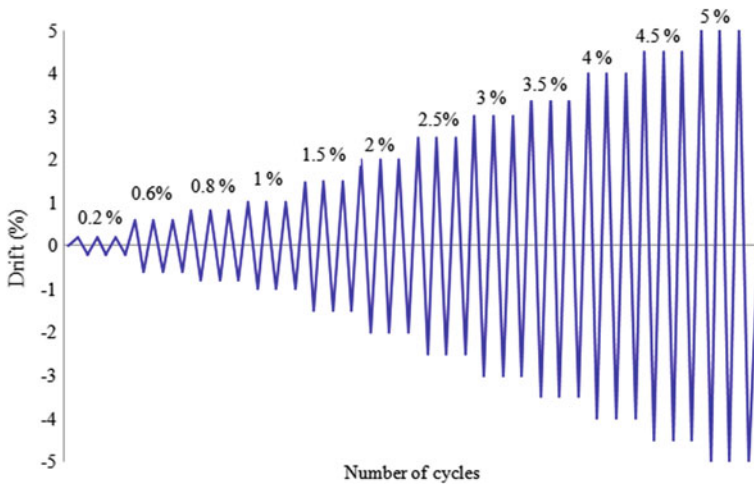


Fig. 5 Loading protocol

test was displacement controlled and the specimen was subjected to an increasing cyclic load up to its 3.5% drift.

The response during testing was monitored by DEMEC gauges and dial gauges. Dial Gauges was mounted unobtrusively on the column, one at the left side bottom of the column and the other at top of beam. A load cell of capacity 100 kN situated between the hydraulic jack and the loading plate measures the static cyclic load applied to the beam. The experimental setup is shown in Fig. 6.



Fig. 6 Test setup in the laboratory

9 Results and Discussion

Experimental results of specimens before and after retrofitting are evaluated. The structural performance of load–displacement exterior beam–column joint was evaluated in terms of ultimate load-carrying capacity, load–displacement hysteresis loops, cumulative energy dissipation, and ductility.

9.1 Experimental Results

9.1.1 Hysteretic Loops

The hysteresis loop is used to measure the behavior of structure starting from elastic range until nonelastic range. It can be obtained by plotting the graph load versus displacement from loading and unloading to complete one cycle of movement. The load–displacement hysteresis loops before and after retrofitting are shown in Fig. 7. From the graphs, it is clearly seen that the trend of load–displacement behavior for specimens before and after retrofitting is similar. However, there is a reduction in the ultimate load after the retrofit.

9.1.2 Energy Dissipation

The energy dissipation is calculated as the area enclosed by the hysteretic loop at a loading cycle. The cumulative energy dissipation of the experimental investigation

Fig. 7 Load–displacement hysteretic curve

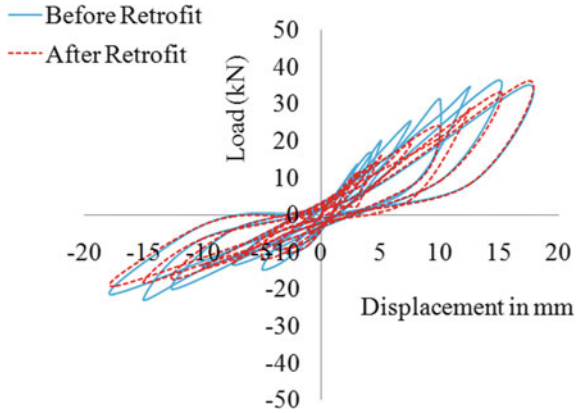
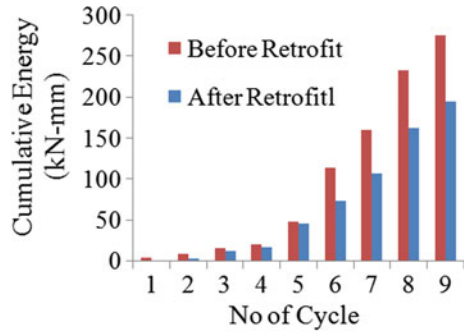


Fig. 8 Cumulative energy dissipation



is shown in Fig. 8. The decrease in energy dissipation for specimens after retrofitting is up to 35% when compared with specimens before retrofitting.

9.1.3 Stiffness

Stiffness is the ratio of the force required to the specified deflection. The specimen after retrofit show greater stiffness than before retrofitting with a difference of 7% is shown in Fig. 9.

9.1.4 Ductility

The ductility measured in terms of displacement ductility, calculated as per ASCE guidelines [16], is presented in Table 1.

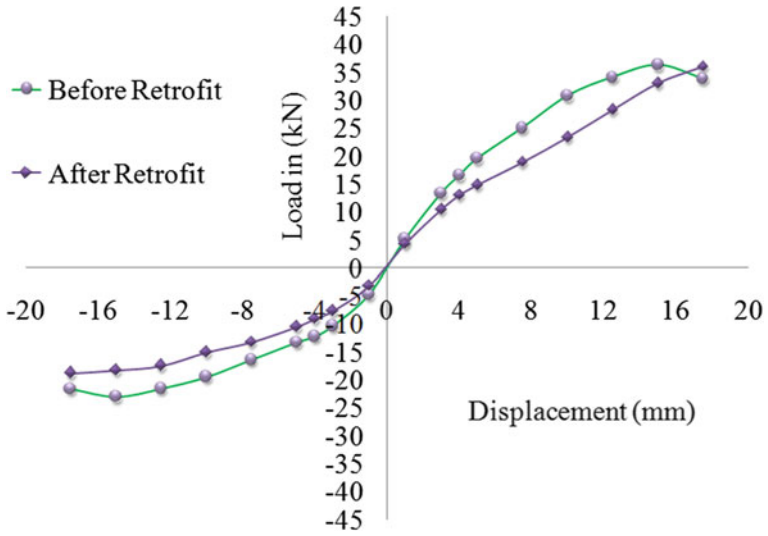


Fig. 9 Load–displacement envelope curve

Table 1 Displacement–ductility

Specimen	Displacement (mm)		Ductility factor
	Yield	Ultimate	
Before retrofit	8.68	17.5	2.02
After retrofit	10.88	17.5	1.61



Fig. 10 Specimen failure before retrofit

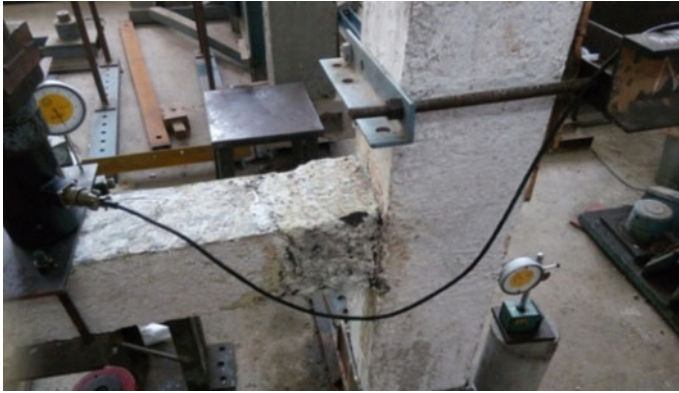


Fig. 11 Specimen after retrofitting

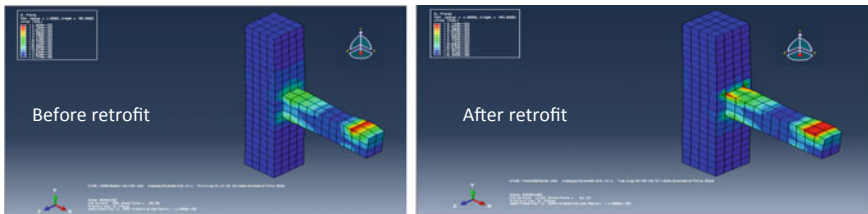


Fig. 12 Comparison of before and after retrofit in ABAQUS

9.1.5 Crack Pattern

The first crack was witnessed at the load level of 10 kN for specimens before retrofit and 19.62 kN for specimens after retrofitting. As the load level was increased, further cracks were developed in other portions of the beam in both specimens. The joint of each specimen are shown in Figs. 10, 11, and 12. The joint failure modes show the specimen failed in flexure in specimen after retrofitting.

10 Comparison of Experimental and Analytical Results

Figures 12 and 13 show the comparative study made between analytical and experimental investigation for specimens before and after retrofitting. From the study, it is observed that the stiffness calculated through ABAQUS is more than the value calculated experimentally.

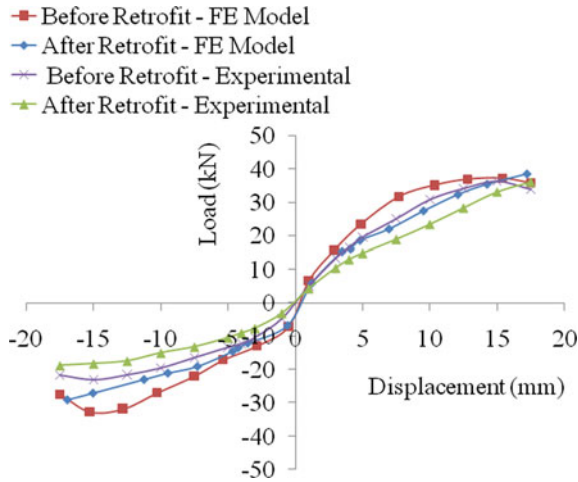


Fig. 13 Comparison of load–displacement envelope

Table 2 Displacement—ductility

Specimen	Displacement (mm)		Ductility factor
	Yield	Ultimate	
Before retrofit-experimental	8.68	17.5	2.02
After retrofit-experimental	10.88	17.5	1.61
Before retrofit-ABAQUS	5.843	17.47	2.99
After retrofit-ABAQUS	8.23	17.09	2.08

Ductility

The comparison of ductility for experimental and analytical model is shown in Table 2.

Energy dissipation

The energy dissipation obtained in ABAQUS is observed to be more when compared to the experimental model [17, 18]. It is found that the energy dissipation for analytical model is 46% more than of experimental. Figure 14 shows the variation of energy dissipation through analytical and experimental.

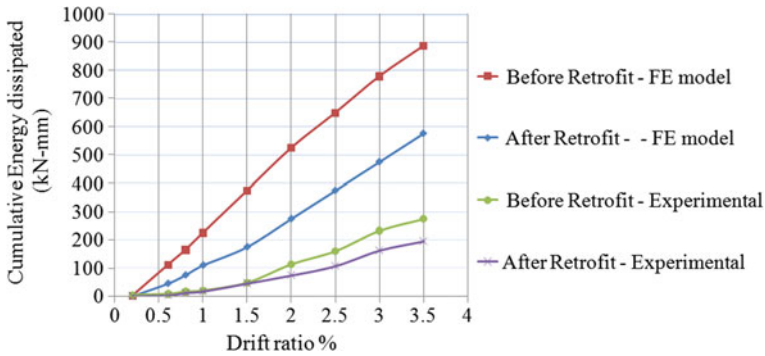


Fig. 14 Cumulative energy dissipation curves and drift ratio

11 Conclusions

Based on the theoretical and experimental study carried out, the following conditions were arrived:

- The ultimate load of the specimens after retrofitting was found to be 1.7% more than that of the specimen before retrofitting in experimental and 2% more in ABAQUS analysis.
- The energy dissipation investigated analytically was 46% more than the value found through experimental analysis.
- The stiffness calculated analytically shows a slight increase of 4.7% compared to experimental values.
- Similarly, ductility performance shows an enormous increase (1.7 times) analytically when compared with experimental results.
- ABAQUS modeling closely predicts the experimental behavior of beam–column joints.

Acknowledgements The financial assistance provided by the University Grant Commission through Rajiv Gandhi National Fellowship for supporting the Ph.D. scholarship is greatly acknowledged by the authors.

References

1. Kareemunnisa Begum S, Harinarayana T (2016) Basement configuration from magnetotelluric studies in Bhuj earthquake epicentral zone, Gujarat, India. *J Earthq Res* 5:177–188
2. Panagiotakos TB, Fardis MN (1999) Estimation of inelastic deformation demands in multi-storey RC frame buildings. *Earthq Eng Struct Dyn* 28:501–528
3. Kulkarni SM, Patil YD (2012) A state-of-art review on reinforced concrete beam-column joints. *J Inf Knowl Res Civil Eng* 2(1):94–115

4. Kam WY, Pampanin S (2009) Experimental and numerical validation of selective weakening retrofit for existing non-ductile R.C. frames. In: Improving the seismic performance of existing buildings and other structures, vol I, pp S7–2
5. Pimanmas A, Chaimahawan P (2010) Shear strength of beam-column joint with enlarged joint area. *Eng Struct* 2529–2545
6. Niroomandi A, Maheri A, Maheri MR et al (2010) Seismic performance of ordinary RC frames retrofitted at joints by FRP sheets. *Eng Struct* 32(8):2326–2336
7. Mahini SS, Ronagh HR (2010) Strength and ductility of FRP web-bonded RC beams for the assessment of retrofitted beam-column joints. *Compos Struct* 9(6):1325–1332
8. BIS (2002) IS 1893 (Part 1): 2002-Indian standard criteria for earthquake resistant design of structures, part 1: general provisions and buildings (fifth revision). Bureau of Indian Standards, New Delhi
9. BIS (2000) IS 456: 2000-Indian standard plain and reinforced concrete-code of practice (fourth revision). Bureau of Indian Standards, New Delhi
10. BIS (1987b) SP 34: 1987-Handbook on concrete reinforcement and detailing. Bureau of Indian Standards, New Delhi
11. Sumer Y, Aktaş M (2015) Defining parameters for concrete damage plasticity model, challenge. *J Mech* 149–155
12. Lubliner J, Oliver J, Oller S, Onate E (1989) A plastic-damage model for concrete. *Int J Solids Struct* 25(3):229–326
13. Lee J, Fenves GL (1998) Plastic-damage model for cyclic loading of concrete structures. *J Eng Mech* 124(8):892–900
14. Hu H-T, Schnobrich WC (1990) Nonlinear analysis of cracked reinforced concrete. *ACI Struct J* 87-S21
15. BIS (1987a) IS 12269: 1987-Indian standard specification for 53 grade ordinary portland cement.,Bureau of Indian Standards, New Delhi
16. ASCE (1982) State-of-the-art report on finite element analysis of reinforced concrete. American Society of Civil Engineers, New York
17. Mousavi SA, Zahrai SM, Bahrami-Rad A (2014) Quasi-static cyclic tests on super-lightweight EPS concrete shear walls. *Eng Struct*. 62–75
18. Wan S, Loh CH, Peng SY (2001) Experimental and theoretical study on softening and pinching effects of bridge column. *Soil Dyn Earthq Eng* 75–81

Study on Effect of Particle Shape on Interlocking



Ashwani Kumar Bindal, Arghya Das and Animesh Das

Abstract The mechanical response of a granular system depends on various factors at macroscopic (continuum scale) and microscopic (grain scale) levels. Interlocking between the aggregates is one of the microscopic features that affect the response of granular assembly. The present study deals with the study of the effect of aggregate shape on interlocking. Aluminum rods of circular cross-section are used as the basic elements idealizing the aggregates under plane strain conditions. A biaxial compression setup is fabricated. The load is applied vertically at a constant displacement rate and the lateral displacements of the vertical walls are measured. These vertical walls are partially restrained by horizontal springs. The stiffness of the rod assembly and the translation and rotation of some selected rods are considered as the surrogate parameters indicative of the degree of interlocking. Rods with square or triangular cross-sections are used as intrusions, at various area percentages. The present study suggests that, in general, the stiffness of assembly increases, and translation and rotation decreases as more angular particles are used in the assembly. However, no appreciable difference in the response is observed between the two types of angular particles (that is, rods with triangular and square cross-sections) used in the present study.

Keywords Interlocking · Angular particle · Biaxial compression · Granular materials

1 Introduction

The mechanical response of any granular system depends on various factors at the macroscopic and microscopic levels. For instance, at the macroscopic level, the overall porosity/volume fraction, confining pressure, and interlocking, etc., determine

A. K. Bindal · A. Das (✉) · A. Das
Department of Civil Engineering, Indian Institute of Technology Kanpur,
Kanpur 208016, India
e-mail: arghya@iitk.ac.in

© Springer Nature Singapore Pte Ltd. 2020
A. Prashant et al. (eds.), *Advances in Computer Methods
and Geomechanics*, Lecture Notes in Civil Engineering 56,
https://doi.org/10.1007/978-981-15-0890-5_38

the load-carrying capacity. On the other hand, microscopic features like grain size, shape, intergranular friction, mineralogy, angularity, etc., also affect the load-carrying capacity.

Interlocking in granular materials, in a qualitative sense, can be described as a state in which particles or grains lock among themselves and provide additional resistance towards deformation. Interlocking is purely a geometrical feature of any granular assembly. Knowledge of granular interlocking is essential in various fields of engineering: in geotechnical engineering, shear strength properties of granular materials depend on interlocking [6]; in construction technology, aggregate interlocking within concrete influences the deformation of structural members [12]; in pavement engineering, load transfer in pavement depends on the aggregate interlocking [9], and so on. Despite the widely recognized importance of interlocking, its quantitative description remains subjective in the literature.

Various researchers quantify interlocking indirectly from different microscopic features of granular materials, for example, friction, cohesion, shape, rotation, and translation. Traditionally, interlocking in granular materials is interpreted as a shearing resistance and thus intergranular friction is enhanced to account for this effect [6, 11, 16–18]. Shearing of locked particles results in overriding followed by dilation in the granular assembly. Owing to such response of granular materials, Matsuoka [13] described shear stress ratio as a summation of interparticle friction and a function of dilatancy rate. Here, this dilatancy term indirectly represents the effects of interlocking. It has been found that particle surface roughness has lesser influence than interlocking in macroscopic friction of any granular assembly [19]. Since dilation effect is rooted in particle rotation, in several studies, interlocking was also modeled as resistance to rotation. For instance, Estrada et al. [5] presented a discrete simulation of granular assembly using a modified contact law that considers separate rolling friction along with the conventional sliding friction. The results show that the relative motion of particles at the contact depends on the frictional resistance; either rolling or sliding, whichever reduces the internal friction. Besides shearing resistance, axial and lateral resistance also enhances with interlocking. Walraven [20] experimentally demonstrated that in concrete deformation, along the crack zone reduces due to aggregate interlocking. In this case, load transfer is guided by the rough concrete surface. Kim and Buttlar [9] showed that in hot mix asphalt, the effectiveness of particle interlocking on stiffness enhances with increased particle-to-particle contact. Thus, the present study emphasizes that particle arrangement needs to be accounted for studying interlocking.

Since interlocking primarily denotes a locked packing of aggregates, the geometry of particles is a crucial consideration. Thus the effect of shape on the deformation characteristics of the granular material has been widely studied as a surrogate measure to characterize interlocking [1, 4, 14, 15]. For quantifying particle shape, sphericity and angularity are typically used as parameters. Several studies [8, 14], based on the numerical simulation of biaxial shearing, reported that angularity affects shear strength and dilation response of granular material. Experimental and numerical studies [10, 15] confirm that interlocking of elongated

particles increase constant volume friction (critical state) during shearing. Since the orientation of the fabric tensor is strongly influenced by the particle shape, such a response was observed [15]. Altuhafi et al. [1] proposed a combined shape parameter accounting for particle packing, sphericity, and angularity of sand. The correlation of the newly proposed shape parameter with shear strength response suggests that shape effects are significant in the low confining condition, while becomes insignificant in the high confinement. Stiffness in granular material also depends on the shape of the particles [7]. In general, the shape dependency on stiffness is twofold, (i) shape effect in particle-to-particle contact, and (ii) shape effect in particle packing. To account for these aspects, Worth and Housby [21], Cascante and Santamarina [3] formulated nonlinear elastic stiffness for granular materials in terms of power law stress function and void ratio function.

Based on the preceding discussion, it is evident that most of the studies focus on the dependency of interlocking on shear response and consequent shear failure mechanism. In addition, shape effects were often analyzed numerically using discrete element modeling without direct experimental validation. In this paper, an experimental study is presented encompassing the effect of particle shape on macroscopic stiffness and particle scale rotational movement. A series of biaxial compression response of granular materials is analyzed to understand the effect of particle shape on the interlocking behaviour. The first part of the paper discusses the experimental setup and method of analysis, while the second part elaborates the results in terms of axial and lateral movement and particle rotation. Finally, a discussion is presented to elucidate the results obtained in light of variation of particle shape.

2 Experimental Program

The main philosophy of the proposed experimental setup is that a granular assembly is vertically compressed while allowing a controlled lateral movement during deformation. Series of such experiments are carried out by varying the shape of the constituent material to study the effect of shape on interlocking [2].

2.1 Test Setup and Materials

Since the identification of particle rotation is one of the objectives of the present study, a two-dimensional biaxial experimental setup is designed. Such biaxial arrangement ensures in-plane particle rotation that can be easily captured using imaging or video photography. Figure 1a shows a schematic diagram of the test setup. The entire setup is confined within a rigid box of dimension 300 mm \times 100 mm \times 110 mm. The granular assembly is contained within two vertical plates

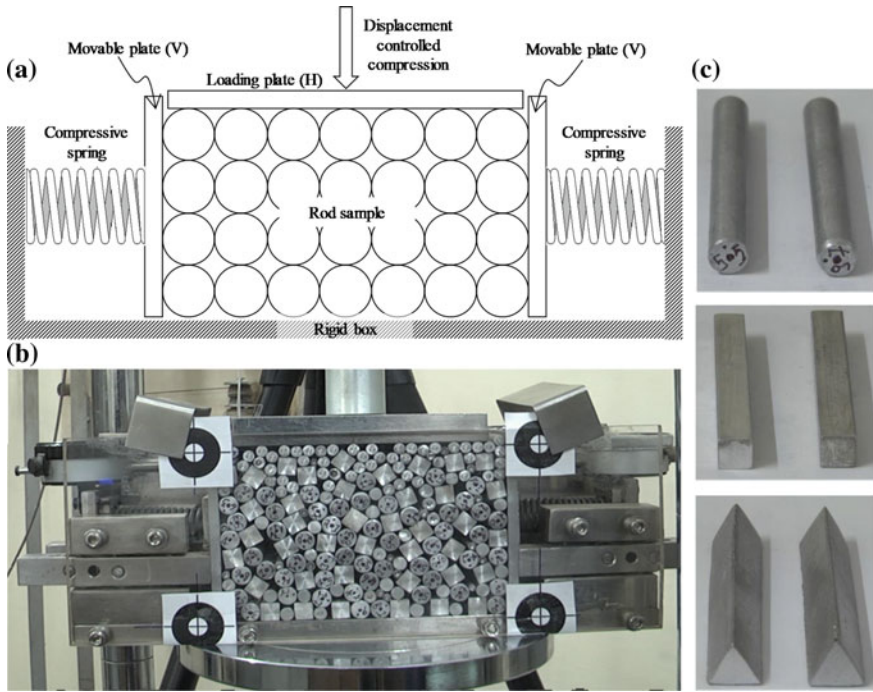


Fig. 1 Experimental setup—**a** schematic diagram; **b** front view of the setup; **c** typical rod elements with circular, square, and triangular cross-section

(identified as “V” in the diagram) that can move in the lateral direction; and a horizontal loading plate (identified as “H” in the diagram), which moves vertically. The H plate is made up of stainless steel. The V plates are made up of 5 mm thick aluminum plates to avoid any rotational instability. In addition, they are connected with a ball bearing arrangement to reduce friction during the lateral movement. The lateral movements of vertical plates are partially restricted using two compression springs (spring constant 0.195 and 0.189 kg/mm). Besides, two dial gauges are fixed on the two plates (not shown in Fig. 1a) to measure the horizontal displacement. Both the springs and the dial gauges are attached to the fixed end walls of the box as shown in the diagram. The pitch, wire diameter, and the overall diameter of the springs are selected by trial and error so that a reasonable deformation of the granular assembly can be achieved in the lateral direction. The base and the backside of the setup are made up of stainless steel while the front face of the box is made up of a 10 mm thick Perspex sheet which (being transparent) allows tracking the movement of the particles during deformation. Reference markers were placed on the Perspex plate at the four corners of the central portion of the box; these markers were used for the calculation of translational and rotational movement of the particles. Figure 1b shows a front view photograph of the experimental setup.

Rod elements with specific geometric cross-section are used as the model granular material in the present study. The main advantage of using such rod elements is that only in-plane translation or rotation is possible, while zero out-of-plane deformation/displacement is ensured along the length direction. Aluminum rods of different basic shapes, i.e., circular (of diameter 3.92, 5.9, 6.8, and 10 mm), square (of side 9.77 mm), and equilateral triangle (of side 14.2 mm) are used in the present study (Fig. 1c). The cross-sectional areas of circular (of 10 mm diameter), square, and equilateral elements are chosen to be the same. Here, aluminum is chosen to reduce the self-weight of the materials, and therefore to reduce its subsequent effect to the response of the granular assembly. The length of the rod is decided in a way that it should not touch the vertical walls located at the front and backside of the setup. The cross-sectional dimensions of the rods are chosen such that the central portion of the box accommodates around 100–120 such elements.

2.2 Test Details

The aluminum rods are placed randomly so that a uniform area ratio is maintained in each test. Care is taken so that these rods do not touch any of the two faces of the box. The packing with the rods of all the circular cross-sections (that is, of four different diameters) is used as the reference since this packing induces minimal interlocking. In the other experiments, the circular rods (10 mm diameter) are replaced with triangular and square cross-sectional rods. Such replacement introduces angularity in the sample and enhances the interlocking in the granular assembly while maintaining area ratio the same. Table 1 shows the different types of samples prepared for testing.

Table 1 Experimental plan

Sl. No.	No. of rods with triangular/square cross-section	Area percent of cross-section (%)	Notations used ^a
1	0	0.00	C0
2	9	7.25	T9
3	25	20.36	T25
4	40	32.52	T40
5	62	56.75	T62
6	9	7.88	S9
7	25	21.85	S25
8	40	34.50	S40
9	62	54.00	S62

^aC = circular; T = triangular; S = square

The loading is applied through the loading plate H. To ensure that the plate H (refer Fig. 1) remains horizontal during loading, it is fixed with the main loading frame, while the entire setup is moved from the bottom with the help of mechanical arrangement in the loading frame. In all the experiments (with different packings), a controlled vertical displacement (0.3 mm per minute) is applied on the horizontal plate. A proving ring attached with the loading plate is used for measurement of vertical force. All the tests are terminated after approximately 20 mm vertical movement of the loading plate.

Two digital video cameras [Panasonic AG—AC120ENU, with 3 MOS sensors and 1920×1080 pixels resolution] are used to record the whole experiment. One camera (camera I) is placed at the front face to record the particle movement and the proving ring reading, while a second camera (camera II) is placed to record the readings of the two horizontal dial gauges from the top. After the test snapshots at a time interval of 1 min, is captured manually from the video recording. From these images, the dial gauge readings and the proving ring reading are noted down for further analyses.

3 Results and Discussion

3.1 Macroscopic Response

Figure 2a shows the vertical stress versus vertical displacement for different area percent of rods with triangular cross-section. It is observed that when percentage rods with triangular cross-section are zero (that is, all the rods are of circular cross-section), the vertical stress is found to be the lowest. With the increase in area percent of rods with triangular cross-section, the vertical stress increases.

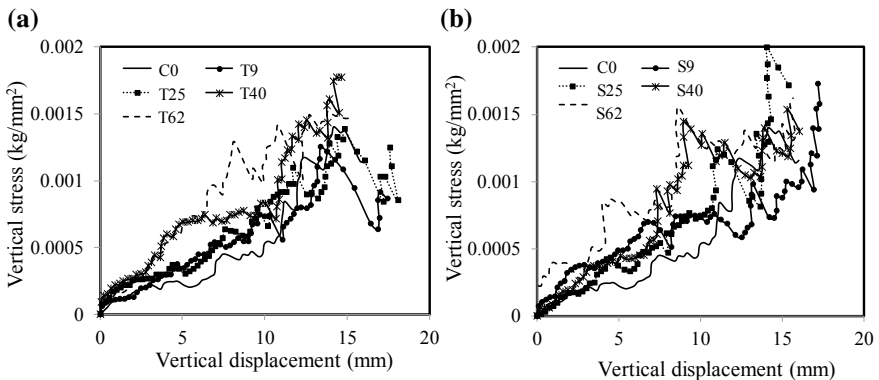
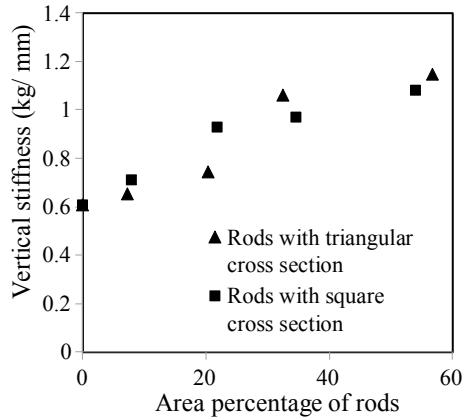


Fig. 2 Vertical stress versus vertical displacement for different area percentages of rods with **a** triangular cross-section and **b** square cross-section

Fig. 3 Vertical stiffness versus area percent of rods with triangular and square cross-sections



Although for lower area percent of intrusion, the increase in vertical stress is insignificant but for higher area percent (say more than 30%), the increase in vertical stress is notable. Similarly, an increase of vertical stress is observed with the increased area percent of rods with the square cross-section (refer to Fig. 2b). The oscillating nature of the curves is attributed to the loss of particle below the loading plate, during the loading stages.

The vertical stiffness of each sample used in testing is calculated by estimating the slope of vertical load versus vertical displacement curve with zero intercepts. Figure 3 shows the variation in vertical stiffness with different area percent of rods with the triangular and the square cross-sections. From Fig. 3, it is seen that with the increase in the triangular and the square particles, there is an increase in the vertical stiffness; that is, the particles are getting more and more interlocked. No appreciable difference is observed between the stiffness response of rods with triangular cross-section and rods with square cross-section.

For each set of experiments, horizontal stress is estimated from the spring stiffness and the displacement of vertical plates. The value of average horizontal stress on the two vertical plates corresponding to 15 mm vertical displacement is plotted in Fig. 4a, b, for rods with triangular cross-section and square cross-section, respectively. In these two graphs, linear trend lines are plotted. From Fig. 4a, it can be seen that the horizontal stress increased approximately 28% when the intrusion of rods with the triangular cross-section is increased from 0.00% to 56.75%. Similarly, from Fig. 4b, it can be seen that the horizontal stress increased approximately 25% when the intrusion of rods with the square cross-section is increased from 0.00% to 54.00%.

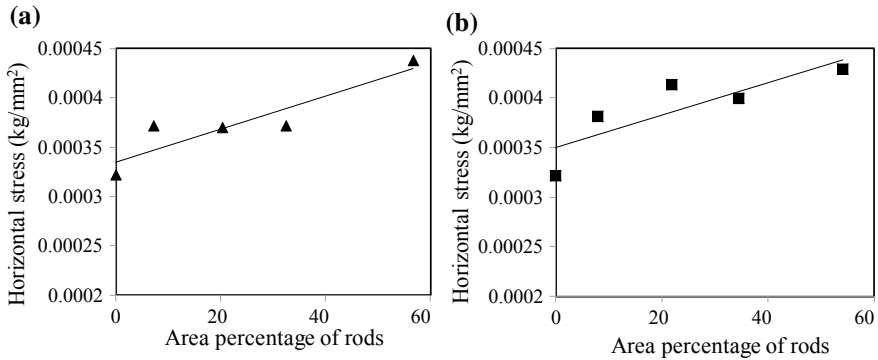


Fig. 4 Horizontal stress versus area percentage of rods with **a** triangular cross-section and **b** square cross-section at (15 mm vertical displacement)

3.2 Translational Response of the Particles

In this section, the movement of the particles during the experiments is presented. In the experimental analysis, 16 circular rods (10 mm in diameter) are chosen for each experiment. For the calculation of rotational movement of the rod elements, an open-source software (Plot digitizer, ver. 2.6.8, <http://plotdigitizer.sourceforge.net>) is used. This software correlates the pixel coordinate of an image with any given Cartesian coordinate system. For calibration purpose, before the start of the experiments, four reference points with known relative distance are marked on the Perspex plate (as shown in Fig. 1b). Naturally, during video recording, these reference points are also captured within the frame. Thus, once the pixel coordinate is calibrated, the location of any point on the image can be determined. Each of the chosen rods with circular cross-section is marked with two dots, one at the center and another is away from the center, i.e., near the side (refer to the top image of Fig. 1c). In addition, an identification (ID) number is also written on each rod. After image digitization, the coordinates of those dots are determined and are subsequently used for the displacement and rotation analyses.

Figure 5 shows three typical plots of particle movement corresponding to C0, T9, and S9. From the figure, it can be seen that the rods placed closer to the sides (i.e., closer to the vertical plates) show more lateral movement than the rods placed closer to middle portion. On the other hand, rods placed closer to the middle portion show more vertical movement than the rods placed closer to the sides. The rods at the bottom are restricted for the vertical movement as well as lateral movement due to the boundary effect. Such movement responses are expected. In T9 and S9, the rods are showing more lateral movement and less vertical movement as compared to the rods in C0.

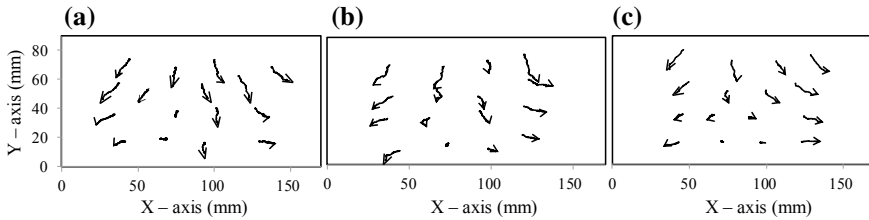


Fig. 5 Typical movement of rods for different area percentages of rods with triangular and square cross-section: **a** C0, **b** T9, and **c** S9

3.3 Rotational Response of the Particles

To compute the rotation of a particle, its direction vectors are computed as per the procedure discussed in the previous section for every image that is captured. The difference in the orientation between the two direction vectors of any particle in two subsequent images provides the rotation of that particle. For every image, the cumulative rotation of rods are calculated for each 1 min interval. In this part of the study, rotation of the rods at the second and third layers is considered only. The rods at first and last layers may have been influenced by the boundary, so their rotation in this present study is not analyzed.

During the initial stage of calculations, the cumulative rotation (clockwise or anticlockwise) of any particle is observed to be quite random. Hence, two approaches, namely, maximum rotation and maximum rotation difference are considered for the calculation of rotation. In the first approach, cumulative rotation of any particle is computed and the maximum rotation is noted. All the side particles are utilized for this analysis, and the central particles are not considered since these did not undergo significant rotation. Figure 6a shows an example plot developed using this approach. In the second approach, the maximum rotation

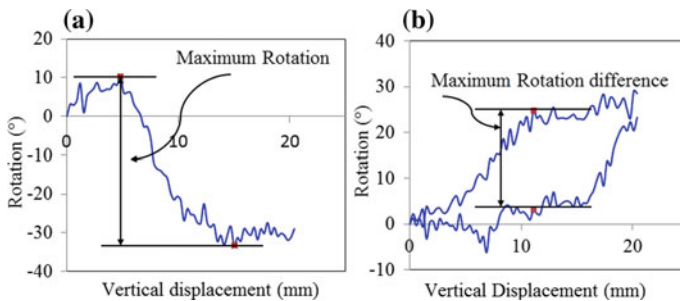


Fig. 6 Typical rotation plots for an individual particle by **a** maximum rotation approach and **b** rotation difference approach

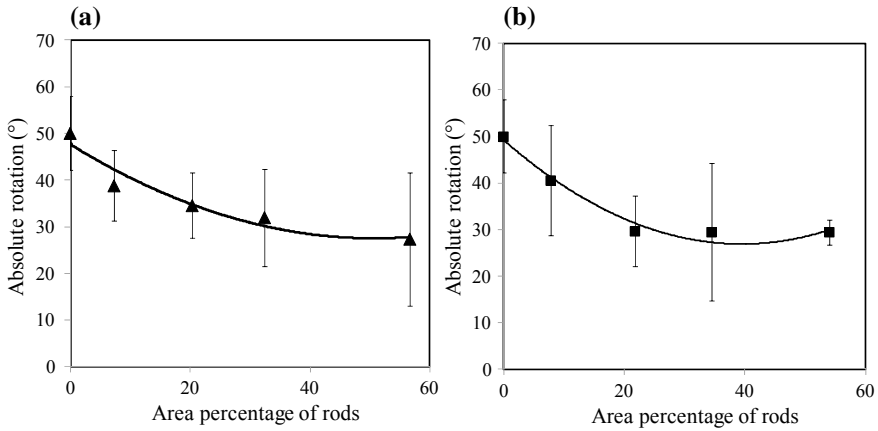


Fig. 7 Absolute rotation versus area percentage of rods with **a** triangular cross-section and **b** square cross-section

difference between the two particles in a row, one being a central particle and another being a particle located at the side, is computed. Figure 6b shows an example plot developed using this approach for the same particle. It is interesting to note that in the present study, the cumulative rotation of any particle ranges between $\pm 40^\circ$, irrespective of particle location or interlocking effects.

Finally, the average of maximum rotation and maximum rotation difference are computed for every experiment. Figure 7 shows the variation in the maximum rotation (that is, the first approach) against the area ratio of two different types particle intrusions, that is, rods with square and triangular cross-section. The plots demonstrate the effect of particle shape since the maximum rotation reduces with the increase of angular rod particles. Approximately, 20° reduction in the rotation is

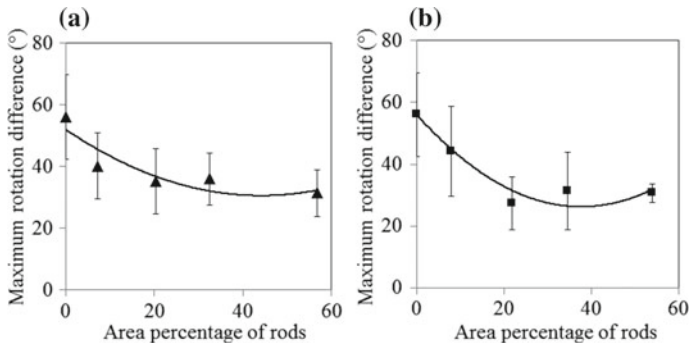


Fig. 8 Maximum rotation difference versus area percent of rods with **a** triangular cross-section and **b** square cross-section

found with 50% intrusion of angular particles. However, there is no appreciable difference observed between rods of triangular and square cross-sections. Similarly, in Fig. 8, the maximum rotation difference (that is, the second approach) is plotted against the area of angular particle intrusion. In this case also, around 20° reduction in the rotation is noticed and no appreciable difference is observed between rods of triangular and square cross-sections.

4 Conclusions

The paper presents an experimental study to explore the effect of particle shape on the interlocking behavior of granular assembly. An experimental setup is fabricated to apply biaxial compression on an assembly of rod-shaped particles with three different geometric cross-sections, namely, circular, triangular, and square. As a surrogate measure of interlocking, macroscopic stiffness and microscopic particle translation and rotation of particles have been analyzed here. The specific conclusions are summarized in the following:

- The analysis suggests a linear increase in the vertical stiffness with the increase of intrusion of angular (square and triangular) rods. However, there is no appreciable difference in the stiffness observed between rods with triangular and square cross-sections.
- Total horizontal stress at the end of the test is found to increase with the increase in the intrusion of angular particles. The horizontal stress increased approximately 28% when the intrusion of rods with the triangular cross-section is increased from 0.00% to 56.75% and the horizontal stress increased approximately 25% when the intrusion of rods with the square cross-section is increased from 0.00% to 54.00%.
- The natural tendency of any granular assembly is to spread in the outward direction with the application of compressive loading. In the present experimental study, it is found that the rods placed closer to the sides show more lateral movement than the rods placed closer to the middle portion. On the other hand, rods placed closer to the middle portion show more vertical movement than the rods placed closer to the sides. In the present study, approximately 20° reduction in the rotation is found with about 54% intrusion of angular particles, compared to the situation when all particles are with circular cross-section. No appreciable difference is observed in rotation between rods with triangular and square cross-sections.

References

1. Altuhafi FN, Coop MR, Georgiannou VN (2016) Effect of particle shape on the mechanical behavior of natural sands. *J Geotech Geoenviron Eng* 142(12):04016071
2. Bindal AK (2018) Effect of particle shape on the interlocking behavior of granular materials. Master's thesis, Indian Institute of Technology Kanpur
3. Cascante G, Santamarina JC (1996) Interparticle contact behavior and wave propagation. *J Geotech Eng* 122(10):831–839
4. Dodds J (2003) Particle shape and stiffness effects on soil behavior. Master's thesis, Georgia Institute of Technology
5. Estrada N, Taboada A, Radjaï F (2008) Shear strength and force transmission in granular media with rolling resistance. *Phys Rev E* 78(2):021301
6. Guo P, Su X (2007) Shear strength, interparticle locking, and dilatancy of granular materials. *Can Geotech J* 44(5):579–591
7. Hardin BO, Richart FE (1963) Elastic wave velocities in granular soils. *J Soil Mech Found Div* 8933–8965
8. Iwashita K, Oda M (1998) Rolling resistance at contacts in simulation of shear band development by DEM. *J Eng Mech* 124(3):285–292
9. Kim M, Buttlar WG (2010) Stiffening mechanisms of asphalt–aggregate mixtures. *Transp Res Rec J Transp Res Board* 2181(1):98–108
10. Li Y (2013) Effects of particle shape and size distribution on the shear strength behavior of composite soils. *Bull Eng Geol Environ* 72(3–4):371–381
11. Liu S, Matsuoka H (2003) Microscopic interpretation on a stress-dilatancy relationship of granular materials. *Soils Found* 43(3):73–84
12. Martín-Pérez B, Pantazopoulou SJ (2001) Effect of bond, aggregate interlock and dowel action on the shear strength degradation of reinforced concrete. *Eng Struct* 23(2):214–227
13. Matsuoka H (1974) A microscopic study on shear mechanism of granular materials. *Soils Found* 14(1):29–43
14. Mirghasemi AA, Rothenburg L, Matyas EL (2002) Influence of particle shape on engineering properties of assemblies of two-dimensional polygon-shaped particles. *Géotechnique* 52(3):209–217
15. Peña AA, García-Rojo R, Herrmann HJ (2007) Influence of particle shape on sheared dense granular media. *Granul Matter* 9(3–4):279–291
16. Rowe PW (1962) The stress-dilatancy relation for static equilibrium of an assembly of particles in contact. *Proc R Soc A Math Phys Eng Sci* 269(1339):500–527
17. Szalwinski C (2017) On critical states, rupture states and interlocking strength of granular materials. *Materials (Basel)* 10(8):865
18. Taylor DW (1948) *Fundamentals of soil mechanics*. Wiley
19. Thornton C (2000) Numerical simulations of deviatoric shear deformation of granular media. *Géotechnique* 50(1):43–53
20. Walraven J (1980) Aggregate interlock: a theoretical and experimental analysis. Doctoral thesis, Delft University of Technology
21. Worth CP, Houlsby GT (1985) Soil mechanics, property characterization and analysis procedure. In: 11th international conference on soil mechanics and foundation engineering. Publication of: Balkema (AA), pp 1–55

Correlation of Shear Wave Velocity with Standard Penetration Resistance Value for Allahabad City



Manjari Singh, S. K. Duggal, Kumar Pallav and Keshav Kr. Sharma

Abstract Shear wave velocity is the most widely used parameter for microzonation studies, site characterization, groundwater engineering, and environmental studies. Field techniques for the measurement of shear wave velocity are generally not economically viable due to deficiency of skillful personnel or unavailability of equipment. The importance of this study is to develop the empirical correlation between standard penetration resistance value (SPT-N) and shear wave velocity (V_s), for Allahabad, U.P, from the existing correlation developed for other cities of India for all soil condition using regression analysis. In this study 83 borehole data is used to calculate the average shear wave velocity (V_s) for Allahabad city at depths of 1.5, 3, 4.5, 15, and 30 for all soil condition. Also average shear wave velocity map for 30 m depth has been plotted and is used to classify the study area as per IBC-2009 (International Building Code). Results show most of the sites fall under C and D category representing soil conditions.

Keywords Allahabad city · Shear wave velocity (V_s) · MASW · SPT-N value · IBC-2009

1 Introduction

Traits of the seismic motion are strongly affected by local site conditions. Local site conditions include depth of soil strata and soil properties. Effects on ground motions due to variations in the geologic conditions of a particular site due to soil softness and total sediment thickness over bedrock are termed as site effect. The

M. Singh (✉) · S. K. Duggal
Department of Civil Engineering, MNNIT Allahabad, Allahabad, India
e-mail: manjarisingh.2508@gmail.com

K. Pallav
Department of Civil Engineering and Surveying, CPUT, Bellville, Cape Town, South Africa

K. Kr.Sharma
Department of Civil Engineering, NIT Jamshedpur, Jamshedpur, India

most severe damages are generally produced by ground shaking and amplified by site conditions, Haloi and Sil [1]. The 1985 Michoacan earthquake occurred in Mexico City, produced severe damages around 350 km away in the city where the presence of soft soil caused significant amplification of bedrock ground motion. The Loma Prieta earthquake (1989) caused tremendous destruction in Oakland region of San Francisco, soft soil areas were badly affected in San Francisco Bay area, whereas nearby hard rock areas were amplified by two to four times, Housner [2]. Thus, local site effects must be considered for evaluating the seismic hazard assessment of the site.

So the above-explained earthquake has shown that local soil deposits and site condition can amplify the ground motion and increase the extent of destructions. Thus, it is very important to classify the area according to its class on the basis of dynamic properties of soil (like shear wave velocity) for site response analysis purposes. Shear wave velocity is the most widely used parameter which describes soil stiffness and used in site characterization, microzonation studies, and dynamic site response evaluation, Kramer [3].

Shear wave velocity is used for determining the shear modulus (G_{max}), which is a vital parameter for dynamic stability analysis of dams and slopes, etc. There are some field methods such as seismic reflection or refraction test, SASW or MASW and cross-hole or down-hole test which is used for estimating magnitude of V_s . The V_s profile can be found from any of the above field tests for a site. The tests are expensive and it requires skilled manpower. Further, it also requires large amount of initial investment for purchasing the instruments as well as the availability of open area at site is also required for the conduction of test. However, SPT is easily obtainable for many sites where geotechnical investigations are accomplished. In this account, an empirical correlation can be developed without much expense for mapping the velocity profile.

In this study, a correlation between V_s and SPT-N have been derived from the existing correlations for all soil available for other Indian cities using regression analysis. Contour map has also been prepared for V_s profile at 30 m depth for Allahabad city.

2 Past Studies in India and Abroad

Numerous researchers have suggested sets of correlation. The basic procedure in forming these correlations is the calculation of V_s by any standard field method and determining SPT-N value. Then it is assumed that there exists a power-law relation between V_s and SPT-N value.

$$V_s = a \cdot N^b \quad (1)$$

where 'a' and 'b' are coefficients based on the type of soil. Also, sometimes, there will be other coefficients to take care of the geological type of soils.

$$V_s = a \cdot N^b \cdot c \tag{2}$$

where ‘c’ is a coefficient based on the geological type of soil like Pleistocene and Holocene. So, after the field tests, regression is done to fit the above equations and the coefficients are determined. The Correlations proposed by numerous researchers are summarized in Table 1.

In India, the mostly used geotechnical test is Standard Penetration Test and many researchers have tried to develop the correlation. Hanumanthrao and Ramana [5] have conducted SASW test in Delhi region and proposed a correlation using regression analysis for all soils, sands, sandy silt/silty sand. Maheswari et al. [6] have proposed empirical equations between SPT-N values and V_s for Chennai city using 200 data pairs obtained by conducting MASW test at thirty locations in Chennai. Anbazhagan and Sitharam [7] have presented a relation of corrected SPT-N value with V_s for Bangalore City. Based on average V_s and SPT-N categorized the city as seismic site class D and C. Sil and Sitharam [8] have proposed correlation for Agartala city based on MASW test performed on 27 locations in the city and developed V_s profile. According to average V_s^{30} the city is categorized in

Table 1 Existing correlation of SPT-N values with shear wave velocity [4]

Researchers	Soil type		
	All	Cohesionless	Cohesive
Ohba (1970)	$V_s = 84.0N^{0.31}$		
Shibata (1970)		$V_s = 32.0N^{0.50}$	
Imai (1970)	$V_s = 76.0N^{0.33}$		
Ohta (1972)		$V_s = 87.0N^{0.36}$	
Fujiwara (1972)	$V_s = 92.1N^{0.337}$		
Ohsaki (1973)	$V_s = 81.4N^{0.39}$	$V_s = 100.0N^{0.33}$	
JRA (1980)		$V_s = 80.0N^{0.33}$	$V_s = 100.0N^{0.33}$
Seed (1981)	$V_s = 61.4N^{0.50}$		
Imai (1982)	$V_s = 97.0N^{0.314}$		
Sykora (1983)		$V_s = 100.5N^{0.29}$	
Yokota (1991)	$V_s = 121.0N^{0.27}$		
Kalteziotis (1992)	$V_s = 76.2N^{0.24}$	$V_s = 49.1N^{0.50}$	$V_s = 76.6N^{0.45}$
Raptakis (1995)		$V_s = 100.0N^{0.24}$	$V_s = 184.2N^{0.17}$
Athanasopulos (1995)	$V_s = 107.6N^{0.36}$		
Jafari (1997)	$V_s = 22N^{0.85}$		
Chien et al. (2000)		$V_s = 22.0N^{0.76}$	
Jafari (2002)	$V_s = 22.0N^{0.85}$	$V_s = 19.0N^{0.85}$	$V_s = 27.0N^{0.73}$
Lee (2008)	$V_s = 137.153N^{0.229}$	$V_s = 98.07N^{0.305}$	$V_s = 163.15N^{0.192}$
Tsiambaos (2011)	$V_s = 105.7N^{0.327}$	$V_s = 79.7N^{0.365}$	$V_s = 88.8N^{0.37}$

Table 2 Correlation of shear wave velocity with SPT-N values for various Indian cities

Researchers	Place	All soil	Cohesionless soil	Cohesive soil
Hanumantharao and Ramana [5]	Delhi	$V_s = 82.6N^{0.43}$	$V_s = 79N^{0.434}$	$V_s = 86N^{0.42}$
Maheswari et al. [6]	Chennai	$V_s = 95.64N^{0.301}$	$V_s = 100.53N^{0.265}$	$V_s = 89.31N^{0.358}$
Anbazhagan and Sitharam [7]	Bangalore	$V_s = 78[(N1)_{60cs}]^{0.40}$		
Sil and Sitharam [8]	Agartala	$V_s = 123N^{0.22}$ $V_s = 116N^{0.27}$		
Anbazhagan et al. [9]	Lucknow	$V_s = 68.96N^{0.51}$	$V_s = 60.17N^{0.56}$	$V_s = 106.63N^{0.39}$
Thaker and Rao [10]	Surat	$V_s = 59.72N^{0.42}$	$V_s = 51.21N^{0.45}$	$V_s = 62.41N^{0.42}$
Kirar et al. [11]	Roorkee	$V_s = 99.5N^{0.345}$	$V_s = 100.3N^{0.338}$	$V_s = 94.4N^{0.379}$
Chatterjee and Choudhury [12]	Kolkata	$V_s = 78.21N^{0.3769}$	$V_s = 54.82N^{0.5255}$	$V_s = 77.11N^{0.3925}$ $V_s = 58.02N^{0.455}$
Mhaske and Choudhury [13]	Mumbai	$V_s = 72N^{0.40}$		

seismic site class D and E. Anbazhagan et al. [9] have developed an empirical equation between V_s and SPT-N for Lucknow city using MASW data of 47 locations and 23 SPT borehole data. Based on the V_s^{30} values city is classified into site class D and class C. Similarly Thaker and Rao [10], Kirar et al. [11], Chatterjee and Choudhury [12], Mhaske and Choudhury [13] have also given the correlation for different parts of India. Presently existing empirical relationships are shown in Tables 1 and 2.

3 Study Area

In the present study, Allahabad city, Uttar Pradesh has been selected. It is located at 25°45' N and 81°84' E in the southern part of the Uttar Pradesh. Ganga and Yamuna rivers flow through the district. Allahabad is a center of trade, politics, learning, and religious festivals.

The Ganga and Yamuna rivers divide Allahabad into three distinct regions: Ganga basin, Yamuna basin, and Dwaba. Ganga Basin lies in Indo Gangetic Plain, have large alluvial sedimentary soil deposits. A Deep borehole report from CGWB (Central Ground Water Board) Allahabad, specifies the basement depth and rock present at the bed of the city. Cross section of the city shown in Fig. 1 indicates Shale, limestone and Sandstone present at the bedrock level and having 100–280 m basement depth. Depth of average water table varies between 6.0 and 7.0 mbgl.

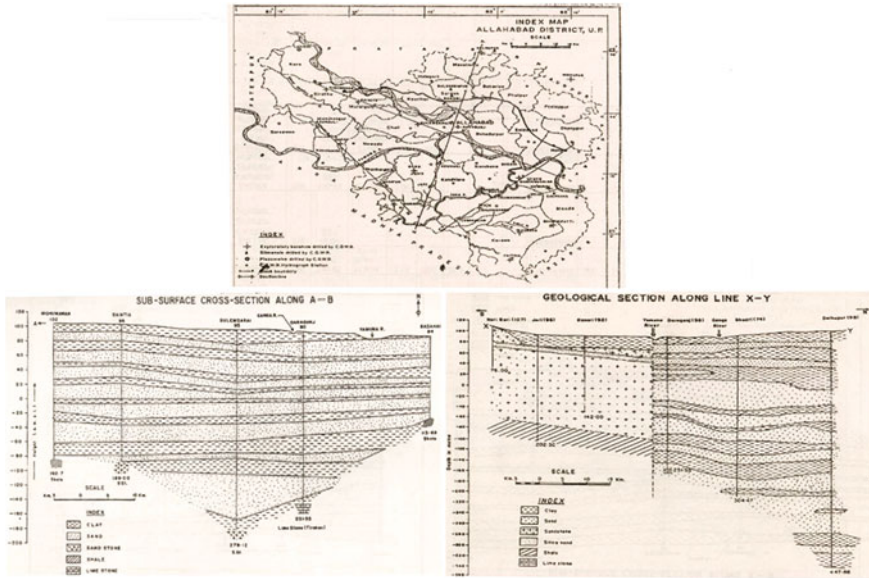


Fig. 1 Geological cross section of district along line A-B and X-Y of district

Numerous existing infrastructures were designed using the recommendation of the IS code but did not incorporate local soil site conditions. As per Indian seismic zonation map, the city belongs to zone-II [14] with Zone factor 0.10.

The city has experienced several earthquakes occurred in U.P. $6.0 M_w$ RaeBareilly (1925) Earthquake; $6.2 M_w$ Bulandshahar (1956) Earthquake; $5.7 M_w$ Gorakhpur (1965) Earthquake; in Country $7.5 M_w$ Dharchulla (1916) Earthquake; $6.5 M_w$ Uttarakhand (1945) Earthquake; $6.0 M_w$ Jabalpur (1997) Earthquake; from neighboring country $8.4 M_w$ Nepal-Bihar (2015) Earthquake; $7.8 M_w$ Nepal (2015) Earthquake. A catalog of the felt intensity of Indian earthquakes from 1636 A.D to 2009 A.D is described by Martin and Szeliga [15].

Allahabad is surrounded by numerous subsurface faults and ridges which increases city’s seismic hazard susceptibility. Details of these faults such as strike, dip, and mechanism (thrust, strike-slip, and normal) are described in Singh et al. [16]; Dasgupta et al. [17], and Kayal [18]. Allahabad city is situated at a distance of nearly 265 km from HFT (Himalayan Frontal Thrust system). It can trigger disastrous earthquake of magnitudes $7.5-8 M_w$, Thakur [19]. According to the collaborated disaster risk management programme UNDP (United National

Development Programme) and Ministry of Home Affairs, the study area is located near Faizabad Ridge, which has been inactive for almost 30 decades. Due to huge seismic gap the ridge is very much stressed, therefore, can cause devastating earthquake in upcoming years, Nadeshda [20]. A report of Uttar Pradesh Earthquake Mitigation Department shows the subduction of Indian Plate under Asian Plate by 5.25 m may produce earthquake of 8 Mw, Nadeshda [20]. Therefore, due to the potential seismic gap and seismicity around the study area, seismic site classification is necessary for the city.

4 Geotechnical Information

Authentic and reliable geotechnical data is of utmost importance for this study hence data was taken from technical institutes, soil investigation societies, government departments, and national laboratories. Total 22 locations were selected across the city; 83 boreholes were drilled at these sites for the collection of following datasets (Fig. 2). Typical borehole information for one of the sites (Balughat) is shown in Table 3.

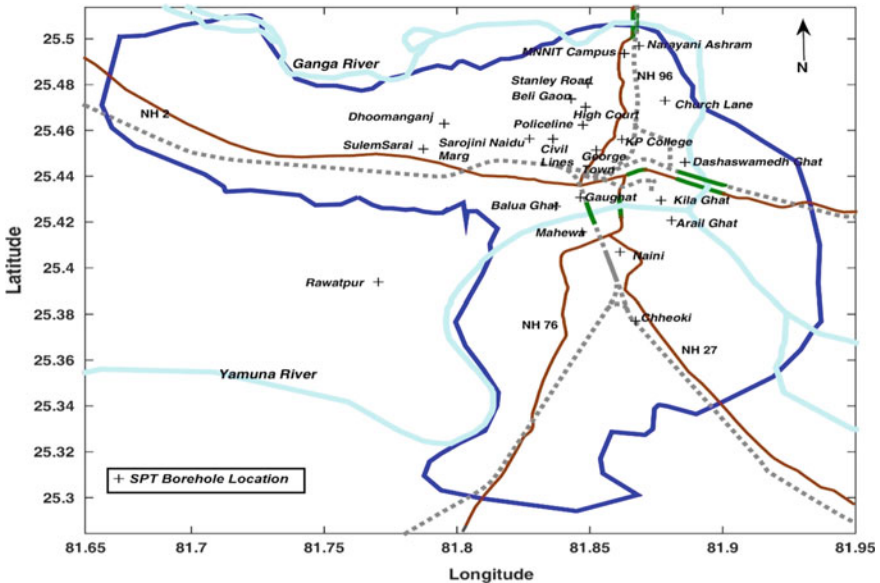


Fig. 2 Locations of borehole

5 Proposed Methodology

In this research, empirical correlation of SPT-N values with V_s has been proposed. By using the correlations listed in Table 2, a linear power regression analysis was done by taking the average of shear wave velocities for each SPT-N values. The resulting correlation for all soil condition from the above analysis is given in Eq. (3).

$$V_s = 73.89N^{0.42}, R^2 = 0.99 \quad (3)$$

In this study, interpolation technique is used to determine average V_s values for intermediate points mapped for the city. The extrapolation scheme suggested by Boore [21] is used to determine the 30 m average V_s where borehole data were not available.

Correlation between \bar{V}_{s30} and \bar{V}_{sd} is used to extrapolate \bar{V}_{s30} . Time-averaged velocity at any depth d is stated by

$$\bar{V}_{sd} = \frac{d}{t(d)} \quad (4)$$

$t(d)$ is time taken to travel 'd' depth is given by

$$t(d) = \int_0^d \frac{dz}{V_{sz}} \quad (5)$$

where, V_{sz} is depth-dependent velocity model. In this method power-law relation was assumed between \bar{V}_{s30} and \bar{V}_{sd} . The correlation is given by

$$\bar{V}_{s30} = a + b \times (\log \bar{V}_{sd}) \quad (6)$$

where 'a' and 'b' denotes regression coefficients and its values of the same for depth ranging from 10 to 29 m are given in Table 4. This correlation gives good results even for shallower depth of 10 m.

To find out the impacts of incoming seismic waves on ground, near surface (30 m) V_s can be determined to characterize the site for calculating seismic hazard. *International Building Code*, IBC [22] used the equivalent V_s for top 30 m depth of soil to characterize the site and the same can be computed as follows:

$$V_s = \frac{\sum_{i=1}^n d_i}{\sum_{i=1}^n \frac{d_i}{V_{si}}} \quad (7)$$

where, V_s = shear wave velocity in meter per second (or feet per second).

d_i = thickness of any layer between 0 and 100 feet (or 30.480 m).

The site classification as per IBC-2009 is shown in Table 5.

Table 4 Coefficients of the Eq. (6)

d	a	b	σ
10	4.2062×10^{-02}	1.0292×10^{00}	7.1260×10^{-02}
11	2.2140×10^{-02}	1.0341×10^{00}	6.4722×10^{-02}
12	1.2571×10^{-02}	1.0352×10^{00}	5.9353×10^{-02}
13	1.4186×10^{-02}	1.0318×10^{00}	5.4754×10^{-02}
14	1.2300×10^{-02}	1.0297×10^{00}	5.0086×10^{-02}
15	1.3795×10^{-02}	1.0263×10^{00}	4.5925×10^{-02}
16	1.3893×10^{-02}	1.0237×10^{00}	4.2219×10^{-02}
17	1.9565×10^{-02}	1.0190×10^{00}	3.9422×10^{-02}
18	2.4879×10^{-02}	1.0144×10^{00}	3.6365×10^{-02}
19	2.5614×10^{-02}	1.0117×10^{00}	3.3233×10^{-02}
20	2.5439×10^{-02}	1.0095×10^{00}	3.0181×10^{-02}
21	2.5311×10^{-02}	1.0072×10^{00}	2.7001×10^{-02}
22	2.6900×10^{-02}	1.0044×10^{00}	2.4087×10^{-02}
23	2.2207×10^{-02}	1.0042×10^{00}	2.0826×10^{-02}
24	1.6891×10^{-02}	1.0043×10^{00}	1.7676×10^{-02}
25	1.1483×10^{-02}	1.0045×10^{00}	1.4691×10^{-02}
26	6.5646×10^{-03}	1.0045×10^{00}	1.1452×10^{-02}
27	2.5190×10^{-03}	1.0043×10^{00}	8.3871×10^{-03}
28	7.7322×10^{-04}	1.0031×10^{00}	5.5264×10^{-03}
29	4.3143×10^{-04}	1.0015×10^{00}	2.7355×10^{-03}

Table 5 Site classifications as per IBC-2009

Site class	Soil profile name	V_s^{30} (m/s)
A	Hard rock	$V_s > 1500$
B	Rock	750–1500
C	Very dense soil and soft rock	360–750
D	Stiff soil	180–360
E	Soft soil	<180

The comparison shown in Fig. 3 suggests that up to SPT-N value 20, predicted relation is considerably closer to the existing relation of Mhaske and Choudhury [13], Maheswari et al. [6], and Seed and Idriss [23]. For all range of SPT-N, Ohasaki and Iwasaki [24], and JRA-Clay [25] including developed relation yield same V_s values. So it is found that the predicted relation is very well matched with existing worldwide relation.

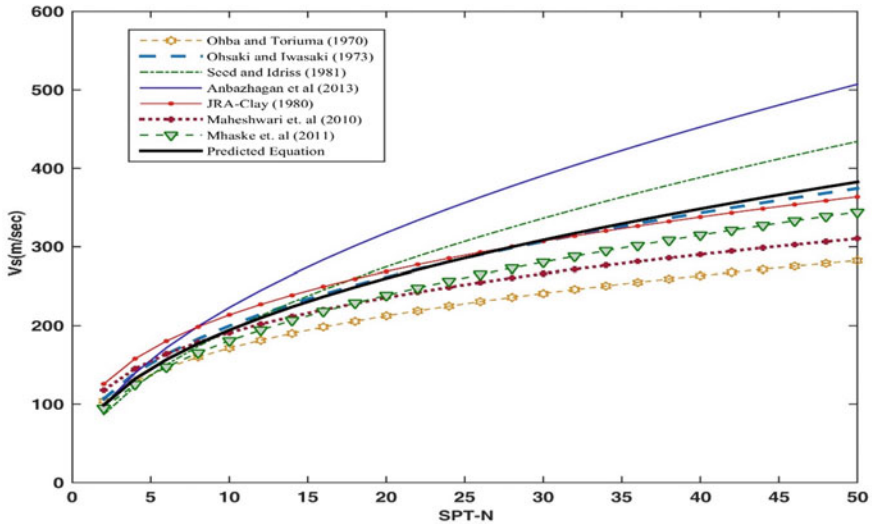


Fig. 3 Comparison of predicted correlation with worldwide correlation

6 Results and Discussion

For site characterization and site response analysis, shear wave velocity is a vital factor. In the current study, V_s is estimated at various depths, viz., 1.5, 3, 4.5, 15, and 30 m depth for Allahabad city using equation proposed in Eq. (3). For few important sites shear wave velocity at various depths have been discussed in following section. As per IBC-2009, estimated 30 m shear wave velocity (V_s^{30}) is used for site classification of the city. Further, contour map has been plotted for the city at 30 m depth (Fig. 4).

V_s (m/s) at 1.5 m depth

The average V_s at depth of 1.5 m varies from 109 to 251 m/s. Minimum velocity obtained is 109.85 m/s for Kila Ghat site and maximum velocity is 251 m/s for Arail Ghat. Estimated shear wave velocity observed in High court is 125.85 m/s; in Church lane is 179.65 m/s and in KP College is 135.45 m/s.

V_s (m/s) at 3.0 m depth

For depth of 3.0 m average V_s ranges from 110 to 366 m/s which indicates dense to medium soil (Table 6). Minimum velocity obtained is 112.01 m/s for SP Marg Civil lines and maximum velocity is 366.09 m/s Arail Ghat. In High court, Church lane, and KP College area the calculated shear velocity observed is 127.65 m/s, 256.89 m/s, and 135.45 m/s, respectively.

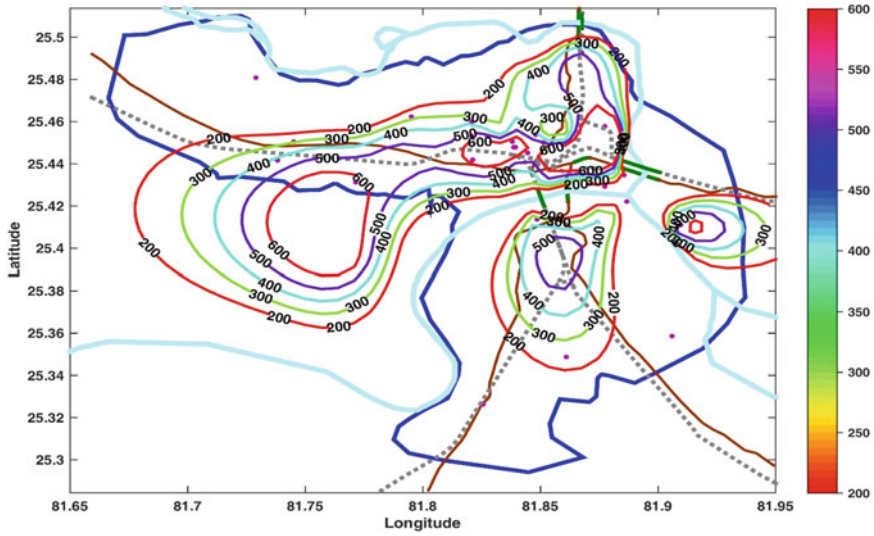


Fig. 4 V_s (m/s) distribution at 30 m depth for Allahabad city

Table 6 Average shear wave velocity, V_s^{30} (m/s) at 30 m depth from ground surface

Sites	Latitude	Longitude	V_s^{30} (m/s)	Site-class
Chheoki railway station	25.3771	81.8671	435.15	C
MNNIT Allahabad	25.4935	81.8629	465.89	C
Central Jail Naini	25.407	81.8614	460.98	C
Sulem Sarai	25.4518	81.7873	458.89	C
Stanley road	25.4804	81.8492	413.21	C
Police line	25.4623	81.8473	355.39	D
Gaughat	25.4308	81.8465	314.72	D
Arail Ghat	25.4207	81.8807	255.29	D
Dhoomanganj	25.4629	81.7951	266.54	D
High court	25.4702	81.8483	466.36	C
Civil lines	25.4563	81.8361	421.08	C
Church lane	25.4612	81.8633	394.13	C
Mahewa (East)	25.4158	81.847	297.95	D
Sarojini Naidu Marg	25.4564	81.8273	367.90	C
Rawatpur	25.3938	81.7704	638.19	C
George town	25.4514	81.8525	397.84	C
KP college	25.4440	81.8541	555.95	C
Beli Gaon	25.4737	81.843	463.59	C
Narayani Ashram	25.4969	81.8684	350.57	D
Baluua Ghat	25.4268	81.8372	300.09	D
Kila Ghat	25.4294	81.8768	183.26	D
Dashaswamedh Ghat	25.4461	81.8858	504.19	C

V_s (m/s) at 4.5 m depth

V_s profile at 4.5 m depth indicates dense to medium soil ranging from 125 to 382 m/s. Minimum velocity obtained is 127.30 m/s for Kila Ghat and maximum velocity is 382.53 m/s Dashaswamedh Ghat. Calculated V_s observed in High court, 185.19 m/s; in Church lane, 176.95 m/s, and in KP College, 312.65 m/s.

V_s (m/s) at 15 m depth

Minimum velocity corresponding to a depth of 15 m obtained is 172.24 m/s for Gau Ghat and maximum velocity is 388.53 m/s BeliGaon. Calculated shear wave velocity in High court is 334.56 m/s, in Church lane is 294.56 m/s, and in KP College is 320.12 m/s.

V_s (m/s) at 30 m depth

For assessment of local site effect, subsoil classification is carried out by estimating average V_s at 30 m depth. The estimated average velocity is ranging from 180 to 640 m/s. Most of the sites are classified as class C and D type which shows very dense soil and soft rock to stiff soil [22]. In High court, Church lane, and KP College area the calculated shear velocity is 466.36 m/s, 394.13 m/s, and 555.95 m/s, respectively and are categorized under class C. In the regions near to river bank like Gau Ghat, Arail Gaht, Balua Ghat, and Kila Ghat the calculated shear velocity is 314.72, 255.29, 300.09, and 183.26 m/s and are categorized under class C. Figure 4 indicates the map of average V_s for a depth of 30 m. Minimum velocity obtained is 183.26 m/s for Kila Ghat and maximum velocity is 638.19 m/s for Rawatpur. Further, 30 m shear wave velocity (V_s^{30}) at all sites of the city is mentioned in Table 6.

7 Validation

Tripathi et al. [26] carried out soil investigation at shallow depth (up to 9 m) using seismic refraction survey for Allahabad city at 68 different locations. Primary wave (P —Wave) have been recorded at various depths up to 9 m for above-mentioned locations. Since this study displays the variation of V_s with different depths for Allahabad city so, in order to validate, it has been converted to P -wave velocity (V_{PS}) using the relation Eq. (8). Three common locations viz. High Court, Church Lane, and KP College have been opted for validation. Shear wave velocity V_s is determined using correlation proposed in Eq. (4) that has been converted to P —Wave velocity (V_{PS}) in order to compare the observed P —Wave velocity (V_P) from seismic refraction survey.

$$V_{PS} = \sqrt{3}V_s \quad (8)$$

Table 7 Velocity profile at different depth

Site	Depth (m)	Calculated V_s	V_{PS} after conversion	V_p observed	Difference (%)
High court	1	124.7902	215.887	200–250	4.2
	3	121.2063	215.887	201	6.8
	4	180.1692	311.693	300–350	4.2
	6	209.9797	375.422	300–400	6.7
	8	212.3930	395.439	300–400	11.4
	9	320.8803	528.171	588.96	11.5
Church lane	1	176.54	305.43	200–250	6.4
	2	253.31	438.23	450–500	8.3
	4	180.68	312.58	300–350	3.9
	6	189.63	328.06	300–400	6.6
	9	305.47	528.47	588.96	11.4
KP college	1	138.39	239.42	200–250	6.0
	3	135.37	234.20	200–250	3.9
	6	186.84	323.25	300–400	8.2
	7	198.59	343.56	300–450	9.1
	8	186.28	322.27	300–400	8.6
	9	303.71	525.42	588.96	12.0

Table 7 shows the velocity profile for three different opted locations. It can be observed from Table 7 that in High Court region, V_{PS} falls in the observed range of primary wave with negligible difference up to 6 m while it increases to 11.5% at 10 m depth. A Similar range is observed in Church Lane site and KP College area.

8 Conclusions

In the current study, 83 boreholes across 22 locations in the Allahabad City of India were selected and geotechnical data was collected from these borehole sites. The relation between V_s and SPT-N is developed for all soil condition for Allahabad city using nonlinear regression analysis. The proposed correlation is validated graphically with other worldwide correlation. The developed correlation was used to obtain V_s profiles at 1.5 m, 3.0 m, 4.5 m, 15 m, and 30 m depth for Allahabad city. The estimated velocity at 1.5 m, 3.0 m, 4.5 m, and 15 m is ranging from 109–251 m/s, 110–360 m/s, 125–382 m/s, to 172–390 m/s, respectively. The average V_s at 30 m depth varies in the range 180–650 m/s, thus the city is categorized as Class C and D as per IBC-2009. Most of the sites (MNNIT Allahabad campus, Chheoki, Rawatpur, Sulemsarai, KP college, and BeliGaon) fall in class C and some of the sites near river bank fall in class D. Estimated V_s values from the

predicted relation are validated with the V_s observed from seismic refraction survey with error range of 3–12% for depth 1–9 m.

Therefore, the proposed correlations can be effectively useful for site response study and hazard analysis of the city.

References

1. Haloi J, Sil A (2015) Seismic site classification of a bridge site over River Barak on Silchar bypass road. *Int J Advanced Earth Sci Eng* 4(1):275
2. Housner GW (1989) Competing against time, Report to Governor Deukmejian of California, Governor's Board of Inquiry on the (1989) Loma Prieta Earthquake
3. Kramer SL (1996) Geotechnical earthquake engineering. Prentice Hall, New York
4. Mert T, Elmon T, Ural DN (2015) A comparative study of soil classifications using international approaches. In SECED Conference: Earthquake risk and engineering towards a resilient world
5. Hanumantharao C, Ramana GV (2008) Dynamic soil properties for microzonation of Delhi, India. *J Earth Syst Sci* 117(2):719–730
6. Maheswari RU, Boominathan A, Dodagoudar GR (2010) Seismic site classification and site period mapping of Chennai City using geophysical and geotechnical data. *J Appl Geophys* 72(3):152–168
7. Anbazhagan P, Sitharam TG (2008) Mapping of average shear wave velocity for Bangalore region: a case study. *J Environ Eng Geophys* 13(2):69–84
8. Sil A, Sitharam TG (2014) Dynamic site characterization and correlation of shear wave velocity with standard penetration test 'N' values for the city of Agartala, Tripura state, India. *Pure Appl Geophys* 171(8):1859–1876
9. Anbazhagan P, Kumar A, Sitharam TG (2013) Seismic site classification and correlation between standard penetration test N value and shear wave velocity for Lucknow City in Indo-Gangetic Basin. *Pure Appl Geophys* 170(3):299–318
10. Thaker TP, Rao KS (2011) Development of statistical correlations between shear wave velocity and penetration resistance using MASW technique. In: Pan-am CGS geotechnical conference, Delhi, India
11. Kirar B, Maheshwari BK, Muley P (2016) Correlation between shear wave velocity (v_s) and SPT resistance (N) for Roorkee region. *Int J Geosynth Gr Eng* 2(1):9
12. Chatterjee K, Choudhury D (2013) Variations in shear wave velocity and soil site class in Kolkata city using regression and sensitivity analysis. *Nat Hazards* 69(3):2057–2082
13. Mhaske SY, Choudhury D (2011) Geospatial contour mapping of shear wave velocity for Mumbai city. *Nat Hazards* 59(1):317–327
14. IS 1893 (2016) Indian standard criteria for earthquake resistant design of structures, part 1—general provisions and buildings, Bureau of Indian Standards, New Delhi
15. Martin S, Szeliga W (2010) A catalog of felt intensity data for 570 earthquakes in India from 1636 to 2009. *Bull Seismol Soc Am* 100(2):562–569
16. Singh SK, Garcia D, Pacheco JF, Valenzuela R, Bansal BK, Dattatrayam RS (2004) Q of the Indian shield. *Bull Seismol Soc Am* 94(4):1564–1570
17. Dasgupta et al (2000) Seismotectonic atlas of India and its environs. Geological Survey of India, Kolkata
18. Kayal JR (2008) Microearthquake seismology and seismotectonics of South Asia, 1st edn. Springer, Berlin
19. Thakur VC (2004) Active tectonics of Himalayan frontal thrust and seismic hazard to Ganga Plain. *Curr Sci* 86(11):1554–1560

20. Nadeshda TNN (2004) Lucknow is on earthquake list. Times of India. <http://timesofindia.indiatimes.com/city/lucknow/Lucknow-isonearthquakelist/articleshow/679471.cms>. Accessed 17 June 2018
21. Boore DM (2004) Estimating V_s (30) (or NEHRP site classes) from shallow velocity models (depths < 30 m). *Bull Seismol Soc Am* 94:591–597
22. IBC (2009) International building code, International code council
23. Seed HB, Idriss IM (1981) Evaluation of liquefaction potential sand deposits based on observation of performance in previous earthquakes. In: ASCE national convention (MO), pp 481–544
24. Ohsaki Y, Iwasaki R (1973) On dynamic shear moduli and Poisson's ratios of soil deposits. *Soils Found* 13(4):61–73
25. JRA (Japan Road Association, 1980) Specification for Highway bridges. Part V, Earthquake Resistant design
26. Tripathi JN, Asharaf S, Singh VB (2011) Shallow seismic refraction survey in Allahabad city (UP), India. *Proc Natl Acad Sci India Sect A-Phys Sci* 81:245–258

Experimental Studies on Controlled Low Strength Materials Using Black Cotton Soils and Comparison of Results with Taguchi Model



B. N. Skanda Kumar, M. P. Naveena, Anil Kumar, A. Shashishankar and S. K. Darshan

Abstract In developing countries like India, due to fast urbanization and rapid development of infrastructure resulted in the use of soft and weak soils around for various Civil Engineering applications. The mechanical behavior of such nature of the soil has to be improved by employing stabilization and reinforcement techniques to make it reliable for construction activities. The black cotton soil is one of the major issues in India. BC soils when exposed to variation in moisture content they undergo high swelling and shrinkage making it more complicated for engineering point of view. The present study investigates the feasibility of controlled low strength material for stabilizing BC soils. The ACI-229R report describes controlled low-strength material (CLSM) as a cementitious material having compressive strength less than 8.3 Mpa (28 days). For the present study, a new greener CLSM comprising Class F fly ash, Cement, Common effluent treatment plant (CETP) Sludge, and Water was developed. The flowability and unconfined compressive strength test was carried out. It was observed from the experimental result that the maximum flowability was 19.8 cm for GF6 and maximum UCS value 0.259 MPa for GF7 mix. After finding the optimum mix, experimental work was carried out by mixing controlled low strength material with black cotton in different proportions. The CBR test was conducted to assess the strength gain of BC soil

B. N. Skanda Kumar (✉)

Department Of Civil Engineering, VTU, CIIRC, Jyothy Institute of Technology, Bangalore, India

e-mail: skandakumar89@gmail.com

M. P. Naveena

Department of Civil Engineering, K. S. School of Engineering and Management, SJC Institute of Technology, Bangalore, Karnataka, India

A. Kumar

Department of Civil Engineering, NMAM Institute of Technology, Mangalore, Karnataka, India

A. Shashishankar

Department of Civil Engineering, AMC Engineering College, Bangalore, Karnataka, India

S. K. Darshan

Department of Civil Engineering, KSSEM, Bangalore, India

© Springer Nature Singapore Pte Ltd. 2020

A. Prashant et al. (eds.), *Advances in Computer Methods and Geomechanics*, Lecture Notes in Civil Engineering 56, https://doi.org/10.1007/978-981-15-0890-5_40

with different proportions of controlled low strength material and it was observed that there was a reduction in overall flexible pavement thickness of 11% by Controlled low strength material as subgrade stabilization. In addition to that, Prediction model was generated using Taguchi's method of design to avoid the conventional trial and error process. The results indicate that there was an increase in the confined compressive strength by increasing the (B/W) ratio.

Keywords Controlled low strength materials · CETP sludge · BC soils · CBR

1 Introduction

The controlled low strength material is a cementitious self-leveling and self-compacting, a cementitious material having compressive strength less than 8.3 MPa at 28 days. The ACI 229R, 1999 and ASTM D 5971-07 define CLSM as "a mixture of soil, fly ash, cement, water, and sometimes admixtures that hardens into material with a higher compressive strength than soil but less than 8.3 MPa". The other names for CLSM are granular fill, K-krete, flowable fill, controlled density fill, liquid dirt, and other trademark names. CLSM can be used for a variety of applications. The production of CLSM is similar to the production of concrete; however, CLSM should not be treated as concrete since coarse aggregates will not be used for the development of CLSM. Industrial waste and by-products from thermal power plants such as pond ash, bottom ash, and fly ash can be used effectively in the production of CLSM [1]. The main advantage of CLSM is that utilization of waste/by-products can be used as constituent materials and thus waste management can be done effectively. The ACI 229R 99 suggests the various nonstandard materials can be used to produce CLSM after suitable testing and if found to satisfy the intended application. In the recent times, other waste and by-products such as foundry sand [2], scrap rubber tire [11], ground granulated blast furnace slag [3], ternary binder blend containing cement, waste gypsum wall boards, GGBFS [4], acid mine sludge [5], cement kiln dust, stone dust and EPS beads [6], incinerated sewage sludge ash and crushed stone powder [7], and waste LCD glass [8] has been reported in the development of CLSM.

Generally, granular fills are widely used for nonstructural filling applications such as trench filling, backfilling, bridge abutment filling, backfill behind retaining walls, and underground pipelines, etc. In applications like trench filling and filling of underground pipelines, it is difficult to obtain the necessary degree of compaction using the conventional compaction equipment [1]. Thus in such situations, controlled low strength materials (CLSM) can be considered as a possible effective alternative. Further, if the compressive strength of CLSM is less than 0.7 MPa 28 days, it is possible for future excavation at a later stage (ACI 229R). For the permanent structural fills the 28 days compressive strength of CLSM should not be less than 8.3 MPa. The main parameters which control the compressive strength of the flowable fills are the constituent elements in the mix, water-cement ratio and the

type of ash used in the mix. The CLSM mixes should have a minimum compressive strength of around 0.44 MPa to provide sufficient support for construction and vehicle loads.

The properties of CLSM can be classified into plastic and in service properties which determine the applicability of CLSM for the engineering applications (ACI 229R) the report describes testing procedures and standards of plastic and in service properties. The plastic properties include flowability, segregation, bleeding, subsidence, hardening time, pump ability, and in service properties Unconfined Compressive Strength (UCS), Unit Weight (Density), Permeability (hydraulic conductivity), Compressibility, Settlement, Excavatability and California Bearing Ratio (CBR).

2 Material Properties

CLSM mixtures used in the present work consisted of proportions of class-F fly ash, CETP sludge, ordinary Portland cement, and water. The mix design was carried out using these industrial wastes/by-products and the feasibility of new CLSM were examined. The primary objective of the work was to maximize the utilization of waste in the development of CLSM. The chemical and physical properties of individual materials are examined as per IS and ASTM standards and the test results are discussed in the subsequent sections.

2.1 Cement

Cement is a primary binding material in CLSM which provides cohesion and strength to the CLSM mixes. ACI 229 R recommends the use of Type-I or Type-II Portland cement in the development of CSLM. Generally, for the low strength CLSM which can be excavated at later stages, the quantity of cement used will range between 1 and 4% [1]. The strength of CLSM depends on the quantity of the cement used and other constituents. For permanent fill, the strength of the CLSM should be more than 8.3 Mpa. For the present study cement used was OPC 43 grade conforming to IS 8112-1989. The physical properties of cement are given in Table 1.

Table 1 Physical properties of OPC 43 grade cement

Properties	Obtained value	Requirements as per is 8112:1989
Fineness	2%	Not more than 10%
Normal consistency	30	27–33
Initial setting time (minutes)	65	Not less than 30
Final setting time (minutes)	215	Not more than 600
Specific gravity	3.16	–

Table 2 Physical properties of Class F fly ash

Properties	Value
Specific gravity	2.04
Blaine's Fineness (m^2/kg)	234
Percent retained on 45 μm sieve	12.2
Percent retained on 45 μm sieve	1.6

Table 3 Chemical analysis of Class F fly ash

Parameters	Test method	Results
Iron as Fe_2O_3 %	ASTM C114-2011b	11.95
Alumina as Al_2O_3 %	ASTM C114-2011b	21.08
Calcium as CaO %	IS:5949:1990 (Reaff. 2010)	5.71
Silica as SiO_2 %	ASTM C114-2011b	47.64
Moisture as MOI %	ASTM C 311-11b	0.23
Sulphates as SO_3 %	ASTM C114-2011b	0.850
Loss of ignition %	ASTM C114-2011b	4.36

2.2 Fly Ash

CLSM is frequently proportioned with fly ash or slag to enhance workability and pump ability, and reduce segregation, bleeding, shrinkage, or settlement. Generally, coal-based fly ash is utilized in CLSM to enhance flowability and segregate resistance. Use of high fly ash content in CLSM is recommended in ACI-229R report. In general, Class F fly ash may be utilized in the range of 60–1200 kg/m^3 . In the present examination, class F fly ash was utilized and was acquired from Raichur Thermal Plant. Physical properties and chemical composition of fly ash are given in Tables 2 and 3.

2.3 Common Effluent Treatment Plant Sludge (CETP)

Various nonstandard materials are utilized in the development of CLSM mixtures depending upon project necessities and after testing their acceptability in CLSM mixtures. In the present study, Common Effluent Treatment Sludge is utilized in various proportions for obtaining CLSM mixes. The physical and chemical testing of CETP sludge has been carried out and it was found that CETP satisfy the general requirements of CLSM. The results of physical and chemical analysis of CETP sludge is given in Tables 4 and 5, respectively.

CETP sludge is generated in huge quantities. For the present study, CETP sludge material was obtained from one of the common effluent treatment plants in

Table 4 Physical properties of CETP sludge

Parameter	Test results
Dry Powder Density (kg/m^3)	
Loose	485
Rodded	571
pH (10% suspension)	9.56
Specific gravity	2.186

Table 5 Chemical composition of CETP sludge

Chemical composition	Base (100)%
Silica	21.6
Aluminum oxide	2.0
Calcium oxide	8.3
Iron	4.3
Magnesium oxide	0.89

Bangalore, Karnataka. The average quantity of sludge generated in one such plant could be in the range of 40–50 tons/month. The disposal of such huge quantities of sludge generated is a big challenge. The sludge being generated across various CETP'S in India, are disposed as landfills causing massive impact on health and environment.

A thorough chemical analysis was carried out on the sludge sample. Table 5 shows the chemical composition and was found that sludge predominantly contains silica and calcium oxide.

2.4 Black Cotton Soil

In India, expansive soils are called as Black Cotton soil. In the present study, the black cotton soil is collected from Gulbarga North Karnataka India. The physical test on BC soils was conducted as per IS: 2720 and the results are shown in Table 6.

Table 6 Physical characteristics of black cotton soil

Description	Value
Liquid limit (%)	54
Plastic limit (%)	20
Shrinkage limit (%)	8.3
Specific gravity	2.8
Free swell Index	High

3 Experimental Program

In the present study, total of nine CLSM mixes proportion were developed. Flowability, unconfined strength and California bearing ratio (CBR) were analyzed and assessed. To determine the maximum and minimum flowability value of CLSM mix, trial mixes were first prepared with different water contents, proportions. Table 7 gives the mix proportion for the GF1 to GF9, series with respect to Fly ash, CETP sludge, and cement. For each series four specimens were casted for water content 25, 29, 30, and 32%. The fixed proportions of materials were collected in a pan and mixed in the dry state and water was added to the dry mix and uniform mortar mix using a pan mixer. The flowability and normal consistency of fresh CLSM were measured by spread flow test and Vicat apparatus. Unconfined compression strength tests were conducted for 28 days. Based on the Maximum value of unconfined compressive strength of the CLSM mix, the CBR test was conducted to carry out the pavement design as per IRC 37-2012.

3.1 Grain Size Distribution Curve

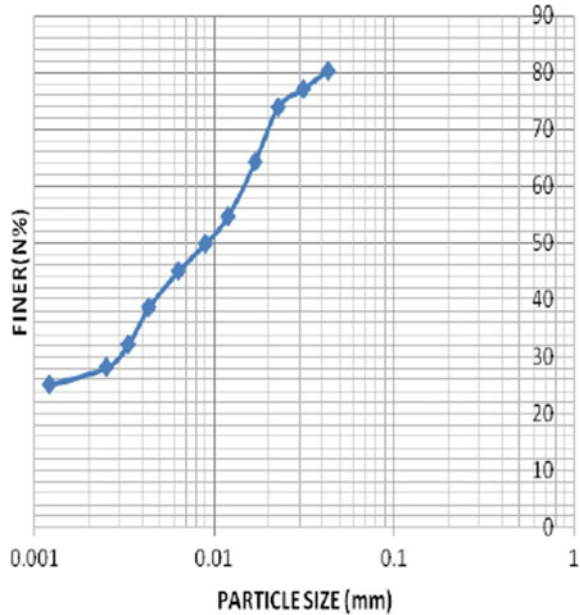
The grain size distribution curve of a black cotton soil carried out using Hydrometer analysis as shown in Fig. 1.

Table 7 Mix proportion of CLSM

Mix proportion	GF1	GF2	GF3	GF4	GF5	GF6	GF7	GF8	GF9
Class F fly ash (gm/100 gm)	65	70	75	80	82	85	90	95	100
CEPT sludge (gm/100 gm)	30	25	20	15	13	10	5	2.5	0
Cement (gm/100 gm)	5	5	5	5	5	5	5	2.5	0
F/C ratio	13	14	15	16	16.4	17	18	38	–
S/C ratio	6	5	4	3	2.42	2	1	1	0

Note Mixes with cement, Class F fly ash and CEPT Sludge are named as GF series and water content is varied as 25, 29, 30 and 32% (by weight of total mixture content)

Fig. 1 Grain size distribution curve of black cotton soil



4 Results and Discussions

4.1 Flow and Strength

The Flowability and unconfined compression strength of GF series are given in Table 8. Most of the mixtures have flow within the specified normal range (15–20 cm) as per ACI229R. The maximum flow was achieved for GF6 mix of 19.8 cm and maximum UCS of 0.259 MPa, for GF7 mix, which indicates the higher water demand of the mixes due to increase in Fly ash content and optimum sludge contents, both are very fine materials. Each mix has been examined for various water content to achieve flowability in the range of 15–20 cm as per ACI 229R.

4.2 Design of Flexible Pavement Thickness

The California bearing ratio test was conducted as per IS-2720 (1987) to assess the strength of the subgrade soil of a pavement. The test was conducted on BC soil amended with different percentages of CLSM. The value of the CBR test was utilized to decide the thickness of the flexible pavement layer as per IRC standards and tabulated in Table 9.

The soil and CLSM were blended and compacted to its optimum moisture content to achieve the maximum dry density. GF7 mix was selected as an optimum

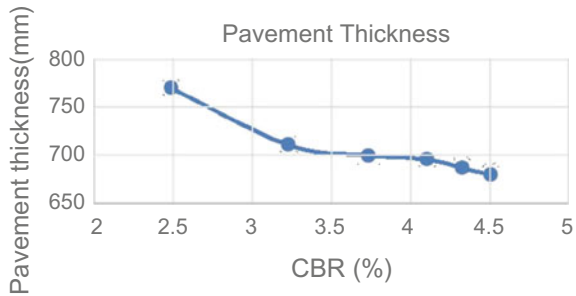
Table 8 Flowability and unconfined strength results for CLSM mixes of GF series

Mix ID	Water percentage	B/W ratio	Flowability (cm)	Average compressive strength (MPa) 28 days
	25	2.8	10	0.196
	29	2.41	15.9	0.183
GF 1	30	2.33	17.1	0.180
F/C = 13	32	2.18	19.7	0.174
GF 2	25	3	10	0.203
F/C = 14	28	2.67	15	0.192
	30	2.5	17.5	0.186
	32	2.34	20	0.180
	25	3.2	10	0.210
GF 3	28	2.85	15.2	0.198
F/C = 15	30	2.66	17.8	0.191
	31	2.58	19.2	0.189
	25	3.4	11.7	0.218
	28	3.03	15.5	0.204
GF 4	30	2.83	18.2	0.197
F/C = 16	31	2.74	19.5	0.194
	25	3.48	11.7	0.220
GF 5	28	3.10	15.6	0.207
F/C = 16.4	30	2.9	18.3	0.200
	31	2.80	19.6	0.196
	25	3.6	12	0.225
GF 6	27	3.3	15.9	0.214
F/C = 17	30	3	18.5	0.203
	31	2.90	19.8	0.200
	25	3.8	12.6	0.245
	27	3.51	15.35	0.259
GF 7	30	3.16	19.25	0.209
F/C = 18	35	2.71	25	0.193
GF 8	25	3.9	13	0.235
F/C = 19	27	3.61	15.45	0.225
	30	3.25	19.5	0.212
	35	2.78	25	0.196
	25	4	15	0.230
GF 9	29	3.44	19.8	0.219
F/C = 0	30	3.33	21.3	0.215
	35	2.87	25	0.199

Table 9 CBR and pavement thickness for selected CLSM mixes of GF 7 series

Mix ID	Particulars	CBR value (%)	Total pavement thickness (mm) as per IRC 37-2012
	Black cotton soil	2.48	770
	BC + 50% CLSM	4.5	680
	BC + 60% CLSM	4.32	687.2
	BC + 70% CLSM	4.10	696
GF 7	BC + 80% CLSM	3.73	700
	BC + 90% CLSM	3.22	711

Fig. 2 Variation between CBR value and pavement thickness



mixture and CBR test was conducted on this mix. Results showed that the CBR value obtained was maximum for BC + 50% CLSM mix. The thickness of pavement was determined as per IRC37-2012.

Figure 2, shows the variation of pavement thickness of black cotton soil and CLSM mix with Various CBR value. It was observed that, as the CBR value decreases, the pavement thickness Increases.

4.3 Analytical Investigation

The Prediction of a CLSM property with Fly ash and CETP sludge and cement was investigated by using the Taguchi method. Design of experiment was performed by Mini Tab software using L9 orthogonal array to accommodate two factors with three levels. These factors were the (B/W ratio) and water content in the CLSM mix. The results indicate that there was an increase in the Flowability by increasing the water content and UCS with increasing (B/W) ratio. In the Taguchi method, analysis results show close to experimental results (Figs. 3a, b and 4).

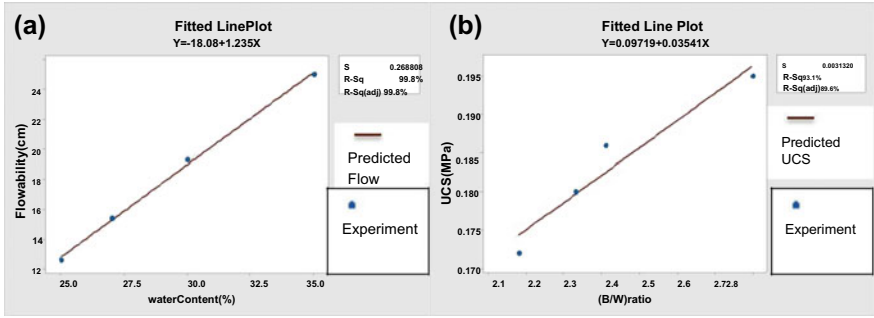


Fig. 3 Validation of Taguchi model for flowability and unconfined compression strength

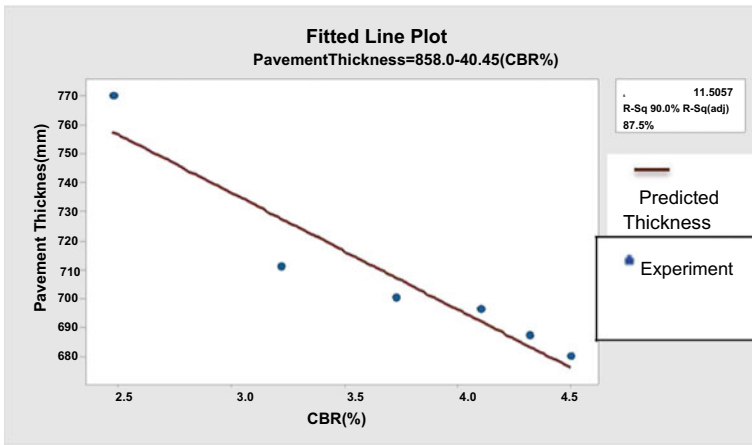


Fig. 4 Validation of Taguchi model for pavement thickness

4.3.1 Comparison of Predicted Values by Taguchi Models and Experimental Results

The Taguchi design model is prepared to predict the values of Flowability, UCS, and Pavement thickness. It is observed from the model result the flowability shows R^2 value of 99.8%, UCS shows 92.16%, and Pavement thickness of 90% generated for GF7 series. The predicted values fairly match the experimental results within the accuracy levels needed for engineering decisions.

5 Conclusions

1. CLSM mixes comprising cement + CEPT sludge + Class F fly ash, attained maximum flowability of 19.8 cm and maximum compressive strengths ranged from 0.196 to 0.259 MPa at 28 days.
2. The validation of Taguchi design models for flow and strength has been examined for GF7 series. The predicted values from Taguchi design models fairly matched experimental values suitable for engineering purposes.
3. The total pavement thickness was found to be 770 mm when black cotton soil as subgrade soil and pavement thickness was reduced to 680 mm when black cotton soil was blended with 50% CLSM (GF7). It is observed there was a reduction in overall pavement thickness by 11% using CLSM as subgrade stabilization.
4. In the present study, the CLSM was developed by utilizing waste and industrial by-products such as CETP Sludge and Class F fly ash and was found to be beneficial for pavement subgrades applications. This could be an effective solution for the burning problems associated with the disposal of waste materials.

References

1. LiniDev K, Robinson RG (2015) Pond ash based controlled low strength flowable fills for geotechnical engineering applications. *Int J Geosynth Ground Eng* 1:32. <https://doi.org/10.1007/s40891-015-0035-1>
2. Naik TR, Singh SS (1997) Flowable slurry containing foundry sands. *J Mater Civil Eng* 93–102
3. Raghavendra T, Udayshankar BC (2015) Flow and strength characteristics of CLSM using ground granulated blast furnace slag. *Am Soc Civil Eng*. [https://doi.org/10.1061/\(ASCE\)MT.1943-5533.0000927](https://doi.org/10.1061/(ASCE)MT.1943-5533.0000927)
4. Raghavendra T, Siddanagouda YH, Jawad F, Adarsha CY, Udayshankar BC (2016) Performance of ternary binder blend containing cement, waste gypsum wallboards and blast furnace slag in CLSM. *Proc Eng* 145:104–111. Elsevier, Sciencedirect
5. Gabr MA, John J (2000) Bowders controlled low-strength material using fly ash and AMD sludge. *J Hazard Mater* 76:251–263. Elsevier Science
6. Marjive VR, Badwaik VN, RamRathanLal B (2016) Experimental studies on controlled low strength material using stone dust and EPS beads. *Int J Eng Technol* 8(4)
7. Fujita R, Horiguchi T, Kudo T, Shimura K (2010) Second international conference on sustainable construction materials and technologies. Università Politecnica delle Marche, Ancona, Italy. ISBN 978-1-4507-1490-7, <http://www.claissse.info/Proceedings.htm>
8. Wang HY (2009) A study of the engineering properties of waste LCD glass applied to controlled low strength materials concrete. *Constr Build Mater* 23:2127–2131. Elsevier Science
9. ACI Committee 229 (1999) Controlled low-strength material (CLSM) (ACI 229R99). American Concrete Institute
10. ASTM D 5971—07 (2007) Standard practice for sampling freshly mixed controlled low-strength material. ASTM International, West Conshohocken, pp 7–9

11. Cheung T, Jansen DC, Hanson JL (2008) Engineering controlled low strength materials using scrap tilerubber
12. IS:2720 (part 16) (1987) Methods of test for soil
13. Indian Road Congress IRC (2012) Guidelines for the design of flexible pavements (Third Revision)

Strength Improvement of Locally Available Sand Using Enzymatically-Induced Calcite Precipitation



P. B. Kulkarni and P. D. Nemade

Abstract In the present study laboratory experiments were conducted for the strengthening of locally available river sand of Bhima river (Maharashtra, India) using sword bean extracted as a urea catalyst in place of microorganisms like *Sporosarcina pasteurii*, which leads to decomposition of urea into ammonia and carbonates. As a calcium source, calcium hydroxide and calcium chloride were considered and mixed separately with sand to observe precipitation of calcite within the matrix of sand. At room temperature, sand matrix with the extract of Sword bean was compacted into a cylindrical specimen and cured for four days and similar specimen without plant extract (virgin sample) was prepared for comparison. With different calcium sources and amounts of urea, unconfined compression tests (UCS) were conducted on treated and untreated sand. It is observed that, with increasing amounts of urea, increase in the UCS for the specimens having calcium chloride has enhanced considerably compared to calcium hydroxide. Sand treated with extract of sword beans has shown higher increase in UCS (324 kPa) as compared to that of without plant extract. It was observed that, calcium chloride is a more effective calcium source when compared with calcium hydroxide.

Keywords Locally available sand • Sword bean extract • Microorganisms • Calcite precipitation • Unconfined compression strength (UCS)

P. B. Kulkarni (✉)

Research scholar, Dr. D. Y. Patil Institute of Technology, Pimpri, Pune 411018, India

e-mail: urpbkulkarni@gmail.com

Vishwakarma Institute of Information Technology, Pune, India

P. D. Nemade

Savitribai Phule Pune University, Pune, Maharashtra, India

e-mail: pravin.nemade@gmail.com

© Springer Nature Singapore Pte Ltd. 2020

A. Prashant et al. (eds.), *Advances in Computer Methods and Geomechanics*, Lecture Notes in Civil Engineering 56, https://doi.org/10.1007/978-981-15-0890-5_41

1 Introduction

Nowadays enhancement of soil properties using biomediated methods like microbially induced calcite precipitation (MICP), Biopolymers, and biofilms are developed [1]. Initially, the precipitation of calcium carbonate due to microbial activity was claimed [2, 3]. Application of MICP using urea hydrolysis is most popular and extensively explored [4]. These carbonate anions (CO_3^{2-}) produced from decomposition of urea, combines with calcium cations to produce calcites (CaCO_3) [2, 5]. The decomposition of Urease by the hydrolysis of urea produces 2 mol of ammonia and 1 mol of carbonate per mole of urea. These carbonate anions produced from decomposition of urea combine with calcium cations resulting in the formation of calcite (carbonate crystals). This calcite mineral closes the gap between the existing sand grains, resulting in the grain/particle movement and thereby improves the strength and stiffness of the sand [6]. The conversion of loose sand into sandstone happens due to filling of pores spaces and cementing sand grains due to production of Urease-induced calcite crystals [2, 7]. The efficacy of these mechanisms was verified for healing concrete cracks [8], waste treatment [9], water erosion control [10], improving liquefaction resistance [11], improving the permeability of porous media, and Cementation in a matrix of loose sandy soil [12]. Bioremediation of weathered building [13], enhancement durability of Building [14], uniform transport, and attachment of bacteria into deep soil layers was studied [7]. Use of MICP in various applications in civil engineering aspects was studied by earlier researchers. Manufacturing of Portland cement leads to generation of large amount of carbon dioxide.

The focus of research in this area was based on its importance due to environment friendly materials and can substitute Portland cement. The various methods to improve effect of MICP using different nutrient, urease enzyme. Different ways to achieve calcite precipitation were carried out by researchers. Lactose mother liquor which is industrial effluent of dairy was used as growth medium as alternative nutrient source [15] for production of microbial concrete [16, 17]. The indigenous microbes which are live cells does have certain limitations in their urease function depending on selection and suitability of nutrients, moisture content, pH, and temperature. Biomineralization of calcite from locally available plant extract is a promising alternative.

In this research, the suitability of locally available plant, sword bean was used. Instead of microbes, sword bean extract as urease catalyst in combination of two different calcium sources were used, to form calcite within the locally available sand. The effect of calcite precipitation using sword bean extract on granular soil was investigated in terms of unconfined compressive strength (UCS). Evidence of calcites precipitation was verified through SEM and XRD test.

2 Materials and Methods

2.1 Sample Preparation and Test Specimens

Extraction of locally available plant sword bean has been carried out. Figure 1 shows the sword bean used for experimentations. Mineralogical composition and engineering properties of Bhima river sand are mentioned in Tables 1 and 2, respectively. The silica content in sand was observed to the extent of 64% and is rounded in shape. Sieve analysis was carried out as per IS and results are shown in Fig. 2, it is well-graded.

Sword bean extract and ureas were mixed in the sand to generate carbonate ions. Precipitation of calcite was obtained by using calcium source, calcium hydroxide $\text{Ca}(\text{OH})_2$, and calcium chloride (CaCl_2). Sword bean extract was varied in the range 0–25 ml and Urea from 4 to 20 gm. Sword bean extract was added to urea, to decompose urea into ammonia and carbonate. The solution thus prepared was kept for three days in sealed condition at room temperature to achieve carbonate solution. An equal amount of extract and urea were added in order to get decomposition of urea fully [18]. Ten grams of calcium source was equally added to all carbonate solutions for achieving yielding of calcite solution. Calcite solution was mixed with sand systematically and mix was divided into three parts. Each portion of mix was compacted in mold of size 50 mm diameter and 100 mm height. Finally sand sample thus compacted was removed from the mold and allowed to air cure for

Fig. 1 Sword bean

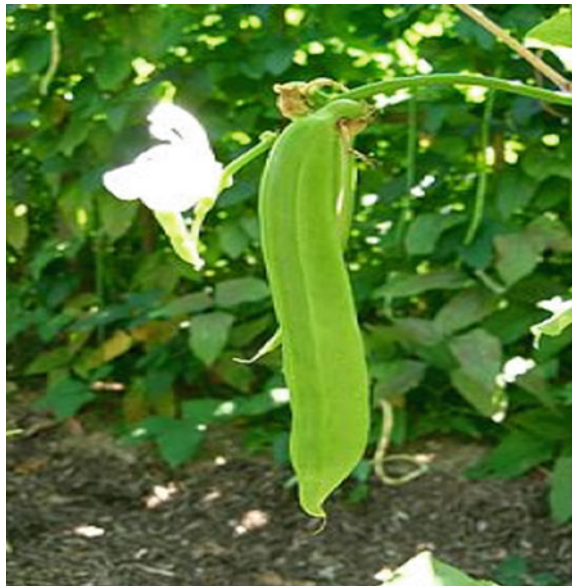


Table 1 Mineralogical composition

Classification	SiO ₂	Al ₂ O ₃	K ₂ O	Na ₂ O	Fe ₂ O ₃	CaO	TiO ₂
Content	64.2	14.07	3.97	1.8	3.91	0.88	0.30

Table 2 Bhima river sand properties

Specific gravity (Gs)	Mean grain size (D50) mm	Effective grain size (D10) mm	Coefficient of curvature (Cc)	Coefficient of uniformity (Cu)	Minimum void ratio (e min)	Maximum void ratio (e max)
2.63	0.38	0.15	0.54	2.66	0.78	1.2

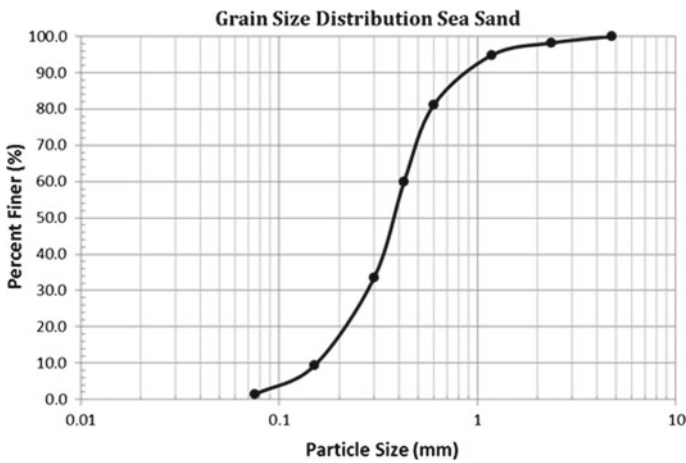


Fig. 2 Sieve analysis of Bhima river sand

three days at room temperature. Triplicate sample of each run was prepared and tested for unconfined compression test. UCs test on cemented sand specimens was carried out at shearing rate of 1% per minute to understand strength and deformations.

3 Results and Discussion

The unconfined compressive stress–strain behavior of Bhima river sand is has been carried out. These results were obtained with calcite precipitation using Sword bean extract, urea, and calcium. Figure 3a and b presents results for specimens treated with calcium chloride and calcium hydroxide as a calcium source. Virgin samples CCL-0 and CCH-0 were prepared without sword bean extract which clearly

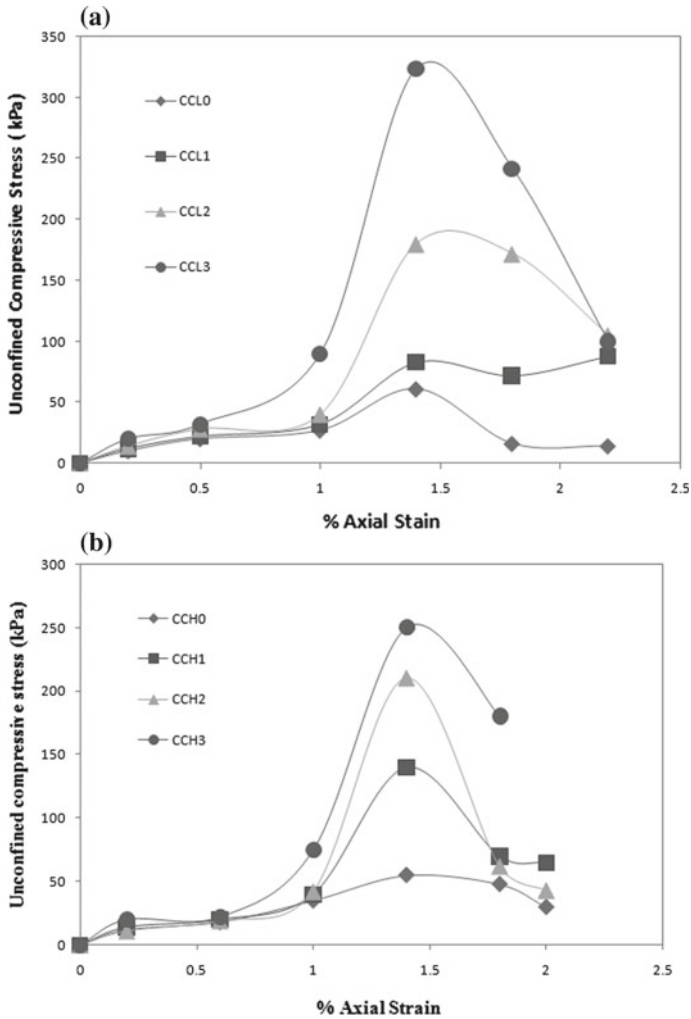


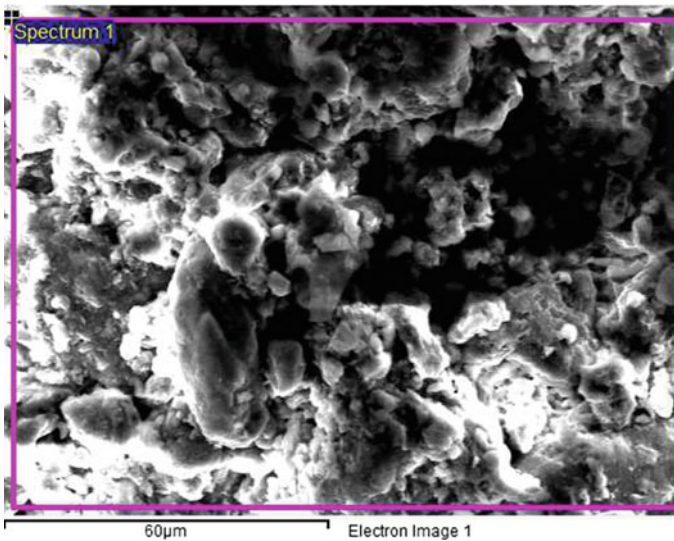
Fig. 3 a Results of unconfined compression test using calcium chloride, b results of unconfined compression test using calcium hydroxide

indicates no calcite precipitation occurred within sand grain matrix, therefore, the specimens CCL-0 and CCH-0 have the lowest UCS values as compared to other specimen having same calcium source. The measured UCS and axial strain along with amount of calcite precipitation is shown in Table 3.

It is observed from Table 3 that UCS strength is directly proportional to increase in urea and sword bean extract and is independent of calcium source used. The maximum value of UCS of 324 kPa was observed for the specimen CCL-3 as seen from Fig. 4. The UCS value of 324 kPa is nearly 5.3 times as that of Virgin samples CCL-0. This is mainly because of calcite precipitation in the specimen

Table 3 Unconfined compression test results

Run no	Calcium source	Sword bean extract (mL)	Urea/water (g/mL)	Water content (%)	Dry density (g/cm ³)	% Axial strain at peak strength	Unconfined compressive strength (kPa)	% Precipitated calcite
CCL-0	CaCl ₂	0	20/40	2.68	1.5	0.79	61	0
CCL-1	CaCl ₂	4	4/40	3.20	1.44	1.8	83	2.30
CCL-2	CaCl ₂	8	8/40	2.52	1.46	2	180	4.85
CCL-3	CaCl ₂	20	20/40	2.1	1.52	1.7	324	6.30
CCH-0	Ca(OH) ₂	0	20/40	1.65	1.4	2.1	55	0
CCH-1	Ca(OH) ₂	4	4/40	0.36	1.42	1.7	140	3.51
CCH-2	Ca(OH) ₂	8	8/40	0.8	1.47	1.75	210	3.8
CCH-3	Ca(OH) ₂	20	20/40	0.4	1.52	1.6	250	4.6

**Fig. 4** Scanning electron monograph (SEM)

CCL-3. A similar pattern of increase in UCS was observed in a specimen having calcium hydroxide as calcium source. The UCS value of the specimen CCH-3 was 250 kPa and is nearly 4.5 times as that of Virgin samples CCH-0. The test result, i.e., UCS of 324 kPa–250 kPa obtained is similar to that of silica sand mixed with 4% Portland cement [19].

It is seen that out of the two calcium source used, calcium chloride is more effective as compared to calcium hydroxide because of higher solubility of calcium chloride as compared to calcium hydroxide at same temperature. The low solubility gives smaller amount of calcium ions dissolved in solution, thereby less precipitation of calcites. It is observed that, when calcium hydroxide was used as calcium

source, large amount of ammonium gas was generated and water gets evaporated at early stage of reaction and the colour of specimen changed to white colour. The % of water content in CCH specimens is on lower side as compared to CCL specimens (Table 3). It also illustrates the UCs test results of all samples with different runs.

4 Scanning Electron Microscopy (SEM), X-Ray Diffraction (XRD)

SEM analysis was carried out to measure cementation by way of calcite precipitation occurred in a sample and the corresponding amount of sword bean extract used. Magnification obtained for each sample was 30, 60, and 100. Figure 4 shows a sample SEM image at 60 magnification. SEM analysis indicates that, use of high amount of sword-bean extract and urea leads to higher amount of calcite precipitation. This trend was noticed in both calcium sources used.

The amount of calcite precipitation in sandy soil can be quantified by methods such as thermogravimetric analysis [16, 17], washing with acetic acid [20], or XRD analysis. XRD analysis was carried out to understand qualitative precipitation of calcite. A small amount of oven-dried sample was collected and crushed from a sample which was tested for UCS. It was crushed to a powder form and was sieved through 0.075 mm.

The results of XRD analysis of specimen CCL-3 using calcium chloride as calcium source gives calcite peak as observed in Fig. 5. From XRD analysis it was revealed that the amount of % precipitated calcite was between 2.3 and 6.30 for CCL specimens and 3.51–4.6 for CCH as mentioned in Table 3. As the amounts of urea and sword bean extract used in each specimen increased, the precipitated calcite gradually increased, regardless of the calcium source.

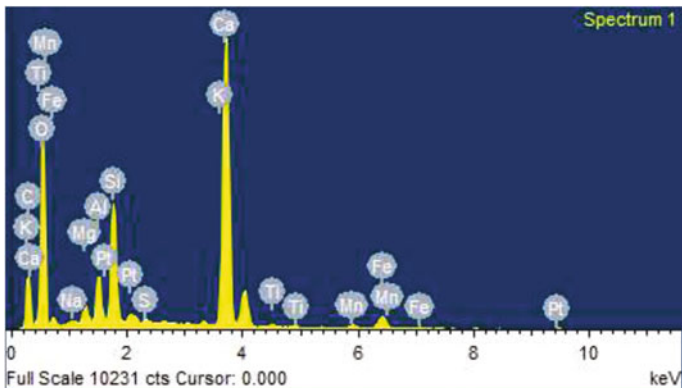


Fig. 5 X-Ray diffraction (XRD)

The calcium chloride as the calcium source has shown highest calcite precipitation, due to high solubility of calcium chloride. The UCS was positively correlated with the precipitated amount of calcite. Other researchers [5, 20–22] also showed that the strength or stiffness of soils increased with increasing amounts of precipitated calcite. They reported that at least 4% of calcite precipitation is required for substantial strength increase.

5 Conclusion

As an alternative to microbes, a plant (sword bean) extract was used to decompose urea into carbonate and ammonium ions. The carbonate ion obtained from decomposition of urea was combined with calcium ion to cause calcite precipitation within the sand. Calcium chloride and calcium hydroxide were used as calcium sources. Bhima river sand was treated with various amounts of sword bean extract, urea, and different calcium sources and then cured for four days. Unconfined compression tests were carried out on the treated sand and the following results were obtained.

UCs strength is directly proportional to the increase in urea and sword bean extract and is independent of calcium source used.

Increase in the amounts of urea and sword bean extract, there is a gradual increase in the % precipitation of calcite.

The maximum value of UCS of 324 kPa was observed, which is nearly 5.3 times as that of Virgin samples, because of calcite precipitation.

The strength of the specimen using calcium chloride was higher than those using calcium hydroxide.

XRD analysis shows that the amount of % precipitated calcite was between 2.3 and 6.30 for CCL specimens and 3.51–4.6 for CCH.

Results obtained are validated with the standard, i.e., at least 4% of calcite precipitation is required for substantial strength increase. Similar results have been reported by [5, 20–22].

Acknowledgements The authors would like to express their sincere thanks to Principal, D. Y. Patil Institute of Technology, Pimpri, Pune. Thanks also to Dr. P. D. Nemade for full support and being the source motivation.

References

1. DeJong JT et al (2013) Biogeochemical processes and geotechnical applications: progress, opportunities and challenges. *Geotechnique* 63(4):287–301
2. DeJong JT, Fritzes MB, Nüslein K (2006) Microbially induced cementation to control sand response to undrained shear. *J Geotech Geoenviron Eng* 132(11):1381–1392

3. Stocks Fischer S, Galinat JK, Bang SS (1999) Microbiological precipitation of CaCO_3 . *Soil Biol Biochem* 31(11):1563–1571
4. Martinez BC (2012) Experimental and numerical upscaling of MICP for soil improvement. PhD thesis, University of California, Davis, CA
5. Whiffin VS, Van Paassen LA, Harkes MP (2007) Microbial carbonate precipitation as a soil improvement technique. *Geomicrobiol J* 24(5):417–423
6. Harkes MP, Van Paassen LA, Booster JL, Whiffin VS, Van Loosdrecht MCM (2010) Fixation and distribution of bacterial activity in sand to induce carbonate precipitation for ground reinforcement. *Ecol Eng* 36(2):112–117
7. Burbank M, Weaver T, Lewis R, Williams T, Williams B, Crawford R (2013) Geotechnical tests of sands following bio-induced calcite precipitation catalyzed by indigenous bacteria. *J Geotech Geoenviron Eng* 139(6):928–936
8. Ramachandran SK, Ramakrishnan V, Bang SS (2001) Remediation of concrete using micro-organisms. *ACI Mater J* 98(1):3–9
9. Chu J, Ivanov V, Lee MF, Oh XM, He J (2009) Soil and waste treatment using biocement. In: Proceedings of the international symposium on ground improvement technologies and case histories, ISGI'09. Geotechnical Society of Singapore, pp 165–170
10. Bang S, Min SH, Bang SS (2011) Application of microbiologically induced soil stabilization technique for dust suppression. *Int J Geo-Eng* 3(2):27–37
11. Montoya BM, DeJong JT, Boulanger RW (2013) Dynamic response of liquefiable sand improved by microbial induced calcite precipitation. *Geotechnique* 63(4):302–312
12. Sari ZN, Yuksekdag AG, Dursun Y, Cinar B (2011) Cementation in a matrix of loose sandy soil using biological treatment method. *Afr J Biotech* 10(38):7432–7440
13. Webster A, May E (2006) Bioremediation of weather-building stone surfaces. *Trends Biotechnol* 24(6):255–260
14. Achal V, Abhijit M, Sudhakara Reddy M (2011) Microbial concrete: a way to enhance durability of building structures. *J Mater Civ Eng* 23(6):730–734
15. Achal V, Mukherjee A, Basu PC, Reddy MS (2009) Lactose mother liquor as an alternative nutrient source for microbial concrete production by *Sporosarcina pasteurii*. *J Ind Microbiol Biotechnol* 36:433–438
16. Park SS, Kim WJ, Lee JC, Choi SG (2014) Effect of microbially induced calcite precipitation on strength of cemented sand. *New Front Geotech Eng GSP* 243:47–56
17. Park SS, Choi SG, Nam IH (2014) Effect of plant-induced calcite precipitation on the strength of sand. *J Mater Civ Eng* 26:06014017–06014022
18. Nam I-H, Chon CM, Jung KY, Choi SG, Choi H, Park SS (2015) Calcite precipitation by ureolytic plant *Canavalia ensiformis* extracts as effective biomaterials. *KSCE J Civ Eng* 19(6):1620–1625
19. Park SS, Kim KY, Choi HS, Kim CW (2009) Effect of different curing methods on the unconfined compressive strength of cemented sand. *J Korean Soc Civ Eng* 29(5C):207–215 (in Korean)
20. Burbank MB, Weaver TJ, Green TL, Williams BC, Crawford RL (2011) Precipitation of calcite by indigenous microorganisms to strengthen liquefiable soils. *Geomicrobiol J* 28(4):301–312
21. Burbank MB, Weaver TJ, Williams BC, Crawford RL (2012) Urease activity of ureolytic bacteria isolated from six soils in which calcite was precipitated by indigenous bacteria. *Geomicrobiol J* 29(4):389–395
22. Van Paassen LA, Ghose R, van der Linden TJM, van der Star WRL, van Loosdrecht MCM (2010) Quantifying biomediated ground improvement by ureolysis: large-scale biogROUT experiment. *J Geotech Geo Environ Eng* 136(12):1721–1728

Bio-treatment of Fly Ash



Archika Yadav, K. Vineeth Reddy, Md. Muzaffar Khan,
G. Kalyan Kumar and Amitava Bandhu

Abstract Fly ash, a waste product from coal combustion, is posing disposal problem all over the world. It is being used in various civil engineering works such as in embankment works and fill materials, etc. The strength of fly ash is very much less compared to the natural soils and hence needs to be improved. A relatively new method of injecting bacteria to bind the soil particles known as Microbial Induced Calcite Precipitation (MICP) was proven to be very effective in the stabilization of poorly graded sands. In the present study, an attempt is made to study the effects of bio-treatment of fly ash using the *Sporosarcina Pasteurii* to promote calcite precipitation from urea hydrolysis. Single staged injection was adopted for introducing bacteria into the fly ash. A standard bacterial cell concentration and varied urea-calcium chloride were adopted for treating fly ash specimens. Unconfined Compression Strength tests (UCS) revealed an increase in strength ranged from 41.19 to 183.31 kPa. Approximately one order of magnitude reduction in the coefficient of permeability values was observed.

Keywords Bio-treatment · MICP · Urea hydrolysis · UCS and permeability

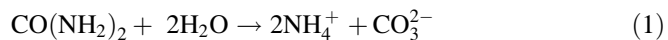
1 Introduction

The infrastructure development is to be supplemented with the competent soil conditions in order to meet the growing needs of society. Availability of such competent soils is decreasing day by day. Hence the available incompetent soils are needed to be stabilized. The conventional ground improvement techniques include densification of soil using mechanical means or by grouting techniques, Karol [1]. On the other hand, production of fly ash, a coal combustion waste products being increased day by day.

A. Yadav (✉) · K. Vineeth Reddy
Civil Engineering, Anurag Group of Institutions, Hyderabad, India
e-mail: archika1993@gmail.com

Md. Muzaffar Khan · G. Kalyan Kumar · A. Bandhu
Civil Engineering Department, NIT Warangal, Warangal, India

Disposal of these waste materials is usually done by filling the low lying areas. Million tons of fly ash being produced requires several hectares of valuable land. Already fly ash found its applications in several ways of civil engineering constructions. Fly ash is being used in the manufacture of cement concrete, soil stabilization, embankment constructions, and so on. Bearing capacity of the embankments constructed using fly ash is comparatively very less. Hence it needs to be stabilized using ground improvement techniques. In recent years, natural and more sustainable biologically based alternative methods have emerged to stabilize the geo-materials, Mitchell and Santamarina [2], Ivanov and Chu [3], DeJong et al. [4]. Bio-stabilization involves the injection of naturally occurring or engineered microorganisms which produce an inorganic cementing material using biological processes, NRC [5]. The process of altering the engineering properties of geo-materials using by-products of a network of chemical reactions being controlled and managed within soil system is referred to as Bio-mediated improvement of soils, DeJong et al. [6]. Experiments on soil strengthening methods utilizing biological means have been restricted largely to laboratory scale studies of calcite precipitation to be used as binding material in sand stabilization and further research is being carried out to evaluate the full potential of this technique. MICP has been proven to be a viable alternative of soil improvement applications such as embankments, liquefiable soil deposits, and reinforcement in subgrade, etc., and the improvement in shear strength of bio-stabilized soil was because of the formation of effective bridges between the sand grains at contact points, Cheng et al. [7]. The urease enzyme released by the bacterial medium plays a key role in biological precipitation of calcite through urea hydrolysis, Bachmeier et al. [8]. The process of MICP could be achieved through many processes. But the MICP through urea hydrolysis is found to be more favorable because of its energy efficiency and ubiquity of urease-producing microorganisms, Khodadadi et al. [9]. The urea hydrolysis promoted by the urease enzyme and the precipitation of calcium carbonate has a productive impact on soil strengthening process, Carmona et al. [10]. MICP is the process of precipitation of calcium carbonate by bacterial means through urea ($\text{CO}(\text{NH}_2)_2$) hydrolysis.



Bio-cemented sand specimens treated using MICP reported reduction in soil settlement, DeJong et al. [6], increase in shear strength of soil, Ismail et al. [11], Chou et al. [12], DeJong et al. [13] and improvement in soil stiffness, Feng and Montoya [14], Montoya and DeJong [15], Lin et al. [16]. Large-scale studies carried on 100 m^3 of sand proved the efficacy of MICP in improving large areas, Van Paassen et al. [17]. The increase in shear strength of treated sand and the produced amount of calcite content may not be proportional to each other, Whiffin et al. [18]. Hence it is necessary to understand the efficacy of the improvement process in order to carry out field applications. In the present study, the MICP process was used to strengthen the fly ash specimens. The aim of the present

research is to develop a new and innovative ground improvement alternative for use of Fly ash in civil engineering practice that utilizes MICP. The objective of this research is to investigate the effects of bio-treatment on the engineering properties of fly ash. For this purpose, a standard procedure was verified and adopted for bacteria cultivation and injection of bacteria into the specimens. The significance of the study is to improve the quality of geo-materials in a reliable and more sustainable way by finding alternatives to traditional stabilization methods.

2 Materials

In the current study, several materials including fly ash, *Sporosarcina Pasteurii* (bacteria) and mixtures of the liquid medium.

2.1 Fly Ash

The fly ash used for the study was obtained from Sri Damodaram Sanjeevaiah Thermal Power Station located in Nelaturu Village of Nellore district, Andhra Pradesh, India. The index properties of fly ash were found based on several experiments as per IS 2720. The chemical composition of fly ash was found using EDAX (Energy Dispersive X-Ray Analysis), presented in Table 1 and the fly ash was identified to belong to Class F according to ASTM C618 [19] since the lime concentration was less than 7%. The fly ash used could be identified as pozzolanic in nature. For successful treatment, compatibility between the fly ash particle distribution and size of bacteria is an important factor. The movement of the microorganism (bacteria), 0.5–3.0 μm in length is to be allowed in the soil pores, Mitchell and Santamarina [2]. The most favorable particle size range was reported as 50–400 μm for bacterial activity to be carried out in soil pores [20].

Table 1 Chemical composition of Fly ash

Chemical constitute	Composition (%)
CaO	4
SiO ₂	60.11
Al ₂ O ₃	26.53
Fe ₂ O ₃	4.25
SO ₃	0.35
MgO	1.25
Na ₂ O	0.22
Loss on ignition (LOI)	0.88

2.2 *Sporosarcina Pasteurii*

The common soil microorganism, *Sporosarcina Pasteurii* (formerly known as *Bacillus Pasteurii*) was used for the study. Freeze-dried vials of *Sporosarcina Pasteurii* were purchased from Microbial Type Culture Collection (MTCC) with catalog number 1761. This bacteria has level 1 biosafety ranking according to the Centre for Disease Control and Prevention (CDC), United States and is suitable for use involving minimal potential hazard to laboratory personnel as well as to the environment. The microscopic view of *Sporosarcina Pasteurii* was shown in Fig. 1. The figure depicts the bacteria to be the rods, generally 0.5–1.2 μm in length. As per MTCC, the optimum conditions for growing this bacteria are the temperature of 30 $^{\circ}\text{C}$, aerobic conditions and proper incubation medium.

2.3 *Liquid Medium*

Agar medium was used to supply nutrients for bacteria when a solid medium was necessary. Liquid Nutrient Broth (LB) medium consisting of four reagents namely Yeast extract (to supply nutrients), Vitamin B (growth factor for bacteria),

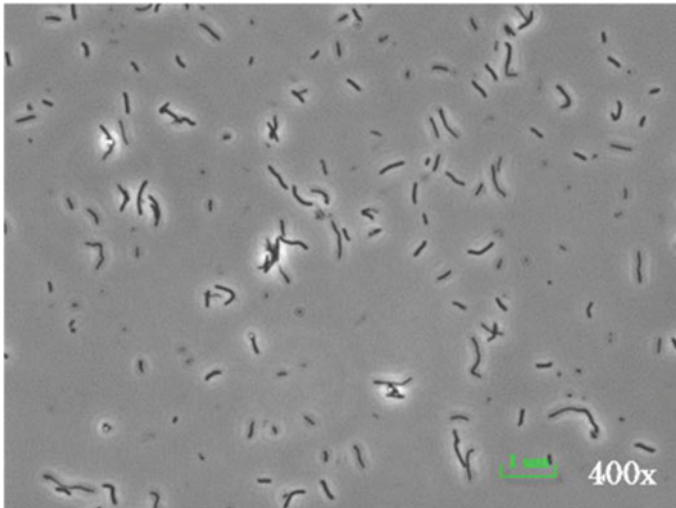


Fig. 1 Microscopic view of *Sporosarcina Pasteurii*

Ammonium Chloride (to provide nitrogen) and other nutrients was prepared. After culturing of bacteria, calcium chloride (CaCl_2) was added a source of Ca^{+2} ions to react with CO_3^{-2} and precipitate calcium carbonate (CaCO_3) that binds the fly ash particles.

3 Methodology

3.1 *Bacterial Cell Solution Preparation*

The original freeze-dried bacteria vial was rehydrated to prepare glycerol stocks. During the test, the bacteria was revived from the glycerol stock using LB medium. Agar solid medium prepared earlier was used for streaking of bacteria with an inoculation loop and were incubated at 37 °C. A seed culture, prepared by mixing a little quantity of lyophilized culture in 100 ml of culture medium and incubating at 37 °C for 24 h, was stored at 4 °C temperature. Then the seed culture was inoculated into the main culture and incubated under agitated conditions at 37 °C for about 48 h to ensure the bacteria reached its maximal population. Now the cells were harvested at 48 °C by centrifugation at 5000 g for 10 min. These cells were now washed twice using 0.1 M sodium phosphate buffer in order to remove any metabolic waste produced during the bacterial multiplication. Bacterial cells were re-suspended in urea - nutrient broth (NB) solution comprising 3 g of NB, 20 g of urea, 10 g of Ammonium chloride and 2.12 g of sodium bicarbonate per liter of deionized water. Finally, the pH value was adjusted to 8.5 using 4 M Hydrochloric acid prior to injection into the specimen.

3.2 *Cementitious Solutions*

The strength gain through MICP depends on the uniform distribution of the calcite formed through urea hydrolysis. For this purpose, at same bacterial cell concentration, the effect of bio-treatment was investigated using four combinations of Urea and CaCl_2 concentrations as shown in Table 3. These cementitious solutions were prepared by dissolving the required amount of mass of urea/ CaCl_2 in distilled water by taking the molecular weights of anhydrous CaCl_2 as 111 g/mol. and that of urea as 60 g/mol.

3.3 Specimen Preparation

PVC molds were used for the preparation of fly ash specimens for bio-treatment. The PVC molds were cleaned thoroughly and to join the two pieces of molds stainless steel clamps and rubber bands were used. Aluminum foil was wrapped inside and at the bottom of the molds to reduce the leakage of the medium during the culture introduction into the specimens. The molds were filled with the fly ash at a density of 12.9 kN/m^3 . The molds were placed in a glass beaker to hold the leakage and the whole setup was then autoclaved to sterilize the sample. For successful treatment, the primary requirement is to ensure the permeation of bacteria and fixation of bacterial cells through the entire specimen. In the present study, among various injection strategies followed in previous researches, single staged injection process (downward flow) was adopted for the fly ash specimen. After injection of bacterial cell solution, the flow was inhibited for 24 h and later permitted to drain under gravity flow through its base. Now the reservoir filled with urea- CaCl_2 solutions was placed directly above the sample top. The flow was stopped for 24 h and then allowed to drain under gravity through its base. Figures 2 and 3 shows the injection of the culture medium into the fly ash specimen and prepared sample, respectively.

Fig. 2 Injection of culture medium into Fly ash specimen



Fig. 3 Prepared Fly ash specimen



3.4 Laboratory Tests

Prior to the bio-treatment, the fly ash samples were tested to identify the index properties. The specific gravity of fly ash particles was found as per IS 2720–part 3 (1) [21]. Grain size analysis was performed according to IS 2720–part 4 [22] and Atterberg limits were found as per IS 2720–part 5 [23]. It was identified that fly ash is non-plastic. The maximum dry density (MDD) and optimum moisture content (OMC) were found according to IS 2720–part 7 [24]. After the bio-treatment the following tests were carried out:

3.4.1 Triaxial Tests

To verify the effects of bio-stabilization, the Unconsolidated Undrained (UU) triaxial tests were conducted on the specimens treated at different cementitious concentrations according to IS 2720–part 11 [25]. Stress–strain curves were obtained using the Data Acquisition and Control system.

3.4.2 Permeability Tests

The coefficient of permeability values of specimens before and after bio-treatment were found using constant head permeability test according to IS 2720–part 17 [26].

The test was performed in the permeability cell of 75 mm diameter and 260 mm height between the perforated plates which is also provided with a loading piston to apply constant axial stress during the test.

3.4.3 Scanning Electron Microscope (SEM) Analysis

SEM image analysis is carried out on treated samples to check the detailed structure of bio-treated fly ash.

3.4.4 X-Ray Diffraction (XRD) Analysis

To see the effects of MICP, XRD tests were performed before and after the bio-treatment. The formation of any new compounds due to MICP on fly ash could be identified using X-ray diffraction patterns.

4 Results and Discussions

4.1 Index Properties

Grain size distribution curve obtained after hydrometer analysis was shown in Fig. 4. The Coefficient of Uniformity (C_u) and Coefficient of Curvature (C_c) values were found to be 3.08 and 1.02, respectively. From C_c value, it could be inferred that the fly ash is uniformly graded. The other index properties along with OMC and MDD were presented in Table 2.

Fig. 4 Grain size distribution curve

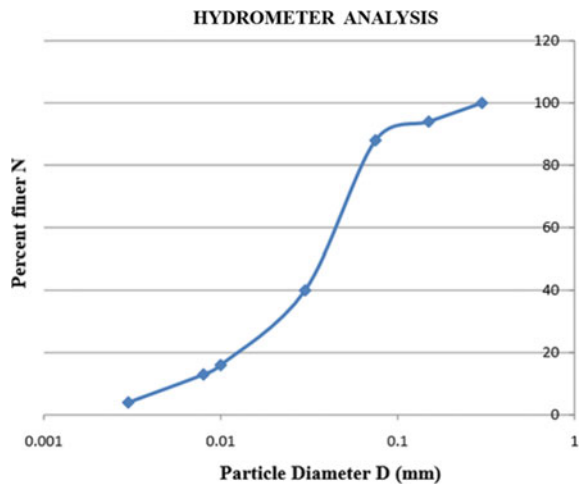


Table 2 Properties of Fly ash used

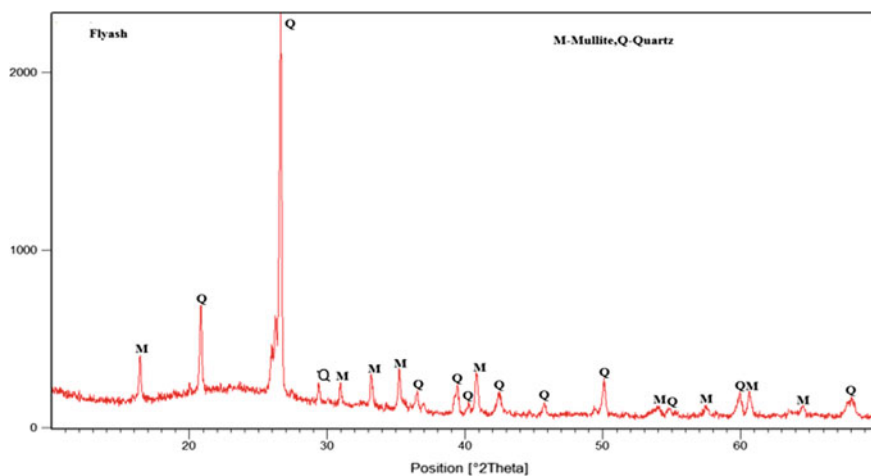
Sl. no.	Property	Value
1	% fines	87
2	Fine sand	13
3	Atterberg limits	Non-plastic
4	Specific gravity	2.09
5	OMC	19.8%
6	MDD	12.9 kN/m ³

4.2 XRD Analysis

XRD images obtained for both untreated and treated specimens were shown in Figs. 5 and 6, respectively. Quartz was found in untreated XRD image. Four main constituents Calcite (CaCO_3), Dolomite ($\text{CaMg}(\text{CO}_3)_2$), Olivine, and Albite which are anhydrous polymorphs of CaCO_3 were identified in addition to Quartz in treated XRD image which was formed through the bio-stabilization process. According to the Mohr's hardness scale, Calcite, Dolomite, Quartz, and Olivine have 3, 3.5, 7, and 6.5 scale hardness, respectively.

4.3 SEM Analysis

The detailed structure of the bio-treated fly ash specimens were identified using SEM images at different magnifications and were presented in Fig. 7. All the particles were flocculated. The surfaces of fly ash particles were found to be rough

**Fig. 5** XRD image of untreated Fly ash

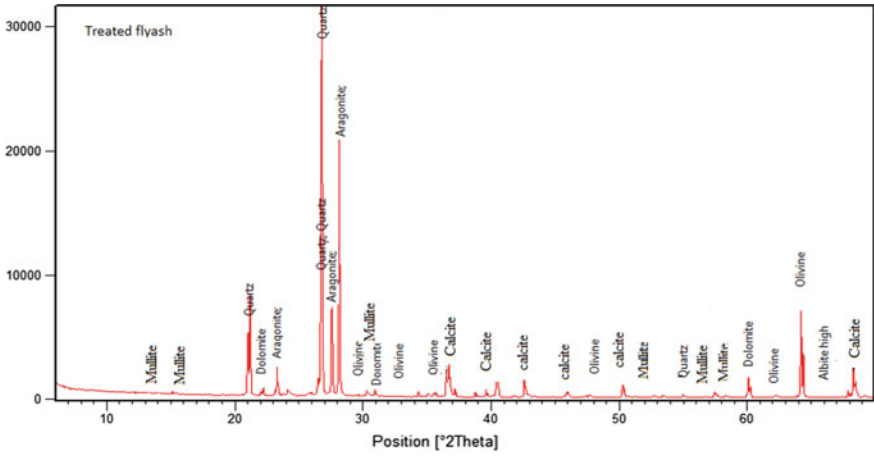


Fig. 6 XRD image of treated Fly ash

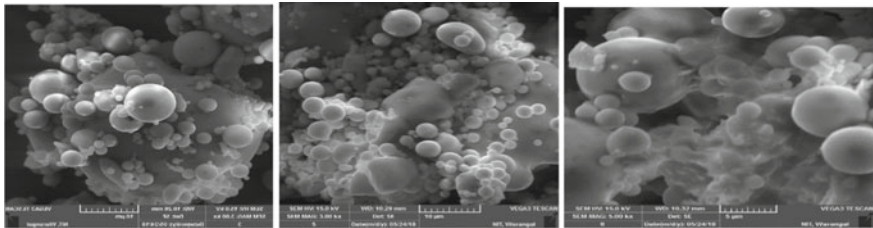


Fig. 7 SEM images of treated Fly ash

and the voids were semi-filled with precipitates. The calcite particles were attached on the surfaces and some layers produced on the surface.

4.4 Triaxial UU Tests

The UU tests were performed on both untreated and bio-treated specimens of fly ash. Prior to the testing, saturation was carried out for specimens using standard procedure until a B-factor value of 0.95 was obtained. The effect of different concentrations of cementitious solutions was assessed by comparing the undrained cohesion values of specimens. The undrained cohesion values of different cementitious solution additions were presented in Table 3. The increased strength was found in a range of 41.19 kPa to 183.31 kPa. From the table, it is depicted that the strength of fly ash sample is increasing with an increase in concentration. The strength is increasing with the concentration of CaCl_2 at same Urea content. This is

Table 3 UCS and permeability values based on various combinations of Urea and CaCl₂

Cementation combination	Urea (M)	CaCl ₂ (M)	UCS (kPa)	Permeability (cm/sec)
Fly ash without bacteria	–	–	37.19	2.59 * 10 ⁻⁴
1	0.1	0.1	46.47	1.36 * 10 ⁻⁴
2	0.25	0.25	164.64	1.02 * 10 ⁻⁴
3	0.1	0.25	183.31	0.29 * 10 ^{-4s}
4	0.25	0.1	171.61	3.64 * 10 ⁻⁵

maybe because of the availability of Ca⁺² ions at higher CaCl₂ contents to form the calcite precipitate giving more strength to the samples. The stress–strain plots of both treated and untreated (w/o bacteria) were shown in Fig. 8. The stress–strain plot for the combination 3 showed a different pattern among all combinations which could be explained with the calcite distribution among the fly ash particles. Because of the availability of more calcium ions the precipitation of calcite was more uniform and thus enabling the specimen to show highly improved behavior.

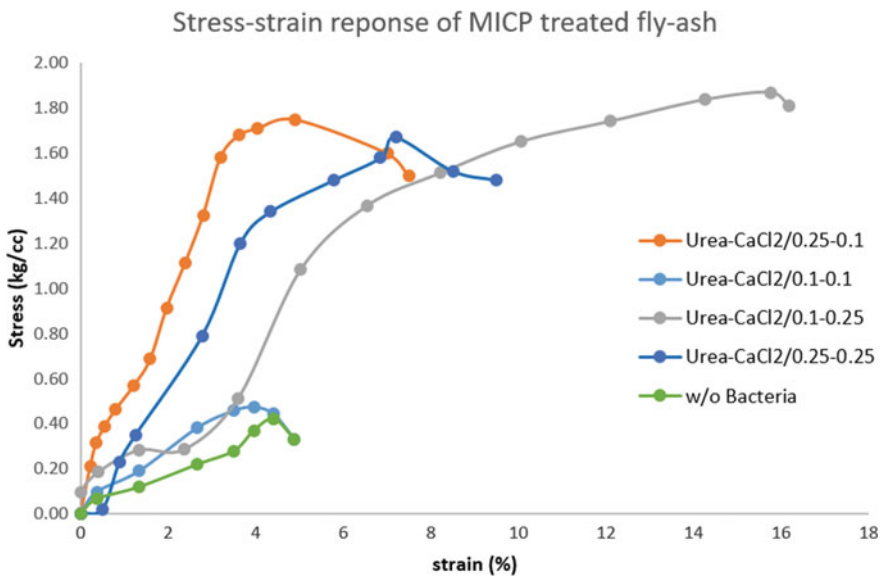


Fig. 8 Stress–strain response of both untreated and MICP treated Fly ash

4.5 Coefficient of Permeability

The coefficient of permeability values of both untreated and MICP treated specimens were presented in Table 3. Each value was verified thrice for each experimental condition. Approximately one order of magnitude reduction was observed in the permeability values. The permeability reduction in the range of about 48–85% was observed. Similar reductions have been reported in various MICP studies conducted on the sand, Soon et al. [27], Whiffin et al. [18] and Yasuhara et al. [28].

5 Conclusions

Based on the investigations carried out the following conclusions are drawn:

- Single-cycle staged injection is significant in fixing the bacteria around the solid interface identified from the strength improvements.
- The undrained strength increased in a range of 25–390% compared to its initial value.
- The permeability coefficient value of treated specimens reduced in a range of 48–85%.
- MICP through urea hydrolysis seems to be a promising and environmental friendly ground improvement technique, but more research is necessary for developing full-scale applications.

References

1. Karol RH, Berardinelli C (2003) Chemical grouting and soil stabilization
2. Mitchell JK, Santamarina JC (2005) Biological considerations in geotechnical engineering. *J Geotech Geoenviron Eng* 131(19):1222–1233
3. Ivanov V, Chu J (2008) Application of microorganisms to geotechnical engineering for bioclogging and biocementation of soil in situ. *Rev Environ Sci Biotechnol* 7:139–153
4. DeJong JD et al (2013) Biogeochemical processes and geotechnical applications: Progress, opportunities and challenges. *Geotechnique* 63(4):287–301
5. NRC (2006) Geological and geotechnical engineering in the new millennium: opportunities for research and technological innovation. National Research Council, National Academies Press, Washington, DC
6. DeJong JT, Mortensen BM, Martinez BC, Nelson DC (2010) Bio-mediated soil improvement. *Ecol Eng* 36(2):197–210
7. Cheng L, Cord-Ruwisch R, Shahin MA (2013) Cementation of sand soil by microbially induced calcite precipitation at various degrees of saturation. *Can Geotech J* 50(1):81–90
8. Bachmeier KL, Williams AE, Warmington JR, Bang SS (2001) Urease activity in microbiologically-induced calcite precipitation. *J Biotechnol* 93:171–181
9. Khodadadi Tirkolaei H, Bilsel H (2015) Statistical modeling of environmental factors on microbial urea hydrolysis process for biocement production. *Adv Mater Sci Eng* 2015

10. Carmona JP, Oliveira PJV, Lemos LJ (2016) Biostabilization of a sandy soil using enzymatic calcium carbonate precipitation. *Proc Eng* 143:1301–1308
11. Ismail MA, Joer HA, Sim WH, Randolph MF (2002) Effect of cement type on shear behavior of cemented calcareous soil. *J Geotech Geoenviron Eng* 128(6)
12. Chou CW, Seagren EA, Aydilek AH, Lai M (2011) Biocalcification of sand through ureolysis. *J Geotech Geo Environ Eng (ASCE)*, GT.0000532:1179–1189
13. DeJong J, Fritzges M, Nüsslein K (2006) Microbially induced cementation to control sand response to undrained shear. *J Geotech Geoenviron Eng (ASCE)* 132(11):1381–1392
14. Feng K, Montoya BM (2015) Influence of confinement and cementation level on the behavior of microbial-induced calcite precipitated sands under monotonic drained loading. *J Geotech Geoenviron Eng* 142(1):04015057
15. Montoya BM, DeJong JT (2015) Stress-strain behavior of sands cemented by microbially induced calcite precipitation. *J Geotech Geoenviron Eng* 141(6):04015019
16. Lin H, Suleiman MT, Brown DG, Kavazanjian E (2016) Mechanical behavior of sands treated by microbially induced carbonate precipitation. *J Geotech Geoenviron Eng* 142(2):04015066
17. Van Paassen LA, Daza CM, Staal M, Sorokin DY, van der Zon W, van Loosdrecht MC (2010) Potential soil reinforcement by biological denitrification. *Ecol Eng* 36(2):168–175
18. Whiffin VS, van Paassen LA, Harkes MP (2007) Microbial carbonate precipitation as a soil improvement technique. *Geomicrobiol J* 25(5):417–423
19. ASTM C 618, Standard specification for coal fly ash and raw or calcined natural pozzolan for use as a mineral admixture in concrete, Annual Book of ASTM Standard 04.02, 2001, p 310
20. Rebata-Landa V (2007) Microbial activity in sediments: effects on soil behaviour. PhD dissertation, Georgia Institute of Technology
21. IS 2720 (1980) Methods of test for soils: part 3 determination of specific gravity/section 1 fine grained soils. Bureau of Indian Standards
22. IS 2720 (1985) Methods of test for soils: part 4 grain size analysis. Bureau of Indian Standards
23. IS 2720 (1985) Methods of test for soils: part 5 determination of liquid and plastic limit. Bureau of Indian Standards
24. IS 2720 (1985) Methods of test for soils: part 7 determination of water content-dry density relation using light compaction. Bureau of Indian Standards
25. IS 2720 (Part 11) (1993) Determination of the shear strength parameters of a specimen tested in unconsolidated undrained triaxial compression without the measurement of pore water pressure. Bureau of Indian Standards
26. IS 2720 (1985) Methods of test for soils: part 17 laboratory determination of permeability. Bureau of Indian Standards
27. Soon WW, Hariharan M, Snyder MP (2013) High-throughput sequencing for biology and medicine. *Mol Syst Biol* 9:640. Pmid: 2330846
28. Yasuhara H, Hayashi K, Okamura M (2011) Evolution in mechanical and hydraulic properties of calcite-cemented sand mediated by biocatalyst. In: *Geo-Frontiers 2011: advances in geotechnical engineering*, pp 3984–3992

A Review of Expansive Soil—Effects and Mitigation Techniques



Trudeep N. Dave and Arshad K. Siddiqui

Abstract The swelling and shrinkage phenomenon in expansive soil is one of the major causes of infrastructure distress for decades. The soils with montmorillonite as primary mineral composition possess property of excessive volumetric variation during drying and wetting of soil. The volumetric changes depend on proportion of clay mineral available, their exchangeable ions, and internal microstructure. The construction of structures on expansive soils experiences tilting, total and differential settlements resulting in cracking of building and basement walls, upheaving of rigid and flexible pavements, cracking and failure of utility lines, and damage to doors and windows. In order to understand the behavior of expansive soil and to determine the extent of damage that may occur many studies have been conducted in the past. Further, to categorize the extent of damage and type of distress that can occur due to expansive soil and probable remedial measures that can be helpful to mitigate swelling pressure, large amount of literature is available. This paper reviews the state of the art research related to different types of distress caused due to expansive soil, severity of cracking damage, remedial measures, and points to be considered while selecting remedial measures for expansive soils.

Keywords Expansive soil · Volumetric changes · Superstructure distresses · Mitigation techniques

1 Introduction

Expansive soils exist in almost all regions of the world. Soil moisture variation due to climatic conditions or variation in groundwater table causes large volume changes in expansive soils. Due to the high swelling and shrinkage potential of these soils, it has high likelihood to cause distresses to Civil Engineering structures.

T. N. Dave (✉) · A. K. Siddiqui
Department of Civil Engineering, Institute of Infrastructure Technology Research
and Management (IITRAM), Ahmedabad, India
e-mail: trudeepdave@iitram.ac.in

© Springer Nature Singapore Pte Ltd. 2020
A. Prashant et al. (eds.), *Advances in Computer Methods
and Geomechanics*, Lecture Notes in Civil Engineering 56,
https://doi.org/10.1007/978-981-15-0890-5_43

519

Construction of residential foundations, highways, railways, airport runways, canals, utility lines, retaining structures, dams, waste disposal sites, and bridges built on/in this type of soils restricts the swelling of soils. This restriction induces swelling pressure, which can cause significant damage to infrastructure if swelling is not controlled. Expansive soils may be categorized as low, medium, high, and very highly expansive [4]. When any construction has been carried out on expansive soil under various environmental conditions without the pre-knowledge of their properties, the damage is severe. Hence, it becomes necessary to understand the consequences of soil swelling on the performance of the structures and associated distresses. It is also important to identify suitable swelling pressure mitigation processes for controlling the distresses. In this context the present work reviews effects and mitigation techniques for expansive soils.

2 Literature Review

Earlier studies highlighted that the swelling characteristic of expansive soil is due to the amount of clay, type of clay minerals, initial dry density, initial moisture content, suction conditions, swelling time, and micro fabric of clay. When the total upward swelling pressure ranges from 20 to 30 kN/m², then it is considered as low expansive soil and if it ranges from 1500 to 2000 kN/m², then it is considered as highly expansive soil [4]. The interaction of structures founded on these soils results in angular distortion and distress within supported structures. In order to understand the distresses and corresponding mitigation methods, a detailed review has been conducted.

The review of the existing state of the art is mainly divided into two parts. The first part explains tolerance limits for various superstructures, the severity of damage based on the damage/distortion observed, and the categorization of distresses caused by swelling/shrinkage phenomenon observed in the expansive soils. Initially the allowable angular distortion of superstructure is explained in Fig. 1 (as per US Department of Army [27]). The method to categorize the severity of damage [5] based on actual data is presented in Figs. 2, 3, 4. The second part is focused on various available methods to mitigate the swelling pressure due to expansive nature of soil so as to safeguard the superstructure against severe damage. It also explains about suitability, method/mechanism involved, advantages, and limitations of these methods.

2.1 *Effects of Expansive Soils*

In order to limit the damage on structures due to differential settlement in expansive soils and associated angular distortion of structures, Fig. 1 presents the allowable angular distortion for different types of the superstructure as suggested by US

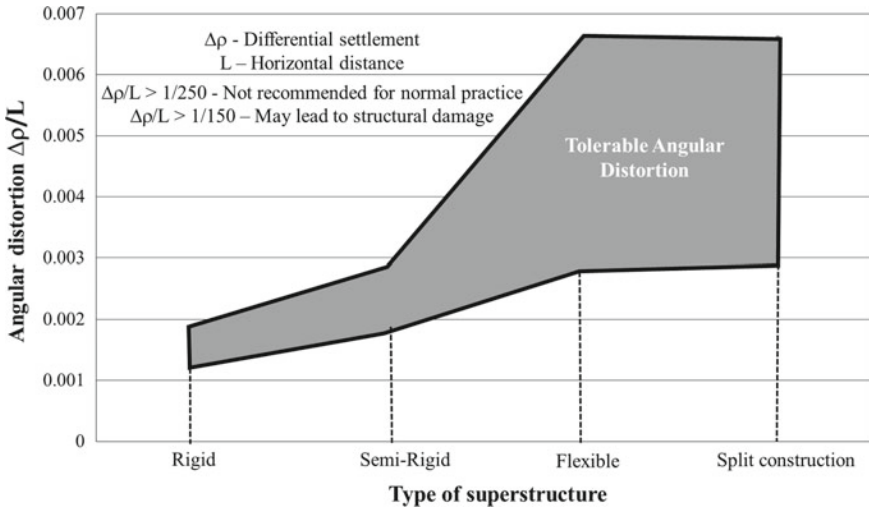


Fig. 1 Allowable angular distortion of the superstructure [27]

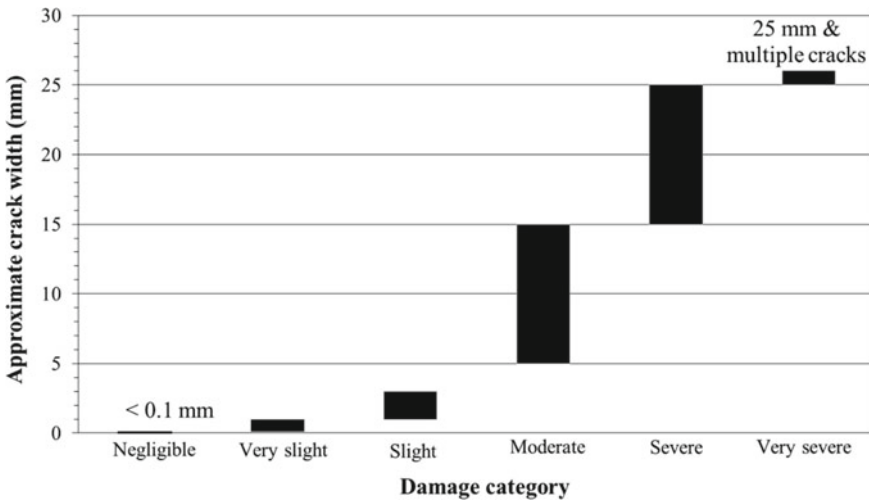


Fig. 2 Categorization of severity—approximate crack width [5]

Department of Army [27]. Further, Figs. 2, 3, 4 presents the different types of distresses and their descriptions. Day [5] categorized types of distresses as architectural, functional or structural. Architectural distresses are associated with building appearance in the form of minor cracks on walls, floor and finishes, cracks on plaster (0.5 mm wide), and cracks on masonry (1 mm wide) as highlighted by [3]. Functional distresses affect the use of the building which includes jammed

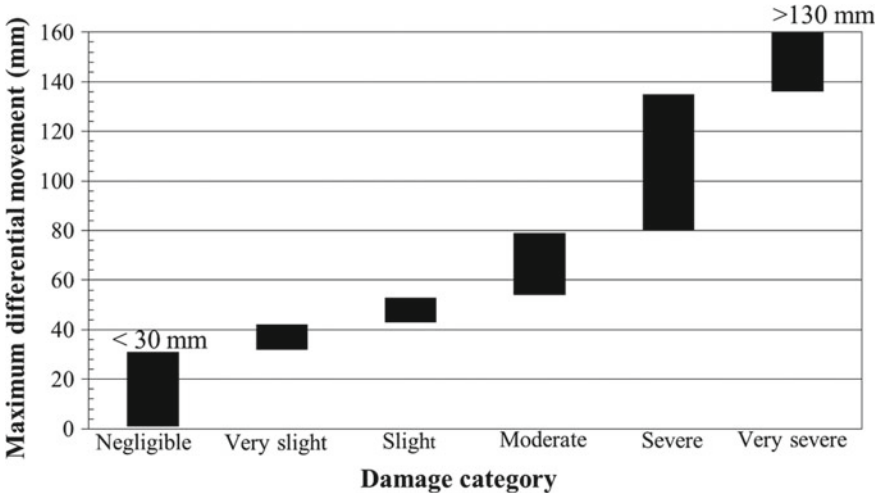


Fig. 3 Categorization of severity—maximum differential movement [5]

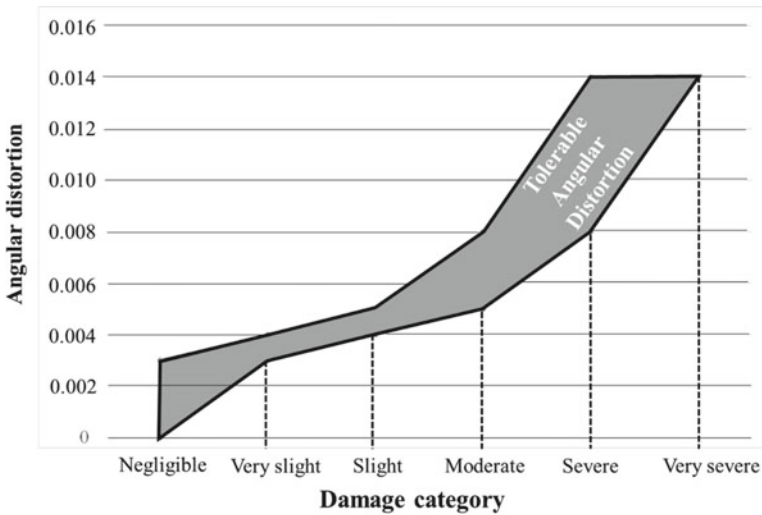


Fig. 4 Categorization of severity—angular distortion [5]

doors and windows, extensively cracked and falling plaster, tilting of wall and floors, deterioration of construction materials, and leaky roofs associated with ground movement. Whereas, the structural distress is mainly in which structural integrity of the building is compromised and building stability is affected such as: cracking or distortions of supporting members like beams, columns, or load bearing walls, and these damages could lead to structural collapse.

For construction of structures in expansive soil, before proceeding to the remedial measures for swelling pressure mitigation, the following information should be sought [19]: (a) Cause and extent of damage (b) Applicable remedial measures (c) Time of implementation of remedial measures (d) Financial liabilities for repair (e) Criteria to be used for the selection of remedial measures and scope of repair work to be employed, and (f) Post repair risk evaluation. Addressing the above requirements will allow to understand various aspects associated with the problem and selecting the most appropriate mitigation method.

2.2 *Expansion Mitigation Methods*

The stabilization of expansive soil is widely used to mitigate swelling pressure due to expansive soils and has been successfully implemented at many sites. According to the mechanism involved, soil stabilization methods can be categorized into physicochemical stabilization, mechanical stabilization, and preventative measures that are recommended for mitigation of swelling pressure in expansive soils. In physicochemical stabilization, stabilizers are mixed or injected into the soil which chemically reacts and improves the engineering properties of soil. Physicochemical stabilizers can be grouped into (a) traditional stabilizers such as lime, cement, and fly ash [1, 15, 22] (b) by-product stabilizers such as granulated ground blast furnace slags, kiln dust, sludge ash, and microsilica [2, 11], and (c) nontraditional stabilizers such as polymers, enzymes, and chemicals [21]. The mitigation methods can also be grouped into removal and replacement, moisture conditioning and compaction control, prewetting, addition of chemical admixtures, moisture control alternatives, and innovative methods.

The use of mechanical stabilization does not modify the chemical properties of the swelling soil. It includes swelling control through compaction [25], soil prewetting, soil mixing with sand [16, 25], reinforcing the soil using geosynthetics and placing compressible geoinclusion between expansive soil and the infrastructure [8]. Preventative measures include excavating and replacing expansive soils with non-expansive soils, soil isolation and installation of subsurface drains [7].

Table 1 summarizes the different methods along with other details for the mitigation of problems associated with expansive soils.

After checking the feasibility about soil treatment to control the heave is done, the choice of the technique should be assessed with respect to the following: (a) Economic factors (b) Relative expected control of volume changes by implementing different treatment alternatives (c) Site-specific conditions such as potential for volume change, moisture variations, degree of fissuring, and permeability (d) Nature of the project (e) Necessary strength of the foundation soils (f) Tolerable movement of the foundation and (g) Time frame available for treatment

The paper attempts to summarize the various effects of expansive soil and methods of mitigation of these effects on the supporting structures. The selection

Table 1 Details of different mitigation methods for expansive soils

<ul style="list-style-type: none"> • Removal (overexcavation) and replacement 	
	Method: expansive soils are over excavated and replaced by non-expansive or treated soils. It depends on the required depth of excavation, allowable heave and location, and cost of replacement fill
<ul style="list-style-type: none"> • Moisture conditioning and Compaction control 	
	Suitability: In case of non-availability of non-expansive fill, swelling properties of soils can be altered by moisture conditioning and compaction control. Compacting the material wet side of optimum and at a lower density but with adequate strength reduces the expansion potential. In some instances, chemical additives can be used together with moisture conditioning
<ul style="list-style-type: none"> • Prewetting 	
	Method: Increasing the water content in the expansive foundation soils will cause heave prior to construction, thereby reducing postconstruction expansion potential
	Reliability: Results are unreliable as the hydraulic conductivity of expansive soils is very low and the time required for adequate wetting can extend up to decades [18]. Many times it can lead to serious loss of soil strength and reduction in bearing capacity. Also, continued migration of water into lower more expansive layers can result in continued heave
<ul style="list-style-type: none"> • Chemical admixtures can be divided into: (a) Traditional materials (b) Nontraditional materials 	
(a) Traditional materials	
1.	Hydrated lime
	Doses: 3–8% by weight of soil
	Reaction: cation exchange, flocculation–agglomeration, lime carbonation, and pozzolanic [12, 17, 26]
	Strength depends on soil type, lime type, lime percentage, and curing conditions
	Suitability: soils with at least 25% passing No. 200 sieve and plasticity index >10 [17]
	Mechanism: lime supplies a divalent calcium cation that can form calcium silicates and calcium aluminum hydrates, which can form physical bonds between particles to increase soil strength
2.	Cement
	Doses: 2–6% by weight of soil
	Reaction: similar to that of lime
	Strength depends on: soil type, cement type, cement percentage, and curing conditions
	Suitability: wide variety of soils including granular soils, silts and clays, when lime is ineffective
	Effect: reduces the liquid limit, plasticity index and volume change potential, increase shear strength, and improve resilient modulus
	Noneffective: for highly plastic clays
	Mechanism: similar to lime except that cement has shorter hydration and setting time
3.	Fly ash
	Doses: Based on application, an extensive testing program is required to decide optimum treatment
	Reaction: similar to that of lime
	Strength depends on soil type, type of fly ash C type/F type, fly ash percentage, compaction, and water control [13]

(continued)

Table 1 (continued)

	Suitability: a wide variety of soils including granular soils, silts, and clays, when lime is ineffective
	Effect: reduces plasticity index, permeability, and expansion potential of the soil and increases stiffness, strength and freeze–thaw resistance
	Mechanism: increases the pozzolanic reaction and improves the gradation of granular soils
(b) Nontraditional materials	
1.	Sodium chloride
	Suitability: more effective in soil with higher liquid limit
	Effect: increases the shrinkage limit and shear strength, also beneficial to control frost heave
2.	Calcium chloride
	Effect: stabilizes the water content changes and hence reduce the volume change potential, beneficial to control frost heave
	Disadvantage: easily leached from the soil and requires at least 30% relative humidity
3.	Potassium chloride
	Mechanism: during the injection process, saturating the soil mass with potassium ions changes the mineralogical characteristics of soil. It forms chemical bond with the crystal lattice of montmorillonite and modifies to illite and reduces its expansion potential [20]
	Limitation: injection into clays soil is difficult because of lower permeability and the distribution of the chemical is questionable
• Moisture control alternatives	
1.	Barriers: In horizontal and vertical directions
	Construction: Impermeable surfaces that extend outward for a considerable distance around the edges of the foundation or floor slab to stabilize water content under slabs or foundations. The vertical barriers should be installed at least as deep as the zone that is most affected by seasonal moisture change [19]
	Materials used: Impermeable membrane consisting of a material such as polyethylene, polyvinyl chloride (PVC), polypropylene, high-density polypropylene, and other types of geomembranes.
	Precaution: Most membranes degrade due to exposure to sunlight. Hence, it should be protected against ultraviolet radiation. Also, the membrane needs to be protected from chemical attack.
	Suitability: Horizontal barriers are more effective if surface drainage is provided to prevent ponding. However, vertical barriers are more effective than horizontal barriers in minimizing lateral moisture migration and maintaining long-term uniform water content distribution
	Comparison: In horizontal barriers, the water content of the soil under the slab increases and the total heave may not decrease appreciably. But, the heave may significantly uniform for the slabs with vertical barriers than for slabs without vertical barriers [6]
2.	Surface drains
	The placement of perimeter drains around the foundations is a common practice to avoid the presence of free water in the soil. However, perimeter drains are not very effective in totally avoiding heave below foundations

(continued)

Table 1 (continued)

• Innovative methods	
1.	Provision of sand blanket [23]
	The Sand was used both as additive material and as spreading layer on expansive soil in the laboratory experiments. It was concluded that the reduction in swelling pressure, in percentage terms, was greater than the added sand in percentage. The clay acts as filler material in the voids formed by the sand particles at lower percentages of sand, thereby reducing swelling pressure is mitigated in occupying denser packing state
2.	Provision of cohesive nonswelling soils [10]
	It was concluded that placing a nonswelling cohesive soil between expansive soil and retaining wall reduced the lateral pressure effectively transmitted by the expansive soil on the retaining wall. Similarly providing nonswelling cohesive soil above expansive soil would reduce the effect of vertical swelling and differential heave on supporting structures such as pavement, buildings, etc.
3.	Provision of combined sand and EPS geofoam layers [8]
	Sand and expanded polystyrene (EPS) geofoam were evaluated as potential stabilizers in improving the swelling behavior of expansive soils. Various thicknesses of layers of sand, layer of geofoam, and combination of sand and geofoam were effectively used in mitigating the swelling pressure
4.	Provision of compressible geoinclusion [9, 24]
	The measured percent swell and swelling pressure reduces substantially with the increase in thickness of EPS geofoam layer. The reduction in swelling pressure due to EPS geofoam is more pronounced for soils with higher swell potential. The high compressibility feature of EPS geofoam accommodates the volume changes due to physical modification in backfill materials behind retaining structures
5.	Provision of the combined surcharge and lime for stabilization [14]
	The surcharge contributes to compensating the swelling effect of expansive soils and hence depending on the type of construction expected, the lime content can be varied considering the surcharge from superstructure

mitigation method requires detailed understanding of the degree of expansiveness of soil; architectural, functional, and structural aspects of supporting structure; type of distresses, extent of distress related damage, economical aspects and constructability issues related to mitigation method. Proper understanding and implementation efforts may lead to more effective performance of structures on expansive soils.

References

1. Al-Rawas A, Hago AW, Al-Sarmi H (2005) Effect of lime, cement and Sarooj (artificial pozzolan) on the swelling potential of an expansive soil from Oman. *Build Environ* 40 (5):681–687
2. Alrubaye AJ, Hasan M, Fattah MY (2017) Stabilization of soft kaolin clay with silica fume and lime. *Int J Geotech Eng* 11(1):90–96

3. Burland JB, Broms BB, Demello VFB (1997) Behavior of foundations and structures: state of the art report. In: Proceedings of the 9th international conference on soil mechanics and foundation engineering. Japanese Geotechnical Society, Tokyo, Japan, pp 495–546
4. Das BM (2008) Advances in soil mechanics. CRC Press, Third Edition
5. Day RW (1998) Settlement behavior of posttensioned slabs-on-grade. *J Perform Constr Fac ASCE* 12(2):56–61
6. Goode JC (1982) Heave prediction and moisture migration beneath slabs on expansive soils. Master's thesis, Colorado State University, Fort Collins, CO
7. Hudyma N, Avar BB (2006) Changes in swell behavior of expansive clay soils from dilution with sand. *Env Eng Geosci* 12(2):137–145
8. Ikizler SB, Aytakin M, Vekli M (2009) Reduction in swelling pressure of expansive soil stabilized using EPS geofoam and sand. *Geosynth Int* 16(3):216–221
9. Ikizler SB, Aytakin M, Nasb E (2008) Laboratory study of expanded polystyrene (EPS) geofoam used with expansive soils. *Geotext Geomemb* 26:189–195
10. Katti RK (1978) Search for solutions to problems in black cotton soils. First I.G.S. Annual lecture, Indian Geotechnical society at I.I.T, Delhi
11. Lin DF, Lin KL, Luo HL (2007) A comparison between sludge ash and fly ash on the improvement in soft soil. *Air Waste Manag Assoc* 57:59–64
12. Little DN (1995) Handbook for stabilization of pavement subgrades and base courses with Lime. Lime Association of Texas
13. Little DN, Males EH, Prusinski JR, Stewart B (2000) Cementitious stabilization. 79th Millennium Report Series, Transportation Research Board, Washington, DC
14. López-Lara T, Hernández-Zaragoza JB, Horta-Rangel J, Rojas-González E, López-Ayala S, Castaño VM (2017) Expansion reduction of clayey soils through surcharge application and lime treatment. *Case Stud Construct Mater* 7:102–110
15. Miller GA, Azad S (2000) Influence of soil type on stabilization with cement kiln dust. *Constr Build Mater* 14(2):89–97
16. Mishra AK, Dhawan S, Rao MS (2008) Analysis of swelling and shrinkage behavior of compacted clays. *Geotech Geol Eng* 26(3):289–298
17. National Lime Association (2004) Lime-treated soil construction manual: lime stabilization and lime modification bulletin 326. National Lime Association
18. Nelson FD, Chao KC, Overton DD, Nelson EJ (2015) Foundation engineering for expansive soils. Wiley
19. Nelson JD, Miller DJ (1992) Expansive soils: problems and practice in foundation and pavement engineering. Wiley and Sons, New York
20. Pengelly AD, Addison MB (2001) In-situ modification of active clays for shallow foundation remediation expansive clay soils and vegetative influences on shallow foundations. In: Proceedings of the ASCE geo-institute shallow foundation and soil properties committee sessions at the 2001 civil engineering conference, pp 192–214
21. Petry TM, Little DN (2002) Review of stabilization of clays and expansive soils in pavements and lightly loaded structures—history, practice, and future. *J Mat Civil Eng* 14(6):447–460
22. Punthuaecha K, Puppala AJ, Vanapalli SK, Inyang H (2006) Volume change behaviors of expansive soils stabilized with recycled ashes and fibers. *J Mat Civil Eng* 18(2):736–751
23. Satyanarayana B (1966) Swelling pressure and related mechanical properties of black cotton soils. PhD thesis, IISc, Bangalore
24. Shelke AP, Dasaka SM (2010) Reduction of swelling pressure of expansive soils using EPS geofoam. In: Proceedings of Indian Geotechnical Conference, pp 495–498
25. Sridharan A, Gurtug Y (2004) Swelling behavior of compacted fine-grained soils, *Eng Geol* 72(1–2):9–18
26. Thompson MR (1968) Lime stabilization of soils for highway purposes final summary report, civil engineering studies, highway series no. 25, Illinois Cooperative Highway Research Program, Project IHR-76, 26
27. US Department of the Army (1983) Technical manual TM 5-818-7, Foundations in expansive soils. Washington, DC

Vibration Control of Flexible Retention Systems



Nisha Kumari and Ashutosh Trivedi

Abstract Infrastructure and facilities built on structures retaining backfill cause significant damage due to large displacement of retaining walls during excessive vibration. The smart materials can be provided to compensate for the deleterious effects of vibration. Smart materials, namely Lead Zirconate Titanate also known as piezoelectric ceramic (PZT) material, are used to minimize the displacement due to the induced vibration and to control the flexible retention system for granular materials. The solution of the displacement control of retaining walls of varying flexibility is indeterminate in a multivariate system. The excessive vibration may reduce the life span of a retaining wall and may get transferred to the critical locations inducing plastic uncontrolled deformations. This paper investigates the response of smart material to control vibration by means of input transformation techniques. The time-domain formulation exploits the vibration as input and output finite settling time for motion excitation vibrations. The finite settling time depends on the natural frequencies and spring constant of vibration of the flexible retaining wall and granular backfill. The numerical analysis concludes that the provision of piezoelectric ceramic (PZT) material describes the specification of finite-time vibration cancelation. Effect of reduction of vibration by using smart material on the flexibility of the retaining structure is presented.

Keywords Smart materials · Flexible retention system · Natural frequency · Vibration control

1 Introduction

Since the past decades, the behavior of retaining walls for dynamic loading has been well investigated. The soil-structure interaction of the soil and the retaining wall makes the analysis of the seismic retaining wall complicated. Limit

N. Kumari (✉) · A. Trivedi
Delhi Technological University, Delhi 110042, India
e-mail: nishasoni.ce@gmail.com

© Springer Nature Singapore Pte Ltd. 2020
A. Prashant et al. (eds.), *Advances in Computer Methods and Geomechanics*, Lecture Notes in Civil Engineering 56,
https://doi.org/10.1007/978-981-15-0890-5_44

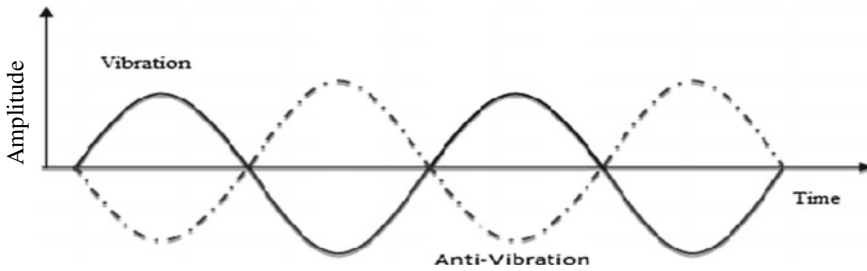


Fig. 1 The amplitude of vibration due to dynamic forces on a retaining wall (bold line) and amplitude of vibration of the PZT patch (dotted line) of equal magnitude and opposite in direction

Table 1 Material properties and chemical formula of the PZT patch

PZT description	Chemical formula	Material properties
Lead Zirconate Titanate PIC-181	$P_b [Zr_{\xi}Ti_{(1-\xi)}]O_3: 0 \leq \xi \leq 1$	Density = 7600–7800 kg/m ³ Elastic stiffness coefficient = 1.0–1.1 × 10 ¹¹ N/m ² Extremely high mechanical quality factor, good temperature and time consistency, suitable for high power acoustic applications and resonance mode

equilibrium and elastic analysis approach are most commonly adopted for dynamic analysis of retaining walls. Flexibility of retaining walls plays a significant role in the design of seismic retaining walls. Recently, smart structures are in trend among civil structures. In smart structures, smart material is used so that different types of actuators and sensors are installed to compensate the effect of vibration due to seismic loading. Figure 1 shows the principle of vibration control consisting of amplitude vibration induced in retaining walls due to dynamic loading and amplitude of vibration of a PZT (Table 1). The principle of vibration control is based on the superposition and destructive interface of amplitude of vibration achieved application of dynamic identical in magnitude but exactly reverse in direction of the amplitude.

In the last 10 years, to understand the dynamic behavior of smart structures many studies have been conducted. Since the natural frequency of structures affect the vibration due to earthquake excitation, it is therefore necessary to analyze the natural frequency of smart structures. The prediction of the natural frequency of retaining walls is found to be a function of two parameters namely height of the backfill and the shear wave velocity [6, 8, 9]. Mukherjee and Joshi [7] proposed a method to optimize a piezoelectric structure based on minimization of the global displacement residue between the design consideration and the current structural configurations for a beam in static and dynamic cases. Irschik et al. [5] have conducted a dynamic shape control analysis for a composite beam-type structure.

Similarly, various methods are proposed to reduce vibration in beams due to dynamic loading [11].

The concept of structure vibration control was given by Yao [10]; according to this, the structure is regarded as a dynamic system whose response variables such as displacement, velocity, and acceleration are functions of time and in which some mechanical properties, typically stiffness ratio and the mass ratio may be adjusted to minimize the dynamic effects of loads under an acceptable level. The purpose of vibration control is to absorb, refract, and reflect the energy induced by the dynamic load. Table 2 shows that a vibration control technique was used to control the problem of a Cartesian robot arm, which was modeled as a flexible cantilever beam with translational base support [2]. The base motion was controlled utilizing an electrodynamic shaker, while a piezoelectric patch (PZT) actuator was bonded on the surface of a flexible beam for suppressing residual arm vibration. This technique

Table 2 Application of PZT material properties in varied engineering fields

Technique used	Theoretical descriptors	References
Piezoelectric control of a robotic arm	Force as a function of time and rotation	Dadfarnia et al. [2]
Admittance monitoring system to structure-test in RC element	Voltage supplied to the circuit, current passing through the PZT, conductance (the real part of admittance), susceptance (the imaginary part of admittance), angular frequency, length of the patch, thickness of the patch, piezoelectric strain coefficient of the PZT, effective mechanical impedance, effective structural impedance, Poisson’s ratio, wave number, Young’s modulus of elasticity and electric permittivity of the PZT patch at constant stress along the diagonal tensorial elements	Bhalla and Soh [1]
Composite beam made of cantilever beam and a PZT patch	The average stress in the PZT and the structural element $(\sigma_P)_{ave} = \left(\frac{6M}{bh_p^2}\right) \left(\frac{(\mu+1)n}{\mu^2n^2 + (4\mu^2 + 6\mu^2 + 4\mu)n + 1}\right)$ $(\sigma_b)_{ave} = \left(\frac{-6M}{bh_b^2}\right) \left(\frac{(\mu^2 + \mu)n}{\mu^2n^2 + (4\mu^2 + 6\mu^2 + 4\mu)n + 1}\right)$	Kerboua et al. [4]
Retaining wall and a PZT patch for vertical loads	The average stress in the PZT and the retaining wall $(\sigma_{PZT})_{avg} = \frac{36M}{bh_p^2} \left[\frac{n(1+\mu)(1+\mu n)}{3\mu^5n^3 + 6\mu^4n^2 + 5\mu^3n + \mu^2n^2 + \mu^2 + 4\mu n + 2} \right]$ $(\sigma_{RW})_{avg} = -\frac{M}{12bh_b^2} \left[\frac{n^2(6\mu^3 + 4\mu^2) + 3\mu^2n + 2}{12\mu^5n^4 + 4n^2(3\mu^4 + 6\mu^3 + 14\mu^2) + 4n(5\mu^3 + 9\mu^2 + 6\mu^2 + \mu) - n\mu^3 + 1} \right]$	Kumari and Trivedi [3]
Horizontal and vertical displacement of a retaining wall bounded with the PZT patch	The horizontal and vertical displacement of vibration $u_x = \frac{F/k_x}{1 - \frac{\omega^2}{\omega_n^2}} \left(\sin \omega t - \frac{\omega}{\omega_n} \sin \omega_n t \right)$ $u_z = \frac{F/k_z}{1 - \frac{\omega^2}{\omega_n^2}} \left(\sin \omega t - \frac{\omega}{\omega_n} \sin \omega_n t \right)$	Present work

where μ is the thickness ratio, n is the modulus ratio, M is bending moment, σ_P and σ_{PZT} are average stresses in the PZT patch, σ_b and σ_{RW} are average stresses in the backfill, u_x is horizontal displacement and u_z is vertical displacement represented in terms of force, spring constant, frequency, frequency ratio, and time in the context of the present study

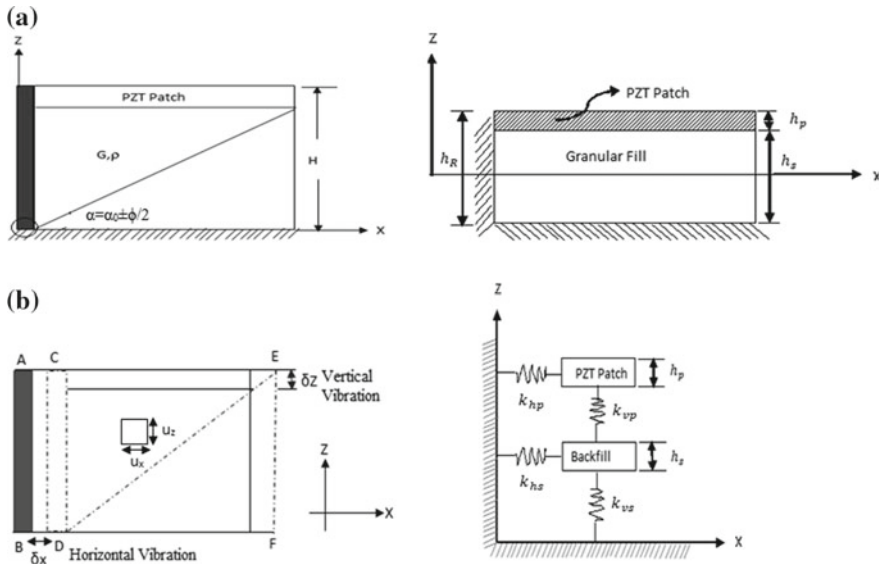


Fig. 2 a Coordinates for soil–wall system represented as a function of shear modulus, density, thickness of backfill, thickness of PZT patch, and the angle of wedge. b Displacement profile represented in the form of spring–mass system

was also used to analyze the stress–strain behavior of a composite beam [4] and a retaining wall [3] by considering the thickness of the PZT patch and Young’s modulus of the material to control the vibration. It can be demonstrated from Table 2 that a strain feedback control action does not include the displacement of vibration in horizontal and vertical direction. In order to further improve the vibration control which is a requirement in the design of the dynamically loaded structure, a PZT patch is utilized to analyze the displacement in horizontal and vertical directions of the retaining wall.

In this study, a flexible cantilever retaining wall has been considered having roller support at the bottom and bounded with the PZT patch on the outer surface of the backfill as shown in Fig. 2(a). The thickness of the backfill is h_b and length L while the PZT patch possesses thickness and length h_p and L , respectively. It is assumed that the PZT patch and backfill have the same width b . It is assumed that the PZT and the granular material are in perfect contact and there is no shear movement or separation at the interface. The chemical formula and material properties of the PZT patch are listed in Table 1. The present model maintains the stress continuity of the soil–wall system. The soil overlaying with the PZT and wall interaction is taken into consideration to examine the dynamic response of the wall.

2 The Principles and Assumptions

The assumptions considered for the analysis of the soil-wall system and the PZT are as follows

- a. The retaining wall is assumed to be flexible, cantilever, and with a constant cross section along the height.
- b. The granular backfill is dry, homogeneous, and isotropic.
- c. PZT and the retaining wall model are linear and elastic.
- d. The wall–soil system is free at its upper surface bound to a rigid base.
- e. The sliding takes place along a shear plane inclined at α_0 , and the soil block below and above this plane is elastoplastic.
- f. The failure takes place along the wedge defined by the angle ($\alpha = \pi/4 = \alpha_0 \pm \phi/2$) as shown in Fig. 2b.

Some of the assumptions are quasi-theoretical leading to a mathematical framework. It is proposed that this simple and basic case is general and can evaluate the physics of transverse vibration of the soil–wall system under an earthquake under the given assumption. The soil–wall system is subjected to transverse seismic excitation. The soil–wall system is overlain on a rigid base with the depth of H from the PZT surface. The wall installed is of length L, thickness t_w ; thickness of the PZT is h_p from the top and thickness of the granular fill is H_s . The Young's modulus of the PZT and wall is E_p and E_R respectively. The vibration induced in the soil–wall system due to transverse seismic excitation can be reduced in many different ways according to the problem; the most common are the stiffness, damping, and isolation. In the present paper, reduction of the vibration stiffness is considered. The stiffness consists of shifting the resonance frequency of the structure beyond the frequency band of excitation. Natural frequency of the excitation of the structure or the natural time period is also an essential part to control the vibration of the flexible retaining system.

The stress of the individual PZT and granular fill layer are the product of strain and modulus of the material of each layer. In pure bending radius of curvature (R), the normal stress σ_n and normal strain ϵ_n in x- and z- direction [3] can be expressed as

$$\epsilon_x = \frac{x}{R} \quad (1)$$

$$\epsilon_z = \frac{z}{R} \quad (2)$$

$$\sigma_n = E \epsilon_n \quad (3)$$

The modulus of the participating layer represents the stiffness variation of the PZT and granular backfill. The generalized relationship between the stiffness (k) and modulus (E) for a retaining wall of length (L) and area (A) is expressed as

$$k = \frac{AE}{L} \tag{4}$$

$$k \propto E \tag{5}$$

3 Equation of Motion for the Soil-Wall System

Figure 2a shows a retaining wall retaining a granular backfill bounded with a PZT patch. This flexible cantilever retaining wall is elastically constrained against rotation at its base. It has been idealized as a spring–mass system. The mass (m) is the total mass of the PZT patch and triangular failure wedge. The displacement is considered on the center of mass as shown in Fig. 2b. The spring constant for the PZT and granular fill are k_1 and k_2 , respectively. This spring–mass system is being subjected to a force $F \sin (\omega t + \beta)$ in the horizontal direction.

The equation of motion is represented by

$$m\ddot{u} + k_{hp}u + k_{hs}u = F \sin(\omega t + \beta) \tag{6}$$

Let $k_{hp} + k_{hs} = k_x$

General solution for Eq. (6) is given as

$$u = a_1 \sin(\omega t + \beta) + a_2 \cos(\omega_n t) + a_3 \sin(\omega_n t) \tag{7}$$

The boundary conditions at time $t = 0$ are presented as

$$u = u_o = 0 \tag{8}$$

$$\dot{u} = 0 \tag{9}$$

Substitution of Eqs. (8) and (9) in Eq. (7), neglecting the terms of damping and considering the force in the phase (i.e., $\beta = 0$), the displacement in x-z direction is represented as

$$u_x = \frac{F/k_x}{1 - \frac{\omega^2}{\omega_n^2}} \left(\sin \omega t - \frac{\omega}{\omega_n} \sin \omega_n t \right) \tag{10}$$

$$u_z = \frac{F/k_z}{1 - \frac{\omega^2}{\omega_n^2}} \left(\sin \omega t - \frac{\omega}{\omega_n} \sin \omega_n t \right) \tag{11}$$

Here, $k_z = \frac{k_{vp}k_{vs}}{k_{vp} + k_{vs}}$ and $\omega_n = \sqrt{\frac{k_z}{m}}$

where the total mass (m) is expressed as

$$m = \frac{\gamma H^2}{2 \tan \alpha} + \gamma B h_p \tag{12}$$

Equation (9) implies the resonance condition. The maximum displacement occurs when the velocity is equal to zero and is expressed as

$$u_{\max} = \frac{F \omega_n t}{2k_Z} \tag{13}$$

Equations (10) and (11) indicate variation of displacement of soil–wall system in horizontal and vertical directions respectively resulting from the contribution of the stiffness of the PZT and the granular material. It is shown in the Fig. 3 that the variation of the displacement ratio for the angular frequency ratio $\omega/\omega_n < 1$ is well below the resonance condition. Equation (13) indicates the maximum displacement when velocity is zero at angular frequency ratios $\omega/\omega_n = 1$ and $\omega_n t = 2\pi$.

Equation (12) shows the total mass of the retained material with the PZT patch on the top of the granular fill. As the failure has taken place along the shear plane at an angle $\alpha = \alpha_0 + \phi/2$, the internal friction angle of the granular material affects the angular frequency of the soil–wall system. The mass of the triangular wedge varies according to the angle of the failure plane, which is the function of the internal friction angle. Since, according to Rankin’s theory $\alpha_0 = \pi/4$, $\alpha = \pi/4$ for a frictionless sliding plane. Figure 4 indicates the angular frequency at $\alpha = \pi/4$ along the frictionless sliding plane and height of retaining wall $H = 8$ m. The ratio of the height of the wall and the PZT layer has been such that, $H/h_p = 3, 4, 6,$ and 8 . As shown in Fig. 4, the angular frequency decreases with increase in H/h_p . It indicates

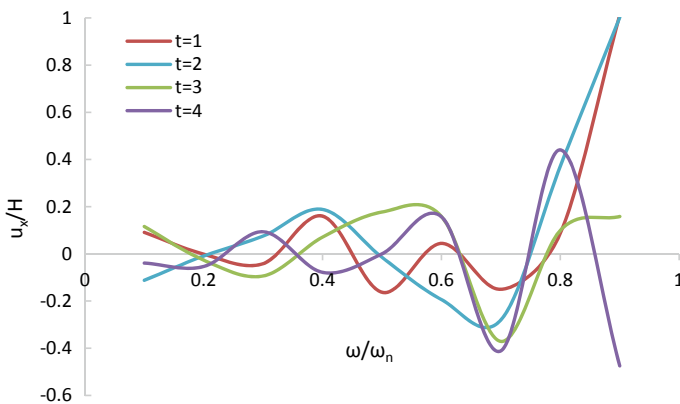


Fig. 3 Displacement ratio variation with the ratio of angular frequency at varied time intervals ($t = 1-4$ s)

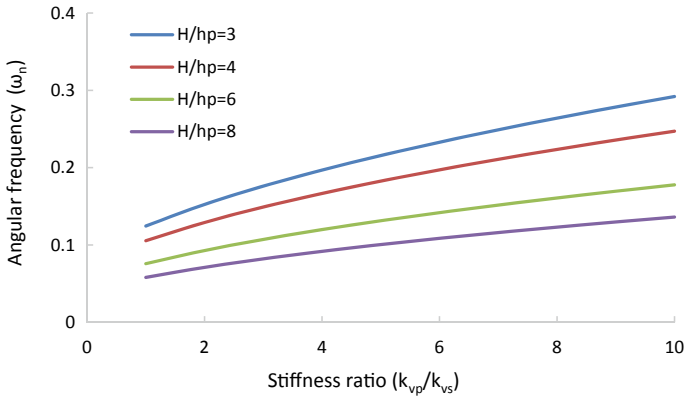


Fig. 4 Variation of the angular frequency with stiffness ratio for frictionless sliding

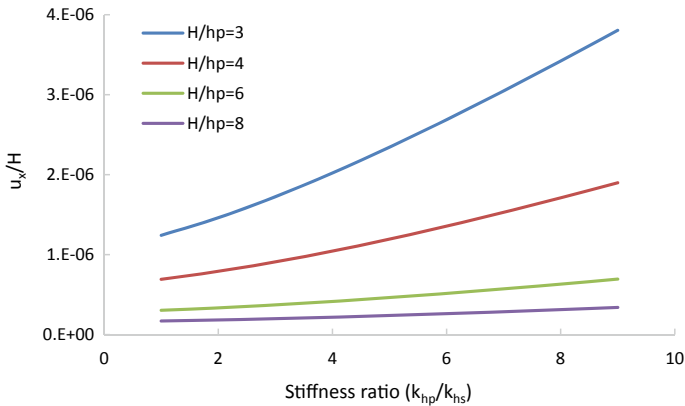


Fig. 5 Variation of displacement ratio with the stiffness ratio of the wall and the PZT at thickness ratio ($H/h_p = 2-8$) at a constant angular velocity at a particular time interval ($t = 3$ s)

that by increasing the thickness of the PZT patch at smaller stiffness ratio, angular frequency can be reduced.

Figures 5 and 6 indicates the variation of displacement ratios u_x/H for different thickness ratio of the wall and the PZT when $t = 3$ and $t = 4$. As shown in Figs. 5 and 6 for $H/h_p = 3$, the displacement ratio shows the variation from 4.E-06 to 7. E-06, i.e., for better results, H/h_p ratio would be greater than 3.

At different stiffness ratio, displacement ratio variations below the resonance frequency, i.e., $\omega/\omega_n < 1$ at different time periods has shown that thickness of the PZT layer is less than one-third of the height of the retaining wall then difference between displacement ratios is smaller. However, displacement ratio variations are

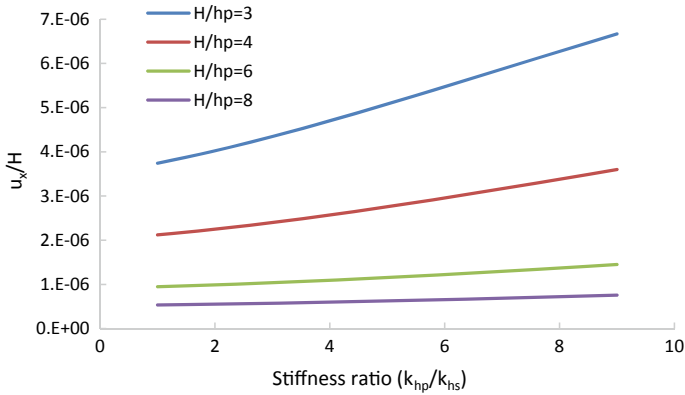


Fig. 6 Variation of displacement ratio with the stiffness ratio of the wall and the PZT at thickness ratio ($H/h_p = 2-8$) at a constant angular velocity at a particular time interval ($t = 4$ s)

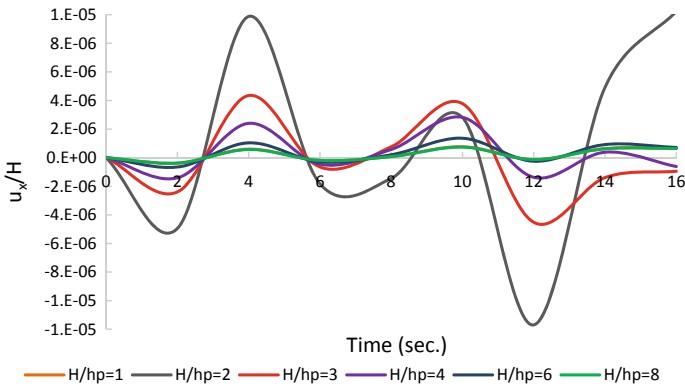


Fig. 7 Variation of horizontal displacement ratio with time at different thickness ratios

very small when the PZT patch less than the one-third of the height of the retaining wall is provided on the outer surface of the granular fill.

Figure 7 shows the variation of the horizontal displacement ratio (u_x/H) with time. The maximum displacement ratio is for $H/h_p = 2$, i.e., thickness of the provided PZT patch should be less than half of the height of the retaining wall.

Figure 8 shows the variation of the vertical displacement ratio with time. It is shown that for $H/h_p = 2$, the displacement ratio is maximum in soil-wall system.

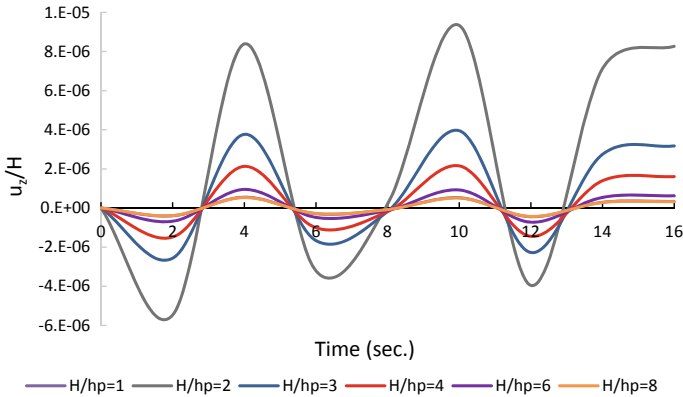


Fig. 8 Variation of vertical displacement ratio with time at different thickness ratio

4 Conclusion

An analysis of the smart structure consisting of the retaining wall with the PZT patch on the upper surface of the granular backfill is presented. On a flexible cantilever retaining wall, and with constant cross section along the height having granular dry, homogeneous, and isotropic backfill free at its upper surface and bounded by a rigid base.

For a model of a flexible linear-elastic retaining wall having a sliding along the shear plane, a solution is developed to quantify the effect of the PZT patch embedded with granular backfill evaluating the displacement and angular frequency of the soil–wall system. In the present study, horizontal and vertical displacement of the soil–wall system and the critical failure plane of a triangular wedge at angle α_0 are considered. Herein, this study can be extended to active case value of α_0 as $\alpha + \phi/2$ and in passive case value of α_0 as $\alpha - \phi/2$. The main conclusions of this study are as follows:

- The material properties and geometrical size of the structure and the PZT patch have a significant influence on the stress–strain curve as visible in Table 2. The present study over and above the past studies has shown the influence of stiffness and mass on the frequency response and displacement of the retaining wall.
- Natural angular frequency of the soil–wall system has been found to decrease with the increasing thickness ratio as shown in Fig. 3. The lower value of the stiffness ratio represents the soil–wall system with low natural angular frequency.
- The variation of displacement ratio for different stiffness ratios has been presented at varied thickness ratios in Figs. 5 and 6. From the results, it is concluded that the amplitude of the displacement increases at thickness ratio more

than one-third; thus, the thickness of the PZT patch should not exceed one-third of the height of the retaining wall.

- Results for the displacement ratio below the resonance frequency have been obtained at the initial time of excitation of angular frequency ratio 0–0.9; the displacement pattern is represented in the horizontal and vertical directions, respectively, as shown in Figs. 7 and 8.
- Results obtained from the variation of the horizontal and vertical displacement ratios with time conclude that at thickness ratio $H/h_p = 2$, maximum displacement takes place in the soil–wall system. Therefore, for an improved design of the smart retaining structure, H/h_p ratio should be more than 3.

The present study shows the potential of PZT applications to control vibrations which consist of mass–spring system in the retaining wall. The present study has been extended to control vibration consisting of shapes, phase difference, damping, and acceleration of dynamic loading.

References

1. Bhalla S, Soh CK (2004) Electromechanical impedance modeling for adhesively bonded piezo-transducers. *J Intell Mater Syst Struct* 15(12):955–972. <https://doi.org/10.1177/1045389X04046309>
2. Dadfarnia M et al (2004) An observer based piezoelectric control of flexible Cartesian robot arms: theory and experiment. *J Control Eng Pract* 12:1041–1053
3. Kumari N, Trivedi A (2018) Application of semi active control strategy for the wall retaining granular fills. In: *Proceeding of China-Europe conference on geotechnical engineering, SSGG*. Springer, pp 978–982. https://doi.org/10.1007/978-3-319-97115-5_20
4. Kerboua M et al (2014) Semi active control of civil structures, analytical and numerical studies. In: *Eighth international conference on material sciences, CSM8-ISM5, Physics Procedia*, vol 55, pp 301–306
5. Irschik H et al (2003) Dynamic shape control of beam-type structures by piezoelectric actuation and sensing. *Int J Appl Electromag Mech* 17(1–3):251–258
6. Matsu H, Ohara S (1960) Lateral earth pressure and stability of quay walls during earthquakes. In: *Proceedings of the 2nd world conference on Earthquake, Tokyo-Kyoto, Japan*, vol 1, pp 165–181
7. Mukherjee A, Joshi S (2002) Piezo-electric sensor and actuator spatial design for shape control of piezo-laminated plates. *AIAA J* 40(6):1204–1210
8. Scott RF (1973) Earthquake-induced earth pressure on retaining walls. In: *Proceedings of the 5th world conference on earthquake engineering, Rome, Italy*, vol 2, pp 1620–1620
9. Wood JH (1973) Earthquake-induced earth pressure on structures. Report No. EERL 73–05, California Institute of Technology, Pasadena, California
10. Yao JTP (1972) Concept of structural control. *ASCE J Struct Div* 98(9):1507–1574
11. Rizet et al (2000) Model control of beam flexural vibration. *J Acoust Soc Am* 107(4):2061–2067

Sequential Drawdown and Rainwater Infiltration Based Stability Assessment of Earthen Dams



Priyanka Talukdar and Arindam Dey

Abstract Earthen dams supporting an upstream reservoir is always associated with the problem of seepage, as water seeks the path of the least resistance through the body of the dam as well as its foundation. Further, due to seasonal rainfall, rainwater can also infiltrate into the earthen dams. Depending on the rate and duration of rainwater infiltration, the stability of the dams is affected. The infiltration of the rainwater into the earthen dams results in the development of pore-water pressures and hydraulic gradients, thus altering the position of the phreatic surface within the embankment, causing consequent deformations. Thus, it is vital to assess the response of earthen dams to the duration and rate of rainwater infiltration during reservoir operating conditions. In this study, considering upstream drawdown conditions, the influence rainfall infiltration on the response of a homogeneous earthen dam has been identified. Coupled stress/pore-water pressure analysis has been carried out for this purpose. It has been observed that the pore-water pressures generated due to the rainwater infiltration adds to the seepage resulting in deformations of the dam faces and reducing the stability of the earthen dams.

Keywords Earthen dams · Transient analysis · Drawdown · Infiltration · Stability · Coupled stress/PWP

1 Introduction

Earthen dam failures are one of the major concerns as they affect the livelihood of people to a catastrophic extent. People across the globe are aware of the devastating effect of dam failures on humankind, and, thus, a unanimity has been developed

P. Talukdar (✉) · A. Dey
Department of Civil Engineering, Indian Institute of Technology Guwahati,
Guwahati 781039, Assam, India
e-mail: priyanka.talukdar1990@gmail.com

A. Dey
e-mail: arindamdey@iitg.ac.in

© Springer Nature Singapore Pte Ltd. 2020
A. Prashant et al. (eds.), *Advances in Computer Methods
and Geomechanics*, Lecture Notes in Civil Engineering 56,
https://doi.org/10.1007/978-981-15-0890-5_45

among governments, industries, and academicians regarding the importance and urgency to study the adverse effect of these failures and to come up with ways to mitigate its impacts. Especially with the current trends in climate changes manifesting harsh climatic sequences, the safety of dams is seeking more importance and public attention as the floods caused due to dam failures, especially in densely populated areas, result in irreparable loss of life and property. The common causes of dam failures include piping, overtopping, and structural failures, which have been investigated by different researchers over the years. However, with the changing climatic conditions, the effect of rainwater infiltration on the stability of earthen dams has become a vital topic of investigation and thorough research.

The water pressure in the soil gets affected by the alteration of boundary flux conditions such as infiltration and evapotranspiration. These boundary flux conditions are governed by rainfall patterns. With rainfall infiltration through the soil pores, the reduction in the shear strength of the soil takes place as the water content of the soil increases. There are studies that have been and being conducted around the world to investigate the complex relationship between slope stability and changes in rainfall patterns. Many studies have been attempted to understand this complex interdependent relationship, which would allow for reliable predictions of potential slope hazards. Fu et al. [3], for instance, identified the soil thickness and rock fragment cover as vital contributing factors to the soil's erosional and hydrological behavior. Thinner soil layers were found to exhibit higher infiltration capacity and lower erosion rates against various rainfall events. Furthermore, it has been reported that landslide events in Italy increase considerably when the rainfall amount and rainfall intensity increases during cold-wet season while the occurrence of slope failure has been found negligible during warm-dry season [1]. The government of Taiwan has detected Central Taiwan as a landslide-prone area, with the predicted increase in the average temperature of Taiwan as 2–3 °C by 2100, as compared to the temperature in 2000, resulting in an increase in the seasonal mean precipitation by 2–26% [8].

The Indian Meteorological Department (IMD) has classified the rainfall intensity on a 24-h timescale as heavy (>6.5 cm/day), very heavy (>13.0 cm/day), and extremely heavy (>20.0 cm/day). The intensity of rainfall has a further category for a short-period violent downpour over a limited area called as a cloud burst (CB). This kind of relatively high intensity of rainfall, which is usually accompanied by thunderstorms, is related to deep convection resulting in bursting and discharge of a whole cloud at once. The studies related to cloud burst phenomenon have gained popularity with time. References available date back to Woolley [11] who studied about floods caused by CB that occurred during the period 1850–1938 in Utah, United States, utilizing the information published in newspaper reports at that time. In India, people residing in the hilly and mountainous Himalayan regions commonly encounter such CB events. However, due to small spatial and temporal scales, the coarse rain gauge network of IMD is unable to capture these events intricately. Such CB events in India have been confirmed from the flash floods caused by the rainfall and the damages it causes to life and property. Review work has been conducted by Dimri et al. [2] on the occurrences of CB in the western

Himalayan regions of India. The work suggests that in the valley folds of the southern rim of the Himalayan region of India, at an elevation range of 1,000–2,500, the occurrences of CB events are maximum.

There are a number of works where studies have been conducted to find the effect of rainfall intensity on the stability of hill slopes. However, not much literature has been found that provides detailed insight into the response of earthen dams to varying rainfall intensity and duration. In this work, an attempt has been made to study the response of a homogeneous earthen dam to three different rainfall intensities (0.09; 0.24; 2.5 m/day) during a reservoir drawdown operation while considering the rainfall occurrence for both high and low durations (5 days and 24 h, respectively).

2 Numerical Model for the Present Study

The model used in the present study consists of a homogeneous earthen dam with an embankment of height 10 m and width 50 m. The upstream slope has an inclination of 2.5H:1V and the downstream slope has an inclination of 2.2H:1V. The section has been chosen as per the recommended guidelines provided for homogeneous earthen dams in IS 12169 [7]. The embankment has a crest width of 3 m and it has a free board of 1 m. The foundation height and width are chosen to be 10 m and 80 m, respectively, as shown in Fig. 1.

2.1 Material Properties

In numerical modeling, the correct assignment of the material models with proper input parameters plays an important role. In Seep/w analysis, the embankment has been modeled using “saturated/unsaturated” material model while the foundation has been modeled using “saturated only” material model. In Sigma/w, the “elastic-plastic material” model has been used to perform the deformation analysis.

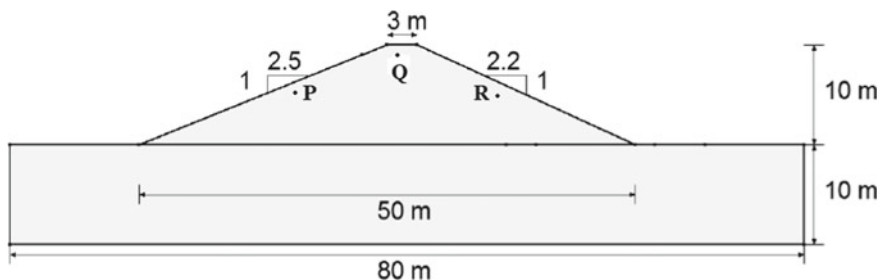


Fig. 1 Model of the earthen dam used in the present study

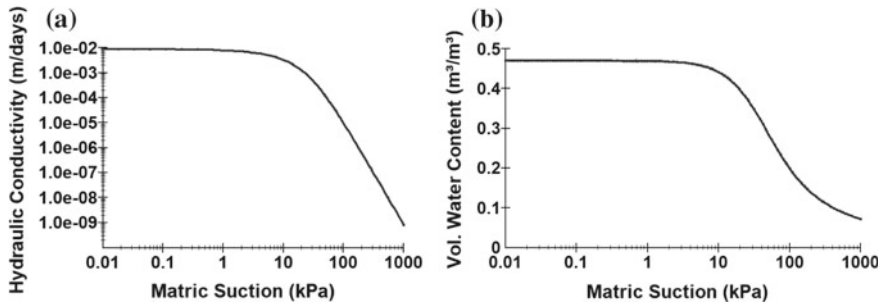


Fig. 2 Characteristics of the embankment material. **a** Hydraulic conductivity function. **b** Volumetric water content function

Table 1 Material properties used in modeling

	Cohesion (kPa)	Friction angle (degree)	Unit weight (kN/m ³)	Elastic modulus (MPa)	Permeability (m/days)
Embankment	10	25	20	15	0.00864
Foundation	12	18	20	30	8.64×10^{-5}

A stability analysis had been performed, with the aid of Slope/w, to obtain the corresponding stability assessment using the “Mohr–Coulomb material” model. The hydraulic conductivity function and the volumetric water content function for the embankment material have been shown in Fig. 2a, b.

The various soil properties used in the modeling have been obtained from the extensive literature survey (Seep/w [4]; Sigma/w [5]; Slope/w [6]; IS 12196 [7]; USBR [9]; USBR [10]) coupled with proper engineering judgment. Table 1 lists the material properties used in the numerical study.

3 Analyses Methodology

The present numerical study has been conducted with the aid of Seep/w, Sigma/w, and Slope/w modules of Geostudio. The main objective of this work was to study the flow and deformation response of earthen dams to three different rainfall intensities during reservoir drawdown operation. The rainfall intensities were classified as heavy rainfall (0.09 m/day), extreme rainfall (0.24 m/day), and cloudburst CB (2.5 m/day). These rainfall intensities are chosen as per the guidelines given by IMD. To achieve this objective, first, different models were simulated for initial steady-state seepage analysis, in Seep/w, to establish the existing pore-water pressures and total head conditions. The initial stress conditions were generated using the in situ analysis of Sigma/w. The drawdown of the reservoir has

been analyzed using the Coupled Stress/PWP analysis in Sigma/w, in which the pore-water pressure generated in the steady-state analysis and stresses generated in the in situ analysis were used to define the initial conditions for the transient state. A drawdown rate of 0.9 m/day has been used in the analysis and this rate of drawdown for the analysis has been chosen in such a manner that the upstream of the dam remains stable even after the drawdown operation. The rainfall infiltrations of different intensities have been simulated from the 10th day after the drawdown operation has been completed. A unit flux boundary condition has been used to simulate the rainfall infiltration. Each rainfall intensity is simulated for two different durations, namely a high duration (infiltration lasting for 5 days) and a low duration (infiltration lasting for 24 h.). A stability analysis has been performed after every stage of simulation, with the aid of Slope/w, to obtain the corresponding stability assessment. The entry–exit specification has been used to define a wide range of circular slip surfaces in the slopes of the dam. Simulation of these hypothetical, yet realistic, scenarios produced results that can be used to understand the behavior of the earthen dams when subjected to sequential drawdown and rainwater infiltration. A detailed analysis of the results obtained from the simulations along with the discussions is provided in the next section.

4 Results and Discussions

4.1 *Transient State Conditions of Reservoir Operation (Flow/Deformation Analysis)*

Transient flow conditions lead to time-dependent variation of pore-water pressure and effective stresses. Transient conditions of reservoir operations include first filling, normal operational cycles, rapid drawdown, seasonal fluctuations in reservoir operation, and flood loading. As an effect of the abovementioned transient loads on the dams (or levee), the time required for a saturation front to move through the core section of the dam or its foundation is also adjudged as a transient effect. In this study, rainwater infiltration scenarios have been evaluated for different rainfall intensities on a homogeneous earthen dam subjected to a prior drawdown operation. The variation of PWP with time near the heel and toe of the dam is shown in Fig. 3 and Fig. 4, respectively.

It is observed that there is no change in the magnitude of pore-water pressures with change in the rainfall intensities. The variation of PWP with varying rainfall intensities is very much dependent on the dissipation of matric suction and rise in the phreatic surface. In case of the homogenous earthen dams without central core or drainage layer, as considered in this study, the embankment material used is a fine material with sufficiently low void ratio and a substantially low saturated permeability. As a result, the varying rainfall intensities could not substantially alter the pore pressure variation within the body of the dam; rather, for any of the

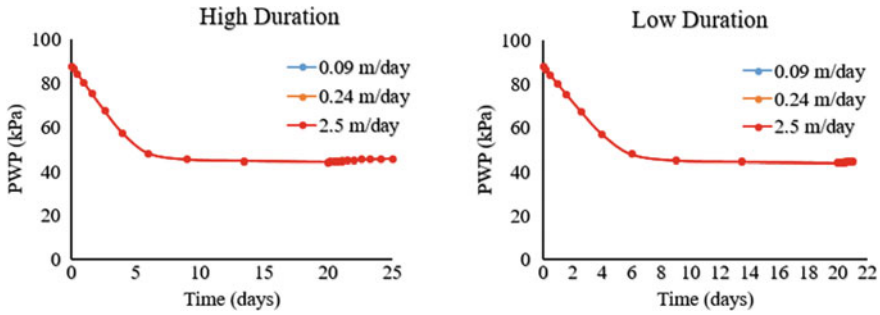


Fig. 3 Variation of pore-water pressure (PWP) with time at the heel of the dam

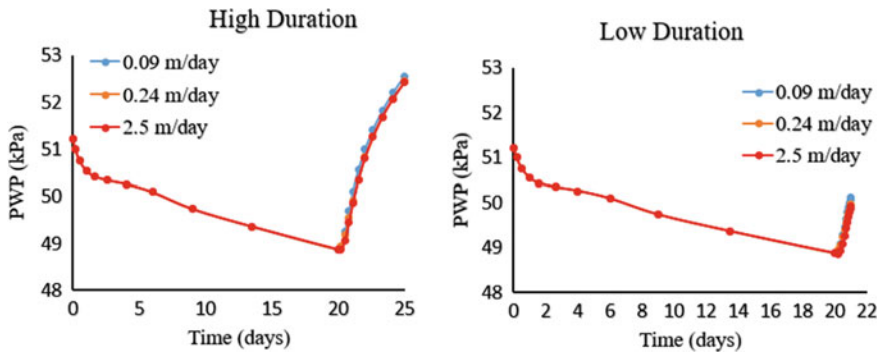


Fig. 4 Variation of pore-water pressure (PWP) with time at the toe of the dam

variations, the maximal infiltration has been effective in major portions of the dam body. Significant rise in PWP with the rainfall duration has been more pronounced in the toe portion of the dam as compared to its heel portion.

As the different intensities did not pronounce any significant variation in the PWP values, the deformation of the dam was studied considering the particular rainfall intensity of 0.09 m/day. The variation of displacement contours, along with displacement vectors, for heavy rainfall intensity (0.09 m/day) is shown in Fig. 5. These variations were measured at the end of the corresponding infiltration periods. The reservoir was drawn down in 10 days, following which rainwater infiltration was simulated from the 10th day after the drawdown event was completed. Thus, the infiltration of rainwater started on the 20th day and it was simulated with a constant rainfall intensity of 0.09 m/day. The rainfall was continued for 24 h. (i.e., from 20th to 21st day) for low duration infiltration while for the high duration infiltration, the rainfall was continued for an additional 5 days (i.e., from the 20th day to the 25th day).

The displacement variations were observed on the 25th day (i.e., 5 days after the onset of infiltration) and on the 21st day (i.e., 1 day after the onset of infiltration)

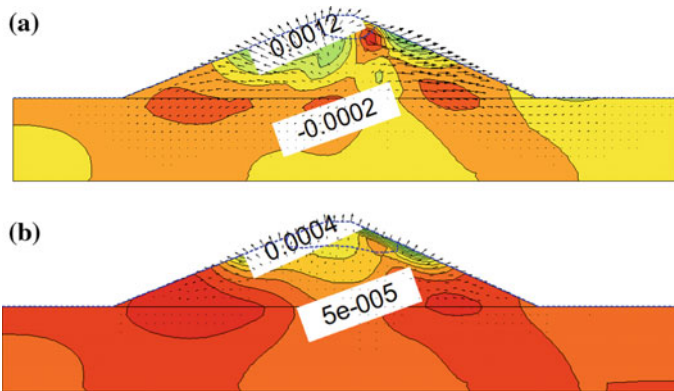


Fig. 5 Displacement contours with displacement vectors showing the deformation behavior of the dam for heavy rainfall intensity (0.09 m/day) measured at the end of infiltration period **a** 5 days for high duration infiltration **b** 24 h for low duration infiltration

for high and low duration infiltration cases, respectively, as shown in Fig. 5a, b. The displacement contour shows that for higher rainfall duration, higher deformation is induced in the dam as indicated by higher magnitudes of the displacement vectors exhibiting heaving of the embankment.

To have a proper understanding about the time-varying deformation behavior of the embankment, the variation of displacement of certain locations of the embankment with time has been studied (considering rainfall intensity of 0.09 m/day). Figure 6 highlights the displacements measured at three different points, namely one at the upstream face (Point P), one below the crest (Point Q), and one at the downstream face (Point R), as shown in Fig. 1.

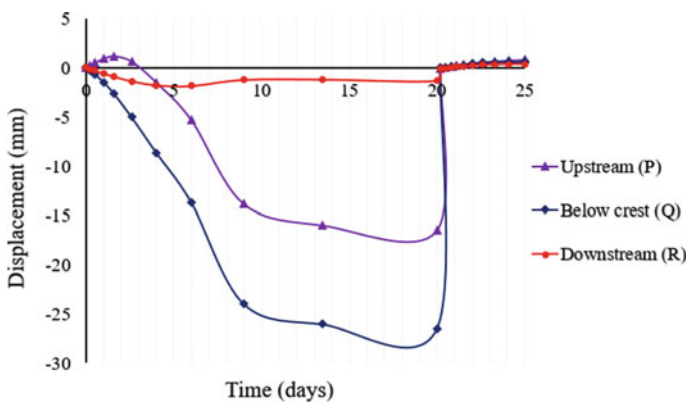


Fig. 6 Variation of displacement with time for a rainfall intensity of 0.09 m/day

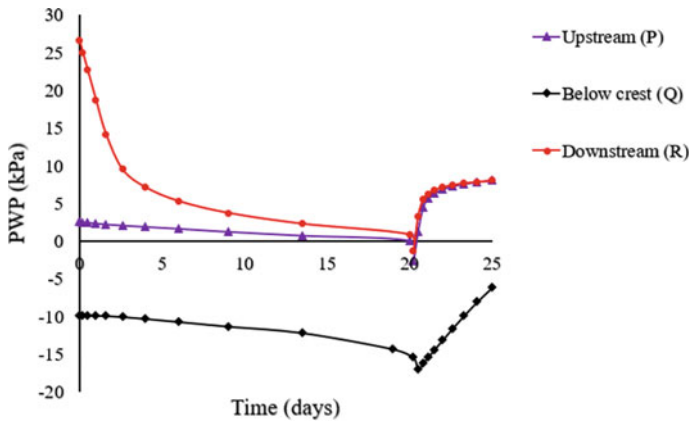


Fig. 7 Variation of PWP with time for a rainfall intensity of 0.09 m/day

It can be observed that the embankment undergoes settlement until the 20th day, which is attributed to the drawdown phenomenon, taking place till the first 10 days, followed by its aftereffect of gradual pore pressure dissipation for the continuing 10 days. Due to the removal of the reservoir water, the gradual dissipation of the excess PWP takes place with time (Fig. 7), inducing settlement at various locations of the embankment. The onset of rainfall is simulated from the 20th day.

On the 20th day, with the inception of rainwater infiltration, the pore-water pressure increases abruptly as observed in Fig. 7. The rainwater infiltration reduces the suction and appends the volume of infiltrated water to the volume of the embankment at the end of the drawdown condition. Such a phenomenon leads to heaving at various locations of the embankment, as shown in Fig. 5.

4.2 Transient State Conditions of Reservoir Operation (Stability Analysis)

Stability analysis was performed for all the models to assess the change of the Factor of Safety (FoS) for the different scenarios. The variation of FoS with time for the upstream and the downstream regions of the dam is shown in Fig. 8 and Fig. 9, respectively.

The factor of safety of the upstream slope of the dam decreases noticeably within a short period during the drawdown operation, attributed to the rapid dissipation of the pore-water pressure from the upstream face of the dam. After the completion of the drawdown of water from the reservoir, FoS becomes almost constant as shown in Fig. 8. Owing to the continual dissipation of excess pore-water pressure through the upstream face for the next 10 days after the drawdown, FoS should have increased due to the enhancement in the effective strength of the dam material.

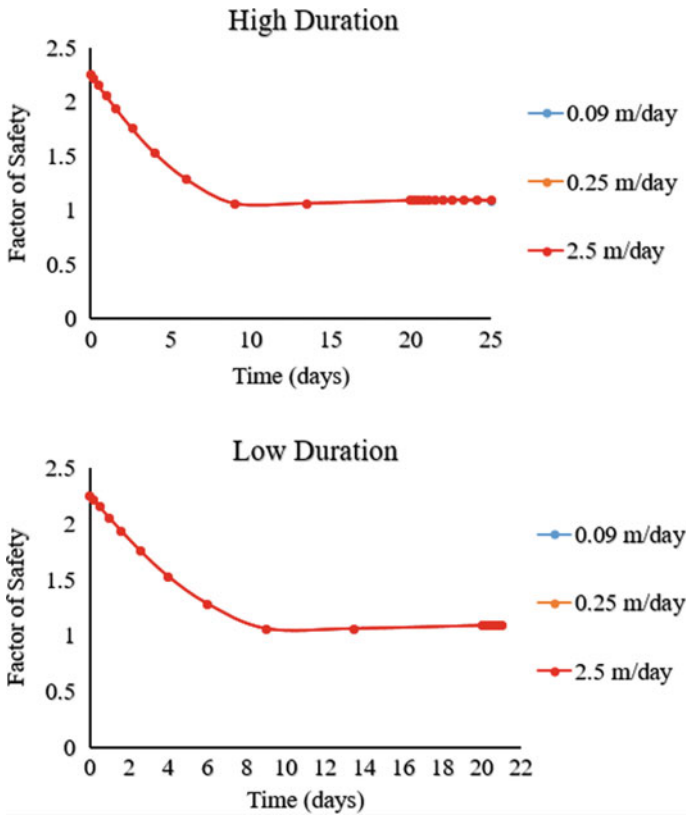


Fig. 8 Variation of FoS with time for the upstream side of the dam

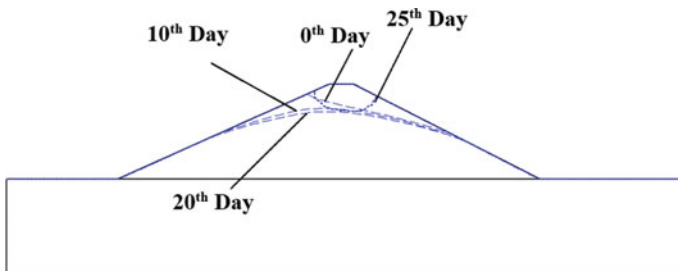


Fig. 9 Position of the phreatic surface at different stages of drawdown and infiltration

However, in the meanwhile, the infiltration of rainwater gradually increases the pore-water pressure, and thus the effective FoS values show almost a constant magnitude. In the downstream portion of the dam, initially, FoS increases due to retraction of the steady-state phreatic line due to the drawdown-induced dissipation

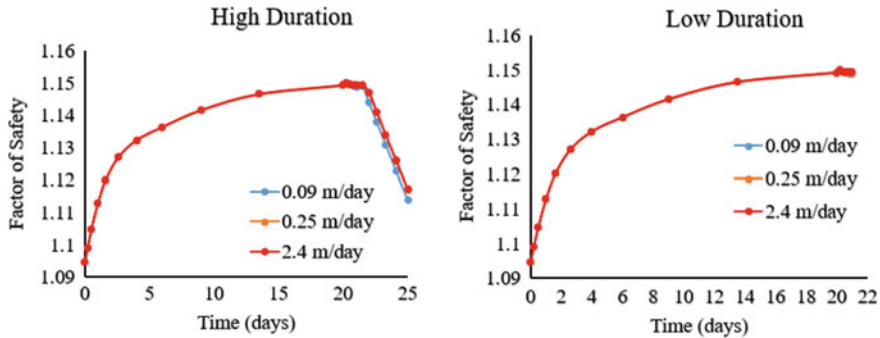


Fig. 10 Variation of FoS with time for the downstream side of the dam

of PWP from the upstream face. Figure 9 shows the typical locations of the phreatic line on the 0th day (initial steady-state condition before drawdown), and its retracted levels on the 10th (at the end of drawdown) and 20th days (at the initiation of the rainfall event).

Later, the infiltration of rainwater leads to sufficient replenishment of the PWP (as shown by the phreatic level on the 25th day in Fig. 9) and thus, a decrease in FoS of the downstream face is observed as shown in Fig. 10. As expected, the higher duration rainfall adds larger PWP in the downstream section of the dam, thus exhibiting a substantial reduction in FoS.

5 Conclusions

The study aimed to understand the behavior of a homogeneous earthen dam when subjected to rainwater infiltration from different rainfall intensities and durations after a drawdown operation of the reservoir has been completed. Following are the conclusions obtained from the analyses:

- (a) There is no change in the magnitude of pore-water pressures (PWP) with the change in the rainfall intensities, resulting in no effect on the stability of the dams.
- (b) Different rainfall intensities did not have any effect on the (PWP) and stability values of the dams owing to the fine material of low permeability used for the construction of homogeneous earth dams.
- (c) It is not the intensity but the duration of rainfall that is playing an important role in the stability of the dams in this study. Higher duration of rainfall results in lesser FoS values and greater PWP values.
- (d) Rainfall infiltration results in heaving of the embankment with the reduction of suction and rise of PWP values.

References

1. Ciabatta L, Camici S, Brocca L, Ponziani F, Stelluti M, Berni N, Moramarco T (2016) Assessing the impact of climate-change scenarios on landslide occurrence in Umbria Region, Italy. *J Hydrol* 541(A):285–295
2. Dimri AP, Chevuturi A, Niyogi D, Thayyen RJ, Ray K, Tripathi SN, Pandey AK, Mohanty UC (2017) Cloudbursts in Indian Himalayas: a review. *Earth Sci Rev* 168:1–23
3. Fu Z, Li Z, Cai C, Shi Z, Xu Q, Wang X (2011) Soil thickness effect on hydrological and erosion characteristics under sloping lands: a hydropedological perspective. *Geoderma* 167–168:41–53
4. GEO-SLOPE International Ltd (2012) Computer program SEEP/W-for finite element seepage analysis', 308 User's Guide, Calgary. Alta, Canada
5. GEO-SLOPE International Ltd (2012) Computer program SIGMA/W-for finite element deformation analysis, 308 User's Guide, Calgary. Alta, Canada
6. GEO-SLOPE International Ltd (2012) Computer program SLOPE/W-for finite element stability analysis, 308 User's Guide, Calgary. Alta, Canada
7. IS 12169 (1987) Criteria for design of small embankment dams, B.I.S
8. Meei-Ling L, Sheng-Chi L, Yu-Ching L (2014) Review of landslide occurrence and climate change in Taiwan In: Ken H, Suzanne L, Luciano P (eds) Slope safety preparedness for impact of climate change, pp 1–24. CRC Press, Fl, USA
9. United States Bureau of Reclamation (2003) Design of small dams. Oxford & IBH, New Delhi
10. United States Bureau of Reclamation (2014) Design standards no. 13: Embankment dams, Chapter 8: Seepage analysis and control
11. Woolley R (1946) Cloud burst floods in Utah 1850–1938. U.S. Government, Washington D.C., pp 1–154

Water-Soluble Super Absorbent Polymer as Self-curing Agents in High-Strength Cement Concrete Mixes



N. T. Suryawanshi and S. B. Thakare

Abstract The ordinary Portland cement is mixed with various mineral admixtures to produce high strength concrete. Mineral admixtures like microsilica and metakaolin are well-known supplementary cementitious materials. Metakaolin is derived from natural pozzolanic material named as kaolin clays; many researchers had tried it to produce high strength concrete. Concrete produced using such natural pozzolana and of low water–cement ratio might not have enough water for hydration process. It would affect adversely the properties of concrete. In this study, high strength concrete is produced using metakaolin and mixed with superabsorbent polymer (SAP) to fulfill the demand of water during hydration process. It also examines the effect of SAP on the mechanical properties of concrete. The study includes use of two types of polymers commercially available, namely polyvinyl alcohol (PVA) and polyacrylic acid (PAA). Concrete is mixed with both types of polymers separately. Concrete specimens are cast by using SAP and without SAP and cured under different curing regime conditions. Polymers are added in varying percentages from 0.2 to 1.0% by the weight of cement. The test results reveal that 0.4% by the weight of cement is the optimum dose of PVA which produces strength that nearly equals to the strength of the control mix and for the same dose of PAA, the strength obtained is about fifty percent of the strength of the control mix. As the strength gets reduces by the addition of polyacrylic acid, this paper aims to describe the effect of polyvinyl alcohol and polyacrylic acid in combination on the properties of concrete. The study reveals that use of superabsorbent polymers in combination and in lesser percentages is more effective in water retention and strength enhancement as compared to air-cured mixes (No curing).

Keywords Natural pozzolana · Supplementary cementitious materials · Water-soluble polymers · Water retention · Mechanical properties

N. T. Suryawanshi (✉)
Savitribai Phule Pune University, Pune, MS, India
e-mail: nt.suryawanshi@gmail.com

N. T. Suryawanshi · S. B. Thakare
JSPM's RSCOE, Tathwade, Pune, MS, India

1 Introduction

Curing plays vital role in the enhancement of properties of concrete. Cement concrete hardens and develops the mechanical properties over the passage of time by the process. The curing process restricts water evaporation from the concrete. Nowadays, traditional methods of curing are ineffective because of various factors like bad workmanship and scarcity of water. Self-curing concrete are produced by the addition of self-curing agents like SAP. Polyethylene glycol is one of the water-soluble polymers found to be effective in water retention and improving the hydration process [1].

High strength concrete (HSC) is produced by using supplementary cementitious materials (SCMs) like silica fume and high reactive met kaolin. From the investigation, high strength concrete produced in low water–cement ratios (below 0.4) restricts entry into the water. It would result in insufficient curing. Water required for the hydration process is not enough and some additional water is required for the curing process. The HSC produced using mineral admixture like metakaolin is susceptible to autogenous shrinkage because of insufficient water for the hydration process. Hence, in this study, an attempt was made to fulfill the demand of water requires for the hydration process by using SAPs. Two types of superabsorbent polymers namely polyvinyl alcohol and polyacrylic acid have been evaluated as self-curing agents. The performance of self-curing mixes was evaluated and the results obtained were compared with the results of moist-cured and air-cured (No curing) mixes.

The purpose of this study is to evaluate the possibility of self-curing using superabsorbent polymers in high strength concrete produced using natural pozzolana and the objective of this study is to find the effect of internal curing on the mechanical properties of HSC produced using natural pozzolana.

2 Experimental Procedures

2.1 *Properties of Superabsorbent Polymers*

Polyvinyl alcohol is a white-colored granular powder. It is soluble in water 5% of polyvinyl alcohol shows pH in the range of 5.0–6.5. It has a melting point of 180–190 °C.

Polyacrylic acid is prepared from monomer Acrylic acids by free radical polymerization reaction. The presence of carbonyl group causes high reactivity of acrylic acid leading to the addition of versatile nucleophiles. PAA is a white, colorless and fluffy powder at room temperature. It is soluble in water and pH of the solution ranges between 3 and 5.

The Empirical Formula of PAA is $C_3H_4O_2$.

In this study, polyacrylic acid in crystal form passing through 150 μ and retaining on 90 μ has been used. These crystals absorb water up to 100–110 times of its weight.

3 Tests on Material

3.1 SEM Test

Scanning Electron Microscope (SEM) provides detailed high-resolution images of the samples. An SEM is a type of electron microscope that produces images of a sample by scanning the surface with a focused beam of electrons. The electrons are interacting with atoms in the sample, producing various signals that contain information about the sample's surface topography and composition. Figures 1, 2, 3, 4, 5, 6, 7 and 8 are the images of the material used for experimental investigation. The sample were tested for SEM and EDX in Savitribai Phule Pune University.

3.2 EDX Test

Energy Dispersive X-ray Spectroscopy (EDX) is an analytical technique used for the elemental analysis or chemical characterization of a sample. During EDX analysis, we normally get elemental composition in both normalized atomic percentage concentration and normalized weight percentage concentration.

Fig. 1 SEM test on cement

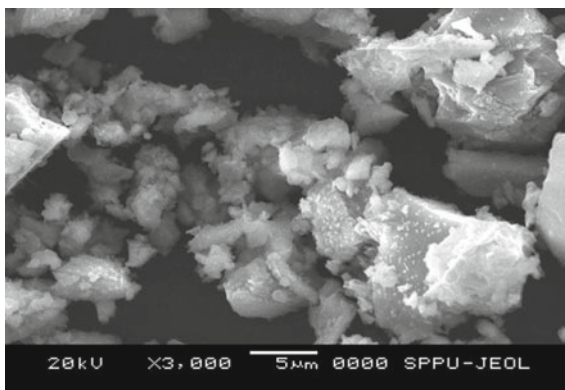


Fig. 2 SEM test on metakaolin

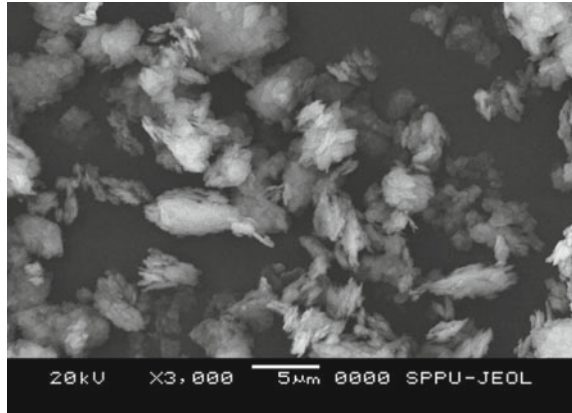


Fig. 3 SEM test on PAA

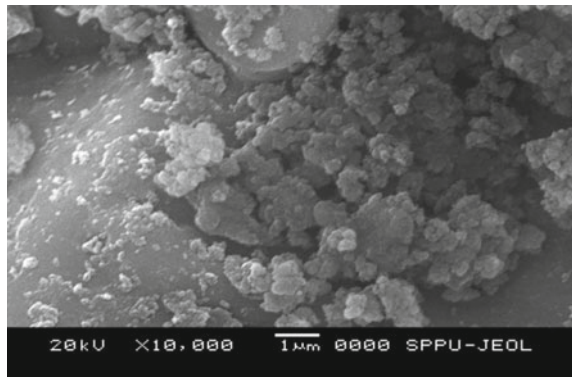
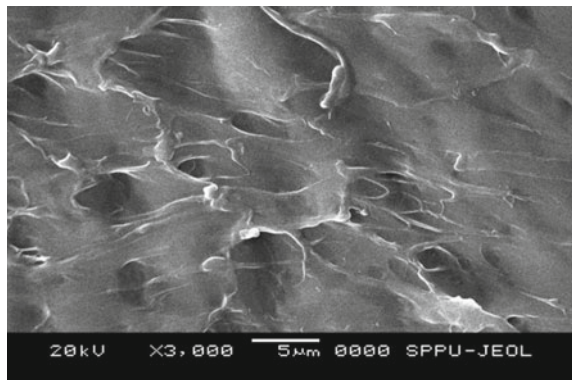


Fig. 4 SEM test on PVA



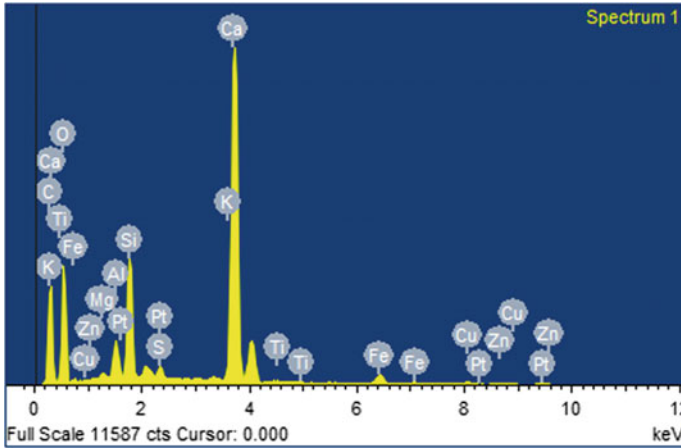


Fig. 5 EDX of cement

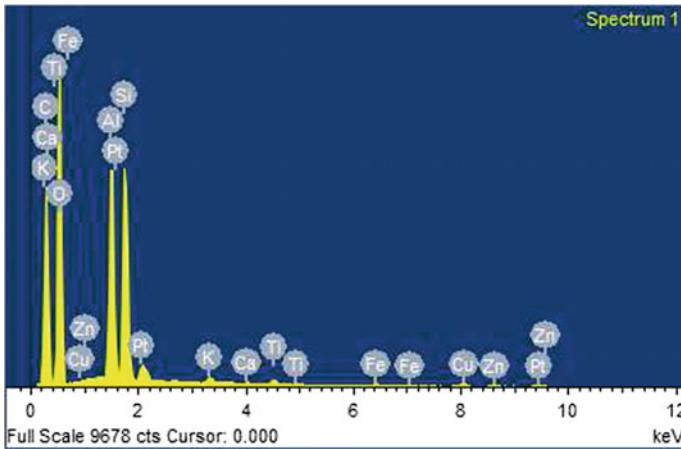


Fig. 6 EDX of metakaolin

3.3 Experimental Program

High strength concrete was prepared by using metakaolin as per IS 10262:2009. The dose of metakaolin finalized from the literature was reviewed [2] and it was 10% by the weight of cement used for casting all mixtures. Concrete was mixed by using horizontal pan mixer. All the ingredients were dry mixed for 2 min. PVA and PAA were added in varying percentages and different mixes were prepared. Table 1

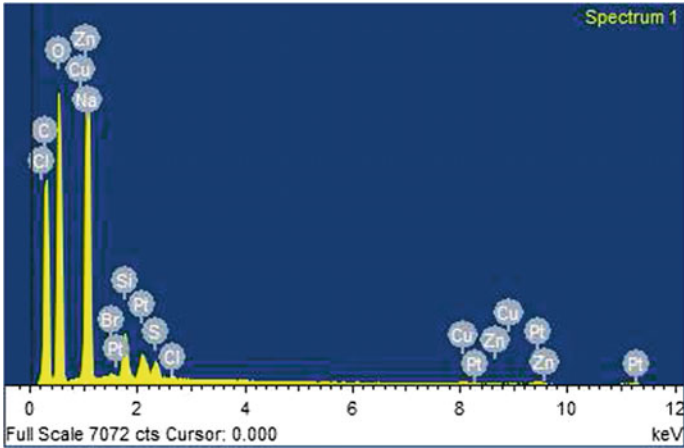


Fig. 7 EDX of PAA

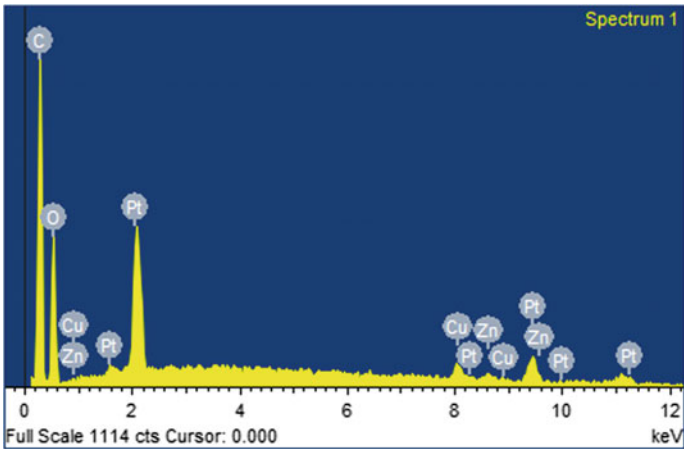


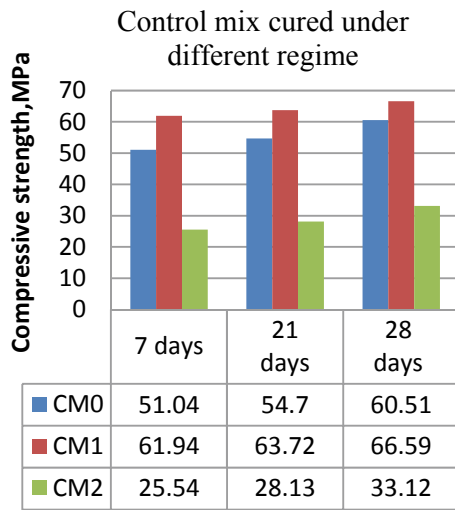
Fig. 8 EDX of PVA

shows the combinations and curing conditions. Half of the mixing water was added gradually with the polymers and superplasticizer. The Superplasticizer used was modified naphthalene formaldehyde sulphonate and the trade name is Sikament-4101NS (Confirms IS 9103-1999). According to Neville (1996), SPs can affect the concrete strength even at constant water–cement ratios. Hence, the dose of Sikament was kept as 1% constant for all mixes. All constituents were mixed

Table 1 Combination of polymers under different curing conditions

Mix no.	Mix type	Curing condition	Tests
CM0	Control mix with OPC	Moist	Mechanical properties: (1) Compressive (2) Flexural (3) Split tensile strength
CM1	Control mix with OPC +10% HRM	Moist	
CM2	Control mix with OPC +10% HRM	Air-dry curing	
SCM1	0.1%(PAA) + 0.3%(PVA)	Self-curing at room temperature	
SCM2	0.2%(PAA) + 0.2%(PVA)		
SCM3	0.3%(PAA) + 0.1%(PVA)		
SCM4	0.4%(PAA)		
SCM5	0.4%(PVA)		

Fig. 9 Compressive strength of control mix



thoroughly for 2 min. After mixing three types of specimens, namely cubes (150 × 150 × 150 mm), beams (100 × 100 × 500 mm), and cylinders (Ø100 mm, length 200 mm), they were cast by using steel molds. The casted specimens were demoulded after 24 h and cured in a laboratory under different curing conditions as shown in Table 1. All the specimens were tested after 28 days for compression, tensility, and flexure load and the results obtained are shown in Figs. 9, 10, and 11. Every day weight loss was observed and percentage weight loss was found as shown in Fig. 12.

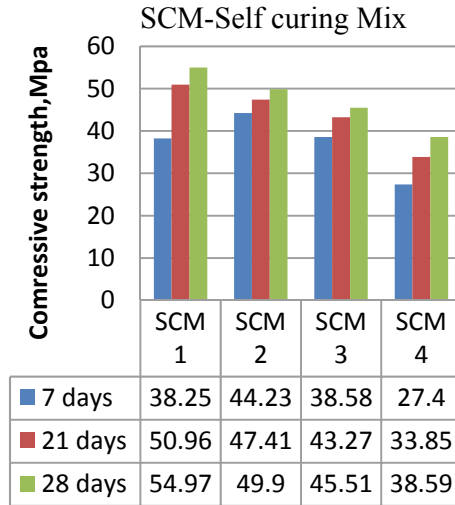


Fig. 10 Compressive strength of self-curing mix

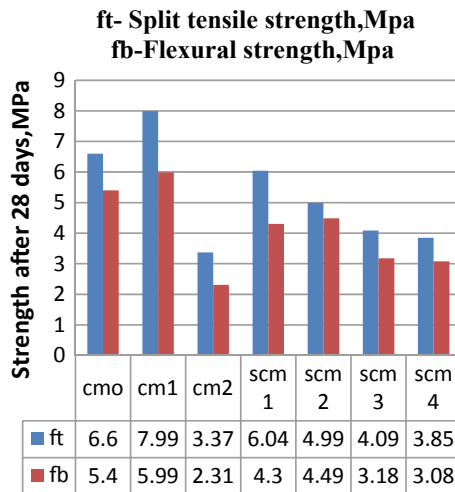
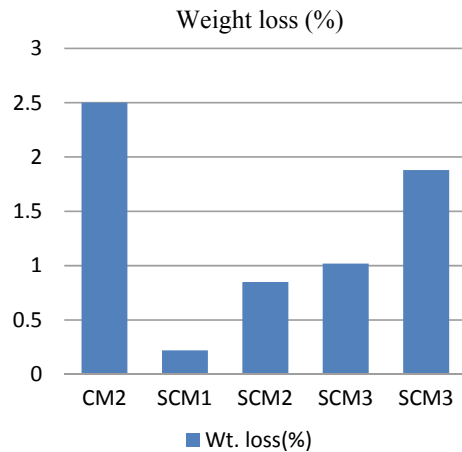


Fig. 11 Split tensile and flexural strength of all mixes

Fig. 12 Percentage weight loss



4 Result and Discussions

4.1 Compressive Strength

Figure 9 shows the compressive strength of the control mix. The control concrete incorporated with highly reactive metakaolin, water cured gives strength 66.59 N/mm^2 and the same concrete cured in air-dry regime means no curing gives the result 33.12 N/mm^2 . It indicates that non-cured mixes produce strength for only about 50% of the strength of water-cured mixes. On the other side, self-cured mix made using polyvinyl alcohol produces the strength equal to 65.42 N/mm^2 that is nearly equal to the strength of water-cured mix.

Figure 10 shows the results obtained of self-cured mix produced by combination; the results obtained were found to decline as the dose of polyacrylic acid increases. For 0.4% polyacrylic dose, the results obtained are 38.59 N/mm^2 ; it's slightly higher than the strength of non-cured mix but about 50% less than the water-cured mix.

The study by Siriwatwechaklu et al. explain that superabsorbent polymers mixed with water form a polymer gel by swelling. The water molecules diffuse in space of the polymer network and hydrate the chain. The process is reversible during the hydration of concrete mix and it would result in collapsing of the superabsorbent polymers [3]. The effect of SAP may be a twofold increase or decrease of compressive strength. Klemm et al. presented that superabsorbent polymers increase the degree of hydration and can prevent the concrete from self-desiccation. Denser paste obtained prevents micro-cracks. However, on the other hand, SAP increases porosity by creation of voids in its collapsed state. The pores may have negative influence on the strength. Therefore, higher the water contents in the concrete, lower is the resulting compressive strength [4]. The study conducted by Reinhardt et al. showed loss of strength by the low cement paste content and increased

porosity. The strength test of the concrete mixed with SAP showed a rather lower result [5].

In the present study, polyacrylic acid (crystal form) has been used and it showed lower strength when used solely as well as in a combination. It may be because of the void formation in its collapsed state as per the findings discussed above.

4.2 Split Tensile and Flexural Strength

Figure 11 shows split tensile strength and flexural strength of the concrete for all curing conditions. The result showed that split tensile strength of the self-cured mix varies from 9 to 11% of the compressive strength of the moist-cured control mix. It also indicates that flexural strength varies from 7 to 9% of the compressive strength of the moist cured control mix.

4.3 Weight Loss

Figure 12 shows the percentage weight loss with time due to moisture evaporation under natural drying conditions for conventional non-cured mix and with self-cured mixes. From the observation made, conventional non-cured mix lost more water relative to self-curing mixes. This indicates better water retention ability (i.e., lower weight loss) of the self-cured mix.

5 Conclusions

From the experimental investigation, the following conclusions can drawn.

- I. Polyvinyl alcohol is used as a self-curing agent in kaolin-based high strength concrete.
- II. The results obtained with addition of Polyacrylic acid are lower than the expected; this is because of more water release during the hydration process. This indicates that polyacrylic acid used in lower percentages may enhance strength properties.
- III. The combination of both the polymers gives the results more than the non-cured mix but not up to the moist-cured mix. However, due to the complicated nature of absorption and desorption, more comprehensive studies are required.

- IV. The use of lesser amount of polyacrylic acid and polyvinyl alcohol in combination may prove effective in water retention and strength enhancement. Hence, further research will be conducted by using diversified combinations with lower percentage.

Acknowledgements First, I would like to express my sincere gratitude to my advisor Prof. S. B. Thakare for the continuous support to my research work, for his patience, motivation, and immense knowledge. In addition, I would like to thank Dr. P. D. Nemade and Dr. R. K Jain, who gave access to the laboratory and research facilities. Without their precious support, it would not be possible to conduct this research.

References

1. El-Dieb AS et al (2012) Water soluble polymers as self-curing agents in cement mixes. *Adv Cem Res (Thomas Telford)* 24(5):291–299
2. Prahallada MC (2012) Effect of replacement of cement by metakaolin on the properties of high performance concrete subjected to hydrochloric acid attack
3. Sirwatwechaklu et al (2010) Superabsorbent polymer structures. In: International RILEM conference on use of superabsorbent polymers and other new additives in concrete. RILEM publications S.A R.I., Lyngby, pp 243–252
4. Klemm et al. Super absorbent polymers in cementitious composites. Glasgow Caledonian University, Glasgow, UK
5. Reinhardt et al (2010) Application of super absorbent polymers in light weight concrete with porous matrix. In: International RILEM conference on use of superabsorbent polymers and other new additives in concrete. RILEM publications S.A R.I., Lyngby, pp 207–212

Pounding Probability of Three-Span Simply Supported Bridge Subjected to Near-Field and Far-Field Ground Motions



Lopamudra Mohanty, Rahul Das and Goutam Mondal

Abstract During earthquake shaking, pounding of decks occurs in multi-span simply supported bridges (MSSS) when relative displacement between two adjacent decks exceeds the available expansion gap. It may cause the failure of a bridge in various ways such as unseating of the deck, pier failure, bearing failure, and local damage to decks and girders. The damage level of bridge also depends on the distance of the bridge from the fault rupture because the properties of ground motion change with distance from the fault rupture. This paper focuses on pounding probability of a three-span highway bridge subjected to three different types of ground motions, namely, near-field ground motion with pulse, near-field ground motion without pulse, and far-field ground motion along the longitudinal direction of the bridge. Finite element analysis of the bridge was performed in OpenSees considering the nonlinear behavior of piers and bearings. Energy dissipation during pounding of decks was also considered. Incremental dynamic analysis (IDA) was performed to obtain the level of earthquake shaking (i.e., peak ground acceleration (PGA)) required for pounding between adjacent decks. Based on the IDA, fragility analysis was performed to obtain the pounding probability of decks. At a particular PGA level, it was found that far-field ground motions resulted in higher pounding probability as compared to near-field ground motions. When gap size was small, pounding probability for near-field ground motion with pulse was found to be smaller than that of near-field ground motion without pulse. However, when the gap size was large, near-field ground motion with pulse caused higher pounding probability as compared to near-field ground motions without pulse.

Keywords Pounding · Near-Field and Far-Field ground motions · Incremental dynamic analysis (IDA) · Fragility curves

L. Mohanty · R. Das · G. Mondal (✉)
School of Infrastructure, Indian Institute of Technology Bhubaneswar,
Bhubaneswar, Odisha, India
e-mail: gmondal@iitbbs.ac.in

© Springer Nature Singapore Pte Ltd. 2020
A. Prashant et al. (eds.), *Advances in Computer Methods
and Geomechanics*, Lecture Notes in Civil Engineering 56,
https://doi.org/10.1007/978-981-15-0890-5_47

565

1 Introduction

In most of the past major earthquakes (for instance, 1979 Imperial Valley earthquake, 1989 Loma Prieta earthquake, 1995 Kobe earthquake, 1999 Chi-Chi earthquake, 2001 Bhuj earthquake, etc.), it has been observed that pounding caused local damage as well as the global failure of simply supported bridges. Also, response of a bridge is dependent on properties of ground motion, the bridge is subjected to (e.g., amplitude, frequency, duration, etc.), which change with distance from fault rupture. Based on the distance from rupture, ground motions are divided into two types, namely, near-field and far-field ground motions. According to CALTRANS [3], near-field is defined by the distance of structure not more than 15 km from the fault. Characteristics of near-field and far-field ground motions recorded from the same earthquake are different. Also, near-field and far-field ground motions have two components, namely, fault-normal and fault-parallel. In most of the earthquake ground motion records, it was found that near-field ground motions contain acceleration, velocity, and displacement pulses with permanent ground displacement. Generally, fault normal component of horizontal ground motion contains pulses [17]. Energy applied to structures by near-field ground motion is much higher than the far-field ground motions and shorter period pulse contains higher input energy as compared to longer period pulse [16].

Only a few research works are available in the literature on seismic performance of bridges subjected to near-field ground motions. Liao et al. [7] studied seismic response of an RC highway bridge subjected to near-field and far-field ground motions and concluded that near-field ground motions show 1.5–2 times base shear and ductility demand of pier as compared to far-field ground motions. Based on a study on single degree of freedom (SDOF) system, Chopra and Chintanapakdee [4] concluded that in near-field ground motion, the velocity region becomes narrower for long period than far-field ground motions, and acceleration and displacement response region become wider for near-field ground motions. They also concluded that fault-normal component causes more deformation as compared to the fault-parallel component of near-field ground motion but the deformation of the fault-normal and fault-parallel components are the same in far-field ground motion. Based on the 1999 Chi-Chi earthquake records, Loh et al. [9] proposed a factor to calculate the seismic force in pier during near-field ground motion. Liao et al. [8] focused on seismic response of isolated and non-isolated bridge subjected to near-field and far-field ground motions and concluded that in the isolated bridge, base shear reduces more in far-field ground motion than near-field ground motion. They also concluded that displacement of girder and base shear mainly depend on the ratio of peak ground velocity (PGV) and peak ground acceleration (PGA). Shen et al. [16] found that near-field ground motion increases the response of isolated bridge when the period of pulse is nearly close to the natural period of the bridge. They also found that if the period of pulse increases, the energy of input pulse decreases. Phan et al. [15] performed shake table tests on bridge pier and concluded that near-field ground motion causes excessive pier displacement. Brown and Saiidi [2] experimentally

studied the effect of near-field and far-field ground motion on identical bridge bents and concluded that near-field ground motion causes more damages in bridge pier as compared to far-field ground motion. Chouw and Hao [5] concluded that spatially varying ground motion demands higher gap size as compared to wave propagation considering only time delay. Billah et al. [1] studied the effect of near-field and far-field ground motions on the retrofitted RC bridge bent and concluded that ductility demand is very high during near-field ground motion. Mosleh et al. [11] studied the effect of near-field and far-field ground motions on multi-span simply supported reinforced concrete (RC) bridge and concluded that far-field ground motion causes more damage in pier as compared to near-field ground motion.

The abovementioned papers mainly focused on the overall performance of bridges subjected to near-field and far-field ground motions. The pounding response of bridges subjected to near-field and far-field ground motions are not discussed in these papers. Therefore, the main objective of this study is to obtain the pounding probability of bridge subjected to near-field and far-field ground motions. Also, the effects of two types of near-field ground motions, namely, near-field with and without pulse have been considered and their effects on pounding probability of decks are compared.

2 Description of Bridge

A three-span simply supported reinforced concrete (RC) highway bridge as shown in Fig. 1 is selected for this study. The span length and width of the bridge are 35 m and 8.5 m, respectively. Decks are supported by a two-cell box girder. The expansion gap between adjacent decks, and between decks and abutments is 40 mm. Fixed and rocker bearings are used alternatively at the ends of girders over the pedestal of size 0.3 m \times 0.5 m \times 0.2 m. The substructure consists of a rectangular cross-section of size 5 m \times 1 m with a wall type pier of height 4 m. Piers are supported on a group of pile foundation.

3 FE Model of The Bridge

The bridge is modeled and analyzed in OpenSees [10]. Details of the finite element model of the bridge are shown in Fig. 2. The decks and girders are modeled as a single unit using linear-elastic beam-column elements and total masses of the deck and girders are uniformly lumped at the node along the beam-column elements and deck edges. Bearings are modeled as nonlinear zero-length elements between pedestal and girder following the procedure proposed by Nielson [13]. Piers are modeled by force-beam-column element and nonlinearity of pier is considered by using rectangular patch elements where nonlinear properties of core concrete, cover concrete, and reinforcement are used. The pedestal is modeled as a rigid element.

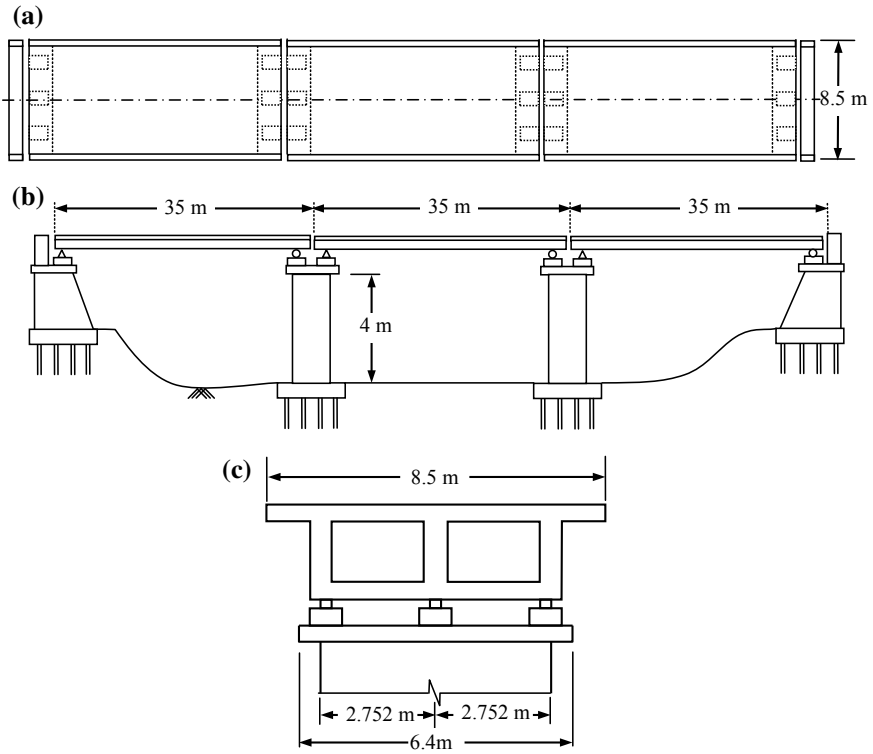


Fig. 1 Details of bridge: a plan, b elevation, c box girder

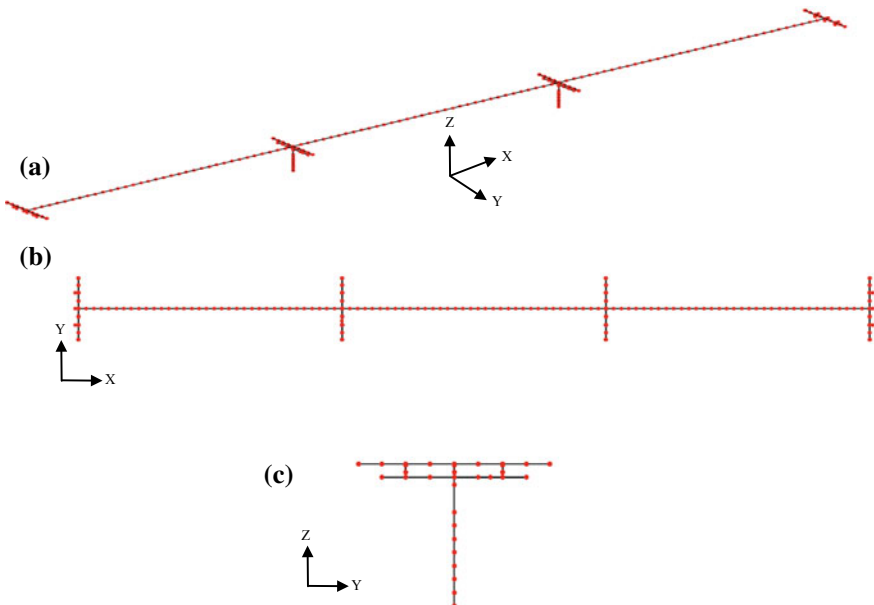


Fig. 2 Finite element model of the bridge: a isometric view, b plan view, c side view

Pounding is modeled using five zero-length impact elements equally spaced along deck edges at each expansion gap. Stiffness of impact elements was calculated based on the formula proposed by Muthukumar and DesRoches [12]. Soil–structure interaction is not considered and the piers are assumed to be fixed at pier cap level. Frequency analysis of the bridge is carried out and the fundamental period of the bridge is found to be 0.325 s.

4 Selection of Ground Motions

In this study, seismic analysis of the bridge is performed using three types of ground motions obtained from PEER motion database [14]. These include (a) 20 near-field ground motions without pulse (NFwoPulse), (b) 28 near-field ground motions with pulse (NFwPulse) and (c) 36 far-field ground motions (FF). Only one type of far-field ground motion is applied because there is no significant difference in response of the structure in case of fault-normal and fault-parallel ground motions when the structure is at a far distance from fault [4]. Details of the three sets of ground motions are given in Tables 1, 2 and 3. From each station, two horizontal ground motion data are taken and applied along the longitudinal direction of the bridge model. Mean acceleration response spectra for three types of ground motions are shown in Fig. 3.

Table 1 Far-field ground motions data

Id no.	Moment magnitude (M_w)	Year	Name of the earthquake	Recording station
1	6.7	1994	Northridge, USA	Beverly Hills–Mulhol
2	6.7	1994	Northridge, USA	Canyon Country-WLC
3	7.1	1999	Duzce, Turkey	Bolu
4	7.1	1999	Hector Mine, USA	Hector
5	6.5	1979	Imperial Valley, USA	Delta
6	6.5	1979	Imperial Valley, USA	El Centro Array #11
7	6.9	1995	Kobe, Japan	Nishi–Akashi
8	6.9	1995	Kobe, Japan	Shin–Osaka
9	7.5	1999	Kocaeli, Turkey	Arcelik
10	7.3	1992	Landers, USA	Yermo Fire Station
11	7.3	1992	Landers, USA	Coolwater
12	6.9	1989	Loma Prieta, USA	Capitola
13	6.9	1989	Loma Prieta, USA	Gilroy Array #3
14	7.4	1990	Manjil, Iran	Abbar
15	6.4	1987	Superstition Hills, USA	El Centro Imp. Co.
16	6.5	1987	Superstition Hills, USA	Poe Road (Temp)
17	6.5	1999	Chi-Chi, Taiwan	CHY101
18	7.6	1999	Chi-Chi, Taiwan	TCU045

Table 2 Near-field ground motions data without pulse

Id no.	Moment magnitude (M_w)	Year	Name of the earthquake	Recording station
1	6.8	1976	Gazli, USSR	Karakyr
2	6.5	1979	Imperial Valley, USA	Bonds Corner
3	6.5	1979	Imperial Valley, USA	Chihuahua
4	6.8	1985	Nahanni, Canada	Site 2
5	6.9	1989	Loma Prieta, USA	BRAN
6	6.9	1989	Loma Prieta, USA	Corralitos
7	6.7	1994	Northridge, USA	LA–Sepulveda VA
8	7.6	1999	Chi-Chi, Taiwan	TCU067
9	7.6	1999	Chi-Chi, Taiwan	TCU084
10	7.9	2002	Denali, USA	TAPS Pump Station #10

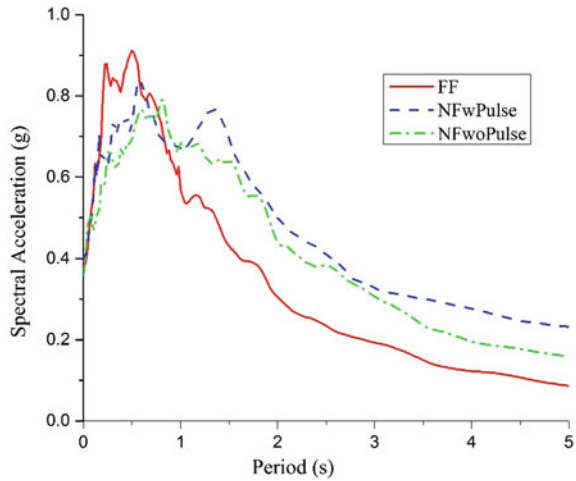
Table 3 Near-field ground motions data with pulse

Id no.	Moment magnitude (M_w)	Year	Name of the earthquake	Recording station
1	6.5	1979	Imperial Valley, USA	El Centro Array #6
2	6.5	1979	Imperial Valley, USA	El Centro Array #7
3	6.9	1980	Irpinia, Italy	Sturno
4	6.5	1887	Superstition Hills, USA	Parachute Test Site
5	6.9	1989	Loma Prieta, USA	Saratoga–Aloha
6	6.7	1992	Erzican, Turkey	Erzican
7	7.0	1992	Loma Prieta, USA	Petrolia
8	7.3	1992	Landers, USA	Lucerne
9	6.7	1994	Northridge, USA	Rinaldi Receiving Station
10	6.7	1994	Northridge, USA	Sylmar–Olive View
11	7.5	1999	Kocaeli, Turkey	Izmit
12	7.6	1999	Chi-Chi, Taiwan	TCU065
13	7.6	1999	Chi-Chi, Taiwan	TCU102
14	7.1	1999	Duzce, Turkey	Duzce

5 Fragility Function Using IDA

Fragility function is mainly used to determine the probability of exceeding a particular damage state (DS) for a particular input intensity (e.g., acceleration, velocity, and displacement). In this study, peak ground acceleration (PGA) is used as the intensity measure (IM) of earthquake motions and pounding between decks is taken as the bridge damage index (DI). Probabilistic seismic demand analysis (PSDA) and incremental dynamic analysis (IDA) are the two commonly used approaches

Fig. 3 Mean acceleration response spectra for three types of ground motions considered in the present study



for deriving fragility functions. PSDA is an easy method, which is based on the survey of damages that occurred in the structures during an earthquake. Although the IDA method demands more computational effort, it is used in this study for fragility analysis because it gives more accurate results as compared to PSDA [6, 18]. The PGA values to cause pounding at a particular expansion gap size is obtained from IDA. Pounding probability at each IM level can be calculated based on the number of damage cases for a particular damage state (*i*) and the total number of simulation cases:

$$p \left[DI \geq LS : IM \right] = \frac{n_i}{N} \tag{1}$$

where *n* is the number of damage cases and *N* is the total number of simulation cases.

Nonlinear time history analyses are conducted at every IM level in this study under the IDA approach. Then the normal cumulative distribution function is used to derive the fragility curve as given in Eq. 2.

$$p \left[DI \geq LS : IM \right] = \int_{-\infty}^{IM} \frac{1}{\sqrt{2\pi}\sigma_{IM}} \exp\left[-\frac{(im - \mu_{IM})^2}{2\sigma_{IM}^2}\right] d(im) \tag{2}$$

Lognormal cumulative distribution function can also be used as shown in Eq. 2 to attain various expansion gap sizes like 20, 40, 60 and 80 mm between decks.

$$p \left[DI \geq LS : IM \right] = \int_0^{IM} \frac{1}{im\sqrt{2\pi}\epsilon_{IM}} \exp\left[-\frac{(\ln(im) - \lambda_{IM})^2}{2\epsilon_{IM}^2}\right] d(im) \tag{3}$$

where μ_{IM} and σ_{IM} are the mean values and standard deviation of IM to reach the specified displacement state as indicated by the normal distribution, and λ_{IM} and ε_{IM} are logarithmic mean values and logarithmic standard deviation, respectively.

6 Results and Discussion

Incremental dynamic analysis (IDA) of the bridge for three types of ground motions are performed for different sizes of expansion gaps such as 20, 40, 60, and 80 mm. The corresponding PGA values to reach 20, 40, 60, and 80 mm, the relative displacement between decks are determined. Based on the PGA values, fragility curves for three types of ground motions are plotted and shown in Fig. 4. From Fig. 4, it is clear that as gap size increases, pounding probability decreases for all three types of ground motions. However, the rate of decrease of pounding probability is more in near-field ground motion without pulse (NFwoPulse) because it does not contain any kind of pulse and pounding occurs mainly due to ground displacement.

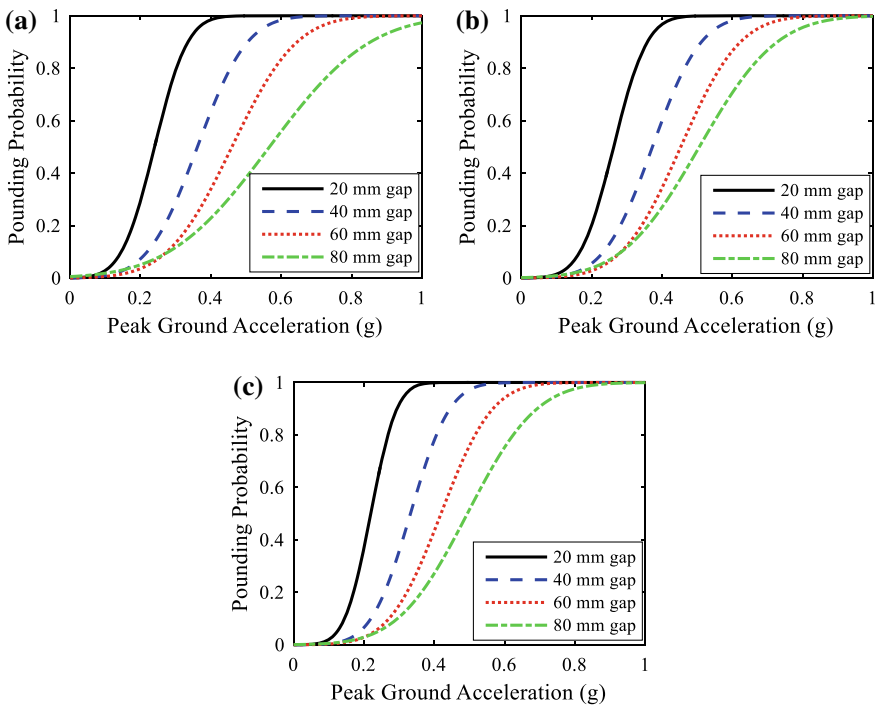


Fig. 4 Fragility curves for pounding of decks in bridge subjected to **a** near-field without pulse, **b** near-field with pulse, and **c** far-field ground motions

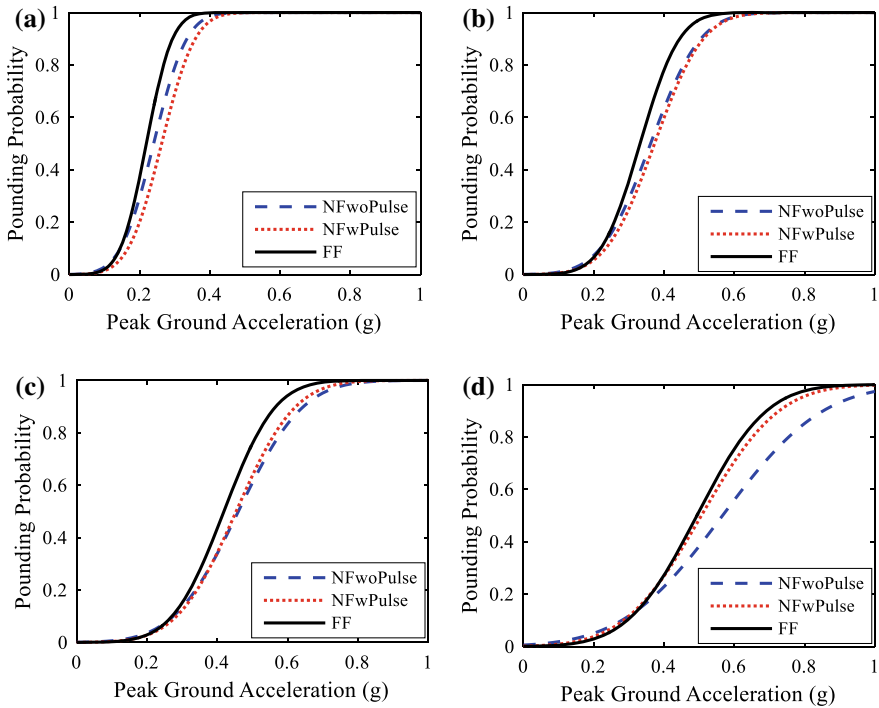


Fig. 5 Comparison of fragility curves of pounding of bridges under three types of ground motions (i.e., near-field without pulse (NFwoPulse), near-field with pulse (NFwPulse), and c far-field (FF)) for expansion gap of size **a** 20 mm, **b** 40 mm, **c** 60 mm, **d** 80 mm

A comparison of fragility curves for different gap sizes is shown in Fig. 5. It can be inferred from Fig. 5 that for every gap size, far-field ground motion (FF) shows maximum probability of pounding as compared to near-field ground motion with pulse (NFwPulse) and near-field ground motion without pulse (NFwoPulse). For example, when PGA is 0.3 g and gap size is 20 mm, probability of pounding for near-field ground motions with and without pulse are 71% and 79%, respectively, whereas pounding probability for far-field ground motion is 91%. This is because the far-field ground motions have a higher acceleration response at the fundamental period of the bridge ($T = 0.325$ s) as compared to response of near-field ground motion with and without pulse (Fig. 3). Mosleh et al. [11] also found a similar trend in column damage. They found that far-field ground motions caused higher probability of column damage than near-field ground motion. At 20 mm gap size, the pounding probability is less for near-field ground motions with pulse as compared to near-field ground motions without pulse because pounding occurred before the development of peak acceleration and peak velocity of bridge span as gap size is small. Therefore, when gap size is small, pounding probability for near-field ground motion

With pulse is less although they contain various types of pulses. However, when gap size is 80 mm and PGA is 0.8 g, pounding probability for near-field ground motion with and without pulse are 96% and 85%, respectively, whereas pounding probability for far-field ground motion is 98%, which is almost same as the near-field ground motion with pulse. Hence, when gap size increases, pounding probability due to near-field ground motion with pulse exceeds the pounding probability due to near-field ground motions without pulse. This is because acceleration and velocity pulse present in near-fault motion with pulse can develop an excessive response of the bridge by giving high input energy.

7 Conclusions

In this paper, fragility curves of pounding are obtained for a three-span simply supported bridge decks with an expansion gap of different sizes, namely, 20, 40, 60, and 80 mm. Fragility curves are developed for three different types of ground motions, i.e., near-field ground motions with and without pulse, and far-field ground motions. Incremental dynamic analysis (IDA) was performed for different gap sizes and different ground motions. Based on the IDA, fragility curves for pounding are drawn and the following conclusions are made for a three-span simply supported bridge.

- (1) Bridges are more vulnerable to pounding when subjected to far-field ground motions as compared to near-field ground motion with and without pulse at the same PGA level.
- (2) When expansion gap size is small (less than 60 mm), there is no significant difference in pounding probability for near-field ground motions with and without pulse. However, when gap size is high (more than 60 mm), pounding probability increases rapidly in case of near-field ground motion with pulse.
- (3) When gap size is 80 mm, pounding probabilities for far-field and near-field ground motion with pulse are almost the same.

In the present study, soil–structure interaction, spatially varying ground motion, and multi-directional ground motions are not considered.

References

1. Billah M, Alam S, Bhuiyan R (2013) Fragility analysis of retrofitted multi-column bridge bent subjected to near-fault and far-field ground motion. *J Bridge Eng* 18(10):992–1004
2. Brown AS, Saiidi MS (2008) Investigation of near-fault vs. far field ground motion effects on a substandard bridge bent. Report University of Nevada, Reno
3. CALTRANS (2004) Seismic design criteria. Sacramento, CA

4. Chopra AK, Chintanapakdee C (2001) Comparing response of SDF systems to near-fault and far-fault earthquake motions in the context of spectral regions. *J Earthquake Eng Struct Dyn* 30(12):1769–1789
5. Chouw N, Hao H (2008) Significance of SSI and non-uniform near-fault ground motions in bridge response II: effect on response with modular expansion joint. *Eng Struct* 30(1):154–162
6. Huo Y, Zhang J (2013) Effects of pounding and skewness on seismic responses of typical multispan highway bridges using the fragility function method. *J Bridge Eng* 18(6):499–515
7. Liao WI, Loh CH, Wan S, Jean WY, Chai JF (2000) Dynamic responses of bridges subjected to near-fault ground motions. *J Chin Inst Eng* 23(4):455–464
8. Liao W, Loh C, Lee B (2004) Comparison of dynamic response of isolated and non-isolated continuous girder bridges subjected to near-fault ground motions. *Eng Struct* 26:2173–2183
9. Liao WI, Loh CH, Chai JF (2002) Effect of near-fault earthquake on bridges: lessons learned from Chi-Chi earthquake. *J Earthq Eng Vib* 1(1):86–93
10. McKenna FT, Fenves G (2001) *The OpenSees Command Language Manual: version 1.2*, Pacific Earthquake Engineering Center, University of California, Berkeley (<http://opensees.berkeley.edu>)
11. Mosleh A, Razzaghi MS, Jara J, Varum H (2016) Seismic fragility analysis of typical pre-1990 bridges due to near- and far-field ground motions. *Int J Adv Struct Eng* 8(1):1–9
12. Muthukumar S, DesRoches R (2006) A Hertz contact model with non-linear damping for pounding simulation. *J Earthq Eng Struct Dyn* 35(7):811–828
13. Nielson BG (2005) Analytical fragility curves for highway bridges in moderate seismic zones. PhD thesis, School of civil and environmental engineering, Georgia Institute of Technology, USA
14. PEER Strong Motion Database (2009) <http://peer.berkeley.edu/ngawest2>. Accessed 16 Dec 2018
15. Phan V, Saiid S, John A, and Hamid G (2007) Near-fault ground motion effects on reinforced concrete bridge columns. *J Struct Eng* 133(7):982–989
16. Shen J, Tsai MH, Chang KC, Lee GC (2004) Performance of a seismically isolated bridge under near-fault earthquake ground motions. *J Struct Eng* 130(6):861–868
17. Somerville PG (2002) Characterizing near fault ground motion for the design and evaluation of bridges. In: *Third national conference and workshop on bridges and highways*, April 29–May 1 2002, Portland, Oregon
18. Zhang J, Huo Y (2009) Evaluating effectiveness and optimum design of isolation devices for highway bridges using the fragility function method. *Eng Struct* 31(8):1648–1660

Review of Seismic Performances of Partial Infill RC Frames



Narayan Muduli, Suresh R. Dash and Goutam Mondal

Abstract Partial infill frames are constructed by filling the bare frame with brick masonry to a certain height throughout the length of the frame. The walls generally restrain a part of the column to deform freely and a leftover portion remains captive which attracts large shear force and shows brittle failure (called captive column failure) during an earthquake, often leading to collapse of the building. Although sufficient experimental investigation has been carried out for infill walls with openings, the same for partial infill frame and recommendations for its modelling in building frame analysis are very limited. This paper collates the performances of partial infill RC frames during major past earthquakes and attempts to provide a review of the major literature on the performance of partial infill frames studied through experiments and numerical models, and their simplified analytical formulations. Further, some available methods to prevent captive column effect are also presented in this paper. The performance of retrofitted partial infill frames, which previously failed due to the captive column effect, studied experimentally by other researchers are also summarised.

Keywords Reinforced concrete frame · Partial infill · Captive column effect · Seismic retrofit

1 Introduction

Masonry infill walls are constructed in a large number of multistorey reinforced concrete (RC) buildings as exterior and interior partition walls. These are considered as non-structural elements during the design of buildings. However, their contribution towards lateral strength, stiffness, and energy dissipation capacity of RC frame can be significant when the building is subjected to earthquake loading

N. Muduli · S. R. Dash · G. Mondal (✉)

School of Infrastructure, Indian Institute of Technology Bhubaneswar, Bhubaneswar, India
e-mail: gmondal@iitbbs.ac.in

© Springer Nature Singapore Pte Ltd. 2020
A. Prashant et al. (eds.), *Advances in Computer Methods and Geomechanics*, Lecture Notes in Civil Engineering 56,
https://doi.org/10.1007/978-981-15-0890-5_48

577

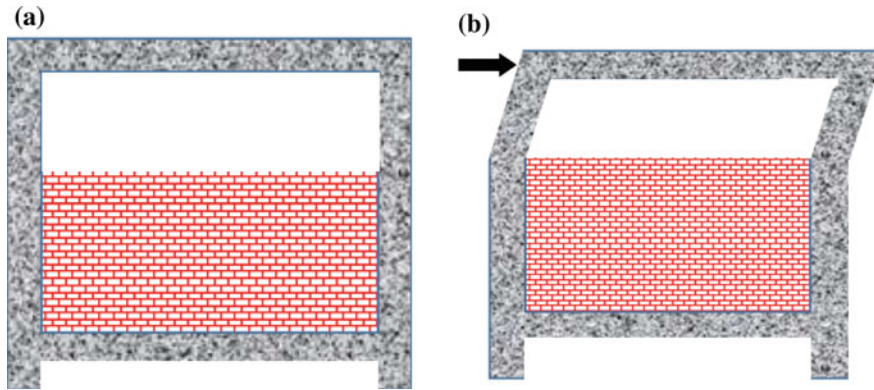


Fig. 1 a Partially filled infill wall; b Captive column failure while subjected to lateral seismic loading

[18, 20, 35] and therefore serving an important role in seismic performance of buildings. However, for architectural and functional reasons such as ventilator openings and lighting, large openings are often provided in the infill walls. Research shows that openings in the form of doors and windows in an infill wall tends to reduce the strength, stiffness, and energy dissipation capacity of infill walls [12, 16, 17, 19, 24].

Sometimes, an infill wall is provided upto a certain height of the frame throughout the length; this, here, is referred to as partial infill (Fig. 1a). Because of opening throughout the length of the wall, the effective height of the adjacent column reduces, thereby the columns are subjected to higher shear force during an earthquake and fail in a brittle manner and this phenomenon is called as captive column effect. This effect is due to the partial insertion of masonry infill which restricts the ability of infill frame to deform laterally, thereby keeping a part of the column captive by those non-structural insertions with the remaining portion deforming laterally (Fig. 1b). The captive column effect proved to be the culprit behind the failure of several buildings during many past major earthquakes. Such type of partial infill frames is quite common in school classrooms, storerooms, corridors and kitchen rooms serving natural lighting and ventilation purposes.

The present study reviews the performance of partial infill RC frames during past major earthquakes. Some preventive measures of premature failure of partial infill suggested by various researchers are also reviewed and presented in this paper. Some of the experimental investigations by other researchers on the performance of retrofitted partial infill frames failed due to captive column effect are also presented in this paper.

2 Past Seismic Performances of Partial Infill RC Frames

In many past major earthquakes, a large number of buildings failed due to short column failure. Some of the past earthquake performances of partial infill frames are depicted below.

2.1 Damage Due to Ventilator Opening

For ventilator opening, infill walls are stopped generally at about 1.5 m from the floor level which makes the columns shorter than their design lengths. Due to this, a part of the column is subjected to shear force higher than it has been designed and thus inadequate transverse reinforcement results in brittle failure of columns as shown in Fig. 2a–c. Sometimes the failure also occurred in infill as shown in Fig. 2d when infill is weaker than the surrounding frame.

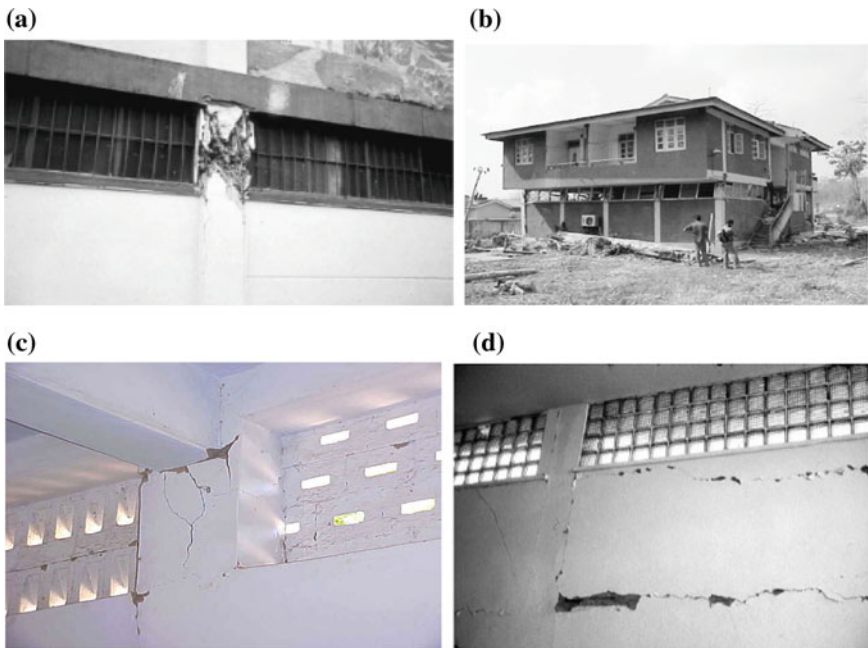


Fig. 2 Building failed due to ventilator opening: **a** Column damage due to captive column effect in 1999 Armenia, Colombia earthquake M (7.2) [8]; **b** the BSNL telephone exchange building damaged due to captive column effect [21] in 2004 Great Sumatra earthquake M (9.2); **c** warehouse damage in 2001 Bhuj Earthquake M (7.7) [10]; **d** undamaged column restrained by weaker clay tile [8]

2.2 *Damage Due to Unintended Use of Masonry Infill Around the Frame*

Various examples of captive column effect were noted mostly because of unintended use of partial infills during various earthquakes. Sometimes, unreinforced brick masonry walls were raised between the columns of the ground storey in multistorey buildings to form boundary wall. Due to this, the column suffered significant diagonal shear cracking. Figure 3a, b show the failure of columns during the 2001 Bhuj earthquake.

3 Past Experimental Studies

To understand the damage caused to buildings during an earthquake due to the presence of partial infill requires a better knowledge of failure mechanism. Generally, partial infill frames failed by the captive column effect and sliding failure in the plane of mortar. Mortar is typically considered to be the weak plane of the masonry structure, therefore cracking is initiated from there. Many researchers have tried to conduct either model-scale test or full-scale test to understand the failure mechanisms and to come up with simplified numerical modelling schemes to implement in the analysis. Some of the important experimental investigations and findings are discussed below.

Chiou et al. [6] conducted a full-scale test on 50% partial infill wall with clay bricks under monotonic loading without considering the effect of gravity load as shown in Fig. 4a. They observed that failure concentrated on the RC frame. However, there were no cracks found in the masonry wall. Many horizontal cracks were found in the left column where the infill wall terminates. However, failure of

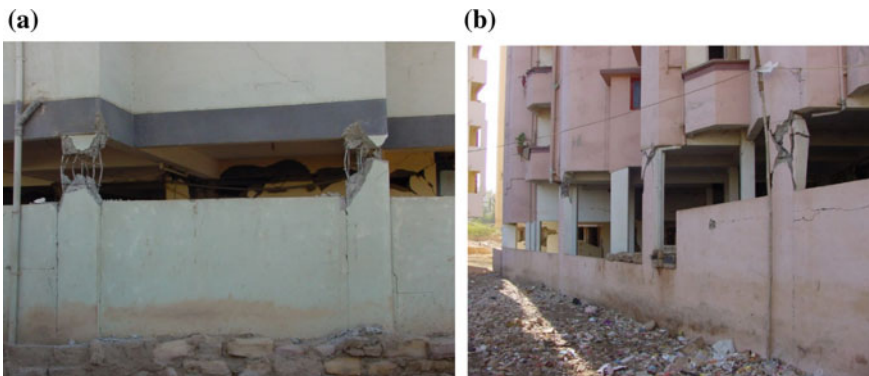


Fig. 3 a Damage to columns of buildings with varying lateral supports from masonry infills; b shear failure in short columns and flexure/shear failure in others [10]

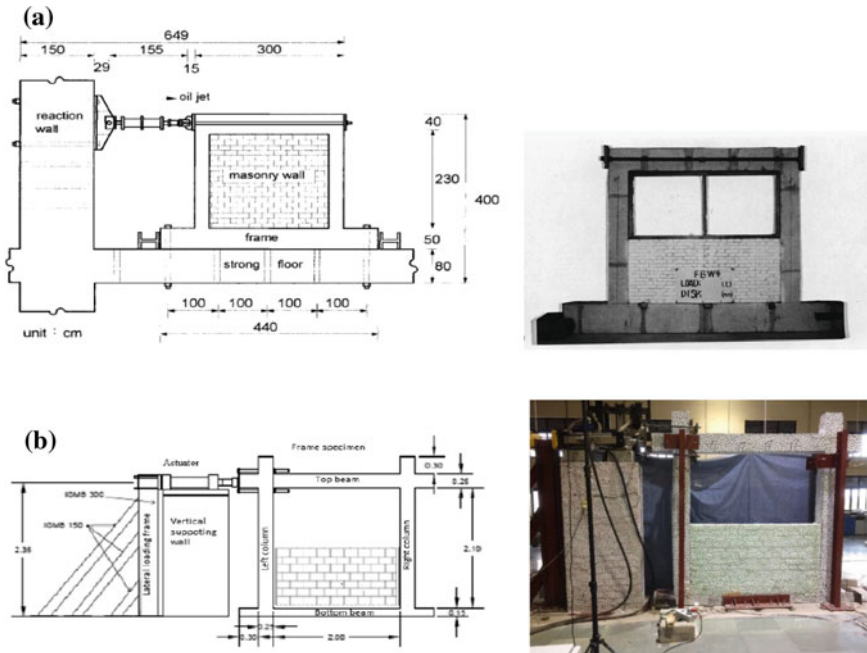


Fig. 4 a An illustration of experimental test setup for partially infilled RC frame [6] and b schematic diagram of the experimental test setup used in the present study [13]

the right column was found to be similar to that of a bare frame. The reason for the different failure mechanisms is that partial infill induces short-column effect on the left column.

Later, Kaushik [13] and Rout [30] conducted an experiment on partial infill using different types of infill material to see its cyclic behaviour. Kaushik [13] conducted full-scale tests on an RC frames having 50% partial infill with fly-ash bricks under cyclic loading without considering the effect of gravity load as shown in Fig. 4b. He observed that the presence of the partial infill wall reduced the effective length of the column and the lower half of the column became stiff resulting in captive column failure. However, lateral strength and energy dissipation capacity of partial infill frames were increased by 2.2 and 3.45 times, respectively, as compared to that of the bare frame. A similar experiment was done by Rout [30] on a partial infill frame with autoclaved aerated concrete (AAC) blocks. Two distinct modes of failure, namely, the diagonal cracking and shear sliding failure of mortar were observed prior to captive column failure. The initial stiffness and lateral strength of 50% partial infill frame were increased by about 77% and 22%, respectively, as compared to that of the bare frame. Niyompanitpattana and Warnitchai [22] conducted a study on the half-scale long-span infill wall with width to height (b/h) ratio 2.7 by considering the effect of gravity load under quasi-static loading. They also found captive column behaviour.

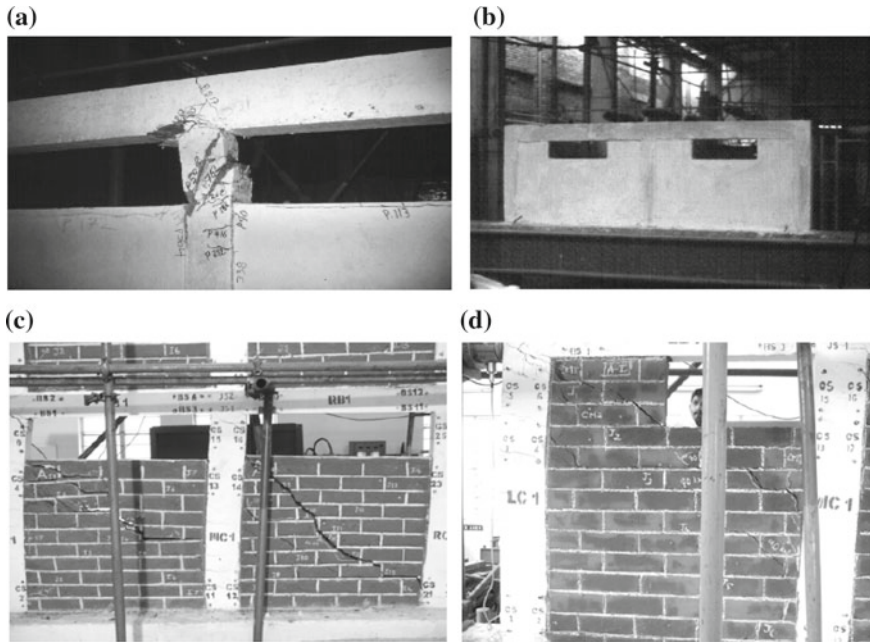


Fig. 5 a, b Partially infilled RC frame and solution [25]; c, d Two-bay two-storey partial infill frame and solution [33]

Pineda [25] performed an experiment on a two-bay one-storey RC frame with partial infill (Fig. 5a). A solution to prevent captive column failure is recommended by adding masonry inserts at both sides of the column as shown in Fig. 5b. Later similar recommendation for the prevention of captive column failure was given by Babu et al. [2], Subramanian and Jayaguru [33] based on experiments on two-bay two-storey RC frames subjected to cyclic loading (Fig. 5c, d). In these experiments, the masonry insert was provided at the bottom storey. It was concluded that masonry insert prevents captive column failure though it increases energy dissipation capacity and stiffness of the partial infill frame.

Huang et al. [9] conducted an experiment on one-bay one-storey non-ductile RC frame (including partial infill) under horizontal cyclic loading. They cast six frames; out of these, three frames were jacketed with carbon fibre reinforced polymer (CFRP). The RC frame was jacketed at the column portion only. They concluded that the strength and ductility of the RC frame were increased due to retrofitting by CFRP. However, minor shear cracks were observed in the beam and masonry infill of the partial infill frame.

Later, Jayaguru and Subramanian [11] conducted an experiment on retrofitted two-bay two-storey RC frame, infilled with clay bricks, subjected to lateral loading. A retrofitting scheme is proposed by using glass fibre reinforced polymer (GFRP) laminates for strengthening infill frame with a captive column defect. The RC frame

was jacketed with GFRP sheets in column and beam–column joint of the lower storey. It was observed that the ultimate strength and stiffness of the retrofitted frame was greater than that of the non-retrofitted frame. In addition, the captive column effect was also prevented by using the GFRP retrofitting scheme.

From the above discussion, it can be observed that the percentage of infill in the frame has a great influence on seismic performance. Large shear force is generated at the column level where the infill wall terminates leading to severe brittle failure of the column. Also, bed shear failure was observed in the infill due to shearing along the mortar plane. Moreover, it has been observed from the experimental studies that this failure pattern is independent of the span length of the frame and amount of gravity loading.

4 Past Analytical and Numerical Studies

A lot of experimental studies and past earthquake reports show that partial infill frame failed mainly due to the captive column effect. It is still a matter of interest to researchers to calculate how much shear force is generated at the location where the wall terminates. On this, some important numerical and analytical studies are discussed below.

4.1 *Finite Element Model*

Chiou et al. [6] were among the pioneers to carry out a detailed numerical investigation on partial infill wall with 50% opening by using discontinuous deformation analysis (DDA). Such analysis can model discontinuous and non-linear behaviour of masonry wall resulting from the failure of mortar and separation of bricks at the initial failure state. They validated the results with experiments and based on principal stress distribution in the RC frame, they concluded that discontinuous masonry wall cannot be modelled by the equivalent diagonal strut.

Later, Taher and Afefy [34] and Singh [31] studied the partial infill wall by the finite element method. Taher and Afefy [34] considered material and geometric non-linearity and found that the strength and stiffness of the entire frame increase with increase in height of the infill. Singh [31] considered separation and sliding at the frame–infill interface and non-linear behaviour of frame elements but infills were assumed to be linear-elastic. He performed a parametric study by considering the height of the infill as a parameter and concluded that the lateral stiffness of the RC frame increases with an increase in the infill height.

Pradeep [27] has performed finite element analysis by giving non-linear properties to the concrete and bilinear isotropic properties to the steel reinforcement. However, infill walls were modelled by a crack failure mechanism in which shear cracking and crushing never pass through the masonry infill, and that cracking

occurs entirely within the mortar and contact surface between the brick and mortar. He concluded that with an increase in the aspect ratio (ratio of length, L_w , to height, H_w , of infill), the initial stiffness and strength of the frame decrease.

Jayaguru and Subramanian [11] conducted non-linear static analysis on a two-bay two-storey RC frame, retrofitted using GFRP composites and subjected to monotonic loading. In this study, partial infill was modelled by adding a virtual beam at the location where the wall terminates. The masonry infill wall was modelled by an infill panel element. The strength of concrete was estimated by L-L model developed by Li et al. [14] which can calculate the strength of the concrete confined by both FRP composite and reinforcement. They validated their numerical results with experimental results that were discussed in the above section of this article.

4.2 Equivalent Diagonal Strut Model

Past researchers have proposed that the lateral force is resisted by the masonry infill by diagonal strut action as shown in Fig. 6a, b. These diagonal struts were found to be capable of representing global effects of infill such as stiffness and strength. Among these researchers, some suggested expressions for equivalent strut width [23, 26, 32]. Numerous study reports can be found for fully infilled frame; however, there is a lack of such reports on partial infill frame.

Later, Manistone [15] had proposed a simplified equation for calculation of equivalent strut width for fully infill wall 'a' (see Fig. 6b) as given in Eq. 1.

$$a = 0.175D(\lambda_1 H)^{-0.4} \quad (1)$$

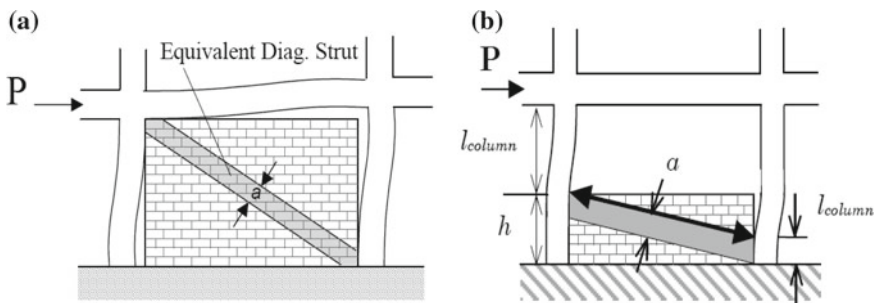


Fig. 6 **a** Equivalent diagonal strut for a full infill frame; **b** diagonal strut model for a partial infill frame [1]

where $\lambda_1 = \sqrt{4 \frac{E_m t \sin 2\theta}{4 E_c I_c h}}$ and $H =$ Height of frame

where E_m , t and h are Young's modulus and thickness and height of infill, respectively; E and I are Young's modulus and second moment of area of the columns, respectively, and θ is the slope of the infill diagonal to the horizontal.

Al-Chaar [1] suggested that the partial infill wall can also be modelled by an equivalent diagonal strut as given in Eq. 1 by calculating the value of λ_1 by replacing the height of the partial infill. If there is any existing damage in the masonry infill, Eq. 1 must be reduced by the reduction factor R_2 :

$$a_{red} = aR_2 \quad (2)$$

where $R_2 =$ reduction factor for in-plane evaluation due to existing infill damage.

Pradhan [28] has also proposed an expression for equivalent strut width (w), validating the same with the previous works, by taking percentage of opening as a parameter as given by the expression in Eq. 3.

$$w = k_x \sin \psi \quad (3)$$

$$k_x = \frac{\pi}{2} 2.29 \left(\frac{E_c I_c h_m}{E_m t h_c} \right)^{\frac{1}{3}}$$

$$\sin \psi = \frac{L_m}{\sqrt{L_m^2 + (h_m - k_x)^2}}$$

where E_c is Young's modulus of the frame, I_c is the moment of inertia of the columns, h_m is the height of the partial infill, E_m is Young's modulus of masonry, h_c is the centre-to-centre height of the frame, L_m is the length of the masonry and t is the thickness of the masonry. He found that when the opening area is more than 70% of the infill area, the opening has no effect on the strut width signifying that the strut width will remain the same irrespective of the aspect ratio. Another study by Pradhan et al. [29] showed that the stiffness of partial infill frame remains the same if the infill wall is provided up to 40% of the height of the column; beyond that height, stiffness and strength of the frame start to increase with increase in infill height.

5 Review of Codal Provisions

Indian standard IS 1893 Part-1, with its recent revision in 2016 [3] has adopted single and multi-strut models to analyse infilled frames. However, it lacks information on partial infill walls. Indian standard code for ductile detailing of RC frame IS: 13920-2016 [4] states that special confining reinforcement is to be provided

over the full height of the column which has significant stiffness variation along its height, which could be due to such partial infill configuration. Also, Eurocode 8 [7] provides similar recommendations for partially infilled walls. This comes from the fact that the height of the infill wall depends upon the choice of the architect and designer. Therefore, the height is unpredictable at the beginning. Moreover, the plastic hinge formation is uncertain as it depends upon the infill wall termination point. Hence, providing the confining reinforcement all through the height of the column provides an acceptable level of ductility and confinement at each section of the column eliminating the uncertainty in the height of the infill.

6 Key Observation and Remedial Measures

The partial confinement of infill can be present in a building due to many functional or architectural reasons. Generally, this type of failure is found in school buildings and kitchen rooms where openings are provided for natural lightening and ventilation purposes. From the above review, it has been seen that the presence of partial infill makes a part of the column captive, which leads to the generation of large shear force in the columns. The column in this condition fails in a brittle manner if not adequately designed for shear.

To overcome this type of effect, many ways are suggested by various researchers. Charleson [5] suggested constructing shear walls on one side which are generally strong and stiff for seismic loading (Fig. 7a). In addition, he suggested that masonry inserts can be provided at the top of the infill (Fig. 7b). Other approaches to prevent these types of short column effect is to retrofit the frame [11] by GFRP, which increases the ductility of the short column and can minimize the failure of the frame. Special confining reinforcement according to IS:13920-2016 [4] code can also be used for the prevention of this type of failure of partial infill frame.

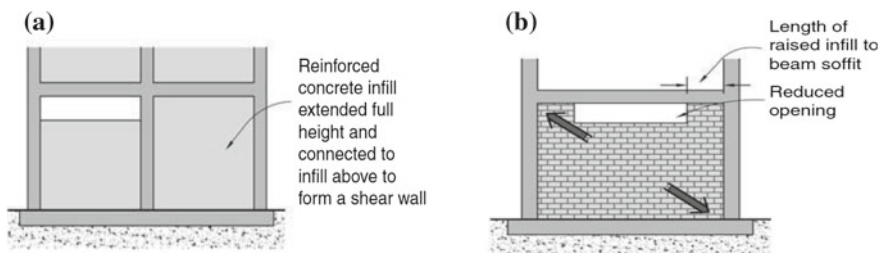


Fig. 7 a One bay completely infilled to form a shear wall; b additional masonry insert [5]

7 Concluding Remarks

In this study, past seismic performances of partial infill walls are critically reviewed. In addition to that, experimental and analytical studies carried out by various researchers are reviewed. From this review, the following key observations can be made.

- (a) Partial confinement of the frame with masonry infill leads to the captive column effect. This type of partial infill is often found in school buildings, kitchen rooms, and corridors. The mechanism enforced here engenders large shear force which is often ignored in the seismic design. From the past earthquake records, it is found that the buildings with partial infill walls are prone to failure by the captive column effect which is brittle in nature.
- (b) Hardly any experimental and analytical studies are done on the partial infill wall to study the behaviour of such wall under dynamic seismic excitation. Analytical studies mostly used the finite element-based technique for this purpose. Also, equivalent diagonal strut methods were devised in these studies. Experimental studies are generally conducted under the action of in-plane loading considering different parameters like percentage of partial infill and some retrofitting techniques to strengthen the frame.
- (c) The foremost solution for the captive column effect is to avoid the occurrence of it in the first place. The non-structural element that obstructs the free deformation of the column should be detached from the vertical column by providing interface elements like pads and shear keys or by using ‘masonry inserts’.

References

1. Al-Chaar G (2002) Evaluating strength and stiffness of unreinforced masonry infill structures. Technical Report ERDC/CERL TR-02-1, U.S. Army Corps of Engineers
2. Babu RS, Venkatasubramani R, Venkatasubramani GS (2011) Seismic strengthening of partially infill RC buildings using brick inserts—experimental investigation on 3D model structure. *J Eng Appl Sci* 6(12):123–30
3. BIS (2016) Criteria for earthquake resistant design of structures, IS1893 (Part 1): 2016. Bureau of Indian Standards, New Delhi, India
4. BIS (2016) Ductile designing and detailing of reinforced concrete structure subjected to seismic force, IS13920: 2016. Bureau of Indian Standards, New Delhi, India
5. Charleson A (2008) *Seismic design for architects outwitting the quake*. Elsevier, Oxford
6. Chiou YJ, Tzeng JC, Liou YW (1999) Experimental and analytical study of masonry infilled frames. *J Struct Eng* 125(10):1109–1117
7. European Committee of Standardization (2003) Eurocode 8: Design of structures for earthquake resistance, Part 1: General rules, seismic actions and rules for buildings, prEN1998-1. Belgium, Brussels
8. Guevara LT, García LE (2005) The captive-and short-column effects. *Earthq Spectra* 21(1): 141–160

9. Huang CH, Sung YC, Tsai CH (2006) Experimental study and modeling of masonry-infilled concrete frames with and without CFRP jacketing. *Struct Eng Mech* 22(4):449–468
10. Jain SK, Lettis B, Murty CVR, Bardet JP (2002) Bhuj/India earthquake of January 26, 2001. *Earthq Spectra* 18(Supplement A):398
11. Jayaguru C, Subramanian K (2012) Seismic behavior of a partially infilled RC frame retrofitted using GFRP laminates. *Exp Tech* 36(5):82–91
12. Kakaletsis D, Karayannis C (2007) Experimental investigation of infilled R/C frames with eccentric openings. *Struct Eng Mech* 26(3):231–250
13. Kaushik A (2018) Evaluation of lateral response of partially infill walls with Fly-Ash bricks through experimental study. MTEch thesis, School of Infrastructure, Indian Institute of Technology Bhubaneswar, India
14. Li YF, Lin CT, Sung YY (2003) A constitutive model for concrete confined with carbon fiber reinforced plastics. *Mech Mater* 35(6):603–619
15. Mainstone RJ (1971) On the stiffnesses and strengths of infilled frames. *Proc Inst Civil Eng* 92(1):381–403
16. Mallick DV, Garg RP (1971) Effect of openings on the lateral stiffness of infilled frames. *Proc Inst Civ Eng* 49(2):193–209
17. Mansouri A, Marefat MS, Khanmohammadi M (2014) Experimental evaluation of seismic performance of low-shear strength masonry infills with openings in reinforced concrete frames with deficient seismic details. *Struct Des Tall Spec* 23(15):1190–1210
18. Moghaddam HA, Dowling PJ (1987) The state of the art in infilled frames. ESEE Research Report No. 87-2, Imperial College of Science and Technology, Civil Eng. Department, London, U.K
19. Mondal G, Jain SK (2008) Lateral stiffness of masonry infilled reinforced concrete (RC) frames with central opening. *Earthq Spectra* 24(3):701–723
20. Murty CVR, Jain SK (2000) Beneficial influence of masonry infill walls on seismic performance of RC frame buildings. In: *Proceedings of the 12th world conference on earthquake engineering*, Auckland, New Zealand, Paper No. 1790
21. Murty CVR, Rai DC, Jain SK, Kaushik HB, Mondal G, Dash SR (2006) Performance of structures in the Andaman and Nicobar Islands (India) during the December 2004 great Sumatra earthquake and Indian Ocean tsunami. *Earthquake Spectra* 22(S3):321–354
22. Niyompanitpattana S, Warnitchai P (2017) Effects of masonry infill walls with openings on seismic behaviour of long-span GLD RC frames. *Mag Concr Res* 69(21):1082–1102
23. Paulay T, Priestley MJN (1992) *Seismic design of reinforced concrete and masonry buildings*. Wiley and Sons Inc, New York
24. Penava D, Sarhosis V, Kozar I, Guljas I (2018) Contribution of RC columns and masonry wall to the shear resistance of masonry infilled RC frames containing different in size window and door openings. *Eng Struct* 172:105–130
25. Pineda JC (1994) *Experimental tests on control of short columns*(in Spanish), PhD, Department of Civil Engineering, University of the Andes, Bogota, Colombia, 43 pp
26. Polyakov SV (1960) On the interaction between masonry filler walls and enclosing frame when loaded in the plane of the wall. In: *Translations in Earthquake Engineering*, Earthquake engineering Research Institute, Oakland, California, pp 36–42
27. Pradeep S (2017) Behavior of reinforced concrete frame with short column effect under lateral cyclic loading. *Asian J Civ Eng* 18(6):879–891
28. Pradhan PM (2012) Equivalent strut width for partial infilled frames. *J Civ Eng Res* 2(5):42–48
29. Pradhan PM, Maskey RK, Pradhan PL (2012) Composite behavior of masonry partially infilled reinforced concrete frames. *Build Res J* 60(1–2):51–60
30. Rout S (2018) Evaluation of lateral response of partially infill walls with AAC blocks through experimental study, MTEch thesis, School of Infrastructure, Indian Institute of Technology Bhubaneswar, India

31. Singh P (2016) Response of RC frame with partial infilled wall subjected to lateral in-plane loading, MTech thesis, School of Infrastructure, Indian Institute of Technology Bhubaneswar, India
32. Stafford Smith B, Carter C (1969) A method of analysis for infilled frames. *Proc Inst Civil Eng* 44(1):31–48
33. Subramanian K, Jayaguru C (2009) Lateral behavior of partially infilled reinforced concrete frames with masonry inserts. *J Civil Eng Res Pract* 6(2):1729–5769
34. El-Din Taher S, El-Din Afefy HM (2008) Role of masonry infill in seismic resistance in RC structures. *Arabian J Sci Eng* 33(2B):291–306
35. Tanjung J, Maidiawati, Nugroho F (2017) Experimental investigation of the seismic performance of the RC frames with reinforced masonry infills. In: *Proceedings of International Conference of Global Network for Innovative Technology and AWAM International Conference in Civil Engineering (IGNITE-AICEE-2017)*, 8–10 August, on sustainable technology and practice for infrastructure and community resilience, AIP Conference Proceedings, 1892:020009-1–020009-8

An Artificial Intelligence Approach for Modeling Shear Modulus and Damping Ratio of Tire Derived Geomaterials



Siavash Manafi Khajeh Pasha, Hemanta Hazarika
and Norimasa Yoshimoto

Abstract Scrap Tire Derived Materials (STDM) mixed with soil are often being used as geomaterials in civil engineering projects for reducing dynamic loads acting on geo-structures and soil liquefaction remediation purposes. On the other hand, any soil dynamic analysis involving STDM needs an estimation of dynamic characteristics of these materials. Predicting dynamic properties of STDM-soil mixture is a complicated task because there are large numbers of factors affecting dynamic properties of mixture, which might have complex relationships with each other within the soil-STDM system. There have been several attempts to evaluate and predict dynamic characteristics of STDM-soil mixtures using simple mathematical expressions. However, all those studies have been focused on case studies of some specific types of STDM and soil mixtures without considering various aspects of their dynamic behavior. This study presents application of artificial intelligence technique in predicting dynamic properties of gravel-tire chips mixtures (GTCM). Two Artificial Intelligence (AI) techniques, Support Vector Machine (SVM), and Artificial Neural Networks (ANN) were employed for modeling shear modulus and damping ratio of TDGM. Test results have shown that shear modulus and damping ratio of the granular mixtures are remarkably influenced by gravel fraction in GTCM. Furthermore, shear modulus was found to increase with the mean effective confining pressure and gravel fraction in the mixture. It was found that a feedforward multilayer perceptron model with backpropagation training algorithm have better performance in predicting complex dynamic characteristics of granular mixture than SVM one.

Keywords Shear modulus · Damping ratio · Tire derived geomaterials · Gravel-tire chips mixture · Support vector machine · Artificial neural network

S. Manafi Khajeh Pasha (✉) · H. Hazarika
Department of Civil Engineering, Kyushu University, Fukuoka, Japan
e-mail: manafi.siavash@gmail.com

N. Yoshimoto
Department of Civil and Environmental Engineering, Yamaguchi University, Ube,
Yamaguchi, Japan

1 Introduction

Approximately 1 billion of waste tires in quantity are generated annually in the world. In 2017, over 1 million tons waste is removed from services and scraped in Japan. One common disposal practice is to dump scrap tires in very large landfills. However, stockpiling of tires Tire stockpiles may increase public health, environmental and fire risk. Therefore, recycling of waste tires is the only solution to properly deal with the disposal of waste tires in landfills.

Over 63% of total scrap tires are being used as fuel for energy production purposes in different industries, while only 16% are reused as Scrap Tire Derived Materials (STDM) such as ground rubber, tire chips, and tire shreds. This may increase the emission of CO₂ to atmosphere and consequently cause climate change and global warming. Therefore, reusing waste tire materials convert the waste tire into a valuable product such as Scrap Tire Derived Materials (STDMs) is highly encouraged.

In recent years, disaster mitigation efforts are concentrated on developing novel technical means to mitigate the risk to the buildings, property, and environment from the earthquake ground motion. However, the key issue is to find a balance between the economic costs of seismic mitigation measures and environmental impacts. Nowadays, STDMs standalone or mixed with soil as Tire Derived Geomaterials (TDGM) are being adopted in several civil engineering applications as alternative non-dilative geomaterials for vibration isolation and liquefaction remediation purposes. Low unit weight, high hydraulic conductivity, and high elastic deformability are some of the unique characteristics of these geomaterials [5, 8, 13]. On the other hand, any dynamic analysis (such as ground response analysis) involving TDGM needs an estimation of dynamic properties of these materials.

Most of previous studies were focused on dynamic behavior of sand-STDM mixtures involved tire chips (TC) particle remarkably larger than sand particle ($D_{50,r}/D_{50,s} \gg 1$ or smaller than sand particles ($D_{50,r}/D_{50,s} \ll 1$ where the $D_{50,r}$ and $D_{50,s}$ are mean diameter of rubber and soil particles respectively [6, 7, 26]. This may result in severe particle segregation due the significant differences in their size, shape, and density.

Recent studies on sand-STDM mixture have already confirmed the effectiveness and efficiency of implementing STDM as an additive material to sandy soil in improving dynamic performance and mitigating liquefaction potential of granular soil [12, 25, 26]. A series of undrained cyclic triaxial and 1-g shaking table tests were performed by Hazarika et al. [14] to study the effect of reinforcing sand with tire chips on the dynamic response of quay walls. They observed that residual lateral displacement of the quay wall was limited in reinforced backfill in comparison to that of unreinforced one.

Feng and Sutter [7] conducted a series of torsional resonant column tests on sand-rubber mixtures. The tests were performed on materials prepared either air-dried or with a small quantity of moisture, using dry spooning or under-compaction methods. They found that shear modulus decreases as rubber

inclusion increases in the mixture. However, damping ratio was found to be not significantly affected by rubber inclusion in the mixtures.

Anastasiadis et al. [2] conducted torsional resonant column tests on sand-rubber and gravely soil-rubber mixtures to investigate small-strain shear modulus and damping ratio of reinforced granular mixtures. They have considered different combinations of sand-tire chips mixture with rubber inclusion in the range from 0 to 35% by mixture weight. They found out that shear modulus tends to decrease by adding rubber inclusion to the sand. However, damping ratio was found to be slightly improved by rubber inclusion in the mixtures.

Nakhaei et al. [18] conducted a series of large-scale consolidated undrained cyclic triaxial tests to obtain shear modulus and damping ratio of sandy-gravel mixed with different percentage (0, 8, 10, and 14% by weight) of granulated rubber at different effective confining pressures. Outcome showed that regardless of level of the confining pressure, shear modulus steadily decreases as rubber content increases in mixture. They concluded that damping ratio decreases with an increase in rubber inclusion in the mixture for the confining pressures of 50 and 100 kN/m². However, this trend was reversed for the confining pressures of 200 and 300 kN/m².

Although sand-tire chips mixture is a conventional ground improvement method for preventing seismic and liquefaction induced structural damage during earthquake. However, low hydraulic conductivity of sand, low bearing capacity of sand-STDM mixture are some of the key issues of utilizing this technique in practice. Gravel and tire chips mixture (GTCM) can provide a solution for the drawbacks of existing method. Gravelly soil possesses higher permeability in comparison to that of sandy soil [11, 13, 22].

Majority of previous empirical models proposed for estimating dynamic characteristics of reinforced granular soils with tire chips are actually modified version of Hardin hyperbolic model [10]. Implementation of such complex empirical expressions may require definition of a large number of parameters that need to be calibrated against experimental data. Furthermore, these models showed poor performance when higher percentage of tire chips are present in mixture. In addition, footings constructed on gravely soil yields higher bearing capacity in comparison to that of sand. In recent years, Artificial Intelligence (AI) technique has been implemented in several fields of geotechnical engineering to predict behavior of sophisticated systems. For instance, ANN technique has been implemented to estimate the soil characteristics soil permeability [19] and shear strength parameters [3] as well as predict the behavior of foundations [20, 24].

There is no study on the dynamic properties of gravel-tire chips mixtures especially in the range of medium to large shear strains. The main objective of this study is to introduce new model using Artificial Neural Network (ANN) and Support Vector Machine (SVM) approaches that can simulate complex dynamic characteristics of GTCM mixtures taking into account important features of granular materials. Therefore, a series of stress-controlled undrained cyclic triaxial tests were conducted on GTCM with different gravel fraction at an effective confining pressure of 50 and 100 kN/m² to examine the influences of gravel fraction and

effective confining pressure on shear modulus and damping ratio of GTCM. The obtained experimental results were used to construct ANN and SVM models for predicting dynamic properties of GTCM.

2 Material Properties and Testing Procedure

A series of large cyclic triaxial tests were carried out on specimens of 100 mm in diameters by 200 mm in height to determine liquefaction resistance and large strain shear modulus of gravel and gravel-tire chips mixtures (GTCM). Figure 1 shows the particle size distribution of gravel and tire chips (TC) used in this study. Other physical characteristics of materials such as maximum diameter of gravel and tire chips particles (D_{max}), coefficient of curvature (U_c), coefficient of uniformity (U_ζ) are also displayed in Fig. 1. The maximum grains size of TC and gravel were limited to less than 1/6 of specimen diameter to avoid the effect of sample size on the results of experiments.

According to JGS 0131, gravel is classified as poorly graded (SP). Regarding to shape and maximum grain size of STD, the specific gravities (G_s) of gravel and tire chips were determined according to JGS-0111 and ASTM 6270-12 recommendations. The specific gravities of gravel G1 and TC are 2.81 and 1.17, respectively. The variation of specific gravity of GTCM is displayed in Fig. 2. In order to investigate the effect of tire chips on packing of binary mixture of GTCM, a series of vibratory tests were conducted on Gravel and GTCM according to JGS-0161 standard.

Maximum and minimum void ratio of GTCM with different volumetric proportions of Gravel (GF) is shown in Fig. 3. As is evident, both maximum and minimum void ratio of GTCM decreases as gravel fraction increases. An empirical expression (Eq. 1) is proposed to capture compaction behavior of gravel and GTCM mixture.

Fig. 1 Particle size distribution of gravel and tire chips

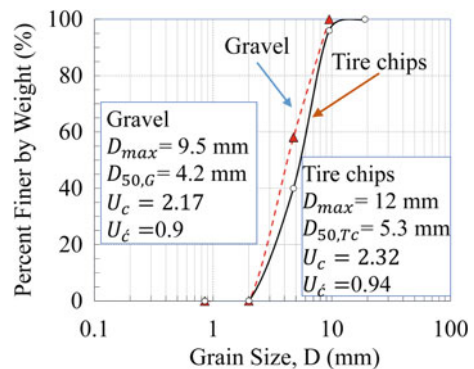


Fig. 2 Specific gravity of GTCM

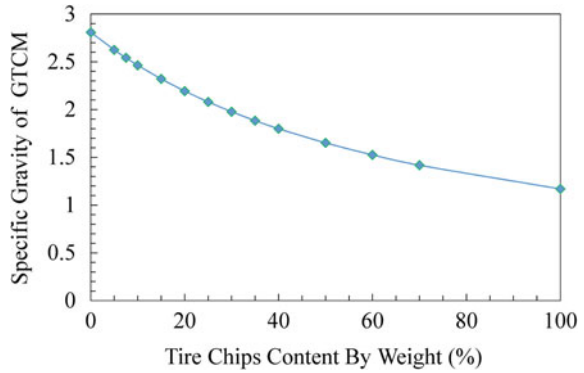
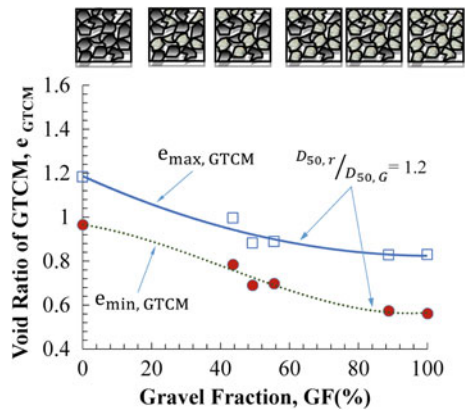


Fig. 3 Maximum and minimum void ratio of GTCM



$$e_{min,GTCM}, e_{max,GTCM} = A + B / \left(1 + 10^{(C - (GF\%) \times D)} \right) D_{50,Tc} / D_{50,G} \approx 1.2, D_{50,Tc} = 6 \text{ mm} \tag{1}$$

where $e_{min,GTCM}, e_{max,GTCM}$ are minimum and maximum void ratio of GTCM for a given gravel fraction (GF) in mixture. $D_{50,G}$ and $D_{50,Tc}$ are mean diameter of tire chips and gravel particles respectively. A, B, C, D are fitting parameters listed in Table 1. Considering theory of packing of a binary mixture, minimum and maximum void ratio of GTCM decreases with increasing gravel fraction, because large particles are surrounded with small particles of the same size, no packing phenomena occurs.

Table 1 Fitting parameters for maximum and minimum void ratio

Parameters	A	B	C	D
Maximum void ratio	0.83	0.35	41.39	-0.05
Minimum void ratio	0.56	0.42	43.26	-0.03

Under-compaction method was used for preparation of specimens. In order to obtain a desired ratio of gravel to tire chips, gravel and tire chips were weighed separately, and then mixed together by hand and placed into mold and sequentially compacted into 10 layers. Samples were saturated by allowing desired water to flow through from the bottom of the samples. 200 kN/m² backpressure was applied to specimens in order to increase degree of saturation ($B > 0.95$). Samples were consolidated to the effective confining pressure of 50 and 100 kN/m². Stress-controlled undrained cyclic triaxial tests were conducted at a constant frequency of 0.1 Hz, relative density of 50% and different cyclic stress ratios ($\sigma_d/2\sigma_{3c}$). Where σ_d and σ_{3c} are amplitude of cyclic deviatoric stress and mean effective confining pressure respectively.

Evaluation of shear modulus (G) and damping ratio (D) can be calculated from following expressions:

$$G = \frac{\tau_{max} - \tau_{min}}{\gamma_{max} - \gamma_{min}} \frac{1}{3} \times \frac{(q_{max} - q_{min})}{\epsilon_{q,max} - \epsilon_{q,min}} \tag{2}$$

$$D = \frac{1}{4\pi} \frac{\Delta W}{W} = \frac{1}{4\pi} \frac{\oint \tau d\gamma}{(0.125 \times \Delta\tau \times \Delta\gamma)} \tag{3}$$

where q_{max} and q_{min} are maximum and minimum deviatoric stresses respectively. $\epsilon_{q,max}$ and $\epsilon_{q,min}$ are maximum and minimum deviatoric strains, respectively. τ_{max} and τ_{min} are the maximum and minimum shear stresses corresponding to the maximum (γ_{max}) and minimum shear strains (γ_{min}), respectively. $\Delta\tau$ and $\Delta\gamma$ are the difference between maximum and minimum shear stresses and shear strains, respectively. ΔW is the area of the hysteresis loop and W is the area of right triangle shown in Fig. 4a. Typical stress–strain hysteresis loop of GTCM is shown in Fig. 4b. A MATLAB code was written to accelerate the calculation process.

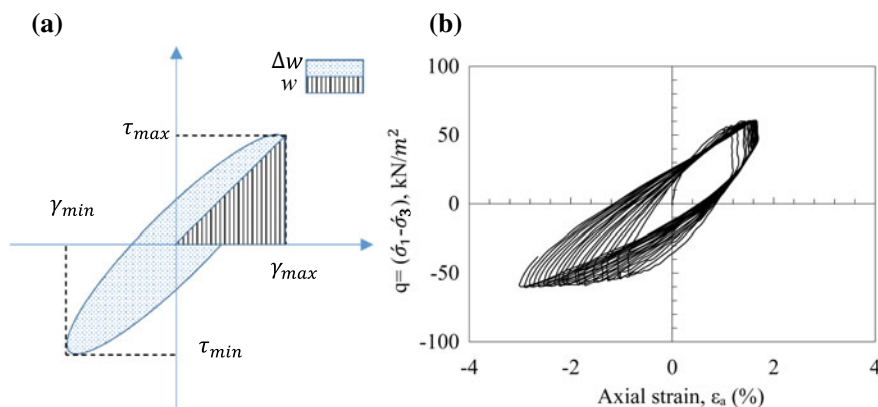


Fig. 4 a Definition of shear modulus and damping ratio of soil. b Stress–strain hysteresis loop of GTCM with GF = 44%, $\sigma_3 = 100$ kN/m²

3 Shear Modulus and Damping Ratio

The shear modulus curves of GTCM samples with different GF (%) are shown in Fig. 5. For the GTCM specimens with GF = 100% and GF = 87% shear modulus decreased drastically with the shear strain within the few cycles of loading, this reduction in shear modulus with an increase in shear strain can be imputed to a decrease in gravel inter-particles contact due to rapid building up of pore water pressure during the cyclic loading. As is evident from Fig. 5, rubber fraction did not significantly affect the shear modulus of specimen with GF = 44 and 30% and shear modulus of specimens at higher shear strains are almost identical.

This is probably because gravel inter-particle contacts are minimal (especially at very high shear strains > 1%) where GTCM matrix is mainly formed by tire chips particle with relatively low stiffness in comparison to that of gravel particles [23]. GTCM samples with gravel fraction GF < 100%, experienced higher deformations resulted in shifting shear modulus degradation curves rightward. Variation of damping ratio of GTCM mixtures with gravel fraction and shear strain is shown in Fig. 6. Damping ratio slightly increases with decreasing gravel fraction from 100 to 44%.

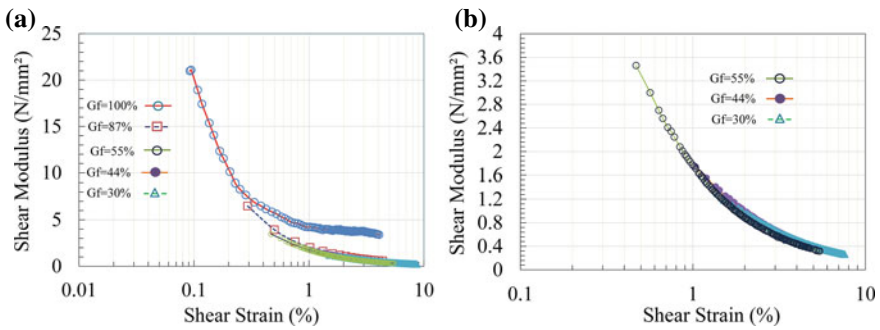
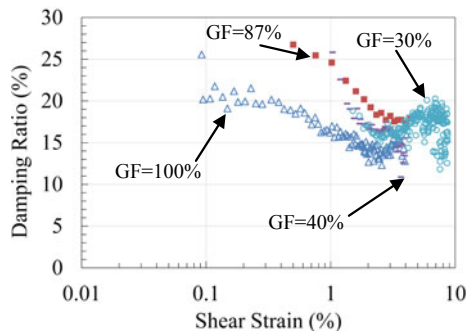


Fig. 5 Effect of gravel fraction on shear modulus reduction curves of GTCM: **a** 30% ≤ GF ≤ 100% **b** 30% ≤ GF ≤ 55%

Fig. 6 Effect of gravel fraction on damping ratio of GTCM



The reduction in damping ratio value may happen due to rapid increase in the pore water pressure during cyclic loadings. High pore water pressure decreases inter-particle contacts resulting in significant reduction in Frictional energy loss in soil skeleton with the number of cycles and axial strain [4, 16, 21].

4 Support Vector Regression (SVR)

Support vector machines (SVM) are popular supervised learning tool in machine learning capable of analyzing data for both classification and regression. This method was first introduced by Vapnik et al. [27] and follows structural risk minimization principle that looks up to minimize upper bound generalization error. If the target variables involve categorical data a SVM model need to be used, however, when the target variables are continuous data Support Vector Regression (SVR) model should be employed.

If a set of observation data are given as $\{(x_1, y_1), (x_2, y_2), \dots, (x_k, y_k),\}$ where $x_i \in \mathbb{R}^n$ input values and $y \in \mathbb{R}^n$. The ϵ -insensitive loss which is the magnitude of the difference between the predicted value and the radius ϵ of the tube function can be expressed as follows:

$$L_\epsilon(y) = \begin{cases} 0 & \text{if } |y - f(x)| \leq \epsilon \\ |y - f(x)| - \epsilon & \text{otherwise} \end{cases} \tag{4}$$

The nonlinear regression function can be presented as below:

$$f(x) = \{(w^T x + b)\} = 0 \tag{5}$$

where b = bias and w = weight vector. The main objective in SVR is to find a function, $f(x)$ that almost has a ϵ deviation from the actual output (y_i). So this goal can be achieved by minimizing the following expression:

$$\psi(w) = \frac{\|w\|}{2} = 0.5w^T w \tag{6}$$

Subject to the following constraints:

$$+y_i - \{(w^T x + b)\} \leq +\epsilon \tag{7}$$

$$-y_i + \{(w^T x + b)\} \leq +\epsilon \tag{8}$$

by introducing slack variables ξ_i, ξ_i^* ($i = 1..n$), optimization function now can be expressed:

$$\psi(\mathbf{w}, b, \alpha) = 0.5\mathbf{w}^T\mathbf{w} + C \sum_{i=1}^m (\xi_i + \xi_i^*) \tag{9}$$

Subject to the following constraints:

$$y_i - \{(w^T x + b)\} \leq \varepsilon + \xi_i \tag{10}$$

$$-y_i + \{(w^T x + b)\} \leq \varepsilon + \xi_i^* \tag{11}$$

where C = constant known as the regularization or penalty parameter. The function in Eq. (9) can be transformed in the form of a

Lagrange functions as follows:

Therefore, the goal would be maximizing the following expression:

$$W(\alpha, \alpha^*) = -\frac{1}{2} \sum_{i,j=1}^n (\alpha_i + \alpha_i^*)(\alpha_i^* - \alpha_i)K(x_i, x_j) + \sum_{i=1}^n y_i(\alpha_i^* - \alpha_i) - \varepsilon \sum_{i=1}^n (\alpha_i + \alpha_i^*)$$

where K is the kernel function and defined as follows:

$$K(x_i, x_j) = \vartheta(x_i)\vartheta(x_j) \tag{12}$$

α, α^* and b are calculated by solving the above expressions considering following condition:

$$\sum_{i=1}^n (\alpha_i - \alpha_i^*) = 0, 0 \leq \alpha_i, \alpha_i^* \leq C, i = 1, 2, 3, \dots, n. \tag{13}$$

The regression function can be rewritten as

$$f(x) = \sum_{i=1}^n (\alpha_i - \alpha_i^*)K(x \cdot x_i) + b \tag{14}$$

Radial basis function (RBF) was used to identify the support vectors along the function surface.

In this study, the comprehensive data sets collected from experimental program were used for the development of SVR model.

Support vector machine-based model for predicting shear modulus and damping ratio of GTCM can be expressed as follows:

$$G = \text{SVR} (GF, \dot{\sigma}_3, \sigma_d/2\dot{\sigma}_3, \gamma) \tag{15}$$

$$D = \text{SVR} (GF, \dot{\sigma}_3, \sigma_d/2\dot{\sigma}_3, \gamma) \tag{16}$$

A data sets consisting of 3006 shear modulus and damping ratio measurements of GTCM was employed in our analysis. 2970 data sets out of 3006 were randomly chosen for training and validation of proposed model whereas the remaining 36 data sets were selected to test the constructed model. Before the training of SVR model, data sets were randomly shuffled, in order to make sure that the model is not learning a specific order and faster convergence is observed. The algorithm utilized for data shuffling was simply relied on selecting two data rows (consisting of the input and outputs) randomly and swapping them together. Figure 7 shows the observed and estimated values of GTCM shear modulus for different gravel fraction at confining pressure of 100 kPa.

It is worthwhile to mention that the SVR models of shear modulus and damping ratio yield the coefficient of determination of $R^2 = 0.95$ and $R^2 = 0.8$ for training data sets. It can be observed from Fig. 7 that SVR model is capable of predicting the complex, nonlinear dynamic behavior of granular mixture with high accuracy. A comparison between predicted and observed values of shear modulus and damping ratio of GTCM for independent new testing data sets is displayed in Fig. 8. It is should be noted that new testing data sets were not used for training the SVR model. The coefficient of determination is reduced from $R^2 = 0.95$ and $R^2 = 0.8$ for training data sets to $R^2 = 0.91$ and $R^2 = 0.71$ for new test data sets of shear modulus and damping ratio models respectively.

Although SVR-based model shows satisfactory generalization ability and can predict shear modulus of granular materials with relatively high resolution, yields slightly lower performance in generalization and estimation of damping ratios of GTCM. Lower performance in prediction of new test data might be result of very disperse nature of damping ratio versus axial strain.

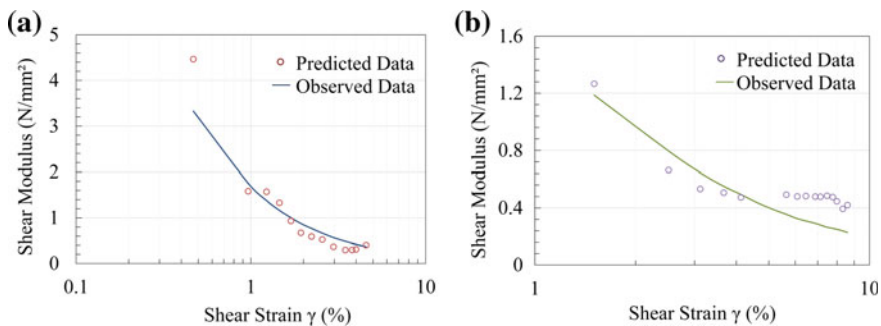


Fig. 7 Comparison between observed and predicted values of shear modulus for training data sets using SVR: **a** GF = 55%, $(\sigma_d/2\dot{\sigma}_3) = 0.25$; **b** GF = 44%, $(\sigma_d/2\dot{\sigma}_3) = 0.3$

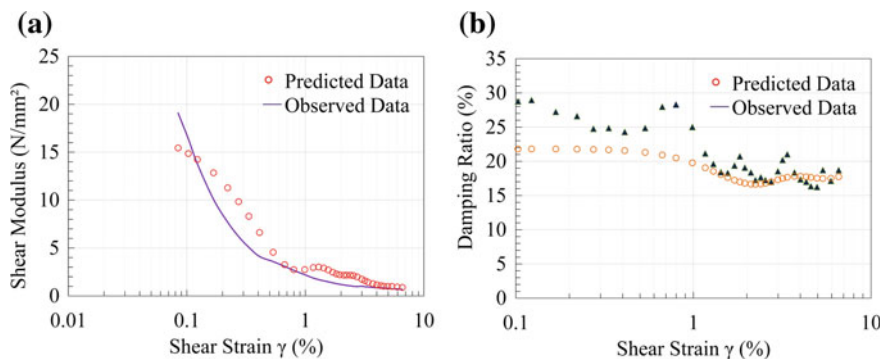


Fig. 8 Comparison between observed and predicted values for new testing data sets using SVR at $GF = 87\%$, $(\sigma_d/2\sigma_3) = 0.25$: **a** shear modulus. **b** Damping ratio

5 Artificial Neural Network (ANN)

Artificial Neural Networks (ANN) are one of Artificial Intelligence (AI) techniques that inspired by function of human biological nervous system and mimics brain problem-solving process. The concept of ANN is first introduced by McCulloch and Pitts [17] but first training algorithm for a feedforward multilayer perceptron is introduced in 1986. The application of ANN in civil engineering is introduced in the early 1990s by Goh [9] which involved the feasibility of ANNs to predict the liquefaction potential of soil. Selection of appropriate ANNs architecture is one of the most essential and complicated tasks of building a model.

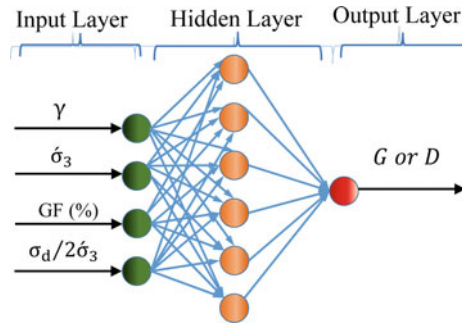
In this study, the feedforward ANN in which information moves forward from the input layer directly towards output layer through any hidden layers was selected. Backpropagation learning algorithm (BPP) which uses the gradient decent laws and is suitable for prediction problems, is implemented. A total number of 3006 shear modulus and damping ratio values of GTCM are used as the database for building ANN model. 36 out of 3006 data sets were selected to independently test the proposed model. The goal of the model is to estimate shear modulus and damping ratio of gravel and GTCM for a given gravel fraction (GTCM) and mean effective confining pressure. The architecture of the network is determined as follows and is illustrated in Fig. 9.

$$\text{Input vector } \{X\} = \{\sigma_d/2\sigma_3, \gamma, \sigma_3, GF (\%) \}$$

$$\text{Output } \{Y\} = \{G\}$$

$$\text{Output } \{Y\} = \{D\}$$

Fig. 9 Structure of ANN model



A MATLAB code is written to determine neurons (nodes) in the hidden layer by a trial and error method. In this method, training of networks starts with minimum number of nodes in the first hidden layer and sum squared error is calculated and compared with the allowable threshold error. If the error exceeds the threshold value, next neuron is added to the hidden layer. The above iterative process is repeated until the desired stopping criterion is met.

In order to reduce time consumed during training process of ANN model, maximum number of neuron in each hidden layer is limited to eight. In order to have an efficient model with high performance and reduce the noise, size of input space and have a smother relationship, the input data are preprocessed using min-max normalization method before training process starts.

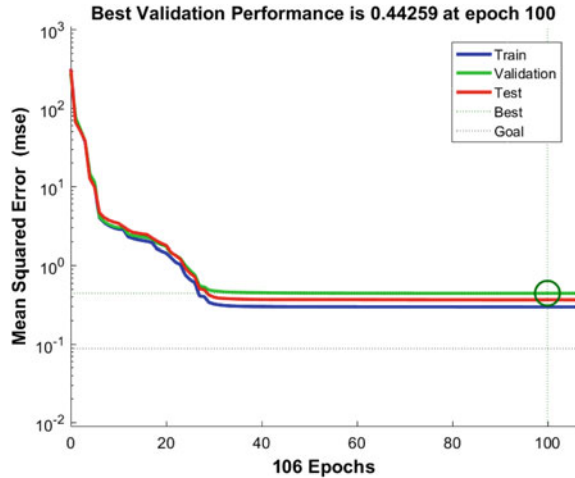
Eight training algorithms have been assessed for this study. The Levenberg–Marquardt algorithm which has been shown to have better performance for training moderate size of a Multilayer Perceptron (MLP) was selected for training the ANN.

The data are randomly divided into three subsets: training (60%), validation (20%), and testing (20%). During the learning or training process, training data sets are used to obtain ANN parameters in each layer (Weights and biases) by minimizing the error function. In order to avoid overfitting the network, the error on the validation data set is monitored during training process. The training will stop when the error on the validation data set begins to rise. Further training of network will over fits data and prevents generalization. At the next stage, the training data set is introduced to the ANN and its performance is evaluated.

In this study, the proposed neural network model has four nodes in the input layer, six nodes in the hidden layer, and one node in the output layer (Fig. 9). Once the ANN performance is evaluated, ANN is utilized to conduct a parametric study. As is mentioned at the beginning of this section, the optimum number of hidden layers and neurons in each hidden layer are obtained based on criterion defined to terminate the training process.

Mean squared error between the target and predicted values of all outputs over all possible configurations were monitored constantly. In order to assess the performance of ANN model, the measured error during the training process is plotted

Fig. 10 Best validation performance of ANN model



with that of error measured during testing process, training will stop where the testing errors start to rise while the training errors constantly decreasing. Training must stop to avoid overtraining and final performance of ANN is measured at this point.

After training of ANN model is over, in order to assess the performance of proposed ANN model in predicting shear modulus of GTCM (Fig. 10), predicted values of model for training, validation and test data sets are plotted against the target values. As can be seen from Fig. 11, there is such a strong correlation between estimated and target values of shear modulus for all three data sets. Figure 12a shows the comparison between the predicted values of shear modulus for GTCM with $GF = 87\%$ at the effective confining pressure of $\sigma_3 = 100$ kPa and stress ratio of $(\sigma_d/2\sigma_3) = 0.25$ by ANN model simulation and laboratory results. It is should be noted that new tested data set was not used for training of ANN model.

As can be seen from the plot, predicted and the measured values of shear modulus are in very good agreement. Performance of ANN model is assessed by

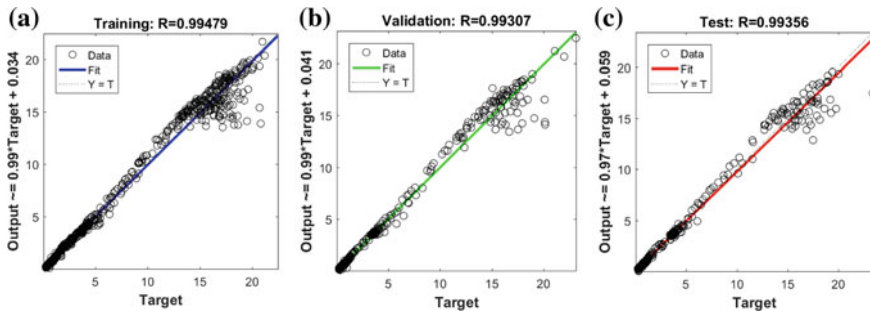


Fig. 11 Performance of the ANN Model over: **a** training; **b** validation; **c** test data sets

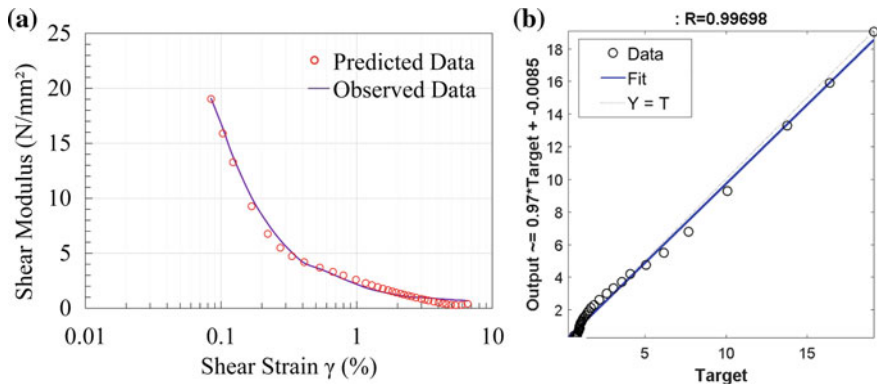


Fig. 12 **a** Comparison between observed and predicted values of shear modulus for new testing data set using ANN at $GF = 87\%$, $(\sigma_d/2\sigma_3) = 0.25$. **b** Performance of the ANN Model over new testing data set

performing a linear regression between the network outputs and the corresponding targets. A very high coefficient of correlation ($R = 99\%$) is obtained for the tested data set (See Fig. 12b).

6 Conclusion

In this study, a series of cyclic triaxial test was carried out to investigate dynamic properties of GTCM as a new TDGM. In addition, Support Vector Machine (SVM) and Artificial Neural Network (ANN) techniques were used to simulate shear modulus and damping ratio of GTCM. The following conclusions can be drawn:

- For a given relative density and confining pressure, shear modulus and damping ratio of GTCM are highly influenced by rubber inclusions for samples with GF from 100 to 44%.
- A feedforward artificial neural network model with backpropagation training algorithm can be employed to model sophisticated dynamic characteristics of granular mixtures with relatively high resolution.
- Outcome of this study shows that the Support Vector Machine with the RBF kernel function shows satisfactory performance on generalization and prediction of the training and test data sets and yields relatively low statistical error.
- Although result of ANN and SVR model showed that both the models are suitable tools for estimation dynamic characteristics of granular mixture in terms of performance parameters, i.e., R-value, RMSE, and ANN-based model yields better performance on generalization of training data sets in comparison to that of SVM.

References

1. ASTM D6270-12: Standard practice for use of scrap tires in civil engineering applications. ASTM International, West Conshohocken, PA, USA
2. Anastasiadis A, Senetakis K, Pitilakis K, Gargala C, Karakasi I (2011) Dynamic behavior of sand/rubber mixtures. Part I: Effect of rubber content and duration of confinement on small-strain shear modulus and damping ratio. *J ASTM Int* 9(2):1–19
3. Besalatpour A, Hajabbasi MA, Ayoubi S, Afyuni M, Jalalian A, Schulin R (2012) Soil shear strength prediction using intelligent systems: artificial neural networks and an adaptive neuro-fuzzy inference system. *Soil Sci Plant Nutr* 58(2):149–160
4. Brennan AJ, Thusyanthan NI, Madabhushi SP (2005) Evaluation of shear modulus and damping in dynamic centrifuge tests. *J Geotech Geoenviron Eng* 131(12):1488–1497
5. Edil T, Bosscher P (1994) Engineering properties of tire chips and soil mixtures. *Geotech Test J* 17(4):453–464
6. Edinçliler A, Baykal G, Dengili K (2004) Determination of static and dynamic behavior of recycled materials for highways. *Resour Conserv Recycl* 42(3):223–237
7. Feng Z-Y, Sutter KG (2000) Dynamic properties of granulated rubber-sand mixtures. *Geotech Test J* 23(3):338–344
8. Foose GJ, Benson CH, Bosscher PJ (1996) Sand reinforced with shredded waste tires. *J Geotech Eng* 122(9):760–767
9. Goh ATC (1994) Seismic liquefaction potential assessed by neural networks. *J Geotech Eng* 120(9):1467–1480
10. Hardin BO (1978) The nature of stress-strain behavior for soils. In: Proceedings of the ASCE geotechnical, Vol 1 Engineering division specialty conference on earthquake engineering and soil dynamics, June 19–21, Pasadena, California
11. Hazarika H, Abdullah A (2016) Improvement effects of two and three dimensional geosynthetics used in liquefaction countermeasures. *Jpn Geotech Soc Spec Publ* 2(68):2336–2341
12. Hazarika H, Kohama E, Sugano T (2008) Underwater shake table tests on waterfront structures protected with tire chips cushion. *J Geotech Geoenviron Eng* 134(12):1706–1719
13. Hazarika H, Yasuhara K, Kikuchi Y, Karmokar AK, Mitarai Y (2010) Multifaceted potentials of tire-derived three dimensional geosynthetics in geotechnical applications and their evaluation. *Geotext Geomembr* 28(3):303–315
14. Hazarika H, Yasuhara K, Karmokar A, Mitarai Y (eds) (2007) Shaking table test on liquefaction prevention using tire chips and sand mixture. In: Proceedings of the international workshop on scrap tire derived geomaterials—opportunities and challenges, Yokosuka, Japan
15. JGS 0111-2009, Test method for density of soil particles, Standards of the Japanese Geotechnical Society. Japanese Geotechnical Society
16. Mashiri M, Vinod J, Sheikh M (2016) Liquefaction potential and dynamic properties of Sand-Tyre Chip (STCh) mixtures. *Geotech Test J* 39:69–79
17. McCulloch WS, Pitts W (1943) A logical calculus of the ideas immanent in nervous activity. *Bull Math Biophys* 5(4):115–133
18. Nakhaei A, Marandi SM, Sani Kermani S, Bagheripour MH (2012) Dynamic properties of granular soils mixed with granulated rubber. *Soil Dyn Earthq Eng* 43:124–132
19. Park HI (2011) Development of neural network model to estimate the permeability coefficient of soils. *Mar Georesour Geotechnol* 29(4):267–278
20. Park JK, Cho DH, Hossain S, Oh J (2018) Assessment of settlement profile caused by underground box structure installation with an artificial neural network model. *Transportation research record*: 0361198118756901
21. Pasha SMK, Hazarika H, Bahadori H, Chaudhary B (2017) Dynamic behaviour of saturated sandy soil reinforced with non-woven polypropylene fibre. *Int J Geotech Eng* 12(1):89–100
22. Pasha SMK, Hazarika H, Yoshimoto N (2019) Physical and mechanical properties of Gravel-Tire Chips Mixture (GTCM). *Geosynth Int* 26(1):92–110

23. Pasha SMK, Hazarika H, Yoshimoto N (2018) Dynamic properties and liquefaction potential of Gravel-Tire Chips Mixture (GTCM). *J Jpn Soc Civil Eng Ser A1 (Structural Engineering & Earthquake Engineering (SE/EE))* 74(4):I_649–I_55
24. Shahin MA (2014) Load–settlement modeling of axially loaded steel driven piles using CPT-based recurrent neural networks. *Soils Found* 54(3):515–522
25. Tsang HH, Lo SH, Xu X, Sheikh MN (2012) Seismic isolation for low-to-medium-rise buildings using granulated rubber–soil mixtures: numerical study. *Earthq Eng Struct Dynam* 41(14):2009–2024
26. Uchimura T, Chi N, Nirmalan S, Sato T, Meidani M, Towhata I (2007) Shaking table tests on effect of tire chips and sand mixture in increasing liquefaction resistance and mitigating uplift of pipe. In: *Proceedings, international workshop on scrap tire derived geomaterials—opportunities and challenges*, Yokosuka, Japan
27. Vapnik V, Golowich SE, Smola AJ (1997) Support vector method for function approximation, regression estimation and signal processing. *Adv Neural Inf Process Syst*

Rutting Performance of PPA-Modified Binders Using Multiple Stress Creep and Recovery (MSCR) Test



Shivani Rani, Rouzbeh Ghabchi, Musharraf Zaman
and Syed Ashik Ali

Abstract In this study, the effect of modifying an asphalt binder using Polyphosphoric Acid (PPA) on its rutting performance was studied using the Multiple Stress Creep and Recovery (MSCR) test. The MSCR test provided the non-recoverable creep compliance and percent recovery of the tested binder blends at the test temperature(s). Those parameters were then used to evaluate the stress sensitivity and rutting potential of the PPA-modified binders and were utilized to determine the binder grade based on the level of traffic. For this purpose, a PG 58-28 binder was blended with different amounts of PPA, namely 0, 0.5, 1.0, 1.5, and 2.0% using a high shear mixer. The MSCR tests were conducted at two different stress levels (0.1 and 3.2 kPa) and two different temperatures (58 and 64 °C). It was found that adding PPA decreases the non-recoverable creep compliance of the neat binder. Consequently, the MSCR grade of the neat binder was found to improve from PG58S-XX to PG58E-XX, when blended with 2.0% PPA. Additionally, the percent recovery of the neat binder was found enhanced due to PPA modification. Therefore, it is anticipated that the mixes containing PPA would sustain a higher level of traffic without undergoing a significant amount of rutting compared to mixes containing non-PPA modified binders. Also, it was observed that the PPA-modified binders can exhibit stiffness similar to polymer-modified binders.

Keywords Rutting · Polyphosphoric acid (PPA) · Multiple stress creep and recovery (MSCR) · Test · MSCR grade · And percent recovery

S. Rani (✉) · S. A. Ali

School of Civil Engineering and Environmental Science, The University of Oklahoma,
Norman, OK, USA

e-mail: shivani.rani@ou.edu

R. Ghabchi

Department of Civil and Environmental Engineering, South Dakota State University,
Brookings, SD, USA

M. Zaman

Civil Engineering, Petroleum and Geological Engineering, Southern Plains Transportation
Center, The University of Oklahoma, Norman, OK, USA

© Springer Nature Singapore Pte Ltd. 2020

A. Prashant et al. (eds.), *Advances in Computer Methods
and Geomechanics*, Lecture Notes in Civil Engineering 56,
https://doi.org/10.1007/978-981-15-0890-5_50

607

1 Introduction

Modifying asphalt binders by blending them with Polyphosphoric Acid (PPA) is found to bump their high-temperature Performance Grade (PG) and therefore, improve the resistance of an asphalt mix to rutting. In recent years, many studies have been conducted on the use of Polyphosphoric Acid (PPA) to improve the mechanical properties of asphalt binders (e.g., [2, 4, 13]). It was found that the addition of PPA significantly increases the stiffness of binders at high temperatures, and depending upon the source of the asphalt binder may improve the low-temperature PG grade as well [1, 4, 7, 8, 10, 11, 13–15]. Subsequently, PPA reduces the sensitivity of asphalt binders to temperature variation and increases their resistance to rutting. Previous studies have also reported that PPA-modified binders had a higher resistance to low-temperature cracking than those containing waxes such as Sasobit[®].

Giavarini et al. [9], Baumgardner [5], Jaroszek [12], and Yan et al. [18] investigated the effects of PPA at a molecular level and reported that PPA increases the concentration of asphaltenes at the expense of saturates, resins, or cyclics in the binder. However, the effect of PPA is dependent on the composition of the base binder. A number of mechanisms such as cross-linking of PPA with asphalt segments, formation of ionic clusters, and cyclization of alkyl aromatics could explain the reason for an increase in stiffness of asphalt binder due to the addition of PPA [5].

The abovementioned effects of PPA were mostly based on Dynamic Shear Rheometer (DSR) test results. However, a DSR test can only determine the high-temperature PG and cannot identify the effect of traffic loading although it is a significant factor affecting the rutting performance. Bahia et al. [3] proposed a new test method, named Repeated Creep and Recovery Test (RCRT), to determine the accumulated strain under repeated stress level of 0.3 kPa. The test was later modified to include two different stress levels of 0.1 and 3.2 kPa and named it as Multiple Stress Creep and Recovery (MSCR) test. In a study conducted by D'Angelo [6], the MSCR test was used to evaluate the rutting performance of neat and polymer-modified binders at high temperatures. It was reported that the performance of polymer-modified binders depends on the amount of polymer and extent of polymer network in the binder. The MSCR test can distinguish the performance between neat and polymer-modified binders. Based on the results in that study, a new grading system was suggested considering the traffic loading. Reinke [17] reported that the high-temperature performance of polymer-modified binders are sensitive to applied stress, and it is important to evaluate the stress sensitivity to assess the rutting potential of those binders.

In the present study, MSCR tests were conducted to evaluate the performance of PPA-modified binders. For this purpose, five different binder blends were prepared with varying amounts of PPA. Based on the MSCR test results, the percent (%) Recovery and non-recoverable creep compliance of binder blends were measured and compared for all the binder blends. The binder blends were subjected to

different stress levels to investigate their stress sensitivity and to evaluate their resistance to rutting. The binder blends were further analyzed to determine their MSCR grade and the maximum sustainable intensity of traffic loading those binder blends that can sustain. Also, the performance of PPA-modified binders was compared with the polymer-modified binders using a polymer curve method.

2 Materials

A Superpave[®] designated grade binder, i.e., PG 58-28, was collected from a local refinery in Oklahoma. Also, a PPA of 105% grade was collected from a local supplier. PPA is available in different grades depending upon the concentration of P₂O₅ with respect to H₃PO₄. PPA is a liquid mineral polymer with high viscosity at room temperature [19]. It is a mixture of polyacids with the general form of H_{n+2}P_nO_{3n+1}, where n ≥ 2 [12]. Since PPA has no water, it can easily be mixed with the asphalt binder in all proportions [1].

3 Sample Preparation

In this study, the collected PPA was blended with the binder in four different amounts, namely 0.5, 1.0, 1.5, and 2.0%, using a high shear mixer. The mixing was performed at 1,000 rotations per minute (RPM) for 45 min. The prepared binder blends are referred to as S1, S1P0.5, S1P1.0, S1P1.5, and S1P2.0, where S1 represents the binder type and “P#.#” defines the PPA and its concentration in the blend. The binder blends were aged in a Rolling-Thin Film Oven (RTFO) for 85 min in accordance with AASHTO T240-13. The MSCR samples were prepared by placing a small amount of RTFO-aged asphalt binder in a 19-mm diameter and 1.5-mm height silicon mold generally used for DSR testing, as shown in Fig. 1.

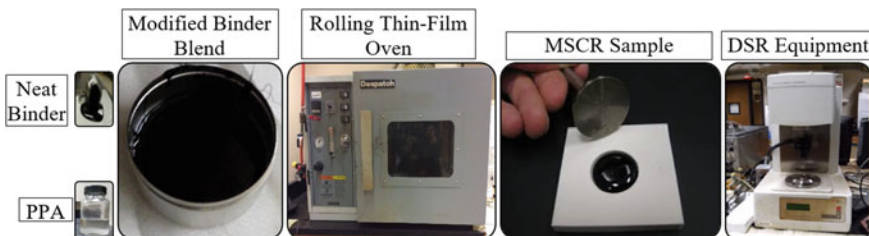


Fig. 1 Sample preparation procedure

4 Laboratory Test

In this study, the MSCR test was performed on the RTFO-aged binders in accordance with AASHTO TP70-09. Accordingly, a binder blend was first subjected to 10 loading cycles at 0.1 kPa stress level followed by 10 loading cycles of 3.2 kPa stress level, as shown in Fig. 2. The loading duration of a cycle was 10 s including 1 s of loading and 9 s of recovery. The test was performed at the base temperature of the neat binder, i.e., 58 °C. Based on the test data, two different parameters, namely, the Non-recoverable creep compliance (J_{nr}) and % Recovery, were calculated using Eq. (1) and Eq. (2), respectively, at both 0.1 and 3.2 kPa stress levels. Then, these parameters were used to characterize the binder blends for the traffic loading, to assign the MSCR grade, and to evaluate their resistance to rutting. Table 1 presents the criteria used to characterize the binder blends.

$$J_{nr} = \frac{\text{Non-Recoverable Shear Strain}}{\text{Applied Shear Stress}} \text{ (kPa}^{-1}\text{)} \tag{1}$$

$$\% \text{ Recovery} = \% \text{ of Recoverable Shear Strain} \tag{2}$$

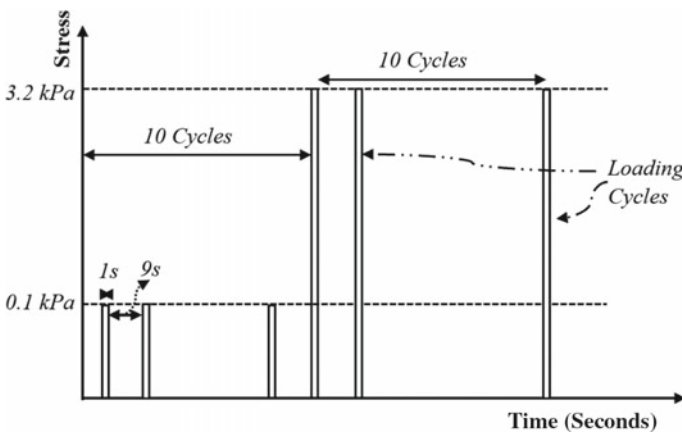


Fig. 2 Loading pattern used in the multiple stress creep and recovery test

Table 1 Traffic loading criteria used for characterization of binder blends (AASHTO M332-15)

Traffic intensity (in million ESAL ^a)	J_{nr} at 3.2 kPa (kPa ⁻¹)	Grade*
<10	>2.0	S
10–30	1.0–2.0	H
>30	0.5–1.0	V
>30	<1.0	E

^aESAL: Equivalent Single Axle Load

*AASHTO M332-15

5 Results and Discussions

5.1 Non-recoverable Creep Compliance (J_{nr})

Figure 3 presents the non-recoverable creep compliance (J_{nr}) values of binder blends measured at the applied stress levels of 0.1 and 3.2 kPa. As shown, the J_{nr} of the neat PG 58-28 binder is 3.0 kPa^{-1} at 0.1 kPa stress level and it increases to 3.3 kPa^{-1} when subjected to 3.2 kPa stress level. The addition of PPA, irrespective of the amount, reduces the J_{nr} value at both stress levels. For instance, from Fig. 3, the J_{nr} value at 0.1 kPa stress level decreases from 3.0 kPa^{-1} to 1.5, 0.7, 0.2, and 0.1 kPa^{-1} due to the addition of 0.5%, 1.0%, 1.5%, and 2.0% PPA, respectively, to the neat binder. Similarly, at 3.2 kPa stress level, the J_{nr} value of the neat binder decreases from 3.3 kPa^{-1} to 0.1 kPa^{-1} when blended with 2.0% PPA. These results indicate that the use of PPA reduces the creep compliance or enhances the stiffness of the neat binder. Therefore, it is expected that the binder blend containing PPA will behave more elastically than the neat binder. As a result, the asphalt mix containing PPA is expected to exhibit a higher resistance to rutting as compared to conventional HMA mixes. This is possibly due to increase in the concentration of asphaltenes in the neat binder due to the addition of PPA ([5, 12, 18]). This increase, in turn, enhances the stiffness of the neat binder and results in lower J_{nr} value. Several other researchers [2, 4, 16] have reported similar observations based on the DSR test results, stating an increase in the rutting resistance of the base binder after modifying it by using PPA.

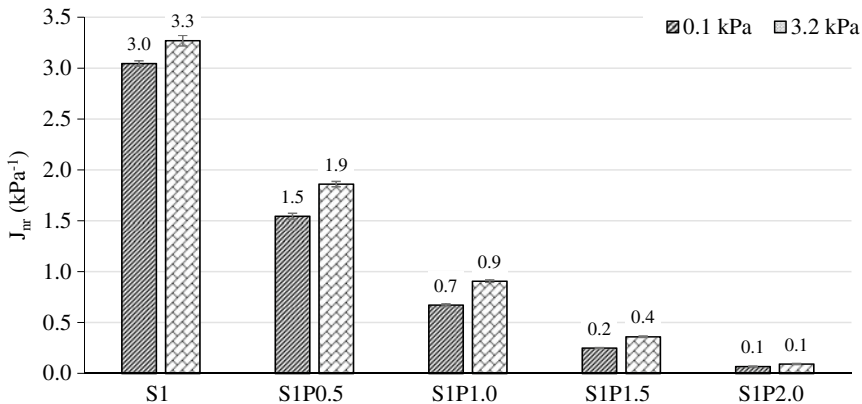


Fig. 3 Non-recoverable creep compliance of binder blends at 58 °C

5.2 Percent (%) Recovery

The % Recovery of binder blends is shown in Fig. 4, measured at a test temperature of 58 °C. As shown, the % Recovery of the neat binder is only 1.9% at 0.1 kPa stress level and 0% at 3.2 kPa stress level. Therefore, it is anticipated that a mix containing only neat binder may experience a high amount of rutting in the field. The addition of PPA improves the % Recovery of the neat binder, as seen in Fig. 4. The higher the PPA's concentration, the higher the increase in the % Recovery of the neat binder. For instance, from Fig. 4, the addition of 1.0% PPA increases the % Recovery from 1.9 to 30.6% at 0.1 kPa stress level and from 0 to 12.8% at 3.2 kPa stress level. The binder blend containing 2.0% PPA has a % Recovery as high as 74.9% at 0.1 kPa stress level and 64.8% at 3.2 kPa level. These results indicated that using PPA enhances the neat binder capability to recover the applied strain under traffic loading. Therefore, it is anticipated that mixes containing PPA-modified binder will exhibit lower non-recoverable permanent deformation or rutting in the field compared to conventional mixes. As noted earlier, this is possibly due to the increase in the concentration of asphaltenes in the neat binder due to the addition of PPA ([5, 12, 18]), which enhances the stiffness of the neat binder and allows a higher recovery of the applied strain under traffic loading.

Furthermore, from Fig. 4, the difference between the % Recovery at 0.1 kPa and 3.2 kPa stress levels for the binder blend containing 0.5% PPA was 75%. The increase in the PPA content to 1.0% reduces this difference to 58%. Further, increase in the PPA to 2.0% results in the lowest difference of 14%. These results indicate that % Recovery of the PPA-modified binders is less sensitive to the applied stresses.

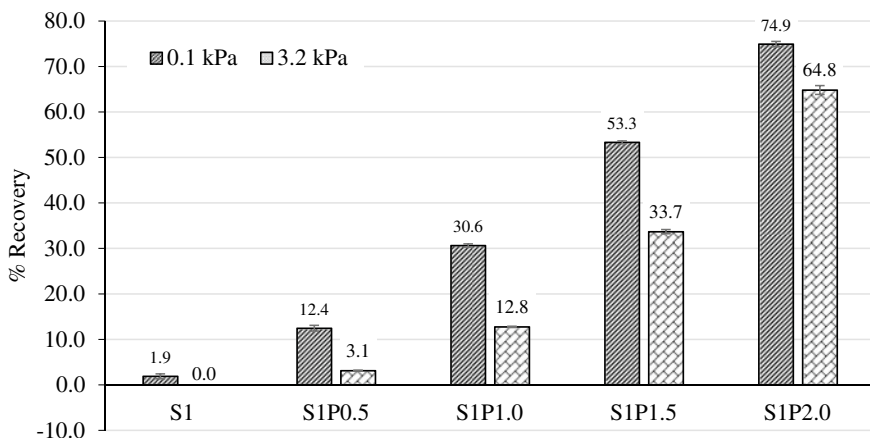


Fig. 4 Percent recovery of binder blends at 58 °C

5.3 MSCR Grade

Based on the J_{nr} value of the binder blends at 3.2 kPa stress level, the MSCR grade was determined in accordance with the AASHTO M332-15 specification. The results are presented in Table 2. It is seen that the MSCR grade of the neat binder was PG58S-XX indicating that the neat binder can be used in areas of low traffic level (<10 million ESAL). The addition of PPA helps improve the MSCR grade of the neat binder. It is evident from Table 2 that the use of 0.5% PPA changes the MSCR grade from PG58S-XX to PG58H-XX. According to AASHTO T332-14 specifications, the binder blends containing 0.5% PPA can sustain 10–30 million ESAL of traffic loading. Further increase in the PPA concentration to 1.0% bumps the MSCR grade to PG58 V-XX, which can sustain a traffic loading intensity of more than 30 million ESAL. The highest MSCR grade of PG58E-XX can be observed for the binder blends containing 1.5% or 2.0% PPA (Table 2). These results indicated that the addition of 1.5% or 2.0% PPA significantly improves the traffic loading level of the neat binder.

5.4 Comparison with Polymer-Modified Binders

The polymer curve is generally used to determine the presence of the elastomeric polymers in the binder blend and to evaluate performance in the field (AASHTO M332-15). It represents the relationship between the J_{nr} value and % Recovery at 3.2 stress level, as shown in Fig. 5. Any binder blend falling above the curve signifies that the blend contains polymer, which would exhibit good % Recovery under applied traffic loading. In this study, this curve was used to compare the PPA-modified binders with the polymer-modified binders. For this purpose, the test data at 3.2 kPa stress level were plotted on the curve, as seen in Fig. 5. It is evident that all the binder blends containing PPA fall under the curve. Only the binder blend containing 2.0% PPA touches the curve. These results indicate that although PPA modification improves the % Recovery and stiffness of the neat binder, it cannot improve their strain recovery capability significantly, as compared to the polymer-modified binders. This may be attributed to the lack of the cross-linking of asphaltenes and maltenes in the binder blend when using PPA alone.

Table 2 MSCR grade of binder blends

Binder blend type	J_{nr} (kPa ⁻¹)	MSCR grade	Intensity of traffic loading*
S1	3.3	PG58S-XX	<10 million ESAL
S1P0.5	1.9	PG58H-XX	10–30 million ESAL
S1P1.0	0.4	PG58V-XX	>30 million ESAL
S1P1.5	0.2	PG58E-XX	>30 million ESAL
S1P2.0	0.1	PG58E-XX	>30 million ESAL

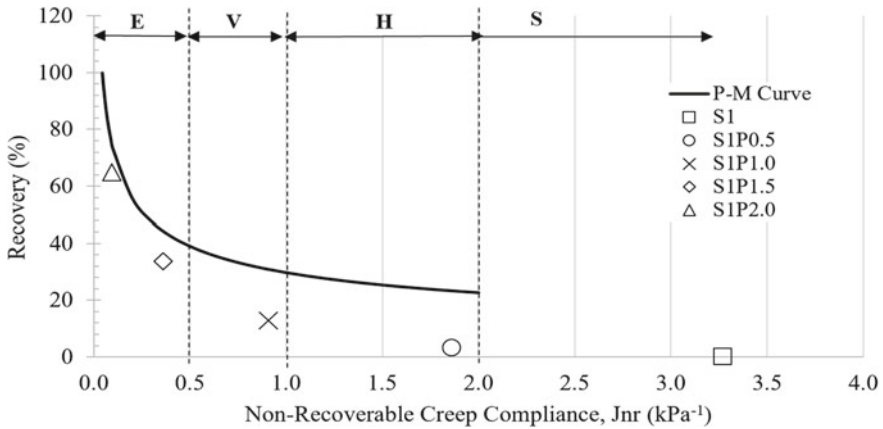


Fig. 5 Polymer curve and its comparison with PPA-modified binders

6 Conclusions

The following conclusions are drawn from the results presented in the preceding sections:

1. The use of PPA reduces the non-recoverable creep compliance of the neat binder, which is an indicator of improved stiffness of the neat binder. Therefore, it is expected that asphalt mixes containing PPA would exhibit a higher rutting resistance compared to conventional HMA mixes.
2. PPA increases the % Recovery of the neat binder. For instance, the binder blend containing 2.0% PPA has a % Recovery of 75% at 0.1 kPa stress level and 65% at 3.2 kPa stress level. Therefore, it is expected that mixes containing PPA-modified binders would recover the applied strain under traffic loading and therefore, exhibit a lower non-recoverable permanent deformation or rutting.
3. The MSCR grade of the neat binder is found to bump from PG58S-XX to PG58E-XX due to the addition of PPA to the binder. Consequently, it is expected that the neat binder would sustain more than 30 million ESAL without undergoing significant deformation under the applied traffic loading.
4. Based on the test data, the PPA-modified binder is found to have a lower strain recovery capability compared to polymer-modified binders.

Acknowledgements The financial support from the Southern Plain Transportation Center (SPTC) and the Oklahoma Department of Transportation for this study is gratefully acknowledged. The authors would also like to acknowledge Haskell Lemon Construction Co. and Valero Refinery for providing the materials for this study.

References

1. Al-Qadi IL, Abauwad IM, Dhasmana H, Coenen AR (2014) Effects of various asphalt binder additives/modifiers on moisture-susceptible asphaltic mixtures. Report No. ICT-14-004, UILU-ENG-2014-2004, Illinois Center for Transportation, Rantoul, IL
2. Arnold TS, Youtcheff Jr JS, Needham SP (2009) Use of phosphoric acid as modifier for hot-mix asphalt. In: Polyphosphoric acid modification of asphalt binders: a workshop, circular E-C160, pp 40–51
3. Bahia HU, Hanson DI, Zeng M, Zhai H, Khatri MA, Anderson MR (2000) A project NCHRP 9-10 Superpave protocols for modified asphalt binders. Draft Topical Report (Task 9), Prepared for National Cooperative Highway Research Program, Transportation Research Board, National Research Council, Washington, DC
4. Baldino N, Gabriele D, Lupi FR, Rossi CO, Caputo P, Falvo T (2013) Rheological effects on bitumen of polyphosphoric acid (PPA) addition. *Constr Build Mater* 40:397–404
5. Baumgardner GL, Masson JF, Hardee JR, Menapace AM, Williams AG (2005) Polyphosphoric acid modified asphalt: proposed mechanisms. *J Assoc Asphalt Paving Technol* 74:283–305
6. D'Angelo J (2010) New high-temperature binder specification using multistress creep and recovery. In: Development in asphalt, transportation research circular, E-C147, Transportation Research Board, Washington, DC, pp 1–13
7. D'Angelo J, Anderson RM (2003) Material production, mix design, and pavement design effects on moisture damage. In: Proceeding of moisture sensitivity of asphalt pavements: a national seminar, San Diego, California, pp 187–201
8. Falkiewicz M, Grzybowski K (2004) Polyphosphoric acid in asphalt modification. In: Presented at Western Research Institute symposium on pavement performance prediction, Laramie, WY
9. Giavarini C, Mastrofini D, Scarsella M, Barre L, Espinat D (2000) Macrostructure and rheological properties of chemically modified residues and bitumens. *Energy Fuels* 14:495–502
10. Ho S, Zanzotto L, MacLeod D (2002) Impact of different types of modification on low-temperature tensile strength and $T_{critical}$ of asphalt binders. *Transp Res Rec J Transp Res Board*, No. 1810, Transportation Research Board of the National Academies, Washington, DC, pp 1–8
11. Ho S, Zanzotto L, MacLeod D (2001) Impact of chemical modification on composition and properties of asphalt binders. *Proc Can Tech Asphalt Assoc* 46:153–170
12. Jaroszek H (2012) Polyphosphoric acid (PPA) in road asphalts modification. *Chemik* 66 (12):1340–1345
13. Kodrat I, Sohn D, Hesp S (2007) Comparison of polyphosphoric acid-modified asphalt binders with straight and polymer-modified materials. *Transp Res Rec J Transp Res Board* No. 1998, 47–55
14. Maldonaldo R, Falkiewicz M, Bazi G, Grzybowski K (2006) Asphalt modification with polyphosphoric acid. In: Fifty-First annual conference of the Canadian technical asphalt association (CTAA), Charlottetown, Prince Edward Island
15. Orange G, Dupuis D, Martin JV, Farcas F, Such C, Marcant B (2004a) Chemical modification of bitumen through polyphosphoric acid: properties-micro-structure relationship. In: Proceedings of the 3rd Eurasphalt and Eurobitume Congress Held Vienna
16. Orange G, Martin JV, Menapace A, Hemsley M, Baumgardner GL (2004) Rutting and moisture resistance of asphalt mixtures containing polymer and polyphosphoric acid modified bitumen. *Road Mater Pavement Des* 5(3):323–354
17. Reinke G (2010) Use of Hamburg rut testing data to validate the use of J_{nr} as a performance parameter for high-temperature permanent deformation. In: Development in asphalt, transportation research circular, E-C147, Transportation Research Board, Washington, DC, pp 14–24

18. Yan K, Zhang H, Xu H (2013) Effect of polyphosphoric acid on physical properties, chemical composition and morphology of bitumen. *Constr Build Mater* 47:92–98
19. Zorn S, Mehta Y, Dahm K, Batten E, Nolan A, Dusseau R (2011) Rheological properties of the polymer modified bitumen with emphasis on SBS polymer and its microstructure. *Road Mater New Innov Pavement Eng* 41–48

2D Coupled Poro-Elastic Analysis for Dynamic Behaviour of CPRF



Patchamatla J. RamaRaju, Pavan K. Emani and Shashank Kothari

Abstract In the present work, the dynamic behaviour of combined Piled Raft Foundation (CPRF) in liquefying soils is studied using numerical simulation techniques. Using OPENSEES, 2D poro-elastic modelling of the soil and the piled raft is carried out. The main focus is the pore pressure generation in the soil, caused by the harmonic excitations in horizontal direction on the raft. Due to impervious nature of the raft and piles, excess pore pressures are observed under the raft. This generation of excess pore water pressure can be critical, due to its adverse effects on stability, and this can be very catastrophic without provision of pore pressure relief in the raft. Besides, the poro-elastic horizontal dynamic impedances of CPRFs are reported.

1 Introduction

The Combined Piled Raft Foundation (CPRF) is being used for nuclear containments, high rise buildings, towers, etc., because of their better settlement characteristics under heavy concentrated loads. But pore pressure development leading to phenomena like liquefaction is often considered as the potential hazard for such foundations. Not many researchers studied the dynamics of pore pressure development in CPRF. Some static studies used non-linear p-y curves to simplify the soil-pile and soil-raft interactions. But under liquefying soil conditions, the soil pressure on piles is more likely to be a function of velocity rather than displacement [5, 7]. Experimental studies were carried out by many researchers, either using shake table or centrifuge, to study the dynamics of coupled pore pressure-deformation analysis on soils only, on soils with foundations and on soils with foundation and structures [8]. Great efforts are done to attain the capability of developing appropriate numerical models for simulating the experimental or field behaviour. For example, Kagawa and Kraft Jr [4] used non-linear Winkler model

P. J. RamaRaju · P. K. Emani (✉) · S. Kothari
Graphic Era (Deemed to be University), Dehradun, India
e-mail: dr.emani.ce@geu.ac.in

for numerical simulation. Emani and Maheshwari [1] presented a hybrid FEM-BEM continuum model to study the dynamics of pile groups with embedded pile caps, which behaves similar to a CPRF. Hall et al. [3] used wavelet transform to study the vibration characteristics of pile group under liquefaction. Collapse load analysis of pile groups embedded in liquefying soils, under lateral and axial loading is presented by Emani et al. [2]. The poro-elastic dynamic behaviour of pile groups and piled rafts is not studied extensively.

In the present study, a coupled pore pressure-deformation 2D model of CPRF is developed in OPENSEES, with simple roller boundaries on sides and bottom. A horizontal harmonic excitation is the source of vibration, as may occur under vibrating machines or inertial loading from superstructure during seismic events. Various frequencies of excitation are used to study the frequency response of deformation characteristics and pore pressure development.

2 Geometric Modelling of CPRF

The CPRF analysed in the present work has a 5×5 floating pile group having an individual pile diameter 'd' of 0.5 m, and a centre to centre spacing of 5d between the adjacent rows of piles in a rectangular grid. The length of all piles is 22.5d, i.e. 11.25 m. The raft is square in plan with a side of 24d, i.e. 12 m. The thickness of the raft is taken as 0.75 m. This system is shown in Fig. 1a. The pile and raft are assumed to be made of M25 grade concrete [6].

In the present work, the CPRF is modelled as a strip foundation for 2D analysis. This will have some error compared to a true 3D model. The soil surrounding the CPRF is truncated at a horizontal (X-directional) distance of 8d from the outer face of raft, and at a vertical (Y-directional) distance of 6d. This truncation can lead to artificial reflections for excitation frequencies above 23 Hz. Therefore, for frequencies beyond 23 Hz there can be some error due to simple roller boundaries, and the error is not estimated in the present work. The FE discretization of the model is

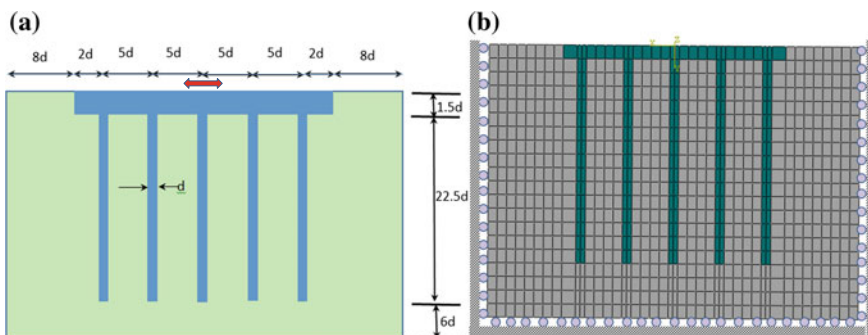


Fig. 1 CPRF a physical system, b 2D finite element model

Table 1 Material properties of soil and the foundation

Soil (sand)	Reinforced concrete (piles and raft)
<ul style="list-style-type: none"> • Saturated Mass Density = 2.0 t/m³ • Shear modulus = 7.5E4 kN/m² • Poisson's ratio = 0.40 • Permeability = 1E-3 m/s 	<ul style="list-style-type: none"> • Mass density = 2.5 t/m³ • Modulus of elasticity = 25,000 MN/m² • Poisson's ratio = 0.25 • Permeability = 1E-10 m/s

shown in Fig. 1b. A total of 880 quadratic u-p elements (quadUP) are used, making the total number of nodes as 945, each having 3 degrees of freedom (2 displacement DOF and 1 pore pressure DOF).

The material properties of the soil and concrete used for CPRF are given in Table 1.

3 Loads and Boundary Conditions

One of the objectives of the study is to determine the horizontal poro-elastic dynamic stiffness coefficients of the CPRF as a function of frequency. This requires an application of harmonic (concentrated) force loading at the plan centroid of the CPRF raft in the horizontal direction (Fig. 1a). Also, gravity loading is applied in the initial step to get the proper initial conditions for dynamic analysis.

At the truncated boundaries, simple roller supports are used. For more accurate solutions to the response, rigorous consistent boundaries need to be used.

The boundaries at the sides and at bottom are taken as impervious boundaries for pore pressure DOF. The only drainage is at the top of the soil at atmospheric pressure.

4 Method of Analysis

The displacement response is solved using Newmark Time-integration algorithm, and the steady-state amplitude is used to calculate the dynamic stiffness coefficient and damping coefficient. This procedure is repeated for various frequencies of the exciting harmonic loading, resulting in the frequency variation of the dynamic stiffness of CPRF. The pre-processing to get OPENSEES input file, and post-processing of the OPENSEES results, are performed in MATLAB.

5 Results and Discussion

The final (at 5.0 s) deformed shape of the soil-foundation system can be seen in Fig. 2, for a 10 Hz harmonic excitation. The peculiar deformations seen around the central pile are found to be due to the built-up of excess pore pressures. The snapshots of excess pore pressure distribution along depth at various locations are shown in Fig. 3.

The pore pressure distributions in the soil along the periphery of the raft and along the length of the piles ① and ③ are shown in Fig. 3 for an excitation frequency of 10 Hz. Even for other frequencies of excitation, the trend is similar. It can be observed that the final excess pore pressures at the outer face of Pile 1 are almost zero, due to drainage conditions available nearby. On the other hand, the pore pressures at the junction of central pile (pile 3) and raft are substantially higher than those at the Pile 1. This excess pore pressure can cause uplift conditions under the raft. The exact reduction in the shear strength of soil caused by build-up of excess pore pressures can only be estimated by non-linear inelastic dynamic or pseudo-dynamic analysis.

The frequency variation of horizontal dynamic stiffness of the poro-elastic soil-pile system is shown in Fig. 4. The dynamic stiffness is the ratio of the amplitude of harmonic excitation force (P_0) and the steady-state amplitude of the displacement response (U_0), multiplied by the cosine of phase lag (ϕ) between the excitation (or source) and response. It can be seen that the local peaks correspond to the natural frequencies of the soil-foundation system. It can also be noted that the peaks are not distinctly visible. This may be due to inaccurate modelling of boundaries.

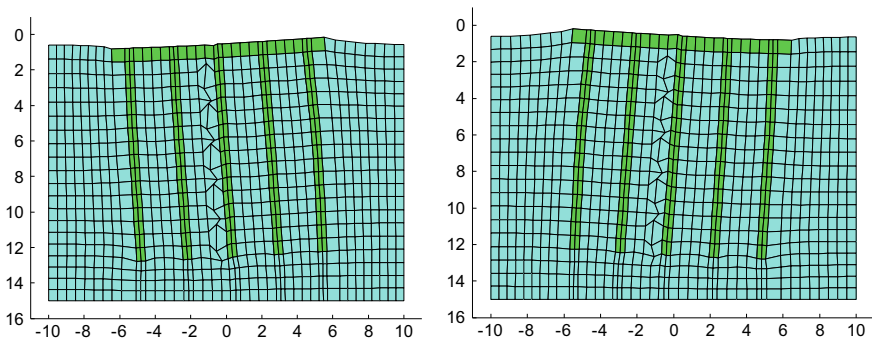


Fig. 2 Deformed shape after 2.5 s and after 2.75 s for 2 Hz excitation

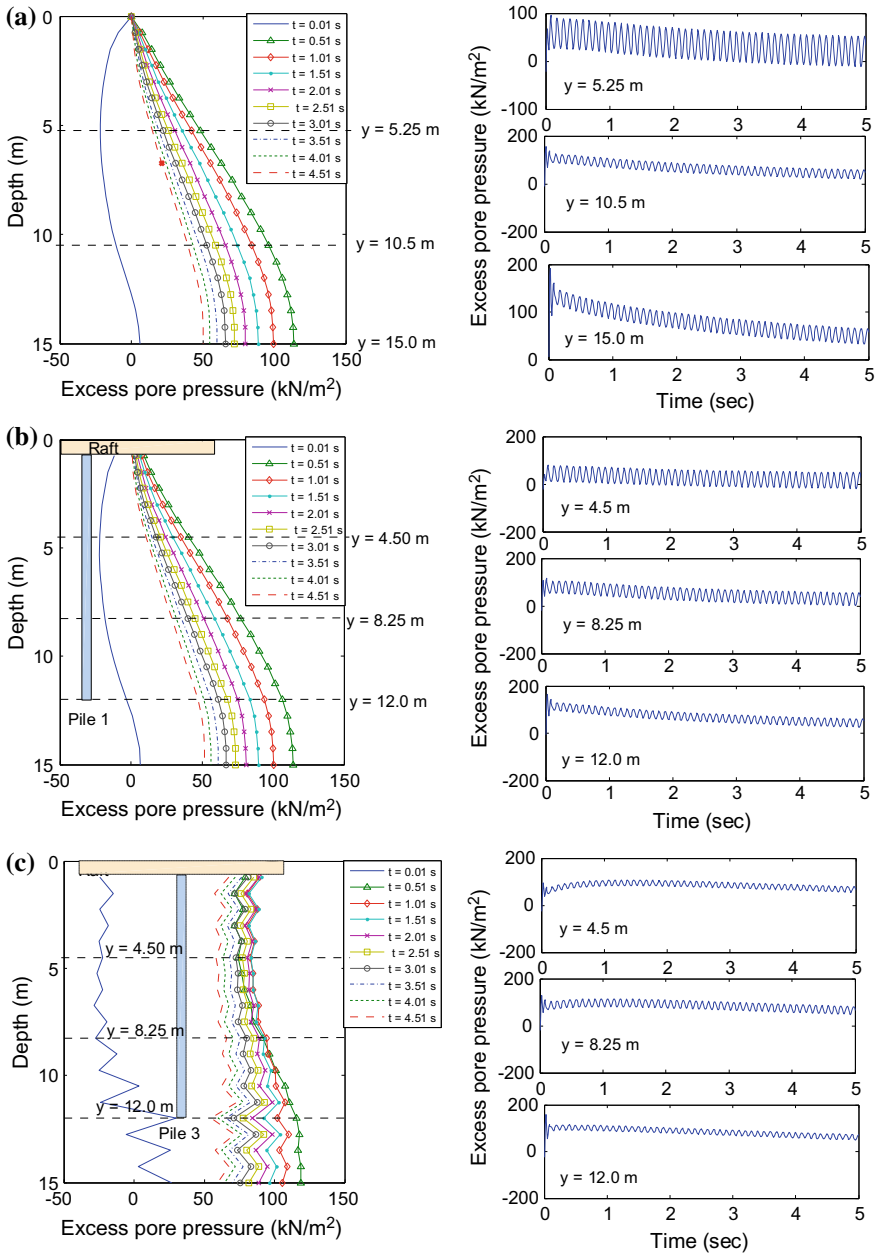


Fig. 3 Excess pore pressure distribution along depth **a** at the periphery of the raft, **b** at the face of Pile1, **c** at the face of Pile 3, under a 10 Hz horizontal excitation on the raft

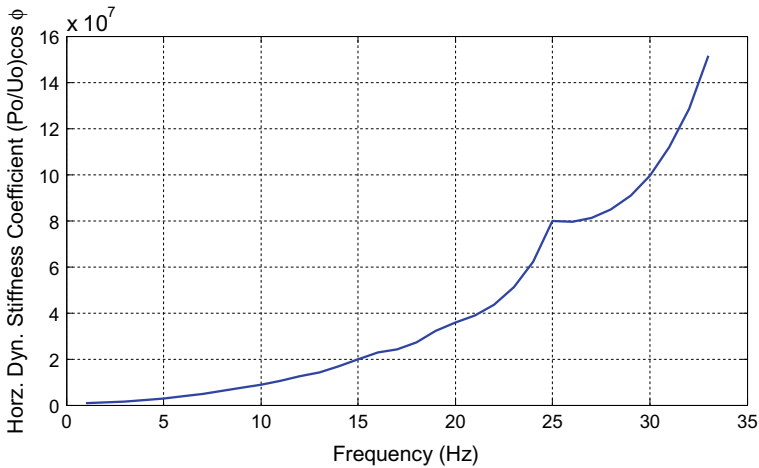


Fig. 4 Horizontal Dynamic stiffness coefficient of the CPRF as a function of frequency

6 Conclusions

The study reports the dynamic analysis results of poro-elastic numerical model of Piled Raft in 2D. The excess pore pressure under the raft can be a source of uplift pressure and can lead to stability problems. Possible pore pressure relief mechanisms need to be designed for avoiding failure modes involving uplift. In addition, the variation of dynamic stiffness with frequency is reported for a frequency range of 1–33 Hz.

Acknowledgements The above research is funded by research grants to the corresponding author from SERB, Department of Science and Technology, GoI, and BRNS, Department of Atomic Energy, GoI, vide sanction No. SR/FTP/ETA-130/2010 and sanction No. 2012/36/49-BRNS, respectively.

References

1. Emani PK, Maheshwari BK (2009) Dynamic impedances of pile groups with embedded caps in homogeneous elastic soils using CIFECM. *Soil Dyn Earthq Eng* 29(6):963–973
2. Emani P, Kothari S, Phanikanth V (2018) Collapse load analysis of reinforced concrete pile group in liquefying soils under lateral loading. *Int J Geotech Geol Eng* (World Academy of Science, Engineering and Technology, International Science Index 134) 12(2):114–117
3. Hall FE, Lombardi D, Bhattacharya S (2018) Identification of transient vibration characteristics of pile-group models during liquefaction using wavelet transform. *Eng Struct* 171:712–729
4. Kagawa T, Kraft Jr LM (1981) Lateral pile response during earthquakes. *J Geotech Geoenviron Eng* 107(ASCE 16735)
5. Kagawa T, Sato M, Minowa C, Abe A, Tazoh T (2004) Centrifuge simulations of large-scale shaking table tests: case studies. *J Geotech Geoenviron Eng* 130(7):663–672

6. Standard I (2000) IS-456. 2000. Plain and reinforced concrete-code of practice. Bureau of Indian Standards, Manak Bhawan, 9
7. Tokimatsu K, Suzuki H, Suzuki Y (2001) Back-calculated p_y relation of liquefied soils from large shaking table tests
8. Tokimatsu K, Suzuki H (2004) Pore water pressure response around pile and its effects on p_y behavior during soil liquefaction. *Soils Found* 44(6):101–110

Performance-Based Evaluation of Building With and Without Soil Flexibility



S. Deepa, I. R. Mithanthaya and S. V. Venkatesh

Abstract Performance-based evaluation of the building by nonlinear static pushover analysis considering the effects of the soil–structure interaction is the main objective of this study. Soil–structure interaction is idealized by Modified Winkler method and elastic half-space Continuum method. Comparison between fixed base and soil–structure interaction method with raft foundation subjected to pushover analysis is performed using the Standards ASCE 41-13 and ATC-40. In the present study of a ten storey building modeled in SAP 2000 V19.2 software as a three-dimensional frame with and without soil–structure interaction is subjected to Pushover analysis. Totally, nine models are modeled under seismic zone 5 for three types of soil (hard soil, medium soil, and soft soil). The performance point of the building is found using Capacity Spectrum Method. The behavior of the building in the form of hinges defines the state of damage in the structure. The results show that performance of the building is more critical when soil flexibility is taken into consideration.

Keywords Soil–structure interaction • Raft foundation • Pushover analysis • Performance point

S. Deepa (✉)

Department of Technical Education, GPT-Udupi, Karnataka, India
e-mail: deepasujayakumar@yahoo.co.in

I. R. Mithanthaya

Department of Civil Engineering, NMAMIT-Nitte, Karnataka, India
e-mail: mith9999@yahoo.com

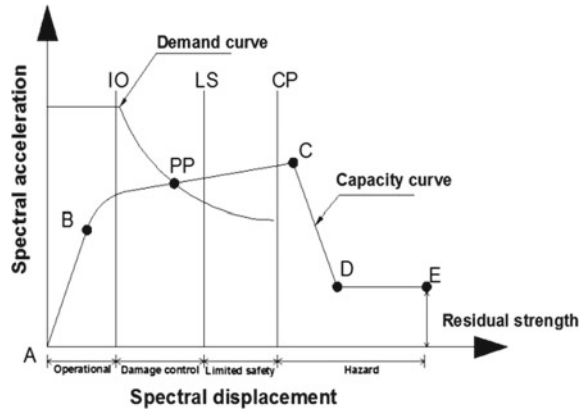
S. V. Venkatesh

Department of Civil Engineering, PESIT-Bangalore, Karnataka, India
e-mail: svvenkatesh@pes.edu

© Springer Nature Singapore Pte Ltd. 2020

A. Prashant et al. (eds.), *Advances in Computer Methods and Geomechanics*, Lecture Notes in Civil Engineering 56, https://doi.org/10.1007/978-981-15-0890-5_52

Fig. 1 Pushover curve



1 Introduction

The nonlinear static method is the more realistic and reliable methodology to depict the performance of structure than linear approach. In the nonlinear static method the structure is subjected to displacement response as the displacement gives better indication of damage than the forces. The linear static analysis predicts only yielding of the structure but it cannot predict the failure mechanism and redistribution of forces during yielding. The nonlinear pushover analysis shows how the building works and displays different stages of failure as given in Fig. 1. The capacity curve is characterized by A, B, C, D, and E which proposes different junctures in a building. As the effect of gravity and lateral loads are included simultaneously in the nonlinear analysis of a structure, it is the gravity load present at the time of lateral loading which is mainly responsible for the nonlinear response of structure to lateral load. The global behavior of the structure is represented by force and displacement curve known as pushover curve projecting the overall capacity of the structure. Capacity curve is generally constructed to signify the first mode response of the structure based on the statement that the fundamental mode of vibration is the major response of the structure.

2 Methodology

The nonlinear analysis method is performed by capacity spectrum method for which three important elements have to be determined such as capacity (Structures ability), demand (displacement of earthquake ground motion), and performance point (Capacity meets Demand).

In the present study, the ten storey building is analyzed as 3D model where columns and beams are assigned hinges as per standards ASCE41-13 and FEMA 440. The gravity loads and lateral loads are applied in corresponding X- and

Y-direction, monitored displacement is given and pushover analysis is carried out by using Saap 2000 V19.2 software. The bare frame is analyzed and the pushover capacity demand curve shows how the structure behaves when it exceeds elastic limit. The maximum displacement response during an earthquake is the demand of the building. The deformed shape of the structure after analysis shows weak points in the form of hinges which denotes various failure modes.

This analysis is performed considering the base of the structure to be fixed. Further, the nonlinear static pushover analysis is performed on structures where the soil is idealized by Modified Winkler method and Continuum method. Considering the Modified Winkler method, the spring supports in six directions which are given by stiffness formulas as per Standards ASCE41-13 and it is tabulated in Table 1. In Continuum method the soil is modeled as solid block and soil properties are assigned for different types of soil. Even though the soil properties are to be analyzed for dynamic analysis, they are subjected to nonlinear static analysis. The hinges are assigned and analysis is performed.

3 Result and Discussion

Results obtained from the analysis of ten storey framed structure for bare frame with rigid base and flexible base subjected to pushover analysis are as below. There is a difference noticed at the performance point where the demand and capacity of the structure meets in all the three types of base condition and soil conditions which are tabulated in Tables 2, 3 and 4. The changes in the formation of hinges at each stage are tabulated in Table 5 for Fixed, Modified Winkler method and Continuum method. It is noticed that there are not much changes observed in the formation of hinges in different types of soil. The results of soft soil are tabulated in each of the support conditions taken. The Pushover curve in case of different support conditions along with deformed shape is shown in Figs. 2, 3, 4, 5, 6 and 7.

3.1 *Base Shear at Performance Point*

The Base shear in rigid support is greater than Modified Winkler and Continuum method. However, the base shear is greater in soft soil compared to other types of soil. This may be due to soil flexibility condition. It is also noticed that Continuum method shows lesser base shear compared to other two methods. The Continuum method shows better results which may be due to the soil and footing taken beneath and around the structure.

Table 1 Stiffens formula as per ASCE 41-13 Standards

Stiffness	Embedment factor	Formula
$K_{x,sur} = GB/(2 - \gamma) * (3.4 * (L/B)^{0.65} + 1.2)$	$\beta_x = [1 + 0.21 * \text{SQRT}(D/B)] * [1 + 1.6 * (Dd[B + L]/BL)^{0.4}]$	$K_x = K_{x,sur} \times \beta_x$
$K_{y,sur} = (GB/(2 - \gamma)) * (3.4 * (L/B)^{0.65} + 0.4 * (L/B) + 0.8)$	$\beta_y = [1 + 0.21 * \text{SQRT}(D/L)] * [1 + 1.6 * (hd[B + L]/LB)^{0.4}]$	$K_y = K_{y,sur} \times \beta_y$
$K_{z,sur} = (GB/(1 - \gamma)) * (1.55 * (L/B)^{0.75} + 0.8)$	$\beta_z = (1 + (1/21 * D/B) * (2 + 2.6B/L)) * (1 + 0.32 * (d(B + L)/BL))^{2/3}$	$K_z = K_{z,sur} \times \beta_z$
$K_{0xx} = (GB^3/(1 - \gamma)) * (0.4 * (L/B) + 0.1)$	$\beta_{0x} = 1 + 2.5(d/B) * [1 + 2d/B * [d/D]^{-0.2} * \text{SQRT}(B/L)]$	$K_{0xx} = K_{0xx} * \beta_{0x}$
$K_{0yy} = (GB^3/(1 - \gamma)) * (0.47 * (L/B)^{2.4} + 0.034)$	$\beta_{0y} = 1 + 1.4 * (d/L)^{0.6} * [1.5 + 3.7 * (d/L)^{1.9} * (d/D)^{-0.6}]$	$K_{0yy} = K_{0yy} * \beta_{0y}$
$K_{0zz} = (GB^3 * (0.53 * (L/B)^{2.45} + 0.51))$	$\beta_{zz} = 1 + 2.6(1 + (B/L))(d/B)^{0.9}$	$K_{0zz} = K_{0zz} * \beta_{0z}$

Table 2 Hard soil–base shear and displacement at performance point

Sl. No.	Particulars–capacity demand curve	Base shear in kN	Displacement in mm
1.	Bare frame with Fixed Support	2212.885	0.016
2.	Bare frame (MWM)	2259.412	0.015
3.	Bare frame (Continuum method)	2061.150	0.018

Table 3 Medium soil–base shear and displacement at performance point

Sl. No.	Particulars–capacity demand curve	Base shear in kN	Displacement in mm
1.	Bare frame with Fixed Support	3009.524	0.022
2.	Bare frame (MWM)	2649.996	0.019
3.	Bare frame (Continuum method)	2253.983	0.022

Table 4 Soft soil–base shear and displacement at performance point

Sl. No.	Particulars–capacity demand curve	Base shear in kN	Displacement in mm
1.	Bare frame with fixed support	3695.518	0.027
2.	Bare frame (MWM)	2687.752	0.025
3.	Bare frame (Continuum method)	2522.664	0.026

3.2 Displacement at Performance Point

There is not much difference noticed in displacement for all three base conditions and also in all three types of soil.

3.3 Hinge Formation at Performance Point

The approximate formation of hinges in fixed base condition at performance point is zero which is in A-B state. However, the number of hinges increases with increase in displacement and reaches the state beyond collapse with 50 hinges.

In case of Modified Winkler method 240 number of hinges is formed at performance point which is in B-IO state. However, the formation of hinges in this case also increases with increase in displacement and reaches a state beyond collapse with 50 hinges

Continuum method shows 116 number of hinges which is in B-IO stage at performance point. However the formation of hinges increases stage by stage and finally at stage beyond collapse shows only one hinge. It can be seen that hinge formation in each stage is less compared to Rigid and MWM.

Table 5 Hinge formation details–pushover curve

Description	Step	Displacement “mm”	B. F “kN”	A to B	B IO	IO LS	LS CP	CPC-C	C D	DE	E	Total
<i>Fixed base</i>												
PP	5	0.025	3467.00	1920	0	0	0	0	0	0	0	1920
B-IO	24	0.117	16193.00	1914	6	0	0	0	0	0	0	1920
IO-LS	33	0.171	21501.18	1720	184	16	0	0	0	0	0	1920
LS-CP	36	0.194	22534.26	1632	258	14	16	0	0	0	0	1920
CP-C	37	0.199	22728.15	1622	260	22	0	0	16	0	0	1920
C-D	38	0.204	22880.37	1622	250	28	4	0	16	0	0	1920
Decrease in BS	51	0.278	23981.44	1554	214	64	8	0	80	0	0	1920
	52	0.281	23957.42	1554	212	58	12	0	84	0	0	1920
C-D	119	0.615	6670.90	1554	212	50	4	0	100	0	0	1920
D-E	120	0.619	6494.77	1554	212	50	4	0	96	4	0	1920
Beyo E	121	0.619	6494.77	1554	212	50	4	0	96	0	4	1920
Beyo E	124	0.635	5666.87	1554	212	50	4	0	92	2	6	1920
<i>Modified Winkler method</i>												
PP	14	0.025	2706.43	1680	240	0	0	0	0	0	0	1920
B-IO	0	0.000	0.00	1864	56	0	0	0	0	0	0	1920
IO-LS	92	0.157	8224.52	1432	486	2	0	0	0	0	0	1920
LS-CP	227	0.363	14682.24	1302	260	356	2	0	0	0	0	1920
CP-C	239	0.381	15151.27	1294	260	346	20	0	0	0	0	1920
C-D	240	0.383	15191.10	1294	256	350	18	0	2	0	0	1920
D-E	284	0.452	16704.28	1282	240	316	4	0	76	2	0	1920
Beyo E	503	0.803	22368.19	1166	292	122	2	0	58	278	2	1920
Decrease in BS	571	0.903	23434.27	1086	280	166	14	0	78	242	54	1920
	572	0.905	23423.26	1084	282	166	8	0	84	242	54	1920
Beyo E	609	0.946	20018.95	1084	278	150	108	2	102	146	50	1920

(continued)

Table 5 (continued)

Description	Step	Displacement "mm"	B. F "kN"	A to B	B IO	IO LS	LS CP	CP-C	C D	DE	E	Total
<i>Continuum method</i>												
PP	7	0.026	2522.75	1804	116	0	0	0	0	0	0	1920
At B-IO	3	0.012	1390.92	1918	2	0	0	0	0	0	0	1920
At IO-LS	23	0.112	5638.87	1564	352	4	0	0	0	0	0	1920
At LS-CP	44	0.222	8290.60	1460	304	152	4	0	0	0	0	1920
At CP-C	45	0.228	8389.18	1456	308	152	3	0	1	0	0	1920
Decrease in BS	53	0.240	8511.39	1450	312	130	0	0	28	0	0	1920
At C-D	46	0.232	8454.16	1452	312	144	8	0	4	0	0	1920
D-E	111	0.472	2585.62	1450	312	122	0	0	32	3	1	1920

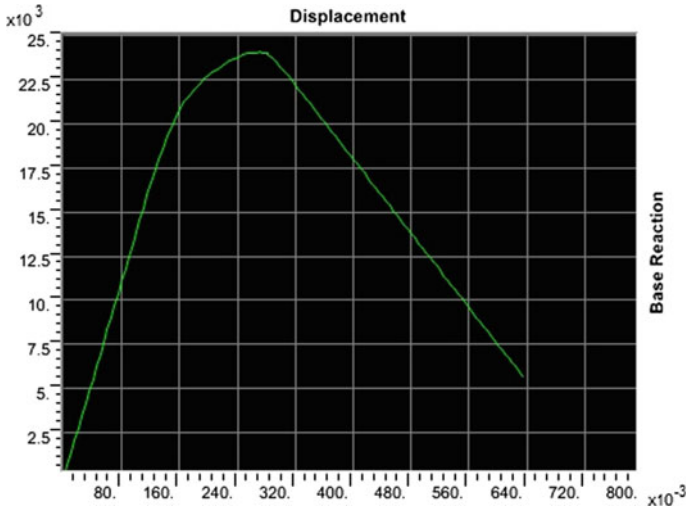


Fig. 2 Rigid base. Displacement versus base shear—capacity pushover curve

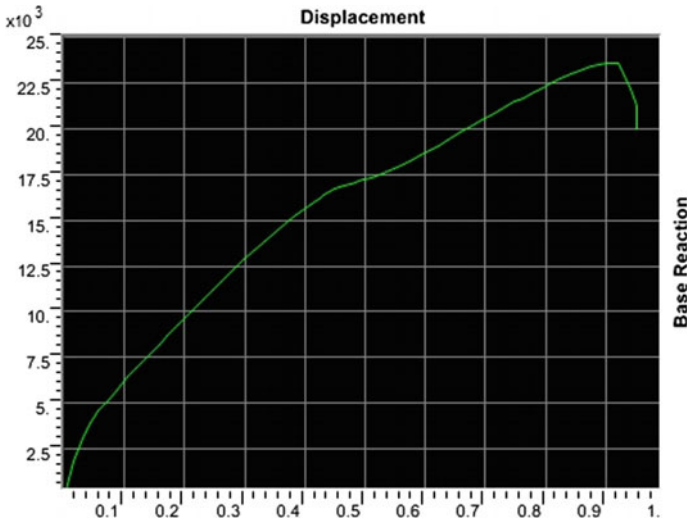


Fig. 3 MWM. Displacement versus base shear—capacity pushover curve

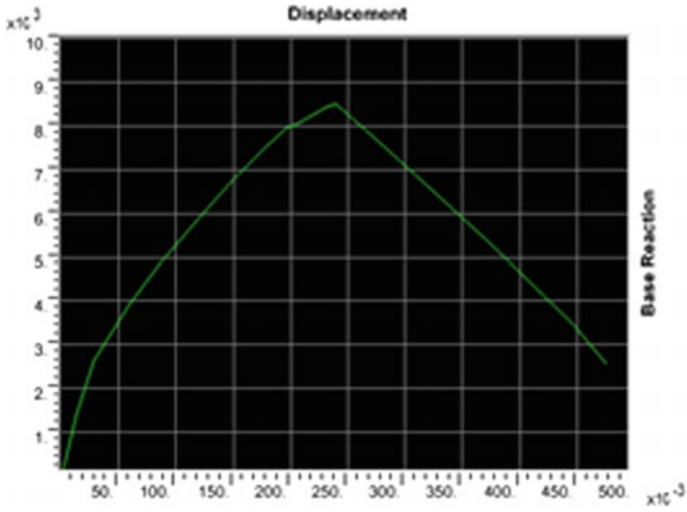


Fig. 4 Continuum. Displacement versus base shear—capacity pushover curve

Fig. 5 Rigid base. Deformed shape of pushover curve

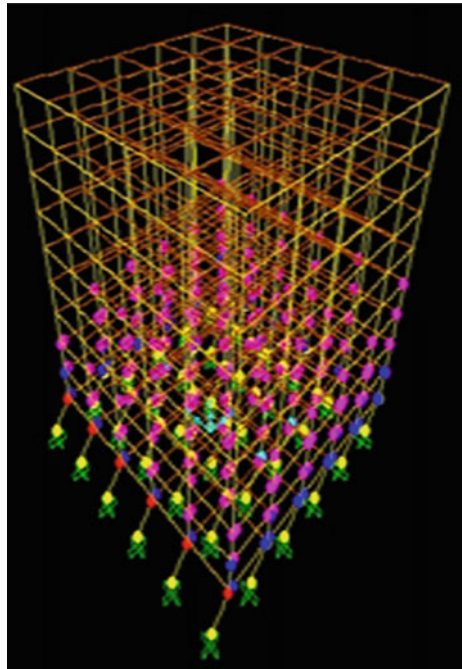


Fig. 6 MWM. Deformed shape of pushover curve

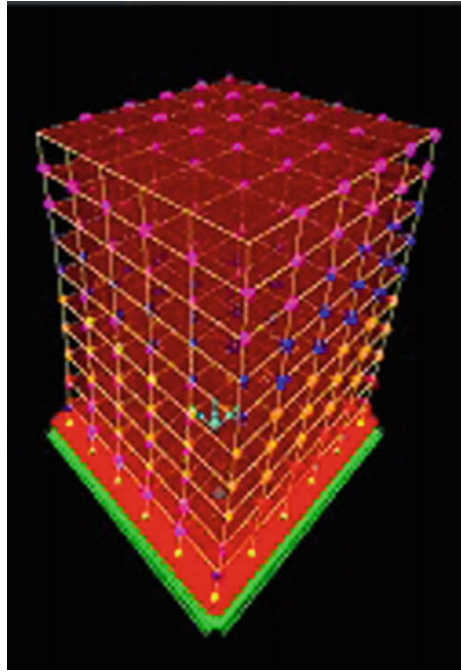
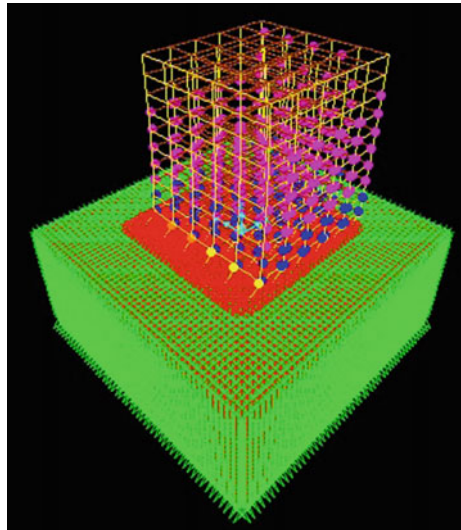


Fig. 7 Continuum. Deformed shape of pushover curve



4 Conclusion

1. Comparing different types of soil Base shear and displacement at performance point is maximum in case of soft soil.
2. Continuum method at Performance point with displacement of 0.026 m and Base shear of 2522.75 kN shows better results compared to rest of the two methods.
3. Considering the hinge formation beyond safety range i.e., C-D stage it shows that the Continuum method with displacement of 0.472 m, Base shear of 2585.62 kN, and 32 hinges formation can be taken as efficient method of analysis compared to MWM (displacement of 0.452 m and Base shear of 16704.28 kN, with 76 hinges) and Fixed support (displacement of 0.619 m Base shear of 6494.90 kN, with 96 hinges).
4. Considering nonlinear analysis parameter mainly Hinge formation, Continuum method shows lesser hinges compared to Fixed and MWM as a result Continuum method can be considered as best method.

References

1. Gamit KD, Amin JA (2017) Application of DDBD and FBD methodology for 8-Story RC frame using IS 1893 spectra. In: ICRASET2017 International conference on research and innovations in science, engineering and technology, 2017, vol 1, pp 69–79
2. Garag V, Karuna S (2016) Effect of soil-structure interaction on regular and irregular, medium RC framed structure. *Int J Sci Eng Technol Res (IJSETR)* 5(5)
3. Mathew AK, Tomer SK, Lovely KM (2015) Effect of soil-structure interaction in seismic analysis of framed structures using Ansys. *Int J Eng Dev Res IJEDR* 3(3):1–9
4. Neethu KN, Saji KP (2015) Pushover analysis of RC building. *Int J Sci Res* 4(8):208–211
5. Parmar MK, Mevada SV, Patel VB (2017) Seismic performance evaluation of RCC buildings with different structural configurations. In: ICRASET2017 International conference on research and innovations in science, engineering and technology, 2017, vol 1, pp 375–380
6. Patil SS, Kalyanshetti MG, Dyawarkonda SS (2016) Parametric study of RC frames with raft foundation considering soil structure interaction using spring. *Int J Sci Dev Res (IJS DR)* 1 (4):63–67
7. Ravikumara HS, Kulkarni SR, Babu Narayan KS (2015) A study on plastic hinge formation in RC frame by nonlinear static analysis. *Int J Res Eng Technol* 04(09):179–182

Application of TS Method in Dynamic UH Model



Zheng Wan, Chenchen Song and Wensheng Gao

Abstract Original Cam-Clay model and modified Cam-Clay model are both two-dimensional elastoplastic models, which are established in p - q space. Von Mises criterion would be adopted if the above models were applied into simulating three-dimensional stress–strain relationship for soils. It is proved that spatial mobilized plane (SMP) or Lade criterion is more consistent with the yield criterion of soil under three-dimensional stress–strain relationship for soils by test results. A dynamic unified hardening (UH) model is combined with SMP criterion directly or generalized by $g(\theta)$ method. The analyzed results have shown that there is volume dilatancy under triaxial extension condition using SMP criterion directly. There are discontinuous yielding surfaces in p - q space using $g(\theta)$ method. Finally, the defects mentioned above could be avoided by transformation stress (TS) method. The comparison between model prediction and test results has demonstrated the superiority of TS method.

Keywords Elastoplastic model · SMP criterion · Lade criterion · Dynamic · Three-dimensional

1 Introduction

Whether original Cam-Clay model or modified Cam-Clay model is established under triaxial compression condition, and thus yield surface and plastic potential surface in the model are expressed in terms of variables p and q .

Z. Wan (✉) · W. Gao

China Academy of Building Research, Research Institute of Base and Foundation, Beijing, China

e-mail: zhengw111@126.com

C. Song

Institute of Structural Engineering and Disaster Reduction, Tongji University, Shanghai, China

© Springer Nature Singapore Pte Ltd. 2020

A. Prashant et al. (eds.), *Advances in Computer Methods and Geomechanics*, Lecture Notes in Civil Engineering 56, https://doi.org/10.1007/978-981-15-0890-5_53

637

If the above models are directly applied to model the stress–strain relationship of soil under the three-dimensional stress condition. The stress–strain relationship under arbitrary stress paths is actually considered as that of triaxial compression condition. Von-Mises criterion in deviatoric plane would be actually adopted as the yield criterion. However, Von-Mises criterion is applicable to metal material yield criterion. By contrast, the SMP criterion or Lade criterion are more applicable to the yield criterion for geomaterials.

In order to apply the above three-dimensional yield criteria to two-dimensional elastoplastic model, many scholars have proposed the method of generalizing the two-dimensional models, e.g. Crouch and Wolf [1].

Zienkiewicz and Pande [2] proposed the method of $g(\theta)$ in 1977, while Nakai and Mihara [3] proposed the t_{ij} method in 1984. The above methods are widely applied in static models, but the prospect of the application to the dynamic model is more brilliant.

Yao and Wang [4] thought that the $g(\theta)$ method is not applicable to the initial anisotropic elastoplastic model, such as the sub-loading surface model of Setouchi et al. [5] or the bounding surface model of Dafalias et al. [6]. If t_{ij} method is adopted, the constitutive equation adopted by the model would be changed.

Yao et al. [7–9] have proposed the transformation stress (TS) method, which is based on the SMP criterion or Lade criterion. The TS method is applied to the anisotropic elastoplastic model mentioned above. It can avoid the problems caused by the $g(\theta)$ method or the t_{ij} method. Hereinto, TS method is applied to the dynamic UH model. And it is superior to adopt the TS method by comparison with the other methods from test results.

The proposed dynamic UH model with over-consolidation stress ratio parameters can reflect the differences of shear dilatancy and the stress ratio due to the different stress paths and stress history. TS generalization method is more simple and reasonable to convert two-dimensional constitutive model dominated by p/q variable to three-dimensional constitutive models.

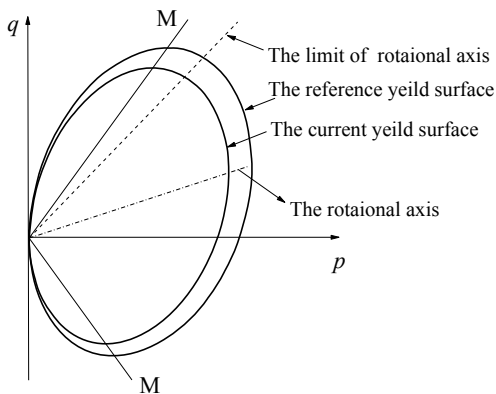
In addition, the disturbed state concept (DSC) constitute model proposed by Desai [10], which uses state variables to mark the state of the soil at each moment, also adopts the state variables to reflect the differences of the variable strength of the soil. Therefore, it can be conveniently applied to the description of the stress–strain relationship for the undisturbed soil. But the state variable is hard to determine.

2 Dynamic UH Model

2.1 Description of the Model

As shown in Fig. 1, the relationship between the reference yield surface and the current yield surface can be established by the over-consolidation parameter R .

Fig. 1 Reference yield surface and current yield surface



$$R = p/\bar{p} = q/\bar{q} \tag{1}$$

where p represents the effective mean stress on the current yield surface, and \bar{p} represents the effective mean stress on the reference yield surface. The q and \bar{q} are the generalized deviatoric stress corresponding to p and \bar{p} . By using the associative flow rule, the plastic potential surface and the current yield surface can be expressed as

$$g = f = c_p \left[\ln \frac{p}{p_0} + \ln \left(1 + \frac{\eta^{*2}}{M^2 - \zeta^2} \right) \right] - H = 0 \tag{2}$$

where M is the critical state stress ratio. $c_p = (\lambda - \kappa)/(1 + e_0)$. The λ is the slope of the normal compression line in the e - $\ln p$ coordinate system. The κ is the slope of the corresponding swelling line, and e_0 is the initial void ratio. The plastic volumetric strain ε_v^p is adopted as the hardening parameter H for the reference yield surface. The slope of the rotational axis is represented by ζ , which can be expressed by its axial component β_{ij} as Eq. (3).

$$\zeta = \sqrt{\frac{3}{2} \beta_{ij} \beta_{ij}} \tag{3}$$

Its geometric meaning is the slope of the rotational axis of yielding surface in the p - q coordinate system. The η^* is the relative stress ratio in the yield surface, which can be expressed as

$$\eta^* = \sqrt{\frac{3}{2} \hat{\eta}_{ij} \hat{\eta}_{ij}} \tag{4}$$

where the component $\hat{\eta}_{ij}$ of the relative stress ratio can be expressed as

$$\hat{\eta}_{ij} = \eta_{ij} - \beta_{ij} \quad (5)$$

where the η_{ij} is the component of the stress ratio tensor, which can be expressed as

$$\eta_{ij} = \frac{\sigma_{ij} - p\delta_{ij}}{p} \quad (6)$$

The hardening parameter H of the current yield surface can be expressed as

$$H = \int \left(\frac{M_f^4 - \eta^4}{M^4 - \eta^4} d\varepsilon_v^p + \frac{\eta}{M} \frac{\partial f}{\partial \beta_{ij}} d\beta_{ij} \right) \quad (7)$$

where the potential strength M_f can be expressed as

$$M_f = 6 \left(\sqrt{k(1+k)} - k \right) \quad (8)$$

where the k can be expressed as

$$k = \frac{M^2}{12(3-M)R^\alpha} \quad (9)$$

where the parameter α is the newly introduced parameter to adjust the evolutionary ratio of the potential strength. The over-consolidation parameter R is expressed as

$$R = \frac{p}{\bar{p}} = \frac{p}{\bar{p}_0} \left(1 + \frac{\eta^{*2}}{M^2 - \zeta^2} \right) \exp \left(-\frac{\varepsilon_v^p}{c_p} \right) \quad (10)$$

where \bar{p}_0 is the pre-consolidation pressure, and the ε_v^p is plastic volumetric strain.

The kinematic process of the rotational axis is determined by the rotational hardening law. The increment of the rotational axis component can be expressed as follow:

$$d\beta_{ij} = \sqrt{3/2} \frac{b_r M}{c_p} (b_l M - \zeta) d\varepsilon_d^p \frac{\hat{\eta}_{ij}}{\eta^*} \quad (11)$$

where b_r is the evolutionary rate of the rotational axis. The b_l is the rotational axis boundary parameter, and the $b_l M$ is the boundary of the rotational axis. The $d\varepsilon_d^p$ is the increment of the plastic deviatoric strain.

2.2 Stress Generalization Method

To generalize the dynamic UH model, a simple direct combination method is adopted. Simply, a static model is considered by using generalization method. When the rotational hardening rule is neglected, the dynamic UH model degenerates to UH model. SMP criterion is directly combined with the UH model. The equation of the SMP criterion is united with that of the yield surface for UH model. The united result of the yield surface is shown in Fig. 2.

Under the triaxial compression condition, the generalized yield surface is the same as the original yield surface. Under the triaxial extension condition, the lowest point of yield surface is F point, while the critical state point is E. Obviously, the lowest point does not coincide with the critical state point. This would result in an unreasonable circumstance in which the plastic strain increment in EF segment is negative, which is conflicted with the test result. Therefore, it is not feasible to directly combine the SMP criterion with the model.

The $g(\theta)$ method based on SMP criterion is combined with the UH model, then the generalized yield surface obtained by $g(\theta)$ method is shown in Fig. 3.

It can be seen from Fig. 3 that, with the increase of mean stress, generalized deviatoric stress increases. However, the yield surface shapes on the deviatoric plane are always geometric similar, so it cannot reflect the shape change of yield surface caused by the increase of mean stress. And it cannot reflect the hydrostatic stress effect. The $g(\theta)$ method is used to reflect the initial anisotropic model, taking the dynamic UH model as an example. The generalized yield surface shape on p - q plane is shown in Fig. 4. It can be seen from Fig. 4 that the discontinuity phenomenon is generated in the transition phase of the triaxial compression path to the triaxial extension path. Therefore, the $g(\theta)$ method is not feasible to generalize the anisotropic model.

Fig. 2 Yield surface of generalized UH model in p - q plane using SMP criterion

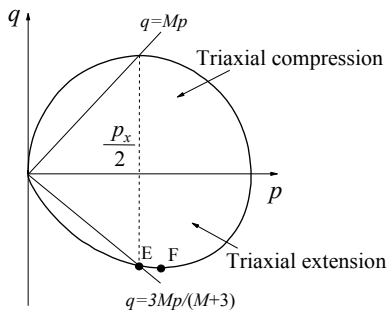


Fig. 3 Yield surfaces of generalized UH model on π -plane using $g(\theta)$ method

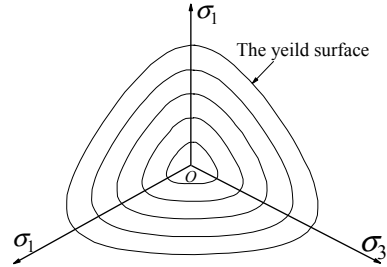
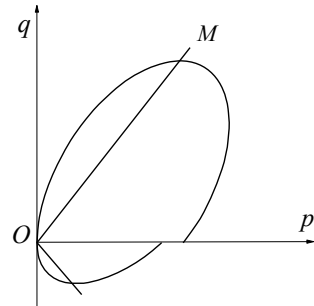


Fig. 4 Yield surface of generalized dynamic UH model on p - q plane using $g(\theta)$ method directly



3 Transformation Stress (TS) Method

The dynamic UH model is generalized by TS method. As shown in Fig. 5, the TS method proposed by Yao and Wang [4] is used to generalize the constitutive model. The solid line in Fig. 5 is the SMP criterion curve in the normal stress space. Because any point of the Mises circle is equivalent with one point on the triaxial compression path. Therefore, the point A can be transformed to the point B of the triaxial compression curve. Then, the SMP criterion in normal stress space is transformed into the Mises criterion in TS space. The equation of TS can be written as

$$\begin{cases} \tilde{\sigma}_{ij} = p\delta_{ij} + \frac{q^*}{q}(\sigma_{ij} - p\delta_{ij}) & q \neq 0 \\ \tilde{\sigma}_{ij} = \sigma_{ij} & q = 0 \end{cases} \quad (12)$$

$$q^* = \frac{2I_1}{3\sqrt{(I_1I_2 - I_3)/(I_1I_2 - 9I_3)} - 1} \quad (13)$$

where I_1 , I_2 , and I_3 are the first, second, and third stress invariants in normal stress space.

The UH model mentioned above is generalized by the TS method, and the shape of the yield surface in the deviatoric plane is shown in Fig. 6. It can be seen from

Fig. 5 SMP criterion in ordinary stress space and Mises criterion in TS space

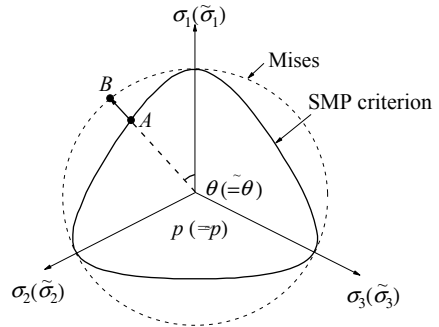


Fig. 6 that, with the increase of the mean stress, the yield surface shapes gradually tend to the circle. The hydrostatic stress effect on the yield surface can be reflected.

The dynamic UH model is generalized by TS method. Then, the shape of yield surface in p - q space is shown in Fig. 7.

In Fig. 7, the dashed line represents the shape of the original yield surface, and the solid line represents the shape of the generalized yield surface using TS method. Therefore, TS method is more feasible to generalize the two-dimensional model.

Fig. 6 Yield surfaces of generalized UH model on π -plane using TS method

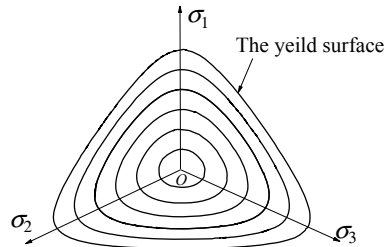
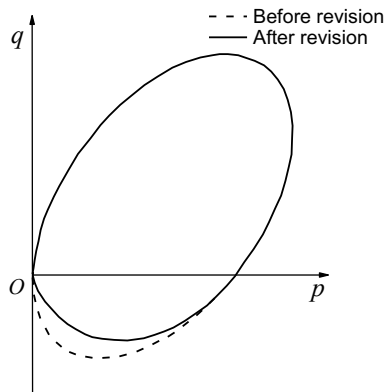


Fig. 7 Comparison between original yield surface and revised yield surface using TS method



4 The Equation of Generalized Dynamic UH Model

The equation of generalization dynamic UH model is proposed. The elastic shear modulus G can be expressed as:

$$G = \frac{E}{2(1+\nu)} = \frac{3(1-2\nu)(1+e_0)p}{2(1+\nu)k} \quad (14)$$

The constant Lamé L is

$$L = \frac{E}{3(1-2\nu)} - \frac{2}{3}G = \frac{(1+e_0)}{k}p - \frac{2}{3}G \quad (15)$$

The generalized yield surface of Eq. (2) can be written as

$$\tilde{f} = c_p \left[\ln \frac{\tilde{p}}{p_0} + \ln \left(1 + \frac{\tilde{\eta}^{*2}}{M^2 - \tilde{\zeta}^2} \right) \right] - \int \left(\frac{\tilde{M}_f^4 - \tilde{\eta}^4}{M^4 - \tilde{\eta}^4} d\varepsilon_v^p + \frac{\tilde{\eta}}{M} \frac{\partial \tilde{f}}{\partial \tilde{\beta}_{ij}} d\tilde{\beta}_{ij} \right) = 0 \quad (16)$$

The stress σ_{ij} in all equations is replaced by $\tilde{\sigma}_{ij}$ in the transformation stress space. Equation (16) is differentiated as follow:

$$d\tilde{f} = \frac{\partial \tilde{f}}{\partial \tilde{\sigma}_{kl}} \frac{\partial \tilde{\sigma}_{kl}}{\partial \sigma_{ij}} d\sigma_{ij} + \frac{\partial \tilde{f}}{\partial \tilde{\beta}_{ij}} d\tilde{\beta}_{ij} - \left[\frac{\tilde{M}_f^4 - \tilde{\eta}^4}{M^4 - \tilde{\eta}^4} d\varepsilon_v^p + \frac{\tilde{\eta}}{M} \frac{\partial \tilde{f}}{\partial \tilde{\beta}_{ij}} d\tilde{\beta}_{ij} \right] = 0 \quad (17)$$

where the stress increment can be expressed as

$$d\sigma_{ij} = D_{ijkl}^e d\varepsilon_{kl}^e = D_{ijkl}^e (d\varepsilon_{kl} - d\varepsilon_{kl}^p) \quad (18)$$

The increment of the plastic strain tensor can be expressed as

$$d\varepsilon_{kl}^p = \Lambda \frac{\partial \tilde{f}}{\partial \tilde{\sigma}_{kl}} \quad (19)$$

where Λ is the plastic factor.

The partial differentiation of the rotational axis is

$$\frac{\partial \tilde{f}}{\partial \tilde{\beta}_{ij}} d\tilde{\beta}_{ij} = \frac{c_p \left[\sqrt{6} \Lambda M b_r \left(b_l M - \tilde{\zeta} \right) \tilde{\eta}^{*2} \left(-2M^2 + 3\tilde{\eta}_{ij} \tilde{\beta}_{ij} \right) \right]}{\left(M^2 - \tilde{\zeta}^2 + \tilde{\eta}^{*2} \right)^2 \left(M^2 - \tilde{\zeta}^2 \right) \tilde{p}} \quad (20)$$

The increment of plastic volumetric strain can be written as

$$d\varepsilon_v^p = \Lambda \cdot \partial \tilde{f} / \partial \tilde{\sigma}_{ii} = \frac{\Lambda c_p (M^2 - \tilde{\eta}^2)}{(M^2 - \tilde{\zeta}^2 + \tilde{\eta}^{*2}) \tilde{p}} \quad (21)$$

By substituting Eqs. (18)–(21) into Eq. (17), the plastic factor can be obtained

$$\Lambda = \frac{\partial \tilde{f}}{\partial \sigma_{ij}} D_{ijkl}^e \cdot d\varepsilon_{kl} / X \quad (22)$$

where

$$X = \frac{\partial \tilde{f}}{\partial \sigma_{ij}} D_{ijkl}^e \cdot \frac{\partial \tilde{f}}{\partial \tilde{\sigma}_{kl}} + \frac{c_p T_{ms}}{(M^2 - \tilde{\zeta}^2 + \tilde{\eta}^{*2}) \tilde{p}} \quad (23)$$

where the T_{ms} can be expressed as

$$T_{ms} = \frac{\tilde{M}_f^4 - \tilde{\eta}^4}{M^4 - \tilde{\eta}^4} (M^2 - \tilde{\eta}^2) + \frac{(1 - \frac{\tilde{\eta}}{M}) M \sqrt{6} b_r (b_l M - \tilde{\zeta}) \tilde{\eta}^{*2} (2M^2 - 3\tilde{\eta}_{ij} \cdot \tilde{\beta}_{ij})}{(M^2 - \tilde{\zeta}^2 + \tilde{\eta}^{*2})(M^2 - \tilde{\zeta}^2)} \quad (24)$$

The increment of the stress tensor can be written as

$$d\sigma_{ij} = D_{ijkl} d\varepsilon_{kl} \quad (25)$$

The elastoplastic stiffness tensor is expressed as

$$D_{ijkl} = D_{ijkl}^e - D_{ijmn}^e \frac{\partial \tilde{f}}{\partial \tilde{\sigma}_{mn}} \frac{\partial \tilde{f}}{\partial \sigma_{st}} D_{stkl}^e / X \quad (26)$$

The elastic shear modulus and the constant Lamé are substituted into Eq. (26).

$$D_{ijkl} = L \delta_{ij} \delta_{kl} + G (\delta_{ik} \delta_{jl} + \delta_{il} \delta_{jk}) - \left(L \frac{\partial \tilde{f}}{\partial \tilde{\sigma}_{mm}} \delta_{ij} + 2G \frac{\partial \tilde{f}}{\partial \tilde{\sigma}_{ij}} \right) \left(L \frac{\partial \tilde{f}}{\partial \sigma_{mn}} \delta_{kl} + 2G \frac{\partial \tilde{f}}{\partial \sigma_{kl}} \right) / X \quad (27)$$

where the X can be expressed as

$$X = L \frac{\partial \tilde{f}}{\partial \sigma_{ii}} \frac{\partial \tilde{f}}{\partial \tilde{\sigma}_{kk}} + 2G \frac{\partial \tilde{f}}{\partial \sigma_{ij}} \frac{\partial \tilde{f}}{\partial \tilde{\sigma}_{ij}} + \frac{c_p T_{ms}}{(M^2 - \tilde{\zeta}^2 + \tilde{\eta}^{*2}) \tilde{p}} \quad (28)$$

5 Test Verification

The test results of the two-way undrained cyclic loading of Toyoura sand and Niigata sand from Tatsuoka et al. [11] and Ishikara et al. [12] were used to verify the generalized dynamic UH model by TS method. The material parameters of the sand are shown in Table 1.

As shown in Fig. 8, the circles represent the test results, and the solid line represents the prediction result of the model. It can be seen from the figure that there is a significant difference between the compression path and the extension path. The critical state strength of compression path is higher than that of the extension path, and the prediction trend is consistent with the test result.

Observing the relationship between axial strain and deviatoric stress, axial strain on triaxial extension path is higher than that on triaxial compression path, which can be predicted by the dynamic UH model adopting TS method.

The cyclic loading test results are shown by Ishihara et al. [12] for Niigata sand in Fig. 9. The material parameters are listed in Table 1. The initial void ratio is 0.737 and the value of initial consolidation pressure is 212.6 kPa. The value of interception of NCL is 0.87 and that of initial consolidation stress ratio is 1.0.

Table 1 Material parameters of

Type	M	λ	κ	ν	b_r	b_l	α
Toyoura sand①	1.287	0.01	0.0035	0.3	0.5	0.95	0.05
Niigata sand	1.48	0.0070	0.0040	0.3	1.5	0.98	0.05
Toyoura sand②	1.24	0.0030	0.0010	0.3	1.5	0.6	0.5

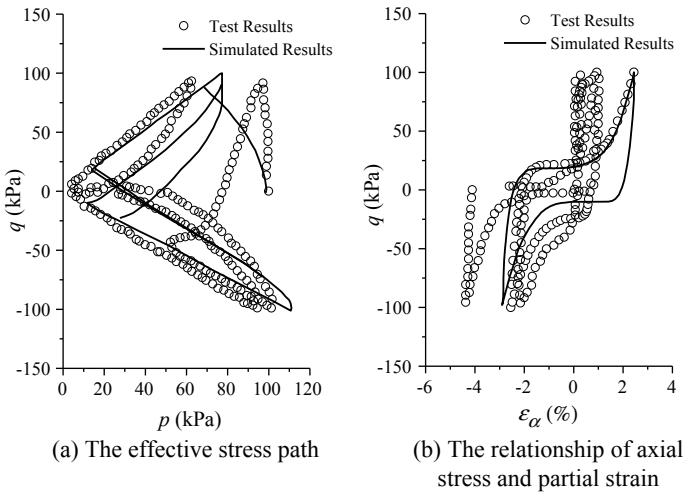


Fig. 8 Comparison between model prediction and test results of Toyoura sand①

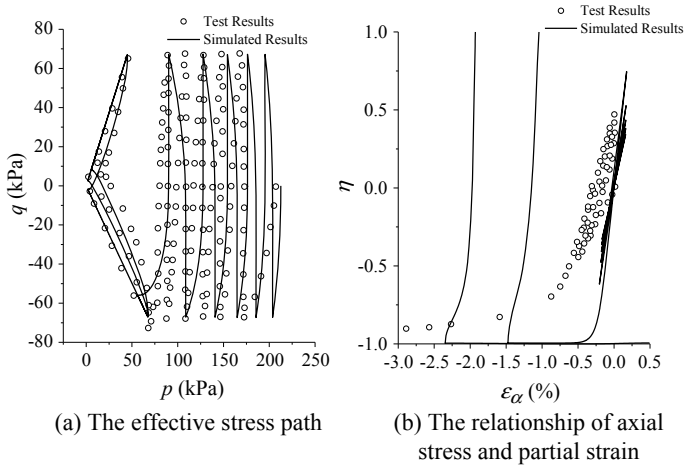


Fig. 9 Test and simulated results of cyclic mobility under undrained condition on Niigata sand

The comparison between test data and prediction of stress path under undrained conditions is shown in Fig. 9a. There is a cyclic mobility phenomenon after five cycles and the loop is formed when the location of stress state is close enough to the origin point. There is a corresponding relationship between deviatoric strain and stress ratio in Fig. 9b. The scope of deviatoric strain is corresponded to the value of mean stress from 60 to 212.6 kPa in Fig. 9b. The mechanical behavior of sand corresponding to the cyclic mobility is unstable while the amplitude of deviatoric strain could be large enough. The trend of deviatoric strain is consistent with the predicted ones.

The test results are shown by circles with a constant value of mean stress path for Toyoura sand② by Pradhan et al. [13]. The materials are quartz of sand which is from Keratin. The initial void ratio is 0.845 while the value of initial consolidation pressure is 98.1 kPa. The value of interception of NCL is 0.969 and that of initial consolidation stress ratio is 1.0. The material parameters are listed in Table 1.

The comparison between test data and prediction is shown in Fig. 10. There is a relation between deviatoric strain and stress ratio in Fig. 10a. The prediction agrees well with that of test results under triaxial compression condition while the value of predicted result is larger than that of test results in triaxial extension condition. The relationship of deviatoric strain to volumetric strain is shown in Fig. 10b. The prediction is in a good agreement with that of test result. The cumulative characteristic of volumetric strain can be fully described. In Fig. 10a, the stress ratio under triaxial compression path is larger than that of triaxial extension path. The corresponding axial strain along triaxial compression path is smaller than that of triaxial extension. This phenomenon shows that the strength and modulus of triaxial compression are larger than those of triaxial extension. As Fig. 10b shows, the volumetric strain along the triaxial extension path is larger than that of triaxial

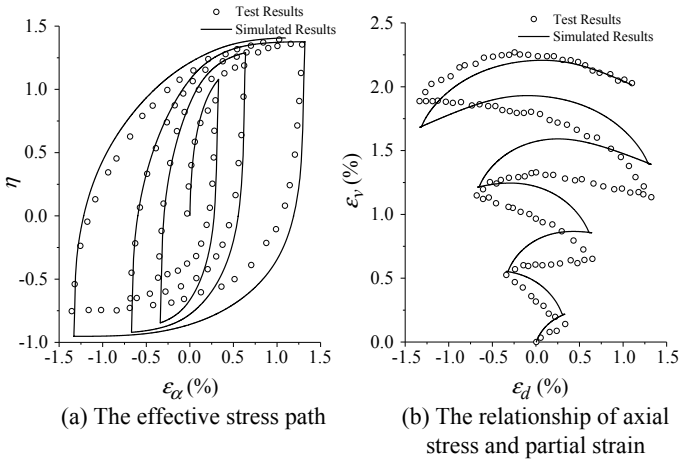


Fig. 10 Test and simulated results with a constant mean stress $p = 98.1$ kPa on loose Toyoura sand②

compression. The modulus of soil under triaxial compression path is larger than that of triaxial extension. The generalized dynamic UH model by TS method can be used to reflect the above difference.

UH dynamic model can be used to describe the basic characteristics of the over consolidated clays such as strain hardening and softening and shear shrinkage and the dilatancy. Although the soil is essentially discrete accumulation body, it also can be described by theory of continuum mechanics. Because the soil is a quasi-solid material formed by its own consolidation, and the loading method adopted is compression shear method, so there is no stretching, also is not the problem of discontinuous discrete effect.

For the differences strength and volumetric dilatancy under variable stress paths, the proposed model is also reasonable. Because the unified hardening parameter is used, and different over-consolidation stress ratios state parameters are adopted to reflect the difference of the initial state, thus it can be considered that the differences of volumetric dilatancy and stress ratio under different stress paths.

6 Conclusions

By studying the generalization methods, the following conclusions are obtained:

- (1) It is not feasible to combine the SMP criterion with the model directly, and it is not feasible to use the $g(\theta)$ method to generalize the anisotropy model. It is feasible to apply the TS method to the static or dynamic model.

- (2) The generalized dynamic UH model using TS method can more reasonably reflect dependency on the stress path of the stress–strain relationship. It is more consistent with test results from the strength property and stress–strain relationship.
- (3) Adopting the TS method, the dynamic elastoplastic model can be applied more simply and rationally without any additional parameters or changes of the original model.

Acknowledgements This work is supported by the National Natural Science Foundation of China (NSFC) (project No. 11402260).

References

1. Crouch RS, Wolf JP (1995) On a three-dimensional anisotropic plasticity model for soil. *Geotechnique* 45(2):301–305
2. Zienkiewicz OC, Pande GN (1977) Some useful forms of isotropic yield surface for soil and rock mechanics. *Finite Element Geomech*, London
3. Nakai T, Mihara Y (1984) A new mechanical quantity for soils and its application to elastoplastic constitutive models. *Soils Found* 24(2):82–94
4. Yao YP, Wang ND (2013) Transformed stress method for generalizing soil constitutive models. *J Eng Mech* 140(3):614–629
5. Setouchi H, Hashiguchi K et al (2006) Extended tangential-subloading surface model for general loading behaviors of soils: application to nonproportional loadings. *Soils Found* 46(4):449–463
6. Dafalias YF, Manzari MT et al (2002) A simple anisotropic clay plasticity model. *Mech Res Commun* 29(4):241–245
7. Yao YP, Zhou AN et al (2007) Extended transformed stress space for geomaterials and its application. *J Eng Mech ASCE* 133(10):1115–1123
8. Yao YP, Matsuoka H et al (1999) A unified elastoplastic model for clay and sand with the SMP criterion. In: *Proceedings of 8th Australia-New Zealand conference on geomechanics*. Australia
9. Yao YP, Hou W et al (2009) UH model: three-dimensional unified hardening model for over consolidated clays. *Geotechnique* 59(5):451–469
10. Desai CS (2000) *Mechanics of materials and interfaces: the disturbed state concept*. CRC Press
11. Tatsuoka F, Toki S et al (1986) Some factors affecting cyclic undrained triaxial strength of sand. *Soils Found* 26(3):99–116
12. Ishihara K, Tatsuoka F et al (1975) Undrained deformation and liquefaction of sand under cyclic stresses. *Soils Found* 15(1):29–44
13. Pradhan T, Tatsuoka F et al (1989) Experimental stress–dilatancy relations of sand subjected to cyclic loading. *Soils Found* 29(1):45–64

Effect of Lime and Cement on Strength and Volume Change Behavior of Black Cotton Soil



Majid Hussain

Abstract Lime stabilization continues to be the widely used technique to control the swell-shrink properties of expansive soils. In this paper, results of an experimental study conducted to understand the effect of lime and/or cement on engineering properties of expansive (Black Cotton Soils, (BCS)) collected from Bharuch, Gujarat India are presented. Effect of lime and cement, curing period and specimen preparation on shear strength and compressibility of untreated and treated BCS is studied. Results from the study showed a decrease in LL and the increase of PL with a considerable reduction in PI. Reduction in PI increased with increasing lime content. Physical mixing of soil, lime and/or cement was achieved by two methods: Method 1 (*mixture of soil and stabilizer(s) was cured and then specimens prepared and tested immediately*) and Method 2 (*specimens of treated soil were prepared, cured and then tested*). Shear strength increased with curing period in the case of cement. Results show that Method 2 of physical mixing of soil and lime is effective in increasing shear strength and reducing the coefficient of compressibility or compression index. Treatment led to a reduction in swell pressures with magnitude profoundly affected by specimen preparation method and the presence of cement along with Cao. Method 2 of physical mixing of soil and stabilizer(s) was found to be efficient in improving the strength and volumetric behavior of BCS.

Keywords Expansive soils · Swell pressure · Unconfined compressive strength · Compressibility

1 Introduction

Expansive soil refers to the soil that can shrink and swell with changing moisture content, due to the presence of montmorillonite mineral. Volumetric changes resulting from imbibition of water exert forces on the structures overlying the soil.

M. Hussain (✉)

Indian Institute of Technology Gandhinagar, Gandhinagar, India
e-mail: majid.hussain@iitgn.ac.in

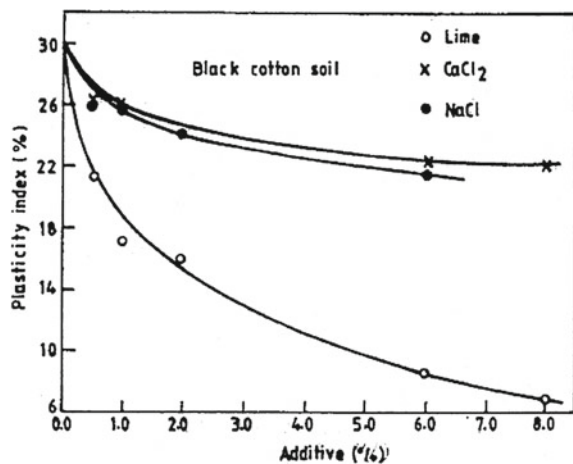
Black cotton soils are predominantly confined to semiarid regions of tropical and temperate climatic zones where annual evapotranspiration exceeds precipitation [5].

India, Australia, Sudan, Chad, and Ethiopia constitute more than 75% (193 mha) of the global BCS cover [4]. In India, one-third of the land area is constituted by these soils. They are predominant in the Deccan plateau region, i.e., in the states of Gujarat, Maharashtra, Karnataka, Andhra Pradesh, Tamil Nadu and Madhya Pradesh [7]. Expansive soils cause more damage to structures, particularly light-weight buildings and pavements, than any natural hazard, including earthquakes and floods [6]. These distress problems have resulted in India too particularly in roads and low rise structures.

Many techniques have been developed to control the damage imposed by the expansive soils [1, 2]. Lime stabilization, a subset of chemical stabilization, is the most widely used and studied technique to control the shrink–swell potential of expansive soils [3]. Fly ash and cement have also been used for stabilization of expansive soils. Pozzolanic property of fly ash makes it a potential building material particularly in combination with lime. The presence of SiO_2 and Al_2O_3 enhances the pozzolanic property of fly ash, which has encouraged numerous stabilization studies in India and abroad. The use of fly ash as an additive may help to increase its utilization eventually leading to lower carbon footprints.

Venkatappa Rao and Ramana [10] presented mechanisms of soil–lime interaction, changes in soil properties, various design methods and guidelines for construction involving lime stabilization of clays including BCS. Exhaustive experimental studies have been reported on the effect of lime on engineering properties of black cotton soils (BCS) [1, 8, 9]. The immediate impact of lime (also Sodium Chloride and Calcium Chloride) on plasticity index of BCS is shown in Fig. 1 [11]. It is evident that CaO exerts maximum influence on the reduction of plasticity index. The chlorides too reduce the plasticity, but compared to CaO , the influence is marginal.

Fig. 1 Effect of Lime ($NaCl$ and $CaCl_2$) on Atterberg limits of black cotton soil (after [11])



Earlier studies mostly focussed on the immediate effect of lime on the engineering behavior of expansive soils. Stabilization of BCS pretreated with lime by using different stabilizers, lime, fly ash, cement, etc. remains unexplored.

In the current experimental study effect of lime and fly ash on the liquid limit (LL), plastic limit (PL), and plastic index (PI) of BCS at different curing periods is explored. Effect of lime and/or cement, curing time and method adopted for physical mixing of soil and stabilizers on strength and compressibility properties of untreated and treated BCS is studied.

2 Material Properties, Testing Programme, and Specimen Preparation

2.1 Material Properties

The black cotton soil studied in the present investigation was collected from Bharuch, Gujarat India. In situ properties were determined by performing tests, as per IS Standards. The fraction passing 2-mm sieve was used for conducting Standard Proctor Compaction, Oedometer, Swell Potential, and UCS tests. Index properties were determined on the soil fraction passing through a 425 μm sieve. Chemically pure CaO , PPC-33 grade cement and fly ash from the Gujarat State Electricity Corporation Limited (GSECL) power plant located in Gandhinagar, Gujarat were used for testing purposes. Physical properties of BCS and fly ash are listed in Tables 1 and 2, respectively.

Table 1 Physical properties of black cotton soil

Property	Value
Bulk density, γ_b g/cc	1.84
In situ water content %	30
% Sand	7
% Silt	33
% Clay	60
G_s	2.66
LL %	69
PL %	31
SL %	10
% DFSI	93
% OMC	24.0
MDD, g/cc	1.46

Table 2 Physical properties of fly ash

Property	Value
% Sand size	20
% Silt size	80
G _s	2.15
LL %	Non-plastic
PL %	Non-plastic
% OMC	29.53
MDD, g/cc	1.18

Table 3 Designed test series for plasticity behavior

Series	% Additive	
	CaO ^a	Fly ash
1	1, 2, 4, and 6	–
2	1, 2, 4, and 6	12.5
3	1, 2, 4, and 6	25

^aAnalytical reagent, assay 95%

2.2 Testing Programme

Atterberg Limits were determined for the different combinations of BCS and *CaO* (Series 1 with chemically pure lime). Two more series, Series 2 and Series 3 were designed to study the effect of fly ash in combination with *CaO* on Atterberg Limits. For Series 2, 12.5% fly ash in combination with 1, 2, 4, and 6% *CaO* was mixed with BCS. In Series 3 fly ash content was 25%. Table 3 presents the mix proportions for the three-test series.

From the considered combinations, BCS + 2% *CaO* from Series 1 was chosen for further studies. To study the effect of *CaO* and cement on strength and compressibility characteristics of untreated and treated BCS five test series as listed in Table 4 were designed. The type and amount of stabilizer(s) added and the method of specimen preparation adopted for each series are also included in Table 4.

Table 4 Test series designed to study the effect of treatment on UCS and compressibility

Series	Combination	Curing period (days)	Specimen preparation method
A	Untreated BCS + 2% <i>CaO</i>	7, 14, and 28	Method 1
B	Treated BCS + 2% <i>CaO</i>	14 and 28	Method 1
C	Treated BCS + 2% Cement	14 and 28	Method 1
D	BCS + 2% <i>CaO</i>	7, 14, and 28	Method 2
E	BCS + 2% Cement	7, 14, and 28	Method 2

Treated BCS = BCS + 2% *CaO* cured for 14 days

2.3 Specimen Preparation Methods

Specimens measuring 38 mm in diameter and 76 mm in height were prepared by moist tamping method to determine the strength characteristics whereas specimens measuring 60 mm in diameter and 20 mm in height were prepared for determining compressibility characteristics of untreated and treated BCS. The specimens were prepared by the following two procedures:

Method 1: Water was added by spraying to the dry mix of BCS and the stabilizer(s) and then thoroughly mixed. The mixtures were then cured. At the end of 7 days, 14 days, and 28 days of curing, specimens were prepared by moist tamping technique and tested immediately. Water content was monitored throughout the curing process and maintained at OMC + 2%. This method was adopted to prepare specimens for Series A, Series B, and Series C.

Method 2: Water was added by spraying to the dry mix of BCS and the stabilizer(s) and then thoroughly mixed. The mixtures were prepared at a moisture content of OMC + 2%. Additional moisture of 2% was provided to enable hydration reactions of the stabilizer(s). After mixing, specimens for UCS and Oedometer tests were prepared and left for curing. At the end of 7 days, 14 days, and 28 days of curing, the specimens were tested. This method was adopted to prepare specimens for Series D and Series E.

Unconfined Compression Strength (UCS) and Oedometer tests, as per IS standards, were performed on specimens prepared at a density of 1.46 g/cc (MDD) and moisture content of 24% (OMC) by moist tamping technique.

3 Results and Discussion

3.1 Influence of Lime and/or Fly Ash on Index Properties of Untreated BCS

Figure 2 shows the effect of various percentages of CaO on the Liquid Limit (LL) and Plastic Limit (PL) of untreated BCS. It is evident that as the CaO content increased LL decreased and PL increased resulting in a considerable decrease in the Plasticity Index (PI). Decreased PI is indicative of improved workability, reduced volume changes, and increased strength characteristics. Previous researchers reported similar results. Venkatappa Rao and Rekhi [11] reported a reduction in PI of BCS from 30% to 7% and 8% on treatment with 8% and 6% of lime, respectively. In the current study, a substantial reduction in PI was observed for an addition of only 1 and 2% CaO . PI decreased continuously with increased CaO content and attained a minimum of 5% at the lime content of 6% at 0 days of curing. Figure 2 shows the effect of the combination of fly ash and lime on the Atterberg Limits of untreated BCS. The reduction in PI in the presence of 12.5% (Series 2) and 25% (Series 3) fly ash was slightly less as compared to Series 1. With increased curing period for Series 1, PI was observed to increase slightly but was

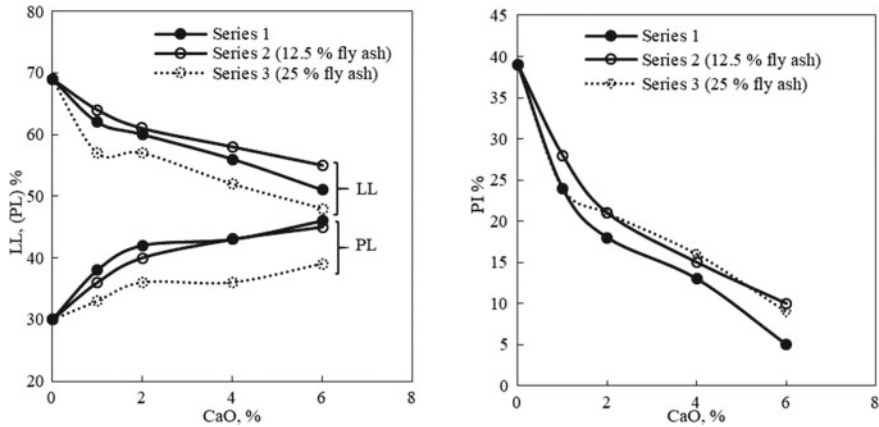
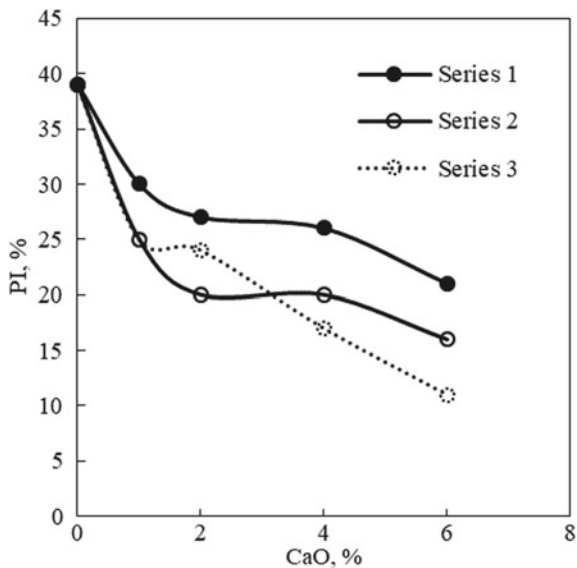


Fig. 2 Effect of fly ash and *CaO* on Atterberg limits of BCS

always less than that of untreated BCS. However, the reduction in PI with curing period was arrested in the presence of fly ash (Fig. 3). This may be attributed to the enhanced pozzolanic action in the presence of fly ash. The reduction in PI was essentially similar for both Series 2 and Series 3.

Availability of fly ash in bulk and its pozzolanic properties makes it a choice for soil stabilization in combination with *CaO*. In this way, the use of fly ash in soil stabilization can address the waste management problem associated with it and also enhance the engineering behavior of problematic expansive soils. In the current

Fig. 3 Plasticity index (PI) at 7 days of curing for Series 1, Series 2, and Series 3



study, the increase in PL at 7 days of curing was more than that at 0 days curing period in Series 1 as compared to that of Series 2 and 3. This might be attributed to the time-dependent pozzolanic property of fly ash.

The addition of lime affects the plasticity characteristics of the soil, and can be used in two stages: (a) modification of the soil and (b) further addition to stabilize the already modified soil. The lime modification is rapid and results in a reduced thickness of diffuse double layer around the clay particles making the soil more friable and less plastic. Reduced double layer thickness makes clay flocculated and coarser.

While the first case, modification of soils, has been researched to a great extent the second case is yet to be explored. In the following sections, the effect of lime and cement, curing period and method of specimen preparation on the strength and compressibility characteristics of untreated and treated BCS is presented. From plasticity test results presented above the addition of 2% CaO was selected for a further study of engineering behavior.

3.2 Effect of CaO and Cement on Unconfined Compressive Strength of Untreated and Treated BCS

Figure 4a shows the results of Unconfined Compressive Strength (UCS) tests performed on the specimens of Series A and Series D. Untreated BCS exhibited unconfined compressive strength (q_u) of 360 kPa at a maximum dry density (MDD) and optimum moisture content (OMC) of 1.46 g/cc and 24%, respectively. Treatment of BCS with 2% CaO increased the strength by a factor ranging from 1.64 to 2.98, depending on the method of specimen preparation. Method 2 resulted

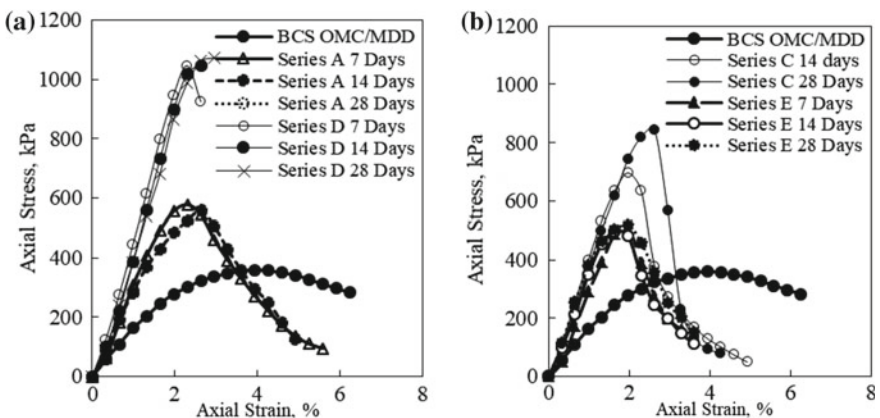


Fig. 4 Influence of specimen preparation method on strength gain characteristics of different mixtures of BCS and stabilizers. **a** Series A and Series D, **b** Series C and Series E

in strength gain factors as high as 2.98 while strength gain factor exhibited by specimens prepared by Method 1 was limited to 2.61. For Series A with specimens prepared by Method 1, strength gain may be attributed to *CaO* as modifier, while for Series D with specimens prepared by Method 2, strength gain might be due to the cementation produced by the binding gel which is the outcome of the reaction between BCS and *CaO*. The increase in strength did not show any remarkable variation within the studied curing periods. The unconfined compressive strength attained by specimens of Series A and Series D at various curing periods is presented in Table 5. Figure 4b illustrates the UCS test results of specimens of Series C and Series E. The results indicated specimens of Series E exhibiting strength gain factor of 1.33, 1.39, and 1.53 at 7 days, 14 days and 28 days of curing period, respectively, with corresponding values of 2.07 and 2.34 at 14 days and 28 days, respectively, for Series C. The specimens of Series C were prepared by Method 1 whereas Method 2 was adopted for preparation of Series E specimens. In both the series strength gain increased with time and could be attributed to the time-dependent hydration reaction of cement. Specimens of Series C effectively contained 2% *CaO* (which acted as a modifier) and 2% cement. Better efficiency in strength gain could be achieved by adding cement to the modified soil. This is because 2% *CaO* acted as a modifier, facilitated the hydration reaction of cement and also made the soil coarser due to which efficiency of cement stabilization was increased.

Series B and Series C were designed to study the effect of *CaO* and cement on the treated BCS (with 2% *CaO*). Treated BCS was cured for 14 days and then treated with 2% *CaO* (Series B) and 2% cement (Series C). After curing for 14 days

Table 5 Effect of lime and/or cement on unconfined compressive strength and compressibility

Series	Dry density γ_d (g/cc)	Water content w (%)	q_u (kPa)	Gain in q_u (%)	C_c	C_r	Swell pressure (kPa)
BCS	1.38	30	175	–	0.25	0.045	0
OMC/MDD	1.46	24.5	360	0	0.210	0.035	400
A 7 Days	1.47	24	578	61	0.152	0.038	250
A 14 Days	1.46	25	560	56	0.174	0.036	300
A 28 Days	1.46	24.5	592	64	–	–	–
B 14 Days	1.45	25	900	150	0.062	0.006	0
B 28 Days	1.43	26.5	941	161	–	–	–
C 14 Days	1.44	26	744	107	0.080	0.022	250
C 28 Days	1.46	24.5	843	134	–	–	–
D 7 Days	1.43	26	1046	191	0.060	0.019	0
D 14 Days	1.44	25	1061	195	0.075	0.018	0
D 28 Days	1.45	24	1072	198	0.082	0.010	0
E 7 Days	1.45	24	480	33	0.047	0.021	0
E 14 Days	1.45	24	500	39	0.071	0.031	0
E 28 Days	1.46	23	550	53	0.058	0.03	85

and 28 days, specimens for Series B and Series C were prepared by Method 1. The stress–strain behavior exhibited by the specimens of Series B and Series C is shown in Fig. 5a. Series B specimens exhibited slightly higher strength gain as compared to Series C specimens. Strength gain factors for Series B specimens were evaluated to be 2.50 and 2.61 at 14 days and 28 days, respectively, as compared to corresponding values of 2.07 and 2.34 for Series C specimens. This might be due to the high clay fraction present in the soil which favors *CaO* as compared to cement. Effectively, the curing periods at 14 days and 28 days for specimens of Series B (*also Series C*) were 28 days and 42 days, respectively, but since there was not any significant effect of time on strength gain in the case of *CaO*, it can be concluded that *CaO* treatment of treated BCS significantly increased the unconfined compressive strength. However, Series C specimens exhibited a significant increase in strength gain with curing period.

Series D and E were designed to study the effect of 2% *CaO* and 2% cement, respectively, on the untreated BCS with specimens being prepared by Method 2. Figure 5b shows the UCS test results for Series D and Series E specimens. Results indicated higher strength gain factors for Series D specimens as compared to Series E specimens. Strength gain factors of 2.91, 2.95, and 2.98 at a curing period of 7 days, 14 days and 28 days, respectively, were exhibited by Series D specimens with corresponding values of 1.33, 1.39 and 1.53 at 7 days, 14 days and 28 days respectively for Series E. As compared to 2% *CaO* (Series D) with same specimen preparation method, strength gain factor was observed to be lower in case of cement (Series E). However, for Series E strength gain factor was found to increase significantly with curing period. This might be due to the time-dependent hydration of cement resulting in the formation of stronger binding gel and thereby improved strength with time.

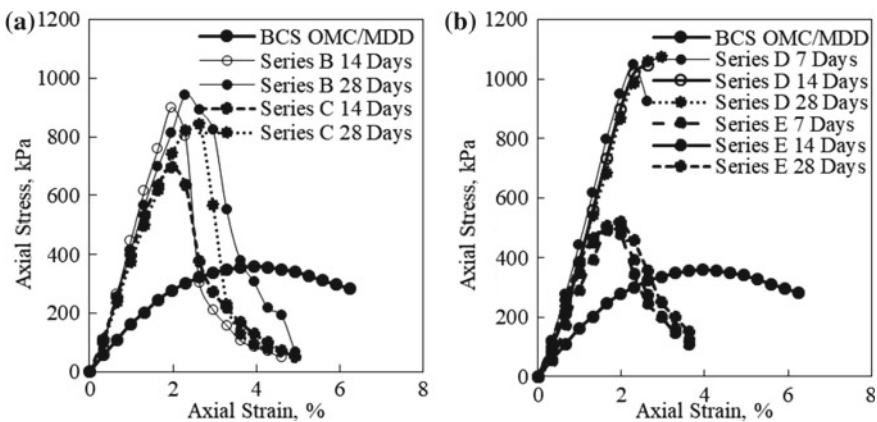


Fig. 5 Effect of different stabilizers on stress–strain relationship of (a) treated BCS Series B and C by Method 1 (b) on BCS Series D and E by Method 2

Comparison of the UCS test results indicating the effect of stabilizer on untreated BCS and treated BCS and also the effect of specimen preparation is illustrated in Figs. 4 and 5. The dependency of strength gain on the method of specimen preparation was reflected in the stress–strain characteristics of different test series. A remarkable change is evident in the peak stress and also the axial strain at peak stress. Addition of stabilizers resulted in increased peak strength of the specimens with reduced axial strain at peak stress. The addition of 2% *CaO* with specimens prepared by Method 2 (Series E) was found out to be most efficient among all the considered series. This improvement could be attributed to the high clay content of the soil. To achieve similar strength gain factor, higher cement content may be required, thereby increasing the cost. Table 5 summarizes the effect of lime and/or cement treatment on the unconfined compressive strength of BCS.

3.3 *Effect of CaO and Cement on Compressibility and Swell Pressure of Untreated and Treated BCS*

From 1-D consolidation test performed at MDD and OMC of BCS specimens, the values of compression index (C_c) and recompression index (C_r) were evaluated to be 0.21 and 0.035, respectively. Figure 6a shows the e - $\log(p)$ relationship for specimens of Series A and Series D at 7 days and 14 days of curing. With the same *CaO* content, Series A and Series D differed only in the method of specimen preparation. Specimens of Series A, prepared by Method 1, exhibited a very large reduction in compressibility with C_c value reducing from 0.21 to 0.152 and 0.174 at 7 days and 14 days of curing, respectively. At 14 days of curing the value of C_c was observed to be higher than that at 7 days of curing but was found to be less than that of the untreated BCS. Similar variations were observed in PI behavior. For Series D wherein the specimens prepared by Method 2, C_c values reduced to 0.06 and 0.075 at 7 days and 14 days of curing, respectively, from an initial value of 0.21. These values were significantly lower than that obtained in Series A for the same period of curing. Method 2 resulted in more significant reduction in compressibility as compared to Method 1 which is in alignment with the strength gain observed in UCS tests. Figure 6b presents the e - $\log(p)$ relationship for Series C and Series E with specimens prepared by adopting Method 1 and Method 2, respectively. However, the specimens of Series C effectively contained 2% *CaO* and 2% cement whereas the specimens of Series E had only 2% cement. C_c reduced from 0.21 to 0.08 at 14 days of curing for Series C whereas for Series E the C_c at 14 days of curing was evaluated to be 0.071. Thus, the addition of 2% cement to untreated BCS and treated BCS resulted in the improvement of compressibility to a similar extent. This could be attributed to the dominant presence of clay in the both the untreated BCS and treated BCS. However, a significant difference could be observed in the strength gain characteristics of specimens of Series C and Series E with specimens of Series C exhibiting higher strength.

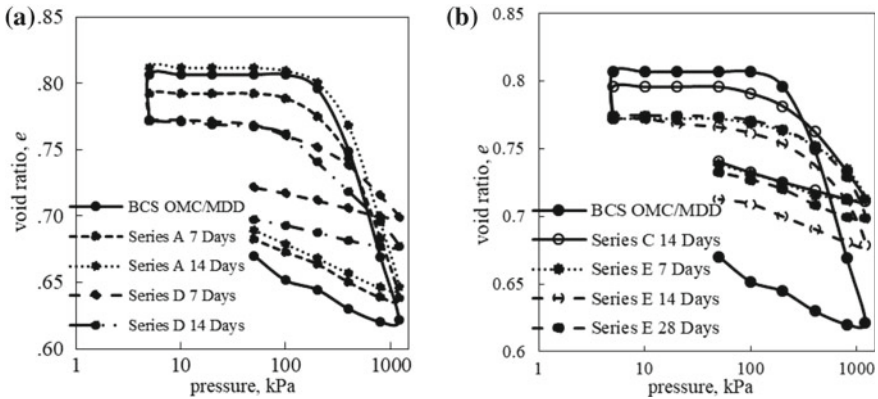


Fig. 6 Influence of specimen preparation method on e - $\log(p)$ relationship of different mixtures of BCS and stabilizers. **a** Series A and Series D, **b** Series C and Series E

Addition of CaO and cement to the treated BCS resulted in a further improvement (decrease) of compressibility characteristics of BCS. The value of C_c reduced from 0.21 to 0.062 and 0.08 at 14 days of curing period for Series B and Series C specimens, respectively, (Table 5). The e - $\log(p)$ relationship for specimens of Series B and C is illustrated in Fig. 7a. The notable decrease in C_c was in conjunction with the gain in strength for Series B and Series C specimens. Corresponding C_r values for Series B and Series C specimens reduced to 0.006 and 0.022, respectively, from an initial value of 0.035 for untreated BCS (Table 5). Specimens of Series B and Series D did not differ much in compressibility characteristics, but Series B effectively had double CaO content as compared to Series D (Table 5). Thus, it can be concluded that Method 2 was more efficient in controlling compressibility characteristics, which is in agreement with the strength gain characteristics. Figure 7b shows e - $\log(p)$ relation for Series D and Series E specimens. Series E specimens showed slightly higher reduction in C_c and C_r values as compared to that of Series D.

Series E exhibited C_c values of 0.047, 0.071, and 0.058 at 7, 14, and 28 days of curing, respectively, with corresponding values of 0.06, 0.075 and 0.082 for Series D. Adopting Method 2 for specimen preparation, treatment with cement reduced compressibility to a greater extent when compared to CaO . This may be because of the increased stiffness due to the quick cementation produced by the hydration products. Recompression index (C_r) reported in Table 5 followed the same trend as followed by C_c . Swell pressure for untreated BCS specimens, moist tamped at OMC/MDD, was 400 kPa. Treatment of untreated and treated BCS with CaO and further with CaO or cement was found to result in reduced swell pressure. It was observed that swell pressure almost vanished in some cases as is evident from the e - $\log(p)$ relation of treated BCS as well as from the results presented in

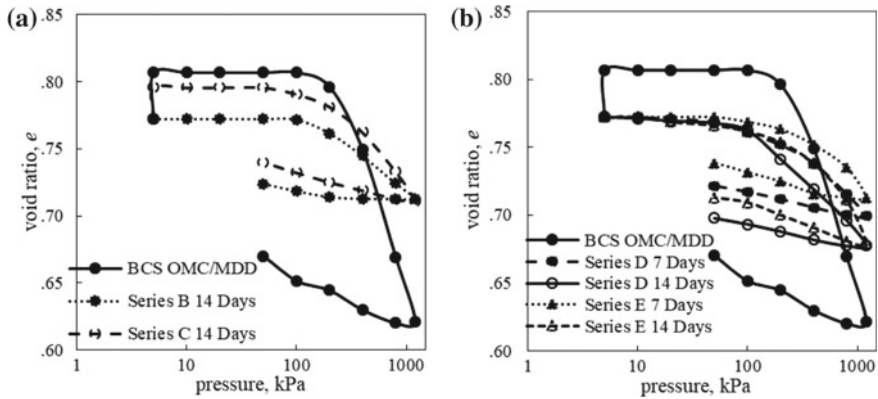


Fig. 7 Effect of different stabilizers on e - $\log(p)$ relationship of (a) treated BCS Series B and C by Method 1 (b) on BCS Series D and E by Method 2

Table 5. It is evident that specimen preparation had a strong impact on swell pressure exhibited by the specimens with Method 2 being efficient as compared to Method 1.

4 Conclusions

The following conclusions have been drawn from this study:

- Addition of CaO and/or fly ash led to a decrease in LL and an increase in PL with a considerable reduction in PI for all percentages of CaO and (or) fly ash.
- Addition of 2% CaO to BCS increased UCS by a factor of 1.61, 1.56, and 1.64 at 7, 14, and 28 days of curing, respectively, while adopting Method 1 of specimen preparation. Corresponding strength gain factors for Method 2 of specimen preparation were higher 2.91, 2.95, and 2.98, respectively. Addition of 2% cement to BCS adopting Method 2 of specimen preparation resulted in strength gain factor of 1.33, 1.39, and 1.53 at 7, 14 and 28 days, respectively. In the case of cement, strength gain was found to increase with time, as expected.
- Addition of CaO /cement to the treated BCS enhanced the strength gain. With an additional 2% CaO , strength increased by a factor of 2.50 and 2.61 at 14 and 28 days of curing, respectively, for additional 2% cement corresponding strength gain factors were 2.07 and 2.34. Strength gain in case of cement exhibited time dependency.
- Treatment of BCS with 2% CaO reduced the value of C_c from 0.21 to 0.152 and 0.174 at 0 and 7 days of curing, respectively, while adopting Method 1 of specimen preparation. With Method 2, C_c decreased to a value of 0.06. Treatment of treated BCS with 2% lime and cement also resulted in similar

values of 0.062 and 0.08 while adopting Method 1. Reduction in C_c was observed in all the test series with a more pronounced effect for Series B, C, D, and E (Table 5).

- Addition of CaO and cement to the untreated and treated BCS resulted in reduced swell pressure. The reduction in swell pressure was significantly affected by the nature of the added stabilizer(s) and specimen preparation method. While untreated BCS specimens exhibited a swell pressure of 400 kPa, it reduced to 250 kPa with the addition of 2% CaO (Series A). With the addition of 2% CaO (Series D) and cement (Series E) and adopting Method 2 for specimen preparation, nearly zero swell pressure were exhibited by the specimens.

Thus lime/cement treatment by different methods can be adopted in real-life situations where strength gain and reduction in swell pressures need to be addressed. The current study reveals Method 2 being efficient in improving the strength and volumetric behavior of expansive soils.

Acknowledgements The support and guidance provided by Prof. G. Venkatappa Rao throughout the study are highly acknowledged.

References

1. Bell FG (1988) Stabilization and treatment of clay soils with lime. Part 1. Basic principles. *Ground Eng* 21:10–15
2. Bell FG (1988) Stabilization and treatment of clay soils with lime. Part 2. Some applications. *Ground Eng* 21:22–30
3. Chen FH (1988) Foundations on expansive soils. Elsevier, Amsterdam, The Netherlands
4. Coulombe CE, Wilding LP, Dixon JB (1996) Overview of vertisols: characteristics and impacts on society. *Adv Agron* 57:289–375
5. Donaldson GW (1969) The occurrence of problems of heave and the factors affecting its nature. In: Second international research and engineering conference on expansive clay soils, Texas A & M Press, pp 25–36
6. Jones DEJ, Holtz, WG (1973) Expansive soils—the hidden disaster. *Civil Eng* 43
7. Katti RK (1979) Search for solutions to problems in black cotton soils. *Indian Geotech J*. 1st IGS Annual Lecture (1978) 9(1):1–80
8. Katti RK, Kulkarni, Radhakrishna N (1966) Research on black cotton soils without and with inorganic additives. Indian Road Congress, Road Research Bulletin, No. 10
9. Sivapullaiiah PV, Sridharan A, Bhaskar Raju KV (2000) Role of amount and type of clay in the lime stabilization of soils. *Proc Inst Civil Eng Ground Improv* 4(1):37–45
10. Venkatappa Rao G, Ramana GV (2000) State-of-the-art report on: lime soil stabilization. Indian Roads Congress, Special Report No. 1
11. Venkatappa Rao G, Rekh TS (1977) Physico-chemical mechanisms governing the plasticity behaviour of soils. *Indian Geotech J* 7(4):261–282

Strength and Deformation Characteristics of Jointed Block Rock Matrix Using Triaxial System



Manish Shah and Arpit Patel

Abstract The strength and deformation behavior of jointed rock was examined in the context of the design of slopes, construction of tunneling, and mining projects due to the presence of natural hair cracks, fissures, bedding planes, faults, etc. Dolomite rock from Gujarat is used for experimental study to find the shear parameters of proposed rock mass matrix. A different rock matrix is formed with providing the vertical and horizontal cuts in different patterns. A different matrix includes the following vertical cuts, two vertical cuts (perpendicular to each other) passing from center of specimen, three vertical cuts (each at every 60°) passing through center of specimen, and four vertical cuts in grid pattern. With above vertical cuts also all specimens were cut in horizontal plane at every (I) $1/6$ of height, (II) $1/3$ of height, and (III) $1/2$ of height. A different matrix is tested using rock triaxial system. The strength behavior was studied using Hoek–Brown strength theory and Mohr–Coulomb strength theory. Results were compared with intact rock and various jointed rock matrix specimens. Orientation of rock matrix shows little increase in cohesion value and decrease in angle of internal friction with increase in number of joints in vertical direction. The typical failure/deformation pattern was observed in jointed rock matrix specimens such as axial failure, block rotation, splitting of blocks through joints, and shear failure.

Keywords Dolomite · Rock matrix · Shear parameters · Failure criteria · Triaxial system

1 Introduction

The behavior of discontinuities between the intact rocks is a subject of investigation of many research workers since it is not possible to deal on the same theoretical considerations as intact rock materials [6]. The sliding is just initiated and the

M. Shah (✉) · A. Patel
Applied Mechanics Department, L. D. College of Engineering, Gujarat, India
e-mail: drmvs2212@gmail.com

© Springer Nature Singapore Pte Ltd. 2020
A. Prashant et al. (eds.), *Advances in Computer Methods and Geomechanics*, Lecture Notes in Civil Engineering 56,
https://doi.org/10.1007/978-981-15-0890-5_55

665

resultant force is inclined at an angle of basic friction from a normal to the inclined surfaces. There are three fundamental components, namely, basic friction angle, peak dilation angle which is equal to the instantaneous incline of the shearing path at peak strength relative to the mean plane, and strength component representation of the failure of the intact material in the form of asperities [1]. It is probable that the dilation angle will be at its maximum value just at the instant when peak strength is passed. From the experimental investigations on nonplanar joints, it has been observed that at low normal stress, a nonplanar joint continues to dilate with increasing shear displacement but at reduced angle, while at high normal stress a nonplanar joint might cease to dilate altogether after passing its peak strength [2]. However, there are not many experimental investigations conducted to clarify this aspect of great significance especially for understanding the shearing behavior of rocks. The work of Barton [2] provides an important step to go further into the realm of shearing behavior of jointed rocks. The uncertainty in predicting the behavior of a jointed mass under triaxial stresses are essentially caused by scale effect and the unpredictable nature of the modes of failure [9] and laboratory tests are often required to assess the strength and deformability of the jointed rock specimens making the exercise quite expensive [11]. In this study, research work has been carried out to address the above problems related to cracks and joint openings in field rock mass with various jointed rock matrix in cylindrical rock specimens to be tested in triaxial test apparatus to study the actual shear parameters and behavior of failure pattern with stress and axial strain characteristics. The results obtained are compared with the strength of intact rock specimen [10].

In the present study, Dolomite rock from Gujarat is used for experimental study to find the shear parameters of proposed rock mass matrix. A different rock matrix is formed with providing the vertical and horizontal cuts in different patterns. A different matrix includes the following vertical cuts, two vertical cuts (perpendicular to each other) passing from center of specimen, three vertical cuts (each at every 60°) passing through center of specimen, and four vertical cuts in grid pattern. With above vertical cuts, all specimens were also cut in horizontal plane at every (I) 1/6 of height, (II) 1/3 of height, and (III) 1/2 of height as shown in Fig. 1c.

2 Theoretical Analysis

The core cutting of cylindrical rock core from dolomite chunk is carried out as per IS-9179-2001 and to make intact and different types of rock matrix patterns cylindrical specimens with aspect ratio 1:2. The rock triaxial test is performed according to IS-13047-2010 and the shear parameters are obtained under different confining pressures like 3, 5, and 7 MPa for the intact and different types of rock matrix specimen patterns of dolomite rock at the constant strain rate of 0.078 mm/min. The joint configuration was varied to achieve the possible modes of failure naturally occurring in the field. The shear parameters of intact and jointed rock specimens were calculated by the following equation.

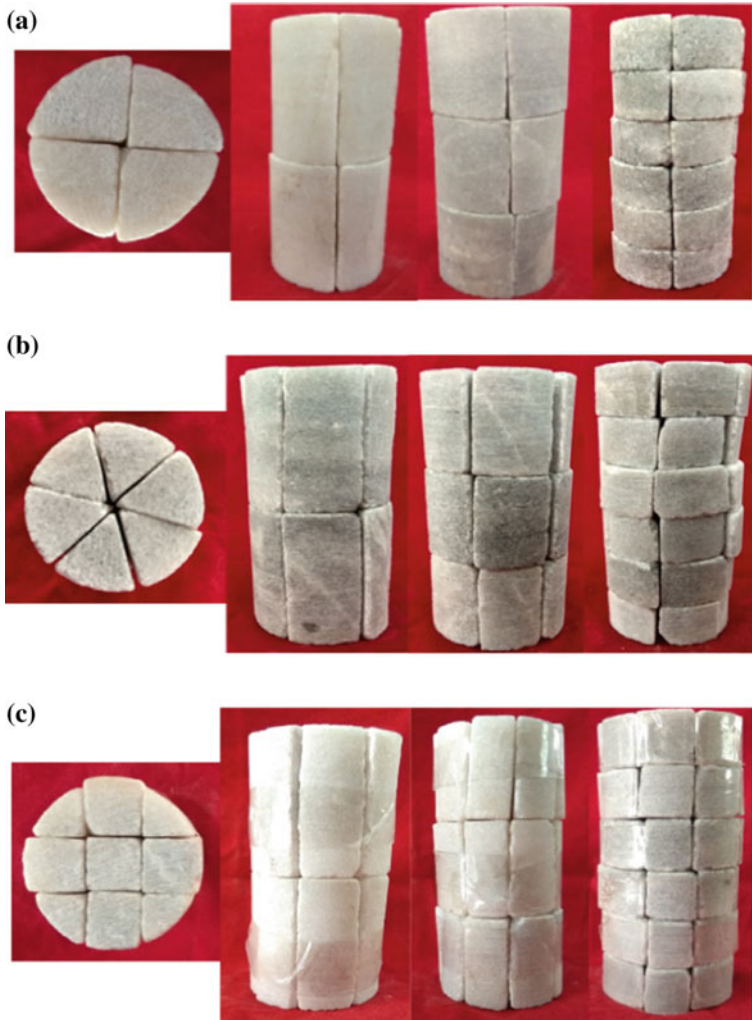


Fig. 1 Rock matrix specimen patterns with different orientations

$$\tau = \sigma \tan \varnothing + c \quad (1)$$

The major principle stresses of intact and jointed rock specimens were calculated by Mohr–Coulomb strength theory and Hoek–Brown theory [5].

As per Mohr–Coulomb Strength theory,

$$\sigma_1 = \frac{2c \cdot \cos \varnothing}{1 - \sin \varnothing} + \frac{\sigma_3(1 + \sin \varnothing)}{1 - \sin \varnothing} \quad (2)$$

where

- σ_1 Major principle stress
- σ_3 Major principle stress
- c cohesion
- \emptyset Angle of internal friction.

As per Hoek–Brown strength theory,

$$\sigma_1 = \sigma_3 + \sigma_c \left(s + \frac{m_b \cdot \sigma_3}{\sigma_c} \right)^{0.5} \quad (3)$$

where

- σ_c Compressive strength of intact rock specimen
- m_b Material constant for rock
- s Hoek–Brown theory constant.

Material constant m_b and Hoek–Brown theory constant s are taken from the (table given by Hoek–Brown).

2.1 Experimental Investigation

Properties of Dolomite Rock:

The cylindrical specimen of intact rock and a different rock matrix with 42 mm diameter and 84 mm height were obtained as per IS 13030-1991 and physical properties of intact dolomite rock specimen are shown in Table 1.

2.2 Modulus of Elasticity

Modulus of elasticity (E) for a different rock matrix is calculated based on the stress–strain relationship of the tested specimen.

Table 1 Properties of dolomite rock

Property	Values
Dry unit weight, γ_d (kN/m ³)	28.4
Porosity (%)	0.3
Unconfined compressive strength (MPa)	58.8
Poison's ratio	0.09

2.3 Geological Strength Index

The Geological Strength Index (GSI) system is used for the estimation of the rock mass strength and the rock mass deformation modulus. The GSI system describes two factors, rock structure and block surface conditions. The guidelines given by the GSI system are for the estimation of the peak strength parameters of jointed rock masses.

3 Results and Analysis

3.1 Shear Parameters and Hoek–Brown Constants

Based on results obtained through rock triaxial test, shear parameters were evaluated for intact and jointed rock matrix specimens as per Mohr–Coulomb strength theory whose values are narrated in Table 2.

Table 2 Cohesion and angle of internal friction of different types of rock matrix patterns

Matrix patterns with notation	Shear parameters		Hoek–Brown constants		Modulus of elasticity E (MPa)
	c (MPa)	θ (°)	m_b	S	
Intact rock specimen, D ₋₁	11.5	35	5.7	1	2500
2-vertical and 1-horizontal cuts, D _{-2V-1H}	5.6	32	3.3	0.33	2032
2-vertical and 2-horizontal cuts, D _{-2V-2H}	7.3	28	2.3	0.24	1941
2-vertical and 5-horizontal cuts, D _{-2V-5H}	10.9	18	1.9	0.19	1878
3-vertical and 1-horizontal cuts, D _{-3V-1H}	5.9	31	3.3	0.33	2214
3-vertical and 2-horizontal cuts, D _{-3V-2H}	5.2	27	1.5	0.15	2031
3-vertical and 5-horizontal cuts, D _{-3V-5H}	4.7	28	1.2	0.12	1570
4-vertical (grid pattern) and 1-horizontal cuts, D _{-4V-1H}	2	42	1.3	0.14	1858
4-vertical (grid pattern) and 3-horizontal cuts, D _{-4V-3H}	5	27	1.5	0.15	1878
4-vertical (grid pattern) and 5-horizontal cuts, D _{-4V-5H}	11	18	1.0	0.11	1133

From the Table 2, it is observed that the percentage decrement in cohesion(c) for various matrixes D_{-2V-1H} , D_{-2V-2H} , D_{-2V-5H} , D_{-3V-1H} , D_{-3V-2H} , D_{-3V-5H} , D_{-4V-1H} , D_{-4V-2H} , and D_{-4V-5H} is observed to be decreased by 51.30%, 36.52%, 5.21%, 48.69%, 54.78%, 59.13%, 82.69%, 56.52%, and 4.34%, respectively, with respect to D_{-I} (intact) rock. The percentage decrement in angle of internal friction (ϕ) for various matrixes D_{-2V-1H} , D_{-2V-2H} , D_{-2V-5H} , D_{-3V-1H} , D_{-3V-2H} , D_{-3V-5H} , D_{-4V-1H} , D_{-4V-2H} , and D_{-4V-5H} is observed to decrease by 8.57%, 20%, 48.57%, 11.42%, 22.85%, 20%, 20%, 22.82%, and 48.57%, respectively, with respect to D_{-I} rock. The strength of various horizontal cuts specimens are increasing moderately as the confining pressure increases because the rock blocks come more close to each other at high confining pressure and it requires more normal load to deform. The load carrying capacity of vertical cut specimen is higher than the horizontal cut specimen and with increase in number of horizontal cut the load carrying capacity of specimen decreases. The percentage decrement in modulus of elasticity (E) of D_{-2V-1H} , D_{-2V-2H} , D_{-2V-5H} , D_{-3V-1H} , D_{-3V-2H} , D_{-3V-5H} , D_{-4V-1H} , D_{-4V-2H} , and D_{-4V-5H} is observed to decrease by 18.72%, 22.36%, 22.36%, 24.88%, 11.44%, 18.76%, 37.2%, 25.56%, 24.88%, and 54.36%, respectively with respect to D_{-I} rock. The modulus of elasticity of jointed rock matrix specimens were noted to decrease as the number of joints increases in horizontal and vertical direction. The modulus of elasticity is observed to decrease as the confining pressure increases for same number of horizontal joints. At higher confining pressure, the parts of specimens are more close to each other which requires high normal load to deform the specimen. Parts of specimen are becoming closer to each other due to application of confining pressure on them. The Hoek–Brown constants “ m ” and “ s ” are varying between 5.7 to 1 and 1 to 0.11, respectively, for intact rock and four vertical and five horizontal cut specimens, respectively. The Hoek–Brown constant (m) is noted to decrease as the number of joints increases for same rock material based on GSI values.

3.2 Stress–Strain Relationship

Figures 2, 3 and 4 shows the comparative plots of stress versus strain for jointed rock matrix with two vertical cut patterns at 3 MPa, 5 MPa, and 7 MPa confining pressure, respectively. The percentage increment in stress with respect to intact rock is observed as 26, 29, and 36% for 3 MPa, the percentage decrement in stress with respect to intact rock is observed as 19, 32, and 52% for 5 MPa and the percentage decrement in stress with respect to intact rock is observed as 21, 36, and 64% for 7 MPa, respectively.

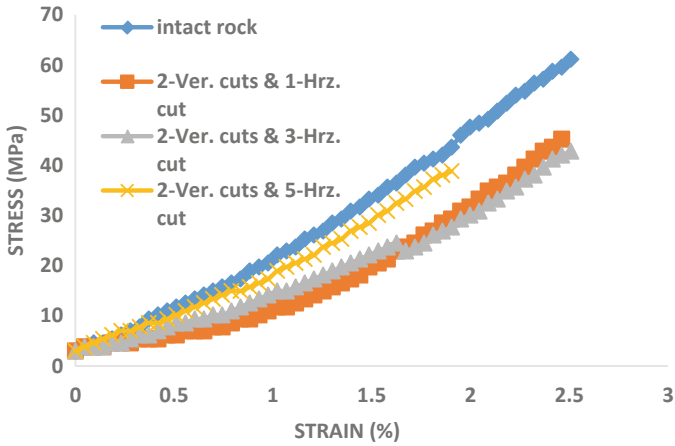


Fig. 2 Comparison of stress–strain of jointed rock matrix pattern (two vertical cut with perpendicular each other) at 3 MPa

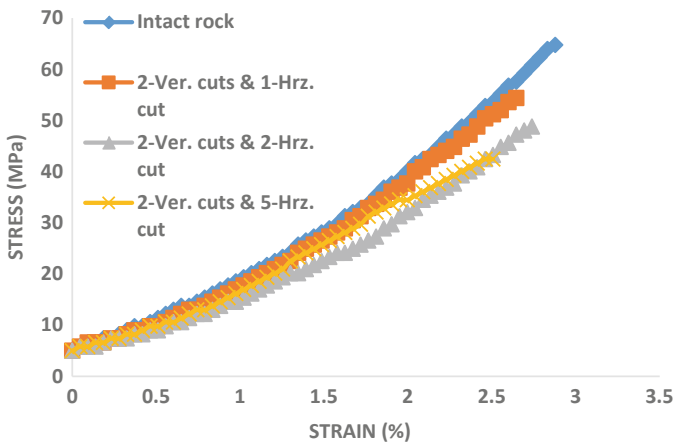


Fig. 3 Comparison of stress–strain of jointed rock matrix pattern (two vertical cut with perpendicular each other) at 5 MPa

Figures 5, 6 and 7 shows the comparative plots of stress versus strain for jointed rock matrix with three vertical cut patterns at 3 MPa, 5 MPa, and 7 MPa confining pressure, respectively. The percentage decrement in stress with respect to intact rock is observed as 29, 50, 53% for 3 MPa, 24, 61, 64% for 5 MPa, and 29, 73, 76% for 7 MPa, respectively.

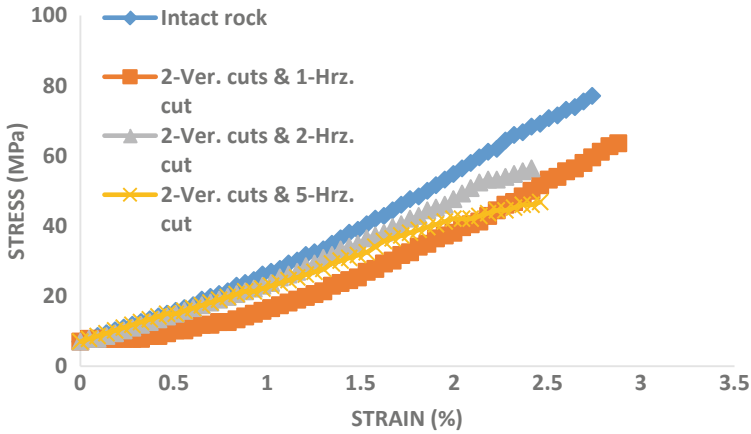


Fig. 4 Comparison of stress–strain of jointed rock matrix pattern (two vertical cut with perpendicular each other) at 7 MPa

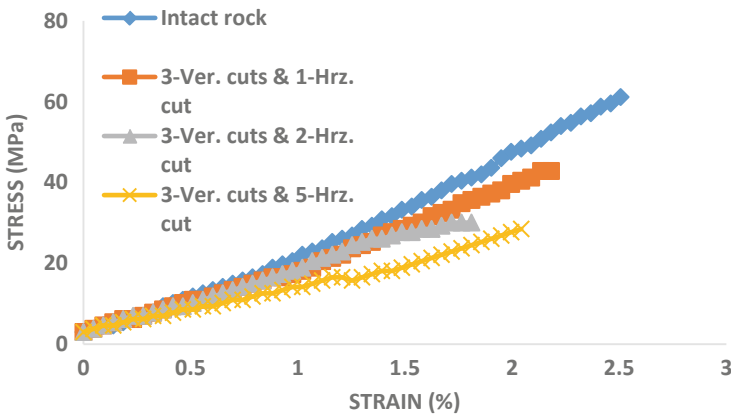


Fig. 5 Comparison of stress–strain of jointed rock matrix pattern (three vertical cut at 60° to each other) at 3 MPa

Figures 8 and 9 show the comparative plots of stress versus strain for jointed rock matrix with four vertical cut patterns at 3 MPa, 5 MPa, and 7 MPa confining pressure, respectively. As the number of joints increasing four vertical and one horizontal cuts, four vertical and two horizontal, four vertical and five horizontal

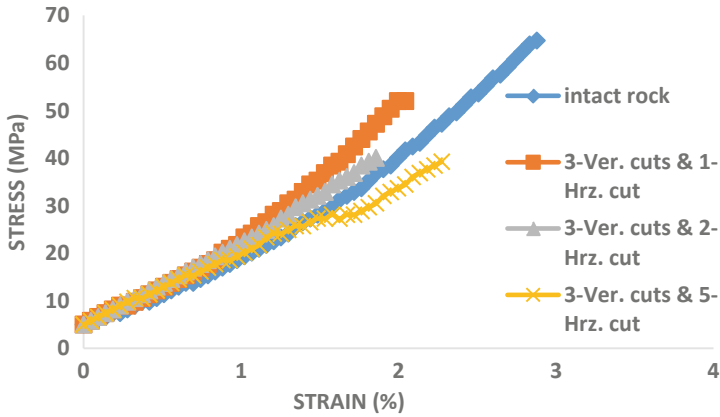


Fig. 6 Comparison of stress-strain of jointed rock matrix pattern (three vertical cut at 60° to each other) at 5 MPa

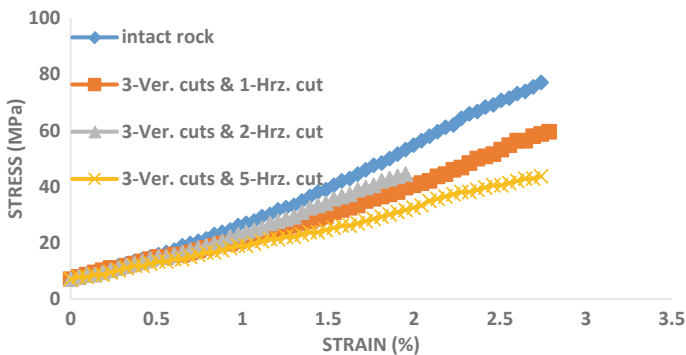


Fig. 7 Comparison of stress-strain of jointed rock matrix pattern (three vertical cut at 60° to each other) at 7 MPa

cuts, the percentage decrement in stress with respect to intact rock is observed as 37, 36, 57% for 3 MPa, 38, 34, 47% for 5 MPa and 34, 39, 51% for 7 MPa, respectively.

3.3 Failure Under Triaxial Compression Test

There were 30 number of specimens (three specimens each of different matrix patterns and intact rocks) tested under triaxial compression test under different confining pressures is shown in Fig. 10. The failure patterns of each specimen were

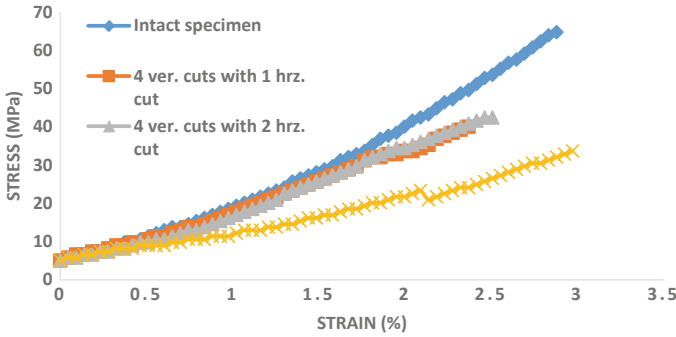


Fig. 8 Comparison of stress-strain of jointed rock matrix pattern (four vertical cuts in grid pattern) at 5 MPa

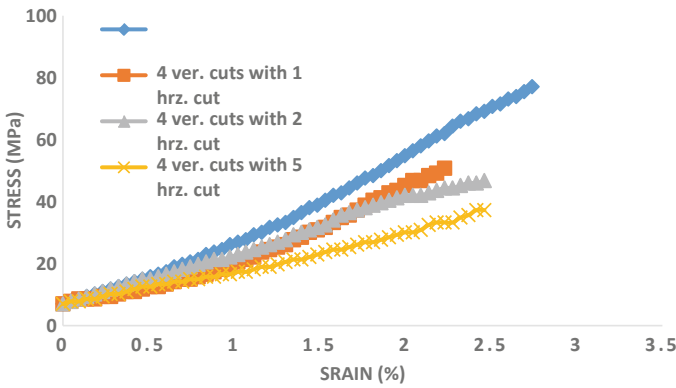


Fig. 9 Comparison of stress-strain of jointed rock matrix pattern (four vertical cuts in grid pattern) at 7 MPa

observed and their corresponding strength values and failure modes are presented in Table 3. Initially in triaxial test, rock specimen shows shear splitting at value of confining pressure 3 MPa, which on increase in confining pressure to 5 MPa, results in multiple fracturing of rock, on further increasing confining pressure value to 7 MPa, specimen get completely crushed.

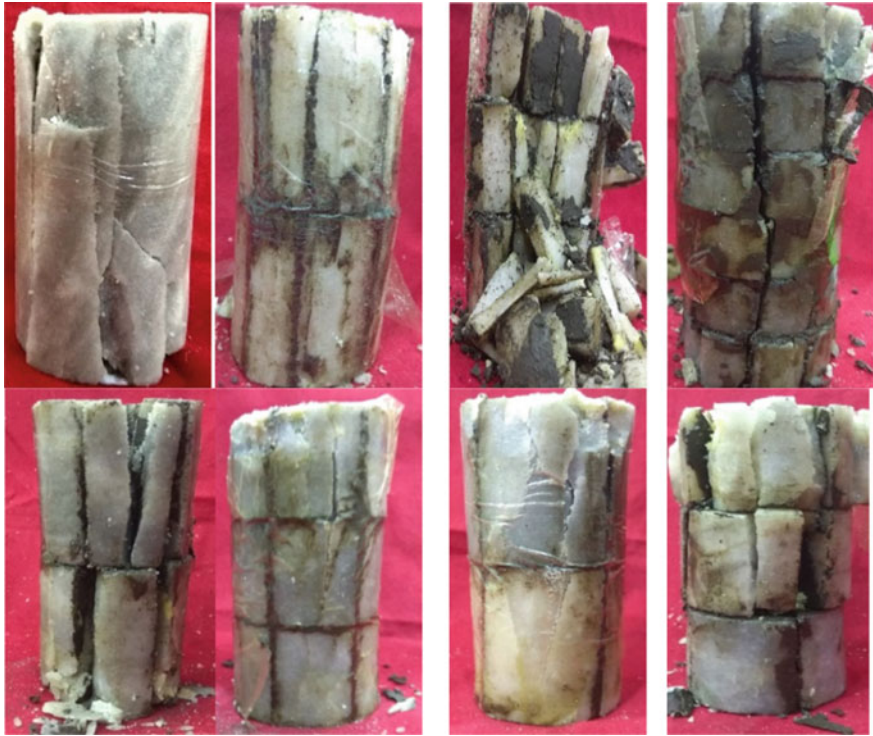


Fig. 10 Different failure patterns in tested specimens

Table 3 Comparison of failure patterns under triaxial compression

Sr. No.	Matrix patterns	σ_3 (MPa)	σ_1 (MPa)	Failure mode
1	Intact rock specimen	3	59.09	Axial failure
2		5	72.21	Axial failure
3		7	80.47	Axial failure
4	Two vertical and one horizontal cut	3	49.07	Axial failure
5		5	57.57	Axial and shear failure
6		7	66.07	Axial and shear failure
7	Two vertical and two horizontal cuts	3	43.28	Axial and block splitting failure
8		5	50.28	Axial, block rotation and block splitting
9		7	56.83	Axial and shear failure

(continued)

Table 3 (continued)

Sr. No.	Matrix patterns	σ_3 (MPa)	σ_1 (MPa)	Failure mode
10	Two vertical and five horizontal cuts	3	36.62	Axial and block splitting failure
11		5	40.88	Shear failure
12		7	44.66	Axial failure
13	Three vertical and one horizontal cuts	3	46.31	Axial failure
14		5	53.76	Axial and shear failure
15		7	61.24	Axial failure
16	Three vertical and two horizontal cuts	3	31.76	Axial failure
17		5	38.57	Axial failure
18		7	44.23	Axial failure
19	Three vertical and five horizontal cuts	3	29.90	Axial and block splitting failure
20		5	37.80	Axial, block rotation and block splitting
21		7	43.41	Axial, block rotation and block splitting
22	Four vertical and one horizontal cut	3	29.86	Axial failure
23		5	40.82	Axial and block split out failure
24		7	50.50	Axial and shear failure
25	Four vertical and two horizontal cuts	3	36.62	Axial failure
26		5	40.88	Axial failure
27		7	44.66	Axial and block splitting failure
28	Four vertical and five horizontal cuts	3	26.69	Block splitting failure
29		5	31.83	Axial and block splitting failure
30		7	36.35	Axial and shear failure

4 Conclusion

The findings from this study as summarized below:

- The value of cohesion (c) is observed to be decreasing and angle of internal friction angle (Φ) is also decreasing with increases when size of opening is increase and increases in angle of joints because as number of joints increases, friction between two rock specimens decreases.
- Strength of jointed rock is dependent on the direction of applied loading with respect to direction of joints. The percentage of error in practical conditions resulting with Mohr–Coulomb theory and Hoek–Brown failure criteria is due to the neglecting pore pressure for all samples due to less porosity of dolomite

rock. Peak values of stress and corresponding strain values increase due to the effect of confining pressure.

- For particularly intact type of rock, the failure behavior was observed to be of hair crack pattern with only axial failure, which was extending throughout the length of specimen. Minute hair cracks were developed which are parallel or at some angle to the vertical direction and they were observed near the vicinity of treated portion of joint due to part resistance of load. Crushed pieces of rock have been observed near the vicinity of jointing area. The jointed rock matrix specimen has failed under different patterns, viz, block rotation under high pressure, splitting through joint due to small blocks, and high number of joints, shear failures, etc.

Rock matrix and its orientation both with respect to vertical and horizontal direction are playing vital role in development of deformation shapes and sliding of tiny rock blocks into weakest plane of failure. The variation in strength parameters is measured with change in rock matrix from one block joint to multiple block joints. Therefore, this type of study becomes very important where rock discontinuities are simulated with matrix pattern, bonding of rock particles simulated with cement binder, simulating number of possible failure planes (vertical, horizontal, and inclined). Simulating in situ rock stresses/overburden stress/induced vertical load as confining pressure through rock triaxial system has given considerable insight to the overall problems associated with a design of tunnels, rock mining, and rock fracturing applications. Even though good comparison of results are obtained using Mohr–Coulomb and Hoek–Brown strength theory, more mathematical models based on actual failures should be adopted.

Acknowledgements The authors are thankful to Dr. G. P. Vadodaria, Principal, L. D. College of Engineering, Ahmedabad and Prof. A. R. Gandhi, Head of Department, L. D. College of Engineering for providing all necessary facilities for this research project.

References

1. Arzua J et al (2014) Strength and dilation of jointed granite specimens in triaxial test. *Int J Rock Mech Sci Direct.* <https://doi.org/10.1016/j.ijrmmms-2014-04-001>
2. Barton N (1973) Review of a new shear-strength criterion for rock joints. *Eng Geol.* [https://doi.org/10.1016/0013-7952\(73\)90013-6](https://doi.org/10.1016/0013-7952(73)90013-6)
3. Cai M et al (2003) Estimation of rock mass deformation modulus and strength of jointed hard rock masses. *Int J Rock Mech Mining Sci Sci Direct.* [https://doi.org/10.1016/s1365-1609\(03\)00025-x](https://doi.org/10.1016/s1365-1609(03)00025-x)
4. Evert H et al (2002) Hoek-Brown failure criterion. In: NARMS-TAC Conference. Toronto. <https://doi.org/10.1007/s00603-012-0276-4>
5. Hoek E, Carranza-Torres CT, Corkum B (2002) Hoek-Brown Failure Criterion— 2002 Edition. In: Proceedings of the 5th North American rock mechanics symposium, Toronto, pp 267–273, 7-10 July 2002
6. Huang D et al (2015) A comprehensive study on the smooth joint model in DEM simulation of jointed rock masses. *Granular Matter.* <https://doi.org/10.1007/s10035-015-0594-9>

7. Kahraman S, Alber M (2008) Triaxial strength of a fault breccia of weak rocks in a strong matrix. *Bull Eng Geol Environ.* <https://doi.org/10.1007/s40098-016-0212-8>
8. Liu M et al (2017) Strength criteria for intact rock. *Indian Geotech J.* <https://doi.org/10.1007/s40098-016-0212-8>
9. Rao KS et al (2016) Rock failure pattern under uniaxial, triaxial compression and brazilian loading conditions. In: *Indian geotechnical conference.* Chennai, India
10. Shah MV et al (2017) Strength characteristics of jointed rock matrixes with circular opening under triaxial compression. In: *Proceedings of 51st U.S. rock mechanics and geomechanics symposium.* California, USA
11. Vergara et al (2015) Large scale tests on jointed and bedded rocks under multi-stage triaxial compression and direct shear. *Rock Mecha Rock Eng* <https://doi.org/10.1007/s00603-013-0541-1>

Fundamental Time Period of Vibration in Seismic Analysis



Prabhat K. Soni, Prakash Sangamnerkar and S. K. Dubey

Abstract Indian seismic code provides expressions to evaluate the fundamental natural period for the seismic analysis of the structures primarily as a function of the height of the building and the length of the structure along the direction of earthquake considered. Building period predicted by these expressions is very useful in practice. Many researchers have performed the studies to evaluate the fundamental natural period of the buildings and found that the different other parameters such as stiffness of the structure, base dimensions, and the number of bays also affect the value of the fundamental time period of vibration of the building. Researchers also found that there is a scope for further improvement in the presently available expressions of time period given in design codes. In this study, effects of the various parameters have been studied and derived an expression to evaluate the time period of vibration.

Keywords Dynamic analysis · Number of bays · Vibration · Stiffness

1 Introduction

Base shear can be considered as one of the most useful parameters for the seismic design of the structures. Estimation of the natural time period is required for the calculation of the base shear of the building. Since the predicted fundamental period is useful for obtaining the expected seismic load affecting the structure, therefore, its precise estimation can be supportive to the accuracy of the design process.

A difference in the determined fundamental period of buildings can be observed between the results by equations of codes and the other methods of computation. In the work of several researchers, many proposed equations of fundamental period of

P. K. Soni (✉) · S. K. Dubey
Maulana Azad National Institute of Technology, Bhopal, MP, India
e-mail: Prabhatsoni15@gmail.com

P. Sangamnerkar
M. P. Housing and Infrastructure Development Board, Bhopal, MP, India

reinforced concrete frames can be observed with expressions having the elements more than height and type of the structure.

Panzer et al. [1], Shan et al. [2] and Olivera and Navarro [3] have pointed out in their study that it is not always possible to estimate the exact value of the natural period, as it depends upon the building configuration, materials used in the construction, and the stiffness of the structure. Sangamnerkar and Dubey [4, 5] have also performed their studies and found that height of the building is not only the parameter but also the stiffness of the structure, plan area of the building, number of bays in both direction, and infill masonry panels should also be considered in deriving the period formula.

Indian seismic code IS 1893 (Part-1)-2016 [6] estimates the fundamental time period of the building by the following expressions:

$$T_a = 0.075h^{0.75} \text{ For R. C. frame building} \quad (1)$$

$$T_a = 0.085h^{0.75} \text{ For steel frame building} \quad (2)$$

$$T_a = 0.09 \frac{h}{\sqrt{d}} \text{ For all other buildings} \quad (3)$$

The Eqs. (1)–(3) of the code, which are formed based on realistic data found using the seismic recordings on real buildings, several computations, testing results of the laboratories, are used to approximate the fundamental period. The purpose of the study can be summarized as to propose a new period equation, which incorporates the effect of the number of bays, plan area of the building, stiffness of the structure, and height of the building.

2 Literature Study

The simplified formula of fundamental time period of reinforced concrete structures has been provided by different codes and researchers by relating this time period to the number of storeys or height of the building. Amanat and Hoque [7] and Verderame et al. [8] have attracted the attention toward the scope of improvisation in the available equations of time period. Verderame et al. [8] showed the results in support of their comment that height alone cannot be adequate to describe the variation in the time period of building in its seismic analysis and the results of this study suggest that different other structural parameters can also be added in these expressions for rapid calculations of the time period. Therefore, they expressed the improvised formula including the plan area in the following manner.

$$T_a = \alpha H^\beta S^\gamma \quad (4)$$

where “ H ” = height of the considered building and α, β, γ are coefficients. “ α ” depends upon the structural system, “ S ” = the product of L_x and L_y , which are the two principal plan dimensions of the building.

Nyarko et al. [9] developed different equations (seven in numbers) considering number of floors, the ratio between the number of bays (in the longitudinal and transversal directions), number of bays parallel to the considered direction, the product of the number of bays (in the longitudinal and transversal directions).

3 Parameters for Analysis

3.1 For Validation of STAAD Software Model

To check the correctness of the computer solution, document number. IITK/GSDMA/EQ 26/V3.0, a design building example of a six-storey building, issued by the civil engineering department of Indian Institute of Technology (IIT), Kanpur (India), has been considered as a datum example.

Assumptions considered: The building is assumed with the use of exhibition or showroom, etc., in the building there has been considered 230 mm thick external walls having plaster thickness 12 mm on both sides.

Slabs are not to be considered at the level of the ground floor and as the tie beams, only ground beams passing through columns are to be considered.

3.2 For Characterization of Parameters Affecting Time Period and Its Effects

Table 1 shows the period formula proposed by the various author in terms of the parameters; N (Number of storey) and H (Height of building). Analysis for validation of software modal has been done as per the parameters considered in

Table 1 Period formula proposed by various authors

Author	Period values
Dunand et al. [10]	0.015 N
Espinoza [11]	0.06 N
Gallipoli et al. [12]	0.016 N
Kobayashi et al. [13]	0.05 N
Lagomarsino [14]	0.051 N
Navarro and Oliveira [15]	0.045 N
Oliveira [16]	0.042 N
Sanchez et al. [17]	0.049 N
Satake et al. [18]	0.015 H

Table 2 Parameters considered for validation of software model

Specification of six-storey building considered as design example	
Considered live load	4.0 (kN/m ²)—typical floors
	1.5 (kN/m ²)—on terrace
Load of floor finish	1.0 (kN/m ²)
Load of water proofing	2.0 (kN/m ²)
Load of terrace finish	1.0 (kN/m ²)
Considered location	Vadodara (Gujarat)
Foundation depth (below ground)	2.5 m
Soil Type	Medium soil (type II) as per IS 1893
Height (storey)	G.F.: 3.5 m, other floor: 5 m,
Number of floors	G.F. + 5 upper floors
Plan area	2.25 × 2.25 m, 3 bay
Seismic zone	III

Table 3 Details of building configuration for analysis

Building configuration		Specification considered	
Type of structure	Multi-storey rigid jointed frames	Material	M-25 (Concrete), Fe-415 (Reinforcement)
No. of storey	G.F. to G + 11, G + 24.	E _c	5000/√f _{ck} N/mm ²
Floor height	3.6 m	f _{cr}	0.7√f _{ck} N/mm ²
No. of grids	3 × 6, 4 × 6, 5 × 6, 6 × 6	Type of soil	Type-II, Medium soil
Thickness of slab	150 mm	Imposed load	4 kN/m ²
Size of columns	1.0 × 1.0 m, 0.75 × 0.75 m, 0.6 × 0.6 m, 0.55 × 0.55 m, 0.45 × 0.45 m	Specific Weight of R.C.C.	25 kN/m ³
Walls- (a) External (b) Internal	200 mm 100 mm	Water proofing	2.5 kN/m ²
Base Dimension	18.0 × 18.0 m, 24.0 × 24.0 m, & 30.0 × 30.0 m	Floor finish	1 kN/m ²

Table 2. Various RC frame buildings were analyzed using a computerized solution with the assumption mentioned in Tables 3 and 4. General arrangement of beams and columns is depicted in Fig. 1.

As mentioned in Tables 3, 4, and Fig. 1, total 120 values of the time period were obtained by performing dynamic analysis on various building/structural configurations, earthquake parameters for the buildings were considered as per the provisions made in the Indian seismic code IS 1893:2016 (Part-I) for earthquake zone III, computer software STAAD is used to analyze the building models. To get the

Table 4 Building configurations for validation of proposed equation

Type of structure	Multi-storey rigid jointed plane frames
No. of storey	G.F. to G + 11
Floor height	3.6 m
Base Dimension	18.0 × 18.0 m, 24.0 × 24.0 m, & 30.0 × 30.0 m
No. of Grids	3, 4, & 5 bays in either direction

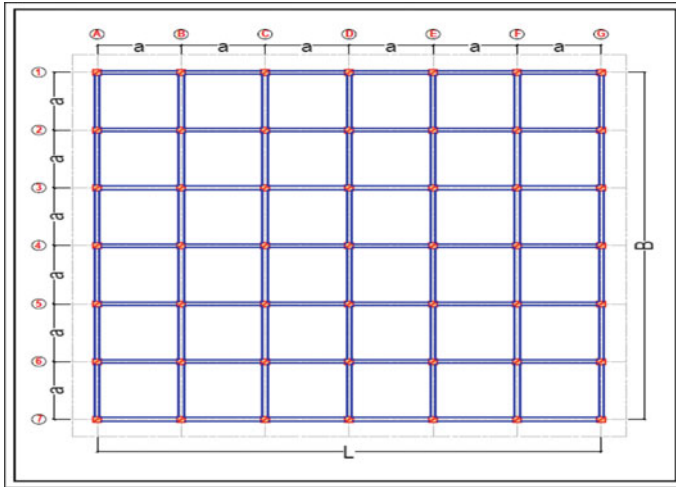


Fig. 1 An example of typical plan of building (6 × 6 grid)

exact value of structural response to earthquake excitation, the response contribution of all natural modes of vibration has been included, generally, first few modes are usually sufficient to derive accurate results.

4 Results and Discussion

4.1 Validation of STAAD Software Model

Table 5 depicts the various response quantities obtained using computer solution and as per the results mentioned in the datum example. It had been observed that fundamental natural period comes out to be 0.9662 s in software analysis against 0.97 s derived in the datum example.

Similarly, base shear is 1260 kN as per analysis performed by STAAD in comparison to 1320 kN calculated in the datum example. Similarly, values of the other responses are very close to each other. Hence, extensive analysis work carried out under the work can be used for deriving some conclusions.

Table 5 Comparison of response quantities obtained from analysis of software model validation

Response quantity	As per solved example	As per STAAD analysis	Percentage variation (%)
Time period (sec)	0.97	0.9662	-0.68
Base shear (kN)	1320.00	1260.00	-4.54
Spectral acceleration	1.402	1.408	0.43
<i>Reaction of floor beam</i>			
• Dead load (kN)	42.20	44.37	4.90
• Live load (kN)	37.50	37.66	4.27

4.2 Study of Different Parameters Affecting Time Period of Building

Considering the parameters mentioned in Tables 3 and 4, the dynamic analysis was performed to get the total 120 values of the fundamental time period as depicted in Tables 6, 7, 8 and 9. Table 6 shows the values with the variable parameters as the grid length, height of the building, number of the bay, and column sizes i.e., stiffness of the columns.

It can be observed, from the tables mentioned above that the values of the fundamental time period go on increasing as the column size reduces, i.e., by reducing the stiffness, the values of the time period increase.

Similarly, it can also be observed that by increasing the bay length, values of the time period also increases. Thus, the tabulated values show that the value of fundamental time period is not only the function of the height of the building. The parameters like the stiffness of the columns, plan area, the number of bays in either direction also affect the time period of the building.

Table 6 Fundamental period of vibration (s) for 4, 5, and 6 m grid length

Number of bays	Column size (mm)											
	1000 × 1000			750 × 750			600 × 600			500 × 500		
	Grid length (m)			Grid length (m)			Grid length (m)			Grid length (m)		
	4.00	5.00	6.00	4.00	5.00	6.00	4.00	5.00	6.00	4.00	5.00	6.00
3 × 6	4.46	5.10	5.92	4.78	5.40	6.23	5.33	5.93	6.75	6.04	6.65	7.48
4 × 6	4.09	4.82	5.71	4.31	5.05	5.96	4.75	5.49	6.42	5.38	6.15	7.11
5 × 6	3.91	4.69	5.60	4.07	4.87	5.82	4.45	5.28	6.26	5.04	5.91	6.93
6 × 6	3.80	4.61	5.54	3.93	4.77	5.75	4.28	5.15	6.16	4.84	5.77	6.83

Table 7 Fundamental period of vibration (s) for grid length 5 m

Column size (mm)	Height of building (m)					
	77.6	63.2	48.8	34.4	20.0	5.6
1000 × 1000	3.8	3.0	2.2	1.5	0.8	0.2
750 × 750	3.9	6.1	2.4	1.6	0.9	0.3
600 × 600	4.2	3.4	2.6	1.8	1.0	0.3
500 × 500	4.7	3.8	2.9	2.0	1.2	0.4

Table 8 Fundamental period of vibration (s) for grid length 6 m

Column size (mm)	Height of building (m)					
	77.6	63.2	48.8	34.4	20.0	5.6
1000 × 1000	4.6	3.6	2.7	1.8	0.9	0.2
750 × 750	4.7	3.8	2.9	2.0	1.1	0.2
600 × 600	5.1	4.1	3.1	2.2	1.2	0.3
500 × 500	5.6	4.5	3.5	2.4	1.4	0.4

Table 9 Fundamental period of vibration (s) for grid length 7 m

Column size (mm)	Height of building (m)					
	77.6	63.2	48.8	34.4	20.0	5.6
1000 × 1000	5.4	7.3	3.2	2.5	1.1	0.2
750 × 750	5.7	4.6	3.5	2.4	1.3	0.3
600 × 600	6.0	4.9	3.7	2.6	1.5	0.4
500 × 500	6.6	5.4	4.1	2.9	1.6	0.4

5 Proposed Equation

There has been done a multiple nonlinear regression analysis on the results obtained out of the dynamic analysis to incorporate the effects of parameters like stiffness of the columns, plan area, and number of bays in either direction. The five different equations of the time period were obtained by analysis.

Here, presenting the following expression as best fit equation to be proposed to allow the design engineers to use it for approximation of fundamental time period of vibration of moment resisting framed structures in a quick and accurate manner by considering the base dimension/plan area of the building, stiffness of structure, and number of bays in longitudinal and transverse direction into account with the height (*H*) of the building. The program SPSS v16 has been used to perform the regression analysis to derive the equation of the following form:

$$T = C_1 \cdot (N_b \cdot N_l)^{C_2} \cdot \left(\frac{A_c}{A_b}\right)^{C_3} H^{C_4} \tag{5}$$

where parameters $C_1, C_2, C_3,$ and $C_4 =$ the regression constants, $A_c =$ the area of column, $A_b =$ the total plan area of the building under consideration, N_b and $N_l =$ the number of bays in the transverse and longitudinal direction, respectively, and $H =$ the height of building.

The regression parameters (four in numbers) were obtained. The data values of the standard deviation of the residuals (σ) and r-squared (R^2) were estimated for each regression. Values of Table 10 indicate how well the regression equation fits the sample Rayleigh data.

R^2 is the residual sum of squares and d_f denotes for degree of freedom. The value of R^2 always lies between 0 and 1, with higher values indicating that the regression model fits the data better. In this study, a value of R^2 is found to be 0.733, 0.833, 0.815, and 0.945 for the different equations.

In presented work, the value of $R^2 = 0.945$ for Eq. (5) indicates that 94.5% of the variation in the dependent variable is explained by the regression model.

Consequently, Eq. (5) with parameters $C_1 = 0.005, C_2 = -0.061, C_3 = -0.55,$ and $C_4 = 1.049$ is to be proposed as the best fit equation from the all other developed equations for determining the approximate fundamental period of moment resisting frames, for the final form of the proposed equation is as follows:

$$T = 0.005 \cdot (N_b \cdot N_l)^{-0.061} \cdot \left(\frac{A_c}{A_b}\right)^{-0.55} H^{1.049} \tag{6}$$

A validation of regression model for above equation was made by performing dynamic analysis on another 108 building models. Here, presenting it with three-, four-, and five-bay building with column sizes 0.55×0.55 m, 0.45×0.45 m plotting the results in Figs. 2, 3 and 4. Results obtained out of the analysis are compared with the results obtained by dynamic analysis performed and the values derived from the period equation were proposed by Verderame et al. [8].

Table 10 Results of regression analysis using ANOVA

ANOVA		
Source	Sum of squares	d_f
Regression	19522.44701	4
Residual (σ)	452.2884999	616
Uncorrected total	19974.73551	620
Corrected total	8282.463489	619

Dependent variable: T

$$R^2 = 1 - (\text{Residual sum of squares}) / (\text{Corrected sum of squares}) = 0.945$$

Comparison of Time Period of building(3-bay, Column size 550 x 550 mm)

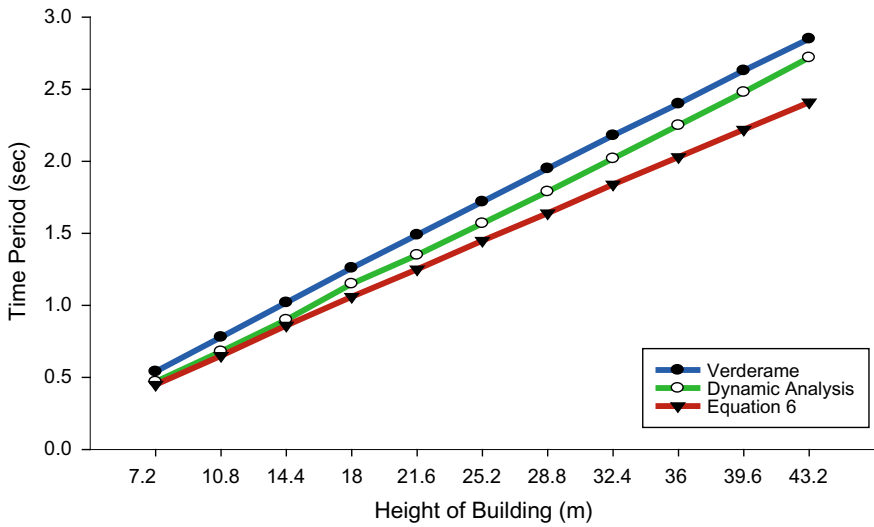


Fig. 2 Comparison of fundamental period of vibration T (three bays–column size 550 × 550 mm)

Comparison of Time Period of building (4-bay, Column size 450 x 450 mm)

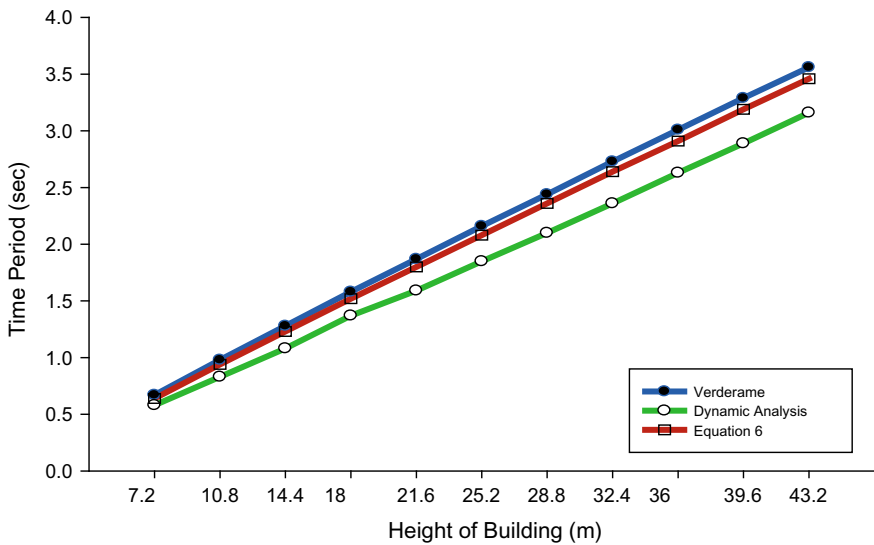


Fig. 3 Comparison of fundamental period of vibration T (four bays–column size 450 × 450 mm)

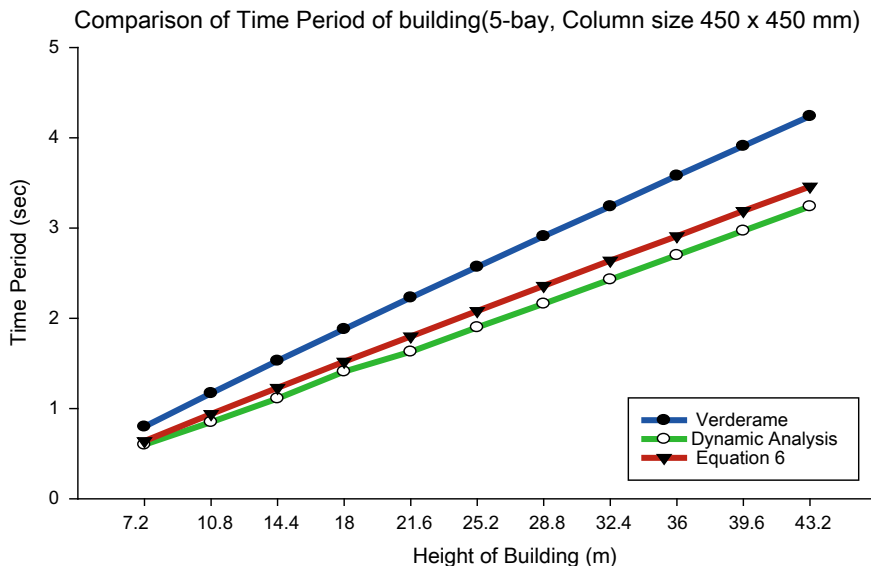


Fig. 4 Comparison of fundamental period of vibration T (five bays–column size 450 × 450 mm)

6 Conclusions

In the view of obtained results, It can be remarked that there are so many parameters which also affect the time period of vibration, out of which, the following parameters other than the height of the building were considered for the time period formula in the present work: (a) Plan area of the building, (b) Total cross-sectional area of the columns, and (c) Number of bays in longitudinal and transverse direction.

The paper provides a new formula for the natural time period of vibration of reinforced concrete moment resisting frame building. It can be observed from Figs. 2, 3 and 4 that the values of time periods from Eq. (6) are almost matching with the values derived by equation of Verderame et al. [8], having observed variation between 5% to 10%. It comes out to be 10–20%, while comparing with the values obtained from the dynamic analysis.

In many cases of the analysis, the values of the time period, obtained from the cited equation, differ on the higher side from the values obtained by the formula of Indian design code IS 1893, which results in base shear reduction and supports to make the economical structural design.

It can be concluded that the paper explores the scope of improvisation in expressions of time period of vibration given in seismic design codes and presents the study to show that the height alone, as a primary factor, seems inadequate to evaluate the time period of vibration precisely. Further, it suggests that the different structural parameters, also with respect to the parameters characterized in this

analysis, other than the height of the building should be incorporated in the simplified expressions of the time period of vibration used in seismic analysis, which can provide better assessment of time period and economy in the structural design.

References

1. Panzera F, Lombardo G, Muzzetta I (2013) Evaluation of building dynamic properties through in situ experimental techniques and 1D modeling: The example of Catania Italy. *Phys Chem Earth* 63:136–146
2. Shan J, Shi W, Wang J (2013) Regional study on structural dynamic property of buildings in China. *Earthq Eng Struct Dyn* 42:1013–1029
3. Oliveria CS, Navarro M (2010) Fundamental period of vibration of RC buildings in Portugal in-situ experimental and numerical techniques. *Bull Earthq Eng* 8:609–642
4. Sangamnerkar P, Dubey SK (2015) Effect of base width and stiffness of the structure on period of vibration of RC framed buildings in seismic analysis. *Open J Earthq Res* 4:65–73
5. Sangamnerkar P, Dubey SK (2017) Equations to evaluate fundamental period of vibration of buildings in seismic analysis. *Struct Monit Maint* 4(4):351–364
6. Indian standard Criteria for Earthquake resistant design of structures-Part-1, General Provisions and Buildings, IS 1893 (Part 1):2016, Bureau of Indian Standards, New Delhi
7. Amanat KM, Hoque E (2006) A rationale for determining the natural period of RC building frames having infill. *Eng Struct* 28:495–502
8. Verderame GM, Iervolino I, Manfredi G (2010) Elastic period of sub-standard reinforced concrete moment resisting frame buildings. *Bull Earthq Eng* (8):955–972
9. Nyarko MH, Morie D, Draganic H, Nyarko EK (2012) New direction based (Fundamental) periods of RC frames using genetic algorithms. In: 15th world conference on earthquake engineering. Lisboa
10. Dunand F, Bard PY, Chatelain JL, Guéguen P, Vassail T, Farsi MN (2002) Damping and frequency from random method applied to in situ measurements of ambient vibrations. Evidence for effective soil structure interaction. In: Proceedings of 12th European conference on earthquake engineering. paper 869
11. Espinoza F (1999) Determinación de las características dinámicas de estructuras. Universidad Politécnica de Catalunya, Tesis Doctoral
12. Gallipoli MR, Mucciarelli M, Vona M (2009) Empirical estimate of fundamental frequencies and damping for Italian buildings. *Earthq Eng Struct Dyn* 38:973–988
13. Kobayashi H, Midorikawa S, Tanzawa H, Matsubara M (1987) Development of portable measurement system for ambient vibration test of building. *J Struct Constr Eng* (Transactions of Architectural Institute of Japan) 378:48–56
14. Lagomarsino S (1993) Forecast models for damping and vibration periods of buildings. *J Wind Eng Ind Aerodyn* 48:221–239
15. Navarro M, Oliveira CS (2004) Evaluation of dynamic characteristics of reinforced concrete buildings in the City of Lisbon. In: Proceedings of 4th assembly of the Portuguese-Spanish of geodesy and geophysics. Figueira da Foz, Portugal
16. Oliveira CS (2004) Atualização das bases-de-dados sobre frequências próprias de estruturas de edifícios, pontes, viadutos e passagens de peões a partir de medicos expeditas in-situ. In: Proceedings of 5th Portuguese conference on earthquake engineering. University of Minho, Guimarães (in Portuguese)
17. Sanchez FJ, Navarro M, García JM, Enomoto T, Vidal F (2002) Evaluation of seismic effects on buildings structures using microtremor measurements and simulation response. *Struct Dyn Eurodyn* 2:1003–1008
18. Satake N, Suda K, Arakawa T, Sasaki A, Tamura Y (2003) Damping evaluation using full-scale data of buildings in Japan. *J Struct Eng ASCE* 129(4):470–477

Case Studies on Ground Improvement for Heavy Infrastructure on Soft Soil Using Basal Reinforcement



Vikalp Kamal, Minimol Korulla and P. S. Meenu

Abstract Design and construction of high embankment or structures on fine-grained and soft soil having poor shear strength parameters have always been a challenging task for engineers which is not only susceptible to higher settlements and shear failures but also in some cases liquefaction. Selection of a proper ground improvement method is the key for economical and sustainable development of any project. With the help of three case studies, this paper intends to present the measures adopted to overcome the complexity faced during the design and construction of such structures for different kinds of soils. This paper also emphasizes on the use of liquefaction hazard assessment and mapping for structures on soils susceptible to liquefaction which is not very much common in contemporary India and explains various measures that can be taken to mitigate it.

Keywords Basal reinforcement · Liquefaction · Gangapath expressway · Embankments · Soft soil · Piled embankment · Stone column

1 Introduction

The contemporary world of rapid infrastructure development has escalated the need of economic, sustainable, and eco-friendly solutions to unavoidable poor soil conditions with low bearing capacities, high consolidation settlement, liquefaction prone characteristics, and high compressibility that could result in failures either due to ultimate or serviceability limit state being reached. Unavoidable construction of embankments and higher structures on such soft soils has been a challenging task for both designers and construction engineers. The embankment on soft soil may fail due to various reasons such as (a) Failure of soft subsoil in shear (failure in bearing capacity) (b) Sliding of embankment fill and underlying soft subsoil (failure along a slip circle) (c) Excessive settlements and also lateral displacements

V. Kamal · M. Korulla (✉) · P. S. Meenu
Maccaferri Environmental Solutions Pvt. Ltd., Gurugram, India
e-mail: m.korulla@maccaferri.com

© Springer Nature Singapore Pte Ltd. 2020
A. Prashant et al. (eds.), *Advances in Computer Methods and Geomechanics*, Lecture Notes in Civil Engineering 56,
https://doi.org/10.1007/978-981-15-0890-5_57

(IRC 113). To safeguard against such failures, various ground improvement techniques such as: (a) Part or full replacement of soft subsoil with soil of better load bearing (b) Preloading and construction of the embankment in stages (c) Deep stabilization of subsoil using admixtures, such as use of lime columns (d) Use of Prefabricated Vertical Drains (PVD) with preloading (e) Use of stone columns to improve the bearing capacity of soft subsoil (f) Use of reinforcing elements, Metallic or Polymer, at the base level and above (g) combination of the above are used. However, conventional construction techniques such as preloading, stepwise construction or replacement are either uneconomic or have ecological restraints and would not provide a satisfactory engineering solution in the required time frame. This paper with the help of three case studies depicts the successful use of economical ground improvement techniques that can be utilized for such soil conditions based on different site conditions and their problems.

2 Mechanisms

2.1 *Soil Replacement (Full or Partial)*

This method involves excavation of weak soil layer and replacing with compacted sand or suitable soil fill; hence, providing a sturdier and less compressible foundation stratum. It is observed that replacement till the depth of 4.5 m is feasible in terms of cost and workability. Moreover, it is demonstrated that removal of 0.5 m to 2 m of soft soil results in the reduction of overall settlement by 27% to 60%, respectively, with respect to when this method is not used [1]. However, this method is not considered viable considering the cost implication and ecological restraints, hence is used in combination with other ground improvement methods for better and economical results.

2.2 *Prefabricated Vertical Drains*

Used in soft clays to accelerate the speed of primary consolidation by two mechanisms (a) By reducing the drainage path to about half of the PVD spacing. (b) Changing the direction of flow of pore water from vertical to horizontal as shown in Fig. 1a. The subsoil gains strength by dissipation of pore water pressure in excess. It is generally noticed that coefficient of hydraulic conductivity is more for horizontal direction due to anisotropic nature of the soil and hence, it reduces the time to achieve the required degree of consolidation from decades to a few months as shown in Fig. 1b. It should be noted that PVD is effective only in conjunction with other techniques such as surcharging, preloading, and staged construction. Moreover, it can be used only in soft soils and is generally terminated

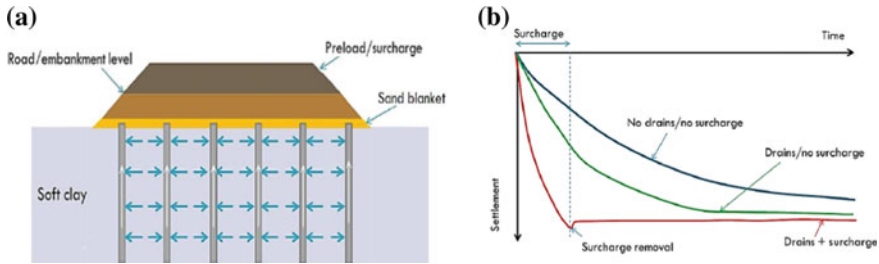


Fig. 1 a Preloading with vertical drain, b Time settlement curve with different conditions

in stronger materials with SPT Number > 7. The guidelines to the design of PVD are given in IS15284-Part 2 and is governed by the time allowed for consolidation. For axisymmetric flow in the unit cell, the average degree of consolidation is given by [2] as follows:

$$U = 1 - e^{\left(\frac{-8T_h}{\mu}\right)} \text{ for } T_h = \frac{c_h t}{D^2}$$

where $\mu = \frac{n^2}{n^2-1} \ln(n) - \frac{3n^2-1}{4n^2}$

$n =$ Drain spacing ratio = D/d

$c_h =$ Radial consolidation index

$T_h =$ Time factor

$D =$ Equivalent soil cylinder diameter influenced by each drain

$s =$ Drain spacing

$d =$ Equivalent diameter of prefabricated vertical drains (PVD)

2.3 Basal Reinforcement

Shear resistance is an important parameter while designing embankments on the soft soil. Inclusion of reinforcing material enhances the stability by mobilizing the tensile strength of the geosynthetics reinforcement and also increase the bearing capacity of the soil [3]. Moreover, the partial reduction in the differential settlement has also been observed due to improved distribution of stresses over the soft soil by implementation of basal reinforcement [4]. Jewell [5], depicted failure mechanism of the embankment in such soils as: (a) lateral sliding of embankment (b) Foundation extrusion or bearing capacity failures (c) Rotational stability failures as shown in Fig. 2. The desired grade of geosynthetics reinforcement required to safeguard from above described failure mechanism for embankment is computed by considering checks as depicted in IRC 113, 2013. It is to be noted that tensile

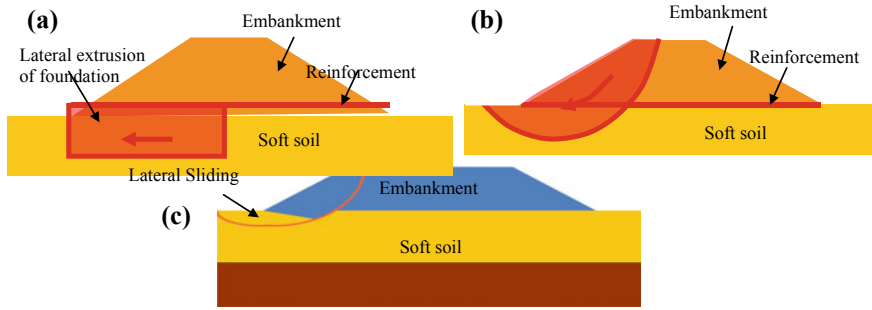


Fig. 2 Mechanism of failures in embankment on soft soil **a** foundation extrusion failure, **b** rotational stability failure, **c** lateral sliding failure

strength requirement for the reinforcement varies with time due to the improvement of shear strength properties of the soft soil during consolidation process. Moreover, the design life of the reinforcement may be considered to be the same as that required for 90% consolidation (IRC 113, 2013). While designing, it is important to ensure the maximum and allowable strains in reinforcement and to assess the desirable strain values because of the fact that smaller the strains greater will be the tensile loading requirement. It has been noted that variation of reinforcement strain from 3 to 6% results in 40% reduction in tensile loads [6]. These strains are also dependent on the type of fill soil.

2.4 Stone Columns with and Without Geosynthetics

Stone columns without geosynthetic reinforcement are usually utilized when ground improvement techniques stated above are not found viable in terms of either design perspective or feasibility. Ground improvement by stone column is usually preferred for soft soils with undrained shear strength range of 7 to 50 kPa. However, for sensitive clay and silt having sensitivity ≥ 4 , this particular technique is not preferred. Stone column not only increases the bearing capacity of the in situ material but also reduces the settlement by acting as a “giant PVD” to accelerating the process of consolidation [1]. These columns transmit loads prominently from the passive earth pressure developed from the bulging of the column and resistance to lateral deformation under superimposed loads [7] as shown in Fig. 3. It is to be noted that stone columns are generally used for embankment heights greater than 2.5 m to distribute more load on the stone column by the principle of soil arching [1].

Generally, the column bulging would be more at the top due to the confinement effect which would be less at the top as the overburden pressure would be less. Further, design guidelines for stone columns can be found in IS 15284-Part 1. However, the stone column has some limitations when it comes to using in soft soil as the interface of both is a mixed layer of clay and stones and prevents the effective

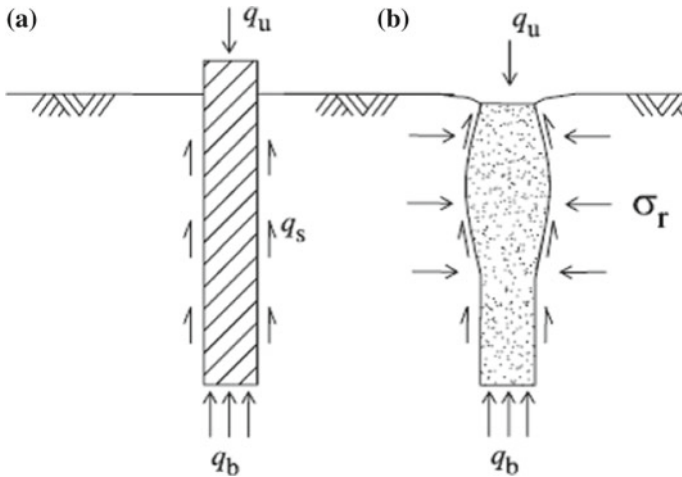


Fig. 3 Mechanism of load transfer **a** a rigid pile, **b** a stone column [8]

drainage because of clogging. The stones get into the surrounding soil because of lower confinement, hence, causing excessive settlement. This limitation can be overcome by encasing stone column with geosynthetics. This provides sufficient lateral restraint and prevents material from intermixing. The geosynthetic layer acts as a separation and filter media. However, for mobilization of ring-force, some radial extension is required to provide shear resistance at the interface which is usually in the range of 1–4% strain in ring direction [9]. Further, design guidelines for the geosynthetic encased stone column can be referred from EBGEO manual 2011.

2.5 Piled Embankment

A piled embankment consists of piles or vertical bearing element along with high-strength geosynthetics reinforcement either in top or close to the base of the embankment following a complex soil–structure interaction. The pile arrangement is generally in a square grid and is driven through unsuitable soil to firm-bearing stratum (see Fig. 4).

The vertical stresses from the embankment are more concentrated in the piles due to the higher stiffness of the pile with respect to the surrounding soil. Moreover, due to differential settlement between stiff pile and soft soil, soil arching is developed. These arches span the soft soil and load is transferred onto the piles and then the hard-bearing stratum [10]. Although the load transferring mechanism is not properly understood, several methods for estimating the magnitude of arching [5, 10–13] are known and used, but does not capture the key characteristics of soil–

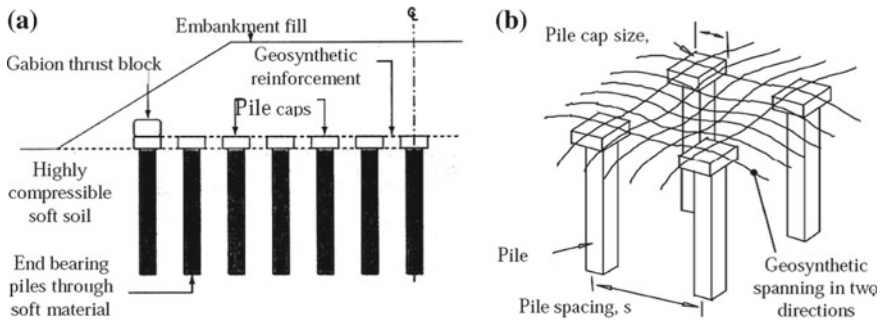


Fig. 4 a Section of a piled embankment, b general layout of reinforcement in piled embankment

structure interaction between them. However, from the literature [14], it was found that in conventional pile-supported embankments the area covered by pile caps is around 60–70% which can be reduced to 10–20% with insertion of basal reinforcement.

The full loading of the embankment, both vertical and horizontal should be supported by the pile group. It should also be ensured that no instability should occur in the operating area of the embankment, resulting in possible differential settlement at embankment’s crest. There are two mechanisms by which the loads are generated in the geosynthetics reinforcement in piled embankment. First, the loads from vertical embankment not supported by embankment arch are transferred to pile cap by the reinforcement. Second, it counteracts the horizontal thrust of the embankment fill which occurs across the width of the embankment only (see Fig. 5).

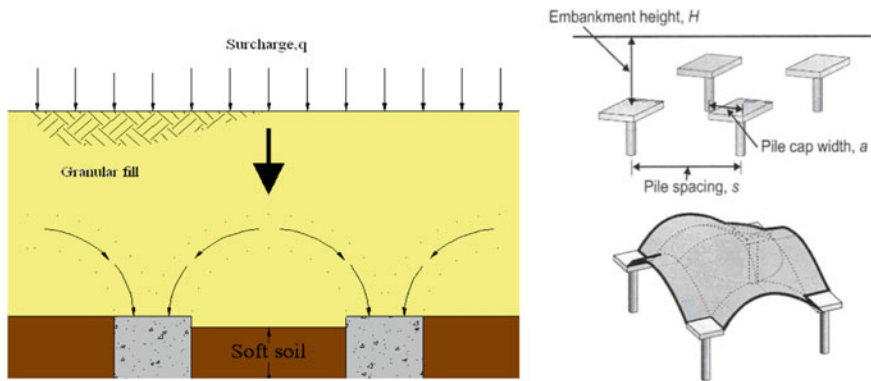


Fig. 5 Arching distribution within embankment fill

3 Case Studies

3.1 Road Over Bridge for Connectivity between Mundra and NH8A, Gujarat

3.1.1 Problem Description

Mundra Special Economic Zone, one of the largest SEZ in India is located in Kutch District of Gujarat state. A ROB was proposed over the railway line that cuts across the connecting road between Mundra and NH8A. The approaches of ROB were proposed to be retained by geosynthetic reinforced soil wall system. However, the in situ soil comprises sandy and clayey silt and found to have inadequate load-bearing capacity to bear the load of retaining wall. Moreover, the water table at the site location was high, and risk of higher settlements due to primary consolidation was a major concern. The preliminary design calculations revealed that the settlement did not fall under permissible limits and hence a ground improvement method resolving the issue of all the problems was required which is economical and sustainable.

3.1.2 Geotechnical Investigations

All the relevant geotechnical investigation to acquire the soil parameters for the further design of the structure was conducted at desired locations. It was found from various tests that the soil up to 3.0 m depth was clayey silt and followed by sand with silt up to 4.5 m depth. This is underlined by sandy silt with traces of clay till 9.0 m depth. Groundwater table was at 1.5 m depth. Moreover, oedometer tests were also conducted at various depths to compute the compression index for settlement calculations.

3.1.3 Solution

Considering the techno-commercial application foundation stratum, groundwater situation and higher consolidation settlements at the site, of all the ground improvement techniques, the stone column with basal reinforcement seemed like a preminent method that was adopted to mitigate all the problems stated above. The maximum wall height for this project was 8.8 m. It is to be noted that all the design checks for reinforced soil wall were conducted as per the guidelines specified in BS: 8006:1995. BS: 8006 advocates limit state principles for the design of reinforced soil wall, wherein, partial factors are applied to materials and loads, and adequate safety margins are ensured under various load combinations. As per the guidelines given in BS:8006, the design has been carried out for three load combinations, i.e., Load combination A, B, and C using partial load factors given in code. The seismic

Table 1 Stone column description

Wall height	8.8 m	8 m	7.2 m	6.4 m	5.2 m and below
Geosynthetics strength	200	200	200	200	200
Stone column diameter (m)	0.6	0.6	0.6	0.6	0.6
Stone column spacing	1.55	2	2	2.2	2.5

design is not covered in BS: 8006. Hence, the seismic design has been carried out based on the guidelines given in FHWA publication “Mechanically Stabilized Earth Walls and Reinforced Soil Slopes. Design & Construction Guidelines; Publication No. FHWA–NHI–00–043”, for load combination C, using pseudo-static Mononobe Okabe analysis. For seismic condition, the factor of safety for respective mode of failure is 75% of static condition as per the guidelines of FHWA.

For computation of base pressures at the foundation level of reinforced soil wall, Meyerhof stress theory as referred in BS:8006 was used. All the load cases were considered, and stresses were computed accordingly for the design of stone column. Further, the design of the stone column was done as per guidelines given in IS 15284 Part-1. The total bearing capacity and spacing of the stone column was computed. It is to be noted that the arrangement of the columns was considered triangular. Moreover, the columns were placed below the entire zone of south side of the ROB but due to better soil condition at the north side, the columns were provided only under reinforced soil wall. Geosynthetics was installed through-out the base of the structure and the surface of the column was covered with free-draining granular fill compacted with 95% of modified proctor density. Table 1 gives the details of strength of geosynthetics and stone column spacing and diameter (see Figs. 6 and 7).

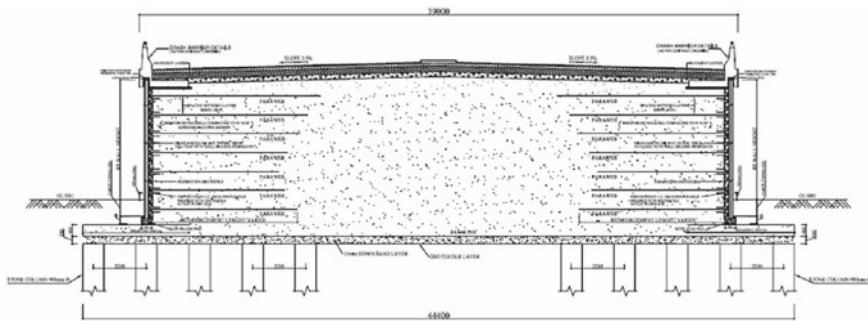


Fig. 6 Typical cross section of reinforced soil wall for high strength geogrid laying



Fig. 7 During construction **a** installation of stone column, **b** laying of high strength geogrid

3.2 *Basal Reinforcement for Gangapath Expressway from Digha to Didarganj*

3.2.1 Problem Description

Along southern bank of the river Ganga in the city of Patna, Bihar a 21.5 km expressway connecting Digha to Didarganj was proposed, of which 13.9 Kms consisted of high embankments of heights varying from 8 m to 15 m. The foundation soil for this mega-infrastructure was mainly, loosely packed sand and fine silt deposits of alluvial soil. This soil is prone to liquefaction when subjected to ground vibration, and it lies in high-risk seismic zone IV. Furthermore, the city is situated largely in the Ganga river basin, which is susceptible to floods due to heavy rains during monsoons season. Hence, there was a need to provide a high embankment which can act as flood control bund. Moreover, due to liquefaction, the ground beyond the toe can suffer lateral flow and loose shear strength resulting in the settlement of the embankment and progressive cracking of the top crest. Hence, stability of embankment in short term and settlement of ground in long term ensuring the protection against scour and slope erosion during floods has made the embankment construction more complex (see Fig. 8).

3.2.2 Geotechnical Parameters

Soil testing was conducted at strategic locations to acquire the information of foundation stratum and several bore log data obtained from the geotechnical investigation reveals that the project location has clayey silt at top layer followed by loose to medium dense silty sand at greater depths along the whole stretch as mentioned in Table 2.



Fig. 8 Initial site conditions

Table 2 Soil parameters at Ganga path

Bore log no.	Cohesion (kPa)	Angle of internal friction (Degree)	Bulk density (KN/m ³)	Depth range (m)
100	0–50	30–28	17.5–19	0–8.5
	0	32–33	19–20	8.5–25
108	0–35	0–32	18–19	0–13
	0–130	5–33	19–20	13–25
110	0–40	5–28	18	0–7
	0–150	5–33	19–20	7–25

3.2.3 Solution

To retain the embankment structure of 8–13 m along the expressway, basal reinforcement technique with a replacement of the top strata was finally adopted. Although, different ground improvement techniques like complete soft soil replacement, usage of PVD's, were discussed and reviewed for the design of embankment. Since the soil is made up of both silt and clay, PVDs may not work effectively and further PVDs require an additional surcharge to be placed while complete replacement of soft soil is not feasible due to large area improvement required, i.e., bottom width of embankment ranged from 70 to 130 m along the complete stretch.

At places where weak soil was found till 9 m depth combination of dynamic compaction, replacement, and basal reinforcement were adopted. Basal reinforcement was chosen considering its faster installation and construction easiness with no loss of stability, availability of wide range of strength 50 to 1300 KN/m. To further improve the strength of foundation soil, high strength geogrid as basal reinforcement at 0.2 m below ground level is adopted. The replacement was done in the range of 0.5 m to 3 m for different locations, where the soil is susceptible to liquefaction, additional ground improvement methods were suggested such as

provision of berms at the embankment’s toe, increasing berm width, densifying the subsoil using dynamic compaction or a combination. This brings the N value higher than the liquefiable limits thus controlling the extent of damage created by liquefaction.

Since the alignment of the expressway is running along the river Ganga, there is a possibility of erosion which necessitated the provision of suitable erosion control and bank protection systems. Hence, for protection of embankment a launching apron of length 20 m with 0.5 m thick gabion mattress and on slopes 0.23 m thick mattress (till HFL) or 0.17 m thick mattress (from HFL to berm level) was suggested. Further, for erosion control along the slope, biodegradable mat was proposed above the berm. Moreover, to control erosion of fines beneath the mattresses, recommendation of a geotextile filter/separator, was made.

3.3 Design of Basal Reinforcement

At Borehole no. 100, Two layers of High Strength Geogrid of Tensile strength of suitable strength has been proposed of length 20 m at the base of embankment for ground improvement with 2 m of soil replacement. All stability checks, i.e., rotational stability of an embankment, lateral sliding stability and bearing capacity checks were done as per equations (Eqs. 1–6) given in IRC 113 and the check for plastic squeezing of the foundation stratum has done as per IRC 75 (Clause no. 3.6.4). Live load (22.8 kPa) has considered as per IRC 6. Apart from this foundation extrusion checks were also calculated by using BS 8006-2010. The summary of the factor of safety achieved and targeted for various checks is shown in Table 3. The embankment stability was checked for both long and short term as the most critical condition for the stability is at the end of the construction, as the reinforcement has to function until the foundation soil gains sufficient strength to support. Also, strain consideration for the geosynthetics were considered as per IRC:113 & BS:8006. However, a proper assessment of desirable strain value is

Table 3 Summary of factor of safety

Height (m)	Applicable borehole no.	Check	Case	Water level at	FOS required	FOS achieved	Remark
9.5	BH 100	Rotational stability	Static	GL	1.4	1.535	Safe
			Static	HFL	1.4	1.762	Safe
			Seismic	GL	1.05	1.064	Safe
			Seismic	HFL	1.05	1.141	Safe
		Bearing capacity	–	–	1.5	1.61	Safe
		Lateral sliding	Static	–	1.5	1.88	Safe

required because of the fact that smaller the strains greater will be the tensile loading requirement. It has been noted that the variation of reinforcement strain from 3 to 6% results in 40% reduction in tensile loads [6]. These strains are also dependent on the type of fill soil.

Moreover, as the area lies under high seismic zone with loose-fine-grained soils, liquefaction can be triggered due to ground motion and vibrations; hence, liquefaction potential analysis was also done to check the susceptibility to liquefaction and necessary economic measures to mitigate it was proposed accordingly. "Simplified Procedure" methodology as described in [15] and IRC-75 is used to assess the liquefaction potential.

As per the simplified procedure, to compute the susceptibility of soil for liquefaction, two variables are required, namely, Cyclic Shear Stress (CSR) which is the seismic resistance of the soil layers and Mobilized shear resistance (CRR) is the capacity of the soil to resist liquefaction. Further, the soil is said to be liquefiable if the induced Cyclic Shear Stress (CSR) is more than mobilized shear resistance (CRR). Hence, if the ratio of CRR to CSR, termed as the factor of safety is greater than one, the soil is non-liquefiable. From the analysis done for the project it was observed that the top strata up to 3 m deep are liquefiable. Hence, the soil replacement of 0.5 to 3 m of the in situ soil or construction of overburden at toe on both sides of the embankment heights ranging from 0.5 to 6 m after closely analyzing the liquefaction potential. Moreover, if the above measures do not make the soil non-liquefiable, other improvement technique such as dynamic compaction is used.

Similarly, all stability checks were done for remaining boreholes also and all the factor of safety were achieved (see Fig. 9).

3.4 Basal Reinforcement in Construction of Piled Embankment for Italian High-Speed Railways

3.4.1 Problem Description

A high-speed railway line was proposed to connect the cities of Napoli and Milano. However, some part of this alignment falls over a soft soil stratum and as per clients specified the requirement for the rate of settlement should not exceed 0.05 m/10 years, and there was a potential concern over the localized differential settlement of the railway embankment while stratifying the construction time requirements. Moreover, the specified area was well-known for spring water, which further escalated the concern of influence of springs on the rate of settlement and subsequent performance of the railway embankment. In addition, the relevant piled embankments are located south of the city of Parma parallel to the A1 (Milano-Bologna) Motorway which curbed the right of way for the construction activity and design (see Fig. 10).

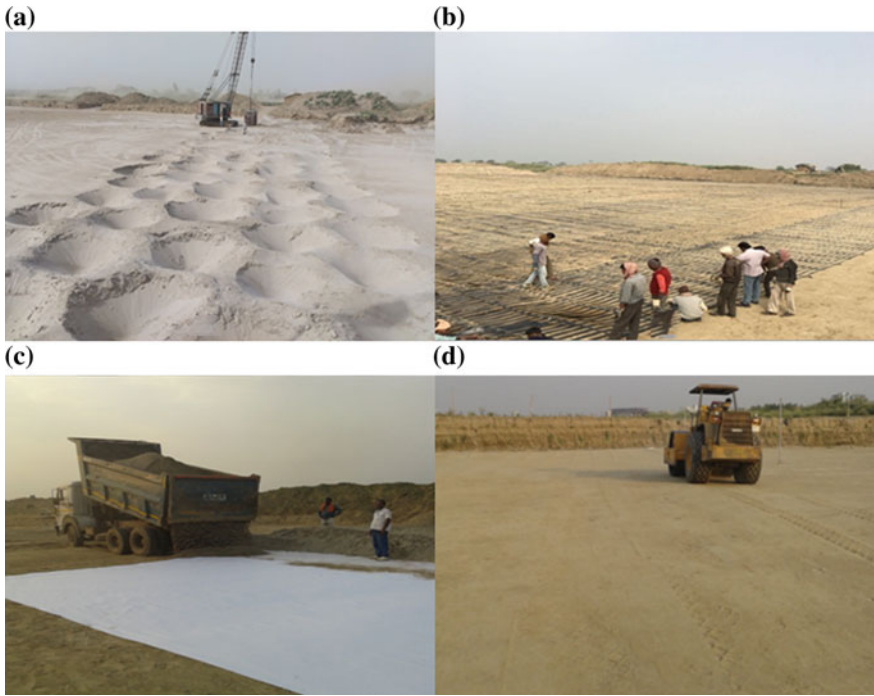


Fig. 9 a Dynamic compaction, b laying of high strength geogrid for basal reinforcement, c Laying of geotextile filter below replaced soil and dumping of soil over it, d Compaction using roller with replaced fill

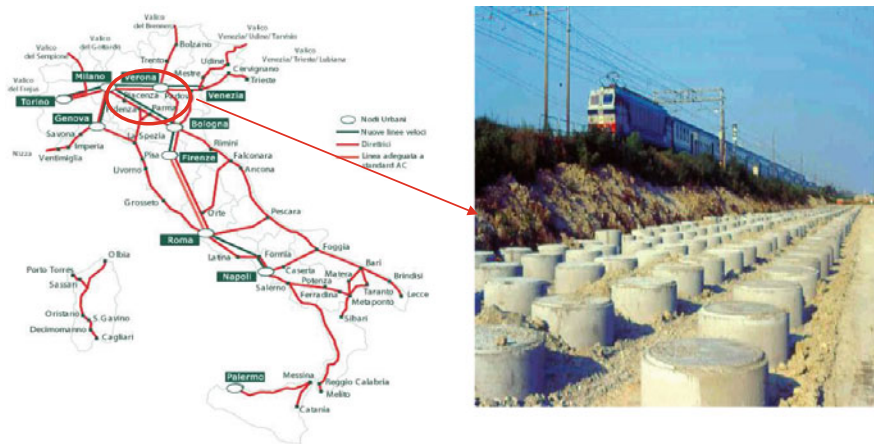


Fig. 10 Site location and high-speed railway lines in Italy

3.5 Solutions

All the traditional consolidation-based method to refrain from the settlement of the embankment were initially considered. However, none of the techniques offered superior technical and cost benefits considering the problems of total and differential settlement with a potential risk of the risen water table due to springs on soft soils. Hence, the choice of a nontraditional solution of the piled embankment was proposed. It is interesting to note that pile caps were not used instead the high tensile polyester geogrid was introduced with a thin layer of sand separating the geogrid and the pile top to uniformly distribute the stresses from the embankment and to further reduce the cost of the structure. A detailed site investigation involving both in situ and laboratory testing was performed and based on the soil parameters obtained the magnitude of the settlement was estimated using elastic techniques. Settlement of the proposed piled embankment was calculated using the consolidation model proposed by Broms [16]. The analysis indicated that the use of piles to support the embankment would reduce the rate of settlement over a 10-year period (3–13 years) by a one-third. The final solution, designed in accordance with BS 8006 [17], consisted of 0.5 m diameter continuous flight augured piles installed at 2 m *c/c* on a square grid. The pile length varied depending on the height of the embankment and the results of the settlement analysis.

A maximum short-term design strain of 4%, with a further 1% creep strain over the design life, was used in the calculation of the tension in the reinforcement. Depending on the height of the embankment, the strength of the reinforcement ranged from 900 to 1050 kN/m. Two layers of geogrid, one in the longitudinal and the second in the transverse direction were installed. In the longitudinal direction, the geogrid was layered resulting in no overlaps and a significant cost saving for the client. In the transverse direction, the geogrid was anchored using 0.5 m of gravel, around which the grid was rapped, to achieve the required anchorage length specified by the design method [17]. The design decision to avoid using pile caps had a significant influence on the required strength of the geogrid. The tensile strength of the geogrid reinforcement was calculated in accordance with BS8006 [17]. This project was the first large-scale use of piled embankment on high-speed railway applications in Italy (see Figs. 11 and 12).

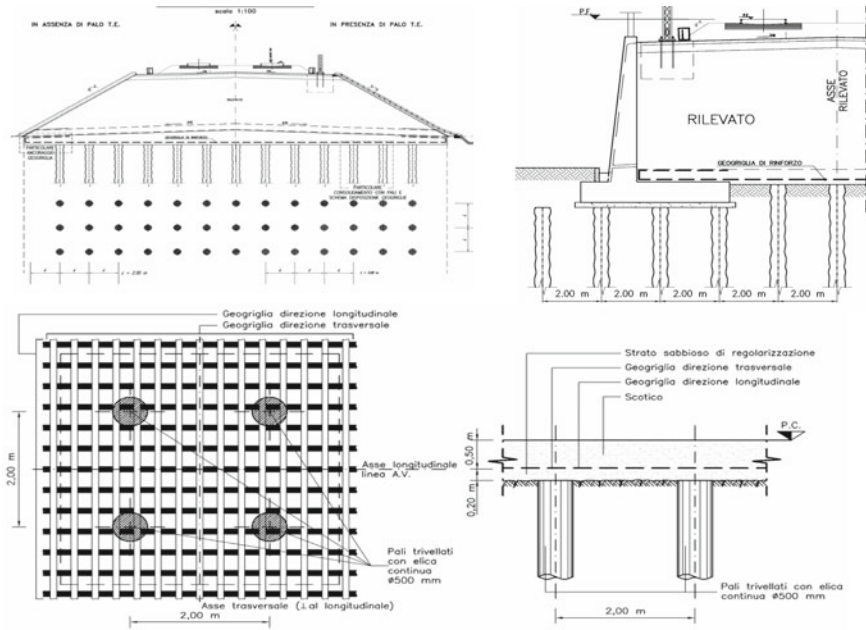


Fig. 11 Plan and cross-sectional details



Fig. 12 Installation of transverse and longitudinal geogrids

4 Conclusion

There are several techniques for improvement of ground improvement. However, the use of an appropriate method plays a vital role in the development and implementation of the project. While designing, an engineer should not only consider the technical aspect of the project but also the economic and ecological implication of the method used. In this paper, an effort was made to revisit various

ground improvement methods and by illustrating various case studies the solution adopted as per the ground situation and techno-commercial advantages was depicted. Moreover, it also emphasizes on the assessment of liquefaction potential that was made and the necessary counteracting measures adopted to diminish its effect such as replacement and removal of the soft soil, use of berm at the toe of the embankment, increasing the width of the berm, dynamic compaction, are depicted to play a major role, prior to the construction and during the service life of an embankment.

References

1. Tan YC (2016) Design and construction of road embankment on soft ground. Sabah Road Day, 5–6 April 2016
2. Hansbo S (1981) Consolidation of fine-grained soils by prefabricated drains. In: Paper 12/22: Proceedings of the 10th international conference on soil mechanics and foundation engineering, vol 3. Stockholm, Sweden, pp 677–682
3. Chu J, Bergado DT, Shin EC, Chai J (2012) Embankments on soft ground and ground improvement. In: GA 2012-5th Asian regional conference on geosynthetics: geosynthetics for sustainable adaptation to climate change, pp 3–24
4. Rowe RK, Li AL (2005) Geosynthetic reinforced embankments over soft foundations. *Geosynthetics Int* 12(1):50–84
5. Jewell RA (1988) The mechanics of reinforced embankments on soft soils. *Geotextiles Geomembranes* 7:237–273
6. Lawson CR (n.d.) Role of modelling in the development of design methods for basal reinforced piled embankments. Eurofuge 2012, Delft, The Netherlands
7. Malarvizhi SN, Ilamparuthi (2007) Comparative study on the behavior of encased stone column and conventional stone column. *Soils Found - Tokyo* 873–885
8. Hughes JMO, Withers NJ (1974) Reinforcing of soft cohesive soils with stone columns. *Ground Eng* 7(3):42–49
9. Alexiew D (2011) Embankments on soft soils, pp 1–16
10. Kempfert HG, Gobel C, Alexiew D, Heitz C (2004) German recommendations for soil reinforcement above pile-elements. In: EUROGeo3, Third Geosynthetic Conference, Munchen, vol 1, pp 279–283
11. Hewlett WJ, Randolph MF (1988) Analysis of piled embankments. *Ground Eng* 21(3):12–18
12. Russel D, Naughton PJ, Kempton GT (2003) A new design procedure for piled embankments. In: Proceeding of the 56th annual Canadian geotechnical conference, Winnipeg, September 29–October 1, Winnipeg, Canada, CD Rom
13. Terzaghi K (1943) *Theoretical soil mechanics*. Wiley, New York
14. Rutugandha G (2004) Geosynthetic reinforced pile supported embankments. Thesis presented to the graduate school of the University of Florida in partial fulfillment of the requirements for the degree of Master of engineering University of Florida, 2004. http://etd.fcla.edu/UF/UFE0004884/gangakhedkar_r.pdf
15. Seed HB, Idriss IM (1971) Simplified procedure for evaluating soil liquefaction potential. *J SMFE ASCE* 97(9):1249–1273
16. Broms BB (1987) Soil improvement methods in Southeast Asia for soft soils. In: Guest Lecture, Proc. 8th Asian regional conference on soil mechanics and foundation engineering, Kyoto, Japan, July, vol 2, pp 29–64
17. BS8006 (1995) Code of practice for strengthened/reinforced soils and other fills. British Standard Institution, London, pp 122–150

18. IRC:113 (1974) Recommended practice for treatment of embankment slopes for treatment of embankment. Indian Road Congress
19. IRC:75 (2015) Guideline for design of high embankment. Indian Road Congress
20. BS:8006-part 1 (2010) Code of practice for strengthened/reinforced soils and other fill. British Standards
21. IS:15284-part 1 (2003) Design and construction for ground improvement—guidelines part 1—stone columns
22. IS:15284-part 2 (2004) Design and construction for ground improvement—guidelines part 2—preconsolidation using vertical drains
23. Recommendations for design and analysis of earth structures using geosynthetic reinforcements—EBGEO, 2012, 2nd edn. pp 201–225

Effect of Fascia Gravity on the Design of Reinforced Soil Walls



Homit Singh Pal and Mohan Krishna Kolli

Abstract The gravity effect of fascia has been neglected in conventional design methods, which results in conservative designs. In this study, an attempt is made to study the effect of fascia gravity on the final design of reinforced soil wall. Along with the gravity effect, the difference in the design methods of flexible faced wall design and rigid faced wall design methods and their impact on the designs is also studied. In this study, it was found that gravity effect helps in reducing lengths of reinforcement by providing resistance in external stability.

Keywords Flexible fascia · Rigid fascia · Gabion fascia · Full height rigid fascia

1 Introduction

Reinforced soil retaining walls have been widely used in road embankments and retaining structures because of their benefits over conventional concrete retaining walls, such as flexibility, durability, aesthetics and cost-effectiveness. The conventional design of these reinforced soil walls is based on limit equilibrium methods, which involve internal stability, external stability and global stability analyses. Conventionally, fascia is provided to prevent local soil failures, erosion and for aesthetic purposes and does not affect neither behaviour nor the design of the wall.

Several fascia systems exist in practice such as wrap-around fascia, welded wire mesh fascia, segmental block fascia, precast concrete panels of partial height or full height fascia, gabion fascia and cast in situ concrete fascia. Fascia systems such as gabions can have impact on the design over other fascia because of its gravity component along with its greater widths. The gravity effect helps in increasing sliding and overturning stability by the additional weight component. This may result in the reduction of lengths of reinforcement in the final design. However,

H. Singh Pal · M. K. Kolli (✉)
Civil Engineering, Indian Institute of Technology Gandhinagar, Ahmedabad, India
e-mail: kolli.mohan@mtech2015.iitgn.ac.in

design codes such as BS 8006 [1], FHWA-NHI(2009) and IRC [2] guidelines for flexible faced wall design, neglect this aspect. As per Tatsuoka [3], Fascia not only helps as an additional gravity component but also can stabilize active mass behaviour of reinforced wall by its global stiffness and toe resistance. Considering the stability effects of fascia, Railway Technical Research Institute (RTRI) of Japan developed guidelines for full height rigid fascia walls which are being used in high-speed railway systems in Japan (Shinkansen). This method uses double-wedge method for the internal stability analysis with short planar reinforcements, while, conventional flexible wall design guidelines recommend higher lengths with single wedge (tie back/coherent gravity) method for internal stability analysis.

In view of the above, the difference in design methods considering gravity effect of fascia on the design of reinforced soil walls is taken up to study. In this study, different fascia systems with different widths are taken and their impact on the final design is studied based on two design methods, with and without considering the gravity effect of fascia.

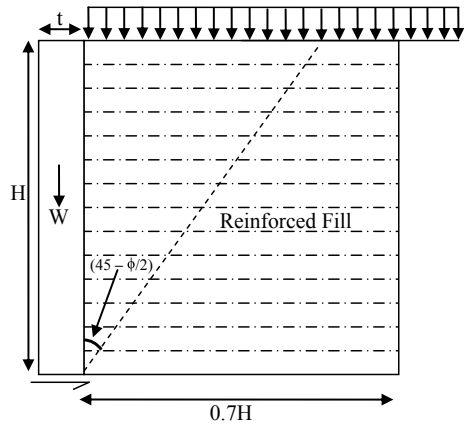
2 Conventional Design Considering Gravity of Fascia

Reinforced soil walls have been designed following the conventional design guidelines such as BS 8006 excluding the fascia gravity in the stability of structure. BS 8006 follows the limit state approach for the design of reinforced soil retaining walls. The minimum length of the reinforcement specified is 70% of the height of the retaining wall. The external stability and internal stability of the reinforced soil walls are considered for two ultimate state of load combinations, which consider specific load factors for different loads. The external stability includes check for the stability of structure against sliding, overturning and bearing capacity failure. Tie-back wedge method is used for accounting the pull out and tension failure of reinforcement. The interaction of the soil and the reinforcements are the primary load-bearing elements of the reinforced soil retaining walls and purpose of the fascia system is to provide aesthetic finish and local support to the reinforced fill. The fascia system is not considered to resist any superimposed load or earth pressure from the retained soil. The advantage of weight effect of fascia system is considered in the modified design for external stability, which allows providing lesser reinforcement length (Fig. 1).

3 Details of Study and Results

Reinforced soil walls of height 5 and 7 m are considered for the study. The length and spacing of reinforcement, backfill properties and the retaining soil properties are assumed same throughout the height of the retaining walls. A uniform surcharge of 25 kPa was considered for calculating forces. The internal friction angle (ϕ) of

Fig. 1 Tie back wedge method as per BS 8006.
 Source BS8006-1:2010



the reinforced fill is considered 30° , vertical spacing of reinforcement (S_v) is taken as 0.3 m and it is assumed that the reinforced soil wall is safe against bearing capacity failure. The design methods followed for the design are tie-back wedge method and double-wedge method. The length of reinforcement required for the safe design has been obtained for different cases, i.e. conventional BS code design and considering the contribution of the weight of fascia systems of different values of thickness along with current BS code design. The minimum strength of the geogrid reinforcement required for safe design is TGU 60 and TGU 80 for 5 m and 7 m wall, respectively (Table 1 and Figs. 2 and 3).

4 Rigid Fascia GRS-RW Using Double-Wedge Method as Per RTRI Guidelines

RTRI design standard includes the fascia system gravity effect in calculation of resistance forces against external forces and earth pressure of the retained ground. The geosynthetic reinforced soil structures have full height rigid facing with high

Table 1 Reinforcement length requirements for BS 8006 modified BS 8006 design for different fascia thickness

Height of wall (m)	Design	Reinforcement length for different fascia thickness for Gabion fascia		
		t = 0.25 m	t = 0.5 m	t = 1 m
5	BS 8006	0.85H	0.85H	0.85H
5	Modified design	0.75H	0.7H	0.6H
7	BS 8006	0.8H	0.8H	0.8H
7	Modified design	0.7H	0.65H	0.6H

Source BS8006-1:2010

Fig. 2 Reinforcement layout for fascia thickness less than 0.5 m

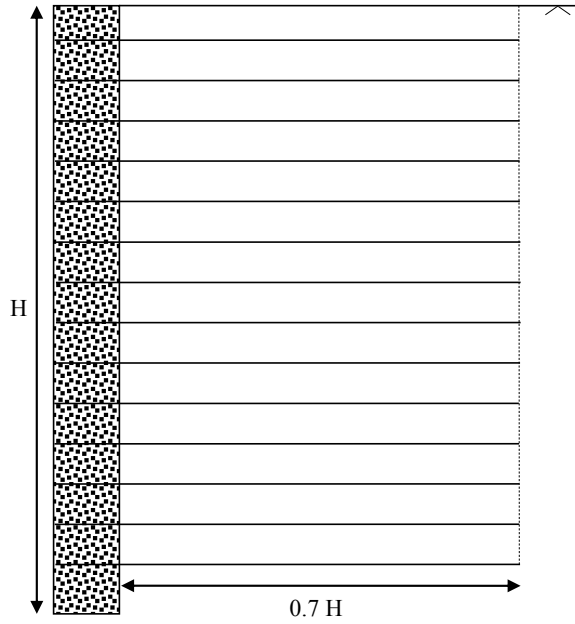
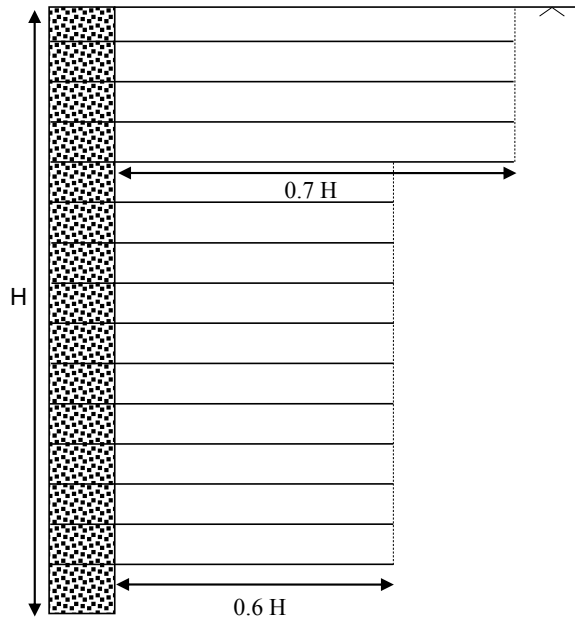


Fig. 3 Reinforcement layout for fascia thickness greater than 0.5 m



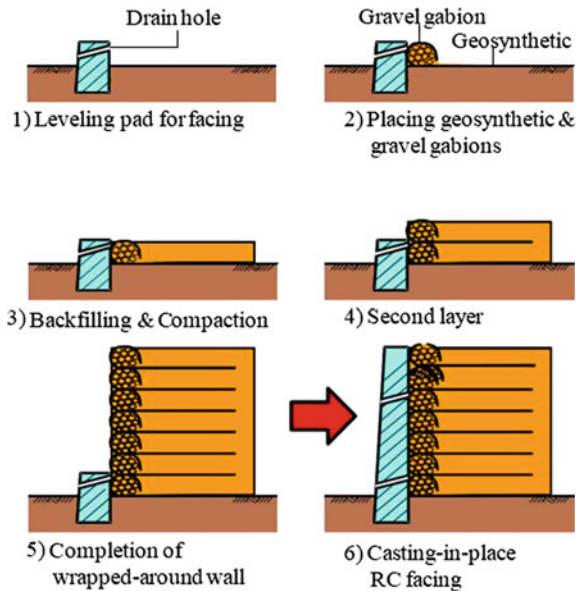
flexural rigidity. The geosynthetic reinforced backfill and the full height rigid facing are integrated together following the RRR (Reinforced Rail/Road with Rigid facing) construction technology which maintains the structural stiffness and the stability of the geosynthetic reinforced soil retaining walls. This connection of the rigid fascia to the reinforcements allows high earth pressure to act on the fascia which generates a confining pressure on the backfill. These reinforced soil walls have produced satisfactory results and are widely used for the high-speed Shinkansen train lines in Japan. A detailed examination of the overall stability of the reinforced soil walls and tensile or pullout failure along with adequate construction management is required for achieving greater strength and better deformation performance.

The full height rigid fascia is constructed by casting in place concrete between the temporary outer concrete frame and the wrapped around wall face after the major residual deformation of the backfill has taken place [4]. Steel bars of diameter 13 mm are anchored as shown in Fig. 5 in the backfill results in firm connection between the reinforced backfill and the fascia system. Geogrid made of poly vinyl alcohol which has high resistance against high alkali environment, is used as reinforcement as the geogrid comes in contact with the high alkaline fresh concrete (Fig. 4).

The design provisions of Geosynthetic Reinforced Structures as per the design standards for Railway Structures are as follows:

1. The minimum length of the reinforcements arranged throughout the height of the wall is maximum of 1.5 m and 35% of the height of the reinforced soil wall with a spacing of 300 mm, which is equal to the thickness of the compacted soil

Fig. 4 Staged construction of geosynthetic reinforced soil—retaining walls.
Source RTRI [5]



layers and for every 1.5 m height one reinforcement layer is extended up to the line drawn from the reinforcement embankment at an angle equal to internal friction angle as shown in Fig. 4.

2. The earth pressure forces are calculated using two-wedge stability analysis and the design response values for GRS retaining walls are calculated using an analysis and an action model relevant to the structure type and loading conditions.
3. The stability of the facing of reinforced backfill retaining walls is analysed by modelling the facing as continuous beam supported by a series of spring representing reinforcement layers subjected to earth pressure forces. The spring constant is taken as tensile force at 5% tensile strain obtained from the tensile tests of reinforcement.
4. The internal stability of the reinforced backfill and reinforcement layers is ensured by calculating the resistance against sliding and overturning. The external stability of the reinforced backfill retaining walls calculated using modified Fellenius method (Figs. 5 and 6 and Table 2).

Fig. 5 Double wedge method as per RTRI guidelines. *Source* RTRI [5]

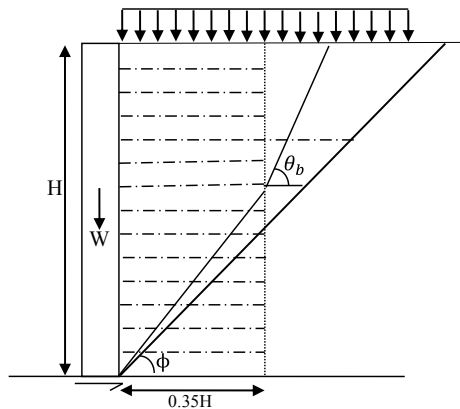


Fig. 6 GRS—RW with full height facing after staged construction. *Source* RTRI [5]

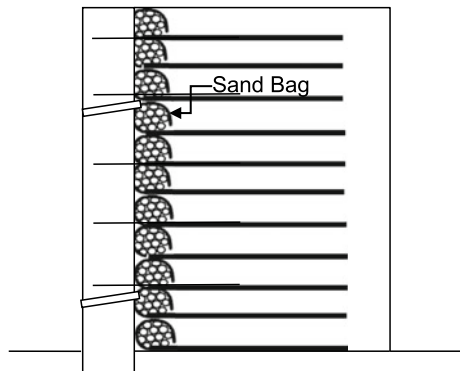


Table 2 Reinforcement length requirements for RTRI double wedge design

Height of wall (m)	Reinforcement length for 0.2 m thick panel fascia
5	0.55H
7	0.45H

Source RTRI [5]

5 Conclusions

In this paper, a comparative study of design of geosynthetic reinforced soil wall is carried out and the design philosophy of Geosynthetic Reinforced Soil Retaining walls following the RTRI guidelines is discussed.

The following key observations are made through this study:

1. The BS code design has been modified with the inclusion of fascia gravity effect for external stability and there is a reduction in length than that of the conventional reinforced soil wall design.
2. The reinforcement length for gabion fascia reinforced soil walls with thickness greater than 0.5 m can be provided with length less than that mentioned in the BS 8006, provided that the top layer reinforcement has sufficient pullout capacity. This can be achieved by increasing the reinforcement length of top layers, providing lower reinforcement length in bottom layers, and thus, also avoiding over safe design.
3. The fascia system is considered as structural component in RTRI design guidelines, where as BS 8006 considers the fascia system for aesthetic purpose only.
4. The design philosophy and the construction technique of reinforced soil walls with RTRI guidelines result in lesser reinforcement in comparison to BS 8006 and IRC guidelines. In addition to that, the staged construction approach of RTRI avoids the chances of fascia failure or differential settlement as the backfill gets completely compacted prior to the construction of the full height rigid fascia.

Acknowledgements We express our deep gratitude to Prof. G. V. Rao for his guidance and valuable suggestions for this work.

References

1. BS 8006-1:2010 Code of practice for strengthened/reinforced soils and other fills
2. IRC:SP:102 (2014) Guidelines for design and construction of reinforced soil walls, Indian Road Congress. FHWA-NHI-10-024 2009. In: Design and construction of mechanically stabilized earth wall and reinforced soil slopes—volume I. U.S. Department of Transportation Federal Highway Administration

3. Tatsuoka F (1992) Roles of facing rigidity in soil reinforcing, Keynote Lecture. In: Proceedings of International Symposium on Earth Reinforcing Practice (IS Kyushu'91), pp 831–870
4. Tatsuoka F, Tateyama M, Koseki J, Yonezawa T (2014) Geosynthetic-reinforced soil structures for railway in Japan. *Transp Infrastruct Geotechnol* 1(1):3–53
5. Railway Technical Research Institute, Japan (2012) Design standards for railway structures and commentary earth retaining structure

Geotechnical and Electrical Resistivity Properties of Gypsum Rich Sands



Raghava A. Bhamidipati and Michael E. Kalinski

Abstract Gypsum rich soils, mostly found in arid regions of the world are known to pose and number of geotechnical engineering hazards, the most common one being collapse settlement. In this research, the influence of gypsum content on the shear strength and collapsibility of reconstituted gypsum sands was studied. Reconstituted specimens of gypsum and sand were prepared with varying amounts of gypsum by weight. Direct shear strength tests and single collapse potential tests were conducted on the soils. The study showed that both the angle of internal friction and collapse potential of the soils increased with increase in gypsum content. The addition of water to the specimens brought about a visible amount of cohesion to the specimens, which were otherwise mostly cohesionless when dried. Next, electrical resistivity testing was conducted on the gypsum sand specimens using the four-electrode box resistivity setup. The influence of gypsum content and volumetric moisture content on five specimens was studied and it was seen that resistivity increased with decrease in moisture, but it did not vary significantly with gypsum content. Pore-water resistivity measurements were made to using a conductivity meter. It was seen that, the presence of gypsum had a marked effect on pore-water resistivity but gypsum content itself did not have a major influence on resistivity. The resistivity measurements normalized with pore-water resistivity were then plotted and it was found that soil with no gypsum had a markedly different profile than those of gypsum sands. Regression models were developed to predict the volumetric water content for gypsum and non-gypsum sands.

Keywords Gypsum · Sand · Collapse potential · Angle of internal friction · Electrical resistivity

R. A. Bhamidipati (✉)
Indian Institute of Technology Gandhinagar, Gandhinagar, India
e-mail: raghava.b@iitgn.ac.in

M. E. Kalinski
University of Kentucky, Lexington, KY, USA

© Springer Nature Singapore Pte Ltd. 2020
A. Prashant et al. (eds.), *Advances in Computer Methods and Geomechanics*, Lecture Notes in Civil Engineering 56,
https://doi.org/10.1007/978-981-15-0890-5_59

1 Introduction

Construction of structures on gypsiferous soils often proves to be very problematic due to collapse settlement. The damages and catastrophic failures of engineering structures built on gypsum soils have been documented in several parts of the world. Collapsible gypsum soils are generally good foundation material under dry conditions but undergo considerable settlement upon wetting. These soils are found in several parts of the world, mostly in the arid regions in the form of saline precipitates (evaporites) [1]. Middle Eastern countries like Iraq, southern Spain, Central Europe, and parts of western United States are some examples of places where gypsum soils are predominantly found. Several irrigation facilities and structures in Spain and Iraq have experienced significant settlement and deformation due to the presence of collapsible gypsum soils [2, 3]. Several dam sites across the world have been severely affected by gypsum karst.

The mineral gypsum is calcium sulfate-dihydrate ($\text{CaSO}_4 \cdot 2\text{H}_2\text{O}$) and it has a Mohs scale hardness of 1.5–2 [4]. It has a specific gravity of about 2.32 and a moderate solubility of about 2.5 g/l in water. These properties of gypsum lend certain unique features to gypsum rich soils. Many researchers in the Middle Eastern countries have studied the geotechnical properties of gypsum soils and the influence of the parameters on collapsibility [5]. Fattah et al. [6] studied the collapse settlement behavior of gypsum sands from Al-Tar region of Iraq using oedometer tests. For the double oedometer tests, they used three soil samples with gypsum contents of 14.8, 44, and 66%. From their testing, they found that the collapse potential of the soils increased with gypsum content [6].

Electrical resistivity profiling is a widely used noninvasive geophysical method for subsurface investigations. The basic principle involves introduction of a direct current or an alternating current into the ground and measuring the resulting potential difference between two points. Numerous factors dictate the electrical properties of earth materials, the most important ones being soil water content, mineralogy, and fraction of fines, grain size, salinity, pore fluid, bulk density, and temperature. Several researchers studied the relationships between soil properties and their geoelectrical characteristics. Archie [7] proposed an empirical method for correlating electrical resistivity of clay-free granular soils with pore-water resistivity and porosity. Kalinski and Kelly [8] estimated the volumetric water content of soils containing 20% clay. They also developed a circular four-probe resistivity cell as an alternative to the Miller soil box for laboratory measurements of soil resistivity. Guinea et al. [9] described how laboratory measurements, theoretical models, and field data could be used to identify commercial useful gypsum rock deposits in northeastern Spain.

For this research, the effect of gypsum content on the shear strength properties and collapse potential of gypsum sands were studied. Also, electrical resistivity technique was used as a possible alternative for characterization of gypsum sands

on a laboratory scale. The influence of gypsum content and moisture content on electrical resistivity was of interest. The following sections discuss the various testing schemes used and the results were observed.

2 Experimental Program

Reconstituted mixtures of ground gypsum and quartz sand (SP) were prepared with varying proportions of gypsum by weight. These mixtures were considered to be representative of gypsum soils occurring in arid regions. Figure 1 shows the grain-size distribution for the sand and gypsum used. Hydrometer analysis was not performed because of the soluble nature of gypsum. The gypsum content (GC%) of the mixtures varied from 0 to 100%. The samples were named M0, M10, and M20, etc., where M stood for “mix” and the number represented the GC%. To study the behavior of these soils, a set of geotechnical tests and electrical resistivity tests were performed. Table 1 shows the specific gravity of some of the specimens used for study. The geotechnical testing program consisted of direct shear testing and collapse potential testing. Electrical resistivity testing was performed to see if variation

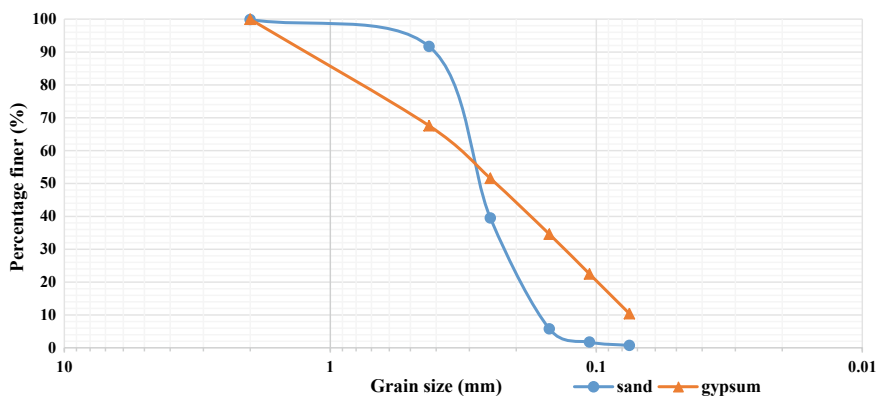


Fig. 1 Grain-size distribution of sand and gypsum used

Table 1 Specific gravity of some gypsum sand mixtures

Soil	Specific gravity
M0	2.63
M20	2.56
M50	2.46
M75	2.38
M100	2.33

in the soil parameters brought about any change in resistivity patterns. The following sections discuss each of these tests and their results.

2.1 Direct Shear Strength Testing

Since the soil used for the study was reconstituted gypsum sand specimens, direct shear testing was deemed suitable for studying the shear strength properties of the soils. Geocomp Shear Trac II equipment was used to perform the direct shear tests. The shear box had depth of 1.1 in. (2.79 cm) and a diameter of 2.5 in (6.35 cm). Gypsum sand mixtures were gently poured into the shear box using a funnel and gently tamped in such a way that the initial void ratio of all the specimens was kept close to 0.67. The direct shear machine was controlled using software named SHEAR. A deformation rate of 0.02 in/min was used. Soil samples were tested under a normal stress range of 15 psi (104 kPa) to 60 psi (414 kPa). Testing was performed under two conditions: (i) testing of dry specimens (ii) testing of wet specimens, 1 h after saturation. The latter was performed to see the possible effect of gypsum as a weak cement agent in terms of cohesion.

The peak shear stresses were plotted against normal. The drained friction angle (ϕ') and drained cohesion (c') for the specimens were calculated from the obtained Mohr–Coulomb failure envelopes. The Mohr–Coulomb failure envelopes are shown in Figs. 2 and 3.

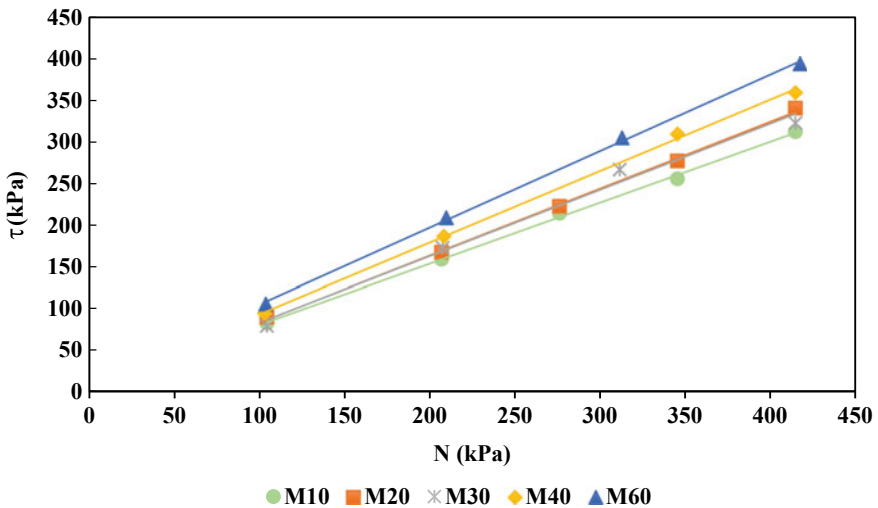


Fig. 2 Shear stress versus applied normal stress for dry specimens

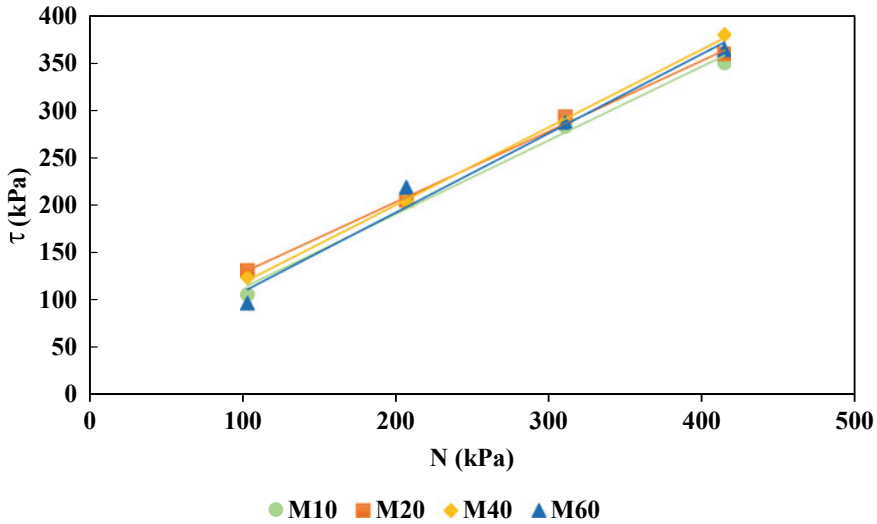


Fig. 3 Shear stress versus applied Normal stress for wet specimens

2.2 Collapse Potential Testing

The collapse settlement of sand was estimated based on a parameter called collapse potential (CP). In this study, CP was measured using the Single Collapse Test [10] in a one-dimensional consolidation load frame [11]. This method was chosen because only a single specimen was needed to perform the test as opposed to two specimens in the double oedometer tests.

Samples of gypsum sand were placed in the consolidation cell and the mass and volume of the sample were noted. This information was used to calculate the initial void ratio of the specimen. Dry gypsum sand mixtures were poured into the cell using a funnel. The specimens had a diameter of 6.35 cm and a height of 1.88 cm. All the specimens had a void ratio of about 0.62. Next, the consolidation cell was mounted in the load frame. The soil sample was then gradually loaded up to 200 kPa. At this point, the sample was inundated with water and left for 24 h. Loading was thereafter continued until a final load of 312 kPa was achieved and then the test was discontinued. The deformation of the sample in the 24-h time period (ΔH) is recorded. Collapse potential of the soil is defined as follows:

$$CP = \Delta H / H_0 = (\Delta e / 1 + e_0) * 100\% \tag{1}$$

where H_0 is the initial height of the sample, e_0 is the initial void ratio, and Δe is the change in void ratio of the specimen. Collapse potential is a measure of vertical strain which in practice would be multiplied by the thickness of a given layer of gypsum sand to estimate vertical settlement at the ground surface. Five different

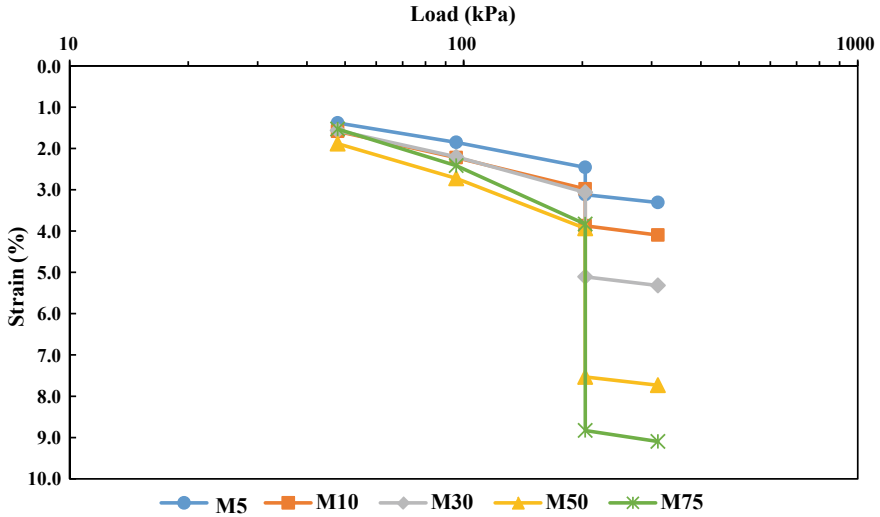


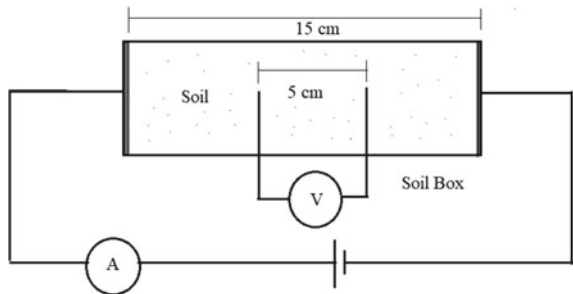
Fig. 4 Vertical strain versus normal stress for the tested specimens in the CP test

samples were tested with gypsum contents ranging from 5 to 75% and the vertical strain was plotted against applied load (Fig. 4).

2.3 Electrical Resistivity Testing

The testing method used in this research was the four-electrode soil box method. The test was based on the *Wenner electrode configuration* (Fig. 5). In this arrangement, four electrodes are placed in a straight line with equal spacing. Current from a steady DC source is applied across the ends of the box, which serve as the outer electrodes. The ensuing potential drop between the two inner electrodes is measured. Resistivity is calculated as K times the ratio of voltage by current, where K is the calibration constant of the box.

Fig. 5 Arrangement for soil resistivity testing



An acrylic rectangular box was used for performing the tests. The dimensions of the box were 15 cm × 6 cm × 6 cm. The separation between the electrodes was 5 cm. A steady DC power source from an Agilent E3620A power supply was used to maintain a steady current flow across the outer electrodes. It was set to supply 6 V DC. A schematic of the test setup is shown in Fig. 5. In this configuration, resistance (R) was calculated as V/I and resistivity of the soil (ρ) was calculated as:

$$\rho = K \cdot (R) \tag{2}$$

where K is the calibration constant of the box. Considering the box had a cross-sectional area (A) of 36 cm² and an electrode spacing (l) of 5 cm, K was determined to be 7.2.

Five samples of gypsum and sand mixtures, M0, M10, M20, M40, and M60 were tested. Tap water was added and mixed with each sample. The moist samples of soil were taken and filled in the box. They were lightly compacted to ensure uniform distribution across the box. The void ratio of all specimens was kept close to 0.6.

Electrical resistivity was measured and plotted against volumetric moisture content (θ). Measurements were taken at regular intervals and the mixtures were allowed to dry naturally. The change in the weight of the box was used to estimate the change in moisture content. Typically, after 3–4 days, when no further weight change was seen, the samples were dismantled and the final moisture content of the soils was found. The results of the tests are shown in Fig. 6.

The excess water initially collected on top of the samples was decanted and set for pore-water resistivity measurements. Pore-water resistivity was measured using an Extech 400 conductivity meter at 20 °C. The device can measure electrical

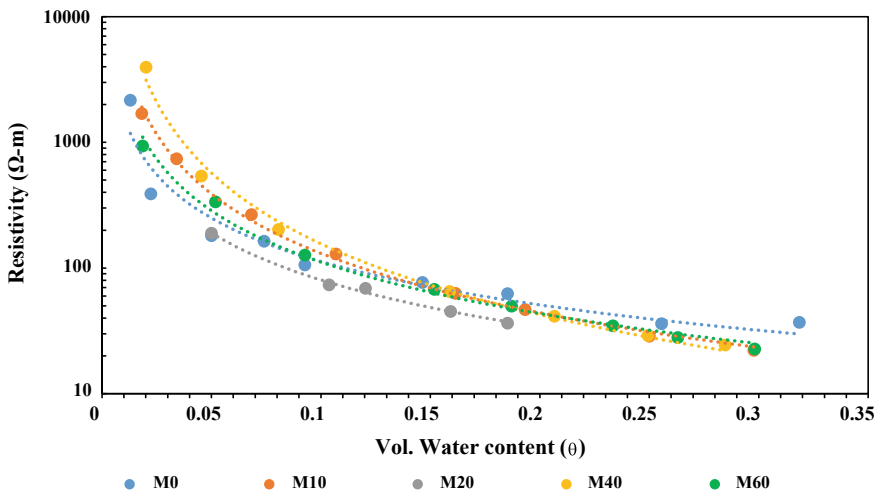


Fig. 6 Resistivity versus volumetric moisture content of the tested specimens

Table 2 Measured pore-water resistivity for the five samples tested

Soil Sample	Pore-water resistivity (Ωm)
M0	9.30
M10	2.85
M20	2.70
M40	3.32
M60	3.03

conductivity, salinity, and the total dissolved solids (TDS) in any solution. Table 2 shows the pore-water resistivity measurements obtained from the different soil samples.

Electrical resistivity of the five specimens was plotted against volumetric moisture content on a semi-log graph. It was found that for all the specimens, resistivity increased with decrease in moisture content. For the tested range of moisture content, the resistivity of the specimens varied between 20 and 3,000 Ωm . This range of observed resistivity values is typical for clays and sands [12]. The general relationship between resistivity and volumetric water content was akin to $y = a \cdot x^{-b}$, where “a” ranged from 0.4 to 1.3 and “b” ranged from 0.9 to 1.4.

The pore-water resistivity measurements of the five specimens is shown in Table 2. It was seen that the electrical resistivity of soil with no gypsum (M0), was measured as 9.3 Ωm . For the other samples, the pore-water resistivity was almost comparable and varied in the range of 2.7–3.3 Ωm . The measurements were taken at a temperature of 20 °C. The lower pore-water resistivity of gypsiferous samples can be attributed to the dissolution of gypsum. Saline solutions have a lower resistivity than tap water, due to the availability of calcium and sulfate ions.

To further utilize this aspect, the electrical resistivity values of the samples shown in Fig. 6 were normalized with their corresponding pore-water resistivity values shown in Table 2. Best fit power curves were used for all the specimens. The resulting values were plotted as shown in Fig. 7. It was found that the normalized resistivity curve for M0 plotted significantly lower than the resistivity curves of the other mixtures. In other words, the normalized resistivity values of gypsum-free soil were much different than that of gypsum soils.

3 Results and Discussion

The results of the different tests conducted are discussed in this section. The specific gravity tests showed a decreasing trend in G_s with increase in gypsum. This was expected because of the lower G_s of gypsum in comparison to sands and clays. From the direct shear strength testing of dry and wet gypsum sand mixtures, it was found that in both the cases, the drained angle of friction increased with increase in GC% (Fig. 8). In the case of dry specimens, the values ranged from 35.5° to 42.7°. The variation was less in the case of wet specimens (36.7–40.0°) (Fig. 8). Because

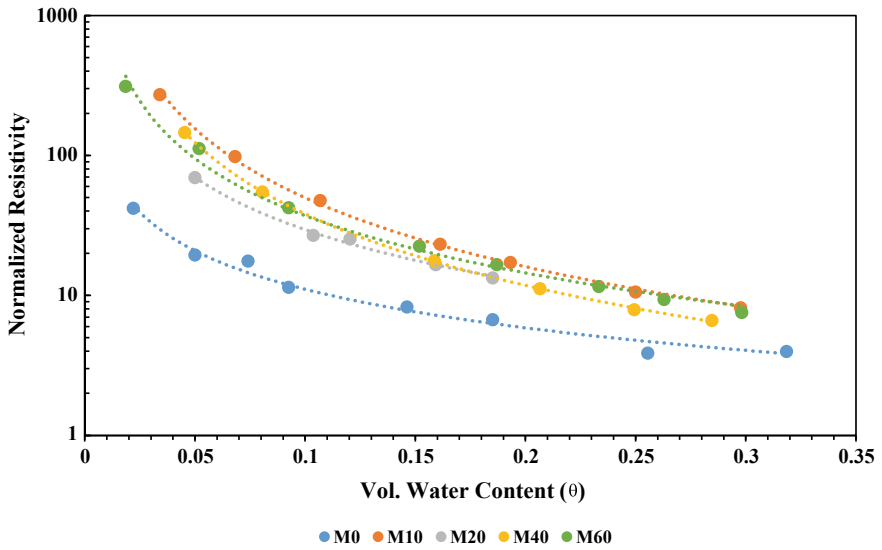


Fig. 7 Normalized resistivity versus volumetric moisture content of the tested specimens

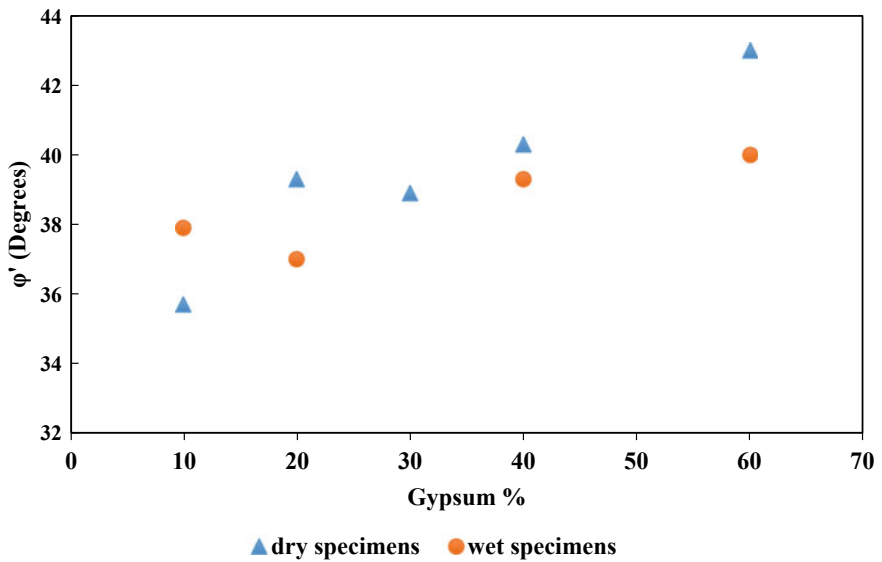


Fig. 8 Drained friction angle versus gypsum content for the tested specimens

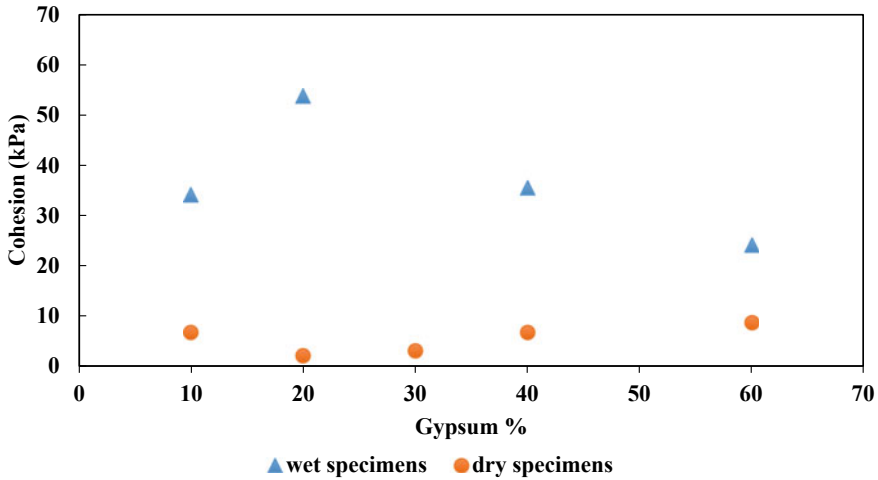


Fig. 9 Drained cohesion intercept versus gypsum content for the tested specimens

of the soft nature of gypsum, the applied normal force crushes the gypsum particles and pushes the specimen into denser configurations. This explains the increase in friction angle. Cohesion was very little for the dry specimens as expected, because of the granular nature of the materials being tested. The wet specimens, however, should have higher values of cohesion, due to the weak cementing action of gypsum coming into play upon wetting. This aspect is shown in Fig. 9. At around 20% GC, the gypsum particles occupy most of the void spaces between the sand particles and the developed weak cementing bonds were stronger. This shows in the slightly higher cohesion value of M20.

The collapse potential tests showed that collapse potential of gypsum sands increased linearly with increase in GC as shown in Fig. 10. This behavior is attributed to the softness and solubility of gypsum. Gypsum is softer than sand and has a higher solubility. Loading and addition of water causes the softer gypsum particles to undergo compression and dissolution, leading to collapse settlement. The trend is in agreement with the results of Fattah et al. [6], wherein, the hydrocollapse settlement of gypsum sands increase in gypsum content.

The electrical resistivity of both gypsum and non-gypsum sands increases with decrease in moisture content. When the resistivity values of the soils are normalized with pore-water resistivity, it was observed that gypsum-free sand had a much lower normalized resistivity than gypsiferous sands. The results from Fig. 7 can be used to develop generalized predictive equations for sandy soils with and without gypsum (Fig. 11). Using a best fit power curve for all the data points of M10, M20, M40, and M60, the following equation was developed with an R-squared value of 0.95:

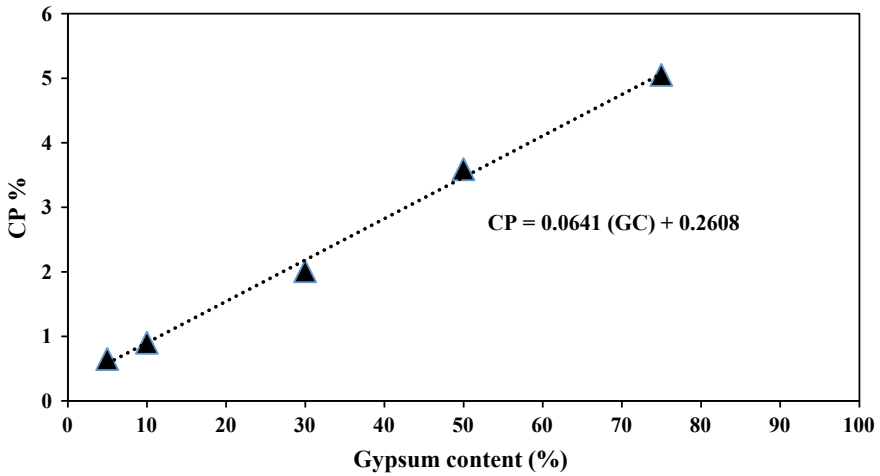


Fig. 10 Collapse potential versus gypsum content

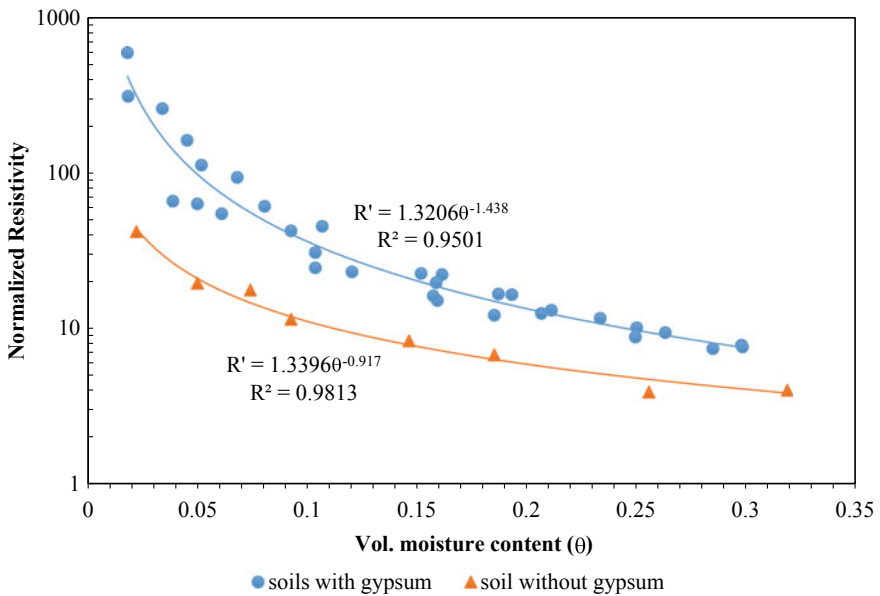


Fig. 11 Generalized resistivity versus volumetric moisture content trends for soils with and without gypsum

$$R' = 1.3206(\theta)^{-1.438} \quad (3)$$

The best fit curve for M0 yielded the following equation with an R-squared value of 0.98:

$$R' = 1.3396(\theta)^{-0.917} \quad (4)$$

Equations 3 and 4, can be used to estimate volumetric water content of potential gypsiferous soils as a function of normalized resistivity.

4 Interpretation of Electrical Resistivity Trends

When dry, both gypsum and quartz are very good insulators. In soils free of clay, any electrical conductivity is mainly due to pore water. This explains why electrical resistivity increases with decrease in volumetric water content. For gypsum sands, under wet conditions an increase in conductivity is brought about primarily due to the dissociation of Gypsum into Ca^{2+} and SO_4^{2-} ions and the availability of water. These liberated ions are partially dissolved in the water and partially adsorbed on the soil surface. Bolan et al. [13] suggested that soil surface acts as surface for adsorbent for Ca^{2+} and SO_4^{2-} ions liberated in the presence of water. Therefore, gypsum tends to dissolve more in saturated soil than in water.

Gypsum belongs to the class of sparingly soluble salts (solubility in water is 2.0–2.6 g/l) [14] gypsum concentrations. Beyond this amount, no further gypsum can be dissolved and addition of gypsum could only result in precipitation. This is why there is no change in resistivity trends beyond a certain concentration of gypsum in the soil. As seen in Fig. 11, the normalized resistivity of the non-gypsum specimen is much different from that of gypsum containing specimens. It is the dissolved gypsum that causes the change in resistivity in the gypsum containing sands.

5 Conclusion

Gypsum sands around the world cause major engineering and construction hazards; therefore, it is very essential to study their engineering properties. This paper discusses the results of some geotechnical and electrical resistivity tests performed on reconstituted gypsum soils. The tests showed that gypsum content is an important parameter dictating the engineering behavior of gypsum sands. Both the internal friction angle and collapse potential of sands increases with increase in gypsum content. Gypsum acts as a weak cementing agent and this can be seen from the slight increase in cohesion values obtained from testing of wet gypsum sands.

Geophysical methods such as electrical resistivity testing can be applied as alternatives to study soils containing gypsum. The presence of gypsum in sandy soils brings about a marked change in the electrical resistivity measurements of the soils. However, the percentage of gypsum itself is not a significant factor in influencing the resistivity patterns. This is because of the low solubility of the mineral gypsum. Based on the observed normalized resistivity values, using Fig. 11, a judgement can be made as to the whether the soil is gypsiferous or non-gypsiferous. The results from this study can be used for preliminary site characterization studies in places where engineering properties of gypsum soils might be of concern. The in situ moisture content of collapsible soils is one of the major factors affecting collapsibility. Using Eqs. 3 and 4, the in situ moisture content of the subsurface soil can be estimated.

References

1. Bell FG (2007) *Engineering Geology*. Butterworth-Heinemann, Burlington
2. Alphen JV, Romero FDR (1971) *Gypsiferous soils: notes on their characteristics and management*. Wageningen, International Institute for Land Reclamation and Improvement
3. Al-Saoudi NK, Al-Khafaji AN, Al-Mosawi, MJ (2013) Challenging problems of gypseous soils in Iraq. In: *Proceedings of the 18th international conference of soil mechanics and geotechnical engineering*, pp 479–492
4. Cooper A, Calow R (1998) *Avoiding gypsum geohazards: guidance for planning and construction*. British Geol Soc, Nottingham
5. Seleam S (2006) Evaluation of collapsibility of gypseous soils in Iraq. *J Eng* 13(3):712–726
6. Fattah MY, Yousif J, Huda N (2008) Long-term deformation of some gypseous soils. *Eng Technol J Iraq*, 1461–1483
7. Archie GE (1942) The Electrical Resistivity log as an aid in determining some reservoir characteristics. *Petroleum Trans AIME* 54–62
8. Kalinski RJ, Kelly WE (1993) Estimating the water content of soils from electrical resistivity. *Geotech Testing J* 323–329
9. Guinea A, Playa E, Riveroi L, Himi M, Bosch R (2010) Geoelectrical classification of gypsum rocks. *Surv Geophys* 31:557–580
10. Knight K (1963) The Origin and occurrence of collapsing soils. In: *Proceedings of the 3rd regional conference of africa on soil mechanics and foundation engineering*, vol 1, pp 127–130
11. Al-Rawas AA (2000) State-of-the-art review of collapsible soils. *Science and Technology, Special Review*, pp 115–135
12. Samouelian A, Cousins I, Tabbagh A, Bruand A, Richard G (2005) Electrical resistivity survey in soil science. *Soil Tillage Res* 173–193
13. Bolan NS, Syers JK, Summers ME (1991) Dissolution of various sources of gypsum in aqueous solutions and in soil. *J Sci Food and Agricult* 527–541
14. Adiku S, Renger M, Roth C (1992) A simple model for extrapolating the electrical conductivity data of gypsum containing soils from reference soil extract data. *Agric Water Manag* 21:235–246